Developing a Holonomic iROV as a Tool for Kelp Bed Mapping

Williamson, Benjamin

Award date:
2013

Awarding institution:
University of Bath

Developing a holonomic iROV as a tool for kelp bed mapping

Benjamin Williamson

A thesis submitted for the degree of Doctor of Philosophy

University of Bath

Department of Electronic and Electrical Engineering

July 2013

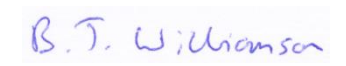

.....

Developing a holonomic iROV as a tool for kelp bed mapping

How can the data from multiple complementary sensors be fused to improve the mapping capability of a holonomic, intelligent, underwater vehicle in the nearshore environment?

Abstract

Kelp beds support a vast and diverse ecosystem including marine mammals, fish, invertebrates, other algae and epibiota, yet these kelp beds can be highly ephemeral. Mapping the density and distribution of kelp beds, and assessing change over yearly cycles, are important objectives for coastal oceanography. However, nearshore habitat mapping is challenging, affected by dynamic currents, tides, shallow depths, frequent non-uniform obstacles and often turbid water. Noisy and often incomplete sensor data compound a lack of landmarks available for navigation.

The intelligent, position-aware holonomic ROV (iROV) *SeaBiscuit* was designed specifically for this nearshore habitat mapping application and represents a novel synthesis of techniques and innovative solutions to nearshore habitat mapping. The concept of an iROV combines the benefits of autonomous underwater navigation and mapping while maintaining the flexibility and security of remote high-level control and supervision required for operation in hostile, complex underwater environments. An onboard battery provides an energy buffer for high-powered thrust and security of energy supply. Onboard low-level autonomy provides robust autopilot features, including station-keeping or course-holding in a flow, allowing the operator to direct the survey and supervise mapping data in realtime during acquisition.

With the aim of providing high-usability maps on a budget feasible for small-scale field research groups, *SeaBiscuit* fuses the data from an orthogonal arrangement of a forward-facing multibeam sonar and a complementary 360° scanning sonar with a full navigation suite to explore and map the nearshore environment.

Sensor fusion, coupled with the holonomic propulsion system, also allows optimal use of the information available from the limited budget sensor suite. Robust and reliable localisation is achieved even with noisy and incomplete sensor data using a relatively basic Inertial Navigation System and sonar-aided SLAM in the absence of an expensive Doppler velocity log or baseline navigation system. Holonomic motion in the horizontal plane and an axisymmetric hull provide the manoeuvrability required to operate in this complex environment, while allowing 3D maps to be generated in-transit.

The navigation algorithms were tested mapping a piling dock and the habitat mapping sensors calibrated using an ‘artificial’ kelp bed of manually dimensioned kelp stipes transplanted to a sheltered but open-water real-world environment. Sea trials demonstrated mapping open ocean kelp beds, identifying clusters of stipes, converting this into a useful measure of biomass and generating a density surface across the kelp bed. This research provides field-proven techniques to improve the nearshore habitat mapping capabilities of underwater vehicles. Future work includes the transition to full-scale kelp bed mapping, and further development of the vehicle and sensor fusion algorithms to improve nearshore navigation.

Acknowledgements

Dr Martin Balchin and Dr William Megill for their guidance and supervision throughout this research.

The Earthwatch Institute, the Engineering Sciences and Physical Research Council (EPSRC) and the University of Bath for continuing to fund this research and the field operations.

All of the companies and organisations who have assisted with funding this research and the underwater vehicles through sponsorship, including: BMT-DSL, Bulgin, Clipper Cargo, EPSRC, Hydro Products, Imagenex, Jem Divers, Maxon Motor, MCMC, SEA, SEACON Europe, The Royal Academy of Engineering, The Royal Society, The University of Bath, Vobster Diving, Weir, Woodland Global, Xsens and the sponsors and organisers of SAUC-E 2008 and SAUC-E 2009.

The 2008, 2009, 2010 and 2011 Bath University Racing Submarine Teams (BURST) for their support with the design, build, construction and testing of the vehicles produced.

Stephen Dolan the Ocean Technologies workshop technician and the Mechanical Engineering Instrumentation Section for their support in the production of the vehicles together with all colleagues and staff at the University of Bath who have offered advice and assistance over the course of this research.

The 2008, 2009, 2010 and 2011 Earthwatch volunteers and crew, the staff and students of the University of Bath, the University of Victoria and the University of Redlands, Hugh Clarke, Patricia Moseley and Laura Williamson for their assistance with the field trials of *Hawthorne 2.0*, *Hawthorne 2.1* and *SeaBiscuit*.

Finally, I gratefully acknowledge the support of my family, thank you.

Table of Contents

List of Figures

List of Tables

List of Abbreviations

2D	2 Dimensional
3D	3 Dimensional
ADC	Analogue to Digital Converter
ADCP	Acoustic Doppler Current Profiler
ADV	Acoustic Doppler Velocimeter
AHRS	Attitude and Heading Reference System
ASCII	American Standard Code for Information Interchange
AUV	Autonomous Underwater Vehicle
BC	British Columbia
BURST	Bath University Racing Submarine Team
C-EKF	Compressed Extended Kalman Filter
CEP	Circular Error Probability
CERF	Coastal Ecosystems Research Foundation
COB	Centre of Buoyancy
COM	Centre of Mass
CSA	Cross Sectional Area
DAQ	Data Acquisition
DoF	Degree of Freedom
DS	Dempster Shafer
DSTL	Defence Science and Technology Laboratory
DVL	Doppler Velocity Log
EGNOS	European Geostationary Navigation Overlay Service
EKF	Extended Kalman Filter
FIL	Filled Array
FIR	Finite Impulse Response
FOG	Fibre Optic Gyroscope
GIB	GPS Intelligent Buoy
GIS	Geographic Information System
GL	Grid Localisation
GPS	Global Positioning System
GUI	Graphical User Interface
HAL	Hardware Abstraction Layer
HDOP	Horizontal Dilution of Precision
HDPE	High Density Polyethylene
IMAQ	Image Acquisition
IMU	Inertial Measurement Unit
INS	Inertial Navigation System
IP	Ingress Protection
IR	Infra-Red
iROV	Intelligent (position-aware) Remotely Operated Vehicle
JCCB	Joint-Compatibility Branch and Bound
KF	Kalman Filter
LAN	Local Area Network
LBL	Long Base Line
LED	Light Emitting Diode
LiPo	Lithium Polymer
LM	Landmark
MC	Monte Carlo
MCL	Monte Carlo Localisation
MDI	Medium Dependent Interface
MDIX	Medium Dependent Interface Crossover
MEMS	Microelectromechanical systems
MHT	Multi-Hypothesis Tracking
ML	Maximum Likelihood
MOSFET	Metal Oxide Semiconductor Field Effect Transistor
NI	National Instruments
NLML	Negative Logarithm of the Matching Likelihood
NMEA	National Marine Electronics Association
NN	Nearest Neighbour
NOF	Not Filled Array
OGM	Occupancy Grid Maps
PC	Personal Computer
PDF	Probability Density Function
PDS	Power Distribution System
PID	Proportional Integral Derivative

PVC	Polyvinyl Chloride
RAM	Random Access Memory
RF	Radio Frequency
RIB	Rigid Inflatable Boat
ROI	Region Of Interest
ROV	Remotely Operated Vehicle
SAUC-E	Student Autonomous Underwater Challenge - Europe
SAUV	Solar-powered Autonomous Underwater Vehicle
SBL	Short Base Line
SCUBA	Self-Contained Underwater Breathing Apparatus
SEIF	Sparse Extended Information Filter
SFF	Small Form Factor
SLA	Sealed Lead Acid
SLAM	Simultaneous Localisation and Mapping
SMC	Sliding Mode Controller
SNR	Signal to Noise Ratio
SONAR	Sound Navigation and Ranging
SSD	Solid-State Drive
SUBMAR	Smart Underwater Ball for Measurement and Actuating Routines
T/F	True/False
USB	Universal Serial Bus
USBL	Ultra Short Base Line
VHF	Very High Frequency
WAAS	Wide Area Augmentation System
WCS	World Coordinate System
XKF-3	Xsens Kalman Filter for 3 Degrees of Freedom

Chapter 1 Introduction

This thesis describes the design, development, field trials and deployment of an underwater vehicle designed to map kelp beds in the challenging nearshore underwater environment.

1.1 Motivation

Kelp beds are the base for a diverse and highly productive ecosystem, yet they are highly ephemeral with very localised variation. Many studies focus on the ecology of these kelp beds, including marine mammals, fish and invertebrates [1-3]. These studies require an estimate of the density and distribution of kelp, and yet techniques to provide these maps have significant opportunities for development.

Kelp stipes are anchored on a rocky substrate in shallow tidal areas. A buoyant pneumatocyst and air filled stipe support a surface canopy. Stipes typically wind around each other to form clusters spread out in great underwater kelp beds. Challenges of kelp bed mapping include high currents, fast flowing tides and shallow water which cause large movements of stipes together with a high risk of entanglement in or damage to the kelp. The stipes and rocky seabed present frequent non-uniform obstacles and navigational landmarks are sparse.

The research aim was to develop a tool capable of detailed mapping of kelp beds from the midwater with a resolution of individual stipes.

1.2 Context

Existing techniques to map the nearshore compromise detail and coverage. Airborne sensing maps only the kelp canopy [4, 5], which is susceptible to damage from storms, boats and marine mammals and stipe density must be inferred with a high uncertainty and low resolution [6]. Ship based mapping using sonar [7, 8] and towfish [9] has been used for submerged vegetation mapping, but this is not possible in canopy forming bull kelp due to damage and entanglement, shallow water environments, poor manoeuvrability and mapping sensors impeded by the surface canopy [10].

Divers are limited by high cost [11], low coverage [1], visibility and positioning, many of which also apply to cameras drops [3]. Underwater vehicles using either sonar [11] or video [12] provide a compromise of detail, shallow water and midwater accessibility, manoeuvrability and coverage [13]. However, existing vehicles avoid operating under canopy forming kelp due to the challenge of this environment and risk of entanglement [14] and significant adaptation is required to operate within bull kelp beds.

Visual and acoustic imaging are complementary in terms of range and detail. For the challenging conditions of the nearshore, the benefits of fusing visual and acoustic mapping are apparent, with sensor fusion used to increase reliability, sensor availability and to combine idiothetic/allothetic sensors, or to increase the information available from low budget sensors [15]. Sensor fusion for navigation is also important, with existing techniques for landmark based navigation requiring a sufficiently diverse environment [16] or artificial markers to be placed beforehand [17]. This research investigated the opportunity to use environmental features (kelp) for navigation.

Sonar fusion is used elsewhere to increase detail and to reduce ambiguity [18], however the novel approach developed in this research fuses multibeam and scanning sonars using an axisymmetric

hull and holonomic propulsion to yield coverage and mapping speed benefits, together with mapping independent of navigation.

Manual kelp detection has been used to process echosounder logs for giant kelp [8, 19], yet given the survey volume from midwater multibeam mapping, significant labour and accuracy improvements are possible from development of realtime autonomous kelp detection algorithms. Validation of sonar detection of kelp is performed either using divers, or separate video surveys in the general area, or from surveys of areas which dry out at low tide [20]. These are all susceptible to errors, yet an underwater vehicle allows co-registered video to be gathered of the exact sonar target at the same time to reduce ambiguity.

Sonar calibration using a known arrangement of kelp stipes has been performed for just stipe detection for a different species, not relating measures of biomass / biovolume to a sonar return [8]. Additionally, Zabloudil et al. [8] struggled to map high kelp densities with a single beam echosounder, so multibeam midwater mapping is proposed to discriminate dense areas of kelp.

Remotely operated vehicles (ROV) and autonomous underwater vehicles (AUV) are complementary in terms of the reliability and security of remote control via a tether and the flexibility and manoeuvrability gained from using an untethered autonomous solution. Remote control of underwater vehicles in high risk areas is still recognised as essential [21], while allowing realtime direction of a survey [22]. Autonomous features ranging from holding a position or course [23] through to teleprogramming or task scheduling [24] all have the potential to relieve an operator of low level control.

An onboard power source would quickly be depleted given the high thrusts required to manoeuvre and operate in the nearshore, and yet a thick tether compromises manoeuvrability [25]. Data-only tethers exist [26], yet the use of an onboard energy buffer trickle charged by a thin flexible tether is undocumented. This research proposed an iROV, an intelligent position-aware ROV, as a hybrid solution.

Vehicles capable of operating at the surface do exist [27], yet vehicles capable of hybrid operation, bridging the air-water interface to register underwater sonar targets using GPS for sonar-aided SLAM underwater is not documented. Axisymmetric holonomic ROVs are rare [28], and exploiting axisymmetry to enable spin mapping is even rarer with only a single vehicle documented [29], incapable of the manoeuvrability required for operation in the nearshore kelp beds. Coupling axisymmetric spin mapping with a forward facing multibeam sonar for vertical resolution and mapping, and a high angular resolution scanning sonar decoupled from vehicle heading is undocumented.

Finally, ROV surveys are typically very expensive when including navigation systems and habitat mapping sensors [14]. In terms of sensing, ‘better’ results can usually be achieved given a greater budget [30], however, the challenge is to achieve high-quality habitat mapping given the limited budget of a small-scale field research operation.

1.3 Background work

Chapter 2 begins with the research context, describing the requirements and biological importance of mapping kelp beds. While a broad array of general purpose vehicles are available, specific design considerations are required for operation in the nearshore. A review of the state-of-the-art of existing techniques for nearshore habitat mapping guided the hardware, software, vehicles and techniques developed in this research.

Practical evaluation of nearshore habitat mapping techniques detailed in the background work in Chapter 3 provided a demonstration of the limitations of existing solutions as well as an insight into the dynamic and challenging environment of kelp beds. A test bed vehicle was constructed to investigate the requirements and opportunities for using underwater vehicles for nearshore habitat mapping. The benefits of holonomic movement, hybrid control and fusion of visual and acoustic data were all seen. This background work was used to inform the development of the iROV *SeaBiscuit* described in Chapter 4.

1.4 Research activities and thesis overview

The iROV *SeaBiscuit* was designed for nearshore habitat mapping on a budget feasible to small-scale research groups. A cylindrical fibreglass shell provided homogenous drag in the horizontal plane and vertical stability, important for midwater mapping. Four thrusters provided horizontal holonomic movement to counteract the effect of tether drag and reduce the risk of tether tangling giving the vehicle complete manoeuvrability. Two vertical thrusters were used for depth control.

A full navigation sensor suite was coupled with forward and downward facing video cameras, a forward facing multibeam sonar and a 360 degree scanning sonar mounted underneath the vehicle. The two sonars were arranged to exploit maximum information using the complementary holonomic propulsion system. The 360° scanning sonar pans around the periphery of the vehicle in a 2D plane, controlled independently of the vehicle heading. This provides object detection, 2D habitat mapping and navigation information. The forward facing multibeam sonar allows objects to be co-registered and profiled in 3D using a vertical swath.

Sonar targets can be registered using GPS from the surface. The vehicle is then able to dive and use this absolute reference to compile a drift-free map using sonar mosaicing, all registered relative to an absolute GPS position. A control system was used to resolve a set point of vehicle bearing and heading into individual motor thrusts for comparison to the vehicle sensors. Using holonomic propulsion, the forward facing multibeam sonar and camera could survey an object as it was passed without adjusting the original course.

Multiple monitors on deck allow dual sonar and dual video to be displayed in realtime to the pilot and scientists, coupled with an intuitive user interface for displaying telemetry, controlling holonomic movement, toggling autonomous features and compiling survey missions from basic building blocks (e.g. hold a depth, heading, course). Realtime supervision allowed modification of the survey in response to rapidly changing conditions and data quality to be ensured the first time around, without the need for costly redeployments.

SeaBiscuit exploited hybrid techniques from the fields of AUVs and ROVs to provide a robust solution for mapping the challenging kelp bed environment. A hybrid control architecture, combining onboard position-awareness and low-level autonomy, allowed survey data to be registered with a position reference and relieved the operator of the tasks of station-keeping and course-holding. Data validity in dynamic conditions was ensured by remote supervision and realtime data verification. Robust, reliable high-level control was provided by maintaining the operator-in-the-loop. A hybrid power-supply also provided the unlimited mission duration and security of a tethered vehicle, with the high-powered manoeuvring thrust required to navigate reliably in and around the full height kelp stipes despite currents.

Sensor fusion provided benefits over using a single sensor, or using sensors in isolation. These benefits included combining drift-free navigation with the robustness and availability of idiothetic

information, the combination of detail and coverage by fusing sonar for detection and video for identification, the extended coverage and resolution in 3D realised by sonar fusion and bridging the air-water boundary to register sonar targets with an absolute GPS position. Utilisation of the same sensors for navigation as well as mapping was developed in Chapter 5 and later demonstrated off a piling dock in Chapter 6.

Development into sonar-aided simultaneous localisation and mapping (SLAM) to supplement low-budget inertial measurements and surface GPS fixes aimed to provide drift free underwater navigation. A manually surveyed piling dock was used to provide a ground truth map, and an instrumented crane was used to hold the iROV in a ground truth location off the dock. Together these allowed the SLAM algorithms to be validated against a known ground truth. A typical mapping accuracy of 40cm or 7% of target range was achieved. Algorithms were written to detect and parameterise features using both sonars, and an Extended Kalman Filter algorithm for SLAM was implemented in LabVIEW using a nearest neighbour method to establish landmark correspondences to previously mapped features.

The same sonars demonstrated for navigation off the dock were also used for kelp mapping. An artificial kelp bed was created to calibrate and validate autonomous kelp stipe detection. A fully dimensioned arrangement of intact kelp stipes was transplanted to a known position off the piling dock. This allowed the sonar processing algorithms to be tuned in constant ground truth conditions to enable optimal and reliable detection of the stipes, towards relating the sonar scans to an absolute biomass and biovolume estimate, rather than simply measurements of relative density.

Following the calibration, operation moved to open ocean kelp bed mapping. The first operation delineated the kelp bed perimeter before mapping the underlying bathymetry. Autonomous image processing algorithms then searched the scan for kelp stipes, using both sonars to create the map. Each stipe was parameterised for computational efficiency, allowing a full reconstruction of the kelp bed without having to store the memory-intensive raw sonar scans.

The field trials culminated in a successful demonstration of open ocean kelp bed mapping using the iROV. Surveys of the same kelp bed from different days were manually registered using overlapping features. Kelp stipes were autonomously parameterised and areas of rock and raised bathymetry delineated by target mass. As well as target validation between sonars and surveying from multiple angles to reduce occlusion, the iROV cameras were also used for corroboration, target identification and density estimates where visibility permitted.

1.5 Summary of conclusions

In conclusion, a staged series of field trials described in Chapter 6 and Chapter 7 demonstrated the successful hybrid concept of an iROV, with capabilities moving towards full-scale kelp bed mapping. The iROV combined manoeuvrability, operational security and reliability with holonomic propulsion to exploit maximum navigation and habitat mapping information while in transit. A modular LabVIEW control system was developed to allow environment adaptive redistribution of video and sonar image processing algorithms between the onboard controllers and surface processing power.

Quantitative mapping of kelp stipes, surveyed from the midwater and decoupled from both surface conditions and the restrictions of a surface vessel has been demonstrated. The map created was more detailed than boat surveys and had a greater coverage and positional accuracy than diver surveys or camera drops, with realtime feedback of results to the operator. Calibration

techniques were also developed to relate these maps to real life measures of kelp biomass and biovolume with realtime target verification.

Compared to the existing field of nearshore habitat mapping, the iROV *SeaBiscuit* provided a compromise between detail and coverage which was ideally suited to navigation in kelp beds. A significant increase in coverage was demonstrated over diver surveys, with financial savings and an unlimited survey duration. Data gathered using video was of a comparable detail to that gathered by the divers, yet a continuous position estimate was provided. However, sonar fusion provided high coverage rates of data co-registered with video, with a quantitative estimate of the position and size of each stipe or cluster of stipes.

Although acoustic mapping from surface vessels provided high-coverage surveys complementary to the iROV surveys, the level of detail available from midwater mapping using the iROV was much greater. Data was acquired free from the occlusion and restrictions of imaging through the kelp canopy, and without the movement and shallow water restrictions of a surface vessel transecting through the kelp bed. Furthermore, small-scale manoeuvrability provided data with a greater spatial resolution and reduced the effects of occlusion, decoupling the survey data from surface conditions.

Chapter 2 Literature Review

2.1 Kelp beds

The upwelling of cold nutrient-rich water along the entire Pacific coast of North America and Canada [31] increases biological productivity in coastal areas, and supports a rich biodiversity of life in the nearshore environment [32]. Fish, invertebrates and marine mammals feed, inhabit and transit through these shallow coastal waters [33].

A wide variety of algae supports this ecosystem, including a vast and diverse community of kelp in shallow rocky areas. The ecosystems of these kelp beds and the associated organisms such as marine mammals, fish, invertebrates, other algae and epibiota [33] collectively make this "one of the most diverse and productive ecosystems of the world" [34] supporting more than ten phyla [33] and are of particular biological value.

Although definitions of the 'nearshore' vary widely between context, kelp flourishes in the photic zone, which in cold clear water ranges from the low tide level to depths of approximately 20-30m, which can extend several km offshore on gently sloping seabeds [34]. Gunderson et al. [35] define rocky reef ecosystems as extending from the shoreline to 40m of depth, supporting fisheries resources of rockfish, greenlings, sculpins, sea urchins and abalone, including several endangered species, and species at risk from expansion of fisheries.

Of particular importance in the context of this research is the species of kelp *Nereocystis luetkeana*, more commonly known as bull kelp. Bull kelp is prevalent along the Pacific coastline of Canada and North America [36], as shown in Figure 2.1 below and is the dominant surface canopy kelp north of Santa Cruz, California [37].

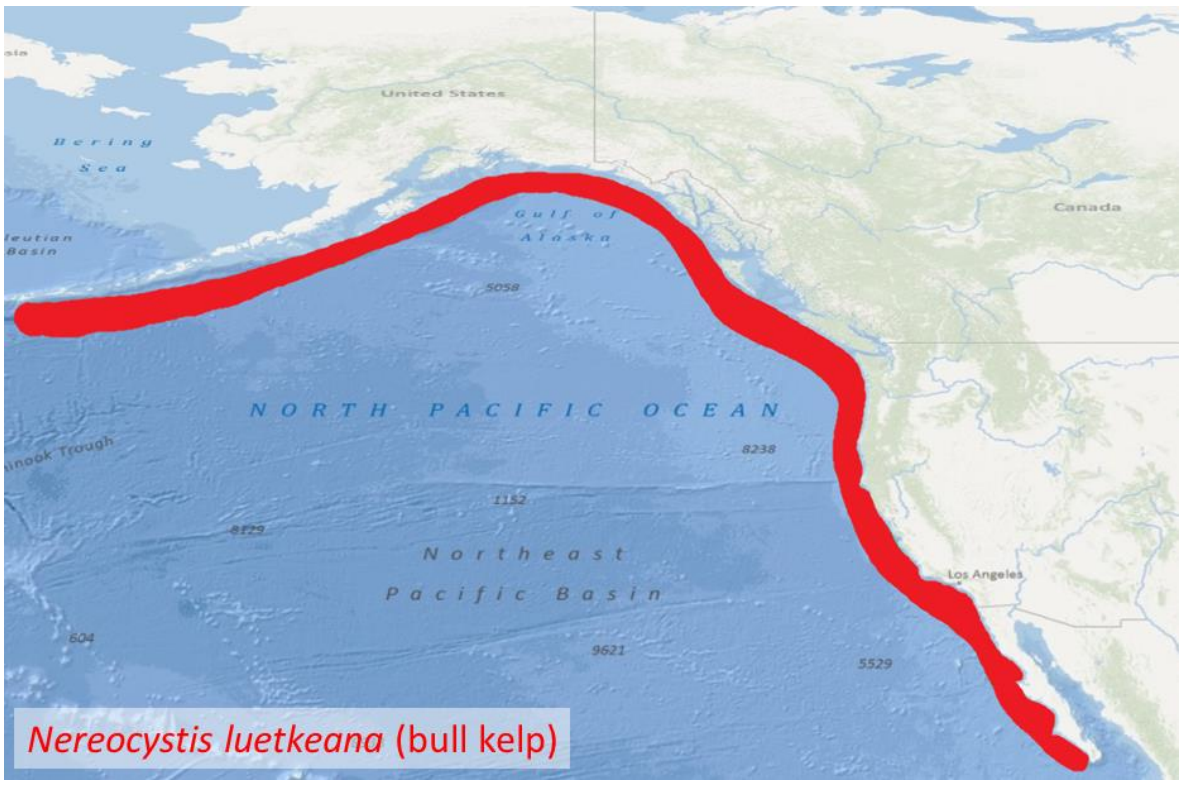

Figure 2.1 - The distribution of *Nereocystis luetkeana* (bull kelp) along the Pacific coast of Canada and North America.

Bull kelp grows on a rocky substrate, either in the nearshore or on rocky pinnacles, anchored by a holdfast in shallow water depths of approximately 10-17 m [1]. Typical lengths are 20-25 m [38]. A single stipe grows (usually annually [37]) upward to the surface where a buoyant bulb (pneumatocyst), typically 5-10 cm in diameter, supports several ribbon like fronds [38] forming a surface canopy which peaks in density and area during July-October [37]. The circumference of the stipe gradually increases with distance from the holdfast and a longitudinal cavity develops in the centre, leaving a surrounding wall 0.5-1.5 cm in thickness [38].

The pneumatocyst and upper portion of the stipe are filled with a mixture of gases, predominantly oxygen and carbon monoxide [38, 39] and the tissue is mainly (92%) water [39]. Figure 2.2 below shows the key elements of a typical specimen.

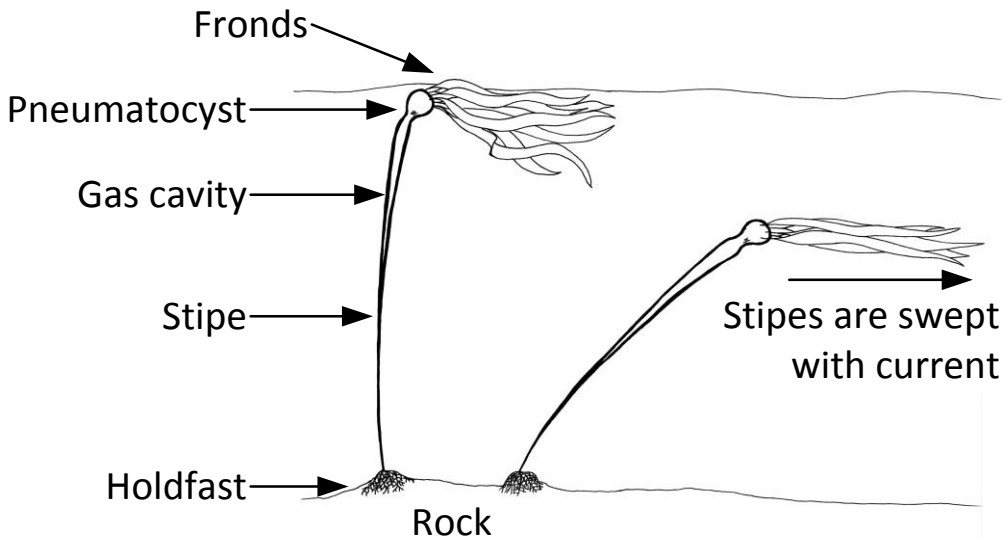

Figure 2.2 - The structure of *Nereocystis luetkeana*.

Stipes grow in tidal areas, often found in regions of high currents and typically wind around each other to form clusters spread out in great underwater kelp forests. These kelp beds support populations of mysids, small crustaceans which form the base of a substantial food-web that includes grey whales dependent on their abundance. Figure 2.3 shows a cloud of mysids and an example specimen under the microscope.

Figure 2.3 - Kelp beds support populations of mysids, small crustaceans. The figure shows a sparse cloud of mysids [40].

Many studies are underway which are centred on these kelp beds with a focus on the ecology which they support. These studies range from mapping the density and species distribution of the mysid shrimp within the kelp beds [3], to sampling the populations of mysids [40], or investigating the acoustic properties of the kelp beds and how grey whales are using passive ambient acoustics

to navigate over great distances [1, 41]. All of these studies require an estimate of the density and distribution of the kelp beds with a resolution considering individual clusters of stipes, yet techniques to provide this data have significant opportunity for development.

2.2 Habitat mapping in the nearshore environment

2.2.1 Importance

Mapping the density and distribution of kelp beds, and assessing change over yearly cycles, are important objectives for coastal oceanography. As the base for a diverse and highly productive ecosystem, mapping and monitoring change in the kelp beds can support fundamental research, such as the studies listed above, but can also be used to develop coastal conservation techniques.

While these kelp beds support a great variety of life, they are also highly ephemeral. Steneck [33] lists thermal events, storms and outbreaks of herbivores as factors which can eliminate entire kelp beds within a year, yet the kelp beds can return nearly as quickly. Changes in water motion, temperature, salinity, nutrients, light intensity, available habitat and invertebrate predation are also listed [42]. The effects of these can be highly localised, with adjacent kelp beds experiencing similar conditions displaying different effects [37].

A >10% decline in canopy area from one year to the next was seen in bull kelp beds in Canada primarily from sand inundating a rocky habitat [37]. Trophic interactions can also have a rapid and significant effect. A commonly cited example is sea urchins grazing on the holdfasts which anchor the kelp stipes; a decline in sea otter population can reduce predation pressure on the sea urchins, leading to increased grazing and a reduced kelp population [37]. Elsewhere, in Alaska, bull kelp is harvested for use in agrochemicals [5]. Careful resource management is required to avoid multi-trophic consequences, including affecting fish abundance and diminishing coastal seabird foraging efficiency [43].

2.2.2 Challenges

The mapping of kelp density and distribution poses significant challenges of operating in the nearshore environment. High currents and fast flowing tides, shallow water and a rocky seabed, together with a high risk of entanglement, fouling or even damaging the very environment being mapped, all serve to compound the difficulty. Additionally, often a large tidal rise and fall proportional to the water depth, coupled with kelp stipes only anchored on the seabed cause large movements of the stipes in tides, waves and wind.

2.2.3 Techniques

Several established techniques exist for nearshore habitat mapping, including specifically mapping kelp density and distribution. However, each technique has its limitations. The applicability of different techniques depends on the scale and resolution of the map required. Techniques range from high-coverage, low-detail satellite surveys, through to aerial surveys, ship-based surveys, underwater vehicles, camera drops, right down to low-coverage, high-detail diver surveys.

2.2.3.1 Satellite and aerial surveys

The canopy forming nature of kelp makes it amenable to mapping using remote sensing techniques [44]. Satellite imagery is very useful for obtaining broad overview maps, for example,

the density and distribution of kelp beds along an entire coastline. However, the low spatial resolution, typically 20m, makes it unsuitable for generating high-resolution detailed maps of individual plant distribution [4]. Airborne hyperspectral or visible spectrum imaging can improve this spatial resolution to approximately 0.5-2m, depending on the imaging altitude and the equipment used [5], with coverage of 1-4 square km per image [6].

However, aerial imaging measures *canopy density* and distribution rather than actual *stipe density* and so the density and distribution of the kelp stipes must be inferred from modelled data [6]. For the applications of the kelp bed maps considered here, including the grey whale feeding habitat studies and the acoustic transmission experiments, it is the *stipe* density and distribution which is important. The use of aerial imaging adds an additional source of uncertainty, particularly when considering the effect of wind and tides on the canopy, together with sea state, cliff shadows, atmospheric visibility and sun glare angle [6].

The surface canopy is also extremely variable in space and time due to the vulnerability of surface material to damage and removal by wave energy during storms [45]. The need to frequently remap the surface canopy is a major disadvantage of aerial techniques given the relatively long-term studies (several months, the feeding season of the grey whales) which are performed on the kelp beds in the field site. However, despite the vulnerability of the surface canopy to change, the stipes themselves are much less vulnerable.

Although the coverage area is very high for satellite imagery and aerial photographs, the resolution is too low for the small-scale maps required for the acoustic grey whale studies and the differences between canopy coverage and stipe density and distribution too unpredictable. Additionally, techniques to generate a 3D map of the kelp bed, add bathymetry data and populate the map with additional information such as mysid density and distribution are all near impossible using aerial techniques. Thus, the trade-off made by aerial techniques to increase coverage while reducing detail is deemed too great for the target application.

2.2.3.2 Ship-based acoustic mapping

Ship-based acoustic mapping provides an increased level of detail, resolution and the ability to generate 3D maps including bathymetry, but at a reduced coverage rate compared to airborne methods.

The tissue of *Nereocystis luetkeana* is mainly (92%) water [39] and so it has a weak acoustic backscatter [46]. Other research has demonstrated acoustic mapping of kelp fronds without a gas cavity [7] using ship-based single and multibeam echosounders to map macroalgae in water depths of up to 20m. Noel et al. [47] map underwater seafloor vegetation using a combination of a surface vessel mounted echosounder and a side scan sonar mounted on a towfish, the results of which are combined using data fusion algorithms. These techniques work well for macroalgae without a gas cavity. The gas-filled portion of *Nereocystis luetkeana*, as described in Figure 2.2, provides a strong acoustic return, thus lending itself further to acoustic mapping using sonar.

However, while ship-based acoustic mapping is suitable for seafloor vegetation [7, 47], it is less effective when mapping surface canopy forming vegetation such as kelp beds of *Nereocystis luetkeana*. For a canopy forming kelp, if the vessel performs a transect[1] under power then it risks tangling either the drive train and/or the scientific equipment with the kelp and damaging the

[1] A transect is defined as traversing a fixed path or known course and recording survey data observed with a position reference. The path is fixed and repeatable to allow spatial comparison and temporal analysis.

environment being studied. Additionally, the vessels typically used for nearshore surveys are unable to provide full manoeuvrability at low speeds and many lack station holding or dynamic positioning capabilities. If the vessel is allowed to drift over the kelp bed with its engines idle to avoid damage to the ship and vegetation or entanglement, then its course is determined by the wind and currents and the risk of tangling is never completely mitigated. If the vessel circumnavigates the kelp bed, directing sonar imaging devices inwards, then the survey range and detail is limited leaving the centre sections of large kelp beds unmapped.

As with any scan taken from the surface, the quality, resolution and understanding of what is happening underwater is much lower than if the sensors and instruments are positioned at depth (i.e. the difference between looking down over the kelp bed, and surveying at depth looking through the kelp bed). Overall, the positioning in latitude, longitude and depth of a surface vessel is not as flexible as that which can be obtained by underwater vehicles, nor can the kelp bed be entered and mapped from the midwater.

Hass and Bartsch [48] provide a recent example of kelp bed mapping using a single beam echosounder and compare the results obtained to geo-referenced underwater video transects and diving transects. One of the significant benefits of acoustic surveys is the ease of data processing. However, the single beam echosounder approach employed by Hass and Bartsch [48] requires interpolation to generate a spatial map from a grid of regular transects. The resulting map is of a lower spatial resolution and detail compared to those required for this research.

Nelson et al. [9] discuss monitoring the temporal and spatial shift of nearshore submerged aquatic habitat in the presence of anthropogenic factors, for example in the proximity of marinas and ports. A combination of underwater video and side scan sonar mounted to a towfish and referenced to the ship's position is used. The benefits from fusing video and sonar in the dynamic conditions of the nearshore are demonstrated. However, the high risk of tangling and lack of small-scale manoeuvrability render a towfish ineffective for mapping the canopy-forming kelp beds proposed in this research.

The applications of kelp bed maps can extend beyond simple habitat mapping; Elwany et al. [19] conducted a study to determine the effects of kelp beds on waves. A combination of side-scan and dual downward facing 200kHz echosounders from a ship-based survey was used to generate local kelp bed maps with a high-resolution considering individual plant density and distribution [8]. Although the post-processing and analysis to identify kelp stipes was performed manually, the constraints and criteria for manually indentifying kelp from sonar scans is applicable to any autonomous processing algorithm.

2.2.3.3 Underwater visual surveys

The most significant disadvantage of acoustic mapping is a lack of detail and resolution. However, this can be supplemented to some extent with visual surveys, either camera drops and tows or diver surveys, to provide high-resolution colour imagery. Visual surveys have the inverse (or complementary) characteristics of sonar surveys. Visual techniques require clear water, good illumination, have relatively poor range and coverage and cannot provide depth perception or ranging (unless stereoscopic techniques are used).

In the kelp beds typical of *Nereocystis luetkeana*, visibility can be as low as <1m depending on water turbidity (verified from the author's own diving experience!). The water turbidity is dependent on a variety of factors and can be highly dynamic and localised. Sea state and benthic composition can combine to cause sediment and silt in the water and the tide speed and direction

can affect the size and density of particles washed from the sediment. Runoff from the land following rainfall or at estuaries can wash particles and nutrients into the water. Additionally, the algal blooms occurring in the spring as sunlight hours increase cause a significant reduction in visibility [49]. The very upwelling of cold nutrient-rich water which supports the ecosystem of the kelp bed also serves to reduce visibility [50].

Thus, visual surveys are useful to complement acoustic mapping with short-range target confirmation and identification. However, for long-range survey, mapping and detection, acoustic mapping has significant advantages for high coverage, yet relatively high detail surveys of kelp beds.

Ship-based underwater visual surveys use a tethered underwater camera, either lowered into the water from the surface vessel at a series of GPS referenced stationary points, or towed through the kelp bed on a transect. However, towing, dragging or dropping passive un-propelled instruments into the kelp bed has the limitation that the position of the instrument is relatively undetermined and uncontrolled. It is hard to accurately place a passive instrument from a surface vessel and the risk of tangling is significant with a moving surface vessel and an uncontrolled towed instrument.

An alternative method of visual surveys to camera drops and tows uses SCUBA divers. The risk of tangling is lower, the survey can be directed and adjusted reactively, movement can be more controlled than a camera drop and measurements and sample collection are possible.

This method was used extensively by Wladichuk [1] to estimate kelp bed density to ground truth acoustic transmission experiments. Figure 2.4 below shows an example image from a transect through a kelp bed, where the length of a diver is used as a reference and kelp stipes are identified through manual video frame analysis.

Figure 2.4 - An example image from an underwater diver kelp bed survey video along a transect in relatively good visibility. Manual video frame analysis is used to identify 7 kelp stipes (or clusters of stipes) shown by red arrows. The length of the SCUBA diver in the frame is used as a reference to calculate a stipe density of 1.75 stipes/m² as there are 7 stipes (or clusters of stipes) in an area of approximately 2m by 2m. Figure and caption adapted from [1].

Figure 2.4 shows relatively good visibility, uncharacteristic of many kelp beds. The labour effort of both data gathering by divers and data processing by manual video analysis is high, the coverage rate is low and there is no estimate of the stipe size or clusters of stipes. These limitations stem partly from the data gathering method of diver surveys, and partly from the limitation of visual surveys over acoustic mapping.

The additional risk, time spent deploying and recovering divers, and the limitation of only being able to perform a few dives per day restrict the usefulness of SCUBA divers when large areas need to be covered or a long duration scan is required. Jones et al. [11] quote that a 2.5km transect mapping submerged aquatic vegetation (eelgrass) was assessed twice in a 4 hour period using an underwater vehicle which included set-up time and vehicle recovery. Jones et al. [11] estimate that the equivalent survey over 500m using 5 divers could take an entire day, depending on conditions and water visibility, costing up to $10k. While the coverage benefits over diver surveys are apparent, a direct comparison to the costs of an underwater vehicle (including capital, deployment and service) is not straightforward.

Additionally, recording scientific data with an accurate position fix while diving is challenging and usually requires predefined simple transect routes or pre-deployed markers. Wladichuk [1] assumes a constant swim speed where the video footage is recorded along a straight transect at a constant speed and depth between two GPS-referenced surface markers.

2.3 Using underwater vehicles for nearshore habitat mapping

Considered by many to be the first remotely operated vehicle, the *POODLE* built by Dimitri Rebikoff in 1953 [51] sparked a revolution in subsea vehicles which the US Navy quickly followed up. The VARE *XN-3* delivered to the US Navy in 1961 provided one of the first controllable underwater video systems [52] and the rest is history. Underwater vehicles today have propagated across the fields of subsea defence, archaeology, security, biology, ecology, oceanography, infrastructure and energy [53, 54]. Enabled by a continual miniaturisation in electronics and power sources, an advance in control algorithms and a drive of expanding exploration, resources and research, the field is continually advancing [55] with the frontiers of autonomy and applications being pushed further and further [56, 57].

Although the field of underwater vehicles is well established, there are still significant opportunities for development to advance the field specific to generating the high-usability maps required for this application of nearshore habitat mapping.

2.3.1 Classification of underwater vehicles

The classification of underwater vehicles varies between sources. Blidberg [58] presents a widely accepted set of definitions which are summarised in Figure 2.5 in the category of *unmanned* underwater vehicles.

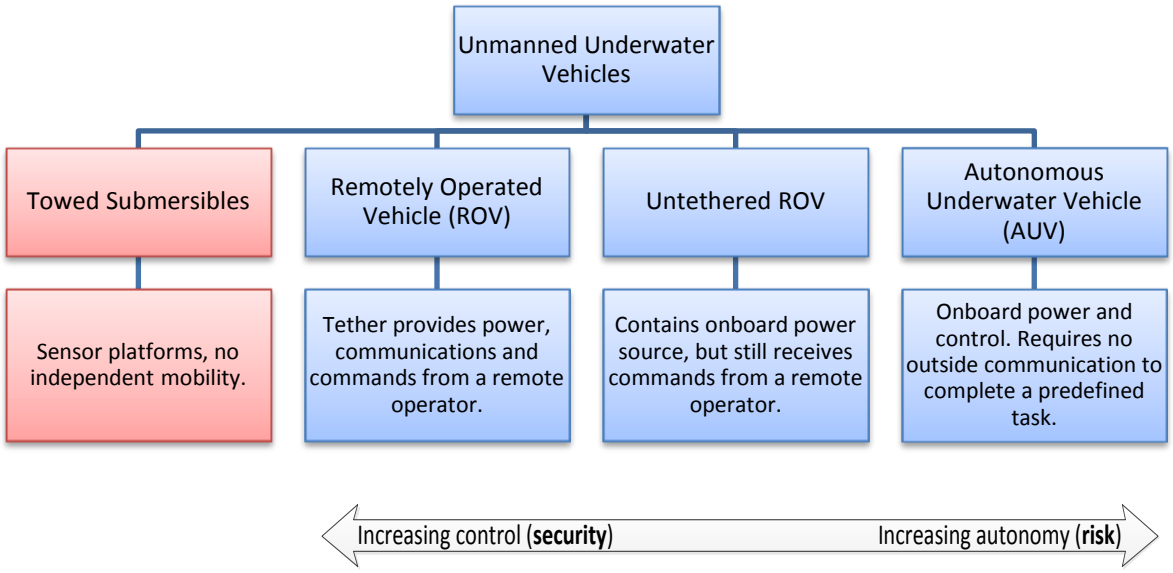

Figure 2.5 - The classification of underwater vehicles (adapted from [58]).

Given the difficulties of using towed instruments in kelp beds, the discussion continues with remotely operated vehicles (ROV), autonomous underwater vehicles (AUV), and the hybrid, an untethered ROV with an onboard power source, no tether, and wireless remote control.

The arrow drawn underneath Figure 2.5 represents increasing autonomy to the right, and increasing control to the left. While this increase in autonomy brings with it benefits (many of which are discussed below), it increases risk and potentially restricts the possible environments into which AUVs can be deployed. Moving to the left brings increasing control, and thus increasing security, but with disadvantages over AUVs (also discussed below). The optimal compromise somewhere along this line to combine the benefits of each end of the spectrum while mitigating the limitations for kelp bed mapping forms the focus of this research.

2.3.2 The requirements and techniques for nearshore habitat mapping

When compared to the alternative survey methods previously reviewed (airborne, ship, camera drops, divers), for many applications, the use of underwater vehicles brings benefits to nearshore habitat mapping. These range from improved resolution, coverage, reliability and flexibility or can extend to a reduction in time, labour and expense.

There are four fundamental requirements for any mobile robot: sensing, control, navigation and propulsion [59]. However, nearshore habitat mapping dictates specific requirements for an underwater vehicle. Each of these are considered in turn, with the specific context of nearshore habitat mapping. The requirements for operating in kelp beds are considered and existing techniques applicable to the use of underwater vehicles for kelp bed mapping are evaluated.

2.3.2.1 Sensing (habitat mapping)

The underlying requirement of the habitat mapping sensors is accurate[2] (low-error) and reliable[3] (repeatable-error) sensing of the elements required to complete the map, in this case, the seabed, the kelp stipes, and any other targets present. All of this is required in the turbulent, dynamic and hostile nearshore environment of kelp beds.

Whichever sensor is used to map the kelp beds, most commonly video or sonar, there are advantages and disadvantages to each which are inherent in the sensing mode, including resolution, range, attenuation and detail, as discussed in section 2.2.3. These factors are present whether the video or sonar scan is conducted using a ship-based method or an underwater vehicle. However, this subsection considers the benefits gained specifically from using the same sensor mode conveyed using an underwater vehicle.

Using a mobile underwater vehicle compared to simply mounting the sonar unit to the surface vessel yields several advantages [13]. Underwater vehicles are able to position the sensors in 3D in the midwater, independently of a surface vessel. A position can be held in currents, or a course navigated independently of the movement constraints of a surface vehicle. Fine precision control of movement and positioning, navigation independent of the surface vessel and independent depth control are all gained as well as the ability to anchor the surface vessel safely out of the kelp bed to avoid shallow water and damaging the kelp. Even *tethered* underwater vehicles are able to extend the operating range of a surface vessel into shallow water, confined spaces, and operating in and around the kelp beds.

Survey data can be gathered without the effects of surface conditions, such as waves and weather, which would reduce the survey quality of a ship-based scan. Through the manoeuvrability of an underwater vehicle, scans can be performed not only around the periphery of the kelp bed looking inwards as a surface vessel would, but also from within the kelp bed looking outwards, thus increasing survey detail and coverage.

Using an AUV, Deneulle and Dunbabin [12] demonstrated successful kelp bed and seagrass mapping using optical techniques in nearshore regions in water depths of 6-10m, yet requiring adequate visibility. Downward facing video and autonomous texture recognition were used to

[2] Accuracy is often defined as "*closeness of agreement between a quantity value obtained by measurement and the true value of the measurand*" and is "*inversely related to systematic error and random error*" [60].
[3] Reliability is used in this context to mean precision, often defined as "*closeness of agreement between quantity values obtained by replicate measurements of a quantity, under specified conditions*" [60].

classify seabed habitats, including leafy kelp, and techniques were proposed to deal with the significant sway of tethered targets in the wave action of the nearshore environment.

Techniques to combine the coverage of a surface vessel with the level of survey detail provided by an underwater vehicle have also been considered. Barrett et al. [13] successfully used an AUV for mapping marine biodiversity in coastal waters in a recent (2010) survey. Information was combined from a ship-based high-resolution multibeam sonar survey of bathymetry with high-resolution position referenced video footage gathered by an AUV navigating a pre-programmed constant-depth course through the surveyed areas. The scientific video footage gathered was also used to cross-reference and correct the vehicle position estimate using image recognition of seabed targets at crossover points along the trackline. The limitations identified by Barrett et al. [13] were the restrictions of water-clarity and the difficulties of estimating the range to and size of survey targets using video data alone.

Therefore, the use of sonar to augment video footage is proposed to improve coverage particularly in low visibility, to reduce survey effort and to allow autonomous image processing and feature extraction algorithms thus removing the need to manually post-process video. Jones et al. [11] discuss the use of an AUV equipped with side-scan sonar to map the boundaries of eelgrass (*Zostera marina*) beds in the nearshore. The requirements are the same as for the kelp bed application discussed in this research, principally delineating (mapping the perimeter of) submerged aquatic vegetation beds in the nearshore to determine area and then populating the map with plant density. The strength of the acoustic sonar echo is driven by abrupt density changes from the surrounding seawater, either increasing density to a solid, or decreasing density to a gas [11]. The gas-filled spaces (lacunae) between the cells of the eelgrass tissue [61] lend eelgrass to acoustic detection [62] in the same way that the gas-filled pneumatocysts of bull kelp are easily detectable acoustically.

Jones et al. [11] used side-scan sonar to delineate areas of eelgrass, however, clutter in regions of high shoot density restricted estimations of plant density. This can be addressed in part through the use of a downward facing (ship-mounted) echosounder capable of discriminating vegetation as a function of vertical height [62], yet the benefits of an underwater vehicle platform are lost. Jones et al. [11] discuss the possibility of using an Acoustic Doppler Current Profiler (ADCP) to populate the map with vegetation density and height, yet the capital costs of such an instrument are high, typically $15k upwards [63].

Instead of surface vessel scans, it is proposed that the combination of a position-aware underwater vehicle, coupled with a multibeam echosounder capable of mapping kelp stipe density over the entire water column can provide an optimal solution for nearshore kelp bed habitat mapping (or indeed any canopy forming kelp). As discussed above, the integration of visual data can provide corroboration and identification of the acoustic target, given short ranges and good visibility.

2.3.2.1.1 Ground truthing habitat mapping sensors

Ground truthing allows sensor data to be reliably interpreted autonomously and a dataset to be expressed using absolute units, rather than simply relative measurements. Given the applications of the kelp bed mapping discussed previously, ranging from supporting ecological research into the kelp bed as an important marine habitat to modelling the acoustic properties of the kelp bed, in each application absolute units of kelp stipe density and distribution are important.

Saade [20] describes a two-part ground truthing process, applied to both multibeam data and aerial imagery, in the context of seabed habitat mapping. The first part is calibration, to relate the arbitrary sensor values (in the case of the multibeam, the strength of the acoustic return) to real-life values. In the case of the kelp stipes, these real-life values are the biomass and/or the biovolume, with an intermediate consideration of the gas volume, as this significantly affects the strength of the acoustic return. The second part is verification, which Saade [20] performs primarily using video transects. The verification phase provides confirmation that the autonomous detection routines are correct, with no false-positives, false-negatives or misidentifications. Saade [20] also uses the verification phase to provide a statistical estimate of the accuracy of the final habitat mapping, both in terms of the accuracy of classification, and the accuracy of positional and dimensional mapped information.

In the context of using underwater vehicles for habitat mapping, this verification through video can be performed by diver surveys or by camera drops. However, self-contained visual verification of classification is also possible using one or more cameras mounted on the vehicle, recording co-registered, synchronised video footage for later playback and examination.

Zabloudil et al. [8] describe their calibration process of surface vessel sonar surveys of the density of giant kelp (*Macrocystis pyrifera*). Although a different species, giant kelp has a similar structure to bull kelp of long stipes anchored by a holdfast and an extensive canopy. However, whereas bull kelp has a gas-filled stipe and a single pneumatocyst supporting fronds at the surface, giant kelp has blades growing over the entire height of the stipe, with each blade supported by a pneumatocyst [64]. The calibration process included considerations of areas of too-high stipe density to distinguish single plants, or smaller stipes which have a reduced acoustic return. Stipe densities greater than 20 plants / 100m² were not distinguishable and not defined in the calibration model. However, for giant kelp, such densities were stated to be infrequent and it is proposed that midwater multibeam scans could distinguish greater stipe densities.

To avoid underestimating density, Zabloudil et al. [8] performed a calibration survey of plants of known dimensions to determine the minimum size at which kelp stipes become acoustically undetectable. This involved harvesting, measuring and transplanting a series of stipes of particular sizes in a known arrangement with appropriately spaced artificial sonar markers for reference [8]. The technique is applicable to any species of kelp surveyed and allows development of a calibration model by comparing the known stipe data with the acoustic return. As well as *calibration* on a manually dimensioned artificial kelp bed, Zabloudil et al. [8] also discuss the technique of *verification* using manually measured sections of real kelp beds.

2.3.2.1.2 Presentation of results

Given the successful mapping of the density and distribution of the kelp stipes, the processing and presentation of the results is important to generate high usability, applicable maps and datasets. There are two options to store and present the kelp stipe data.

The first considers the representation and mapping of individual stipes. An established consideration of habitat mapping is the large datasets of high-resolution imagery produced [13]. While recorded footage is useful to play back for later analysis and mission review, often more efficient storage techniques are available which are also more useful for later analysis and post-processing. Using a combination of image processing and feature extraction algorithms, features pertinent to the survey application (in this case kelp stipes) can be extracted from the raw sonar imagery during acquisition and stored in a compact, efficient parametric representation. Although

this is at the expense of an increase in computing power required for on-the-fly realtime image processing, the reduction in data storage requirements is significant. It does however require survey targets which are amenable to autonomous detection. Techniques to autonomously detect and parameterise the kelp stipes are discussed in the later implementation sections.

The second option represents stipe density as an interpolated surface over the delineated kelp bed area. Given the high currents and turbulent wave action of the nearshore, the kelp stipes often wrap around each other, forming clusters. Additionally, given the wave action and tidal flow, the position of the individual stipes and the clusters can often vary significantly, as the long stipes, only anchored at the holdfast on the seabed, sway back and forth. This movement can be relatively uniform across the kelp bed from tidal flows, with the majority of the stipes not moving relative to each other, but all moving in the same direction by approximately the same magnitude. However, it can also be much more unpredictable, from wave action and wind causing the stipes to move relative to each other in a highly dynamic manner. A significant change in the apparent map can be seen from one scan to the next, even over a few seconds. Therefore, although consideration of the individual stipe size and position is important, given the errors discussed above, it is also useful to consider an average density of kelp stipes (biomass/biovolume), represented as a density surface, delineated by the kelp bed boundaries.

This is useful as a 2D density, gathered at a constant midwater height across the kelp bed, to allow relative measurements and observations to be made between stipes, but also interesting to consider in 3D given the changing characteristics of the kelp stipe, from the holdfast right up to the fronds of the canopy. The technique of presenting interpolated density as a 2D surface has been used previously with a ground truth calibrated scale and combined with a bathymetric map [8]. This presentation is useful both for immediate analysis, but also for recognising and quantifying trends from year to year and is easily expanded to join several local submaps.

Geographic Information Systems (GIS) are often used for the interpretation and analysis of both terrestrial and marine habitat mapping, and a whole field of marine GIS has developed rapidly [65]. Bickers [66] uses these tools for the analysis and interpretation of results, allowing the comparison of the various ‘layers’ of data, from a digitised chart, aerial photography, 3D bathymetry, sonar overlays as well as classified data.

2.3.2.2 Sensing (navigation)

Navigation of underwater vehicles is not trivial, with radio frequency (RF) signals, including GPS attenuated quickly underwater [67], and sonar errors from reflections, reverberation, attenuation, multiple paths, occlusion, a variable speed of sound and a varying frequency response of targets [46]. Even sensors such as inertial measurement units, utilising accelerometers and gyroscopes to sense positional changes, are prone to significant cumulative errors if uncorrected [68].

Estimating the position of observed targets (seabed, kelp, etc.) is fundamental to the aim of habitat mapping. This turns a simple camera and sonar platform which can be piloted through the water to record footage for later playback into a useful scientific mapping tool. If the footage gathered can be referenced with a position, then quantitative analysis of habitat density and distribution can be performed, rather than simply playing back previously recorded footage.

All targets are recorded with a position relative to the vehicle, as no uniquely identifiable landmarks are available with a prior known position. For example, the sonar records targets with a range and bearing to the current vehicle position. Therefore, the mapped data is only as

accurate as the vehicle position estimate when it was gathered. To generate useful (accurate and reliable) maps of the nearshore habitat, accurate and reliable, drift-free position information is essential [69] yet this is an outstanding challenge [70].

In particular, accurate and reliable navigation *on a budget* using *imperfect sensors* in the *hostile nearshore environment* is a current problem. The turbulent and dynamic environment causes the sensor characteristics and capabilities to vary continuously, thus compounding the difficulties. This is identified as a key opportunity for development and one of the subjects of this research. Advances in the capabilities and reliability of nearshore underwater navigation will have benefits to all applications of underwater vehicles.

Although progress over recent years has advanced the field of underwater navigation, both in sensing hardware and data processing, the three underlying methods remain much the same, (1) dead reckoning and inertial navigation, (2) acoustic navigation and (3) geophysical navigation [71]. When conditions permit, visual navigation and radio navigation is also possible. These techniques are considered in the following sections, with a review of the current state of the art, together with the applicability to navigation in the target nearshore environment.

2.3.2.2.1 Information available

While considering the navigation sensors, it is important to distinguish between the two types of information available: *idiothetic* and *allothetic* sources [72, 73].

Idiothetic literally means 'self-proposition' and is the information proposed by the robot's internal sensors on its current position, or a *dead reckoning* estimate. Dead reckoning is the process of estimating the current position based on a previously determined position, a *fix*, and advancing that position based on estimated speed over elapsed time and course. In terms of a land based robot, this can mean the odometry of wheel rotation. However, for the underwater vehicle, speed and course can be predicted by the electrical power applied to the thrusters and measured using accelerometers. As with any dead reckoning system, this process is prone to large cumulative errors. As each new position estimate is calculated solely from previous positions, the error in position grows with time [68].

It is therefore important to use *allothetic* information to complement the idiothetic dead reckoning system. By contrast, allothetic refers to external stimuli or cues, such as objects observed with vision and sonar systems, or surface GPS position fixes. Although the allothetic information appears to be more useful, it is not always available. However, idiothetic dead reckoning information is always available. For example, in turbid or deep water, objects may not be visible using sonar and cameras, and satellite GPS fixes are not available underwater.

Additionally, allothetic information is subject to perceptual aliasing – that is two different locations perceived as the same location, or two observations of the same location recorded in error on the map as distinct locations [74]. Perceptual variability occurs when the same place varies in appearance over time [75]. In the underwater environment, tides, turbidity, vegetation growth, decay or damage can all cause perceptual variability, which, if not interpreted correctly, can also lead to perceptual aliasing.

Allothetic information can also be heavily affected by external interference, e.g. sonar noise, visual turbidity, ferromagnetic interference with compasses and magnetometers, GPS signal loss, etc. As the following sections describe, the lack of absolute navigation data inherent in all underwater navigation, i.e. a lack of drift-free information, is compounded in the nearshore.

2.3.2.2.2 Dead reckoning and inertial navigation

As Leonard et al. [71] state, the simplest method of maintaining a position estimate of the vehicle is to integrate the vehicle velocity in time to update a previous position estimate with the distance travelled. However, whether the vehicle velocity is estimated from the power applied to the thrusters, or measured by water speed and a compass, the presence of an ocean current will add a component of speed which is not accounted for [71]. Thus, in the nearshore environment, where such currents are common from tide and wave action, simple dead reckoning based on thrust applied or relative water speed is highly unreliable.

Inertial Navigation Systems (INS) use accelerometers and gyroscopes (inertial measurement units, or IMUs) to sense linear and angular accelerations. These accelerations are integrated twice in time to yield a change in position from the last estimate [76]. They are capable of measuring fast accelerations and are not susceptible to external factors, such as ferromagnetic disturbances [15]. However, like all dead reckoning systems, they are prone to large cumulative errors building up over time (drift) if an absolute reference is not regularly available. As it is the acceleration which is sensed, any error is increased in magnitude during the double integration to yield displacement. INS are also prone to electrical noise and temperature drift.

All of these problems mean that commercially available INS which have both good small-scale precision and good long duration accuracy are very expensive [77]. Recent advances and miniaturisation of components readily yield INS units suitable for mounting on underwater vehicles capable of a position drift of less than 0.1% of the distance travelled, CEP[4] (the IXSEA PHINS III [79] and Kearfott T-24 [80]). However, the cost of these units is well above the typical users of the kelp bed habitat maps, including the grey whale and coastal ecosystems research organisations supported by this research. Lower cost units are available, but given the relatively small accelerations experienced by underwater vehicles, these cheaper units are prone to large cumulative errors if used alone for navigation [15].

Additionally, the power consumption of the two units considered here is 15-30 watts [78], and both are relatively large in size (the IXSEA PHINS III is 180×180×160mm and weighs 4.5kg [79]). When considering the target application, a compact highly-manoeuvrable vehicle capable of navigating in and around the confined and complex environment of the kelp beds, the size, weight and power consumption are all important considerations.

It should be noted that even with the prohibitively high cost, and large size, weight and power consumption, each of these units use several other sensors to achieve the specified positional drift. Amongst other sensors (pressure/depth, sound speed), these units use a Doppler Velocity Log (DVL) to achieve the positional accuracy stated. In pure inertial mode, the IXSEA PHINS III achieves a positional accuracy of 0.6 nautical miles / hour CEP, or approximately 31 metres / minute CEP [79]. Given the small-scale operation in and around the kelp beds, this high rate of positional error per minute renders it unsuitable in inertial mode alone. Hence, the principle of using other sensors to increase the positional accuracy is continued in later sections.

Doppler Velocity Logs, or Acoustic Doppler Current Profilers (ADCP) are based on the fundamental principle of Doppler shift, that "*an acoustic signal, which has been either transmitted or received by a moving object, will be shifted in frequency by an amount proportional to the velocity of the*

[4] As Panish and Taylor [78] describe: "*CEP refers to the Circular Error Probability, or a circle about a mean value which includes 50% of the population*". For the INS described above with a positional drift of 0.1% of distance travelled, CEP, if it travels 1km, it is expected that 50% of the time the position drift when estimating its new position after 1km travelled will be less than 1 metre.

moving object" [81]. When used for the navigation of underwater vehicles, the velocity of the vehicle relative to the seabed can be used to estimate positional changes by detecting this frequency shift. When the seabed is not visible, or obscured (e.g. by turbulence or midwater vegetation) then the relative movement of the vehicle to the surrounding water can be sensed, however this has no correction for tidal flow and is less suitable for the high current regions of the nearshore.

As the DVL estimates position changes by sensing velocity and integrating it over time, it too is prone to cumulative errors, as with other dead reckoning systems. This drift, whether the DVL is used independently or to support an INS as described above, limits its operation as a sole source of navigational data.

Recent developments have brought the size and weight of DVLs within the capabilities of being carried on a small underwater vehicle: Teledyne-RD Instruments has developed the Self-Contained, Phased Array, Explorer DVL which is 327×124×124mm in dimensions with remote electronics 241×84×88mm [82] and approximately 0.5kg transducer weight in water [83]. However, these dimensions still contribute to increasing the overall size and weight of the required compact, manoeuvrable vehicle.

The second key constraint is budget, and suitable DVL units are often out of the budget constraints of the intended users of the habitat mapping underwater vehicles. As with all dead reckoning sensors, including the INS and DVL solutions discussed here, a higher budget usually means increased performance. The drift, inherent in all-dead reckoning sensors, reduces with higher price sensors, yet the constraints of the application dictate achieving the navigational accuracy required with the limited budget available.

2.3.2.2.3 GPS navigation

For terrestrial and aerial navigation, GPS is widely used as coverage is generally good and a global (geodetic) position is provided [84]. For small-scale navigation and surveying, such as the kelp bed mapping discussed here, GPS is used to register the resulting maps in the World Coordinate System (WCS) and to bound cumulative errors, but the precision of a few metres at best of standard GPS (even with WAAS[5]) [87] is usually coupled with other sensors to increase the accuracy [88-90].

As previously discussed, GPS signals are quickly attenuated underwater [67]. Techniques for extending the benefits of GPS underwater using acoustics are discussed in a following section. The alternative is for the vehicle either to operate with an antenna at the surface, or to return to the surface for regular GPS fixes.

The former, operating with an antenna at the surface, can be achieved by the vehicle conducting surveys from the surface. However, this leaves the vehicle prone to tangling with the kelp fronds, and susceptible to surface wave action. Habitat mapping quality is also reduced, caused in part from the sonar operating through the attenuating bubble layer (section 2.3.2.2.6) and from video at a long range from the target and through reduced surface visibility. Surface operation also prevents the vehicle from surveying the kelp bed from the midwater, often causing the canopy to obscure measurements.

[5] Wide Area Augmentation System (WAAS) is used to increase the accuracy of GPS in selected areas by providing correctional data from terrestrial transmitters [85, 86].

An alternative technique to providing a surface antenna for GPS is to either tow a surface antenna from the midwater, either continuously, or sporadically when required and recover the antenna when not in use, or to release expendable antennas, either cabled or with an acoustic communication channel [91]. However, any towed antenna is prone to tangling in the kelp canopy as the vehicle manoeuvres and expendable antennas are an expensive option. Whether towed or untethered antennas are used, there is also an error introduced from the position difference between the antenna and the vehicle, coupled with the precision of a few metres at best [87] of GPS. Techniques to minimise these effects using low-drag cables and to correct this error using acoustic relative positioning have all been explored [92]. While they are perhaps suitable to long-duration straight-line survey operations, for the small-scale manoeuvres in closed quarters in the kelp bed, with high currents and frequent turns, the complexity and risk of tangling is too high to be feasible.

The latter solution, the vehicle returning to the surface to receive a GPS position, can be used intermittently throughout a mission to bound the errors from dead reckoning sensors such as INS, where the surfacing frequency is proportional to the drift of the INS system. However, the surfacing and diving process expends time and energy, risks the vehicle in surface wave action while a satellite fix is obtained [93], again risks tangling at the surface, and by the time the vehicle has returned to depth any accuracy gained can easily have been lost during the dive.

A novel alternative technique to extend the benefit of GPS to tethered ROVs is through the use of a ‘Smart Tether’. The principle, patented in 2008 [94] and manufactured by KCF Technologies [95], is a completely non-acoustic system which uses orientation and pressure sensors placed at regular intervals along the tether to estimate the tether shape. The relative position of the tethered vehicle to the surface support vessel can then be estimated from the tether shape and registered in the world coordinate system from GPS fixes obtained by the surface vessel. This allows underwater survey data to be registered with a GPS position without the need for the vehicle to surface. The Smart Tether system has been successfully deployed into confined yet static small-scale enclosed environments, most notably a series of underground flooded tunnels systems, to allow successive sonar scans to be co-registered without relying on cross-correlation and co-registered landmarks alone [96].

The benefits of using Smart Tether navigation are the same as any other non-acoustic navigation system: problems from acoustic reflections, noise, or obstructions are all avoided [97]. However, the cost is relatively high, and the accuracy obviously dependent on the application – tether length, and the number and radius of bends in the tether will all reduce the initial few-metre precision of GPS to a lower accuracy underwater. Thus augmentation from other onboard sensors is still required [83].

2.3.2.2.4 Geophysical navigation

If an accurate a priori map of the operating environment is available, then one approach to provide drift-free globally referenced positioning is geophysical navigation. The principle is to match sensor data with an a priori map, given the assumption that there is sufficient spatial variation in the parameters being measured to avoid perceptual aliasing [71]. The most appropriate method for the nearshore is navigation by bathymetry, given the varied topography of the nearshore seabed surrounding the kelp beds.

Over long durations where small-scale accuracy is not required, terrain-based navigation is used with great success [98], using maps either gathered by the vehicle prior to operation in a specific

mapping mode, or using conventional marine charts [99]. Global navigation can be achieved and exploration effort can be reduced through these methods. When operating over large areas, the search space and computational complexity from navigating from a priori maps alone is high, and often other techniques (inertial navigation, DVL) are used to limit the search area [71].

The reliability of navigation using an a priori bathymetric map depends on the accuracy of the map used [71]. Given the small-scale positional accuracy required by the underwater vehicle, the accuracy of traditional marine charts is insufficient – these typically have 10m contour lines, represent the complex rocky pinnacle supporting a kelp bed as a single height, and have depth markers often several tens or hundreds of metres apart. Therefore, often a specifically created map needs to be surveyed, either by the vehicle with an alternative position reference, or by a ship-based bathymetry survey. The time and complexity of this initial map-gathering is proportional to the map resolution, and therefore proportional to the navigational reliability of the vehicle.

However, the principle of using terrain *aided* navigation, that is using terrain navigation for global position estimation with other navigation sensors used for smaller-scale local navigation [100], is recognised as a strong technique. Furthermore, in the specific application of the kelp bed, there are additional environmental cues available for navigation, principally the kelp stipes themselves. If treated with sufficient positional uncertainty due to their tethered movement in water currents, although no a priori map exists, through techniques of concurrent localisation and mapping discussed in later sections, these too have the potential to assist navigation.

2.3.2.2.5 Acoustic navigation

Techniques using sonar to recognise and navigate from bathymetry were discussed in the preceding section and techniques to navigate from sonar landmarks are discussed in the next section. However, acoustic navigation can also be used in a simpler manner. Many existing techniques for the navigation of underwater vehicles in the nearshore environment involve environment modification, such as establishing beacon systems in the environment to be covered [101-104]. The difference in arrival time between acoustic ‘pings’ from transducers at known positions can be used to triangulate the position of a mobile vehicle underwater.

Calculating the range and bearing to the assumed stationary transponders allows for local navigation, however, if the global latitude/longitude of the transponders is known, then the vehicle can infer its global (geodetic) position while underwater. If the transducers are at the surface, on a buoy or a ship, then this latitude/longitude can be established using GPS and transmitted using the acoustic signal to allow for drifting transponders.

Various techniques have been developed to try to extend the benefits of GPS underwater and Crowell [92] references two patents [105, 106]. In both cases, although the implementation differs, the principle is to replicate the GPS system using acoustic transmission underwater. GPS positions can be encoded and transmitted acoustically and the time of arrival from several beacons compared with the encoded GPS timestamps to calculate distance. This is the principle of a GPS intelligent buoy (GIB), a surface buoy which provides communication and therefore positional information between the boundary of the surface and subsea. The buoy tracks its position via GPS and is also itself capable of being tracked by underwater vehicles via acoustics [107].

The field of acoustic positioning, called baseline navigation, is well established [108, 109], and is split into three subclasses depending on the separation of the active sensing elements, Long

Baseline (LBL), Short Baseline (SBL) and Ultra-Short Baseline (USBL) [110]. However, in each case, the underlying principle is the same and a series of transducers, or transducer arrays, is used to aid navigation by measuring the difference in arrival time of acoustic pulses.

From an application point of view, the principal difference between the technologies (LBL, SBL, USBL) is the configuration of the baseline stations. Figure 2.6 below shows the different configurations. Exact specifications for beacon spacing vary between systems and applications but the proportional orders of magnitude shown below are correct. Variations and permutations on the above three general categories are widely used [111, 112].

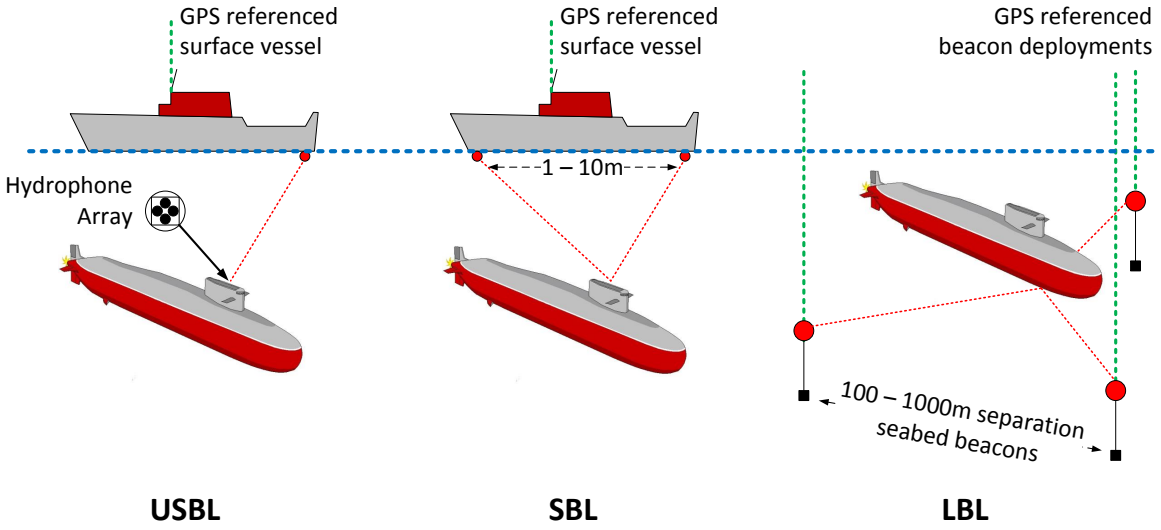

Figure 2.6 - The three main techniques for acoustic 'pinger' navigation underwater are Ultra Short Baseline (USBL), Short Baseline (SBL) and Long Base Line (LBL). LBL uses GPS position referenced beacons separated by a few hundred to a few thousand metres, SBL uses beacons spaced 1-10m apart allowing them to be mounted on a GPS tracked surface vessel, and USBL spaces the receivers by a few cm to create the baseline. Figures adapted from [15, 110, 113].

USBL systems are used over short ranges. A hydrophone array is used to measure time or phase differences in the arrival of an acoustic signal between individual elements of the hydrophone array, with a spacing of a few centimetres. This allows relative positioning to a surface vessel, or absolute positioning if the surface vessel is GPS referenced [15, 110, 114]. Compared to SBL and LBL systems, the initial cost and the operating cost and complexity is the lowest with no requirements for beacons to be deployed and recovered from the seabed [111]. Considering the application for kelp bed mapping, of the three baselines, USBL is the most suitable. However, detailed calibration is required, and redundancy is not inherent in the case of signal occlusion or interference [111].

SBL beacons are typically spaced a few to a few tens of metres apart, allowing them to be mounted on a surface vessel with a GPS receiver. This system provides a compromise between the two extremes of USBL and LBL, not requiring beacons to be deployed but still requiring multiple transponders to be mounted (and calibrated) on the surface vessel [111].

LBL systems establish transponder stations throughout the operating environment spaced from few hundred to a few thousand metres apart, either anchored in known fixed positions, or tracked with GPS. LBL provides good positional accuracy independent of water depth, redundancy and wide coverage [111]. However, the systems are typically expensive and complex [111]. Additional operational time, complexity and risk are introduced by deploying and recovering transponders in the hostile nearshore environment. Navigation solutions which do not require environment modification are preferred, partly for operational reasons and partly for the security of equipment being damaged or lost [99].

Although acoustic navigation is used across a range of fields for underwater navigation, it is not without its general limitations which must be considered. As with any relative navigation system, the positional measurements gathered are only as accurate as the position fix of the reference station in the world coordinate system [71]. Therefore, whether transponders are anchored and positioned using GPS, carried on a surface vessel, or free floating, all accuracies are referenced to GPS, and/or the anchored stability of buoys.

There are also acoustic limitations, in particular considering the shallow water of the nearshore environment. Reverberation from the surface and seabed can create multipath interference which can cause errors if confused with the direct arrival [71] or attenuate signals through destructive interference [111]. Disturbed sediment in the high flow regions of the nearshore, coupled with vegetation and a varied topography can attenuate or occlude acoustic signals which require an acoustic line of sight to operate.

Acoustic noise at the receiver also serves to reduce positional accuracy. This noise can be from a variety of sources. Ambient noise from waves, wind, rain, vessel traffic and marine life is common although less of an issue than other sources. Vickery [111] quotes heavy rain causing an increase of 15-25dB over background levels at 10kHz and shallow water approximately 9dB over deep water in the same sea state. Thus the wave and current action of the nearshore needs to be taken into account, as does noise from the kelp stipes in the flow. Noise from the operation of the underwater vehicle itself (thrusters, other acoustic instruments) can also be a limiting factor [111].

As with other acoustic navigation systems, for accurate operation, the varying speed of sound underwater needs to be measured and accounted for. Whereas in deep water, the speed of sound varies relatively slowly with depth, in the shallow water of the target nearshore environment, different salinities and water temperatures interact in a turbulent and unpredictable manner. As the speed of sound varies, often dynamically over the course of a deployment [71], this can cause ray bending and errors in the measurements [115]. Furthermore, in the confined and complex nearshore, objects, vegetation and bathymetry can obscure the acoustic line of sight and turbulent shallow water can become aerated, therefore degrading acoustic baseline tracking performance [116].

Acoustic positioning techniques, with these limitations and a low data rate, are often used in conjunction with inertial navigation systems, which although having a higher data rate, are prone to large cumulative errors. Although not always available, the errors of the acoustic positioning system are not prone to drift and can be used to bound the cumulative errors (drift) of an INS [117].

2.3.2.2.6 Sonar navigation

The more complex and sophisticated development of acoustic navigation is the use of active sonar for imaging, target recognition, identification and mapping.

Compared to vision, frame rates are often lower (in part due to the lower speed of sound), resolution and detail are lower, yet depth perception/ranging is inherent and sonar scans operate independent of visibility and light levels. Similar to acoustic navigation, sonar navigation is compromised by occlusion, secondary and multipath echoes and reverberation including off the sea surface when operating in shallow water. The varying speed of sound and perturbation from the aerated layer of water called the ‘bubble-layer’ found at the surface [46] also limit shallow water use. The bubble layer can reach from the surface to several metres deep, is dependent on

sea state and wind speed, is highly absorbent to acoustic signals, and causes backscattering and attenuation for sonar observations at the surface [46]. However, overall the use of sonar for navigation is highly successful with many applications, including nearshore shallow water operation.

In structured or partially structured environments [118], sonar can be used to recognise objects as navigational landmarks to assist with mapping and navigation [16]. When navigating in open-water unstructured environments, one option is to place artificial sonar markers to aid with navigation in areas otherwise sparse of navigational landmarks [17]. However, environment modification entails logistical disadvantages discussed previously, together with the unreliability of tethered markers in the high currents found in the nearshore. The alternative is to rely on a sufficiently diverse natural environment, with adequate identifiable acoustic features to enable navigation without environment modification [119, 120].

Given a sufficiently diverse environment, usually the seabed, then navigation aided by sonar in unstructured environments is possible [121], given the same requirements that terrain-aided visual navigation imposes – that is, proximity, visibility and diversity of the seabed [122]. However, in the kelp beds, as discussed in the section on terrain-aided navigation, given occlusion of the seabed by vegetation and the lack of an acoustically diverse seabed, this technique is challenging. The occlusion of targets by dense concentrations of gas-filled kelp stipes, whether the occluded targets are further kelp or the seabed, is a common one, as Smith [123] puts it "*a case of not being able to see the forest for the kelp*".

2.3.2.2.6.1 Single beam echosounders

An echosounder emits a single ping, and the returns (echoes) correspond to targets in the direction of the ping, but as the cone spreads, targets are included which are not directly collinear with the echosounder [46]. To build up an image of either bathymetry or the midwater is complex, as the echosounder must be panned over the target to image it, similar to raster scanning.

Successful techniques to correct mechanically panned echosounders for vehicle movement, and using probabilistic scan matching to enable navigation in *structured* marine environments have been previously demonstrated [124, 125]. The correction for vehicle movement during a scan is essential to reliable mapping and scan matching – without it, the vehicle must either be reliably stationary for the entire duration of a scan limiting operation, or risk objects being 'smeared', distorted, appearing twice, being missed altogether or incorrectly corresponded to previously observed features.

Side-scan sonars provide a one dimensional scan line formed from a very narrow beam (≈1°) in the horizontal plane perpendicular to the direction the vehicle is travelling in and wide (≈50°) in the vertical plane, thus spreading out sideways from the vehicle [46]. One beam is emitted on each side of the vehicle, and used to image the seabed as the vehicle moves. Although there is significant ambiguity in estimating bathymetry and targets from the side-scan returns, side-scan sonar has been successfully used for underwater vehicle navigation, provided that the bathymetry is diverse enough to present sufficient detectable features [120].

While errors due to movement during a scan can be corrected to some extent by robustness to sensor errors in mapping algorithms, if not handled correctly, they can cause significant mapping errors. Each sonar ping can be registered in 3D space using other sensors, and the sensor fusion

algorithms discussed later allow the 'folding back' of information to allow one sensor to correct another to yield an overall improvement in navigation capability.

2.3.2.2.6.2 Multibeam echosounders

The alternative to single beam mechanically-panned or vehicle-panned echosounders is multibeam echosounders. Multibeam units transmit several beams using an array of transducers to image an entire swath simultaneously generating a 2D spatial plot of acoustic return intensity [46]. This allows maps to be generated much more quickly, but also more reliably as the entire swath is imaged at the same time, so positional deviations of the vehicle or the targets during the scan do not occur.

Multibeam sonars are typically used for terrain-aided bathymetric navigation, provided the seabed is sufficiently diverse and within the field of view [126] or used in a forward-looking configuration for obstacle avoidance, midwater target tracking and navigation relative to static targets in the water column [127, 128]. In general, the cost, size, power consumption and processing requirements increase between single beam echosounders and multibeam units, before increasing further when considering the latest development of multibeam echosounders, 3D imaging sonars.

3D imaging sonars, such as the Echoscope manufactured by CodaOctopus Ltd. [129], typically retail for $165,000+ [130] and are thus outside the budget of this application, yet methods to achieve the same results on a fraction of the budget become one of the main points of this research in later sections.

2.3.2.2.6.3 Sonar fusion

Sonar fusion is often cited as an opportunity to increase detail, correct artefacts and reduce ambiguity by combining the information from multiple sonar frequencies, modes, beamwidths and configurations [18]. Concurrent acquisition of multiple sonar sensors avoids errors in registration when overlaying multiple datasets gathered at different times and reduces survey time and cost as only a single survey need be performed [131]. However, either sufficiently separate operating frequencies are required to avoid cross-talk and interference [131], or synchronisation of the transmit pulses is required [18, 132]. Development of realtime adaptive triggering of different sensors based on autonomous analysis of the incoming acoustic data, the realtime range to the target being imaged and the coverage of each device, can be used to interleave the various acoustic pings to maximise resolution while minimising crosstalk [27].

2.3.2.2.7 Visual navigation

Compared to other navigation and mapping sensors, in particular sonar, visual sensors are cheap, compact and under suitable conditions, can yield a high level of detail and resolution for both mapping and navigation [133, 134]. A great deal of success has been achieved in the field of computer vision for landmark detection, location and identification in AUVs worldwide [135] and successful visual-aided underwater station keeping [136-138], cable tracking [139] and benthic mapping [140] are widespread. However, the processing power required to process visual data is often high [133], and thus the power consumption of the vehicle is increased indirectly.

Given the difficulties discussed previously of using visual sensors for underwater habitat sensing, the same limitations of illumination, visibility, brightness and contrast variation, non-uniform

colour attenuation and a lack of ranging and scaling apply to using visual sensors for navigation [141]. However, considering applicability to the nearshore environment, the two most suitable techniques for visual navigation are detecting markers and seabed tracking.

The first technique requires artificial visual markers to be placed in the environment to use as landmarks to assist with navigation, either at known a priori locations, or at unknown but stationary locations. Although some development work into the algorithms at the University of Bath [142-145] has demonstrated identification and tracking of underwater visual markers in confined environments, this technique has limited application in real-world open ocean environments. In kelp beds, the limitations are the same as deploying acoustic beacons for navigation; the logistics of deployment and recovery, the high currents affecting the position of markers, and specifically for vision, often low-light and low-visibility conditions restrict the usefulness of these markers.

The alternative technique, seabed tracking using visual navigation, sees more widespread use in the open ocean [146], but again, operating environments and conditions are restrictive. Whilst the kelp beds are often in shallow water and so the seabed is in close proximity, it is rare that the visibility is such that the seabed is visible from the midwater. Additionally to observing the seabed in sufficient clarity, the tracking algorithms require a sufficiently diverse seabed [147] and unless uniquely identifiable landmarks exist for correspondence to later re-observation, seabed tracking is a form of dead reckoning and is prone to large cumulative errors [148].

Hybrid systems exist, which are capable of visual-aided navigation from seabed tracking when the seabed is sufficiently diverse, and recognising artificial user-deployed markers on the seabed in areas of low-variability, or low-visibility [149].

2.3.2.3 Uncertainty

As the robot finds itself operating in often unstructured and inherently unpredictable environments, yet still requiring an accurate navigation system, it is important to appreciate the uncertainties associated with the problem. If uncertainty is defined as ‘operating without definite and complete information’, then the five commonly cited [150-152] sources of uncertainty for mobile robots can be adapted and supplemented when considering uncertainty in an underwater application:

Uncertainty arises from the inherently unpredictable, unstructured and often dynamic nature of the robot’s operating **environment**. Ocean currents, wave movement, dynamic untethered or anchored targets can all serve to increase environmental uncertainty,

Sensors are inherently limited in what they can perceive arising from two factors. Firstly, the range and resolution of a sensor is subject to physical laws – for example, cameras cannot see through opaque objects, environmental conditions determine the perceptual range, and the spatial resolution of a sensor is finite. Secondly, sensors are subject to noise, aliasing, ghosting (false positives) and missed objects (false negatives); the information is often incomplete and imperfect.

Mobile ‘free’ robots (implying operating free from constraints on their degrees of freedom) have a large degree of uncertainty associated with their **movement**. With every unconstrained Degree of Freedom (DoF), the uncertainty increases. For example, there is a relatively low-level of uncertainty associated with a robot operating on a rail or track system (e.g. a train). However, increasing the degrees of freedom to allow unconstrained 2D mobility (e.g. a car) increases the

uncertainty. If the full 6 DoF are unconstrained (e.g. an airplane, submarine, or underwater robot) then the level of uncertainty associated with movement is high. In each DoF, not only will the actual movements differ from the expected, but the robot is also likely to be subject to external forces affecting its movement. The tether can act as an unpredictable constraint on movement, with nonlinear drag characteristics and the danger of entanglement.

As **models** are abstractions of the real world and incompletely represent the underlying physical processes of the robot and its environment, they are inherently inaccurate. These inaccuracies translate into uncertainties when using the model and must be accounted for [152].

Mobile robots often impose constraints on the **computing power** that can be carried onboard, in terms of physical dimensions and electrical power available. Additionally, as robots are realtime systems, their operation can also be constrained by the computing power available. This forces algorithms to achieve a timely response, which in many algorithms is achieved by approximation – sacrificing accuracy for speed.

As Thrun et al. [150] state, the ability to cope with uncertainty in both perception and action is critical to building successful robots.

2.3.2.4 Sensor fusion

The difficulties of navigating underwater, many of which are compounded in the nearshore, have been identified in previous sections. In many environments, navigation from a single sensor alone is not possible, due to inherently limited sensing conditions underwater [15]. However, as discussed, benefits can be achieved in terms of navigation accuracy and reliability through sensor fusion. This technique provides an improvement in information (accuracy, reliability, speed) by combining information from multiple sources (a priori information, multiple measurements, multiple sensors).

2.3.2.4.1 Levels of sensor fusion

There are three commonly distinguished levels of sensor fusion applicable to nearshore navigation, commonly represented as *signal*, *pixel* and *feature* based sensor fusion [153, 154].

Signal level fusion combines signals from similar sensors to produce a composite signal in the same form as the original components, but in some manner 'better' (accuracy, reliability, information content, etc.). Spatial and temporal registration is required between the similar sensors for fusion to occur [15]. A common example of signal level fusion is combining INS with GPS.

Pixel level fusion is the equivalent at a pixel level, where multiple images (from the same or different sensors/modalities) are fused to obtain a 'better' image [15]. As above, registration between images is required, and thus content and resolution usually have to be similar.

Feature level fusion includes the commonly cited example of combining sonar for detection with vision for identification. In this case, objects in the real world have already been discriminated from their surroundings as features, so either sensory or mapped data can be incorporated into the fusion, with temporal and spatial registration augmented by the correspondence of new measurements with previously recognised objects. Thus, feature level fusion is the most flexible way to fuse different sensor modalities, as the sensor-specific conversion from sensor data to the abstract feature level has already been performed.

A second distinction is also commonly made between direct and indirect sensor fusion. McKee [155] defines direct fusion as combining data from a set of heterogeneous or homogenous sensors and historical values of sensor data, whereas indirect fusion uses a priori knowledge and human input.

2.3.2.4.2 Direct sensor fusion

Considering specifically the direct fusion of multiple measurements from different sensors, if disparate sensors are used, then shortcomings in one sensor or modality can be overcome by others to yield a more reliable overall estimate.

As an example, the sonar is able to provide low-resolution data over a high range, irrespective of darkness and turbidity, the opposite (*complementary*) characteristics to the vision system. Thus, vision proves useful for *identification* over a short range, but sonar is more useful for long range *detection* of objects and benefits can be gained from the combination of the two [156].

If the control system of the vehicle is aware of the sensor capabilities, then operation can be tailored to exploit maximum spatial coverage. When searching for, or mapping an object in the water, an initial sweep using the sonar can be used to detect the presence or absence of objects in the water over a long range. The locations of these objects are then flagged on the map (range and bearing) for later investigation. The vehicle can then move closer to each of these objects in turn for closer inspection and identification by the camera.

Extended temporal coverage can be realised by combining the benefits of relatively slow to update sensors with those much faster, for example, the relatively slow update speed of a mechanically-panned sonar with a fast updating accelerometer.

Sensor fusion also allows the combination of idiothetic and allothetic sensors: robustness against interference is gained from using idiothetic information, while drift and cumulative errors are avoided using allothetic sensors [157]. A regularly cited example for underwater vehicles is the combination of dead reckoning INS measurements [89, 90] with drift free GPS updates when surfacing, with particular application when operating at shallow depths [158]. This technique is often expanded to include acoustic methods, to increase the information available when acoustic conditions permit [88] or extended to include visual sensing when visibility and visual diversity permit [156]. Inherently scalable sensor fusion architectures allow additional sensors to be integrated directly into the fusion algorithms to incorporate their benefits [159].

Finally, sensor fusion provides a technique to maximise the accuracy and reliability which can be obtained from the low-cost limited sensing available in the nearshore. For example, a very high budget Fibre Optic Gyroscope (FOG), DVL and USBL system can yield a drift of a few metres per hour with a DVL aided INS, which the use of a USBL transponder can bound a drift-free error of a few metres or less [117]. On a lower budget, Majumder et al. [156] describe a framework for combining information from several physically different sensors into a single composite multi-dimensional scene description to provide more robust navigation and mapping than if a single sensor mode was used alone. The principle of this research is similar, to use sensor fusion to increase accuracy and to bound drift, yet on a significantly lower budget.

2.3.2.4.2.1 Redundancy and voting

There are a variety of techniques to perform direct sensor fusion. Simple averaging of multiple sensors can lead to misinterpretations in the case of sensor failure [160]. Perhaps the simplest

technique to provide fault-tolerance or to compensate for sensor unavailability is to provide redundant sensors measuring the same quantity/space and to exclude the non-functioning unit. This can either be implemented with three or more sensors measuring the same quantity with a voting algorithm [161] or with two or more units with a fail-silent behaviour [162].

The highly dynamic environmental conditions of the nearshore can rapidly cause one sensor modality to become ineffective, for example cloudy water obscuring vision. Sensor fusion provides a framework to automatically use alternative modalities for continuing navigational reliability and robustness Even with the same sensor modality, multiple corroborating measurements of the same domain increase confidence [163].

This process of 'deciding' which sensor to use can be developed to intelligently select a sensor based on a confidence measure or suitability to a task, e.g. vision for short range, or sonar for long range. Alternatively 'guiding' can be used to focus one sensor onto part of the scene [160], for example, long range detection of objects by sonar for later investigation and identification with vision. Guiding range sensors using intensity images is a long established technique [164]. However, this is sensor integration; sensors are used sequentially which does not necessarily provide redundancy [160].

Provided the sensors can be correctly characterised, it can be proved that sensor fusion performs better than simply selecting the best sensor [165, 166]. Elmenreich [167] distinguishes between imprecision and uncertainty, stating that sensor fusion allows multiple independent measurements of the same property to be fused with a better precision than an individual measurement alone. Uncertainty however, depends on the measurand rather than the sensor, and arises when one sensor cannot measure all of the attributes of an object, or when an object is occluded, etc. Again, with sensor fusion, this uncertainty can be reduced [167]; each of the sensors provides only a small piece of information, and sensor fusion is used to compile the overall estimate.

2.3.2.4.2.2 Probabilistic fusion and Gaussian filters

A more sophisticated technique represents the uncertainty associated with mobile robot operation, including each sensor, with probability distributions [168]. This combination using Bayesian estimation theory was first formalised in 1985 [169] and shown to be a simple form of Kalman filter [170]. Kalman filters rely on recursively updating a state estimate with a prediction and then a correction from another source. The weighting of the prediction and correction is determined by uncertainty [171]. The technique was extended to manipulate and integrate uncertainty in perception, by characterising sensor uncertainty [172].

These probability distributions allow information to be represented over a whole space of possible hypotheses rather than just a single 'best guess' of what might be the case in the world, allowing a mathematically sound representation of ambiguity and degree of belief [150]. By representing the uncertainty associated with each sensor, an informed fusion of sensor data is possible. The central conjecture of Thrun et al. [150] when considering the implications of probabilistic robotics is "*a robot which carries a notion of its own uncertainty and that acts accordingly is superior to one that does not*".

To achieve probabilistic fusion, each sensor has to be modelled by a probability distribution, commonly a Gaussian distribution. The representation assumes a mean value is measured, but that measurements are corrupted by noise/uncertainty/errors represented by the variance of the Gaussian distribution [160]. Correspondence, registration and consistency checks between

multiple measurements are commonly performed by maximum likelihood estimates [160] or using the Mahalanobis distance between distributions [173], a distance measure based on correlations between variables of an unknown sample set to a known one [174].

Probabilistic approaches are widely deployed to applications of underwater sensor fusion. Techniques to deal with the varying availability of sensors underwater are also in existence. For example, Rendas and Lourtie [175] describe a system to maintain navigation accuracy over long duration surveys. The system uses arrays of LBL beacons carefully spaced at intervals throughout the mission. When in range, the LBL system is used to yield a relatively high positional accuracy and when out of range it relies on sonar, DVL and depth sensors for navigation. The switching process between when the LBL beacons are available, or not, is autonomous and the sensor fusion system adapts to incorporate this additional information using a variable dimension Kalman filter. When accelerations are detected, the vehicle switches to a larger order Kalman filter used for manoeuvring, however, when a long straight line path is being followed, a lesser order Kalman filter is used. In this case the sensor fusion takes place at the signal level [15].

For comparison, Loebis et al. [15] present an example of feature level fusion: an AUV used to track and survey underwater cables using vision in regions of varying visibility. The cable is frequently lost from view, however a high-level controller and 2D-position model of the cable are used to predict the most likely region of the cable within the image to reduce the processing time of searching the entire image. When the cable is not visible in the image, then the 2D-position model is used for navigation to predict where the cable is likely to return to the field of view and this is used to navigate the vehicle through periods of low visibility [176].

Probabilistic approaches typically place weaker requirements on the accuracy of models, thus algorithms are more robust to simpler sensor models. Additionally, by considering the full uncertainty rather than just the most-likely guess, probabilistic techniques are typically more robust in the face of sensor limitations, sensor noise, environment dynamics, etc. [150], making them ideally suited to the underwater environment where often a noisy and incomplete dataset is compounded by a dynamic environment.

However, despite this broad applicability of probabilistic approaches for sensor fusion, there are disadvantages, requiring a careful application-specific selection of the sensor fusion technique. Durrant-Whyte [177] identifies the four main perceived limitations as the *complexity* required to specify all required probabilities in order to correctly apply the methods, *inconsistencies* between specifying beliefs and obtaining deductions of state, the required *precision* of models when uncertainty is high, and the difficulty of representing *ignorance* or ‘uncertainty about uncertainty’. The need to specify independent probability distributions, and a sensitivity to dynamic environments are also cited as limitations of probabilistic approaches [178].

The most commonly cited limitation is computational complexity resulting from considering the entire probability density, rather than just a single most-likely hypothesis [150]. Additionally, as most robot worlds are continuous there is a need to approximate the world into discrete points for evaluation by the algorithm. As the resolution with which the world is discretised into is directly proportional to the computational time required and the accuracy of the results, the resolution used is an important consideration. In some cases, the uncertainty can be approximated tightly with a compact parametric model such as discrete or Gaussian distributions. In other cases, such approximations are too crude and more complicated representations must be employed [150].

Estimation techniques like the probabilistic approach described above can be extended to symbolic information using reasoning and inference techniques in the presence of uncertainty using constraints [174] which can again be managed using Bayesian techniques [179].

2.3.2.4.2.3 Dempster Shafer theory

Alternative methods of sensor fusion also exist, the two most commonly used are the Dempster Shafer (DS) theory of evidence and fuzzy set theory [178].

The DS theory [180] provides a framework to combine evidence from independent sources by assigning probability to propositions [160]. The result is a belief function which takes into account all of the available information, and which can provide a measurement of conflicting sources. Compared to Bayesian approaches, where all probabilities must be clearly defined and thus which can limit their application, DS approaches allow a distinction between ignorance (uncertainty) and contradiction [181], or the distinction between uncertainty and risk [182]. Thus, when prior probability distributions are not completely modelled or known, a degree of ignorance (or uncertainty about uncertainty [177]) can be specified in the DS theory.

As described by Hackett and Shah [160], the DS theory is based upon an interval of uncertainty. Defining proposition A, then $s(A)$ denotes the support for proposition A and $p(A)$ is the plausibility of proposition A. The interval between $p(A)$ and $s(A)$ is the interval of uncertainty $[s(A), p(A)]$ about proposition A. If the uncertainty is zero, then this is the same as a Bayesian approach as the support for proposition A is equal to the maximum likelihood. Support is the total positive effect a body of evidence has on a proposition, whereas plausibility represents the total extent to which a body of evidence fails to refute the proposition [160].

Thus the DS theory differs from the Bayesian approaches discussed in the previous section, as the interval of uncertainty can be used to represent uncertainty surrounding a proposition. The Bayesian approach can only use a single probability value to represent the probability that the proposition is true, thus requiring more complete information as the interval of uncertainty cannot be represented. Additionally, Bayesian approaches require independent measurements by definition, and inconsistencies develop when measurements are related [160].

Depending on the application, in high-risk applications, it can be safer to be undecided about a hypothesis, than to act wrongly based on a marginally higher belief of one of several conflicting hypothesis. Thus the capacity for ‘ignorance’ about a situation is, in some applications, considered an advantage of the DS theory [182].

Differences in computational complexity between Bayes and DS implementations vary between applications with some sources stating reduced complexity over Bayes implementations [183-185]. However, the consensus for the majority of applications appears to be that DS implementations incur a higher computational complexity [186].

2.3.2.4.2.4 Fuzzy set theory

Fuzzy set theory, or approximate reasoning [187], is a third, less common method used for combining imprecise assertions and inferences which can be applied to the fusion of several uncertain sensor measurements, although more widespread for supervisory control and high-level data fusion tasks [177].

Although application and implementation specific, fuzzy logic approaches have been cited to perform better in unstructured environments [188] and have a higher robustness to outliers [189]. However, robustness to outliers and filter divergence between two different hypothesis can be avoided by using fuzzy logic techniques to develop an adaptive Kalman filter [190], thus combining the benefits [15]. Even this however has its limitations, relying on trial and error to generate the fuzzy rule based algorithms [15]. Techniques to optimise the fuzzy systems were reviewed by Loebis et al. [15] to include genetic algorithms [191, 192], neural networks, chemotaxis, alopex and simulated annealing [193, 194]. The conclusion drawn is that no one fusion method is the perfect solution, and the associated benefits and limitations must be compared on an application-specific selection process.

2.3.2.4.3 Indirect sensor fusion

Indirect fusion was defined as using information sources like a priori knowledge about the environment. If the robot was simply placed in a new environment and left to localise and map its environment using just its onboard sensors then this is direct fusion. However, if information can be provided to the robot in advance, for example the geometry and dimensions of the tank it is operating in, or a topographical map of the seafloor, then this gives the sensor fusion algorithm one more source of data when considering the localisation and mapping. A priori information need not be 100% accurate as no measurements ever can be, and it is the task of the sensor fusion algorithm to assess the reliability and accuracy of a priori information as it does for the realtime sensor data.

Indirect sensor fusion is less common than direct fusion, but includes the examples discussed previously in section 2.3.2.2.4 on geophysical navigation where a priori maps of the operating environment are fused with ongoing sensor measurements to improve the navigation capability.

Several implementations of integrating terrain-based navigation into sensor fusion algorithms already exist which use either pre-existing a priori bathymetric profiles of the study area or a bathymetric map gathered on-the-fly. The benefits of navigation by matching a local bathymetric scan with a reference map avoids the use of transponder based positioning systems which require costly and time-consuming deployment and recovery in the study area [195]. Similar research integrating a priori underwater map-aided navigation comprising a database of benthic depths has also been implemented by Karlsson and Gustafsson [196] using a Bayesian probabilistic framework for surface vessels. This was developed for underwater vehicles by Di Massa [197] where the accuracy of results depends on the bathymetric variability in the operating environment (it is difficult to localise in sparse featureless environments).

Tracking the seabed with reference to a priori bathymetric scans provides drift free, absolute measurements compared to a dead reckoning DVL system. Additionally, bathymetric tracking using sonar does not require clear water or such close proximity as seabed tracking using vision.

Integrating terrain-based navigation provides corroborative information from a single depth measurement to either a pre-existing bathymetric profile chart (indirect sensor fusion) or to a simultaneously constructed map (direct sensor fusion). However, a topographically and acoustically diverse benthic composition is required for navigation using detailed small-scale sonar seabed topography tracking alone [70]. Instead, as Newman and Durrant-Whyte [70] state, navigational robustness and reliability in both natural and artificial environments can be achieved through a *fusion* of inertial and sonar information.

Usually the underwater vehicle begins in a new environment with no prior knowledge of its surroundings. However, any a priori knowledge which can be provided to the vehicle in advance aids its autonomous navigation and operation. In some cases, the user is able to confirm simple details about the operating environment, for example when operating in a uniform environment (e.g. a harbour or tank) the user can confirm the dimensions and depth of the tank and that a flat floor extends over the entire area. When operating in a dock environment the user can confirm the shape and acoustic (sonar) characteristics of the dock pilings even if the user is not able to confirm actual positions. The benefits of including the remote operator in the control system (user in the loop) in certain scenarios and applications are discussed further in the iROV sections below (2.3.2.6 and 2.5).

Alternatively, in some cases a complete or even incomplete topographical or landmark based map can be provided in advance – for example by digitising marine topographical charts, or by performing a high-speed low-detail GPS referenced sonar scan of the operating area in advance by a surface vessel. Techniques such as these can accelerate autonomous operation of the underwater vehicle by providing a broad overview of the study area in advance which the vehicle can then populate with detail as it explores.

Any a priori information, provided it is recorded with an appropriate certainty, is useful to the vehicle – as is any information gathered during the autonomous exploration, provided it is recorded with an appropriate uncertainty estimate. A small number of distinctive landmarks recorded on the map with a high certainty and GPS latitude and longitude can aid the robot greatly in quickly mapping its environment and provide a reference in the world coordinate system of latitude and longitude.

2.3.2.4.4 General limitations of sensor fusion

Sensor fusion, regardless of method, is not without criticism or its limitations.

As Fowler [198] stated: "*This is a great idea provided the input data are a good quality. Massaging a lot of crummy data doesn't produce good data; it just requires a lot of extra equipment and may even reduce the quality of the output by introducing time delays and/or unwarranted confidence… Be wary of proposals for synergistic systems. Most of the time when you try to make 2 + 2 = 5, you end up with 3 ... and sometimes 1.9.*"

Compared to a single measurement, or simple best sensor selection method, complex sensor fusion methods incur a computational penalty [165] dependent on sensor resolution, particularly relevant given the limited processing power onboard an underwater vehicle. Considering a generalised framework, the computational complexity can be seen as follows [15]. Information from different sensors needs to be co-registered in the same temporal and spatial coordinate system, correspondences established of which features in one sensor refer to the same aspect/feature in the other, followed by fusion of the two data sources (with a variety of methods discussed later in 4.7). Following fusion, inference of a conclusion based on the uncertainty of the source data is required, with reconfiguration of the mission / sensing strategy to direct the next measurement to reduce this uncertainty [15].

When assessing the benefits of sensor fusion, the measures of performance used are often specific to the application, but in general include the accuracy, reliability and reaction time [199]. An assessment of the incremental benefits gained from integrating an additional sensor to the suite is also an important consideration [200] given the finite cost, space, weight and power budgets available to the underwater vehicle.

2.3.2.4.5 The opportunities for nearshore sensor fusion

As Majumder et al. [156] acknowledge, the techniques and benefits of multi-sensor fusion have been investigated for several years, but the development and application of these theoretical solutions to real-world applications is the cutting edge of research into mobile robot navigation. This research seeks to develop techniques for fusing data from multiple complementary sensors to improve the navigation capabilities of underwater vehicles in the notoriously difficult to navigate in and hostile nearshore underwater environment.

In the dynamic nearshore environment, operating conditions can change rapidly, often in the short period of a mission, particularly when moving between the different operating regimes. Such conditions can include varying depth, varying proximity to visual and sonar landmarks, varying proximity to ferromagnetic structures, murky or dark water, varying sea-state, tides, currents and water movements causing sudden fast accelerations or long steady movements, which can all affect the information available.

For example, as the water becomes turbid, cameras are less effective, or, as the vehicle passes magnetic environmental anomalies (such as ferrous structures), inaccuracies can appear on the magnetic compass data. Not only must the sensor fusion algorithm combine the data from each of the sensors to improve the reliability and accuracy of the overall position estimate, but it must also be able to cope with the dynamic characteristics of each of the sensors.

Nearshore sensor fusion also provides an opportunity to realise the benefits (e.g. accuracy, robustness, etc.) of significantly higher budget sensors by intelligently fusing the data from multiple lower budget sensing modes, a recurring theme of this research.

2.3.2.5 Localisation and mapping

The previous sections have considered the navigation sensors, and techniques to fuse the information from selected sensors to improve the reliability and the accuracy of information. This information is used for underwater navigation, that is, tracking the position of the vehicle and mapping the environment. This allows survey data to be recorded with a position reference and permits varying levels of autonomous control.

With this goal, it is important first to define some terms: **localisation** and **mapping** are defined below and **navigation** is considered in the following section (2.3.2.6).

Localisation is the process of estimating a robot's position in an external reference frame from sensory data when the robot is placed at an unknown location in the environment and has to localise itself from scratch [201, 202]. The pure problem of localisation assumes a known map. Cox [157] states that 'using sensory information to locate the robot in its environment is the most fundamental problem to providing a mobile robot with autonomous capabilities'.

If there is no map of the environment available then the robot has no a priori information available to it. The problem then becomes one of **mapping** – the pure problem of mapping assumes that the location of the robot is known [203].

However, in many cases, the robot is placed at an unknown position and has no knowledge of a map – in this case, the problem becomes one of **Simultaneous Localisation and Mapping (SLAM**), first coined by Leonard and Durrant-Whyte in 1991 [204].

A variety of localisation and mapping techniques exist, including well established techniques for SLAM which can be applied to underwater navigation. A series of reviews over recent years have updated these techniques [71-73, 150, 171, 205, 206]. Those most applicable to the nearshore navigation application are discussed here.

2.3.2.5.1 Geometric probabilistic SLAM (Gaussian filters)

The same probabilistic framework introduced earlier for sensor fusion (2.3.2.4) can be applied to SLAM. In the case of Gaussian filters, the estimate of the robot's state is represented by a mean value, centred on the most likely value, with a variance (or covariance for multivariate distributions) representing the level of uncertainty. Features in the environment which can be used for navigation are stored on the map as landmarks, and also parametrically represented by a mean and (co)variance of a Gaussian (normal) function.

Probabilistic SLAM provides the same benefits as probabilistic sensor fusion, including computational efficiency resulting from the parametric representation, and the ability to track and act on uncertainty. Probabilistic SLAM is also capable of global localisation with no a priori information [150]. This is otherwise called the *kidnapped robot problem*, where a mobile robot must either recover from localisation failure, or must localise itself and map an environment with no a priori information and no global positioning device (such as GPS) [207].

The most common technique to solve the SLAM problem is the Extended Kalman Filter (EKF) [208], a development of the standard Kalman Filter (KF), introduced previously in the context of sensor fusion (2.3.2.4).

The standard Kalman filter recursively estimates a state estimate using a prediction/correction cycle. However it requires data and models to be linear, and so cannot be used, for example, with circular orientation data, etc. The requirement for data and models to be linear is overcome by the Extended Kalman Filter (EKF). The EKF linearises the data to allow the standard KF process to be used. First used for SLAM in 1987 [209], the EKF is now widespread for mobile robot SLAM, including extensively underwater [16, 17, 121, 147, 210-212].

Although the parametric representation provides computational efficiency by discarding unnecessary data, the EKF SLAM algorithm is still not the most efficient solution. The EKF SLAM has quadratic complexity[6] [208], so the run time increases proportional to the number of landmarks in the map squared. The memory requirements are also proportional to the number of landmarks squared. Thus, landmark selection is an important consideration for EKF SLAM. Too few landmarks and the map and localisation accuracy is compromised and the uncertainty in the robot's positional estimate can grow too large for Gaussian filters to be effective. Too many landmarks causes the computational complexity to slow the frequency of updates, again compromising accuracy. Techniques for map management to reduce the number of tracked landmarks, such as correct association of features to avoid duplicates, or decaying spurious observations, are discussed later in this document. When working with large numbers of landmarks, mutual exclusion techniques can be applied to reduce the computational complexity

[6] The time complexity of an algorithm refers to the amount of time taken to run the algorithm based on the number of elementary operations performed, expressed as a function of the length of the input to the algorithm represented as a string [213]. Therefore the time taken to run an algorithm with constant time complexity does not depend on the size of the input, and the run time of an algorithm with linear complexity increases linearly with the size of the input.

along with efficient searching and outlier rejection, for example only considering nearby landmarks when operating in a large environment [150].

One alternative to using the EKF is to pre-process the sensor data to be linear so that the standard KF can be used with significant computational savings [89]. Further techniques include the compressed EKF SLAM algorithm (C-EKF) which simplifies the covariance matrix (discussed later) used to store and track landmarks. This technique reduces the computational complexity to be linearly proportional to the number of landmarks [214].

In many SLAM implementations, the mapped environment is sparse, with isolated landmarks spread intermittently throughout [215], hence there are opportunities again to increase the algorithm efficiency by joining several detailed local submaps [216]. Provided the distances between landmarks are not too great, a map sparse of landmarks can be suitable to localisation. However, it is not necessarily suitable for mapping or autonomous navigation, including path-planning [208].

Techniques towards more detailed yet still computationally efficient representations include Scan-SLAM [217] and VorSLAM [208]. Scan-SLAM represents landmarks by templates composed of raw scan data, rather than as parameterised features (Gaussians) in the standard EKF SLAM approach [217]. The EKF algorithm is still used for probabilistic localisation and mapping, yet Scan-SLAM allows landmarks with arbitrary shapes to be accurately represented permitting more robust data association.

Similarly, VorSLAM represents landmarks as isolated features in the map using the EKF, but around each landmark, a more detailed map represents the environment [208]. This provides a more complete representation of complex unstructured environments, allowing sensory information which cannot be modelled as geometric parameters, such as the Gaussians used in EKF SLAM, to be represented using arbitrary shapes if required, or the more standard points and lines while maintaining efficiency [208]. Voronoi division[7] is used to build the local maps, ensuring maximum computational efficiency in the representation by ensuring no overlap of local maps and correct scaling. The local maps also have the potential to reduce data association errors when working in confusing environments [208]. A compromise is provided between the efficient landmark based representation and a full but highly memory-intensive representation of the environment.

The unimodal Gaussian representation works well for local position tracking where the uncertainty is relatively small. As an example, Thrun et al. state a rule of thumb that if the standard deviation for the orientation is greater than ±20° then linearisation effects are likely to make the EKF algorithm fail [150]. The opposite is true for nonparametric filters which are better suited to global localisation problems or local localisation with a high uncertainty.

To meet the limitation of representing a single belief with a unimodal distribution, an extension of the same compact and efficient EKF algorithm but capable of tracking multiple hypotheses was developed in 1979. The multi hypothesis tracking (MHT) EKF uses multiple Gaussians to represent and track multiple hypotheses [219] with a corresponding increase in computational complexity [150]. This has since been updated and widely used for underwater navigation [220, 221]. Multi hypothesis tracking (MHT) Gaussian filters can use negative information to some extent by decaying mixture components (possible hypotheses) that failed to observe a landmark.

[7] Voronoi division divides a plane of points into convex polygons such that each polygon contains exactly one of the points. The polygons are specified such that any position in a given polygon is closer to the generating point than to any other point [218].

A major disadvantage of Gaussian filters is the inability to model hard spatial constraints. These can be better approximated using MHT algorithms but are still hard to model. The example used by Thrun et al. is 'the robot is close to a wall but cannot be inside the wall' [150]. It can be seen here, that if the belief that the robot is close to a wall is represented by a Gaussian, then the Gaussian is going to overlap with the wall suggesting that, albeit with a low probability, the robot is within the wall which contradicts the hard spatial constraint. MHT algorithms can approximate hard spatial constraints using mixtures of Gaussians but the spatial constraint is never definite – the analogy is approximating a square wave with a Fourier series of sinusoidal waves.

2.3.2.5.2 Graph SLAM

A second common technique for SLAM represents the environment and state as a sparse graph of constraints. The Graph SLAM algorithm uses nonlinear optimization to generate the map and the robot's location throughout the map [206].

Computational complexity is nearly opposite to the EKF methods discussed above. Whereas the EKF SLAM algorithm integrates every new piece of information to update the state estimate of the vehicle and the map, the Graph SLAM algorithm accumulates new information into the graph without resolving it. Therefore, updating the Graph SLAM algorithm with new information is computationally relatively simple, whereas updating the EKF can be complex depending on the map and state size [150].

As the EKF method incrementally and recursively updates the state and map estimates, the algorithm can run indefinitely. Conversely, the Graph SLAM algorithm retains all information, all robot path estimates, all landmark observations and associations, and all map data. Thus for long durations, the Graph SLAM algorithm can grow to be unmanageable. However, provided a pre-determined dataset size is known in advance, the Graph SLAM algorithm can more efficiently manage maps which are many orders of magnitude larger than the EKF method [150].

Hybrid solutions have been developed to combine the computational efficiency of topological methods with the detail of metric maps [222]. The computational complexity of the EKF and C-EKF algorithms discussed previously can be further reduced to constant time using the sparse extended information filter (SEIF) SLAM algorithm [215]. This combines the benefits of the EKF algorithm, which performs online SLAM and maintains a current estimate of vehicle state, with the computational efficiency of the offline Graph SLAM algorithm, which simply accumulates information and turns the accumulated information into a map using inference, after all data is acquired [150]. However, the EKF is often favoured for landmark SLAM over potentially more efficient information filters as the covariances are available for data association without any further computation [16].

More recently (2012), techniques to solve the kidnapped robot problem using hybrid metric/topological maps have been proposed capable of global localisation [223]. These techniques use the Bayesian (Kalman) filters introduced previously, but combine topological maps similar to the Graph SLAM techniques. This hybrid solution seeks to avoid the environmental detail often lost in topological techniques [223], where parametric representations discard local detail, or environmental detail is lost in between features.

2.3.2.5.3 Nonparametric filters

The EKF and Graph SLAM techniques introduced above represent the vehicle's state and features in the environment parametrically. This leads to a compact and efficient representation when applied to suitable scenarios and applications. Particle filters however are the opposite, and represent state and the map non-parametrically by discretising the continuous state space into a finite number of values.

Occupancy grid maps (OGM) represent a map of the environment as an evenly spaced array of variables where the state of each element of the grid represents the presence or absence of an object with a binary 1 or 0 [150]. Initially, with no a priori knowledge, the entire grid is 'undefined' and 1s and 0s are filled in as either positive or negative knowledge provides further information. Inverse measurement models are used to populate the grid as the robot explores. The inverse measurement model for each sensor reasons from effects (measurements) to causes (occupancy) [150]. For example, given a sensor measurement and pose, which OGM cells can be confirmed as empty and which can be confirmed as occupied. However, the standard OGM algorithm does not maintain dependencies (for example the position of one landmark relative to another) in the estimate of occupancy.

The quality of the representation and the computational complexity are dependent on the number of values used for the approximation, i.e. the map resolution. An application specific compromise has to be reached, which can include a variable resolution. In large, sparse areas of open space, a coarse grid resolution is used to reduce computational complexity. However, in complex, detailed, highly-populated areas a finer grid resolution is used to allow an accurate representation.

Landmark selection also has the same compromise on complexity versus accuracy of the representation. If too many landmarks are used then the computational complexity can become unnecessarily high; conversely, if too few landmarks are used, then the localisation algorithms can fail in sparse areas.

Particle filters are well suited when the state, measurements, or environment cannot be approximated by a parametric representation (a Gaussian for the EKF) and a more complex representation is required. The computational complexity is proportional to the complexity of the representation. Techniques which can adjust the representation complexity in realtime, in response to the perceived complexity of the state and the computational resources available, are called resource adaptive algorithms [150].

Particle filters have been used with success for underwater navigation when the environment is complex with multimodal multidimensional density functions, albeit at a greater level of computational complexity [139]. Two examples are grid localisation (GL) and Monte Carlo localisation (MCL). These algorithms are able to process raw sensor measurements without having to extract features. This allows them to process negative information, for example the absence of an object can be confirmed which allows for more robust localisation. Because GL and MCL algorithms are non-parametric they are not bound to a parameter representation such as the unimodal distribution used by the EKF localisation algorithm. In particular, this allows for representation of beliefs which do not satisfy a Gaussian approximation and allows multiple hypotheses to be represented and tracked.

However, the computational efficiency of the parametric representation used in the EKF SLAM algorithm and its variants is lost when using GL and MCL techniques [150]. Parametric algorithms

such as the EKF can be very computationally efficient if implemented correctly. Computational complexity is increased in the MHT algorithm, and by the nature of their non-parametric representation, GL and MCL algorithms usually increase computational complexity further [150].

A significant advantage of nonparametric filters is the ability to localise in dynamic environments. This overcomes the requirement for Gaussian filters, that the world is static and the only variable is the robot's pose. Normally, dynamic environments can only be accommodated by probabilistic approaches if the dynamic variable is independent at each time step in the same way as sensor noise is accommodated. However, if the environment variable is persistent over several time steps, for example a moving boat, then the parametric algorithms discussed previously are likely to fail. If nonparametric filters are used, then either state augmentation or outlier rejection can be used to deal with dynamic environments.

State augmentation includes the dynamic state in the state estimated by the filter. However this increases complexity with the more dynamic variables introduced [150]. Outlier rejection aims to reject measurements likely to be caused by unmodelled environment dynamics. Although this has the potential to be more efficient than state augmentation, if localisation is temporarily lost and the robot must perform global localisation, there is a danger that every measurement will be rejected as an outlier, requiring careful evaluation to avoid [150].

2.3.2.5.4 SLAM – state of the art

The challenge of *simultaneous* localisation and mapping with no a priori information is complex. However, to many, the problem of SLAM in structured environments with good sensing is widely regarded as a solved problem [171], at least at a theoretical and conceptual level [212]. Algorithms have been developed which are able to solve the SLAM problem for small/medium structured underwater environments [16]. However, these algorithms make several assumptions on the sensory information available and the structure of the environment, and are thus not yet suitable to SLAM in the unstructured kelp beds. As Durrant-Whyte and Bailey discuss [171], substantial issues remain in practically realising more general SLAM solutions, in particular developing the theoretical solutions through to real-world implementations for challenging environments.

Even as of late 2011, fully autonomous underwater SLAM in dynamic, unstructured environments such as the nearshore is still an open challenge to realise practical implementations and solutions [224]. When dealing with the limited sensing available in the kelp beds, to achieve robust reliable results on a budget is far from a solved problem [206]. It is in this niche that this research seeks to advance the field; to improve the navigation capabilities of underwater vehicles operating in the hostile nearshore environment.

Frese presents a recent (July 2010) interview in Künstliche Intelligenz [225] with two of the leading names in SLAM and mobile robot navigation, Sebastian Thrun and José Neira on whether or not the problem of SLAM is solved. The consensus of these two leading authorities in the field is that SLAM for basic structured environments with good sensing is solved as far as basic research is concerned. However, the understanding of SLAM with limited sensing in large and/or dynamic environments is still in its infancy [206]. Particularly, the ability to not only ignore the effects of dynamic objects but to include them in the model, to monitor and update changes in the environment and to compute semantically meaningful models not just geometric maps of the environment are all identified as opportunities for research [225].

Of particular importance to this work is the identification by Neira that 'because the pressure to publish is very important in many places' and that 'development and implementation is less publishable than new theoretical results' that previous research has not thoroughly explored real-world applications [225]. Thrun also reinforces the issue that SLAM for real-world partially structured (or unstructured) environments with real-world sensing, particularly in the absence of GPS or similar, is still largely an unsolved problem. Thrun *and* Neira conclude that the focus of work now should shift to implementation and development of SLAM in real-world applications with impact and benefit to society rather than *solely* continued theoretical development [225].

This sets the research context – to take a target application and requirements specification, and to both design from scratch and adapt existing solutions (and algorithms) to the specified purpose, before proving and developing the solution in a **real-world** environment. The real-world environment of interest is the dynamic, nearshore environment with often dynamic sensing and varying sensor availability, and crucially, with the constraints of a limited budget and reduced sensor capabilities.

2.3.2.5.4.1 Efficiency and robustness

Theoretical solutions to the SLAM problem have been known for many years. In 2001, Dissanayake et al. [226] presented a theoretical solution before demonstrating an implementation on a land based robot. Dissanayake et al. [227] concluded that theoretically SLAM was well understood and that the focus of research into real-world implementations of SLAM should shift to computational efficiency [228]. SLAM implementations with more than a few tens of landmarks were stated to become computationally intractable due to 'the need to maintain the knowledge of the relative relationships between all the landmark estimates' in the map [228].

Since this work performed by Dissanayake et al. [227, 228], great advances in computationally efficient SLAM implementations have been made and in mobile computing power, and the efficient techniques developed further [229]. Thrun et al. [150] provide a seminal review of many of the leading techniques developed in recent years which is updated in the more recent publication [206]. Now, in more recent years, the focus of research is shifting from computational efficiency to experimental evaluation and robustness in the real world [225]. This is prompted in part by the rapid advances in computational power available, but together with the advances in applications and environments in which mobile robots are being deployed.

2.3.2.5.4.2 Future development of SLAM techniques

As early as 2002, Thrun identified operation in dynamic unstructured environments, efficient map representation, and integration of mapping with robot control for exploration as key areas for ongoing research into SLAM [230]. Although there have been many advances in the field since this article, these issues remain current even today.

Jiang et al. [231] provide an up-to-date (2009) review and summary of recent developments in EKF SLAM with perceptions of the current prospect of future research trends for EKF approaches to SLAM. Jiang et al. [231] identify suitable map representation of the environments, including mixed and layered maps with 3D considerations as being of particular importance to ongoing research.

With relevance to the nearshore application, the map representation is particularly important. Considering a layered map, vertical objects can be observed in the current (2D) plane which can

then be developed into a 3D representation for further inspection. In some cases, the position and configuration of the 2D landmarks can be sufficient for navigation, thus allowing computational efficiency. The 3D representation may only be required for user feedback of the survey data, or when the vertical characteristics of a landmark vary with height; hence the application of layered maps.

The second relevant perception by Jiang et al. [231] with regard to this research is the identification of the benefits of EKF SLAM using multi-sensor fusion, the benefits of which set the context for the multi-sensor navigation system implemented in this research. Jiang et al. [231] identify a reduction in data association errors and improvement in the robustness of feature detection as the two most important benefits. Both of these are realised in this research and were discussed earlier (for example, fusing the data from sonar and video for a combination of detection and identification).

2.3.2.5.5 Applicability to nearshore SLAM

Landmark selection is of particular importance for nearshore SLAM. Navigational landmarks are selected based on the target operating environment and what is likely to be observed – for example, dock pilings, rocks on the seabed, kelp stipes, the shore line, etc. As Thrun et al. [150] state, the key to successful localisation lies in successful data association – that is correctly identifying the correspondence between observed landmarks and those recorded on the map. Techniques such as multi-hypothesis tracking add robustness to data association errors when working with sparse landmarks, or when landmarks can be easily confused or spuriously detected, by allowing multiple location hypotheses to be tracked until a confirmation can be made. Implementations of accurate, robust data association for nearshore SLAM are considered in section 5.3.4 demonstrated in the field trials of *SeaBiscuit* in Chapter 6.

The theoretically solved problem of landmark SLAM for structured environments is gradually starting to propagate to the challenging underwater environment. The benefits of landmark SLAM for navigation when compared to techniques such as DVL, high precision INS and USBL/SBL/LBL systems are great. These benefits include drift free navigation, an increased immunity to noise and interference, the ability for geodetic navigation, no requirement for environment modification and beacon deployment and a significantly increased accuracy, reliability and robustness of navigation for a fraction of the budget. Techniques for autonomous image processing and feature extraction from underwater sonar and video data are also in constant development, including techniques to use both multibeam [126] and mechanically panned sonars [125] for navigation using EKF-SLAM in the nearshore. Significant advances have been made in recent years and this section considers some of the frontiers of research and their significance to the application of nearshore underwater navigation.

Ribas et al. [16] have developed a recent (2007 & 2008) navigation system for AUVs in manmade structured and partially structured environments such as dams, harbours and marinas. The navigation system uses a combination of feature extraction from continuous sonar scans and updates from a DVL tracking the seafloor and water velocity. This system works well and uses similar wall detection algorithms for landmark based SLAM to those developed in this research when operating in a structured environment. The addition of a DVL to the vehicle used by Ribas et al. [16] increases the budget of the vehicle but allows for an additional source of navigational dead reckoning information.

Folkesson et al. [211] also provide an example of tracking and navigating from artificial targets using sonar and in the absence of a relatively expensive DVL sensor. Folkesson et al. [211] develop several useful techniques for working with Gaussian probabilistic representations of sonar targets for SLAM when the errors and uncertainty are non-Gaussian. However, for the sonar tracking to work, clearly identifiable sonar targets are required in the target environment; Folkesson et al. [211] used 12 artificial reflectors for their test. Although this represents an important move away from supplementing navigational information with a DVL, it still places requirements on deploying sonar landmarks.

The move to unstructured natural environments represents a great challenge for image processing and feature extraction algorithms, as well as the algorithms for identifying corresponding features between successive scans. Eustice et al. [147] discuss a technique for visual tracking of the seafloor using techniques from optic flow to provide successive approximations of the movement of the vehicle from one video frame to the next. This technique has the benefit of not requiring any environmental modification or the deployment, positioning, calibration and then recovery of any additional infrastructure (for example LBL); however, the technique is not without its limitations.

Visual tracking of the seabed requires a combination of clear water, good illumination, operation in close proximity to a relatively flat topography of seabed, and a sufficiently visually diverse benthic composition to allow navigation from just successive images. Mahon and Williams [121] expand this technique to successfully combine visual and sonar tracking of the seafloor which allows for higher water turbidity, operation at higher altitudes from the seafloor but requiring an acoustically diverse benthic composition instead of (or as well as) a visually diverse seafloor.

Visual/acoustic tracking of the seafloor using cameras or sonar units and DVL seafloor tracking is similar in principle. Each has a set of operating conditions which restrict its use in some environments. However, due to the inherent expandability and flexibility of the sensor fusion and navigation algorithms developed in this research, if the target operating environment conditions allow, these technologies can be easily integrated into the navigation algorithms for an increase in navigation capabilities and a corresponding reduction in uncertainty.

2.3.2.6 Control and navigation

Navigation is the general process of selecting, maintaining and updating/adapting a desired course (a safe and suitable path) from one point to another using the information from both localisation and mapping [203]. As well as ensuring accurate maps, precise control and accurate navigation is required in the confined, complex environment to avoid damage, entanglement with the kelp stipes, and to manoeuvre in the highly varying bathymetry and rocky pinnacles typical of a kelp bed. If the vehicle size is kept to a minimum to reduce the risk of tangling and to aid deployment and recovery, and the vehicle is designed with the budget of a small-scale research group in mind, then the sensor suite which can be fitted to the vehicle for navigation is limited further.

There are two approaches to this navigation. The first is a triggered pre-programmed response to an external stimulus. Mapless navigation can be achieved by reactive decision making based on the information contained within an image/scan, using optic flow, or feature tracking between frames [232].

The second, more sophisticated navigation strategy dramatically enhances the capabilities of mobile robots and interprets the environment as some form of cognitive map, either spatial,

topographical or some other form. Cognitive maps [233] not only enable path-planning capabilities but also the use of current perceptions, memorised events and expected consequences, additionally allowing detours and shortcut behaviour [234]. To be effective, this strategy needs to combine information from the past, present and future (planned actions, predicted events) [235].

A critical review of the successful techniques and state of the art of the control and navigation of underwater vehicles follows, which can be applied to operation in the nearshore environment, specifically kelp bed mapping. A distinction is made between remotely operated vehicles (ROVs) and autonomous underwater vehicles (AUVs) using the definitions of each from section 2.3.1. There are successful examples of each being deployed into similar environments and for similar tasks, yet limitations are identified with both approaches.

2.3.2.6.1 Remote control (ROVs)

The definition of an ROV implies remote control and supervision, and a remote power source, both transmitted to the underwater vehicle using a tether (or more occasionally, just remote control, either through a data-only tether, or acoustically) [58].

The benefits of remote control are operational security, both from an operator controlling the vehicle, and from the possibility of the tether being used as a recovery line. The operational security provided and the high-power available via the tether is well suited to operation in the nearshore, where the unstructured environment and dynamic conditions often dictate difficulty in implementing fully autonomous navigation and control. Additionally, through the tether, there is no limitation on a finite energy source carried onboard the vehicle, thus no limit on the duration of missions, and high-powered manoeuvring thrusters and instruments can be used more freely [25]. This is particularly applicable to manoeuvring accurately and reliably in the confined, complex environment in the tidal currents and wave action often found in the nearshore.

Although there are limitations to the use and suitability of ROVs to all applications, some are increased in the nearshore. The limitations of a tether restrict the operating range of the vehicle without moving the support vessel, both from the finite tether length, but also the restriction of the vehicle towing the tether behind it. Untethered remote control is possible, but the bandwidth via acoustic communication for sensor feedback is low with interference common in the nearshore [236, 237]. The onboard power source also becomes finite and the security of the tether is lost [238].

Additionally, in the complex arrangement of kelp stipes, tangling is a frequent risk unless careful controlled navigation and manoeuvring is performed. Pacunski et al. [14] deliberately avoid operation of their small-scale ROV under canopy forming kelp, specifically *Nereocystis luetkeana*. Hence, precise positioning and high manoeuvrability are required for operation in and around canopy forming kelp beds.

Although the labour requirements for ROV operation are less than that of, for example a diver survey, there is still a need for the continuous concentration and operation of a skilled surface operator. Tether management is also required to ensure the correct amount of tether is in the water: too much and the vehicle risks tangling, too little and its movement is restricted [25].

Large-scale ROVs are often used for deep water habitat mapping [239, 240], although ROVs have also seen successful use for shallow water nearshore habitat mapping, when the application is carefully selected. Parry et al. [241] successfully used an ROV for benthic identification and

mapping in 10-15m of water depth using video with structured lighting projected to provide scale to the images. This overcomes the limitation of scaling and ranging using video, but the limitations of visibility are still a recognised issue in some circumstances.

As is common for nearshore fisheries surveys, Smith and Shull [242] used a small-scale ROV for rockfish surveys in shallow waters, again using structured lighting for scale. Harrold et al. [243] used ROV video surveys at a low altitude (0.5m) for mapping macroalgal drift from kelp forests (*Macrocystis pyrifera*) into nearby canyons. In deeper waters, Reynolds et al. [244] surveyed fisheries and fisheries habitats using a combination of co-registered side-scan sonar from a surface vessel and visual observations from ROVs.

In these examples, the sensors are well suited to the requirements, primarily manual species/habitat identification in relatively clear water. The use of ROVs is necessitated by the environment complexity, the budget, the requirement for manoeuvrability and to dynamically adjust the mission course in response to realtime sensor feedback.

Pacunski et al. [14] define the small class of ROVs by cost with a limit of <$150,000 (which is considerably higher than the low budget considerations of this research) and go on to describe their successful operation of 'small' ROVs for shallow water surveys (<200m, again greater than this research). The benefits of small ROVs (cost, coverage, ease of logistics) are demonstrated and the apparent underutilisation of small ROVs for nearshore survey work is concluded [14].

2.3.2.6.2 Full autonomy (AUVs)

The opposite end of the spectrum to the ROVs discussed above is a fully autonomous untethered underwater vehicle (AUV) [58]. Energy autonomy is provided by an onboard power source, or by harvesting energy from the environment [245, 246] and control autonomy is provided by onboard 'intelligence'. The level of this intelligence varies from a simple set of pre-programmed sequential operations, to programmed responses or decision making capabilities able to react to circumstances encountered.

Energy and control autonomy bring great benefits to many applications, including the flexibility of not requiring a tether together with reduced labour and logistical support. However, if the application is not correctly selected, energy and control autonomy can be limitations. Energy autonomy restricts the power budget available for sensing and movement, hence fitting high-power sensors, or expecting a high thrust or long duration missions dictates a large, heavy AUV. Equally, control autonomy is only as successful as the variety of scenarios which the programmer can predict in advance to pre-program reactions to foreseen scenarios. Developing sufficient intelligence to react to any given development or circumstance in the real world is an ongoing challenge for all mobile robotics, with difficulties compounded in the dynamic and diverse underwater environment.

Hence, the applicability of ROVs and AUVs to different environments and tasks is an important selection process. Recent (2011) AUVs are highly capable for autonomous undersea inspection [69], yet even so, the challenges of the nearshore environment are still limiting their deployment. Recent development to expand their use to the nearshore is ongoing, with applications for AUVs mapping submerged aquatic vegetation (eelgrass) already successful [11]. Mapping kelp beds of *Nereocystis luetkeana* still poses such a challenge from the full height stipes, canopy [14] and challenging conditions such that modified surface vessels are still widely (as of 2012 [10]) used for survey and mapping of this environment [247].

The benefits and limitations of using AUVs in kelp beds can be seen. The benefit of not having a tether to tangle around the kelp stipes is significant. Additionally, the surface vessel can be at a safe distance with no risk of affecting the measurements. However, the power required to manoeuvre in this environment around the obstacles, and to transect an accurate course or hold a station in the high currents found in the kelp beds is prohibitively high for a compact vehicle to carry its own power source. There is a compromise between correcting the motion of the vehicle, and correcting the readings of the sensors, the latter of which requires less power. However, a compact manoeuvrable vehicle is still required for this application to be able to map the kelp beds in high detail from close proximity, or even from inside the kelp bed looking outwards. The limitations of a tether tangling can be mitigated to some extent by careful piloting and mission planning, and given a correctly rated tether with strain relief, allows for recovery of the vehicle by retracting the tether rather than trying to dock an AUV in high swells.

Considering control autonomy, the highly dynamic environment of the kelp beds, where sea-state, tides and weather can change quickly, and conditions are unique to each kelp bed, make it hard to pre-program complete autonomy for the complex environments. Instead, the security and reliability afforded by remote supervision and control allow dynamic conditions to be dealt with and the mission adjusted while in progress. The need for remote control and supervision in high-risk areas is still recognised as essential [21]. In scientific applications, remote control provides the essential realtime feedback of results, allowing the investigation (often in unknown environments) to be directed in realtime to maximise the scientific benefit [22]. Remote supervisory control also allows the surface support vessel to be repositioned as necessary, and ensures the security of the vehicle while continuing to generate a useful and accurate map.

Thus a dichotomy exists between control autonomy and remote control and supervision, where risk is set against labour requirements. Similarly, the decision between energy autonomy versus a remote power supply contrasts the flexibility of tetherless operation with the restrictions of a finite power budget. With further considerations of additional vehicle complexity over ROVs (and thus potential unreliability & uncertainty) and costs with a near-unlimited ceiling as vehicle sophistication increases [11], the optimum solution for kelp bed mapping in the nearshore is proposed as a compromise between both extremes, a hybrid to yield combined benefits while minimising limitations.

2.3.2.6.3 Hybrid solutions

Given the often-specific applicability of ROVs and AUVs identified above, the opportunity for an optimal compromise has been identified for nearshore habitat mapping, specifically surveying the density and distribution of kelp beds. The AUV/ROV hybrid developed in this research combines the benefits of each, while seeking to minimise the limitations imposed by the two control modes.

Hybrid Control

The degree of autonomy integrated into ROVs varies, and the line between AUV and ROVs is not always clearly defined. In further offshore or deep water work, the need for hybrid systems where the benefits of AUVs are used to reduce labour requirements and ship support, but where either task complexity or environmental risk dictate, ROVs are still essential [21, 248, 249]. There are also successful hybrid solutions applicable to nearshore habitat mapping. Although the bandwidth of underwater acoustic communications is limited, usually to telemetry and control rather than full sensor (video/sonar) feedback [236, 237], untethering is one step in hybridisation, or developing autonomy for ROVs [238].

One alternative to untethering is to deploy a very thin, lightweight (often fibre optic) tether, which maintains the high-bandwidth sensory feedback, yet does not transmit power [250, 251]. This does not provide any tensile strength for recovery of the vehicle in the case of a failure, and can still tangle, although the tether can be cut, the vehicle goes free and then is capable of surfacing (or continuing autonomously [251, 252]) while the tether is recovered. While this solution was proven in depths of over 2200m, there is still an inherent risk of tangling in the nearshore environment with any tether [250]. A similar version of the vehicle using this thin fibre optic tether, the *Nereus* hybrid underwater vehicle, is capable of operating as an untethered AUV for surveying broad areas, or with the lightweight fibre optic tether connected for high bandwidth (multi-gigabit [253]) realtime feedback of video and data when operating in an ROV mode [26, 254].

An often-cited benefit of AUVs is the reduction in labour requirements from not requiring continual supervision and piloting by a remote operator [23, 255]. However, where conditions dictate the requirement for remote high-level operator control, steps can be taken to implement onboard low-level control of basic manoeuvres. These often comprise basic 'autopilot' functions, such as maintaining a heading, depth, and sometimes even course, all despite external influences (tether, currents, manoeuvring) [23, 249, 256] and serve to relieve the remote operator of some of the tedious, labour intensive fine scale control which can easily distract from the overall mission. The implementation of these hybrid control architectures often comprises a hierarchy, ranging from full autonomy with operator supervision, to operator defined waypoints followed autonomously despite external forces, through to direct manual control [249].

Low-level control of underwater vehicles is not trivial [257], due to non-linear dynamics (e.g. movement is not proportional to thrust which is not proportional to electric current), external disturbances, parameter variation during operation and uncertainties [255]. However, techniques such as Proportional Integral Derivative (PID), fuzzy [23] and sliding mode controllers [255, 258, 259] have been developed to solve this control problem. Varying levels of control are used depending on the application requirements, ranging from relatively simple depth control [23, 260] through to correcting for wave motion [261, 262] before finally the development of full dynamic positioning [263].

The level of automation can be developed one step further, through remote high-level control, where manoeuvre commands are sent or scheduled by a remote operator [264, 265]. Complex movements and process can be compiled using elemental manoeuvres (such as a set point for trajectory, orientation, path, wall following, hovering and target tracking) through to fully automatic way point navigation [24] allowing the operator to quickly and easily define an operation, or even redefine on-the-fly, without having to resort to time-consuming low-level control. Fraga et al. [264] define this difference as 'teleprogramming' rather than 'teleoperation', but it is defined elsewhere as task scheduling.

As with each level of increasing autonomy, the reduction in labour requirements allows an operator to concentrate on the unfolding survey in realtime, adapting the operation to optimise the quality of data, thus ensuring in realtime that the gathered data is suitable [249]. This not only ensures the security of the vehicle, but also avoids only discovering fundamental data flaws during review and post-processing. Given the dynamic conditions of the kelp beds, with a limited time and budget available for survey operations, ensuring a suitable dataset first time around is essential. Realtime semi-autonomous correction of the sensor platform position during a survey also reduces the amount of motion correction required in post-processing, avoiding any degradation of data and image quality [27].

Hybrid Power Supply

There is the also the opportunity for a hybrid power supply to bring benefits to nearshore operation by combining the AUV solution of an onboard finite battery with the ROV solution of a surface (unlimited) power source transmitted by tether. The aim is to preserve the benefits of each, while reducing the limitations in the target nearshore application. This hybrid-power tether is distinct from the hybrid-communications tether used by *Nereus* [26, 254].

The hybrid power tether provides the security of an onboard battery supply in the case of a tether-disconnect, while the need for a large and heavy battery pack resulting in a less compact manoeuvrable vehicle is avoided by the continual trickle charge from the surface. Conversely, a high-drag, thick diameter tether is avoided without limiting operational power for sensing and the required high-thrust in the nearshore by maintaining an onboard energy buffer. Thus, when a sudden surge of power is required, for example to accelerate, to avoid a collision, or to correct for wave movement, the onboard batteries can provide the surge of power, while the relatively thin tether can provide a continual 'trickle' charge to replenish the energy used over a longer duration allowing unlimited mission duration.

Existing AUV habitat mapping solutions are often limited to moderate or low current environments, as coastal currents (stronger than 1 knot for example [13]) impede the ability of the AUV to maintain a course heading or steady speed over the seafloor. Thus the hybrid power supply techniques discussed here provide a necessary solution to enable the endurance and manoeuvrability required to carry out accurate transects or for station keeping in the currents found in kelp beds. The trickle-charging tether provides a continuous energy supply for small-scale study areas. When greater coverage is required, the surface support vessel can follow the underwater vehicle trailing the tether [14]. Alternatively, redeployment from a new anchor site is possible.

Existing hybrid solutions often make use of a power tether and onboard battery to allow operation in different distinct modes (ROV or AUV) [266], or provide onboard power with a lightweight data-only tether [251, 252, 267-269], but the use of the onboard battery as a buffer is much less well documented. As well as permitting a thin low-drag tether, the system reduces the required power transfer down the tether, reducing cable cost, increasing safety through lower tether voltages and reducing the expense of onboard power conversion. Typical long distance ROV tethers use voltages upwards of 1500V AC at 400Hz to minimise loss in high power (20kW) tethers [270].

2.3.2.7 Mission planning

When considering the control of the vehicle, at higher levels of autonomy, mission planning describes both the sequencing and scheduling of the operations required to achieve the intended task(s). This includes reacting to unforeseen circumstances (such as when a task cannot be completed) or a changing environment. Most intelligent behaviour, even in humans, is based on prior knowledge not realtime searching. For this reason, the AUV needs precise instructions, of not just how to attempt a particular mission, but also *when* to attempt it.

Silva et al. [271] discuss a three-layer control architecture, starting with a layer to abstract the hardware from the control algorithms. This *hardware abstraction layer* (HAL) is normally provided by the operating system for standard computer peripherals and ports, but for the AUV it is extended to cover the message formats, timings, parsing and fault tolerance of the AUV specific peripherals and actuators. Silva et al. [271] continue with the *functional layer* which provides

motion and navigation operations, localisation and mapping before finally the *coordination layer* deals with mission planning, task selection and scheduling. Silva et al. [271] built this hierarchical tri-layer structure into a successful AUV control architecture with a fully integrated simulation environment.

A few years later, in 2005, El Jalaoui et al. [272] built upon the work performed by Silva et al. [271] to implement a more robust, modular and upgradable control system. El Jalaoui et al. [272] redefine the titles of the tri-layer architecture to be a Global Supervisor, Local Supervisors and Low-Level Control Modules with several reaction (control) loops throughout. The core implementation and principles are the same as the previously discussed tri-layer control architectures. However, the implementation differs and potentially allows for more upgradeable and evolutionary mission definitions which are easily adapted to new scenarios by providing the user with a series of objectives to build a mission. Each objective contains a set of sub-objectives which reflect the capabilities of the given AUV. Any change in the actuation or sensing capabilities of the AUV is reflected in the definition of new objectives available to the user when building a mission, thus facilitating straightforward upgradeability of the control architecture.

Palomeras et al. [273] again build on the work done previously and again define a tri-layer hierarchical control structure. Palomeras et al. [273] identify that the missions for which classical AUV mission controllers are usually developed have unstructured and very large environments to explore. In such situations, the trajectory of the AUV is calculated to optimize the energy efficiency. However, the control algorithm developed by Palomeras et al. [273] is optimised for robot reactivity to the environment, rather than the energy efficiency. The example quoted by Palomeras et al. [273] is the autonomous inspection of a structured environment, such as a dam, in which the robot must avoid the walls while following a trajectory.

To implement full autonomy, the mission planning algorithm is required to be robust in the presence of unexpected hardware failures or external environmental changes. The capability to reconfigure the mission plan to recover from failures and to use alternative combinations of the remaining resources allows, where possible, successful completion of as many of the original mission objectives as possible.

As Patrón et al. state [274], the majority of current AUV mission planning solutions are procedural and static. Hagen [275] defines a flexible mission planning algorithm, but one which is only able to react to environmental or machine changes which can be predicted in advance (a priori) by the programmer and a suitable response programmed in.

Pang et al. [276] develop an improvement to the basic procedural and static mission planning techniques with a reactive technique called behaviour based planning. The technique allows the mission plan to be adjusted in response to sensor data. Reactive systems typically use few variables to model the environment as decisions are based in realtime on acquired data [277]. However, while this technique allows for reactive mission planning to a changing environment, the mission plan is still only capable of reacting to changes which can be predicted and programmed for a priori by the operator. Evans et al. describe an architecture which mixes reactive and deliberative collision avoidance and escape architectures to provide mission planning with an awareness of the known fixed environment, and robustness when faced with the changing unpredictable environment [278].

Patrón et al. summarise these earlier approaches which justifies their evolution of a declarative goal-based solution for adaptive mission planning [274]. This allows higher levels of autonomy than the waypoint-based approaches to mission trajectory planning and allows the mission plan

to adapt and recover from failures and external changes [274], of particular importance when operating in unpredictable environments. The principle of the technique is to repair and reuse parts of a mission plan where possible given a failure of a system or an environmental change, rather than a less robust approach which would simply terminate the uncompleted mission.

Given the sensing available, and the highly dynamic nearshore environment, it is important to define the level of autonomy that is realistically possible. A compromise between high-level autonomy and the risk involved needs to be made. The higher the autonomy, the greater the risk, and while the mission planning techniques discussed here can be used for full autonomy, a more suitable application to the nearshore is the hybrid control discussed previously, where tasks can still be scheduled using these mission planning frameworks, but high-level control remains with the remote operator.

2.3.2.8 Vehicle hull configuration

There exist a great variety of underwater vehicle hull configurations, but these can be split into four distinct classes, each designed to suit their application.

The first is the traditional 'torpedo' shaped vehicle, with a propeller at the stern, and control surfaces and variable buoyancy used to perform turns and depth changes. The National Oceanography Centre *AUTOSUB* is a good example [279]. These vehicles are often untethered AUVs referred to as flight vehicles [280] and designed for long duration surveys to yield maximum range (hence low-drag) for the finite energy carried. They are however of limited manoeuvrability, with control surfaces requiring a flow to be effective, and often incapable of lateral translation. Thus, they are highly suited to their application, but highly unsuitable for navigating in and around the kelp beds.

Torpedo shaped *ROVs* exist and have been successfully used in applications where high-speed or forward propulsive efficiency is more important than manoeuvrability, and management of a thin, flexible tether is possible [281]. In some cases the application dictates a torpedo shaped hull, for example under ice surveys deployed through boreholes. In this case, manoeuvrability and remote control are required, yet deployment of a useful payload through a 20cm diameter borehole dictates a torpedo shaped hull configuration [282]. Thrusters are used for manoeuvring and lateral translation, and any forward propulsive efficiency from the hull design is incidental.

The second of the common vehicle hull configurations is the 'glider', again designed for long duration untethered operation, but increasing range by ascending to the surface, then gliding forwards during descent following a sawtooth or triangular wave depth profile over distance and time. There are options to extend the range of these vehicles by energy harvesting, either from solar power at the surface [245, 246, 283] or using the temperature difference across depths (thermoclines) [284]. Again, these vehicles lack small-scale manoeuvrability, rendering them unsuitable for kelp bed mapping.

The third class considers vehicles designed for manoeuvrability rather than long distance propulsive efficiency, and thus are often used in tethered applications where the vehicle operates in finite proximity to a surface vessel, and has higher power requirements to perform the inefficient small-scale manoeuvres. In the large class (over several thousand kg) and medium class (several hundred kg) of ROV, these vehicles are often cuboid shapes with little to no hydrodynamic fairing, as propulsive efficiency is less of an issue with an unlimited surface power supply and at low speeds. Instead, maximising useful payload while maintaining compactness for manoeuvrability in confined spaces often leads to open frame designs [285].

The Smart ROV *Latsis* is designed for multi-mode operation via easily configurable buoyancy fitted to the top of the vehicle [286]. As well as typical submerged ROV operation, *Latsis* can be towed at the surface, with the sonar units sufficiently submerged to reduce any noise from bubbles and the buoyancy designed to reduce wave-induced motion. Alternatively, the vehicle can manoeuvre itself at the surface, with movement and positioning independent of the constraints of a surface vessel, for example near hazards or in confined spaces [27].

As the vehicles move towards the smaller classes of ROV (<100kg), hydrodynamic efficiency starts to be an issue, to ensure that the vehicle is capable of propulsion and station keeping with the relatively smaller amounts of thrust compared to vehicle mass and tether drag. However, little is currently done to optimise the hydrodynamic efficiency, as the unlimited power source is still available through the tether. Of particular interest to the nearshore environment are vehicles which have a low hydrodynamic drag, firstly to optimise thrust for the limited electrical power available in a thin, flexible tether, but secondly to aid station keeping and manoeuvrability in the dynamic currents of the kelp beds.

Thus, a fourth class of vehicles contains small, compact, hydrodynamic and highly manoeuvrable ROVs. This field is relatively limited at present but is growing; HydroVision produce the highly manoeuvrable *Hyball* ROV which is designed around a spherical structure to support the 360° rotation of the camera through a meridian view port [287].

DepthX is an AUV designed to map subterranean flooded environments, so manoeuvrability is essential rather than forward propulsive efficiency [288]. Four thrusters are mounted at 90° to each other for horizontal manoeuvrability and two vertical thrusters are used for depth control. An elliptical shell both reduces the chance of entanglement and supports an array of echosounders mounted around its periphery for 3D SLAM and obstacle avoidance. The vehicle is 2.13m in diameter, 1.52m in height and weighs 1272kg in air. An optional data-only fibre optic tether can also be used for remote control and debugging.

DepthX was later developed to *ENDURANCE* and adapted for mapping under ice in Antarctica [29]. Modifications included the addition of an Imagenex Delta T multibeam sonar for mapping, and development of the navigation system, originally designed for flooded caves and caverns, for operation in unenclosed environments [289].

Saucer designs are occasionally used to provide omnidirectional drag properties in the horizontal plane, to enable horizontal translation in any direction without the need to rotate to face the direction of travel. The Duke University AUV *Charybdis* [28] uses three horizontal thrusters for translation and rotation, and one central vertical ducted thruster for depth control to provide a highly manoeuvrable vehicle.

Highly manoeuvrable AUVs have also been developed which use oscillating fins for propulsion rather than conventional screw propeller thrusters. One of the most prominent is *Transphibian*, now developed by iROBOT [290]. Designed for environmental monitoring in the surf zone and very shallow water, the combination of ballast tanks and oscillating fins allow either free swimming, or crawling along the seabed.

In the much smaller sampling class of vehicles, a spherical design is used to minimise drag in all directions and to minimise any risk of tangling or becoming stuck, particularly important when operating in confined process flows, pipes and chambers. The *SUBMAR* robot, developed by the Helsinki University of Technology, is a miniature (≈10.8cm diameter) spherical underwater robot. Although it contains no means of active propulsion, active buoyancy control allows it some

control over its movements through industrial process flows. It contains onboard environmental sensors, batteries, communications and control modules as well as a sample acquisition / reagent release tank [291].

Considering the nearshore environment, with dynamic and unpredictable currents in all directions from waves and tides, a 'saucer' hull configuration is proposed to minimise hydrodynamic drag in the horizontal plane while favouring omnidirectional manoeuvrability and maximising stability in pitch, roll [292] and vertical translation.

The rotationally symmetric design aids omnidirectional movement and station keeping in the horizontal plane as the hydrodynamic drag is identical in each direction. This simplifies the control algorithms, and allows the vehicle to translate in any direction with no efficiency penalty. The hull design also enables the panning of directional sensors while underway to extend their coverage with no complex control and no increase in power required from translating in a direction off-axis.

Vertical (translational) stability is important for the application to aid the vehicle in efficiently and accurately maintaining a constant height to provide repeatable kelp survey results across the rapidly changing kelp stipe diameter with height [38]. Vertical stability is difficult to control due to the combined effects of buoyancy, gravity and tether weight [260] – the problem of buoyancy is compounded as non-rigid components, including foam material added for buoyancy, compress at depth leading to instability in vertical control. If unchecked, this can either lead to oscillations from an underdamped system wasting a lot of power trying to hold a depth, or worse, lead to depth safety limits being exceeded, collisions, tangling and irregular survey data.

In terms of practically realising a useful payload volume in the underwater vehicle, a saucer can be simplified to an oblate spheroid, or more practically for manufacturing, a flat, wide cylinder.

2.3.2.9 Propulsion

The nearshore presents a high risk of entanglement, fouling or even damaging the very environment being mapped. Accurate and controlled propulsion is required in conjunction with the navigation system to manoeuvre in the confined, complex environment to avoid damage, to hold a station and to transit an accurate course despite currents. The requirement is to be able to position the sensors accurately and reliably, correcting for the movement of the waves [261] and currents with opposing thrust (station holding). While the sensor measurements can be corrected in software for the movement of the vehicle to some extent, accurate positioning is still required to avoid tangling and damage.

There exist a great variety of underwater propulsion methods which trade thrust, efficiency, stealth and cost to name but a few. A review of possible propulsion techniques is summarised here with consideration to the key requirement of manoeuvrability dictated by the kelp bed environment.

Control surfaces only become effective above a certain operational velocity and are therefore inappropriate for the manoeuvrability required for station keeping and small-scale movement in a complex confined environment [293, 294]. Buoyancy control can provide efficient vertical control and the ability to hold a vertical position with zero energy expenditure but is often slow to provide rapid vertical changes in position [295]. Therefore, the high-thrusts required to hold a position despite external water movements from currents and tides necessitates the use of thrusters.

In their simplest form, a set of fixed thrusters mounted at opposing angles as discussed in the following section can provide a high degree of manoeuvrability [296], well suited to operation in the presence of the currents [297]. Depending on the number of thrusters fitted, the vehicle can either be underactuated, fully actuated, or overactuated [298]. The distinction is whether the vehicle has fewer controls than degrees of freedom (underactuated), the same number (fully actuated), or more controls than degrees of freedom (over actuated).

In mechanics, degrees of freedom (DoF) are the set of independent displacements that completely specify the displaced position of an object. As movement underwater can occur in three dimensions (3D), there are three translational degrees of freedom and three angular rotational degrees of freedom. By definition, translation is movement without rotating, and rotating is angular movement about an axis.

The three translational DoF are usually referred to as *x*, *y*, and *z* as shown in Figure 2.7 below. In the body-axis system, this Cartesian coordinate system is orientated so that positive *x* translation corresponds to forward motion of the craft, positive *y* translation is sideways right motion and positive *z* translation is downwards motion.

The three rotational degrees of freedom correspond to rotation about the three perpendicular axes, often referred to as θ*x*, θ*y* and θ*z*. Conventional naming defines *roll* as rotation about the *x* axis, *pitch* as rotation about the *y* axis and *yaw* as rotation about the *z* axis. From the point of view of the origin, looking in the positive direction of an axis, clockwise rotation about the axis corresponds to a positive angular motion.

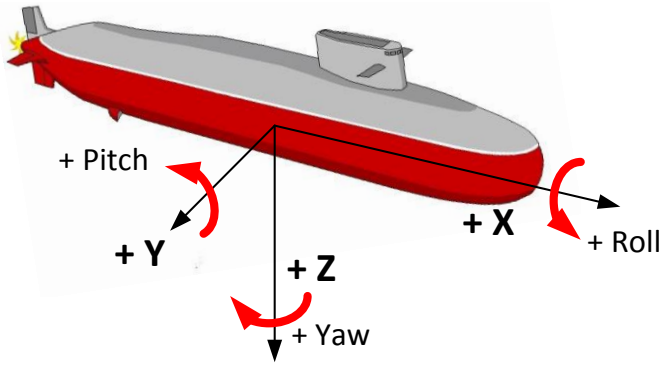

Positive **X** = forward translation (surge)
Positive **Y** = right translation (sway)
Positive **Z** = downward translation (heave)

Positive **Pitch** = Rotation about Y (nose up)
Positive **Roll** = Rotation about X (right wing down)
Positive **Yaw** = Rotation about Z (clockwise)

Figure 2.7 - The 6-DoF of a body in 3-dimensional space using the Cartesian body-axis system. Submarine image [113].

2.3.2.9.1 Holonomic motion

By definition, a holonomic platform has the same number of controllable degrees of freedom as there are total degrees of freedom available [299, 300]. Thus, an underwater vehicle capable of controlling its movement in all 6 DoF is said to be holonomic, dictating either fully actuated or overactuated propulsion (redundancy). For true holonomic control, translation and angular accelerations are decoupled from each other, allowing independent accelerations in any direction. For example, the robot can be rotating about its axis while also translating in a linear direction.

The majority of 'flight' underwater vehicles (torpedo-shaped hulls, gliders, etc.) are non-holonomic, usually incapable of lateral translation when stationary, and many steered by control surfaces are incapable of varying vehicle attitude and heading unless underway. Water movement orthogonal to the available thrust degrades navigation and mapping accuracy, while also increasing the risk of damage and tangling [290].

However, many of the vehicles designed for manoeuvrability rather than high speed or forward efficiency integrate movement in several degrees of freedom (such as the *UHD, Hyball, DepthX, ENDURANCE* and *Transphibian* all discussed above). Thus, considering the confined, complex nearshore environment, with unpredictable flows in any direction and the need for careful tether-aware navigation, the benefits of increased manoeuvrability provided by holonomic propulsion are clear.

Four opposing thrusters mounted at 90°, to each other as shown in Figure 2.8 below, can be used to provide holonomic motion (omnidirectional thrust) in the horizontal plane, similar to the *DepthX, ENDURANCE*, and *UHD* vehicles discussed previously. By varying the speed and direction of each of these thrusters independently, the vehicle is able to control its movement in every degree of freedom in the horizontal plane: forward and backward translation, left and right translation as well as rotation.

Additionally, the vehicle is able to perform any simultaneous combination of movements while also accelerating or decelerating in any degree of freedom at the same time. This gives the vehicle a great degree of manoeuvrability. For example, it can be moving diagonally while also rotating about its axis as it moves – highly beneficial for the nearshore kelp bed mapping application. The axisymmetric hull of the *DepthX*, *Endurance* and *Charybdis* vehicles above exploit this benefit [28, 29, 288]. If this system is combined with a means of depth control, for example vertical thrusters, then a vehicle capable of manoeuvring in 4 DoF is provided.

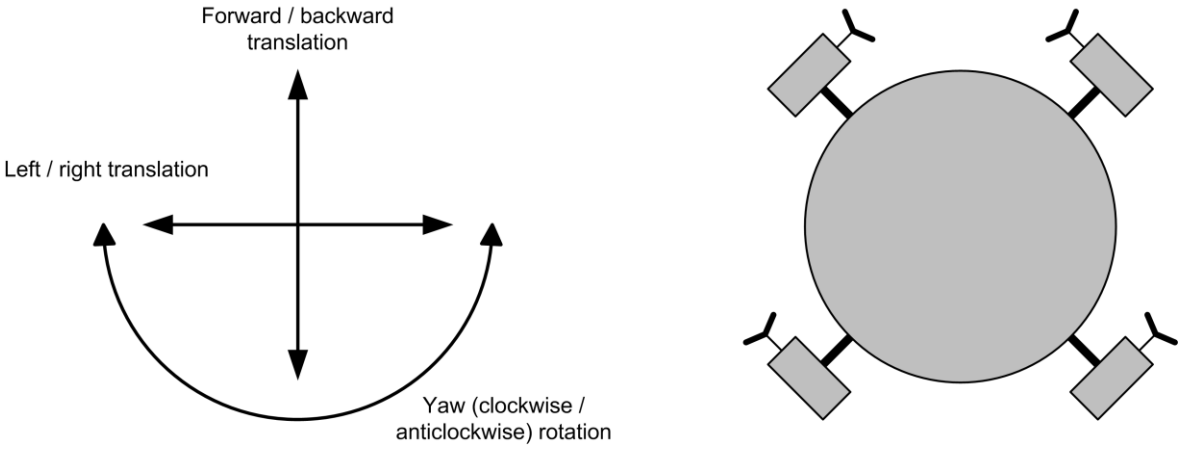

Figure 2.8 - Horizontal holonomic movement allows for any simultaneous combination of translation and rotation in the horizontal plane.

For operation in the kelp beds, translation in 3D is crucial to the mobility of the robot. Yaw control is also important to orientate directional sensors. Therefore, the propulsion system must be able to sense and control movement in these 4-DoF. However, considering the application of kelp bed mapping, an important simplification can be made which greatly reduces complexity: little functionality is lost if *true 6-DoF holonomicity is simplified to holonomic motion in the horizontal plane*. For the intended mapping, control over pitch and roll is not beneficial and instead unnecessarily increases complexity. Instead, pitch and roll can be kept constant and as close to 0° as possible to minimise any angular corrections which would need to be applied to sensor data.

Thus, manoeuvrability is provided by holonomic motion in the horizontal plane, but simplicity, reliability and efficiency are increased by simplifying the propulsion from 6-DoF to 4-DoF.

Stability in pitch and roll can be designed into the vehicle. If the centre of mass (COM) is positioned near the bottom of the vehicle and the centre of buoyancy (COB) near the top directly and centrally above, then upward stability is ensured [301], like the keel of a sailboat. The separation distance between the COM and COB is called the metacentric height [297]. Although in turbulent environments, the pitch and roll of the robot will inevitably deviate, under steady-state conditions the vehicle should return to an upright position.

Compared to vectorable thrusters, which rotate to align the axis of the thruster with the desired direction of vehicle movement [302], fixed opposing thrusters are a simpler, more reliable design, yet introduce inefficiency. The case of forward vehicle movement is shown in Figure 2.9 below. The desired movement of the vehicle is resolved into the individual thrusts required by each motor and the speed and direction of each motor is then controlled accordingly. Each of the four motors produces a thrust which sum to give the overall movement of the vehicle. The red arrows in Figure 2.9 represent the component of thrust cancelled out and thus represent inefficiency introduced by the fixed axis opposing thrusters. For the intended low-budget application, with a continual power source available through the tether, the advantages of simplicity and reliability outweigh any efficiency gains from using vectorable thrusters.

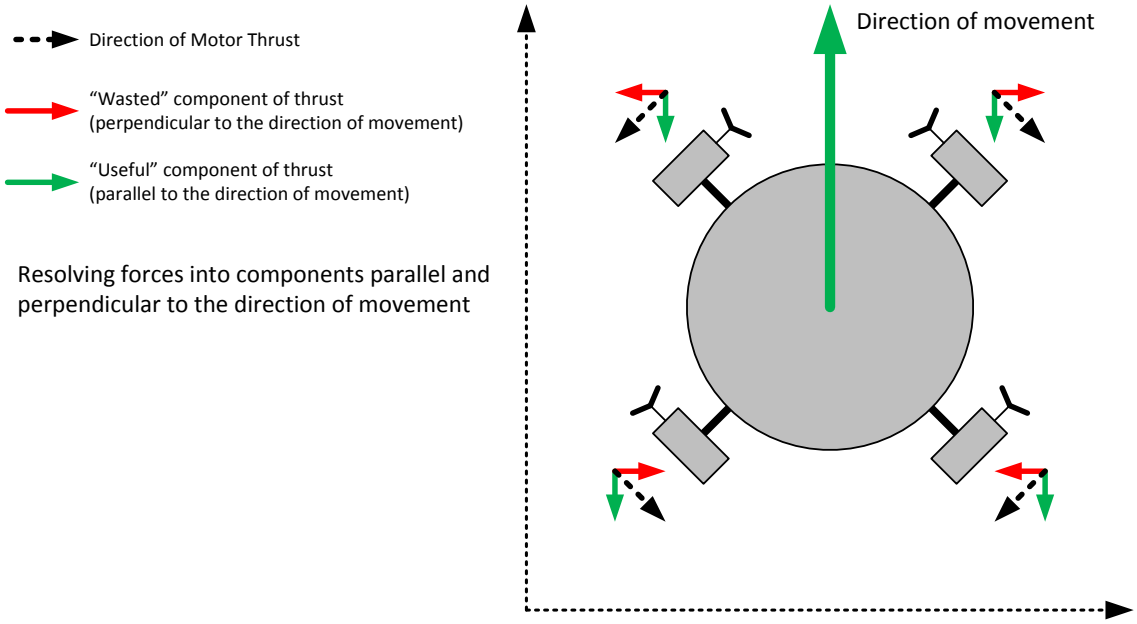

Figure 2.9 - Holonomic movement in the horizontal plane is achieved by 4 opposing thrusters, each mounted at an angle to each other. The speed and direction of each thruster is independently varied and sums together to produce an overall driving force.

2.3.2.9.2 The benefits of holonomic motion

The manoeuvrability provided by holonomic motion permits reliable operation in the confined, complex kelp beds. It also allows navigation between the kelp stipes to gather survey data at an increased detail or sonar scans from inside the kelp bed facing out while easily avoiding obstacles. Additionally, this manoeuvrability partially offsets the limitations of operating as a tethered vehicle, as the risk of tangling and effect of tether drag can be reduced by holonomic motion.

The improved manoeuvrability also permits sensing and mapping with directional sensors while underway. For example, directional sensors such as a multibeam sonar unit and underwater

cameras can be mounted on the front of the vehicle facing forwards. However, full 360° 3D map data of the surroundings can be gathered by the vehicle rotating about its vertical axis as it moves through the water, thus scanning the forward facing sensors over its surroundings as it traverses a planned course. This is highly beneficial considering the limited budget of the target application as it allows the benefits of more sophisticated sensors to be achieved through holonomic control. For example, the benefits of expensive 3D imaging sonars discussed earlier can be partially reconstructed by the combination of a multibeam sonar and the holonomic scanning technique.

For localisation purposes, a 360° spin while holding a stationary position will yield a sonar map of the surrounding environment, including walls, rocks, obstacles and objects in the midwater. This technique, coined 'spin-mapping' was exploited on the axisymmetric AUV *DepthX* to provide 360° sonar mapping of subterranean flooded caves and tunnels while descending [288, 303]. The axisymmetric shape meant little energy was expended maintaining a rotation once started of approximately 10°/s [303] due to the very low rotational drag [288].

Coupled with an appropriate sensing system, holonomic movement capabilities also enable station keeping, that is hovering over a fixed point at a constant height, or maintaining a fixed distance from either a stationary or moving target/vessel [296, 299]. If the vehicle is required to hold a position in the water despite swells and currents, for example for sensing and recording applications, then feedback from the positional sensors measuring deviations in position in 3D can be fed directly to the motor controller requesting corrective holonomic thrusts in 3D.

In the shallow water nearshore environment, the vehicle is likely to be subjected to large and periodic wave induced hydrodynamic forces, as well as turbulent flow around objects and outcrops, and sustained tidal flow. When working with a *remotely* operated vehicle, requiring an operator to continually correct for these movements is an exhausting task, whether it is to ensure the safety of the vehicle or to perform a survey [304]. It also occupies the operator's time and concentration when better productivity could be achieved if the operator was free to focus on the mission at hand [23]. An improvement in the performance of *remotely* operated vehicles is therefore quantified through an increase in the accuracy of operation and a reduction in labour requirements for continual manual position adjustment [305]. When operating in the currents and flows of the tidal nearshore environment, station keeping and the ability to hold a course autonomously are a necessity.

Techniques and control architectures for dynamic positioning and way-point tracking of vehicles in the presence of *constant* ocean currents [297] and optimal efficient path-planning in fast-flowing bi-directional estuarine environments [306] are already well established. Methods of efficient environment-aware path-planning include techniques to avoid fighting high-currents to conserve power and to 'ride' favourable currents. These techniques developed for estuarine environments [306] can be developed to the dynamic currents and obstacles found in the nearshore environment to ensure efficient operation [307].

Detecting and correcting for wave disturbances is also an important consideration, either for station keeping operations, or when underway. Existing techniques use a variety of sensors and a Sliding Mode Controller (SMC) to exploit sustained flows of the bulk of the surrounding water and the periodic movement of waves to provide predictive control, yielding more effective and more efficient compensation than simple reactive control alone [258].

The sensors used for station keeping depend on the application and the suitability of each sensing technology. Riedel and Healey [258] use an Acoustic Doppler Velocimeter (ADV) and motion

package whereas Leabourne et al. [305] exploit the clear water and close proximity of their vehicle to the seabed to provide station keeping capabilities using vision technology.

2.3.2.10 Machine health

Reliability and security can be approached in many ways. The requirement is always present: for any application, the reliable completion of a mission, successful recovery of the data, and a safe and reliable recovery of the vehicle intact are all imperative. A common distinction is made between *reliability* and *survivability* [274]. *Reliability* relates to vehicle failures due to the internal hardware components of the vehicle. *Survivability* on the other hand relates to vehicle failures due to external factors or damage.

There are several techniques for increasing survivability, that is avoiding vehicle failures due to external factors or damage. For example, an increased environmental awareness and collision avoidance can reduce damage from external factors. Patrón et al. [274] reference recent improvements in rules of collision [308] and wave propagation techniques [309] for obstacle avoidance and escape scenarios [278], all in the context of improving the vehicle's survivability to external factors and damage.

Reliability, that is avoiding vehicle failures due to the internal hardware components of the vehicle, is achieved through careful mechanical and electrical design with consideration of the target environment and requirements. This ranges from material selection to mechanical strength and from failsafes to safety factors. The methods of achieving reliability which are built into the vehicles developed in this research are discussed in later sections. However, every decision taken and every design produced is with reliability in mind and critical judgement is exercised at every step. The result is a vehicle which demonstrates significant advances in reliability over previous generations.

The second method of achieving reliability in particular, but also to some extent survivability (from now on referred to synonymously) is to either detect *before* a fault or potential failure has occurred and apply corrective action, or to detect a failure *in progress*. From this, either corrective action can be applied, the results mitigated, or in the worst case, the mission terminated to ensure safe recovery of the vehicle and data. This is the principle of machine health which relies on two stages: fault detection and fault reaction. Elsewhere, this is termed *detection*, *diagnosis*, and *accommodation* [310].

2.3.2.10.1 Fault detection hardware

The first aspect of the machine health system is fault detection. Deciding on what to measure in order to detect potential problems and establishing safe operating limits are critical steps in implementing a successful and effective machine health system. For every possible mode of failure identified, a risk assessment covering the likelihood of failure, the severity of the consequences of failure and the effort in detecting the failure provides a three-fold measure of whether a machine health sensor should be implemented.

Sensors typically implemented include water ingress (leak/humidity), temperature, pressure (over/under), power (voltage/current high/low) and thruster speed.

2.3.2.10.2 Fault detection algorithms

It is as important to avoid false negatives, which may result in faults being overlooked, as it is to avoid false positives, which may cause unnecessary delays searching for non-existent faults. Several methods are available to filter the data obtained to reduce the possibility of false positives and false negatives. Healey [311] describes a method using Kalman filters and batch least squares which relies on a combination of predicting the sensor output based on the vehicle's operation and then updating the prediction with actual measurements.

For example, if the speed of a motor was increased by the mission control program, then the machine health Kalman filter would *predict* an increase in motor driver temperature, the amount determined in advance through calibration. A short time later, this temperature increase would be sensed (*update*) by the temperature sensor monitoring that motor driver. The *prediction* would match the *update* and the machine health algorithm would deem that the system is acting as normal. If the motor speed was not adjusted then the *prediction* would be no change in temperature of the motor driver and the *update* would be no change if the system was acting correctly. If the *update* was any different to this then the machine health algorithm would detect that there was a problem with the system. Combining predictions with updates in this filtering technique can reduce the frequency of false alerts [311].

Changting et al. [312] present a technique for fault detection and diagnosis based on Bayesian networks. This technique uses Bayesian (belief) networks to detect failures when complicated and often only incomplete or inconclusive data is available. The network relies on the causal dependencies of each mode of failure and calculating the probabilities of a fundamental failure given the sensor data available at that moment. It has the possibility to detect a fault at an earlier stage than using independent, individual sensor readings, thus often allowing corrective action to be taken before it becomes too late to rectify and the mission has to be aborted.

This use of a Bayesian network is particularly useful as many potential faults can only be measured indirectly. For example, a jammed propeller can be detected by a rise in motor current and a rise in motor and motor driver temperature. Each of these sensors can be used indirectly to infer the probability that the propeller has jammed. Modelling the relationship between the connected set of electrical, mechanical and computing components can allow detection of faults with cause-effect patterns across different subsystems, without necessarily requiring a dedicated sensor for each fault condition [310].

Decentralised control of machine health systems adds safety and reliability. The use of dedicated microcontrollers allows for corrective actions to be taken even in the event of a main computer crash, or flooding of that compartment [313].

2.3.2.10.3 Fault reaction

The second component of the machine health system concerns the fault reaction [314]. By monitoring trends and setting 'warning limits' then corrective action can be taken before a fault develops (incipient fault detection), for example an overheating motor can be slowed down before it becomes critical.

If a safe operating limit is exceeded, despite attempts at corrective action, then emergency actions can be taken if redundant systems are not available. For example, if water ingress is detected, all systems are shut off and an emergency surfacing routine is activated, followed by

isolating the batteries and recovery by divers tracking an underwater strobe or surface VHF beacon.

2.3.2.10.4 Fault tolerant control

Overall reliability can be obtained by exploiting the redundancy built into the system to continue to operate despite a fault. Kanti Podder and Sarkar [315] as well as Li Ping et al. [316] present an adaptable framework for fault tolerant thruster control for a vehicle with similar holonomic thruster capabilities to those discussed above. This framework allows the redundancy in the propulsion system to be exploited by the machine health and mission planning systems in the case of a fault.

Autonomous damage detection through a comparison of control input and detected output is a crucial step in fault tolerant control, before steps to reconfigure the system to allow safe recovery or mission continuation can be taken [317]. Many existing AUV/ROV systems simply trigger an emergency surfacing / shutdown routine if a fault is detected, yet in many cases redundancy and reconfiguration can be used to continue a mission safely [317].

In vehicles with a high level of autonomy, Patrón et al. [274] discuss a framework for an adaptive mission plan which seeks to obtain a successful mission outcome, despite any occurring failures, by the nature of adaptive planning and fault reaction. As Patrón et al. [274] state, when presented with an unexpected hardware failure the focus of the mission should shift to ‘reconfigure’ itself to use alternative combinations of the remaining functional hardware resources – this is the adaptability required of a robust mission plan which makes optimal use of the machine health and redundancy capabilities of a vehicle.

2.4 General opportunities for the development of underwater vehicles

Figure 2.10 below identifies a series of general opportunities for development in the field of underwater vehicles identified as part of this literature review.

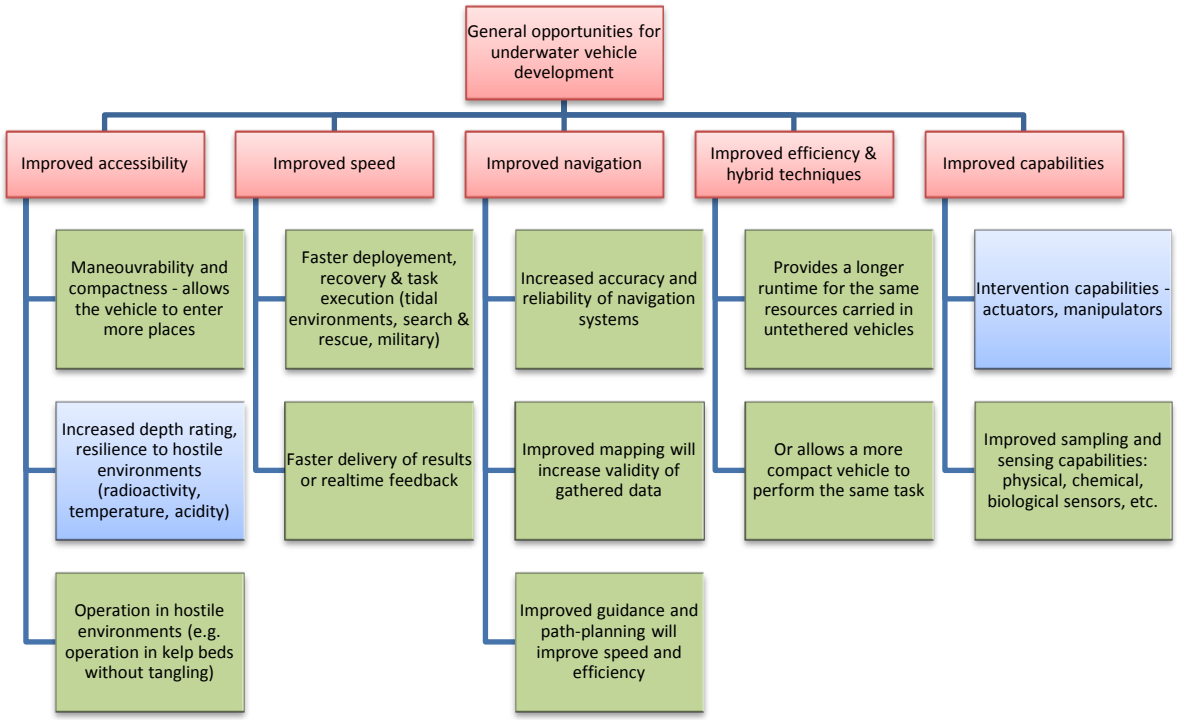

Figure 2.10 - General opportunities for underwater vehicle development. Items in green are addressed or advanced through this research, items left in blue are deemed not required for the kelp bed mapping application.

From Figure 2.10, it can be seen that improvements to the navigation capabilities will yield improvements to the entire operation of an underwater vehicle, autonomous or not. More accurate and reliable navigation improves the accessibility of the vehicle, allowing reliable operation in confined spaces, improving speed and efficiency with less time wasted on incorrect movements or inefficient exploration, and allows for an increase in the sophistication of the tasks the vehicle is capable of. Improved manoeuvrability is also seen to increase the accessibility of the vehicle, together with improving the mapping capabilities and operational reliability (e.g. tangling). Finally hybrid techniques are shown to provide a longer runtime for the same vehicle dimensions, and allow a more compact manoeuvrable vehicle.

2.5 The opportunity and benefits of iROVs for nearshore habitat mapping

The applicability of underwater vehicles to surveying and mapping the density and distribution of kelp beds has been identified, together with an assessment of the different techniques for sensing, navigation, control and propulsion. Based on the literature review and the requirements identified in section 2.3.2, the optimum solution of a hybrid AUV/ROV, the *position-aware, intelligent-ROV* (or **iROV**) is proposed, with the following summarised benefits to nearshore habitat mapping:

It is proposed to combine holonomic horizontal propulsion with a complementary axisymmetric hull shape to enable manoeuvrability, station keeping and reliable operation in the currents of the nearshore. The holonomic propulsion system also allows in-transit panning of directional sensors

over objects of interest while maintaining the original transect course. This novel approach allows greater sensor coverage and faster surveys.

Large ROV surveys can cost upwards of $10,000 per day or $1,000 per day for equipment lease of a small-scale ROV and associated equipment [14]. Typical purchase prices for mini-ROVs range from $100,000 to $150,000 for the Deep Ocean Engineering Phantom HD2+2 and Saab Seaeye Falcon respectively [14]. On a much smaller scale, with less manoeuvring power, and with less capability for payload or sensing, the VideoRay Pro 3 costs approximately $28,000 [14]. However, these costs do not include ancillary yet required equipment, such as tracking and navigation systems, habitat mapping sensors such as imaging sonars or high resolution cameras with laser ranging systems, all of which can add upwards of $15,000 - $150,000 to the initial price of the ROV [14].

In terms of sensing, 'better' results can usually be achieved given a greater budget, however, the challenge is to achieve high-quality sensor data given a limited budget to suit a small-scale research operation [30, 146]. The approach is similar to that attributed to Rutherford of '*we have little money, therefore we must think harder*'. One objective is to move towards the benefits of 3D imaging sonars on a fraction of the budget by combining holonomic propulsion with cheaper directional 2D multibeam sonars.

A hybrid control strategy is proposed to allow reliable nearshore operation while reducing the labour requirements typical of a fully remote controlled underwater vehicle. The proposed iROV, an intelligent hybrid of autonomous low-level control, position awareness with localisation and mapping capabilities, is deemed the optimal solution for kelp bed mapping while maintaining the security and data quality of remote high-level operator control and supervision. The mission can be adjusted reactively and in realtime, yet low-level control is automated to reduce labour requirements and improve transect accuracy. The hybrid power solution of an onboard buffer for high-power manoeuvring in currents and the security of a local uninterruptible power supply with the unlimited mission duration enabled by remote surface trickle charging is also proposed to be an optimal compromise of the two techniques. Finally, sensor fusion is proposed to provide accurate localisation in the nearshore with a limited budget for sensors, and while maintaining a compact vehicle capable of being launched and recovered off a small research boat and capable of surveying in and around the confined kelp beds.

It is through this unique and novel concept of an iROV that the rest of the research progresses, through background work, design, development, field trials and finally the results and analysis of actual kelp bed mapping trials.

Chapter 3 Initial Work and Background

3.1 Introduction

As an initial study into the requirements and challenges of kelp bed mapping, a test bed vehicle, *Hawthorne 2.0* was constructed in July 2008. *Hawthorne 2.0* included holonomic propulsion and a basic underwater navigation system and successfully completed confined water trials deployed as an ROV. The vehicle was then modified for sea trials in the nearshore environment (*Hawthorne 2.1*) where it underwent successful deployment as an ROV, providing a holonomic sensor platform and early development as an iROV adding basic positional-awareness, navigation and mapping capabilities.

The three design concepts of these test bed vehicles were reliability, flexibility and budget. Reliability was ensured in design, through innovative features such as automatic pressurisation of the housings, and in operation through machine health sensors and fault tolerant holonomic propulsions. Flexibility was provided by a modular hardware and software interface system, allowing different sensors to be easily integrated and software reconfigured in the field, often on-the-fly during a mission. The entire system was designed for a budget feasible for small scale coastal ecology groups with a base cost of £2500 and the flexibility to add habitat mapping sensors as the budget permitted. Innovative techniques were used to exploit maximum benefit from the limited budget, such as using holonomic movement to extend the information available from habitat mapping sensors.

This chapter provides a brief overview of the design, development and field trials of *Hawthorne 2.0* and *Hawthorne 2.1*. The results of these field trials informed the development of the iROV *SeaBiscuit*, providing practical information on the requirements and challenges of kelp bed mapping to supplement the literature review. The vehicles also allowed new systems to be trialled in the open ocean without having to rely solely on simulation and provided a baseline point of comparison against which improvements could be measured.

A high degree of manoeuvrability was found to be essential for operating in the cluttered environment coupled with unpredictable currents and the risk of tether tangling. The benefits of holonomic movement to provide complete manoeuvrability were demonstrated, together with the benefits of panning habitat mapping sensors independently of vehicle course. High instantaneous thrust was required for collision-avoidance or manoeuvring around kelp stipes while trailing a tether, requiring a surface power supply without an unduly restrictive tether.

Although full autonomy was seen to be a source of high risk and unreliability, autonomous features similar to an autopilot were demonstrated. These hybrid control features relieved an overloaded operator, allowing full focus on the survey data while basic manoeuvres or station-keeping were performed autonomously.

Finally, the requirement for and benefits of sensor fusion were demonstrated in the open ocean kelp beds. This sensor fusion spanned both navigation and habitat mapping sensors. Long term navigation using solely a low budget INS was demonstrated to be impossible due to drift, yet short term inertial measurements of wave-induced motion fused with regular updates from landmark based sonar observations to bound the drift were investigated. Fusion of video for short-range, high-detail identification with sonar for long-range low-detail detection was also demonstrated.

3.2 Requirements

Based on the literature review, the opportunity for a compact, highly-manoeuvrable vehicle capable of kelp bed mapping in the nearshore was recognised. The need for a low initial cost to suit small-scale coastal research groups was also identified, as was the need for sufficient flexibility and modularity to later expand the capabilities of the vehicle as required. These were formalised into the following requirements specification for the test vehicle *Hawthorne 2.0*.

1. An underwater vehicle capable of mapping the density and distribution of bull kelp with an operational depth of 30m and a safety limit of 50m.
   1.1. A vehicle sufficiently rugged and reliable to be launched and recovered from a small surface vessel in open ocean conditions.
2. Operation from a tether with remote realtime high-level control and supervision of results.
3. Sensors capable of underwater positioning and navigation in nearshore environments.
4. A propulsion system with sufficient power to operate in the currents of the nearshore, and sufficient manoeuvrability for confined environments, precise positioning and accurate transects.
5. A flexible, easily modified test platform for the development of holonomic control and navigation algorithms and sensor hardware.

3.3 Test platform: *Hawthorne 2.0*

In response to the requirements specification above, the underwater vehicle *Hawthorne 2.0* was designed and built. To accelerate the production of the test platform and development towards the objectives of this research it was decided to reuse a chassis and pressure vessel from a previous vehicle, *Hawthorne* pictured below in Figure 3.1 [318]. The limitations and restrictions from the previous design were removed and this allowed the test platform to be completed and operational relatively quickly. A full electrical and software redesign and a mechanical rebuild from the previous chassis were performed to adapt the vehicle to the requirements specified above to produce a reliable, adaptable and versatile test platform.

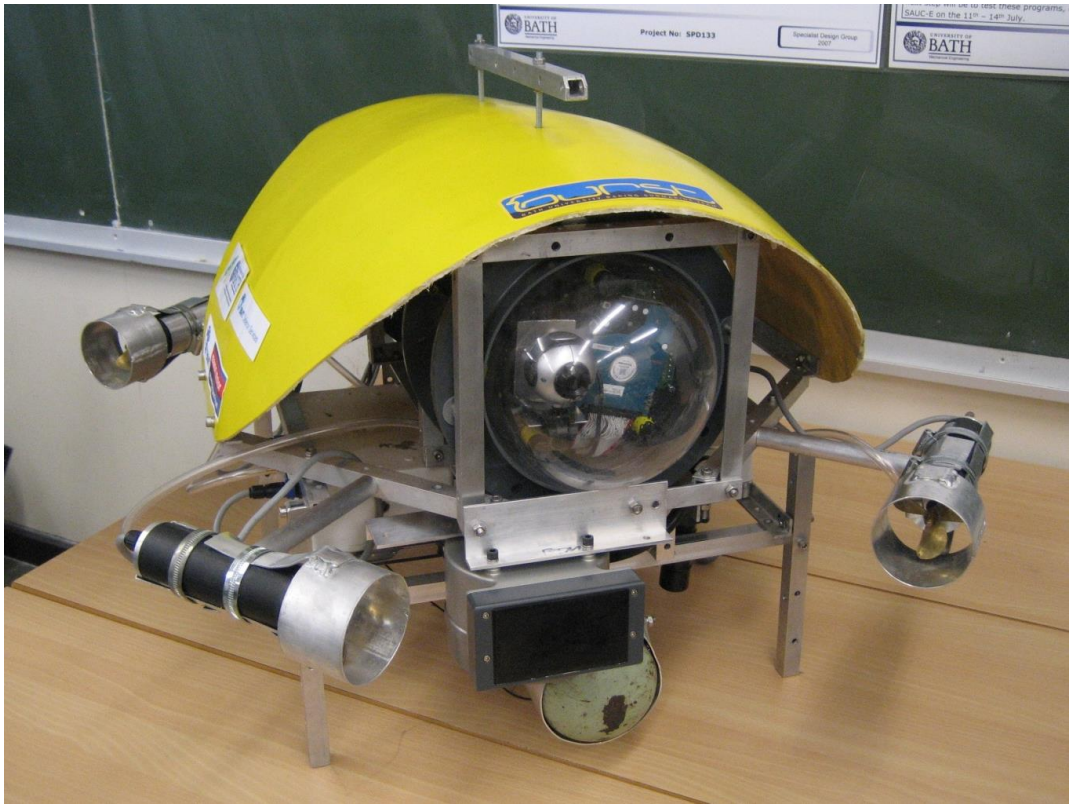

Figure 3.1 - The underwater vehicle *Hawthorne* (pictured) provided the chassis and pressure vessel for *Hawthorne 2.0*. Image from [318].

3.3.1 **Specification**

An overview of the specification of *Hawthorne 2.0* follows in Table 3.1.

Table 3.1 - *Hawthorne 2.0* specifications

Frame:	Reconfigurable aluminium open-frame, bolted together to allow for easy collapse and reassembly (for shipping), modules supported on brackets.					
Pressure vessel:	200mm diameter PVC cylinder					
Mass in air:	50kg fully equipped					
Control:	EPIA PX10000G Pico-ITX motherboard with 8GB SSD, 1GB RAM, ARTiGO housing					
Visual Processing:	EPIA EN15000PD mini-ITX motherboard with 2GB SSD, 1GB RAM, PicoPSU					
Software:	Microsoft Windows XP Professional, National Instruments LabVIEW					
Sensing:	Imagenex Delta T 837 Multibeam sonar Forward & downward facing Logitech QuickCam S5500 Cameras NASA NMEA Gimbal-stabilised marine compass SparkFun 6DoF v2 IMU (3DoF Gyroscopes, 3DoF Accelerometers) Keller PAA21SR 0-2.5bar absolute external pressure transducer Forward facing Navman 3100 echosounder for target ranging (adjustable to face downwards) SiRFstar II GPS Receiver Extensive machine health & diagnostic sensors (temperature, voltage, current, pressure)					
DAQ:	NI USB-6009 Data Acquisition					
Connectivity:	Surface:	Wi-Fi Remote Desktop				
	Submerged:	Umbilical LAN Remote Desktop				
Thrusters:	Horizontal:	4 ×	Maxon	RE36 118798	70W	Brushed DC Motors
		4 ×	Rivabo	Brass 535-075 M5	75mm	Propellers
	Vertical:	2 ×	Maxon	RE36 118798	70W	Brushed DC Motors
		2 ×	Rivabo	Brass 535-075 M5	75mm	Propellers
Propulsion:	Holonomic propulsion in horizontal plane, vertical translation (depth), stable in pitch and roll.					
Motor Control:	3 × Polulu dual-channel MD03A Reversible H-Bridges driven by custom AVR motor controller					
Power:	Computers and sensors:	2S 12V 4Ah SLA batteries (24V 4Ah overall)				1h30 runtime (2.5A)
	Motors:	2S 12V 12Ah SLA batteries (24V 12Ah overall)				0h25 *minimum* runtime (30A)
	Umbilical power supplied at 24V external connection					
Pressurisation:	Main body, battery box and motor modules maintained at slightly above ambient pressure at depth and regulated with an external pressure regulator and compressed air cylinder.					
Buoyancy:	Buoyancy compensation and trim provided by extruded polystyrene foam.					

3.3.2 **Design concepts**

When developing the vehicle for operation in the nearshore kelp beds, every feature was designed with three concepts in mind: reliability, flexibility and budget. An overview of some of the major features of the vehicle is presented in this section.

3.3.2.1 Reliability

The primary concern when designing an underwater vehicle is its operational reliability (including survivability). For field operations, downtime caused by an unreliable vehicle can be costly in terms of time, money and lost research data. Furthermore, the sensors and equipment carried are often of high-value and their safe recovery is essential. For this reason, several safety features were built into *Hawthorne 2.0*.

Machine health sensors were used to continually report the state of the vehicle, allowing problems to be identified early, and action taken to avoid risking the vehicle. These machine health sensors included battery voltage and current, ambient temperature of the main pressure vessel and key components, internal pressure and leak detection. Further reliability was provided by the onboard power supply. Even when the vehicle was operating with a tether, the onboard

batteries allowed for the safe recovery of the vehicle and data if the tether became damaged or had to be disconnected.

The main pressure vessel comprised a 200mm PVC tube, sealed at one end, with a precisely machined insert containing the electronics. This insert was sealed with double barrel O-rings and locked in place with a retaining clip. The main pressure vessel, peripheral and thrusters housings were connected to a pressurised air system. This maintained the internal pressure of the vehicle at slightly above ambient throughout a survey using a SCUBA tank and regulator. When ascending, a dump valve released the excess air pressure. This failsafe system meant any minor leak would cause air to bubble out rather than allowing any ingress of water. As the hydrostatic pressure difference (pressure difference between the inside and outside of the hull when diving) was maintained at close to zero, the seals and pressure vessels did not need to be rated to the depth of operation. Instead, less-expensive IP67[8] solutions could be used. Whereas other small underwater vehicles often incorporate compressed air cylinders, for example the iROBOT *Transphibian* discussed in the previous chapter [290], these are used for buoyancy control rather than the novel approach to housing pressurisation used in *Hawthorne 2.0* which allowed less-expensive housings to be used with greater reliability.

Although the 3 litre tank (pressurised to 220 bar, thus containing ≈660 litres) was a finite restriction on the operating time of the vehicle, under normal operation, this far exceeded a typical survey duration. When all of the seals were intact, air was only expelled when ascending, as the dump valve equalised the internal pressure to be slightly above ambient. For example, ascending from a submerged depth of 20m to 10m would cause an internal pressure change of the internal gas volume of all pressure vessels (of the order of a few litres) from ≈3 bar to ≈2 bar and the order of a few litres of air would be expelled. As kelp bed surveys were usually conducted at a constant depth to ensure repeatable results, the air capacity carried allowed for several surveys before it was depleted. In between surveys, the tank pressure was verified by a submersible pressure gauge fitted to the tank. When in operation, a depleted supply was sensed by monitoring any drop in the pressure differential maintained between the internal and external pressure.

The vehicle was trimmed to be slightly positively buoyant so that, in the event of a failure, the vehicle would float to the surface, allowing for easy location and recovery. Although this required a small amount of energy to continually overcome this buoyancy using the vertical thrusters, the gain in reliability was preferable.

3.3.2.2 Flexibility

Both the hardware and software of *Hawthorne 2.0* were designed to be as flexible as possible to allow straightforward reconfiguration.

Similar to the ROVs discussed in Chapter 2, the chassis of *Hawthorne 2.0* was built around an open frame to allow straightforward expansion and development with opposing thrusters for manoeuvrability. Mechanical flexibility was achieved through the modular, expandable frame allowing for straightforward reconfiguration or for different parts to be fitted or removed altogether. New hardware could be bolted onto the brackets provided. To compensate for the

[8]The Ingress Protection (IP) rating defines a standard level of protection for an object from ingress of particles, liquids, etc. In this case, IP67 denotes protection from submergence in water up to a depth of 1 metre, compared to the higher level of IP68 protection which denotes submergence in depths of greater than 1m, specified by the manufacturer. [319]

buoyancy effects of adding new hardware, the final buoyancy of the vehicle was trimmed by adding or removing small pieces of foam.

Features to allow adaptation between different applications and environments included a modular design for sensors, actuators, peripherals and power supplies to be easily added, removed or upgraded. This was achieved through a common standard of plugs and interfaces for internal and external peripherals as described in Appendix A. Spare external sockets were provided for auxiliary peripherals and a 5V/12V/24V power bus together with a USB/LAN connection were readily available at each connection point.

The software was written in National Instruments LabVIEW to be completely modular. Sensor subroutines could be started depending on which sensors were present and the overall mission planning program for task scheduling could be adjusted on-the-fly for redefining missions during operation. The vehicle was also re-configurable between autonomous and remote operation on-the-fly as an initial implementation of the iROV concept developed in the introduction. Limited confined water field trials with energy and control autonomy are documented in section 3.4.

The capability of holonomic movement and control also contributed to the overall flexibility of the vehicle. Complete freedom of movement underwater yielded benefits in sensing, mapping and survey operations as well as flexibility when navigating in confined environments. Holonomic motion facilitated careful and precise movement to reduce the risk of entanglement when operating in environments such as kelp beds, of particular importance when operating with a trailing tether.

3.3.2.3 Budget

Hawthorne 2.0 was built with limited research funds therefore the budget for parts had to be considered. The total cost of the base platform was approximately £2500. This made the benefits of underwater vehicles readily available to small-scale research groups where existing commercially-available solutions would be out of their budget. The base sensor-package of *Hawthorne 2.0* was simple, but allowed for more complex sensors (such as the Imagenex Delta T Multibeam sonar, used later) to be added and easily interfaced.

3.3.3 Design summary

With reference to the requirements specification in section 3.2 the following features of *Hawthorne 2.0* are highlighted:

1. The 30m depth rating was achieved by a combination of suitably specified pressure vessels and reliability ensured by a dynamic air-pressurisation system.
    1.1. The vehicle was designed to be of lightweight yet strong and rugged construction with an aluminium frame supporting a fibreglass cover. For field use, an alternative aluminium protective frame was fitted as detailed below.
2. The vehicle was capable of energy autonomy and freedom from a tether by carrying sufficient battery power onboard the vehicle for 1h30 of runtime or unlimited operation via the tether. The batteries could either be recharged in-situ in 4 hours or trickle charged when the vehicle was on standby between missions. When conditions or the application dictated, the vehicle was able to operate on a combined power and communications tether, capable of sustaining the power requirements for continuous unlimited operation, while providing realtime feedback of all results for operator intervention / control if required.

2.1. When a tether was not being used, a wireless communication link was available. This allowed autonomous operation: the vehicle could dive, carry out its mission and then, upon surfacing, the data could be downloaded and the next mission initiated over the wireless link.

3. The sensor suite used for underwater positioning and navigation was listed in Table 3.1.
   3.1. Using a combination of the positional information provided by the navigation sensors and the science sensors (dual cameras and the multibeam sonar), the vehicle was capable of gathering the kelp bed visual and sonar survey data required for the kelp bed mapping application.
4. *Hawthorne 2.0* used a combination of four opposing thrusters for holonomic horizontal movement (as per Figure 2.8 earlier) and two vertical thrusters for depth control. This system of opposing thrusters provided great manoeuvrability underwater (section 2.3.2.9.1). Speeds of approximately $1ms^{-1}$ could be achieved, with a turn speed of approximately $90°s^{-1}$.

3.4 Confined water trials

Hawthorne 2.0 underwent successful testing and development before being modified to have basic autonomous capabilities, including path-following, sonar and vision image processing and feature recognition and basic mission planning. The vehicle secured joint-second place at the 2008 Student Autonomous Underwater Challenge-Europe (SAUC-E) [320, 321] as detailed in the co-authored paper [322].

The 2008 SAUC-E competition was hosted by DGA (Direction Générale pour l'Armement) and held at IFREMER (Institut Français de Recherche pour l'Exploitation de la Mer), Brest, France. The competition was held in the deep wave basin, a saltwater tank 12.5m wide by 50m long and varying in depth from 10m to 20m [323]. The deep water and the visibility and corrosion issues associated with salt water provided a realistic test environment for the open ocean field application.

Six university teams from across Europe competed in a challenging event with tasks involving underwater search and localisation, passing through confined spaces and gates, identifying and avoiding decoy gates and objects, mapping the underwater environment and surfacing in specific locations. With success in the competition judged by quality of design, ingenuity of solutions, quality of engineering, communication and documentation as well as successfully and accurately completing the tasks in the shortest possible time, *Hawthorne 2.0* was awarded joint second place.

For an initial entry, *Hawthorne 2.0* demonstrated accurate control and good manoeuvrability. Preliminary development into vision [143] and sonar [324] image processing was carried out, with the vehicle able to recognise underwater targets, the first step in autonomously navigating an underwater course.

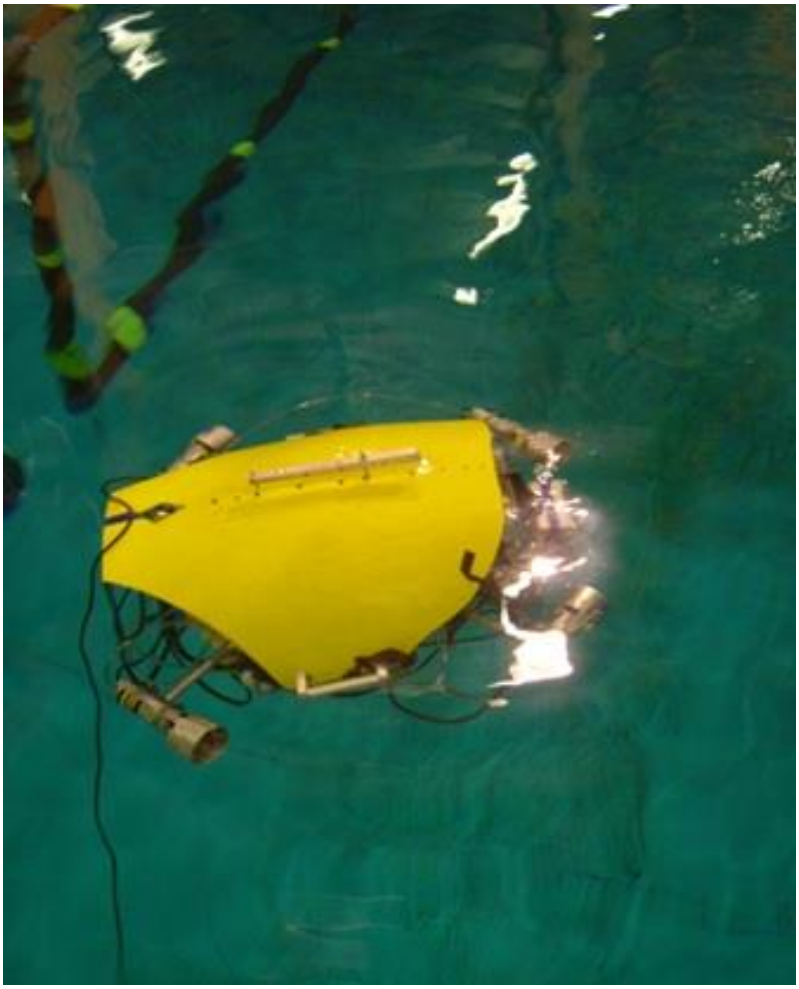

Figure 3.2 - *Hawthorne 2.0* at the surface of the competition tank ready for launch with the data cable connected.

Figure 3.3 - *Hawthorne 2.0* at the competition on its qualifying run. The vehicle is seen submerged to about 2 metres in autonomous mode without a tether attached and about to navigate through the qualifying gate.

3.5 Modifications for open ocean: *Hawthorne 2.1*

Following these successful confined water trials, *Hawthorne 2.0* underwent a series of extensive modifications before sea trials towards the development of a vehicle capable of kelp bed mapping.

Although the competition was designed to simulate real-life applications of AUVs, the requirements of the vehicle for field operations were still very different from the closed, stable environment of the competition test tank. With depths of up to 30m, poor visibility, rough ocean conditions, saltwater operation, a damp service & repair environment and water & air temperatures as low as 8°C, the field conditions were hostile. With these harsh conditions in mind, some of the modifications made in response to these conditions are discussed in this section.

3.5.1 Redesigned hull and protective frame

The relatively sleek and streamlined hull shown in Figure 3.1 was used to enter the competition. Points in the competition were available for a lightweight vehicle; therefore *Hawthorne 2.0* was designed not only to be as light as possible but also to have the smallest possible main hull volume (pressure vessel). This reduced the overall buoyancy of the vehicle and meant that extra weight did not need to be added to achieve neutral buoyancy. In actuality, the vehicle was slightly positively buoyant for safety reasons.

Although this hull design achieved success in the competition it would have restricted field operations; internal space for electronics was limited and the frame was not suitable for rough handling on the deck of the research vessel, and so several changes were necessitated. The hull and superstructure of the vehicle were replaced with a much stronger rigid frame as shown in Figure 3.4 below and the vehicle revised to *Hawthorne 2.1*.

This provided a much more rugged vehicle and afforded more protection to the delicate components enclosed by the frame. The frame allowed for protected transport and storage of the vehicle on deck as well as easier launching and stowage onboard the support vessel with several lift points for manoeuvring the vehicle on deck. The frame also provided a useful mounting point for future additional components, thus adding to the flexibility of the vehicle.

Although the new layout reduced the hydrodynamic efficiency of the vehicle slightly, as most of the kelp mapping was conducted on a tether, the energy available for continual manoeuvring, station keeping and navigating was in effect unrestricted when the surface tether was present.

An external battery pack was added, seen in yellow in Figure 3.5 below. Moving the batteries to this external housing created more space in the main pressure vessel and allowed rapid changes (within a few minutes) of discharged batteries without having to wait for the batteries to be recharged.

The new frame also allowed a larger main pressure vessel to be fitted. Although this increased the buoyancy of the vehicle, this was partly offset by the increased frame weight and it provided much needed internal space for the added electronics required for field operations, such as the INS. By using the same diameter pressure vessel, the previously used insert and back panel could simply be slid out of the old pressure vessel and sealed into the new housing (much like a piston).

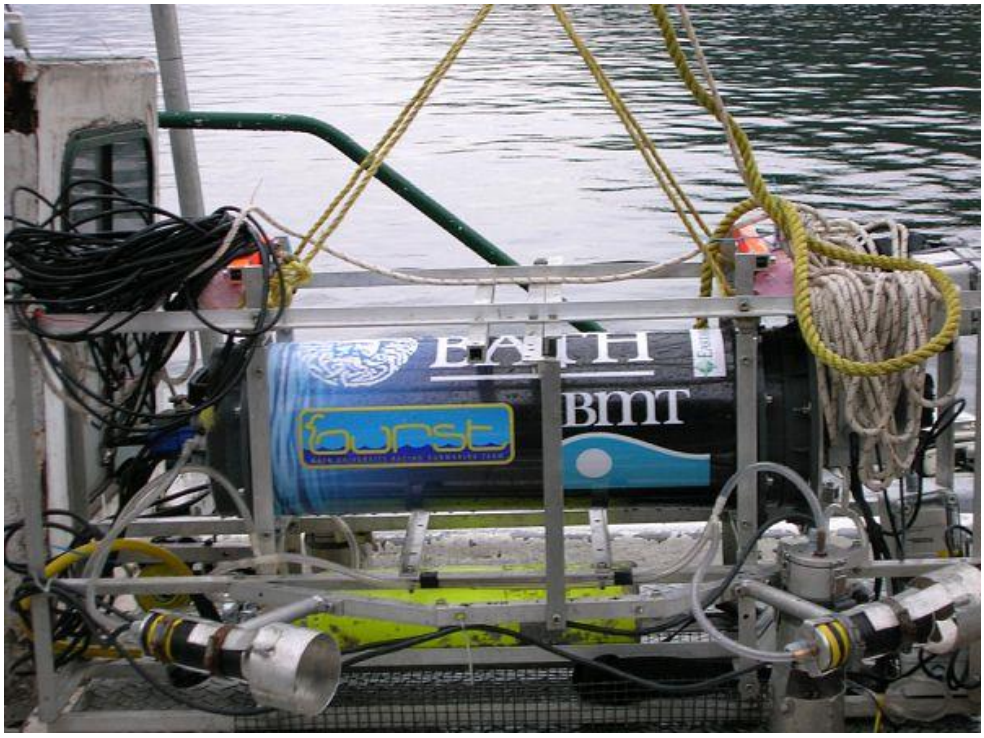

Figure 3.4 - The modifications made to *Hawthorne 2.0* for ocean use included the addition of an aluminium frame enclosing the vehicle for ease of lifting and protection of the fragile components and connectors (seen on the left of this picture). A larger main pressure vessel was mounted into the strengthened chassis. The clear plastic PVC tubes running to each thruster were used for air pressurisation, using the yellow air tank seen at the base of the vehicle.

Figure 3.5 - Preparing to launch *Hawthorne 2.1* from the 37ft research vessel *Stardust* in Rivers Inlet, British Columbia, Canada. The yellow battery pack fitted to the top of the vehicle allowed for fast (<60 seconds) changes of the batteries without interrupting power to the computers using a dual connector design (make-before-break).

Figure 3.5 above shows the vehicle being prepared for launch on the deck of the research vessel *Stardust*, and Figure 3.6 below shows the vehicle captured by a diver about to commence a survey in the sea trials conducted on 12-Sept-2008.

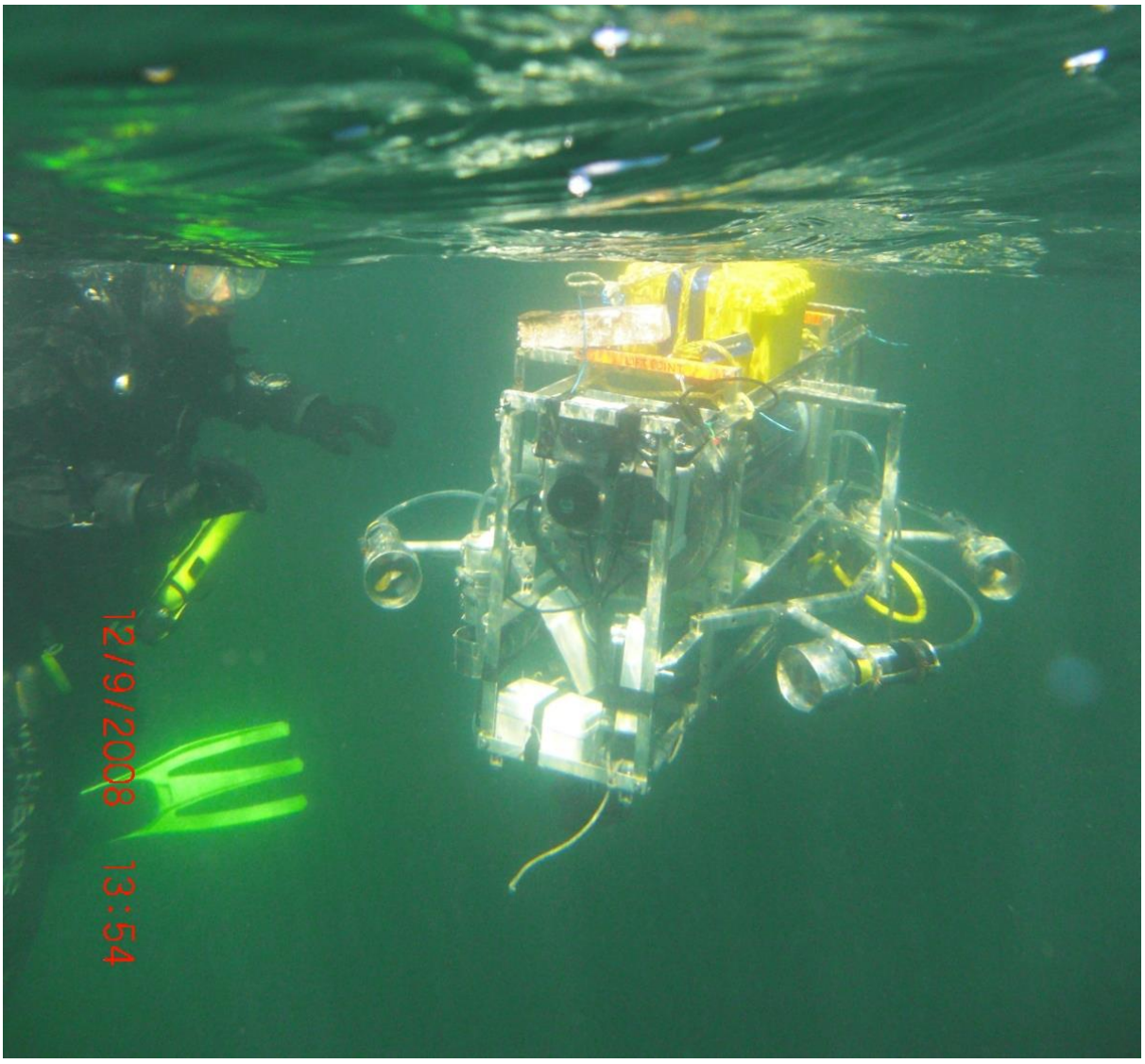

Figure 3.6 - *Hawthorne 2.1* is seen at the surface commencing a dive to approximately 20 metres to conduct a video survey of the kelp bed during sea trials on 12/09/08. A support diver was on standby for this initial test. Image credit Templeton, 2008.

3.5.2 Custom host vessel for launching, tracking and operations

For testing and deployment of *Hawthorne 2.1* in the field, a custom host vessel was designed for launching, operation and recovery of the vehicle. The key requirement of the vessel was a stable platform from which the vehicle could be raised and lowered in and out of the water in a controlled fashion for testing. It was also necessary to carry a surface power supply (in the form of sealed lead acid batteries) and provide a platform for the laptop(s) used for operator control and feedback. This allowed straightforward testing, research and development on the prototype vehicle.

Based on these requirements, the custom host vessel shown in Figure 3.7 was constructed. It is based on the materials already available to the research group and provided a stable, low-budget platform which could carry 4 passengers, the vehicle and all of the necessary support equipment.

Figure 3.7 - The *ZapCat*, used for deploying and operating the underwater vehicle during sheltered testing.

The vessel was based on a catamaran design for stability when lifting the vehicle, with a two-person kayak used for each hull. A superstructure made of wood rested on the kayaks with foam padding used to prevent damage to the fibreglass kayak hulls. The superstructure was strapped onto the kayaks using ratchet straps such that any shifting of the frame or straps would not release the kayaks, allowing the kayaks to be held securely without applying excess pressure to the hulls.

A wooden A-frame was mounted over a removable deck allowing the ≈50kg vehicle to be raised and lowered via a block and tackle. The removable deck could be inserted to transport the vehicle and allow basic servicing to be carried out at sea. A 5hp outboard engine was fitted to the transom to propel the vessel at up to 9 knots. Paddles were also carried for close manoeuvring.

The vessel had a very shallow draft with a tilting outboard engine, allowing operation in shallow coastal waters, as well as in kelp beds without the risk of becoming entangled. Although not suitable for rough seas, the vessel was capable of operating in and around sheltered kelp bed research sites. The high degree of manoeuvrability of the *ZapCat* allowed the holonomic motion of *Hawthorne 2.1* to be easily tracked from the surface during development. However, for ocean deployments, the stable platform of the larger research vessel pictured in Figure 3.9 was used.

3.5.3 **Addition and integration of an inertial navigation system**

Navigation in the closed, uniform SAUC-E competition environment (a tank of predefined dimensions) was relatively straightforward. A horizontally mounted echosounder, which measured the distance to the nearest wall straight ahead, coupled with the compass bearing, the pressure sensor measuring depth, and prior knowledge of the tank dimensions allowed a full 3D positional fix to be made at any time.

Figure 3.8 shows this principle, where a 360° rotation of the vehicle in any position in close enough range to a wall was sufficient to localise the vehicle. This was dependent on the maximum range (150m) of the horizontally mounted echosounder; the useful range reduced significantly as submerged depth reduced. The principle is similar to that of spin-mapping employed by *DepthX* [288, 303] discussed in 2.3.2.8. Although the sensing employed by *DepthX* was more sophisticated (arrays of ranging echosounders) and the environment complexity greater (flooded tunnels and caves), the principle of exploiting holonomic movement to aid mapping is similar.

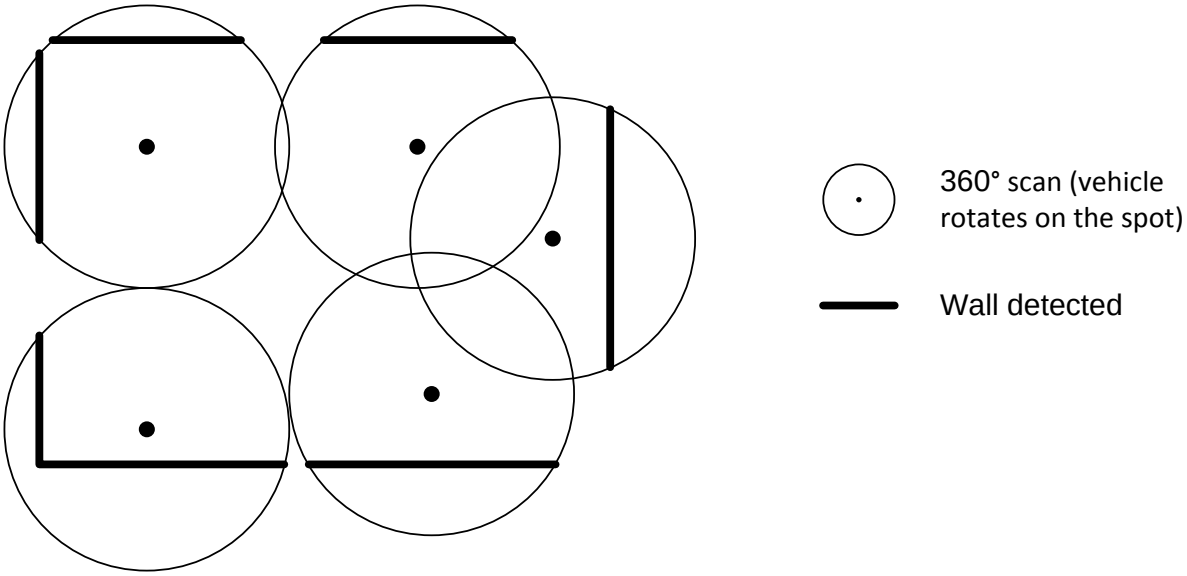

Figure 3.8 - The mapping technique used for Hawthorne 2.0. Each time an object is discovered, the vehicle rotates 360° while scanning its distance from the wall and compass bearing. This information is then integrated into the map.

However, in an open environment (non-uniform, no prior knowledge, or no known fixed landmarks), 3-D navigation is much more challenging. The difficulties of underwater open ocean navigation were discussed earlier. In developing a navigation system for *Hawthorne 2.1*, GPS data was available at the surface and accurate to within a few metres. A low-budget inertial navigation sensor was added to evaluate the performance of 'dead reckoning' of vehicle position to allow navigation between surface GPS fixes. One of the objectives of the field trials was to evaluate what useful data could be gained from the INS, for both long term underwater navigation (and how this translated into real-world accuracy), and for short term detection of sea movements (tides, currents and swells) with an eventual aim of underwater station keeping.

3.6 Sea trials

The sea trials were seen as an opportunity to verify the operation of the vehicle in its target environment as a useful field research vehicle as well as a test bed to identify limitations and opportunities for development.

Further objectives included:

1. To discover the issues involved with deploying and operating an underwater vehicle from the research vessel in the target nearshore environment.
2. An evaluation of the performance and applicability of the newly fitted prototype INS.
3. To investigate the challenges of obtaining useful scientific video footage in an ocean setting compared to the previous tests which had all been performed in closed tanks and pools.
    a. This included adapting the movement control and guidance subroutines for use in the rough ocean conditions to obtain steady video footage.
    b. It also included an investigation and measurement of currents and swells with an eventual aim of station keeping and correcting both course and heading by gathering sensor data for these movements.

The 2008 field season ran from August to September and the vehicle was successfully deployed several times off the Pacific coast of Canada. The culmination of the formal sea trials of *Hawthorne 2.1* were carried out over 5 separate days in September 2008 off the coast of British Columbia. A brief description of these tests and the conditions and location are noted in Table 3.2 for reference.

Prior to these tests, several preliminary trials were performed to check the operation and reliability of all components and to fine tune the sensing and control subroutines. A methodical and incremental approach was used for testing and, where possible, systems were tested independently of each other. This ensured that each system was performing correctly before integrating the next system. This not only ensured that a failure or error in one system would not compromise other parts of the vehicle, but also aided in troubleshooting.

Table 3.2 - Index of 2008 field trials

01-Sept-2008	03-Sept-2008	09-Sept-2008	11-Sept-2008	12-Sept-2008
Evening test in sheltered water of Skull Cove, Bramham Island. IMU logs basic movement subroutines, video log recorded by onboard colour camera.	Evening test in sheltered water of Skull Cove, Bramham Island. Increased video resolution and low-light optimisation. Tuning of PID control subroutines for following a compass course & holding a depth	Afternoon test in sheltered water of Skull Cove, Bramham Island. Video log recorded by IR underwater camera mounted to vehicle frame.	Deep water tests from *Stardust* moored at Dawson's Landing, Rivers Inlet. Movement routines at 20m depth, video logged by IR underwater camera.	Open water tests from *Stardust* at (51°02.659N 127°32.711W) in a 10m depth kelp bed. Sea swells 0.5m. Logging of vehicle movement in rough seas at and below surface with compensation of movement subroutines. Video logged by IR underwater camera.

Figure 3.9 - Deploying *Hawthorne 2.1* off the research vessel *Stardust* into a kelp bed in the 2008 field trials (image credit, Templeton 2008). The yellow battery box mounted on top of *Hawthorne 2.1* can be seen in the foreground between the camera and *Stardust*. A support diver is on hand in the water and the surface support crew can be seen on deck manning the tether, remote monitors and on hand for launch and recovery via the boom.

Figure 3.9 above shows a successful deployment viewed from the water just before *Hawthorne 2.1* commenced a dive. When considering the general objectives to '*verify the operation of the underwater vehicle in its target environment as a useful field research tool*' as well as '*a test bed to identify limitations and opportunities for development*' then the field trials can be considered a success and provided great benefit to the development of subsequent generations of vehicles.

The operation of *Hawthorne 2.1* was verified several times in a variety of nearshore environments typical of the field application, including the target environment of a kelp bed. The benefits of underwater vehicles as a research tool to the coastal ecosystems research group were demonstrated. Several opportunities for development were identified and are considered in the following sections.

3.6.1 The performance, accuracy and benefits of the INS

As described in section 3.5.3, a low budget Inertial Navigation System (INS) was added to *Hawthorne 2.1* to compensate for the reduced visual navigation information available from the cameras in turbid water, the lack of visual landmarks in the natural environment, and when operating without GPS information underwater.

The objective was to investigate what useful data could be gained from the INS for long term underwater navigation and 3D position estimation, and how this translated into real-world accuracy as well as a quantitative evaluation of the performance, accuracy and applicability of the INS to direct future development into the navigation hardware and software. Additionally, short term detection of sea movements (tides, currents and swells) was investigated with an eventual aim of facilitating underwater station keeping.

3.6.1.1 IMU hardware

The Inertial Measurement Unit (IMU) used was a 6 Degree-of-Freedom (DoF) board manufactured by SparkFun Electronics, USA, and sold as a 'SparkFun 6Dof v2'. The IMU used a triple axis accelerometer (Freescale MMA7260Q) [325] and three orthogonally mounted MEMS gyroscopes (Analog Devices ADXRS300) [326].

The gyroscopes had a dynamic range of ±300°/s and the accelerometers had an adjustable sensitivity of ±1.5g, ±2.0g, ±4.0g or ±6.0g (for all tests performed on *Hawthorne 2.1*, the sensitivity was set to ±1.5g for maximum small-scale accuracy). These ranges were appropriate to the maximum accelerations encountered by the vehicle while in operation. Strapdown calculations were performed to remove the component of gravity seen in each accelerometer axis depending on vehicle operation – the algorithm details are discussed later in section 4.6.5.4.1.

The sensor outputs, temperature and reference voltages from the gyroscopes and accelerometers were multiplexed (Texas Instruments CD74HC4067) to the 10-bit ADC on the microcontroller (Microchip PIC16F88). If all data channels were used, sampling occurred at approximately 107Hz. The microcontroller then transmitted the data as a continuous ASCII stream over a RS-232 connection [327]. To interface with the rest of the vehicle electronics, this data stream was either read by another microcontroller for pre-processing or transmitted directly to the onboard control PC via a TTL to RS-232 converter (Maxim MAX232) at 57600bps.

3.6.1.2 Data logs

All mission parameters, telemetry data and navigation readings from the INS were logged for diagnostic purposes and to allow playback and review of missions once the vehicle had been recovered. All mission data, sensor data, video recordings and optional sonar data were logged with a timestamp to allow for synchronised playback of all of the data simultaneously. When all of the subroutines were running on the underwater vehicle control PC, data logging occurred at approximately 18Hz. Onboard video capture reduced the mission log frequency to 16.4Hz.

Table 3.3 below lists the data recorded in each log using the naming conventions of linear and angular accelerations of the underwater vehicle, as defined in Figure 2.7 earlier. With this logged data, realtime analysis could be performed while the mission was in progress as well as full post-processing analysis. Playback of the log files also allowed simulation and algorithm development without having to deploy the vehicle.

Table 3.3 - Logged data

Mission Log:	**Inertial Navigation System Log:**
Timestamp	Timestamp
Compass heading	Pitch Rate
Desired course	Pitch Voltage Reference
Fly by compass (T/F)	Pitch Gyro Temperature
External pressure	Roll Rate
Target depth	Roll Voltage Reference
Fly by depth (T/F)	Roll Gyro Temperature
Individual motor thrust values	Yaw Rate
Horizontal movement command	Yaw Voltage Reference
Vertical movement command	Yaw Gyro Temperature
Front thruster turn (T/F)	
	X Acceleration
GPS latitude & longitude	Y Acceleration
GPS time & date stamp	Z Acceleration
GPS HDOP[9]	
GPS Speed over ground	Supply voltage reference
Fly by camera (T/F)	

3.6.1.3 Error detection and correction

Although errors in the data stream were rare, error detection and correction routines were used to prevent errors from having an effect on the output data. Each sample in the data stream was time-stamped by the receiving program as it arrived in synchronism with the rest of the mission log. If a sample failed any part of the error check, it was simply discarded and the next sample used instead. This did not affect the accuracy of any subsequent integration of the IMU data as the timestamp of dataset was used as the time-base for the integration. This provided a simple, yet effective error correction method for datasets where the error rate was low.

Errors were detected in a number of ways using a custom error detection algorithm. This included parsing errors in the data-stream (incorrect data length, number of items, absence of start and terminating character), checking each sample was within the bounds of the ADC limits as well as a user defined rate threshold which specified the maximum amount a sample can change by from one time period to the next. This was usually defined by the maximum rate of the sensor.

[9] Global Positioning System (GPS) Horizontal Dilution of Precision (HDOP) is a term used to describe the geometric strength of satellite configuration on GPS horizontal positioning accuracy. Closely spaced satellites, obstructions to the signal and a lack of satellites all increase the value of HDOP and reduce the accuracy of a horizontal position fix. An error estimate of a position fix can be made using the value of HDOP. [86]

3.6.1.4 IMU calibration

The first step of integrating the INS into the control and navigation systems of the underwater vehicle was to calibrate the IMU sensors.

3.6.1.5 Accelerometers

The accelerometers were supplied with a 3.3V regulated supply and output a zero value of 1.65V. In the ±1.5g sensitivity setting, the output varied by 800mV/g with a linearity of 1% of full scale output [325].

Therefore, as the acceleration varied by ±1.5g, the voltage output varied by: 0.8×±1.5g = ±1.2V with 1.65V as a centre point, giving an overall voltage output range of 0.45-2.85V. When approximated to a digital value by the 0-5V window 10-bit ADC, this voltage range corresponded to values of 0.45/5×1024=**92** and 2.85/5×1024=**584** with a centre point for zero acceleration of 1.65/5×1024=**338**. This is represented in Figure 3.10 below.

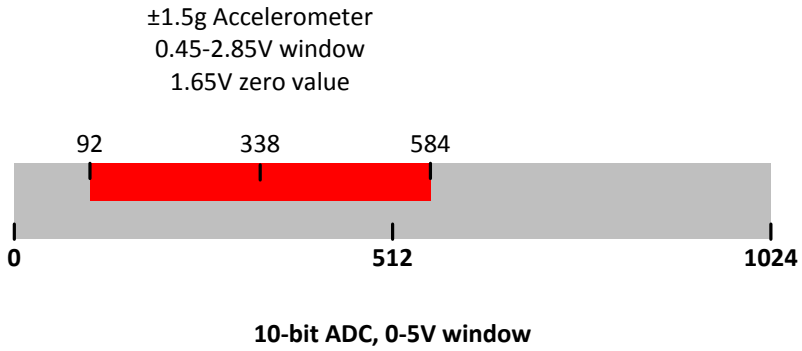

Figure 3.10 - ADC conversion of accelerometer values.

For the range of ±1.5g this gave an output range of 584-92=492. Therefore the resolution, or smallest noticeable component linear acceleration of the system, was ±1.5g/492=3g/492=0.00610=6.10mg over the range ±1.5g. This corresponded to a resolution of 0.0598m/s² over the range ±14.71m/s².

Therefore: Linear Acceleration (m/s²) = (Raw ADC Value – 338)*0.0598

3.6.1.5.1 Gyroscopes

The gyroscopes were supplied with a 5V regulated supply and output a zero value of 2.5V. They operated over the range of ±300°/s with a sensitivity of 5mV/°/s and a linearity of 0.1% of full scale output [326].

Therefore, as the angular velocity varied by ±300°/s, the voltage output varied by: 300×0.005 = ±1.5V with 2.5V as a centre point, giving an overall voltage output range of 1-4V. When approximated to a digital value by the 0-5V window 10-bit ADC, this voltage range corresponded to values of 1/5×1024=**205** and 4/5×1024=**819** with a centre point for zero angular velocity of 2.5/5×1024=**512**. This is represented in Figure 3.11 below.

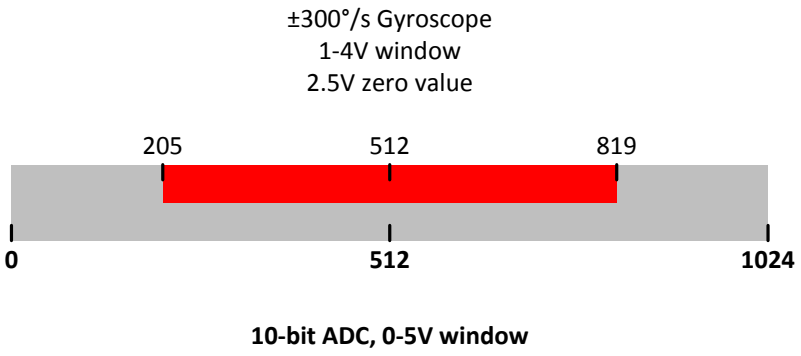

Figure 3.11 - ADC conversion of gyroscope values.

For the range of ±300°/s this gave an output range of 819-205=614. Therefore the resolution, or smallest noticeable component angular velocity of the system, was ±300°/s/614=600°/s/614=0.977°/s over the range ±300°/s.

Therefore: Angular Velocity (°/s) = (Raw ADC Value – 512)*0.977

The temperature output from each gyroscope could be used to correct for the effects of temperature drift. The temperature sensor provided a 2.5V output at 25°C which varied by 8.4mV/°C. This corresponded to a change in ADC output value of 1.72/°C. Although not used, this feature is ready to be used for software compensation of the gyroscope rate output if required in future developments and all temperature data was logged during missions. Continual monitoring of the ambient temperature inside the main pressure vessel using the machine health sensors verified any temperature fluctuations were less than a few degrees Celsius.

3.6.1.5.2 Verification

In the absence of any laboratory force calibration equipment or tilt tables, the datasheet calibrated values were assumed with an accuracy, known sensitivity and known (limit of) nonlinearity. In-situ verification to an absolute reference source was possible for some axes of movement as detailed below in Table 3.4.

Table 3.4 - Reference data sources available for IMU calibration

Linear acceleration	Angular acceleration
X & Y acceleration – GPS sensor on the surface outputs latitude and longitude X & Y acceleration – forward facing multibeam sonar unit (integrated later) measures acceleration towards a known stationary object in the water Z acceleration – pressure sensor (calibrated for sea water temperature and salinity) measures depth Z acceleration – depth sounder measures altitude (height above seabed)	Yaw – electronic compass provides a gimbal-stabilised (±30° in pitch and roll) reading of magnetic north Pitch and roll – were neither measured nor controlled at this stage. The vehicle was trimmed to float with 0° of pitch and roll and would return to this upright position from any deviation in attitude.

Two of the simplest and most accurate verifications were comparing integrated yaw angular acceleration against the absolute compass data and comparing integrated linear z-axis acceleration against the absolute pressure sensor.

Figure 3.13 below shows an example dataset for yaw rate and compass from a relatively long test (35 minutes) on the 9-Sept-2008 in sheltered waters, removing rough seas as one potential source of error in the calibration process. Although the compass sensor updated slowly (2Hz) it was useful for calibration as it provided *absolute* reference data compared to the *relative* (dead reckoning) data from the gyroscopes. A series of clockwise and anti-clockwise turns were performed with periods of holding a heading to simulate a typical mapping mission.

The colour code shown in Figure 3.12 applies to this plot and to all following plots.

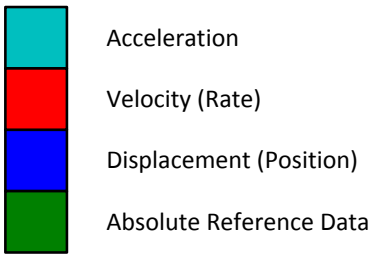

Figure 3.12 - IMU graph colour code – applies to angular and linear measurements.

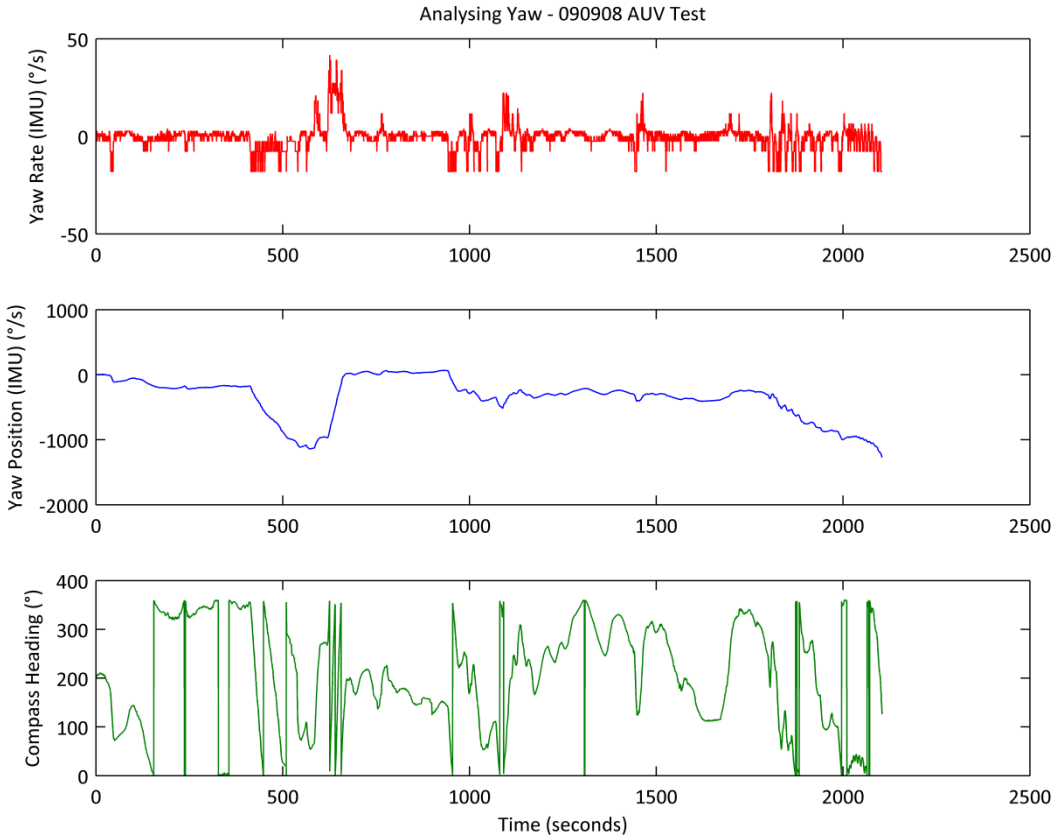

Figure 3.13 - A long duration (35min) gyroscope test in sheltered waters comparing the yaw angle integrated from the gyroscope (shown in blue) with the yaw angle from the compass.

The gyroscope output (rate of turn, shown in red) was integrated once (shown in blue) to give angle of turn from a starting position zeroed with respect to the compass data for comparison. For computational simplicity, a cumulative trapezium integration [328] using the difference in timestamps from one sample to the next was used. The compass data (shown in green) was converted from a wrapped 0-360° range to continuous heading data to track the number of turns. When the vehicle turned clockwise and the bearing increased from 358° to 359° the bearing would then normally reset to 0°. Instead, when using continuous degrees, the heading continued to 360° and 361° thus recording that one complete clockwise rotation had been made. Figure 3.14 below shows the yaw angle (the integrated yaw rate) and the compass data plotted using continuous degrees.

Figure 3.14 - Comparing the integrated yaw angle from the gyroscope with the reference compass data using the dataset shown in Figure 3.13 previously. Angles were converted to continuous (wrapped) degrees.

As can be seen by inspection of Figure 3.14, even over the relatively long 35 minute duration of this test, there was a relatively good correlation between the absolute compass data and the dead reckoning IMU data. Further verification runs were performed and the dataset above represents typical performance. However, two limitations on performance were noted.

Due to the gyroscope sensitivity and the ADC quantisation resolution of 1°/s, quantisation errors were significant at low turn rates. A slow turn of less than 1°/s was underestimated (or missed) by the gyroscopes and slow turns at a rate of a few degrees per second were quantised to the nearest degree. Thus, a sustained slow turn caused a significant drift. This can be seen to some extent in the plot above in Figure 3.14 as periods of discrepancy between the absolute compass data and the dead reckoning INS data. It was only through approximately symmetrical clockwise and anticlockwise movements that the drift remained close to zero after 35 minutes. In the opposite conditions, high-rate short-duration turns (up to 20°/s) could also be missed due to the sampling rate (logging at >20Hz).

In both cases, although the INS data was immune to interference from operating close to ferrous structures and updated at a faster rate than the 2Hz compass, the measurements were subject to the same limitations of all dead reckoning data, cumulative errors. The data presented in Figure 3.14 was from a relatively long duration test of 35 minutes. This was representative of a typical dive length for the underwater vehicle.

The accuracy can be improved by a higher resolution ADC and a more accurate gyroscope, both at a higher budget. However, as can be seen from the figures, the current hardware provides a good approximation of yaw angle during high-turn rates, yet requires absolute yaw angle updates from the compass at regular intervals to correct drift, particularly during periods of slow turn rate. From this example, the drift (up to approx. 50° in places) is unsuitable to navigation and mapping.

Thus the benefits of sensor fusion using complementary sensors demonstrated through the combination of the absolute drift free compass data with the high update rate, electromagnetic immune gyroscope data. A useful addition to this basic INS (which is addressed in Chapter 4) is a 3 DoF magnetometer, to remove the reliance on the mechanically gimballed marine compass used (described later) and to allow gyroscopic measurements to be regularly corrected with a high-rate absolute 3D estimation of inclination.

The second verification example proposed integrating the z acceleration data to estimate vertical position (depth) for comparison to the external pressure sensor, again a comparison of a dead reckoning sensor with an absolute measurement. The three plots below in Figure 3.15 compare the integrated z acceleration data (velocity) and the double integral (position) with the external pressure sensor. The three plots represent different dive profiles to a range of depths (0-16m) and over a range of durations up to 700s to provide an extensive comparison. The 0.5m discrepancy in the zero point of the external pressure sensor curve (green) represents the calibrated zero point: when the top of the vehicle hull was at the surface, the pressure sensor was submerged by 0.5m.

The first set of plots show a typical dive profile during mapping operations. As can be seen from the external pressure (the lowest part of the graph), this test contained a deep dive to over 15 metres over a total duration of 7.5 minutes with a maximum dive rate of 0.13m/s and a maximum ascent rate of 0.29m/s. The plateau at 15m on the pressure sensor graph represented the maximum pressure readable by the pressure sensor. As discussed in the introduction, bull kelp grows in water depths of 10-17 m [1], and so while the vehicle was rated to depths of 30m for safety, accurate mapping was not required at depths of >15m. Thus the 2.5 bar absolute pressure sensor was selected to maximise sensitivity (and therefore accuracy) over the required range. The IMU Z position graph shows a truer representation of the continued dive to approximately 18m, albeit underestimating the rate of descent and ascent. Comparing the IMU estimate of Z position to the absolute reference data from the pressure sensor, shows that an *approximation* of the dive profile could be made using just the INS. However, no accurate measurements of small movements could be made, and all of the subtle characteristics of the dive profile shown by the pressure sensor were lost in the IMU data.

The same effect can be seen on the second set of plots in Figure 3.15, this time for a shallower (3m), shorter (200s) dive. Again, the INS Z-axis accelerometer (blue) provided an approximation of the true dive profile (green), but with a very low accuracy and a large drift over these 200s. The inaccuracies were again due to the large cumulative error from the double integration. Fine level detail of the dive profile was lost in the double integration due to the large amount of noise obscuring the small accelerations. The double integral averaged the acceleration data giving the smooth curve shown for Z position, as seen in the third set of plots in Figure 3.15 for a longer 700s dive. Underestimates of the dive and ascent rate could be attributed to quantisation errors and non-linearity as previously discussed.

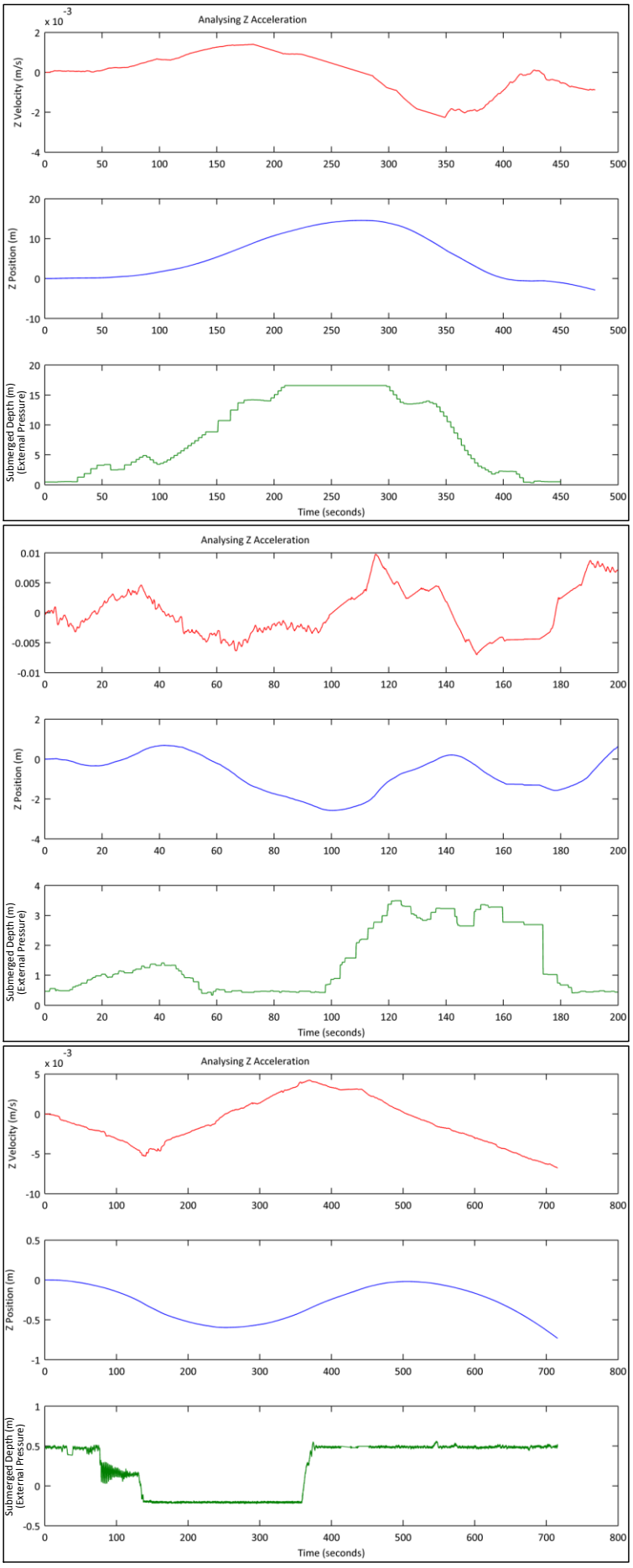

Figure 3.15 - Comparing the INS measurement of depth (z position) with the external pressure measurement across three different depth ranges and time durations. Integrated accelerometer data (velocity) is shown in the top plot (red) in each case, and the double integral (position) is shown in blue. The green plot shows the external pressure sensor calibrated to vehicle depth in metres.

Figure 3.16 shows an example of the raw data output from the IMU ADC for Z acceleration. The example shows the same period as that shown in the first set of plots in Figure 3.15 (so this represents a gradual dive to 18m from 0-250s and then a gradual ascent from 250-500s). As can be seen from the graph, there was a large amount of noise present which obscured the data – this was electrical noise rather than just movement of the vehicle in the water – the pressure sensor updated at a similar rate and at a comparable resolution and did not show these oscillations.

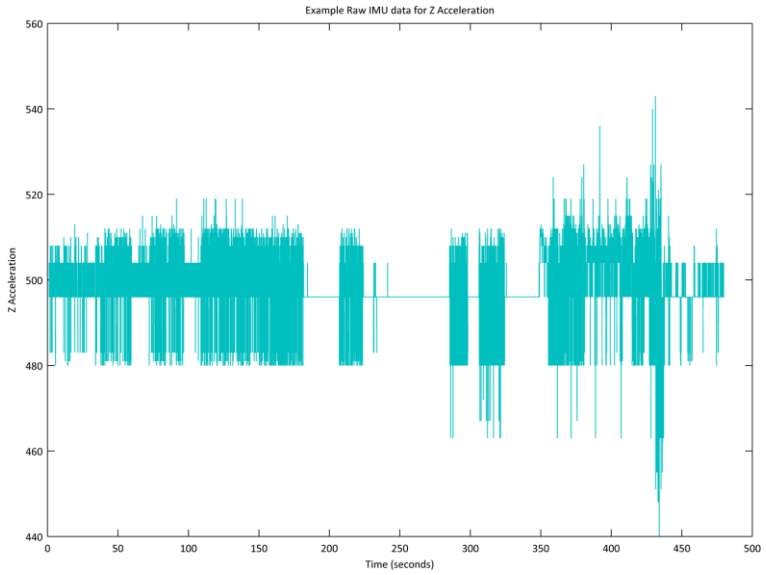

Figure 3.16 - Example raw IMU data for Z acceleration showing the same period as the first plot in Figure 3.15.

It can be seen that INS data alone could not provide the small-scale accuracy required for underwater navigation in confined environments. The lack of accuracy was further compounded by the sensitivity of the ADC. Even at this most sensitive setting of ±1.5g, the accelerations produced by the vehicle used only a small part of the ADC window. This introduced a large quantisation error and reduced accuracy.

A high-linearity, low-noise amplifier between the accelerometers and ADC was later implemented to amplify the accelerometer output to fill more of the 10-bit ADC window (±1.5g over 0-1024 levels), reducing quantisation errors and in effect increasing sensitivity. The compromise was that the accelerometer could be more easily saturated by large accelerations, requiring careful selection of the amplifier gain. This amplifier was implemented post-season, together with the addition of a superior, low-noise, high-sensitivity INS detailed later in section 4.6.5.

The accelerometers used for all three axes in *Hawthorne 2.1* were identical, the magnitudes of acceleration were also comparable and so a similar result and degree of accuracy was seen for all three axes. It was difficult to present a signal to noise ratio as the amplitude of the signal constantly varied depending on the movement of the vehicle. However, bench tests of the IMU sensor (while powered up in the vehicle enclosure to simulate the operating conditions in terms of temperature, interference, power supply fluctuations, etc.) were used to observe the noise present on the ADC outputs. The noise was a random fluctuation, individual to each output from the ADC (therefore individual to each channel of the multiplexer – the ADC only has a single channel). The fluctuations were always within certain limits about the zero value, an average of which can be seen as ±2 levels on the ADC output. When considered over the entire 10-bit window of the ADC, this represented a relatively small error of ±0.2%. However, considering this error over the smaller ADC window of each sensor, this equates to an error of ±0.41% on the accelerometer and ±0.33% on the gyroscope.

In practice, the error was even larger than this as even the largest active accelerations the underwater vehicle was capable of, or the roughest sea movements it was likely to encounter (passive accelerations), were smaller than the maximum operating range of the sensor. Therefore the full scale deflection of the ADC window was never used for each sensor. The effect of the noise on the results was compounded when the constant value of noise was applied to the much smaller scale changes in ADC value encountered under normal operating conditions of the vehicle. This can be seen in Figure 3.16 - even the maximum accelerations experienced by the vehicle when performing this dive used only a fraction of the total ADC window (0-1024).

Noise filtering algorithms could be applied (and indeed, the double integration serves to average the data), however, any averaging performed would risk obscuring the details which are already obscured by noise.

3.6.1.6 INS data for long term navigation and short term station keeping

In Chapter 2, the importance of combining drift free allothetic information with the more robust dead reckoning idiothetic information from INS was identified. The difficulties of navigating from INS dead reckoning data alone, even with very high budget sensors was also shown.

The results presented in this chapter, detailing the trials of an INS in *Hawthorne 2.1* for navigation in the nearshore environment have demonstrated the approximate accuracy and performance which can be achieved with a very low budget sensor. While useful to provide an approximation of movement, due to the drift inherent in any INS coupled with the high-noise and low-sensitivity present in this IMU, inertial navigation systems are not suitable as a single source of long term underwater navigation.

As identified in Chapter 2, this supports the argument for sensor fusion, integrating the idiothetic robust INS data into the sensor fusion framework with regular updates from an absolute (drift-free) sensor. The fusions presented in this chapter (compass and pressure sensor) work well to demonstrate the benefits of sensor fusion, but for some axes (e.g. x and y position) an absolute position estimate is not always available – e.g. no GPS underwater, and landmarks not always available for navigation. In these cases, the reliance of the navigation algorithm on the dead reckoning high-drift INS data becomes greater in between absolute position updates; even with its high drift, the INS is the only available data source in some instances.

While the data shown in the previous section shows that the accelerometers cannot be used for long term position estimation due to the large drift errors, they can be used for short term measurement of ‘impulse’ forces applied to the vehicle. The importance of station keeping has been identified previously, including when capturing video footage and generating sonar maps of the environment, as well as reducing operator load in the nearshore. In each case, it is necessary to hold a position and attitude (angular position), despite ocean currents and swells and to be able to track an accurate and steady course in rough conditions. For the example of station keeping, when the vehicle is trying to maintain a position despite external forces, the accelerometers are poor at detecting gradual movements in position from tides and currents due to the cumulative effects of drift masking any movement estimate. However, for detecting the sudden (often periodic) movement due to waves and swells, the accelerometers are ideal. Figure 3.17 shows the raw accelerometer output over 12 seconds measuring the passive movement of *Hawthorne 2.1* in relatively rough seas from a test carried out in open water on 12-Sept-2008.

For the reasons discussed previously, the IMU data cannot be calibrated to any specific unit; additionally clipping in the negative x and z directions can be seen from miscalibration of the offset zero point saturating the ADC. However, in each of the 3 axes of movement, the vertical and horizontal components of the wave motion can be seen. The data shown here was captured close to the water surface in the nearshore causing increased disturbances. Although the disturbances from wave action reduce with increasing depth, the need for either correcting the movement of the vehicle (station keeping) or correcting the data gathered (tracking underwater position) is still present.

A significant advantage of the holonomic movement capabilities of *Hawthorne 2.0* and *Hawthorne 2.1* is that a perturbation of the vehicle in any direction by ocean currents and swells can be corrected for by simply applying thrust in the opposite direction. Provided sufficiently accurate and responsive data is available from the IMU and the thrust capabilities of the vehicle exceed the swell states, it is possible for the vehicle to hold station in rough conditions.

The short time duration means drifts will not accumulate and the nature of the forces mean that a general indication of the force needs to be measured as quickly as possible in order to provide sudden short burst of corrective thrust. An exact measurement of each periodic deviation is not absolutely necessary, it only needs to be as accurate as the corrective force which can be applied by the thrusters. Thus this rapid measurement is ideally suited to the characteristics of the accelerometer data.

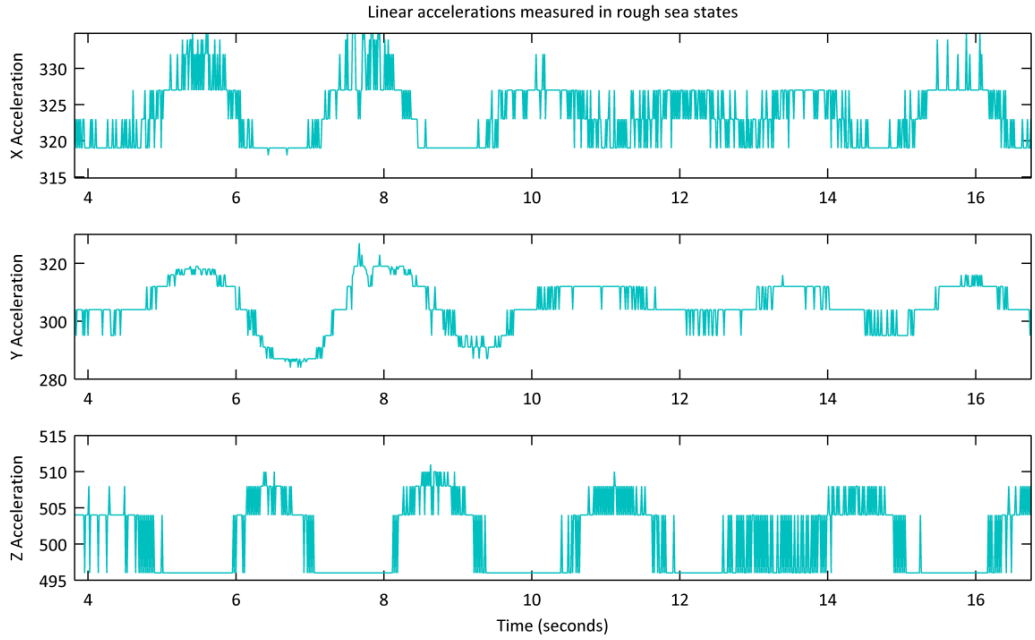

Figure 3.17 - Example 3-axis linear accelerations measured in rough sea states. A 12 second excerpt from a test on the 12/09/08 is shown.

This is an example of the second level to the proposed sensor fusion algorithms – a *strategic* level above the signal fusion level as discussed in section 2.3.2.4 [15]. This strategic level needs to be aware of the characteristics of each sensor and the situations when it can be of use. This means exploiting positive characteristics of sensor data while rejecting a sensor's characteristics when they are a detriment (e.g. not using accelerometers for long term position information due to drift), it is also important to realise the benefits of each sensor and the situations when it can be employed to great effect in *improving* the navigation capabilities.

The strategic level of the sensor fusion algorithm needs to be capable of dynamic adjustment of the biasing of the algorithm in response to changing conditions and therefore the changing

characteristics of the sensor. For example, sudden movements would call for an increase on the bias of the accelerometers but a reduction in sonar bias (the sudden movements would be missed by the slower response sonar). Conversely, when operating close to the water surface in turbulent conditions, the effectiveness of the sonar is impaired so the bias on sonar information needs to be reduced. Sensor fusion algorithms exist which are capable of performing this biasing, for example the extended Kalman filter introduced earlier (section 2.3.2.4.2.2).

A dual-level sensor fusion algorithm is proposed, capable of low-level numerical fusion of sensor data, but also with a strategic level capable of assessing both environmental conditions and the task at hand and dynamically adjusting the sensor bias to maintain an optimal position estimate by exploiting sensor characteristics.

3.6.2 The challenges of obtaining useful scientific video / sonar footage

The third objective of the sea trials was an evaluation of the challenges of obtaining useful scientific video / sonar footage in an open ocean setting. Several adaptations were made for this purpose, including adapted movement and guidance subroutines for use in the open ocean conditions in order to obtain steady footage and to track an accurate course despite currents and swells. Studies into station keeping, including the correction of swells and wave action, as well as techniques to track underwater position are discussed in other sections.

A variety of imaging devices were fitted to *Hawthorne 2.1* for imaging and recording of the underwater environment, including colour video cameras and monochrome infrared cameras depending on the conditions specific to each kelp bed. Section 2.2.3.2 identified the need to supplement video footage with sonar scans, both to increase range and coverage, but also when operating in turbid water or in areas of poor illumination [9]. Initial trials were conducted using the Imagenex Delta T multibeam sonar to supplement the video footage, of particular use at depth and when operating in poor visibility under the kelp canopy. The integration of the Delta T is detailed in later chapters and becomes a focus of this research.

Frameworks to support both the low level direct fusion of idiothetic and allothetic sensors, as well as the high level fusion of sonar and video were introduced in section 2.3.2.4 [15]. The principle of this multi-level fusion is that each sensor has individual qualities and optimum operating conditions. However, often the best dataset is comprised of imagery captured from more than one of these devices simultaneously [9]. This helps to overcome both the limitations of finite-performance sensors, low-budgets, and the limitations of the underwater environment. For example, video can be used to add detail to sonar logs, infrared cameras can improve visibility and the sonar and video cameras provide a complement of detail, resolution and range.

Whether the data is forward facing video and sonar to be played back later with location information for identifying positions, or downward facing video and sonar for generating a mosaic map of the seabed, underwater positional information is crucial. This localises any footage and allows accurate comparisons to be made between different areas, observations to be made on the conditions and habitat of each location, and for accurate maps to be generated. It also allows comparisons to be made between surveys conducted at different times but known to be in the same place. Accurate position information is required to turn the vehicle from simply an inspection tool to a useful biological / ecological / geographical research tool capable of gathering useful survey data. Techniques towards underwater navigation were provided in part by the INS, compass and pressure sensor already fitted to *Hawthorne 2.1*. However, accuracy improvements were an important opportunity for development in subsequent vehicles

3.7 Conclusions

Hawthorne 2.0 was completed in July 2008 and included a basic underwater navigation system. The vehicle served its purpose as a test bed for the development of underwater navigation and control strategies and demonstrated the benefits of holonomic motion. With its single sensor navigation system, the vehicle highlighted several opportunities for development and provided a baseline for comparison of the sensor fusion navigation and holonomic control algorithms developed later in this research. The test bed also allowed new systems to be trialled in the open ocean without having to rely solely on simulation and informed the development of future generations of underwater vehicles including formalising several of the standards developed in Appendix A.

Hawthorne 2.0 saw initial development into autonomous operation. The techniques and advantages of operating both as an AUV at the SAUC-E competition and as ROV during the field season were both seen. At the competition, basic autonomous navigation techniques were demonstrated in the confined environment [322]. In the summer of 2008, the vehicle underwent several modifications for the field operations, including a redesigned hull and protective frame, redesigned tether, software flexibility between ROV and AUV modes, additional underwater imaging devices and expanded underwater navigation sensors. The upgraded vehicle, *Hawthorne 2.1*, saw successful deployment as an ROV supporting grey whale habitat and coastal ecosystems field research in Canada.

The field season was dual-purpose; one aim was to demonstrate the feasibility and benefits of using underwater vehicles for the study, inspection and survey of kelp beds. In this respect, *Hawthorne 2.1* successfully proved the feasibility of operation in the open ocean and gathered several useful video datasets of the kelp beds, both in colour and in IR illuminated monochrome. The advantages of using underwater vehicles to perform the surveys over divers, camera drops and tows were demonstrated with benefits of financial and time savings as well as increased coverage and detail [11, 13]. The coastal ecosystems research group committed to the future development and use of underwater vehicles. Gathering scientific video footage was demonstrated, together with the manoeuvrability provided by holonomic propulsion [288] and the importance of realtime supervision and control to data validity [22]. However, several opportunities for development were identified.

3.7.1 Opportunities identified for development in future vehicles

There are general improvements to be made with each new revision of underwater vehicle including extended efficiency, miniaturisation without sacrificing strength, speed, endurance, manoeuvrability, sensing capabilities and accuracy. Based on the field trials of *Hawthorne 2.1*, three specific areas for development for nearshore habitat mapping were identified to inform development of the next generation of vehicle detailed in Chapter 4. These comprised development of the underwater navigation system including sensor fusion, the integration of sonar for kelp bed mapping and the development of the holonomic iROV concept.

3.7.1.1 Development of underwater navigation and sensor fusion

As highlighted in section 3.6.1, the most important improvement to be made was to increase the capabilities and performance of the navigation system. Improvements to the underwater positional accuracy of the vehicle would yield benefits in a host of other areas. These included improving the usefulness of sensory data captured through improved positional data [69] and

station keeping [263], improvements in the manoeuvrability of the vehicle from an increased integration of the navigation system and movement control algorithms [288] and an increased reliability when operating for long periods underwater. An increase in efficiency from effective path-planning, in reliability from improved collision avoidance and in the autonomy of the vehicle would all be facilitated by improvements in the navigation capabilities [157]. Improving the accuracy and reliability of the underwater navigation system, without sacrificing the low-cost and flexibility of the existing system, was the immediate focus of vehicle development, covering both navigation hardware and software.

Hawthorne 2.1 demonstrated the capabilities of single sensor navigation using a suite of *unlinked* sensors comprising a compass, GPS, pressure sensor and an echosounder to measure altitude. A low budget INS was added to evaluate its performance in the nearshore. In summary, the gyroscopes provided a useful measure of inclination and provided a complementary dataset to the mechanically gimballed compass, while the accelerometers were not accurate enough for underwater position tracking alone. However, short-term accelerometer measurements of wave-induced disturbances were demonstrated with a view to station keeping [261].

The test bed *Hawthorne 2.1* showed that navigation of an underwater vehicle using solely an INS of this order of magnitude of budget was infeasible. The drift, errors and noise were too large to allow accurate tracking of position for any useful length of time underwater. The isolated sensor system was not sufficient for underwater positioning, and it was this premise which directed the research and development of a combined, 'sensor-fusion' approach to the underwater positioning and navigation system [15].

This single-sensor navigation system provided a baseline of performance from which later improvement could be measured. As discussed in later sections, the proposed improvements were twofold: to supplement the existing INS with a higher specification model to improve the quality of the INS data, and to supplement the INS data with navigation data from additional complementary sensors [15].

This sensor fusion was proposed at two levels. The first, a low-level combination of absolute and relative sensors to combine the robustness of dead reckoning with drift free absolute updates [89], together with a second strategic level which was able to assess the changing conditions and make continual decisions as to which sensor combinations are the most reliable and accurate given the current environment, conditions and mission [160].

This process of 'sensor-fusion' underlies the principle of this work and is discussed in depth in later sections: improvements in underwater navigation and mapping can be gained using a complementary set of sensors [167]. Reliability and flexibility could also be added by mitigating, at least in part, the effects of sensor failure and varying sensor availability (e.g. changing conditions, depth, etc.) [329].

3.7.1.2 Integration of sonar for kelp mapping

A development of the proposed sensor fusion was at the feature level [15], to supplement the existing successful video mapping of kelp stipes with sonar scans, as identified in the literature review. As discussed in section 2.2.3.2, this complementary pair of sensors had the potential to increase coverage, detail and reliability when operating in the hostile nearshore conditions [329]. The limitations of kelp bed visual surveys were seen, in particular in poor visual conditions and with limited coverage. The addition of sonar mapping to augment visual mapping had great potential [11], enabled by the manoeuvrability benefits of the holonomic sensor platform [288].

3.7.1.3 The holonomic iROV concept

Finally, flexibility between ROV and AUV operation with a 'hybrid mode' of autonomous-assisted remote operation was demonstrated in the field trials of *Hawthorne 2.1* as essential to ensuring reliable operation and data validity in the dynamic nearshore environment [249]. As conditions could quickly alter within a few metres and within the duration of a few minutes, realtime feedback of the results and operating environment to a remote operator was essential. Basic hybrid control techniques to reduce the operator load were demonstrated on *Hawthorne 2.1* exploiting the holonomic capabilities of the vehicle, including holding a heading and depth despite external disturbances. Further development of both the navigation system and hybrid iROV control system was used to aid these station keeping operations, with development towards scheduling basic manoeuvres into complete survey patterns [249].

The importance of selecting either remote control, autonomous control or a hybrid operating mode which best suited the operating environment and dynamic conditions was identified in the literature review [21] and during the field trials. This was used to inform development of the hybrid iROV concept. For example, when operating in a complex environment with no prior knowledge, complete remote control was maintained. Then, when the operator needed to focus their attention on another task, for example inspecting the video or sonar data, a position could be held or a course steered autonomously [256, 263]. Thus, the reliability and security of remote monitoring and high-level control was maintained but low-level control could be automated. Similarly, through the hybrid power supply, a thin, flexible tether could be used while allowing full manoeuvring thrust and an unlimited mission duration.

Coupled with further development of the hybridised control system, further development to exploit the benefits of holonomic motion was also proposed. Although the thrusters fitted to *Hawthorne 2.0* and *Hawthorne 2.1* were capable of holonomic propulsion, the hull designs were not complementary to holonomic manoeuvrability, in particular the oblong open frame of *Hawthorne 2.1*. The development of a more streamlined hull which maintained the flexibility and modularity of upgrades had the potential to improve manoeuvrability when operating within the kelp beds and to reduce the chance of tangling. The benefits of an axisymmetric hull to enable unrestricted panning of directional sensors was recognised from other vehicles [288], however has not been implemented for vehicles of the size, budget and capabilities suitable to nearshore mapping developed in this research.

Chapter 4 Test Platform: the iROV *SeaBiscuit*

4.1 Introduction

Based on the requirements identified in the literature review in Chapter 2, with the concluding section proposing the opportunity for a hybrid solution for kelp bed surveying and mapping, and the background work presented in Chapter 3, this chapter details the development of the iROV *SeaBiscuit*.

In Chapter 3, *Hawthorne 2.0* demonstrated preliminary autonomous capabilities at the SAUC-E 2008 competition and its revision, *Hawthorne 2.1*, demonstrated the benefits of using underwater vehicles for kelp bed mapping during sea trials. The challenges identified in the literature review of navigating in the nearshore environment were explored, together with the limitations of a single-sensor underwater navigation system. These limitations highlighted the benefits and application of a multi-sensor approach to nearshore navigation and the benefits of holonomic motion both for station keeping and for manoeuvrability.

This background work informed the development of the holonomic, intelligent, position-aware hybrid ROV (iROV) *SeaBiscuit*, completed in 2009. *SeaBiscuit* was designed for the same nearshore application as *Hawthorne 2.1*, yet built on the strengths of flexibility between ROV/AUV operation, holonomic propulsion and navigation, and the flexibility of a modular, re-configurable, multi-purpose frame, hardware, sensing and software. This chapter provides a design overview of *SeaBiscuit* across the areas of mechanical, electrical, machine health, sensing and software.

SeaBiscuit was designed with several novel features to address the limitations identified with *Hawthorne 2.1* and alternative habitat mapping techniques discussed in the literature review. Chiefly, these comprised improvements to the navigation and mapping sensor suite in terms of accuracy, extended coverage and modality, the combination of absolute and relative sensors, a sensor-fusion algorithm designed to combine data from multiple sensors to improve the quality of navigation, and improved autonomous holonomic control algorithms.

Hybrid iROV control provided a novel solution to reliable operation in the nearshore, relieving the operator of low level control while allowing realtime data supervision and survey direction. This was complemented by a hybrid power supply, providing an onboard energy buffer for high power manoeuvring thrust with an unlimited survey duration using a thin flexible tether. The technique of spin mapping identified in the literature review was extended from a single high-budget vehicle designed for closed static environments [29] to the challenging conditions of the nearshore using a multibeam sonar with vertical resolution and a scanning sonar with a scanning sector independent of vehicle heading. The cylindrical hull and complementary holonomic propulsion system were designed to exploit maximum habitat mapping and navigation information from a limited budget sensor suite to enable 3D mapping and localisation while underway. The opportunity identified to integrate sonar mapping of the kelp stipes to augment video footage was also implemented in *SeaBiscuit*.

4.2 Overview of *SeaBiscuit* design

Named after both the round, flat marine animal that its circular shell resembles and the champion racehorse, the intelligent, position-aware iROV *SeaBiscuit* represented many significant advances over its predecessors. The aim was to build upon the requirements identified from *Hawthorne 2.0* and *2.1* to provide a survey sensor platform capable of operating and navigating in the nearshore environment. Figure 4.1 below shows the finished iROV and Figure 4.2 on the following page gives a systems overview of *SeaBiscuit*, together with the specifications in Table 4.1.

Figure 4.1 - The iROV *SeaBiscuit*, the second generation underwater vehicle pictured in Canada, ready for field trials.

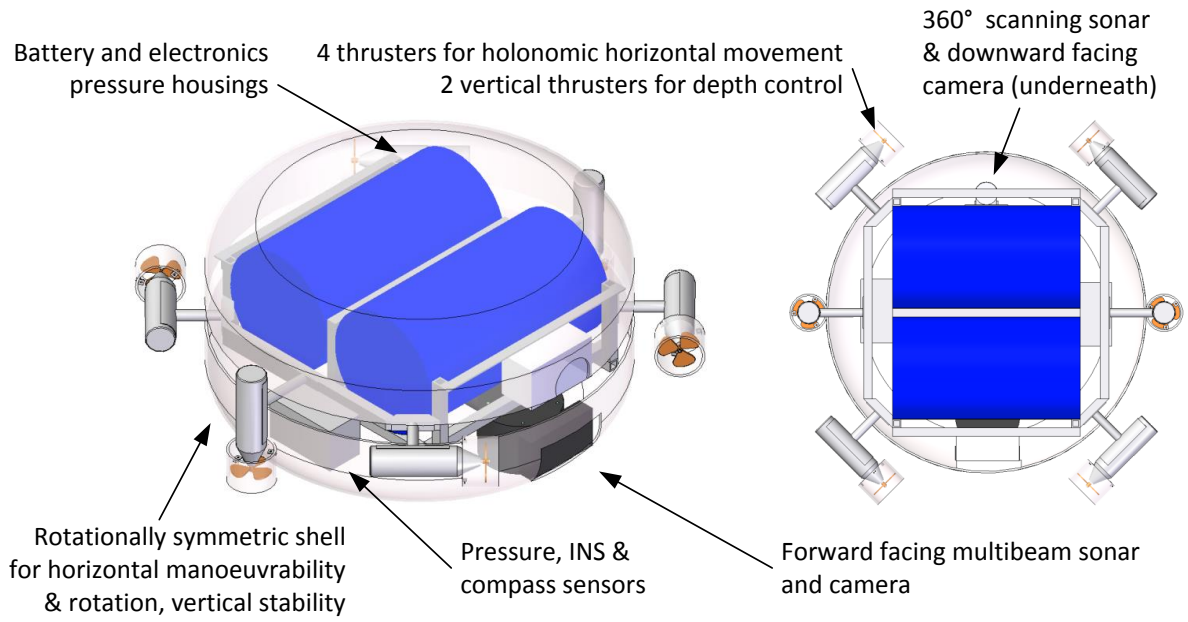

Figure 4.2 - A summary of the key features of the iROV *SeaBiscuit*.

Table 4.1 - *SeaBiscuit* specifications

Dimensions:	850mm L × 950mm W × 460mm H assembled overall 65kg in air fully equipped					
Frame:	Reconfigurable aluminium open-frame, bolted together to allow for easy collapse and reassembly (for shipping), modules supported on brackets. 45° motor frame and sensor mountings are welded aluminium to ensure repeatable mounting. Protective and hydrodynamic fibreglass shell encasing all items except for thrusters.					
Pressure Vessels:	Dual 225mm diameter HDPE cylinders with aluminium bulkheads contain batteries, computing, signal processing and communications equipment. Custom made aluminium peripheral housings for cameras, navigation equipment, antennas, tether & switch box, cable junction boxes.					
Computing:	Dual EPIA PX10000G Pico-ITX motherboards with 8GB SSD, 1GB RAM, ARTiGO housing					
Software:	Microsoft Windows XP Professional, National Instruments LabVIEW, C++, OpenCV					
Sensing:	Imagenex Delta T 837 Multibeam Sonar Imagenex Model 852 Ultra-Miniature Scanning Sonar Forward & downward facing Logitech QuickCam S5500 Cameras NASA NMEA Gimbal-stabilised marine compass SparkFun 6DoF v2 IMU (3DoF Gyroscopes, 3DoF Accelerometers) Xsens MTi 6DoF IMU (3DoF Gyroscopes, 3DoF Accelerometers, 3DoF Magnetometers) Keller PAA21SR 0-2.5bar absolute external pressure transducer SiRFstar III GPS Receiver Extensive machine health & diagnostic sensors (temperature, humidity, voltage, current, leak detection, housing pressure)					
DAQ:	National Instruments USB-6008 and USB-6009 USB Data Acquisition Units (Analogue Input 14-bit, 48kS/s, Analogue Output, Digital I/O)					
Connectivity:	Surface:	Wi-Fi (dual) Remote Access (Control, Data, Telemetry, Mission Data)				
	Submerged:	Umbilical LAN Remote Access (Control, Data, Telemetry, Mission Data)				
Thrusters:	Custom built aluminium oil filled thruster housings.					
	Horizontal:	4 ×	Maxon	RE36 118798	70W	Brushed DC Motors
		4 ×	Rivabo	Brass 535-075 M5	75mm	Propellers
	Vertical:	2 ×	Maxon	RE36 118798	70W	Brushed DC Motors
		2 ×	Rivabo	Brass 535-075 M5	75mm	Propellers
Propulsion:	Holonomic propulsion in the horizontal plane, vertical translation (depth), stable in pitch and roll.					
Motor Control:	3 × Polulu dual-channel MD03A Reversible H-Bridges driven by custom AVR motor controller					
Power:	Computers and sensors:	2S 12V 4Ah SLA rechargeable batteries (24V 4Ah overall)				1h30 runtime (2.5A)
	Motors:	2S 12V 12Ah SLA rechargeable batteries (24V 12Ah overall)				0h25 *minimum* runtime (30A)
	Umbilical power supplied at 32V external connection					
Buoyancy:	Buoyancy trim provided by extruded polystyrene foam moulded under the shell.					

4.3 Mechanical systems

SeaBiscuit used the same motor layout as its predecessors, *Hawthorne 2.0* and *Hawthorne 2.1* to achieve the same benefits of redundant holonomic movement (section 2.3.2.8). However, the frame, shell and internal configuration were completely redesigned. As seen in the following sections, this redesign allowed greater reliability and flexibility when operating in the kelp beds.

4.3.1 Frame and shell

All components were contained within a 700mm diameter circular, fibreglass hull, formulated to give the iROV homogenous drag in the horizontal plane. This simplified the holonomic control algorithms and allowed great flexibility for maximising the benefits of omnidirectional horizontal movement exploiting the axisymmetric hull. The shell also provided protection of the delicate internal components when deploying, operating and recovering the vehicle.

All stages of manufacture of the upper and lower shells were conducted 'in-house', from the initial development of a polystyrene plug (Figure 4.3) through to building the mould from which identical shells could be produced. Layers of gel coat, fibreglass matting and epoxy resin were used to create a strong but lightweight final shell of approximately 4mm in thickness. This in-house manufacturing allowed complete customisation of shell (and indeed most of the other parts used on the vehicle, including the frame, peripheral housings, thrusters and pressure vessels).

The fibreglass shell was supported by a strong but lightweight aluminium frame. Aluminium, stainless steel and brass were used throughout construction to limit corrosion depending on the qualities of material required (lightweight, strength, and low-friction & non-ferrous strength respectively). A sacrificial zinc anode provided protection from the damage due to seawater through galvanic corrosion.

Emergency switches were easily accessible at the rear of the vehicle for safety reasons. The heavier battery housing was positioned at the rear of the vehicle to counteract the pitching moment forces generated by the heavy multibeam sonar mounted forward on the vehicle.

Figure 4.3 - The polystyrene foam plug used to form the hull mould, finished with filler to remove surface irregularities.

Figure 4.4 - The unpainted fibreglass shell showing the internal aluminium frame and two pressure vessels.

4.3.2 Pressure vessels

The watertight containers used to house the batteries and the bulk of the electronics were designed and manufactured in-house. The two containers consist of ID 195mm plastic pipe 400mm long with 15mm wall thickness. These pipes, originally designed for water transport, are rated to pressures of up to 10bar. In order to create watertight housings, the ends were sealed with bespoke aluminium top hats, each possessing a nitrile barrel O-ring situated within recesses on each of the end caps (see Figure 4.5). The tapers included in the lips of the pipe ensured a watertight seal which became increasingly effective at greater depths as the external pressure compressed the O-ring into the taper. The caps were secured with adjustable latches (Figure 4.5) as an additional precaution against the end caps being accidentally knocked off.

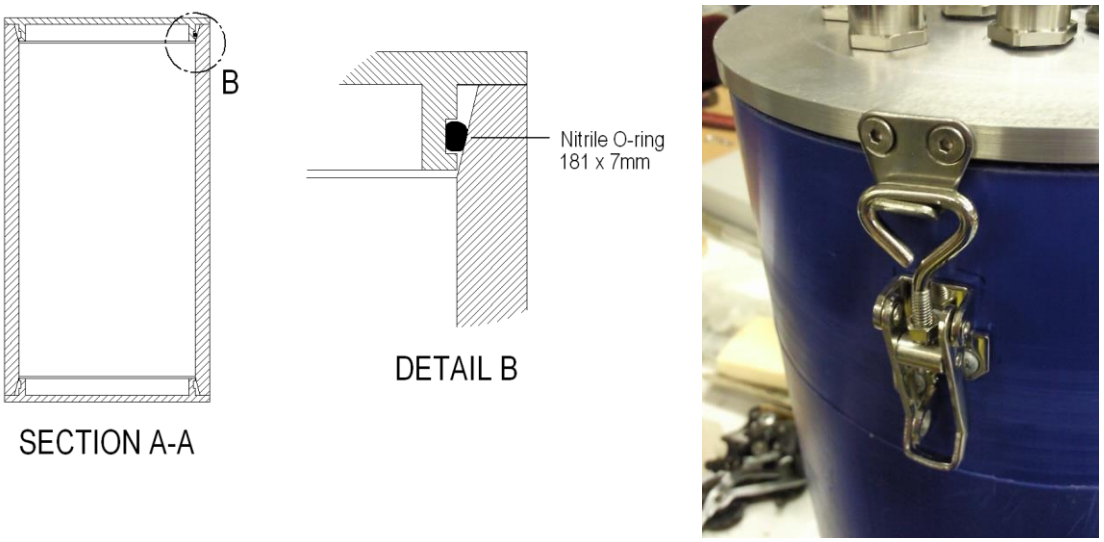

Figure 4.5 - The sealing arrangement of the main pressure vessels (L) Pipe section with O-ring and end cap detail (R) The adjustable-tension end cap retaining latch (4 per end).

The peripheral housings are of a similar design to the proven main pressure vessels but of smaller dimensions as shown below in Figure 4.6. These smaller housings used a transparent polycarbonate faceplate to allow cameras to be mounted inside the housings or to allow inspection or diagnostic lights. The housings were sealed with a nitrile O-ring. Re-usable silica gel sachets were installed in all of the housings to prevent humidity from the damp sea air condensing at low temperatures at depth and causing corrosion or damage to the electronics.

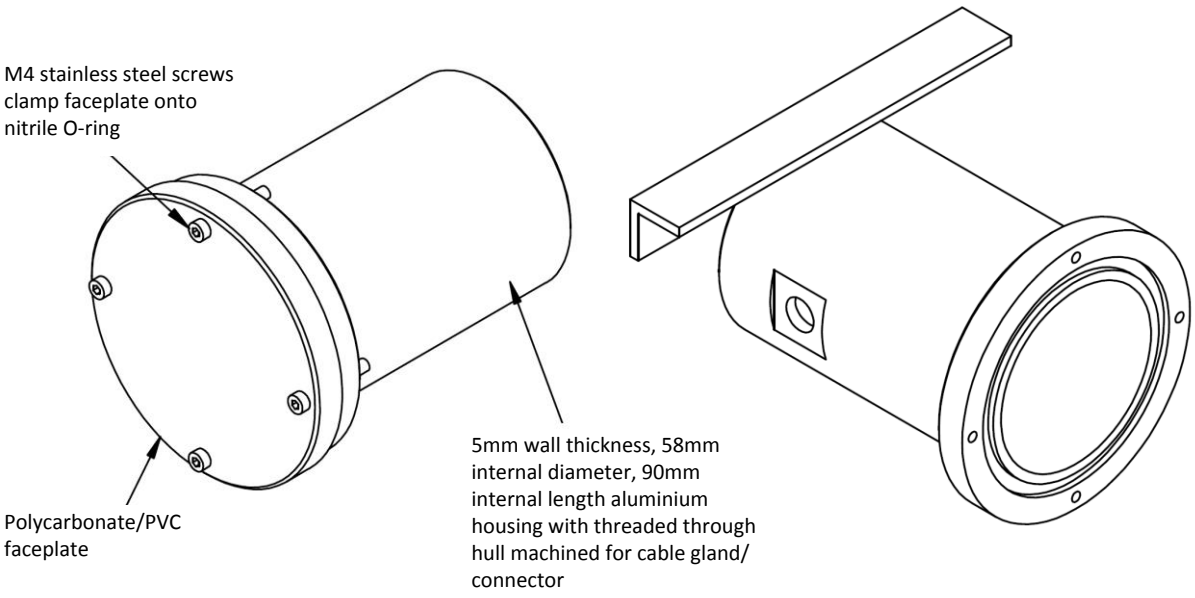

Figure 4.6 - Example aluminium peripheral housing with a clear polycarbonate faceplate sealed by an O-ring.

An option when designing the pressure vessels was to fill them with an electrically inert fluid, for example mineral oil. This incompressible fluid would allow thinner-walled, smaller, lighter-weight housings. However, the benefits gained for this shallow water, therefore relatively low pressure, application were deemed negligible when compared to the added difficulty of adjusting, upgrading and altering the internal components of what was still a system under development. This technique was however implemented on the thruster housings (section 4.3.5). In this case, the benefits gained were significant as the thrusters represented a more finished product with less ongoing development and therefore less frequent access was required, and sealing a rotating thruster shaft is more complex.

4.3.3 Connectors and through-hulls

A serious reliability issue with *Hawthorne 2.0* and *2.1* was the risk of water ingress through the bulkhead connectors. Although the connectors used were of the correct pressure specification, they were mechanically fragile and if damaged, would allow water into the pressure vessels.

To provide electrical and waterproofing reliability, SEACON WET-CON connectors were fitted to *SeaBiscuit*. Wet-mateable connectors were used in applications where the components needed to be frequently removed from the vehicle for testing and development. This supported the design principle used throughout of flexible, modular, reconfigurable systems and also simplified repair and replacement. A common standard of connectors was used throughout the vehicle (detailed in section 4.4.4). 10-bar rated nickel-plated brass cable glands were used of varying sizes for the through-hulls which did not need to be disconnectable.

4.3.4 Buoyancy and pressurisation

Hawthorne 2.0 and *2.1* used an active pressure compensation system to maintain the internal pressure of all housings and thrusters at slightly above ambient pressure throughout a mission. This system reduced the weight and manufacturing complexity of the housings as they could be rated for a much smaller pressure differential than the true vehicle depth. However, the weight added by the air cylinder offset any gain. The air supply was also finite and, as it was exhausted, the weight of the vehicle changed by a few hundred grams thus altering the buoyancy and requiring corrective thrust.

To increase the efficiency and reliability of the vehicle, the active pressure compensation system was removed in *SeaBiscuit*. All pressure vessels and peripheral housings were replaced with >5 bar rated housings, thus allowing unlimited runtime (using the tether to charge the batteries) without having to refill air cylinders. The buoyancy of the vehicle was still trimmed to 0.5% positive buoyancy using polystyrene foam to enable straightforward recovery of the vehicle should systems fail.

4.3.5 Thrusters

SeaBiscuit used six reversible variable speed thruster units arranged in the same layout as on *Hawthorne 2.0* and *2.1* to provide holonomic movement in the horizontal plane and vertical control of depth. This system of using opposing thrusters to achieve holonomic motion was discussed previously in section 2.3.2.9.1.

The thrusters were upgraded from the PVC housings containing lower power and lower efficiency 12V brushed motors used on *Hawthorne 2.0* and *2.1*. These required an external air supply to prevent water ingress and the lower efficiency reduced the runtime of the vehicle considerably. Significant reliability, power and efficiency gains were made from the upgrade to these 24V thrusters. Each motor could be adjusted to run at any percentage of the top speed of approximately 1500 RPM, and was capable of producing 15N of thrust at top speed.

To increase the reliability and performance of the thrusters over those used on *Hawthorne 2.0* and *2.1*, a new thruster housing was designed and built in-house to suit *SeaBiscuit*. Through in-house design and machining, the cost was kept significantly lower than a commercial thruster unit and the parts could be customised exactly to suit the requirement. Aluminium housings were used to enclose DC brushed motors as shown in Figure 4.7.

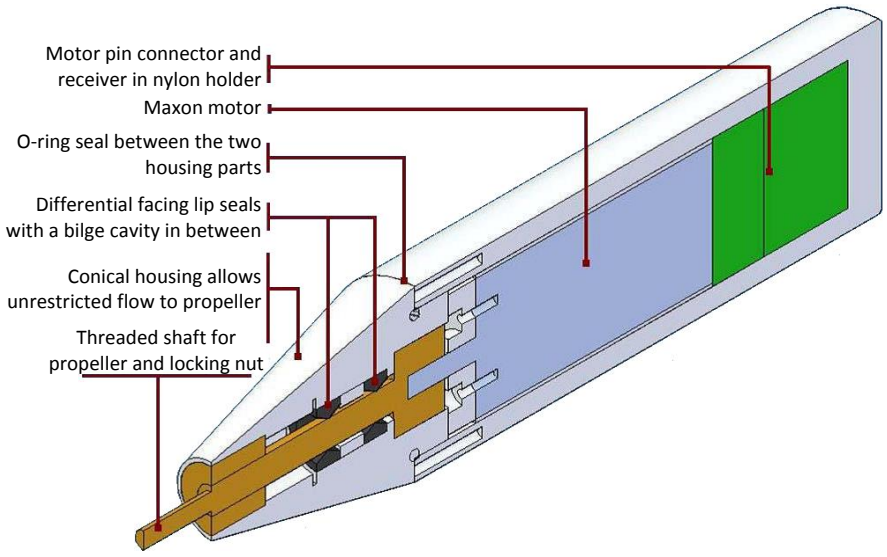

Figure 4.7 - Section view of thruster housing [322].

A thruster unit consisted of a 70 mm brass, three-blade propeller attached to a high-torque Maxon RE36 70W DC graphite brushed motor in a sealed aluminium housing, shown in Figure 4.7. The conical shaft seal unit used a bayonet fitting to secure the motor to the rear of the housing with a locking key for a quick, reliable fastening. A replaceable brass bushing was pressed into the aluminium conical end cap to support the propeller shaft. This held the shaft straight in the lip seals to minimise vibration and therefore the possibility of water ingress.

The tapered motor housing reduced hydrodynamic drag as water was accelerated over the housing by the propeller thus improving efficiency. It also allowed a larger intake for better reverse thrust efficiency [322].

The housings consisted of two main parts, bolted together and sealed with a compressed O-ring. With the correct manufacturing tolerances, the O-ring seal between the two sides of the housing was reliably waterproof. To prevent water ingress around the rotating propeller shaft, two lip seals were used, with an oil-filled bilge cavity between them. One lip seal faced outwards to resist the increased water pressure upon diving and a second lip seal faced inwards to prevent the oil leaving the housing in the case of a reverse pressure differential – e.g. temperature changes (hot thrusters, cool ambient temperature) or transporting the vehicle by airfreight at high altitudes.

To allow the motors to be run at high power (>300W) to provide the sudden impulses of thrust required for station keeping in rough conditions without overheating, the motors were sleeved into the aluminium housing to allow a good thermal conductivity with the housing wall. As the housing was cooled by the water flowing over it, it acted as a large heat sink. The thruster housings were also oil filled to cool and lubricate the motors.

Propeller nozzles were fitted increasing the performance of the motors through thrust augmentation by concentrating the flow aft, in addition to being a crucial safety feature. A fine mesh screen was also fitted around both sides of the nozzles to prevent any foreign bodies entering the thrusters, of particular importance when operating in the kelp beds.

The thruster housings were filled with lightweight hydraulic oil designed to inhibit rust and oxidation. This not only prevented corrosion when operating in the damp environment but also protected the motor from any ingress of water. The oil was virtually incompressible compared to air and so resists the deformation of the seals under high external pressures allowing the thrusters to operate at a much greater depth than if they were air filled.

The oil was inspected and changed together with the lip seals on a regular service schedule; typically the oil was inspected after each series of deployments and the lip seals changed if water ingress detected. An inspection point via the easily removable cable gland allowed the oil level and quality to be examined without having to disassemble the motor and disturb the seals. This allowed a failing seal to be changed in plenty of time without risking damage to the motor.

A sensor framework and associated wiring is in place (although not yet implemented) to complement the existing machine health system by sensing the motor temperature to detect sticking or overloaded thrusters and also to measure the conductivity of the oil, thus alerting the system to water ingress.

The four horizontal thrusters were mounted with their propellers facing forwards so that when the vehicle was moving with a forward component, the propellers were leading. This allowed a relatively undisturbed flow of water to reach the propellers; in reverse, the flow has to pass over the thruster housing, and various mounting brackets. It was proved experimentally that the

thrusters were more efficient in this orientation with the propeller leading [330]. As the vehicle was expected to spend more time moving with a forward component than a backward component, the thrusters were mounted for maximum efficiency most of the time.

The vertical thrusters were mounted with the propellers facing downwards which maintained the propellers submerged in the water when the vehicle was floating at the surface. This downward mounting orientation allowed a high waterline, thus enabling surface wireless transmission with the antennae out of the water while still submerging the propellers to allow the vehicle to dive when required. In addition, the propeller units are more efficient when the water enters the propeller through the nozzle and is accelerated out through the back of the nozzle and over the motor housing [330]. The vehicle was designed to be positively buoyant as a failsafe and so, because much of the time is spent driving the vehicle downwards to counteract this buoyancy, the vertical propeller units were orientated to provide maximum efficiency when driving the vehicle downwards (the most common direction).

4.4 Electrical systems

The electronics and electrical systems in *SeaBiscuit* underwent a complete redesign and rebuild from those which were tested in *Hawthorne 2.0* and *2.1*. This built on the strengths of *Hawthorne 2.0* and *2.1* yet increased reliability, performance, efficiency and sophistication. A brief summary of the electronic systems is contained in the following sections.

4.4.1 Systems overview

Figure 4.8 shows the overall systems layout of *SeaBiscuit*. To improve reliability, wherever possible the high current components such as the motor drive and battery charging circuits were isolated from the sensitive sensing and control systems, either by ensuring physical separation of the cabling as far as possible, or by using separate pressure vessels.

The ‘Battery Tube’ contained all of the high-current, high-heat output heavy electrical systems such as the batteries, charging systems, surface/battery changeover relays, battery isolators and motor drive electronics. This was physically isolated from the ‘Computer Tube’ which contained all of the computers, microcontrollers, signal processing, auxiliary navigation equipment and communications equipment. The sensitive navigation equipment was further isolated from all electrical noise and electromagnetic interference from high-current cabling, ferrous materials and the thrusters in a third aluminium housing underneath the vehicle. This modular design afforded reliability but also flexibility in testing, repairs and upgrades.

For safety, emergency power switches were fitted on the rear of the vehicle with a separate isolator for the motors and for the computers. This allowed the motors to be stopped in an emergency without necessarily stopping the computers. Magnets affixed to emergency pull cords activated reed switches which in turn operated the battery isolators.

The physical separation of each peripheral housing and the use of bulkhead connectors rather than cable glands also improved reliability when considering fault propagation. For example, water ingress from the exposed and easily damaged antenna box, could not spread through cable glands to more crucial components. In the case of the tether box, plugs were connected and removed regularly and therefore it was most susceptible to damage. However, by the provision of a separate tether box, any water ingress could not propagate further, avoiding damage to the contents of the computer or battery tubes.

The overall electrical layout is split into sub-systems and is discussed briefly in the following sections.

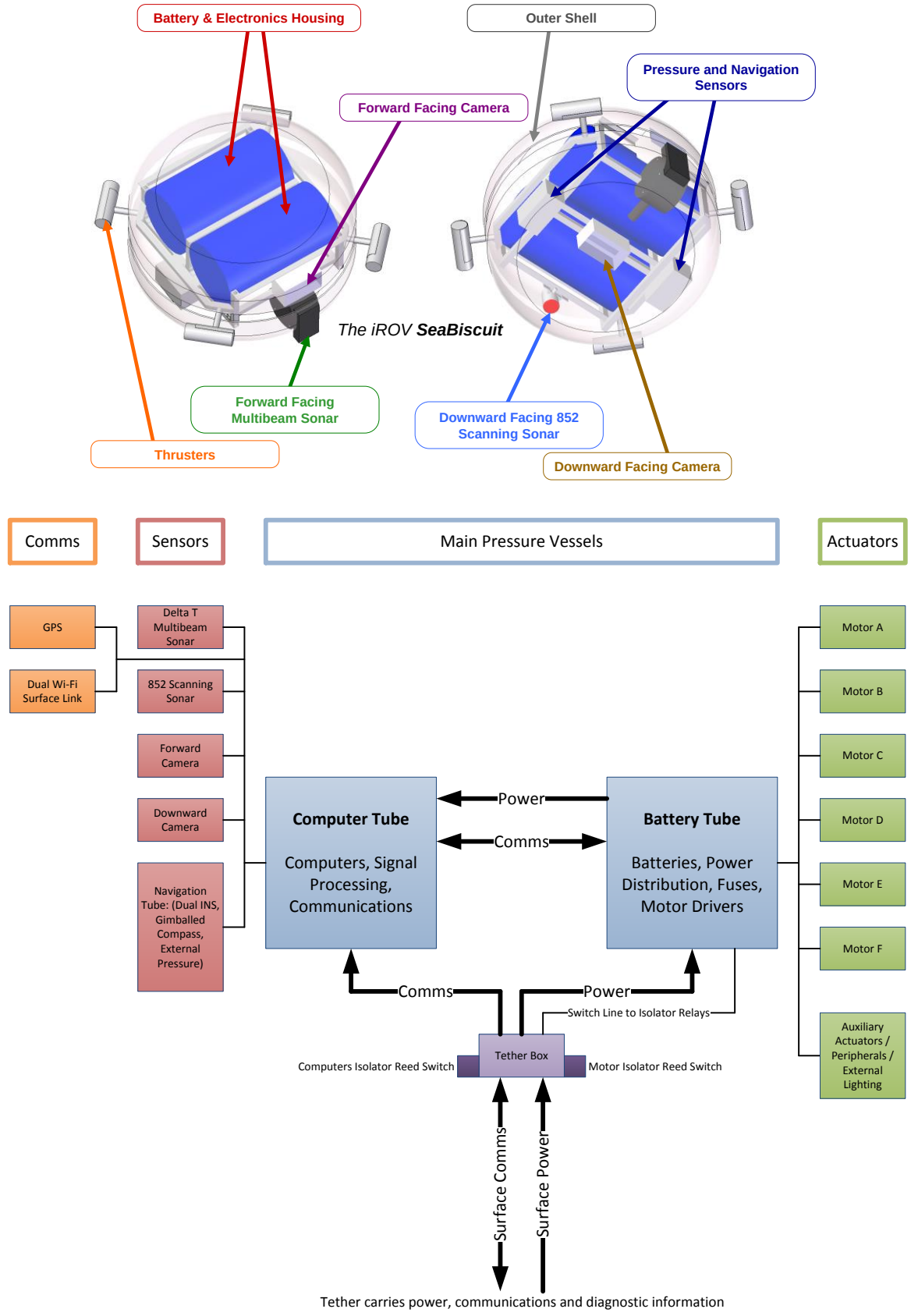

Figure 4.8 - Summarised systems overview of *SeaBiscuit* showing opportunity for expansion via auxiliary actuators and peripherals.

4.4.2 Tether and communications

The tether provided three functions: power for charging the onboard batteries, communications and control and a safety line. Figure 4.9 shows the key functionality and full details are provided in the standards detailed in Appendix A.

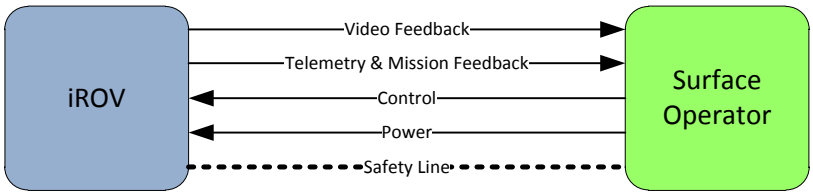

Figure 4.9 - The functions performed by the tether.

An onboard Local Area Network (LAN) was used to interface the high-bandwidth devices contained on the vehicle (control PC, vision PC, sonar) and indirectly all sensors and actuators. This onboard LAN was linked to the surface station router via the communications line (CAT6 Ethernet) where one or more laptops on the surface connected via cables or surface wireless.

The Ethernet tether facilitated straightforward testing and diagnostics, control, programming, sensor feedback and viewing sonar/video data in realtime. A Graphical User Interface (GUI) (discussed in the software section 4.7) allowed full remote control from the surface and sensor feedback. The network was also used to download data, to plan and initiate the next mission and to toggle the various autonomous functions.

LEDs on the rear of the vehicle, mounted behind the clear tether box cover, provided simple diagnostic information (power on, charge on). These were controlled via a USB data acquisition board on the vehicle. Ethernet independent diagnostic lines allowed these to be monitored at the surface via unused conductors in the communications tether.

Via the surface (optionally wireless) network, the sensor data was archived and streamed about the vessel, allowing researchers to view the incoming data and to direct the survey. Additionally, when operating with a live surface vessel (not-anchored) the skipper was able to view the survey in progress and position the surface vessel accordingly.

A wireless (Wi-Fi) data link replicated all of the tether communication functions when the vehicle was at the surface for flexibility through a high-gain waterproof antenna mounted in a separate antenna box on top of the vehicle connecting to the surface station router. This separate antenna enclosure was partly to raise the GPS and Wi-Fi antennas out of the water for increased signal strength while still keeping the sonars underwater, but also meant if the antenna became damaged and leaked, the leak would not compromise the main computer housing.

A 4-core 6A power cable provided a dual surface supply and charge line to both vehicle power circuits. SEACON WET-CON wet-mateable connectors were used to terminate the tether with automatically isolated pins on the vehicle, allowing for underwater connection and disconnection in the water.

Finally a safety line was attached to the vehicle, allowing it to be towed or recovered while providing strain relief for the tether cables.

The tether used for initial trials was 30m however, longer tethers are possible, limited by the 100m maximum length IEEE 802.3ab Ethernet specification [331]. For operation in the nearshore

environment, the surface vessel was always in close proximity and the maximum tether length was not a restriction on operation; longer tethers would also increase the risk of tangling.

Although power was carried by the tether, the battery pack on the vehicle was always present onboard. This was partly for reliability reasons and partly for performance issues. By carrying the battery power onboard, should the tether become damaged or disconnected then the vehicle could continue to function safely and be recovered without losing data.

The onboard battery pack also allowed a much smaller diameter cable to be used in the tether – the power supplied from the surface was current-limited to the diameter of the cable. This power was used to run the computers and to continuously trickle charge the batteries on board. When the high-current motors were run, the onboard batteries supplemented the tether power supply. The voltage drop over the length of the tether was also less of a problem with the low current trickle charge as the voltage drop is proportional to current.

Foam buoyancy floats were fitted along the length of the tether to maintain neutral tether buoyancy. This meant the weight of the tether would not prevent the vehicle from descending and ascending freely. A minimum tether thickness was also important as the tether thickness determines its drag; in order to maintain manoeuvrability, the vehicle still needed to be able to turn freely and quickly without the tether pulling on the vehicle [25]. The lighter, smaller diameter tether reduced the control issues with towing a long cable behind the vehicle.

4.4.3 Power supply and distribution

Onboard power was provided by two independent Sealed Lead Acid (SLA) battery packs as detailed in Table 4.2. The batteries were recharged in-situ via the surface tether. One battery pack was used to power the 24V thrusters and the other used for the sensitive computers, control electronics and sensor systems. This dual supply system isolated the sensitive electronics from electrical noise, interference and voltage sags caused by the high current operation of the thrusters. The system improved reliability and improved the quality of sensory measurements. It also allowed the computers to operate independently of an exhausted motor battery pack, allowing the vehicle to return to the surface passively, signal the end of its mission and then download the mission data before being recharged ready for the next mission.

Table 4.2 - Battery pack specifications

	Batteries used:	Capacity:	Runtime off batteries:
Computers, sensors and control electronics:	2 * Yuasa NP4.0-12	24V (2*12V) 4Ah (48Wh)	2hours assuming maximum loading
Motors:	2 * Yuasa NP12-12	24V (2*12V) 12Ah (144Wh)	40mins assuming 18A [20% thrust] continuous running at 100% duty cycle

The surface tether was capable of fast charging the batteries and supplying sufficient power for all computers and sensors, together with moderate thruster use. The runtime figures provided above are conservative estimates based on maximum loading if the tether was not used. In reality, a longer duration running off batteries could be achieved if sensors were only turned on when required and the motors rarely ran continuously at 100% duty cycle. All circuits were fused, including the surface supply and an overall fuse protected each battery supply. Battery isolators allowed maintenance to be carried out safely.

The batteries were contained in a separate housing to the computers and sensors to provide as much isolation as possible between the high current drive systems and the sensitive electronics. However this also allowed the vehicle specific batteries, motor drivers and cabling to be semi-permanently installed in the vehicle whereas the separate computer unit and sensors could be

removed, either for development and upgrades or to be used on a separate vehicle using the common interface standards detailed in Appendix A.

The battery housing also contained the isolation relays, the custom built microcontroller used to generate the high frequency motor Pulse Width Modulation (PWM) signals, the motor drivers, and a variety of sensors to monitor the state of charge and condition of the batteries.

Sealed Lead Acid (SLA) batteries were initially selected for their low cost and straightforward charging methods [332]. However, it was recognised that much higher energy densities were available from alternative battery chemistries such as Lithium Polymer (LiPo) cells. However, these space and weight savings, or alternatively longer runtimes, came at a price [333]. The cost of LiPo cells was considerably higher and the charging methods more complex. The power distribution system was designed to be adaptable between cell chemistries and voltages so the battery type can easily be swapped in the future if required.

A complex arrangement of changeover and isolator relays (section Appendix B) ensured the exposed pins on the tether box at the rear of the vehicle remained automatically isolated and unpowered until the tether was connected. This not only ensured safety if the pins were accidentally shorted during launch or operation, but also prevented electrolysis and corrosion of the pins when connected/disconnected underwater. A blanking plug was provided for additional protection.

The tether was powered at 32V DC and switch mode power supplies converted this to the various voltage levels required throughout the vehicle, thus mitigating any problems with a variable voltage supply or voltage drop. The supply voltage input was also wide-range. This allowed a coarse power supply to be used to run and charge the vehicle – for example, the 12/24V alternator output typical of a research vessel could be used directly.

The machine health system, discussed later in section 4.5, measured voltage and current throughout the vehicle, which allowed both the remote operator and the machine health algorithms to monitor the system.

4.4.4 Standard connectors and protocols

The common standards and protocols for connectors and interfaces implemented on *Hawthorne 2.0* and *2.1* were implemented on *SeaBiscuit* with some revisions. These standards have been adopted on all other pieces of underwater equipment and instrumentation built in the Ocean Technologies Laboratory at the University of Bath. Further details are contained in Appendix A.

The standard for connectors uses the SEACON WET-CON series of wet-mateable connectors. All connectors are keyed to ensure the correct orientation of insertion, with different pin configurations signifying different interfaces. Peripherals, actuators and sensors could all be swapped and interchanged between positions on *SeaBiscuit* and other vehicles and equipment.

Table 4.3 - Standard connectors and protocols

3 pin	24V PWM and polarity controlled actuator with optional data feedback, e.g. a thruster, lights
4 pin	USB with a high-current 5V line capable of powering peripherals and sensors
5 pin	RS485 with an optional 24V power supply
6 pin	USB connection with the high-current 5V line and an additional 12V option
8 pin	Ethernet with an optional 24V Power over Ethernet option (e.g. tether, sonar)
4 pin (large)	Dual-circuit power distribution (tether, battery and computer tube input / outputs)

Wherever possible, two data protocols were used. USB was used for low-bandwidth peripherals for the ease of multiplexing many peripherals using USB hubs. To allow for many peripherals on one bus, the 5V USB line was boosted with a high current supply. Ethernet was used when high-bandwidth was required (e.g. multibeam sonar, inter-computer communication) or long cable runs were necessary (e.g. tether).

By using these common standards for connectors and communication protocols, the principle of reliability of 'if it fits, it works' was applied throughout for simplicity of field operation.

4.4.5 Motor drivers

SeaBiscuit used a custom motor controller, built around an Atmel AVR Microcontroller to receive commands from the computer over an RS232 connection to control the speed and direction of each motor with 500 possible speed levels in each direction. The microcontroller generated the 6 simultaneous PWM signals required to drive the motors. 3 × Polulu dual-channel MD03A Reversible H-Bridges (VHN3SP30) were used to drive the 6 thrusters. These motor drivers were fitted with heat sinks and cooled by a recirculating fan.

4.4.6 Battery management

Each battery was charged with a constant current for the bulk charge, then a constant voltage for the float charge as detailed in Appendix B. Charger temperature, charge and discharge current, voltage, battery temperature and the housing pressure from any hydrogen gas given off were monitored during charge/discharge operation. A low-voltage cut off circuit protected the batteries from deep discharge.

4.4.7 Computers and control system

The proven dual computer setup from *Hawthorne 2.0* and *2.1* was used in *SeaBiscuit*, but upgraded to dual EPIA PX10000G (1 GHz, speed stepped for efficiency) Pico-ITX Series motherboards with 8GB SSD, 1GB RAM in an ARTiGO housing. When compared to the previous Mini-ITX boards, the Pico-ITX series were approximately 25% of the footprint and had a lower power consumption (<10W) for a comparable processing power. Both computers ran Windows XP Professional for ease of development and remote management and used solid state hard drives for reliability (mitigation of problems associated with humidity, condensation, pressure changes, vibrations, shocks) and for performance and efficiency.

One onboard computer performed high-level control, mission-planning, mapping, navigation and machine health while a second computer performed the processor-intensive vision and sonar processing. The computational load was redistributed depending on the mission in progress and the sensors in use. All algorithms were written to run on either computer with a full communication system established between the two computers to allow seamless interoperability. Space and wiring was provided for a third computer of the same form factor to provide increased onboard processing power, for example, separating vision, sonar and mapping, or increasing the frame rates of both sonars while mapping.

All timing critical operations, such as generating the motor control PWM signals and navigation timing were offloaded to dedicated microcontrollers. This allowed for realtime operation where necessary but retained the flexibility of interfacing with the main control computer. In the case of the navigation timing, the vehicle's heading and position were estimated from an integration of

angular velocity and linear acceleration respectively. Therefore the accuracy of the vehicle's state estimate depended not only on the accuracy of the measurement, but also crucially on the timing of the integration operation. Future developments could offload the machine health core systems to dedicated microcontrollers for further reliability.

4.5 Machine health

Recalling the literature review in Chapter 2 into the principle of machine health, and techniques for fault detection, fault reaction and fault tolerant control, an extensive network of machine health sensors, controllers and algorithms was built into *SeaBiscuit*, demonstrating significant advances over *Hawthorne 2.0* and *2.1*.

4.5.1 Fault detection

Each sensor used an appropriate interface circuit to drive and read the sensor, and if necessary condition and amplify the output. The analogue or digital sensor outputs were then interfaced to a set of National Instruments USB Data Acquisition (DAQ) Cards (USB-6008 and USB-6009) strategically placed throughout the vehicle in each of the three main pressure vessels (navigation, computer and battery containers). These DAQ cards allowed the data to be read directly into LabVIEW control programs where additional filtering was performed.

For each sensor, an upper (and lower if necessary) working limit and a safety limit were defined from a combination of operational testing under normal conditions and from the sensor datasheet. The sensors implemented in *SeaBiscuit* are listed below:

Water ingress:

Humidity detectors were installed in each pressure vessel to detect slow leaks, the potentially damaging effect of condensation and saturation of the silica gel desiccant sachets. Leak detectors measured continuity across separated conductors to detect the more rapid ingress of water.

Communication failure:

A communication failure to a peripheral was assessed based on the importance of that peripheral for the current mission. If the peripheral was essential then the mission was aborted. For a non-essential peripheral, the fault was logged to be inspected after the mission completed.

A communication failure to the surface operator when operating in iROV mode terminated the current mission, turned off all motors for safety and implemented an ascent either for recovery or for diagnostics using the surface wireless connection. A continual ping (a 'heartbeat') monitored the communication link with a timeout period to allow for momentary interruptions.

Navigation sensor failure:

If a fault with a navigation sensor was not detected then it could either reduce the navigation capabilities of the vehicle, or in the worst case, provide otherwise unnoticed false readings, causing errors in mapping and localisation. If uncorrected, this could cause the vehicle to exceed its safe operating depth or cause a collision, both of which would lead to more serious problems.

The sensor fusion navigation algorithm continually compared estimates of the same state from multiple sensors (e.g. vertical position was measured by external pressure, dead reckoning, sonar-detected altitude etc.). If a discrepancy arose between sensors then the incorrect readings were

discounted. This was realised by a simple voting algorithm (section 2.3.2.4.2.1). In the case of a faulty sensor, provided sufficient information was available from other sensors, the mission could continue using the built in redundancy of the design.

Overheating:

Thermistors and Resistance Temperature Detectors (RTDs) were installed on all key components to measure ambient temperatures in several zones. Overheating could cause damage to components or incorrect readings from sensors such as those used for navigation.

Overheating electronics or navigation sensors were shut down and, provided sufficient systems remained, the mission continued with reduced capabilities. The computers were 'speed-stepped' which reduced processor speed either on overheating or when at idle to reduce energy consumption and heat output.

Thrusters:

A framework was designed to measure the temperature of both the motors and the motor drivers to throttle back overheating motors/drivers using the built in redundancy of the system. Wiring was installed to measure motor temperature and rotational speed, however these sensors have not yet been implemented.

Sticking or jammed motors were detected by monitoring the current drawn by each motor with respect to the PWM voltage applied. At a later stage, speed feedback of the motors could also be used to detect sticking or jammed thrusters. A short burst in the opposite direction was sometimes enough to clear the propeller mesh screen of seaweed or debris. A persistent jammed or sticking motor was disabled and the built in redundancy of the propulsion system allowed the mission to continue to some extent.

Internal pressure:

The internal pressure of the main housings was monitored – any increase in pressure at depth (after temperature compensation) indicated a failing seal and the mission was aborted. The internal pressure of the battery tube was monitored to verify that any hydrogen gas given off by the sealed lead acid batteries was being correctly vented by the pressure relief valve.

Power Supply:

The surface power supply was continually monitored when present as was the battery voltage and current. The battery charge voltage, current and temperature were also monitored and the charger output thermally ramped to protect the chargers.

The state of charge of the batteries was monitored by voltage measurements but also by monitoring the charge and discharge currents over time. This allowed mission decisions to be made by monitoring the amount of energy remaining. For example, when operating from the tether, the vehicle speed could be reduced to allow the onboard battery buffer to recharge.

4.5.2 Fault reaction

Fault reaction is the second part of the machine health system. If a working limit was exceeded then corrective action was taken to try to bring the fault back within working limits. If the fault continued to develop, and the safety limit was exceeded, then an emergency mission abort was performed.

In the case of hybrid user-operated mode, a series of dials and warning lights on the graphical user interface provided a clear, concise and easy to see at a glance overview of the essential systems of the vehicle. Temperature, humidity, pressure and leak detection for all key systems were displayed and, if warning limits were exceeded, the user was notified and encouraged to adjust the operation to bring the levels back under control. If the fault continued to develop then the system was overridden by the machine health algorithm which safely aborted the current operation, allowing the vehicle to surface for recovery.

The fault specific reaction is briefly summarised in the section above which discussed individual sensors. In the case of a communications failure, the algorithms were written to be 'failsafe' – i.e. if a positive acknowledgement that the system is ok was not received then a fault is assumed to be present and the appropriate corrective action taken.

4.6 Sensing and algorithms

Based on the observations and conclusions from the test bed underwater vehicle *Hawthorne 2.0* and *2.1*, the navigation suite underwent a complete redesign with the addition and integration of several new sensors:

1. Upgraded forward and downward facing cameras – increased resolution and improved low-light sensitivity.
2. The addition of an Xsens MTi 6DoF Inertial Measurement Unit (3DoF Gyroscopes, 3DoF Accelerometers, 3DoF Magnetometers).
3. The use of the Imagenex Delta T multibeam sonar for navigational data as well as gathering scientific survey data.
4. The addition of an Imagenex 360° Model 852 Ultra-Miniature Scanning sonar for 360° horizontal plane long range detection.

This section provides a brief summary of the various navigation sensors fitted to *SeaBiscuit*. The hardware specifications are provided together with the software algorithms required to extract useful navigational data from each sensor. A measure of the uncertainty associated with each sensor is also considered, together with an approximation of the sensor characteristics. The sensor characteristics include modelling the environmental conditions which affect the performance of each sensor. The effect of changing environmental conditions on the *dynamic* accuracy and reliability of each sensor is also considered, including techniques for assessing the dynamic accuracy and reliability autonomously.

At this stage, each sensor is considered individually and it is not until the following chapter that the sensor fusion algorithms are introduced. The chapter on sensor fusion details the algorithms used to evaluate each estimate based on an uncertainty value and then use its contribution to update the vehicle position.

4.6.1 Navigation sensor suite overview

Table 4.4 provides a summary of the type of navigational data each sensor was *most commonly* used for and where possible a brief summary of any conditions required for the sensor to operate. The distinction between absolute and relative sensors or idiothetic and allothetic is also included. The diagram should be interpreted in conjunction with the notes following it.

Table 4.4 - A matrix overview of the navigation sensor suite showing the data most commonly used from each sensor. The red, green blue colour coding is used to discriminate between x, y and z position respectively, and roll, pitch and yaw angle respectively. See following text for detailed discussion.

	Mechanically Gimballed Compass	External Pressure Sensor	Xsens MTi 6 DoF IMU	Xsens MTi 3 DoF Magnetometer	852 Scanning Sonar	DeltaT Profiling Sonar	GPS	Forward Facing Camera	Downward Facing Camera	Stereo Vision Forward Cameras	CMPS03 Compass	SparkFun 6 DoF IMU	Any additional sensors
Roll Angle (θ_x)			**RELATIVE** Susceptible to drift	**ABSOLUTE**								**RELATIVE** Susceptible to drift	
Pitch Angle (θ_y)			**RELATIVE** Susceptible to drift	**ABSOLUTE**								**RELATIVE** Susceptible to drift	
Yaw Angle (θ_z)	**ABSOLUTE** Provided θ_x&θ_y<30° for gimbals		**RELATIVE** Susceptible to drift	**ABSOLUTE**				**ABSOLUTE** Provided a landmark is visible		**ABSOLUTE** Provided a landmark is visible	**ABSOLUTE** Provided θ_x&θ_y==0° so removed	**RELATIVE** Susceptible to drift	
X Position			**RELATIVE** Susceptible to drift		**ABSOLUTE** Provided a landmark is visible	**ABSOLUTE** Provided a landmark is visible	**ABSOLUTE** Only at surface		**ABSOLUTE** Provided seabed is visible and distinct	**ABSOLUTE** Provided a landmark is visible		**RELATIVE** Susceptible to drift	
Y Position			**RELATIVE** Susceptible to drift		**ABSOLUTE** Provided a landmark is visible	**ABSOLUTE** Provided a landmark is visible	**ABSOLUTE** Only at surface		**ABSOLUTE** Provided seabed is visible and distinct	**ABSOLUTE** Provided a landmark is visible		**RELATIVE** Susceptible to drift	
Z Position		**ABSOLUTE** Relative to an origin defined at the surface	**RELATIVE** Susceptible to drift			**ABSOLUTE** Relative to an origin defined at the seabed		**ABSOLUTE** Provided a landmark is visible		**ABSOLUTE** Provided a landmark is visible		**RELATIVE** Susceptible to drift	
					If θ_x θ_y θ_z are known.			If θ_x θ_y = 0 or corrected for.					

The axes referred to in Table 4.4 were defined earlier in Figure 2.7 (page 66), where the origin of the z-axis (vertical) is defined as water surface. This is important when considering the *depth* of the vehicle beneath the water surface versus the *altitude* of the vehicle above the seabed. For example, when calculating Z position with the Delta T sonar, it is the *altitude* rather than the *depth* which is measured (provided the seabed is visible). The seabed is rarely flat and a uniform distance from the water surface, making inference of the *depth* from sonar measurements difficult unless the water surface can be reliably detected on the sonar scan. However, the external pressure sensor provides an accurate and reliable complementary measurement of submerged *depth*.

Considering the Delta T sonar, if θ_x θ_y θ_z are known, then the X, Y and Z position of the vehicle can be calculated if known stationary sonar targets are observed, or stationary sonar targets are reobserved and corresponded between successive frames. Conversely, if the X, Y and Z position of the vehicle is known relative to a known sonar target, then θ_x θ_y θ_z can be calculated. This second case however is less useful when considering what information is usually known from other sensors. Hence Table 4.4 only shows the most common information extracted from each sensor. Further details associated with each sensor are presented in the sensor specific following sections.

The greyed out sensors to the right in Table 4.4 show sensors which are not currently fitted to the vehicle. The CMPS03 compass sensor and the SparkFun 6 DoF IMU were both superseded by more accurate and reliable models (details of which are discussed in following sections). Stereo vision cameras to add depth perception to visual data have not yet been implemented.

The final dashed entry to the right in Table 4.4 represents the ease with which additional sensors can be integrated into the hardware and software framework. For example, as and when the budget allows or the application dictates, supplementary higher quality sonar and INS units could be added. Sensors such as Doppler Velocity Loggers (DVL), USBL (Ultra Short Base Line) units or GIB (GPS Intelligent Buoy) surface markers could also be integrated.

When considering if the sensor framework is complete, or at least adequate for a mission, a scan across each row of the matrix in Table 4.4, (representing each degree of freedom or axis of movement) quickly highlights any sensory shortcomings. A good mix of relative and absolute measurements of each degree of freedom can be verified. The trade-off between relative and absolute sensors (drift versus robustness to external disturbances and a requirement for external landmarks / satellites / etc.) was explored in previous sections.

The omission of a DVL is noted given the literature review in Chapter 2 identifying possible benefits for nearshore navigation. Although subject to cumulative errors due to dead reckoning, with limitations on operating in shallow water with turbulence and midwater vegetation and with size and budget constraints, the use of DVL navigation was considered for *SeaBiscuit*. However, it was the budget limitation which prevented its integration, in trying to maintain the total cost of the vehicle suitable to small-scale field research operations and in trying to achieve optimum navigation capabilities in the nearshore on a budget. A DVL would have perhaps provided more useful positional information than the Imagenex multibeam Delta T sonar, and would not have required sonar landmarks to navigate from. However, the budget was not available for *both* of these relatively expensive instruments and the multibeam sonar was required anyway for habitat mapping. Therefore, the focus was to use the multibeam sonar for these dual purposes – habitat mapping and navigation information, which followed the design principle of trying to achieve optimum navigation on a budget through innovative techniques.

The following sections provide an overview of the each sensor's hardware, software, application suitability and characteristics.

4.6.2 Magnetic compass

A NASA Marine Instruments NMEA (National Marine Electronics Association) Marine Compass Sensor provided a mechanically gimballed fluxgate reading of yaw angle (θ_z), giving a stable reading in up to ≈±30° of pitch and roll of the vehicle. However, although this provided a stable reading, it had a relatively slow update rate of ≈2Hz and a relatively slow response time to sudden angular accelerations (mechanical damping). These characteristics are complementary to the 3D magnetometers discussed in section 4.6.5 and, when coupled using the sensor fusion algorithm, provide a reliable estimate of yaw under all conditions of operation.

The accuracy of the compass is quoted as ±1° and the resolution as 0.1° [334]. In section 3.3.2.3 the aim of providing accurate and reliable navigation on a low budget, and using innovative algorithms to supplement low-end sensors was discussed. This compass was a relatively inexpensive unit representing only one class higher than the non-gimballed hobbyist unit which the NMEA compass superseded. The previous model fitted, a Devantech CMPS03 electronic compass using a Philips KMZ51 magnetic field sensor, provided a much faster update rate of ≈85Hz, however errors were quickly introduced if a pitch or roll angle was applied. The combination of the NMEA compass and the 3D magnetometer (detailed below in section 4.6.5) provided a superior output in every respect, hence the removal of the CMPS03 sensor.

The NMEA 0183 output was interfaced through an RS232 to USB converter into the navigation USB bus. Power was provided via a 12V supply at <0.1A. A simple NMEA 0183 sentence parser read the data stream, performed basic error detection and then output the bearing with a timestamp to the navigation algorithms.

The data provided by the compass sensor was absolute meaning that each new reading did not depend on a previous reading. This meant the positional information was not prone to drift

causing large cumulative errors to build up over time. However, the measurement was dependent on external factors (the Earth's magnetic field) thus making it susceptible to interference or errors. This was a trade-off with relative sensors which can be seen in the matrix in Table 4.4.

The compass output a bearing relative to magnetic north and in normal ocean environments the output was reliable. However, when operating in industrial or commercial environments, for example, docks, piers, harbours and tanks, or when operating close to a surface support vessel, interference from these nearby ferrous structures could affect the reading. The sensor fusion algorithms were used to evaluate the magnetic compass reading against other measures of yaw angle to detect and mitigate the errors.

4.6.3 External pressure sensor

The external pressure sensor (Keller, PAA21SR, 0-2·5 bar absolute) was used to estimate the submerged depth of the vehicle. The centre of the blue fibreglass shell (and thus the welded aluminium frame beneath) was defined as the centre of the X and Y axis of the vehicle. The top of the blue shell was defined as the zero point in the Z axis. Thus, when the vehicle was at zero depth, the waterline was level with the top of the shell. The vertical motors were submerged ready for diving, the sonar units were submerged for scanning and the GPS and Wi-Fi antennas were out of the water for communication.

The pressure sensor was calibrated for each operating environment. For the kelp bed mapping operation the vehicle was typically operating in 11°C, 3% salinity sea water. Different calibration values were used in different environments to allow for the varying water density.

The analogue output voltage was read by a National Instruments DAQ (Data Acquisition) card (USB-6009). The analogue voltage was converted to a depth reading and basic error detection was performed. The sensor was typically sampled at 10Hz and has an error band of <2% over 0-50°C (1% typical – error band included linearity, hysteresis, zero and span offsets, temperature effects and repeatability) [335].

The pressure measurements were absolute, therefore each new reading did not depend on previous values. The effects of vehicle movement affecting the measured pressure were avoided to some extent by housing the pressure sensor within the fibreglass shell. However, the sensor was susceptible to wave motion causing an increased water pressure, hence mapped data was referenced in the z-axis to the seabed where possible as the tide and wave height determined how high (in altitude) the vehicle was able to ascend. It was possible to estimate wave height and sea state while underwater by combining the multibeam sonar measure of altitude to the external pressure sensor measurement of depth.

4.6.4 Global Positioning System (GPS) receiver

SeaBiscuit was fitted with a SiRFstar III GPS receiver which was mounted in the antenna housing on top of the vehicle. A USB interface connected the GPS unit to the navigation computer. The accuracy of the GPS system was primarily dependent on the number of satellites available and typically a few metres at best. The antenna housing was mounted as high as possible on the vehicle to ensure the best possible satellite reception when the vehicle was at the surface. The SiRFstar III receiver was also WAAS/EGNOS enabled (Wide Area Augmentation System / European Geostationary Navigation Overlay Service) which allowed for enhanced accuracy when operating in areas with WAAS/EGNOS coverage.

4.6.5 Inertial navigation system

As originally described in section 3.6.1.1, the test bed *Hawthorne 2.1* was fitted with a SparkFun 6 Degree of Freedom (DoF) Inertial Measurement Unit (IMU) for the 2008 sea trials. At the end of section 3.6.1 it was proposed to use an additional amplifier to amplify the analogue output of the accelerometers to improve the sensitivity of the accelerometers and allow small accelerations typical of underwater navigation to be detected by the ADC.

A suitable 3-channel low-noise amplifier was designed and fitted. This amplifier did increase the sensitivity of the accelerometer circuit and reduced the quantisation error of the ADC by allowing the small magnitude accelerations to fill the full 10-bit ADC window, reducing drift to some extent. However, the accuracy was still deemed insufficient for the navigation of *Hawthorne 2.1* and later vehicles.

The overall Signal-to-Noise Ratio (SNR) was not improved. The amplifier, although low-noise, still introduced further noise onto the signal. From the conclusions drawn in section 3.7 the SparkFun IMU was shown to be insufficient as a sole source of navigation information. The SparkFun IMU was replaced with a more accurate and sophisticated IMU, the Xsens MTi and the data used by the sensor fusion algorithm rather than independently for navigation. As discussed in section 3.3.2.3, with the aim of using innovative algorithms to achieve a high level of underwater navigation on a restricted budget, the Xsens MTi INS was a relatively low budget unit and was one of the cheapest INS units commercially available above the hobbyist class of units.

A brief comparison of the specifications to justify this upgrade follows in Table 4.5. This table is only a brief overview to demonstrate that the Xsens MTi INS was a more accurate, reliable and capable INS which also included calibrated 3-axis magnetometers. More detailed specifications can be found in the Xsens MTi technical documentation [336].

Table 4.5 - A comparison of IMU hardware

	SparkFun 6DoF v2 IMU	**Xsens MTi INS**
Gyroscopes:	300°/s max turn rate Sensitivity: 0.977°/s	300°/s max turn rate Sensitivity: 0.0092°/s
Accelerometers:	±1.5g maximum Sensitivity: 0.0598m/s²	±1.7g maximum Sensitivity: 0.000505m/s²
Magnetometers:	Not present	3 axis calibrated magnetometer
Update rate:	107Hz	120Hz
Factory calibration:	No, raw ADC output, requires calibration	Yes, calibrated output values
Internal filtering:	None	Internal Kalman filtering (user selectable scenarios) of gyroscope and magnetometer data to orientation output
Approx. cost:	£200	£2,000

The Xsens MTi INS was mounted in the isolated navigation tube underneath the vehicle, centred on the vehicle frame and mounted rigidly and in an accurately repeatable position. The magnetometers were separated as far as possible from ferrous materials and electromagnetic interference.

The effect of constant ferromagnetic materials on the vehicle was corrected for in 3 dimensions by performing a 'hard and soft iron calibration' on the MTi using an Xsens software module 'Magnetic Field Mapper'. This updated the calibration values stored on the device. *Non-deterministic* electromagnetic or ferromagnetic disturbances, for example caused by high-current cabling, or when operating in close proximity to ferromagnetic structures, could not be corrected for but the effect of this was largely avoided by the internal filtering which combined readings

from the gyroscopes and magnetometers to give an output inclination. This filtering technique aimed to avoid the drift of the relative gyroscopes while avoiding the external interference affecting the magnetometers and is discussed further in section 4.6.5.2.

The Xsens MTi was connected to the navigation tube USB bus via the Xsens-supplied RS232 to USB converter. The filtering, smoothing, temperature and voltage compensation and calibration operations which were previously performed on the SparkFun IMU data output were not required as they were all performed internally to the Xsens MTi. Instead, a simple parsing algorithm read the output data stream to extract the acceleration, inclination (either separate gyroscope and magnetometer data or the internally filtered combined estimate) and status measurements. Basic error detection was performed on the output data stream before the parsing algorithm output the data with a timestamp to the navigation algorithm.

As the accelerometers and gyroscopes were relative sensors, each new integrated position estimate depended solely on the previous (t-1) estimate. This made the positional information robust to external interference but prone to large cumulative errors and drift. The magnetometers were the opposite; they were susceptible to external electromagnetic interference, but did not exhibit any drift as each new reading was an absolute reading of the Earth's magnetic field and not dependent on any previous cumulative estimate.

The software operations to convert the INS data into useful navigation information are now considered. The data processing and sensor fusion algorithms were expandable to all inertial navigation sensors to improve code reuse and efficiency.

4.6.5.1 Orientation output

The standard orientation output of the Xsens MTi sensor was three Euler angles, defined in Euclidean space in a right-handed coordinate system, as the orientation of the sensor coordinate system (**S**) in the earth coordinate system (**G**) as follows.

$R_{\phi}^{X} = \text{Rotation about the X axis by } \phi \text{ degrees } (Roll) \quad defined\ from\ [-180° \ldots + 180°]$

$R_{\theta}^{Y} = \text{Rotation about the Y axis by } \theta \text{ degrees } (Pitch) \quad defined\ from\ [-90° \ldots + 90°]$

$R_{\psi}^{Z} = \text{Rotation about the X axis by } \psi \text{ degrees } (Yaw) \quad defined\ from\ [-180° \ldots + 180°]$

There is a mathematical singularity in the definition of Euler angles when the pitch angle approaches ±90°, so called gimbal lock. Other output methods of expressing orientation, such as direction cosine matrices and quaternions [336], can be used to overcome this singularity by providing a redundant and complete representation of the orientation of the sensor. However, the conceptual simplicity, human readable for operator-in-the-loop control and straightforward integration of Euler angles into the SLAM and sensor fusion algorithms can all be maintained by mitigating the effect of this singularity. This is commonly achieved by preventing the vehicle from ever deviating far from 0° in pitch [337, 338], thus ensuring that during normal operating the pitch angle never approaches ±90°. In *SeaBiscuit*, this was achieved through a high metacentric height, coupled with the wide cylindrical shape, which both ensured that the pitch and roll angles of the vehicle never deviated far from 0° during normal operation and thus the vehicle attitude was maintained with maximum separation from the singularity.

4.6.5.2 Internal filtering of gyroscope and magnetometer data

The gyroscope (angular velocity) and magnetometer (angular position) outputs were internally filtered by proprietary Xsens MTi algorithms to give an overall inclination output of pitch, roll and yaw angle in degrees. A detailed specification is provided in the Xsens MTi Technical Documentation [336] and a brief summary is provided here.

The filter, a 3 DoF Xsens Kalman Filter (XKF-3), used the signals from the gyroscopes, accelerometers and magnetometers to compute a 'statistical optimal 3D orientation estimate of high accuracy with no drift for both static and dynamic movements'. The XKF-3 filter, similar to the EKF discussed in the sensor fusion section 2.3.2.4, used measurements of gravity (from the accelerometers) and magnetic north (from the magnetometers) to compensate for the drift in inclination estimate using integration of the gyroscopes alone. This drift compensation is otherwise referred to as an Attitude and Heading Reference System (AHRS).

The assumption was made that the *average* acceleration due to movement was zero, and thus the direction of gravity was observed and used to stabilise the attitude estimate of the gyroscopes. The orientation of the MTi in the gravitational field was accounted for so that centripetal accelerations or asymmetrical movements did not cause a degraded orientation estimate. This assumption of zero mean acceleration was valid for most moving objects, provided the time period over which this zero mean was considered was correct for the object in question.

During this time period the rate gyroscopes must have been able to track the orientation to a high degree of accuracy. In practice, this limited the amount of time over which the assumption held true. For the class of miniature MEMS rate gyroscopes used in the MTi this period of time was about 10-20 seconds maximum.

For applications when the operating scenario did not adhere to the assumption of the internal filter, the accuracy of orientation estimates using the XKF-3 would be severely degraded. When the movement did again match the assumptions, the XKF-3 would recover and stabilise over time. To optimise the assumption for different operating applications, a series of user selectable scenarios was available, including a marine option. This option was optimised for low, long term accelerations and mild magnetic disturbances. Further details on the XKF-3 filtering process are contained in the Xsens MTi Technical Documentation [336].

4.6.5.3 Vector navigation

Some common definitions of vector navigation are introduced below to support the processing of the INS data. These are available in many engineering textbooks, or in the Xsens MTi technical documentation [336]. The unit vectors $\hat{\imath}$, $\hat{\jmath}$ and $\hat{k}$ are defined as vectors with unit length (1) and being codirectional with the X, Y and Z axis as follows:

$$\hat{\imath} = \begin{bmatrix} 1 \\ 0 \\ 0 \end{bmatrix} \qquad \hat{\jmath} = \begin{bmatrix} 0 \\ 1 \\ 0 \end{bmatrix} \qquad \hat{k} = \begin{bmatrix} 0 \\ 0 \\ 1 \end{bmatrix}$$

The rotation of a vector around a specific axis can be achieved by multiplying the vector by the appropriate rotation matrix defined below to yield the new rotated vector.

$$R_{\phi}^{X} = \begin{bmatrix} 1 & 0 & 0 \\ 0 & \cos\phi & -\sin\phi \\ 0 & \sin\phi & \cos\phi \end{bmatrix}$$

$$R_{\theta}^{Y} = \begin{bmatrix} \cos\theta & 0 & \sin\theta \\ 0 & 1 & 0 \\ -\sin\theta & 0 & \cos\theta \end{bmatrix}$$

$$R_{\psi}^{Z} = \begin{bmatrix} \cos\psi & -\sin\psi & 0 \\ \sin\psi & \cos\psi & 0 \\ 0 & 0 & 1 \end{bmatrix}$$

These rotation matrices can be combined by multiplying them together:

$$R_{\phi}^{X}R_{\theta}^{Y}R_{\psi}^{Z} = \begin{bmatrix} \cos\theta\cos\psi & \sin\phi\cos\theta\cos\psi - \cos\theta\sin\psi & \cos\phi\sin\theta\cos\psi + \sin\phi\sin\psi \\ \cos\theta\sin\psi & \sin\phi\sin\theta\sin\psi + \cos\phi\cos\psi & \cos\phi\sin\theta\sin\psi - \sin\phi\cos\psi \\ -\sin\theta & \sin\phi\cos\theta & \cos\phi\cos\theta \end{bmatrix}$$

This combined rotation matrix allows for any combination of rotations about any of the three axes. For example, an alternative orientation output of the Xsens MTi was the above rotation matrix providing the *unit-vector components of the sensor coordinate system* **S** *expressed in the earth coordinate system* **G**, that is $\mathbf{R_{GS}}$. Thus, the output $\mathbf{R_{GS}}$ defines the orientation of the sensor (**S**) expressed in the earth coordinate system (**G**) by specifying a series of rotations of a vector in the sensor coordinate system (**S**) to the earth coordinate system (**G**). The unit vectors of **S** are found in the columns of $\mathbf{R_{GS}}$, so column 1 of the rotation matrix $\mathbf{R_{GS}}$ is $\mathbf{X_S}$ expressed in **G** and so on for the other two columns. If the sensor (coordinate system **S**) was aligned with the earth coordinate system **G**, then the output rotation matrix would be as follows:

$$R_{GS} = \begin{bmatrix} 1 & 0 & 0 \\ 0 & 1 & 0 \\ 0 & 0 & 1 \end{bmatrix}$$

This shows each of the unit vectors, so $\mathbf{X_S}$ expressed in **G** has a unit component of X and zero components of Y and Z, showing that the coordinate systems are aligned.

Two properties of a rotation matrix are that the norm of the matrix is always equal to 1 and a rotation (e.g. $\mathbf{R_{GS}}$) followed by the inverse rotation (e.g. $\mathbf{R_{SG}}$) naturally yields the identity matrix $\mathbf{I^3}$ (any rotation performed is undone by its inverse yielding no-rotation – the identity matrix is simply each of the unit vectors, so when used as a rotation matrix, no rotation is performed).

$$\|R\| = 1 \qquad\qquad R_{GS}R_{SG} = I^3 = \begin{bmatrix} 1 & 0 & 0 \\ 0 & 1 & 0 \\ 0 & 0 & 1 \end{bmatrix}$$

A vehicle coordinate system (**V**) was also defined, which was referenced to the rigid aluminium frame of the vehicle. As is was the orientation and the position of the vehicle (V) with reference to the world around it (**G**) that is required, rather than the movement of each sensor (**S**), it was more useful to convert each piece of sensory information from the individual sensor coordinate system (**S**) to the vehicle coordinate system (V). Provided that the mounting of the sensor onto the vehicle's chassis remained constant, the rotation matrix to convert the Xsens output data to the desired vehicle coordinate system ($\mathbf{R_{VS}}$) was a one off calibration process. The following rotation matrices were used to convert the sensor coordinate system to the world coordinate system:

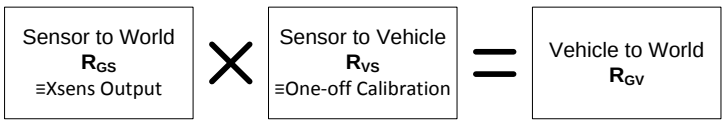

Similar calibration and coordinate system transformations were applied to the other sensors to abstract sensor mounting from the high-level navigation of the vehicle.

4.6.5.4 Linear accelerations

The Xsens MTi measured linear acceleration in the three orthogonal axes of the sensor coordinate system (**S**). Two operations were needed to process this data. Firstly a strapdown algorithm was used to subtract the acceleration due to gravity from the sensor readings to estimate the 'free' acceleration (2nd derivative of position). Secondly the linear acceleration data was converted from the sensor coordinate system (**S**) into the more useful world coordinate system (**G**).

4.6.5.4.1 Strapdown operation

The acceleration due to gravity (g) was subtracted from the accelerometer readings in order to estimate the acceleration of the vehicle (2nd derivative of position). This 'strapdown' operation is named thus because the Inertial Measurement Unit (IMU) is 'strapped down' to the vehicle [76] and so the INS is subjected to the same rotations as the vehicle. The alternative is to mount the inertial measurement unit on a gimballed platform, such that it is always flat and level with the z-axis of the sensor always aligned with g. The advantage of a gimballed system is computational efficiency in that the strapdown calculations need not be performed. The disadvantages however are the mechanical complexity and cost of creating an accurate, rugged, low-friction gimbal system capable of transmitting power and data to the circuitry on the measurement platform.

The gravity vector can be defined (in ms^{-2}) in the world coordinate system (**G**) as the following (a static value of 9.81m/s² is assumed for this operation):

$$G_G = \begin{bmatrix} 0 \\ 0 \\ -9.81 \end{bmatrix}$$

As the positive direction of Z is defined as being skyward, gravity has a negative component of Z only. This needed to be subtracted from the accelerations measured by the INS. If the sensor was upright and stationary then it would be a trivial matter of subtracting -9.81 from the measurement of -9.81 which would be measured by the Z accelerometer. However, this case only applies when the sensor was flat in attitude. Although the vehicle was stable in pitch and roll, some deviation was inevitable. In this case, there would be a component of gravity appearing in each of the other axes in varying magnitude and direction. Therefore the gravity vector needed to be rotated from the earth coordinate system (**G**) to the sensor coordinate system (**S**) by the appropriate angle in each axis where it was subtracted before any further operations were performed. The operation was thus:

$$G_G R_{SG} = G_S$$

$\mathbf{R_{SG}}$ is the inverse of the rotation matrix discussed earlier and was used to rotate a vector in the earth coordinate system to the sensor coordinate system. The inverse of a rotation matrix is simply its transpose such that $\mathbf{R_{SG}}$ could be calculated from $\mathbf{R_{GS}}$ discussed previously, as follows:

$$R_{SG} = R_{GS}^{-1} = R_{GS}^{T}$$

As the orientation output of the Xsens sensor was $\mathbf{R_{GS}}$ this could simply be transposed (the rows became the columns and vice-versa) to yield $\mathbf{R_{SG}}$ which was then used to rotate the gravity vector. The resultant gravity vector $\mathbf{G_S}$ was then subtracted from the linear acceleration output.

4.6.5.4.2 Output coordinate system

Following the strapdown operations, the output accelerations were converted from the sensor coordinate system to the world coordinate system. This was done using a similar calibration matrix which represented the mounting of the sensor with respect to the vehicle, as was used for the output orientations previously.

Post-strapdown acceleration measurements were in the sensor coordinate system (**S**) output in the vector $\mathbf{A_S}$:

$$A_S = \begin{bmatrix} x_s \\ y_s \\ z_s \end{bmatrix}$$

This vector was multiplied by the rotation matrix R_{GS} to yield the accelerations of the **sensor** in the world coordinate system (**G**). A further (previously determined) rotation matrix $\mathbf{R_{VS}}$ was used to correct for the mounting of the sensor on the vehicle to give the accelerations of the **vehicle** in the world coordinate system (**G**) as follows:

$$A_S R_{GS} R_{VS} = A_G$$

4.6.5.4.3 Integration method

The accelerometers were used to measure linear acceleration in each axis of the sensor coordinate system (as discussed above). The conversion from acceleration to position was performed using a cumulative double integration. It was here that any small error in acceleration was increased in magnitude and became a large cumulative error (drift) in position if not otherwise corrected. This emphasised the importance of combining the relative accelerometer data with a drift free absolute position estimate.

For computational simplicity, a cumulative trapezium integration was used where the time base was the difference in timestamps from one sample to the next [328]. This allowed the cumulative position estimate to continue even if an accelerometer measurement was delayed. This integration method was suitable provided that the time interval between samples was short and the rate of change was low [328] and worked well in this application of *SeaBiscuit*. Alternative numerical integration methods are available, many of which sacrifice computational cost for integration accuracy [339]. However, for this application, integration errors tended to have zero mean and were negligible compared to the noise and accuracy of the IMU.

4.6.6 **Sonar**

SeaBiscuit was fitted with two Imagenex sonar units as pictured in Figure 4.10, deliberately selected to provide different but complementary characteristics. These sonars were used to provide realtime information on the location and orientation of the vehicle with respect to its surroundings, as well as any objects or landmarks surrounding it. The sonar was complementary to vision in that, although it had a relatively low detail and resolution, it could operate over long (100m) ranges, provide depth perception and ranging and did not require clear water or illumination, thus providing robustness when integrated with the cameras. The navigation information from the sonar units was integrated into the sensor fusion network for the overall navigation of the iROV as well as for object detection, identification and mapping.

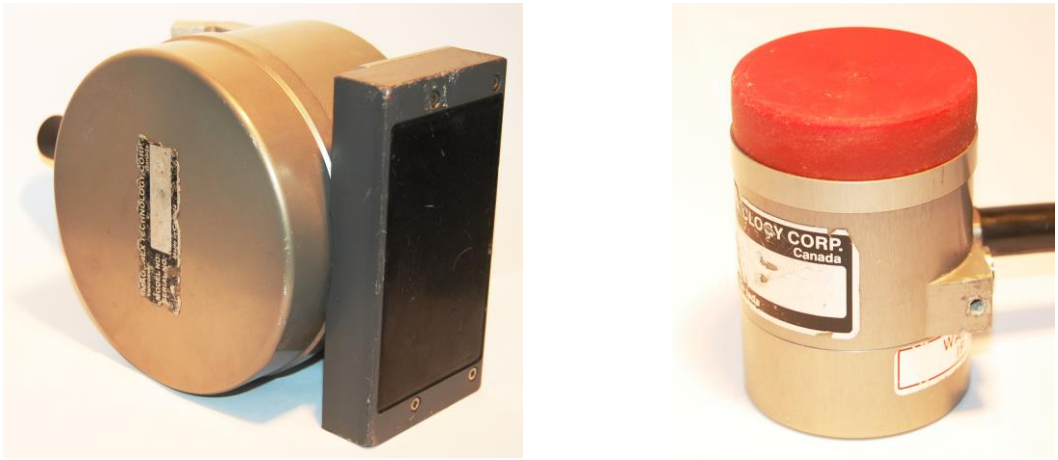

Figure 4.10 - Two sonar units were fitted to *SeaBiscuit*, the Imagenex Model 837 Delta T Multibeam Sonar (left) and Imagenex 852 Ultra-Miniature Scanning Sonar (right), both used for navigation and habitat mapping.

4.6.6.1 852 scanning sonar

The Imagenex Model 852 Ultra-Miniature Digital Scanning Sonar fitted to the underside of the vehicle emitted a single beam 22° high in the vertical plane and 2.5° wide in the horizontal plane which was mechanically panned through a full 360° around the vehicle in a similar fashion to a radar on a boat. A frequency of either 675kHz or 850kHz was selected depending on the application. Higher frequencies generally gave better resolution but a shorter range.

With an adjustable range of up to 50m, adjustable resolution, gain, and the ability to complete a full 360° scan of 120 pings (3° per step) in approximately 6 seconds, this unit was ideal for generating a map of the immediate surroundings of the vehicle. Individual pings could be selected and scheduled as required, allowing a specific sector to be scanned. Alternatively, to increase the scanning speed, the polar resolution could be reduced to 6° per step which allowed a full 360° scan containing 60 individual sonar pings to be completed in 3 seconds.

If the vehicle was passing an area of interest on one side, then the scanning sector could be directed to focus on the area of interest with only an infrequent verification over the remainder of the radius to check that there were no new objects present. This provided a higher scanning speed of the sector of interest.

For each sonar ping, 500 bytes were returned, with each byte representing a distance from the sonar head up to the maximum selected range. For example, if the maximum range of 50m was selected, then each byte represented 10cm radial increments extending outwards from the sonar head (the worst-case resolution). Using the 5m range setting, the radial resolution was theoretically 1cm. Each of these bytes, or range bins, contained an intensity value representing the strength of the acoustic return for that range. Calibration is discussed in a later section (6.3.5), but these intensity values were initially used for relative comparison only.

Although in theory, if the vehicle was held stationary, the sonar could quickly (in 6 seconds) build up a map of the vehicle's immediate surroundings, in practice, several items had to be taken into account. The fundamental problem was movement of the vehicle with respect to its surroundings during a scan. These vehicle movements were split into translation and attitude effects.

Translation during a scan, particularly horizontally, would have resulted in map errors if uncorrected, most commonly the resulting map becoming 'smeared' with targets recorded with incorrect absolute and relative positions and incorrect dimensions. The robot either needed to

hold a stationary position while a scan was in progress, or more realistically, needed to be capable of correcting each individual sonar ping for any movement of the vehicle [16].

Algorithms were written to register individual radial pings from the 852 sonar into an overall 2D scan to allow object detection and mapping. Each individual ping was registered using the vehicle attitude; pitch and roll angle were used to correct pings and yaw angle was used to register the individual ping on the 2D scan. The 852 sonar provided scans in 2D (no vertical resolution) which were registered in 3D, with vertical position provided by other sensors, such as the pressure sensor (depth) and multibeam sonar (altitude). When registering radial pings from the 852 sonar into an overall 2D scan, an input was also provided to register each ping with an x and y vehicle position to allow correction for vehicle movement. As discussed previously, the INS was used to provide short (i.e. the 6 seconds scan duration) estimates of vehicle movement, with accuracy compromised by drift, yet sufficient for short duration estimates of vehicle movement. Longer duration (i.e. greater than 6 seconds) estimates of vehicle movement, with greater accuracy independent of drift, were provided by the localisation algorithms discussed in Chapter 5. These localisation algorithms used the relative movement of landmarks which could be identified to be stationary and apparent in successive scans to estimate vehicle movement.

4.6.6.2 Delta T profiling sonar

The second sonar unit fitted to *SeaBiscuit* was the Imagenex 837 Delta T Multibeam Profiling sonar, trialled briefly on *Hawthorne 2.1*. A 260kHz beam, 3° wide in the horizontal plane and with a spread of 120° in the vertical plane, was used to detect objects on the seafloor, in the midwater ahead of the vehicle through to objects floating on the sea surface.

The multiple receiver system meant an entire frame was captured simultaneously, eliminating any problems from the vehicle moving during a sonar scan, as experienced with the 852 scanning sonar. Each Delta T ping was corrected for vehicle attitude and images were captured, viewed and stored at up to 20 frames per second.

The Delta T sonar measured the backscattering strengths (in dB) of all targets, relative to a source level of 190 dB re. 1 µPa at 1 m (Patterson, pers. comm., 2012). Pulse lengths varied with the range setting (for example, 0.12 ms at 20 m range). Data was received at a resolution of 480 beams spread over a 120° beamwidth and parsed to 120 beams giving an angular resolution of 1°. There were 500 range bins for each beam, with a maximum range of 100m, giving a radial resolution of 0.2% of the range, or 1-20cm depending on which range setting was used.

Similar image processing algorithms were used to detect objects or features using the forward facing profiling sonar as for the 360° scanning sonar. These algorithms are discussed in following sections. This allowed information from the either sonar to either corroborate or correct the other.

Although the forward sonar was fixed facing in one direction and had to be panned with the vehicle, when compared to the 852 scanning sonar, the Delta T had an increased range, better resolution and the ability to distinguish objects in the vertical plane. A similar 360° scan about the vehicle periphery was achieved by panning the vehicle through 360° and recording data from the profiling sonar while tracking the heading of the vehicle, which also allowed landmarks to be registered in 3D with a vertical height. Although *SeaBiscuit* was capable of completing a full 360° rotation in a few seconds due to the low rotational drag, panning at a lower rotational speed allowed a greater radial resolution of Delta T pings with a ping repetition rate of up to 20 Hz.

4.6.6.3 Complementary holonomic propulsion system and navigation sensor suite

The two sonar units were selected and mounted as shown in Figure 4.11 to extract maximum navigational information using the complementary holonomic propulsion system and navigation sensor suite. The 120° swath of the Delta T was normally centred with ±60° about the horizontal plane. However, in some applications, it was advantageous to decline the sonar downwards. For this purpose, a series of calibrated mounting positions were available, the most common being 40° of declination. When operating near the surface, this reduced the number of beams exiting the water surface and directed more of the centre beams downwards towards the kelp bed. It also allowed the bathymetry directly below the vehicle, and to some extent (10°) behind the vehicle, to be imaged.

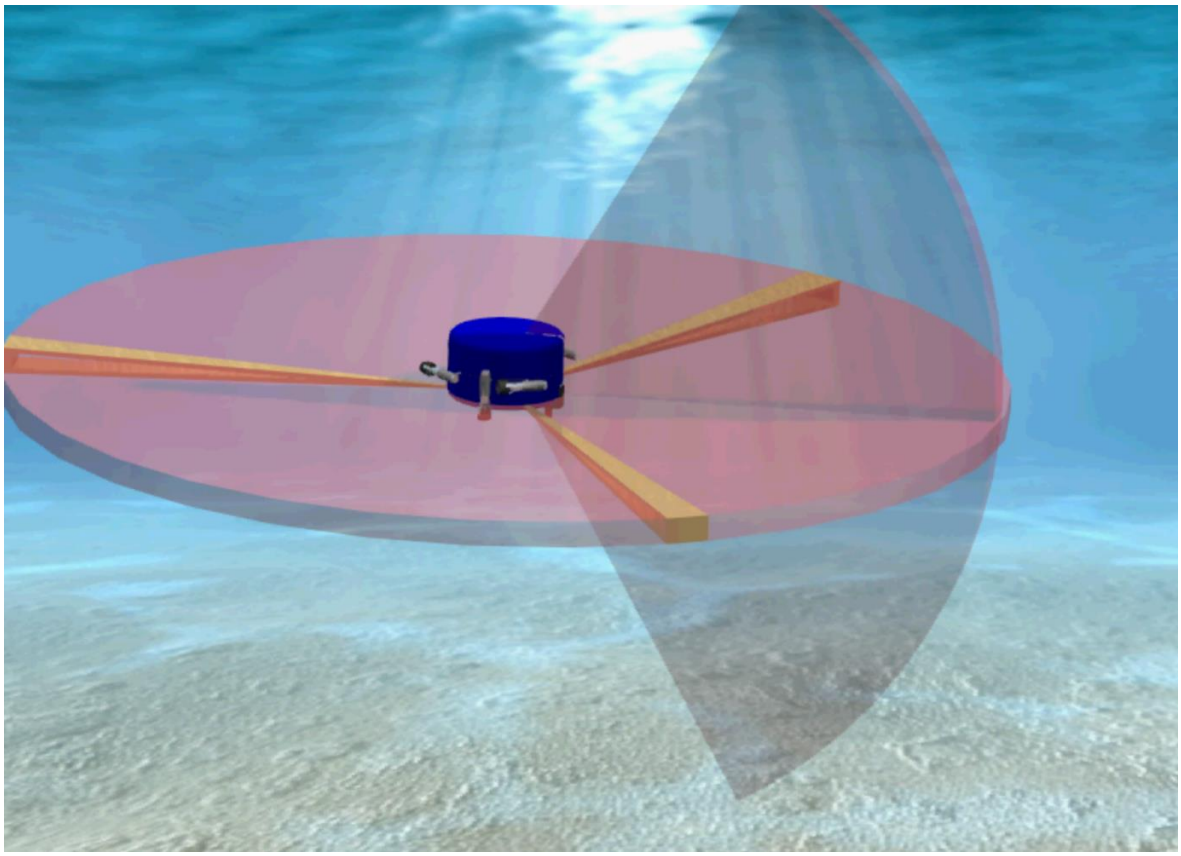

Figure 4.11 - The dual-sonar scanning technique of *SeaBiscuit* allowed for 360° object *detection* and for 3D object profiling and *identification* while underway. It also allowed for co-registration of objects in 3D between the two sonars. The 360° scanning sonar panned around the periphery of the vehicle independently of the direction the vehicle was facing in a 2D plane and the forward facing multibeam sonar allowed objects to be co-registered with the scanning sonar for identification in 3D. Using the holonomic propulsion capabilities, the forward facing directional sensors could survey an object as it was passed without adjusting the original course – i.e. the vehicle was capable of omnidirectional movement in the horizontal plane while independently *facing* in a different direction. Image render Snider, 2010.

Mounting the Delta T in a forward facing position with the multibeam swath aligned vertically, as shown in Figure 4.11, allowed a 3D representation to be built up for *identification* of objects *detected* using the 852 sonar. This dual-sonar arrangement also allowed for objects to be co-registered in 3D allowing a 3D representation to be built up for profiling applications and provided inspection with multiple frequencies (260, 675, 850 kHz).

The capability of holonomic motion also aided navigation in-transit by allowing the directional sensors (sonars and cameras) to be panned independently of course. This allowed a 3D representation to be gathered of the environment, without deviating from a pre-planned straight

transit, by rotating the iROV about its axis while underway. The benefits of generating a 3D map from several panned Delta T scans registered with the INS and 852 sonar allowed the benefits of a 3D imaging sonar to be achieved (and more) without the typically high cost.

3D imaging sonars, such as the Echoscope manufactured by CodaOctopus Ltd. [129], typically retail for $165,000+ [130]. This unit provides a 50×50° angular coverage with 128×128 beams resolution. Similar results were gained for a fraction of the cost, using the complementary holonomic propulsion and navigation system on *SeaBiscuit* to provide 120° vertical by 360° azimuth angular coverage, thus furthering the design concept of using innovative algorithms and techniques to extract the maximum benefit from a limited budget vehicle. Chapter 6 and Chapter 7 contain some of the results of the sonar mapping capabilities of *SeaBiscuit*.

To record underwater landmarks with an absolute reference in real-world latitude and longitude, this sensor arrangement allowed the GPS receiver to be operational at the surface but with the sonars underwater and facing downwards (with the Delta T at 0° or 40° of declination). In normal sea states, the ≈40cm submerged depth of the two sonar units when the top of the vehicle was at the surface was sufficient for basic close range (<10-20m) mapping. This allowed the registration of an observed underwater sonar target with a GPS fix by sonar scans at the surface, before the vehicle dived and used this absolute reference to build up a drift-free map using sonar mosaicking, all with an absolute reference to a GPS latitude and longitude. Using the sensor fusion algorithms to weight a GPS update with a high certainty, regular updates by surfacing to update the GPS fix were also possible. This technique is demonstrated in Chapter 6 for the mapping of a piling dock.

Similar to the hybrid ROV *Latsis* [27] discussed earlier, *SeaBiscuit* was also ideally positioned at the surface to either commence a scan, or to carry out a surface survey: the horizontal motors were submerged for manoeuvring, the vertical motors were submerged ready for diving, the sonar units were submerged for scanning and the GPS and Wi-Fi antennas were out of the water for communication.

4.6.6.4 Sonar image pre-processing

Pre-processing converted polar data from each sonar (a series of range bins for each ping) into a 2D Cartesian array. Two arrays were produced, a ‘Not-Filled Array’ and a ‘Filled Array’.

The ‘Not-Filled Array’ (NOF) mapped each polar range bin for each sonar beam to the nearest neighbour (NN) Cartesian coordinate as shown in Figure 4.12 below. This provided a computationally efficient method for mapping polar data into Cartesian space. Taking the Delta T sonar as an example, with 120 beams each with 500 range bins, this required 60,000 operations per sonar image. However, as shown in Figure 4.12, the distance between beams towards the outer part of the scan represented continuous objects as disjointed features, potentially causing one large object to be detected as several smaller objects by the image processing algorithms.

The ‘Filled Array’ (FIL) represented the divergence of beams with increasing range by ‘filling’ the gaps between beams, providing a truer representation of the sonar return. The exaggerated example shown in Figure 4.12 below illustrates this. The simplest method interleaved each main beam with several interpolated sub-beams. This increased computational complexity. For the Delta T example, interleaving each main beam with three interpolated sub-beams spaced at 0.25° increased computational complexity to 120 × 500 × 4 = 240,000 operations per sonar ping.

An alternative, which provided a complete FIL array for any beam spacing, was to set each element of the filled Cartesian array to the nearest neighbour value when the polar data was mapped to Cartesian space. Cartesian elements outside of the sonar swath were set to zero. This FIL mapping was the inverse of the NOF array: the FIL array iterated through every Cartesian element, setting the value to the NN polar value; the NOF array iterated through every polar element, setting the corresponding value of the NN Cartesian coordinate. The NN FIL array incurred further computational complexity. The 120 beam, 500 range bin Delta T sonar data was mapped onto a Cartesian array of dimensions 868 × 500 pixels, thus requiring 434,000 operations per sonar image. This was still feasible for realtime operation using the onboard controllers.

Incorporating bilinear interpolation, rather than just selecting the NN element, can provide increased accuracy when mapping polar data into Cartesian space. However, the accuracy benefits were deemed marginal compared to the overall sonar accuracy, and the additional computational overhead significant for realtime operation.

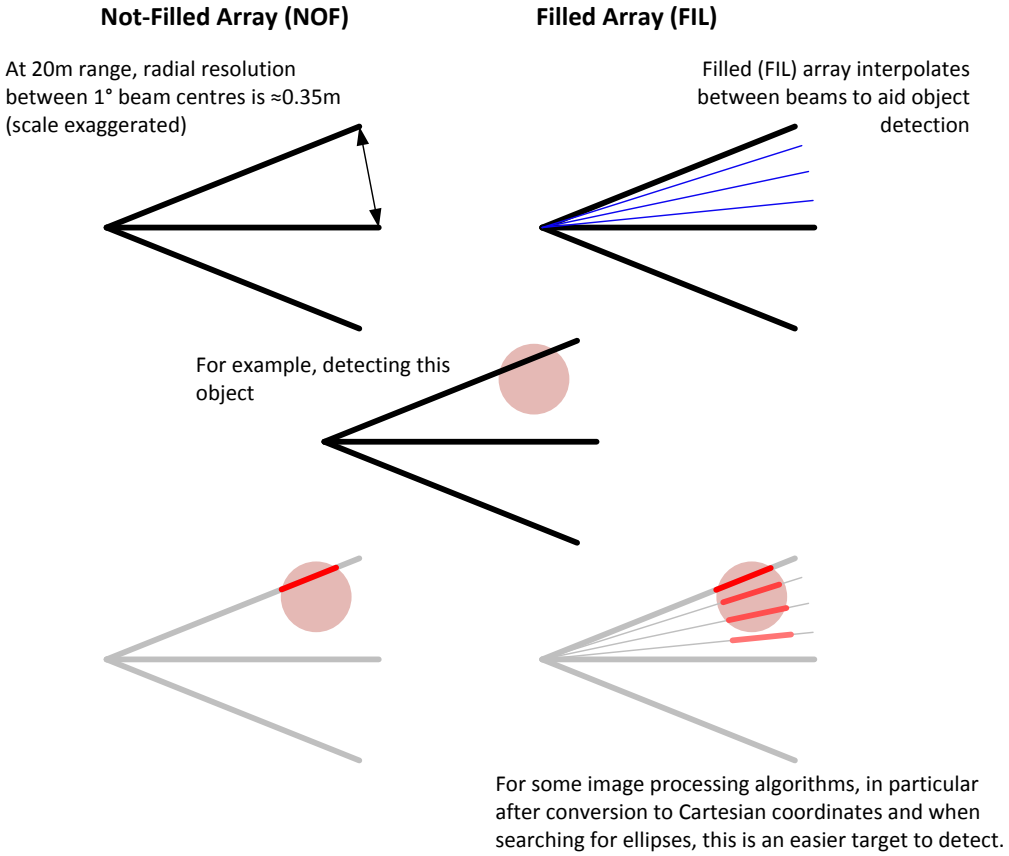

Figure 4.12 - Polar sonar data was compiled and converted to Cartesian coordinates and stored in an array (NOF) for image processing. To aid with image processing, in particular, searching for ellipses, a second filled array (FIL) was created by interpolating 3 beams at equally spaced intervals between the 1° spaced multibeam pings and the 3° spaced 852 sonar pings (using the mean values of surrounding cells). This assisted with feature detection at high range where the Cartesian resolution was low, as shown in the lower part of the diagram.

Each NOF/FIL array was timestamped to relate it to position and inclination data gathered simultaneously (see section 4.6.8 on the timing of sensor data from asynchronous sensors with different timebases and sampling intervals). An entire NOF/FIL array was created at the same time by the Delta T multibeam sonar. For the 852 scanning sonar, each ping was corrected for pitch, roll, yaw and position, taking potentially 6 seconds to compile a 360° NOF & FIL array using these corrected pings. The NOF/FIL arrays were compiled incrementally as data was gathered. Any gaps in the data were either intelligently filled by selective ‘re-scanning’ or left to be filled in by subsequent scans. However, the important distinction was made in the data between a zero return due to an area which had not yet been scanned, and an area which had been scanned and confirmed to be empty.

4.6.6.5 Sonar image processing

Given the corrected NOF/FIL arrays from each sonar, a variety of image processing methods were used to extract useful navigation data from each sonar. Feature extraction and tracking algorithms were used to extract useful information from the often noisy and incomplete sonar images. Algorithms were written in LabVIEW and using the IMAQ Vision and Motion toolbox.

Sonar image processing algorithms for navigation in the *competition environment* were developed in conjunction with two undergraduate Masters student projects supervised by the author [324, 340]. The algorithms developed were capable of recognising artificial landmarks from a pre-defined catalogue using the Delta T sonar and provided a useful demonstration of sonar navigation in a structured environment. However, for operation in the field environment, recognisable landmarks were sparse, not known a priori and often dynamic.

Thus, the algorithms presented here were developed for kelp bed habitat mapping and nearshore sonar-aided navigation, integrating the 852 sonar and navigation suite, as well as providing SLAM capabilities in the open ocean environment. This section presents an overview of the sonar image processing operations performed, the techniques and algorithms developed, and the implementation, integration and adaptation of the algorithm outputs to the specific navigation of the iROV *SeaBiscuit*.

The sonar image processing tasks were split into two sections: general sonar-aided navigation and application-specific sonar tasks.

1. General sonar-aided navigation algorithms were used to search the sonar scan for landmarks of any type that were *stationary* and *uniquely identifiable* which could be used for navigation.
2. Application-specific sonar processing algorithms were applied when a specific target known a priori needed to be found, mapped and/or tracked given the application. This included several of the SAUC-E competition targets (e.g. walls, corners, pipelines, buoys).

The two sonar image processing tasks are considered in turn in the following sections.

4.6.6.6 Sonar-aided navigation

General sonar-aided navigation algorithms were written to search the sonar scan for features that were *stationary* and *uniquely identifiable* and thus could be used as landmarks for sonar-aided navigation. Object identification, tracking, correspondence to other objects and registration on the map were all performed by the SLAM algorithms discussed in section 5.3. Further details of the sonar image processing and feature detection algorithms are considered in the context of the nearshore application using a piling dock (Chapter 6) and kelp bed (Chapter 7). Several pre-processing operations were performed to reduce the chance of landmarks being misidentified and to reduce the computational load when searching for landmarks to enable processing at a high frame rate. These pre-processing algorithms are considered in the following paragraphs.

Figure 4.13 below shows a typical raw Delta T sonar scan with the seabed and water surface annotated. In each 852 and Delta T sonar scan, the seabed was *detected* and delineated (if observable). All regions below the seabed (including secondary echoes) were zeroed to reduce the computational load of detecting false-positive landmarks only to later reject them. Allowances were made for the seabed not being a straight line and approximations of an uneven seabed were made using a series of ellipses, discussed in later sections. The algorithm required tuning,

depending on the bathymetry and the strength of reflection, including correctly setting the gain of the Delta T sonar, as well as the tolerance and threshold levels for seabed detection.

The water surface was also *calculated* using a combination of the pitch and roll sensors and the pressure sensor which allowed the reflections from the water surface to be delineated and any secondary echoes above the surface to be zeroed.

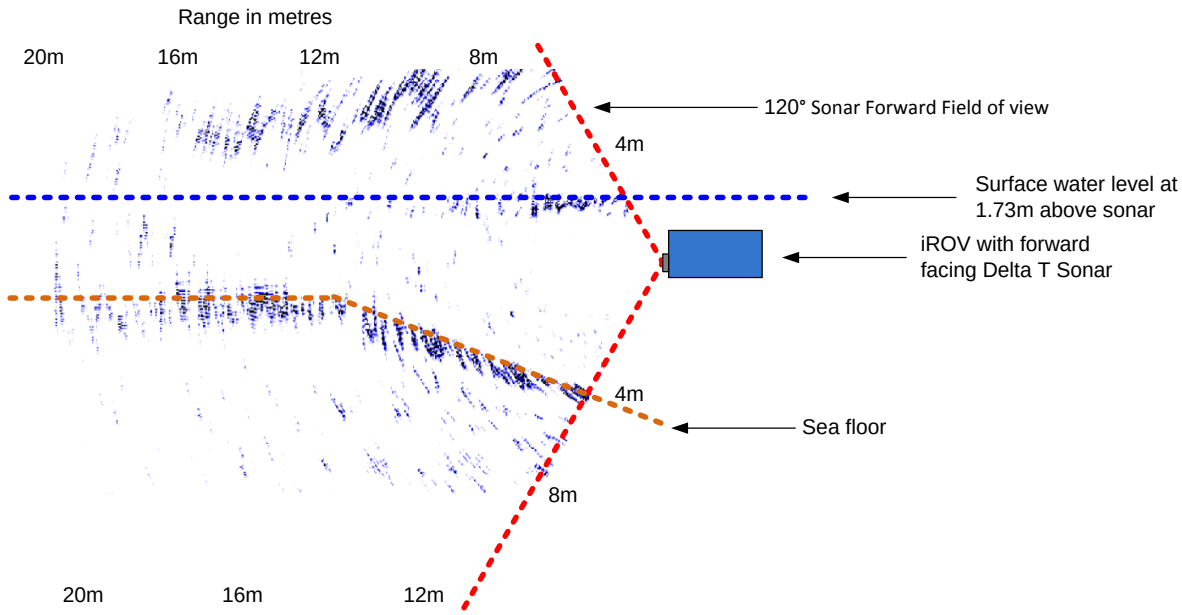

Figure 4.13 - An annotated forward facing Delta T sonar scan with the water surface and seabed indicated.

With the water surface and seabed removed, any objects visible in the field of view were then analysed with the aim of finding *uniquely identifiable* and distinguishable *stationary* objects.

To ensure a high-level of integration between the sonar image processing and the overall iROV navigation code, the tasks of identifying objects and relating them to previously mapped objects were performed in the higher-level navigation code. This allowed an awareness of the other sonar and navigation sensors to determine whether the observed objects were stationary and suitable for use as navigational landmarks. For sonar-aided navigation, the output of the image-processing algorithm for each sonar was the position of any observed objects in the sonar coordinate system, together with several defining characteristics as shown in Table 4.6 below.

The communication protocol shown in Table 4.6 was developed in conjunction with Webster [324] and Birtles [340] to abstract the sonar image processing algorithms from the high-level navigation code. This allowed development of the sonar image processing algorithms independently of the high-level navigation algorithms, and allowed complete modularity when developing algorithms for the competition-specific targets or for operation in the nearshore. Abstraction was also provided between the sonar type, allowing the same protocol to interface with the navigation algorithms for both the Delta T and 852 sonar, together with any further sonar units which may be used in the future.

Table 4.6 - Sonar object detection - data output protocol

ID:	Class:	Description:
0	Object Number	When multiple objects were observed on a single scan they were numbered consecutively. When sonar based tracking was performed, each *new* object was assigned a new number.
1	Bearing	The bearing (°) of the object to the vehicle in the sonar coordinate system. The higher-level navigation algorithms converted this to a global bearing.
2	Range	The range (m) to the centre-of-mass of the object, corrected for the sonar range setting.
3	Orientation	Objects were approximated as ellipses. The orientation of the long axis of the ellipse which approximates the current object was returned. Complex or disjointed landmarks (or the seabed) were represented by many ellipses which are returned as distinct objects.
4	Area	The area (mass) of the object in pixels, specific to the sonar gain setting.
5	Ellipse Ratio	The ratio of the long axis of the ellipse to the short axis, e.g. a circular object would have an ellipse ratio = 1.
6	Identifier	For mission/application specific sonar image processing (discussed below), the sonar image processing code attempted to identify the object based on its characteristics. 0 = unidentified or the object did not match any catalogued objects 1 = seabed (complex seabeds were represented by several ellipses) 2 = pipeline on the seabed 3 = midwater object 4 = wall 5 = piling 6 = gate 7 = corner
7	Identifier confidence	The confidence with which the object was identified. For example, for a wall, the confidence was the ratio of the solid portion observed to the non-solid portion.
8	Partially observed	This returned true if the object extended to the edge of the scan, suggesting that it was part of a larger partially-observed object and required further investigation to be able to identify it completely.
9	Tracking score	When tracking was performed by the sonar algorithm rather than the supervisory navigation algorithms, the tracking score represented the certainty with which and object was being tracked. It ranged from -5 to +5. If an object was not tracked between frames, the score was decremented. Every time it was reobserved, the score was incremented. If the score fell below -5 it was removed from the list of tracked objects. To avoid compounding errors, tracking and map maintenance was usually performed by the higher-level navigation algorithms which had the advantage of knowing the location and orientation of the vehicle, its movement and the data from all of the other sensors.
10	Tracking confidence	The tracking confidence related the accuracy of the predicted tracked position of the object with the actual measurement seen by the vehicle

4.6.6.7 Application-specific sonar image processing

Application-specific sonar image processing algorithms were used in addition to the standard landmark detection algorithms used for general navigation. The application-specific algorithms searched for specific objects or patterns which matched a predefined application-specific catalogue or set of characteristics. In the SAUC-E competition (section 6.2) this included pipelines on the seabed, objects tethered in the midwater (designed to simulate mines), surface vessels or walls, and corners of harbours and tanks to be surveyed [324, 340]. Further object-specific image processing for the dock survey and kelp bed mapping field applications are discussed in Chapter 6 and Chapter 7.

As an example of Delta T application specific image processing, the detection of a corner is considered here. Figure 4.14 below shows an example image of the corner of a tank imaged by the Delta T sonar [324]. Although the concrete walls of the tank were continuous, the noise, ghosting, distortion and incomplete data can all be seen. The sonar image-processing algorithms were robust in a variety of conditions and were still able to recognise the data shown below as a corner, a useful navigational landmark.

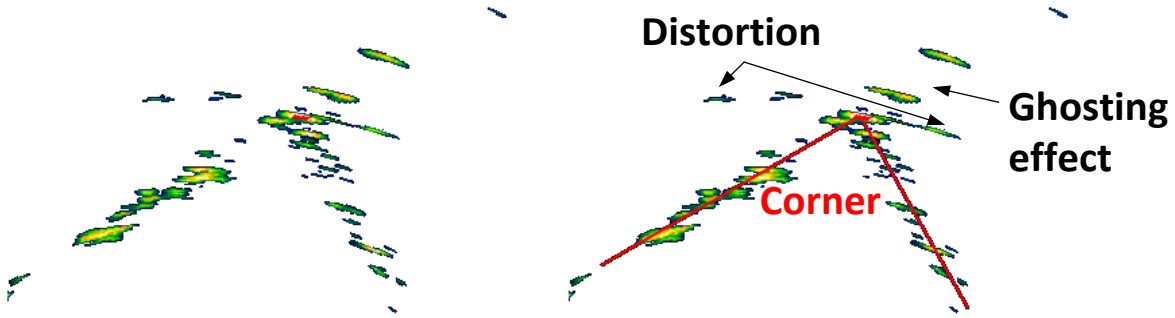

Figure 4.14 - The difficulties of accurately locating a corner from a typical sonar image [324]. The raw image is shown in the left figure, and the corner and noise are annotated in the right figure.

Corners were identified by finding two pairs of particles or features that formed an inclusive angle close to 90° and fell within a similar orientation. A corner was then located by plotting a line through the centre of masses of the pairs of particles, as illustrated by Figure 4.15.

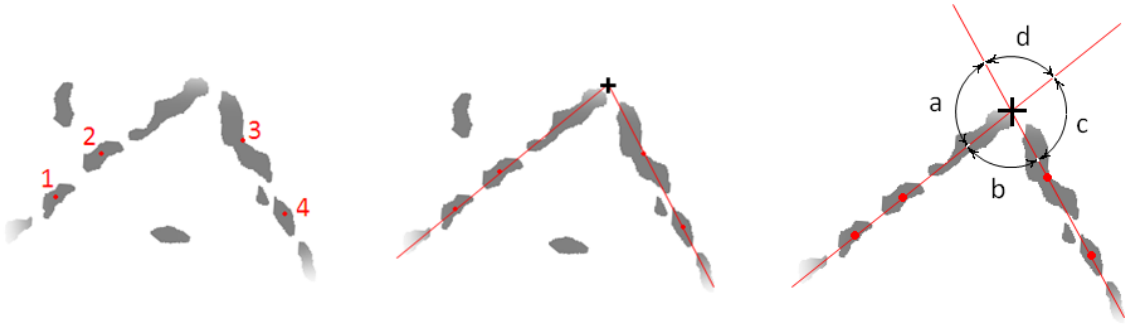

Figure 4.15 - Detecting and calculating the orientation of a corner from a sonar image [324].

Further details of the competition-specific object detection algorithms are provided in the references [324, 340] and are not directly relevant to the open ocean kelp bed mapping application.

4.6.7 Cameras

Two cameras were used to provide visual feedback of the vehicle's environment, to record scientific video footage, to assist a remote operator in iROV mode and for navigation using visual landmarks. One camera was mounted centrally at the front of the vehicle facing forwards and covered a similar field of view to the forward facing multibeam sonar. The second camera was mounted centrally underneath the vehicle facing downwards. This combination allowed objects and obstacles to be detected both in the midwater ahead of the vehicle as well as on the seafloor underneath the vehicle and provided good visual coverage for both the competition and field applications.

The cameras used were Logitech QuickCam S5500 webcams capable of capturing either video at a resolution of 640×480 pixels at up to 30fps or high resolution stills at resolutions up to 1280×1024 pixels. The footage was either captured and processed onboard or encoded and streamed in realtime over the network to a surface operator.

Although the cameras were capable of capturing colour video at a resolution of 640×480 pixels at 30 frames per second (fps), the vision processing and video encoding software operated at a slower rate. The computers used in the vehicle were deliberately selected to be low-power consumption small-form-factor (SFF) computers and so the processing power available was not high. This limited the rate of processor intensive operations, including vision processing. However, due to the relatively slow dynamics of the vehicle, the slower rate of vision processing and capture (≈15fps) was sufficient for smooth and accurate control. The cameras were interfaced by

USB to the dedicated vision processing computer which ran the processor intensive image processing algorithms at this high frame rate without slowing down other mission critical operations.

The dual webcam arrangement provided good results for user feedback and scientific video capture, as well as enabling steps towards autonomous visual navigation in artificial environments such as the SAUC-E competition. Under suitable conditions (range, illumination, visibility) the cameras were capable of imaging the kelp stipes. This was used for density estimates using manual image processing techniques similar to Wladichuk [1] (section 2.2.3.3) and for user confirmation of sonar targets (e.g. mysids, fish, kelp stipes, benthic composition) either in realtime or in post-processing. Some example image captures are shown in Figure 4.16 and Figure 4.17 below.

The forward facing video camera were used to identify, delineate and estimate the density of swarms of mysids. Video was recorded at 10-30 fps. Although the mysids are visible in these low-resolution 320*240 video snapshots, they were easier to distinguish in the video.

Fish species identification and abundance estimates were also possible.

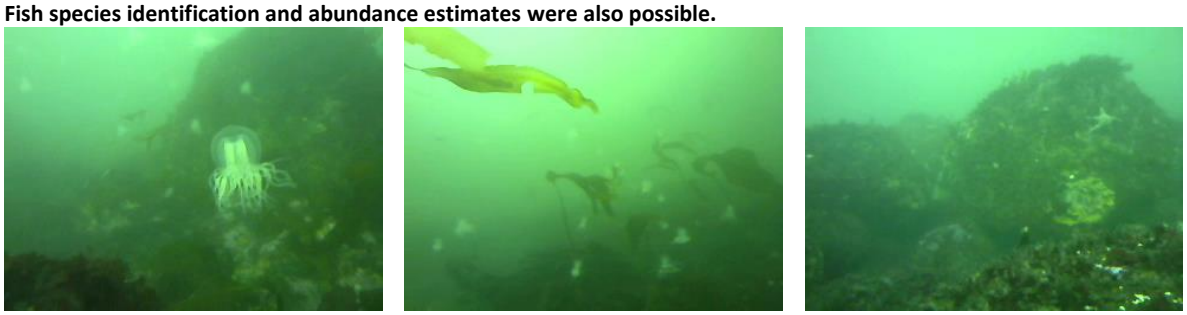

Jellyfish were frequently observed, again species identification was possible. The cameras were also used for benthic species and habitat identification.

Kelp species identification, together with density and distribution estimates were possible where visibility permitted, within a range of a few metres.

Figure 4.16 - A series of example images captured by *SeaBiscuit* in typical visibility during the 2011 field trials.

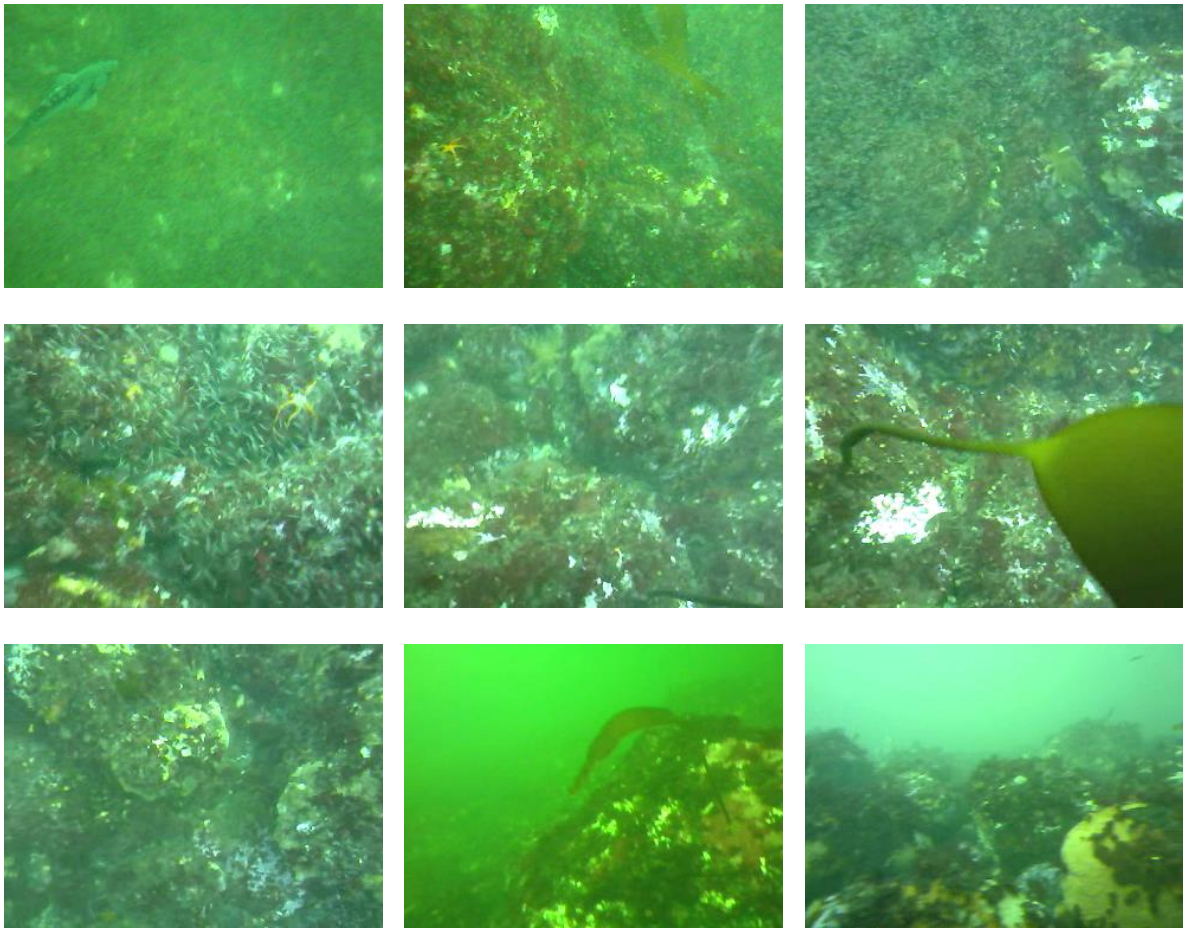

Figure 4.17 - The downward facing camera was also used for detecting the presence of mysids as well as benthic habitat and species identification. The upper images show swarms of mysids in varying densities, whereas the two lower images on the right hand side show seabed images from the forward facing camera for comparison.

An infrared illuminated (IR) underwater camera was added to augment imaging in low-light conditions. The reduced light levels were influenced by a number of factors, including: turbidity (particles / plankton suspended in the water), weather conditions, time of day, operation at greater depths and under the kelp canopy.

The IR camera not only had better performance at low light levels, but also included a set of IR LEDs to provide illumination. The disadvantage of the IR camera was the information lost in transition to monochrome. The lower quality of the scientific video footage captured compounded difficulties in recognising objects underwater, for both the operator and the vision processing software. Figure 4.18 shows an example image showing part of a kelp bed which can be compared to Figure 4.16 to see the loss of information in monochrome.

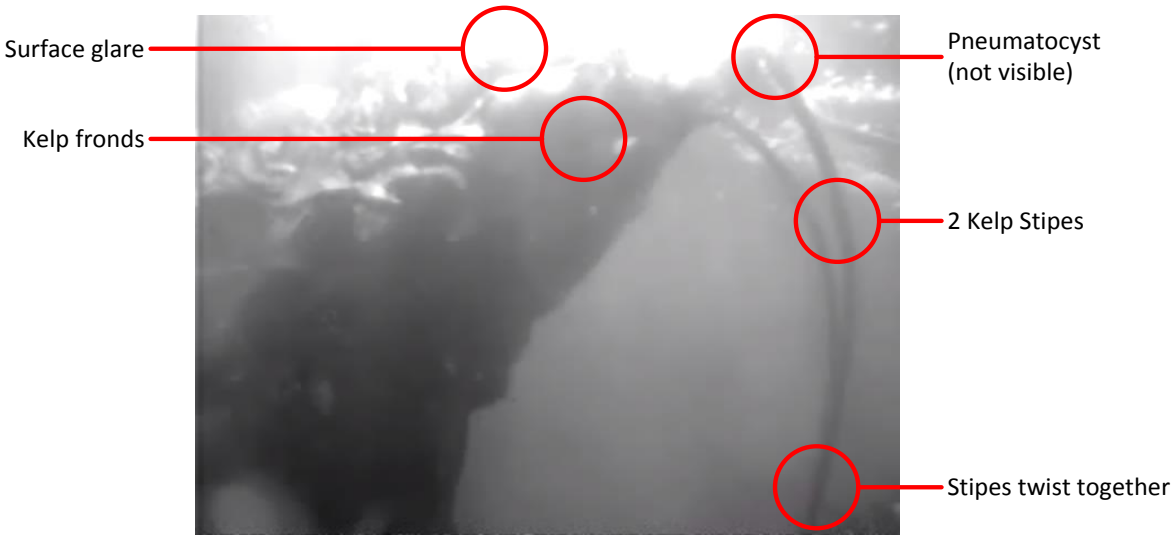

Figure 4.18 - A sample image captured with the IR camera showing a pair of kelp stipes and trailing fronds. The IR image can be compared to Figure 4.16 to see the information lost in monochrome.

4.6.7.1 Visual navigation

While the cameras were mainly used for recording scientific data, as a navigation aid for the remote operator and for identifying sonar targets, some initial development towards visual navigation was also conducted. This was prompted by the entry of *Hawthorne 2.0* and *SeaBiscuit* into the SAUC-E competitions. When operating in the relatively clear and well-illuminated tanks, particularly at the depths required for the competition (<10m), the video quality was sufficient for navigation as shown by Figure 4.19 to Figure 4.21 on the following pages.

A common communications protocol between the self-contained image processing algorithms, the sonar image processing algorithms and the overall SLAM and sensor fusion algorithms ensured modularity, allowing visual navigation to be used when conditions permitted. Due to the limited application of visual navigation in the kelp beds, the focus of this research was not specifically to develop image processing algorithms. Of more interest was how the navigation information from the cameras could be integrated into the sensor fusion algorithms to improve the overall navigation capabilities of the vehicle. In future development, if water clarity and illumination permit, there is the opportunity to aid navigation in the kelp beds by deploying artificial visual markers for recognition as navigational landmarks [135].

The development of image processing algorithms for competition-specific visual navigation was the focus of several Masters projects [142-145], the latter three co-supervised by the author. A brief overview of the integration of the self-contained image-processing algorithms developed by Ruckser [144] to the target applications of *SeaBiscuit* is presented here. The algorithms were used to search for objects and landmarks, either to identify observed objects against a known catalogue based on feature extraction and pattern recognition, or to store new unidentified objects in the catalogue for later re-identification and correction. The competition-specific object recognition algorithms included detecting gates as shown in Figure 4.19, used in conjunction with the sonar for navigating the vehicle autonomously through confined spaces.

Algorithms were also written to detect coloured markers or flashing beacons on the floor / seabed (Figure 4.20) or coloured buoys and flashing lights in the midwater (Figure 4.21). Figure 4.21 also highlights the difference in visual quality between detecting targets in clear chlorinated tanks and in murky saltwater environments. The image processing algorithms were robust (and

included a learning capability) for colour variations and worked well in low light environments. Additionally the algorithms could be used with illuminated targets such as flashing beacons to improve long range detection.

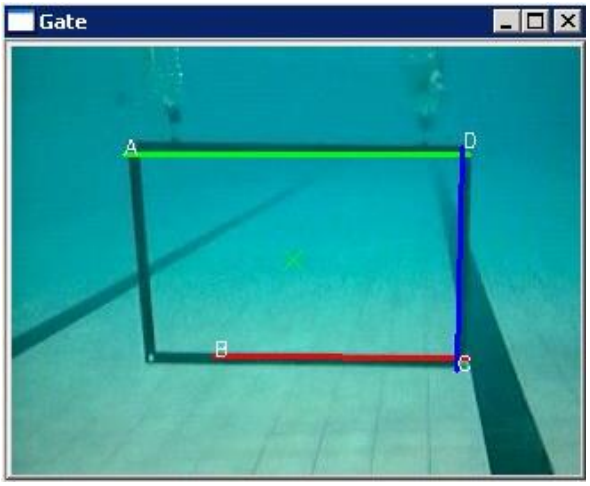

Figure 4.19 - The gate finder algorithm used to navigate the vehicle through confined spaces at the competition. Gates were detected, in conjunction with the sonar, using at least three edges to allow for the gate being partially observed [142].

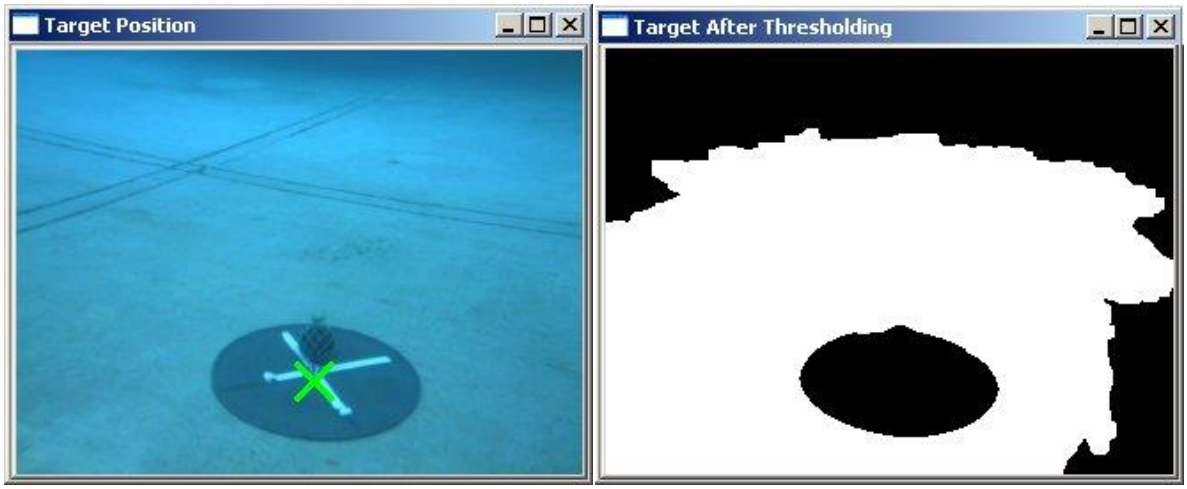

Figure 4.20 - The image processing algorithm searching for a visual marker on the floor / seabed (either a coloured marker or a flashing beacon) using the colour difference between the marker and the surroundings [142].

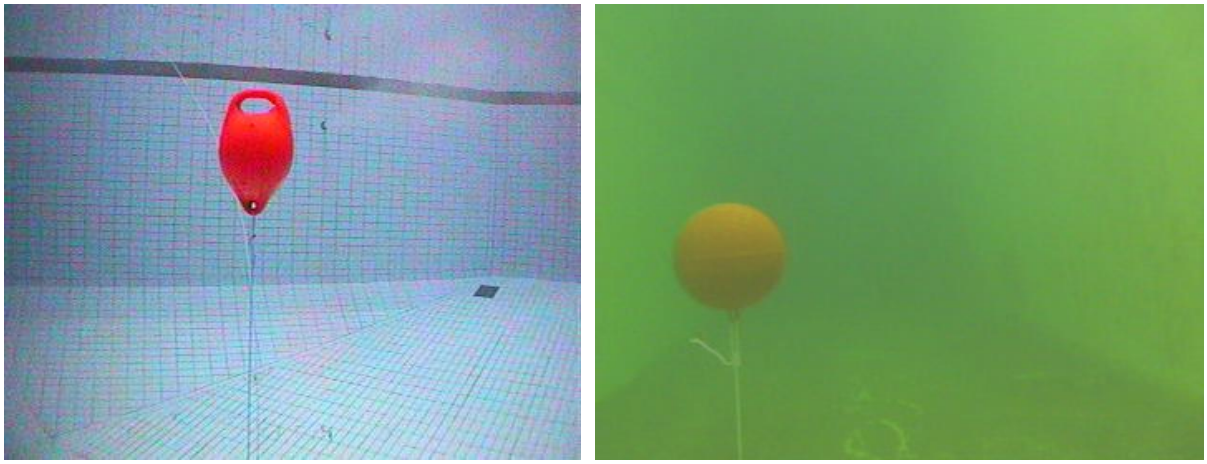

Figure 4.21 - The difference between locating a red marker buoy in clear chlorinated water and murky saltwater. This highlighted the need for adaptable, robust image processing algorithms and the usefulness of underwater beacons and strobes. Left SAUCE-E test image credit [341]. The right image shows the red buoy at a range of several metres, imaged by *Hawthorne 2.0* in the saltwater test tank at the SAUC-E 2008 competition.

4.6.7.1.1 Detecting, identifying and tracking objects by vision

Vision processing algorithms were written in C++. The Open Source Computer Vision Library (OpenCV) already contained many of the appropriate filters and algorithms implemented in C/C++, thus reducing development time.

Underwater objects were detected by a combination of colour, shape, position and relative movement. Detected features were then compared to existing tracked objects to provide reliable detection and identification of objects, robust to the effects of murky water, poor illumination and the absorption and scattering of light underwater. The colour change and degradation, noise, blurring and poor contrast (all increasing with target distance and depth) were mitigated as far as possible by the robust algorithms.

Considering analysis by colour, the image was segmented using an a priori colour sample of the object which was being searched for. An eigenmodel was built for the sample colour to ensure that the colour classification was robust against the significant colour changes with distance underwater. Each colour was treated as a point in a multi-dimensional space, and in order to classify a colour, the Mahalanobis distance [173] was calculated to decide whether a given colour was the target colour. If the distance was small enough, the respective colour was added to the eigenmodel, thus allowing the model to evolve and to learn new shades belonging to a colour group [342]. This 'learning' capability added robustness and reliability to the vision processing algorithms when operating in a variety of environments and conditions. After the image was segmented by colour, the shape of the identified segments was analysed to determine if it matched the target's shape.

A Kalman filter was then used to track the object and to predict the target location if the visual track was lost or the target was moving. The Kalman filter, as discussed previously, predicted the object location based on the uncertain and often incomplete information available to the vision system and applied a correction when the object was reobserved [342]. At each time interval, if the object position was known, the filter was provided with the object's location along with a confidence measure of the correctness of the measurement. This allowed the vision system to maintain a continuous estimate of the target's location, and provided robustness to interference, short occlusions and reflections.

Whereas the object tracking and recognition capabilities of the sonar code were integrated into the higher level SLAM code, some object tracking capabilities were left in the vision processing code. As autonomous visual navigation was not used in the field application, such tight integration was not necessary. The self-contained vision processing software also allowed the processor-intensive processing to be offloaded to the second onboard computer. The data gathered from the sonar units was of a lower resolution, lower bit-depth and lower frame rate than the visual data from the two cameras and thus the processor usage was much lower.

4.6.7.1.2 Navigating confined spaces by vision

For navigating through confined spaces and openings, for example in between the pilings of a dock, or through the gates in the competition, an algorithm was developed with Ruckser to detect and identify underwater 'gates' by vision [144]. Due to the small surface area and potential for its outline to be confused with other parts of the scene, the gate required a less generic approach than the general object detection algorithms discussed above. The Discrete Hough Transform [343] was used to create a set of the lines in the image in conjunction with a quality measure (a

mixture of the expected trigonometric properties of the gate) to identify the lines most likely to represent the gate. The quality measure operated on three randomly selected lines at a time, so that the gate could be partially obscured/off-screen and still be recognised. The distance to and orientation of the gate was then calculated from the estimated location of its four corners. With this estimate, the vehicle could then map and attempt to navigate through the gate, using the downward facing camera to confirm when the gate was passed [144]. Figure 4.19 above shows a screenshot of the algorithm in operation.

4.6.8 Timing of sensor data

Synchronism of all sensor readings was essential to high-accuracy navigation. When comparing readings taken by different sensors at slightly different points in time, then unless the vehicle and its entire surroundings were constant, a difference in readings would be expected. The difficulty was compounded with multiple sensors, each with a different (and often varying) timebase. One option was to attempt synchronous updates to synchronise all sensor readings. If, for example, a positional update was calculated every second and a compass provided a bearing every second but not synchronised with the first time interval, then the reading could be interpolated in between samples to synchronise the timebases.

The alternative approach was an asynchronous (event driven) update of the navigation system. In this case, the navigation algorithm only updated the positional estimate every time a new piece of information became available. For continuous sensors, these were still sampled at a pre-selected timebase. However, for discrete, varying timebase sensors, information was integrated into the algorithm as and when it became available.

Using an asynchronous update, the most up-to-date positional estimate was always available to the navigation and path-planning algorithm, together with the timestamp when it was calculated, so that the user and any mission planning code was aware of any delayed readings. The asynchronous update allowed the optimal use of each piece of sensory information and allowed greater flexibility when dealing with dynamic sensing capabilities, varying sensor availability and a varying amount of computational power available.

The clocks of the two computers were prone to drift by several seconds per hour depending on temperature. To ensure that logged data recorded on the two onboard computers, as well as any surface computers, was synchronised for later post-processing and analysis, a third party software tool was used to regularly (every minute) compare the timestamps between the computers and to correct any drift. The software ‘ClockWatch Star Sync’ developed by Beagle Software also allowed synchronisation to GPS time, either using regular GPS updates of the surface control computer, or when the underwater vehicle surfaced and regained a GPS signal itself.

4.6.9 Calibration of sensor data

Two calibration operations needed to be considered for each sensor to ensure reliable and accurate data. The first, where required, was calibrating an output in arbitrary units (e.g. volts, pixels) to useful navigational units (e.g. degrees, metres). The second was calibrating the mounting of each sensor to a common reference frame on the vehicle.

The first operation, calibration to real units, was covered on a sensor-specific basis in the above sections. In many cases, the operation of a sensor varied depending on the operating environment, for example, calibrating the pressure sensor for salinity and depth, tuning the gain

and frequency of the sonar or calibrating the magnetometers for the soft and hard iron fields on the vehicle. These calibration operations were performed independently and when required, for example when changing operating environment. The usual calibration process was to examine datasheet values – for example, the pressure sensor, in salinity *s* and temperature *T*, an output of *v* volts corresponded to a depth of *d* metres. These values were then validated by experimentation. For the pressure sensor, the vehicle was submerged to a number of precise depths over the full scale range and the ground truth depth was measured by alternative means, for example a tape measure.

The second operation, calibrating the mounting of each sensor with respect to a common reference frame on the vehicle, was performed each time the vehicle configuration was changed. This was avoided to some extent by repeatable, fixed sensor mounting positions. Alternatively, when flexibility of mounting was required, the sensor was mounted in a series of selectable, definite discrete positions which were easily confirmed in software without requiring recalibration – for example the declination angle of the Delta T multibeam sonar.

As discussed previously, much of the frame and structure of *SeaBiscuit* was bolted together to allow reconfiguration in the field and easy shipping. However, when trying to calibrate several sensors to a known reference frame on the vehicle it was important to use a reference which was not going to change. Therefore, all navigation sensors were calibrated (aligned and positioned) with respect to the rigid welded aluminium octagonal frame. The vehicle coordinate system x and y axes were defined as aligned with this frame and the origin of each axis was centred within it. The top of the blue shell was defined as the zero point in the z axis (section 4.6.3).

The following table summarises the calibration process for each of the navigation sensors:

Table 4.7 - Navigation sensor calibration operations

Sensor:	**Calibration Required:**
NMEA Compass	Yaw angle of mounting on vehicle (Pitch and Roll are mechanically gimballed)
Pressure	Position on vehicle relative to defined zero depth point Calibration of measured volts to metres of water pressure Calibration factor for salinity and water temperature (≈3% and 11°C)
Cameras	Calibration of position and mounting angle of both cameras on vehicle Field of view calibration (therefore relation of screen pixels at a given resolution to measured angle which was combined with range using the sonar to give an object size)
Sonar	Calibration of position and mounting angle of both sonars on vehicle
Inertial Navigation	Pitch, Roll and Yaw angle of mounting on vehicle

Calibration of the mounting position and angle of sensors on the vehicle either involved manual measurement using external instruments, or holding the vehicle at a known position/attitude and reading the sensor value. The values were then recorded in a calibration matrix in the software.

4.7 Software

The software was re-written for *SeaBiscuit* to account for the limitations observed on the test bed vehicles *Hawthorne 2.0* and *2.1*. The algorithms required to read, process and extract useful positional information from the navigation sensors were summarised above in section 4.6. The sensor fusion algorithms are discussed in section 5.2 and the autonomous navigation algorithms, including simulation, are presented in section 5.3. This section provides an overview of the general software architecture together with details of the iROV control system.

4.7.1 Graphical User Interface and iROV control

The main program was written in National Instruments LabVIEW with the same benefits of modularity, code reuse and flexibility described in the sections on *Hawthorne 2.0* and *2.1*. The overall structure was written as a series of interacting projects to allow deployment between the different controllers available. The two computers fitted onboard (a third was briefly fitted to increase onboard processing power) and any number of surface computers can all run the different pieces of code, and a full communications system of software variables was set up, allowing all variables to be accessed from any machine. Thus, depending on the task at hand, the processing power could be allocated to favour sonar image processing, for example, to yield a higher frame rate, or to favour video image processing, etc.

Figure 4.22 below shows the overall program architecture (the simulation and playback software is not shown – see section 4.7.6 for details). Working downwards from the top of Figure 4.22, the top section shows the interaction of low, medium and high-level sensing and control with the iROV Operator Graphical User Interface (GUI). Interaction (input and output) was provided across all three levels of the hierarchical software architecture and is discussed in more detail below.

The central blocks shown in the program architecture in Figure 4.22 represent the centralised control, in increasing levels of autonomy shown by the green arrow. These ranged from basic ROV control by a remote operator, to enabling various autonomous features for hybridised AUV/ROV control, to using SLAM to provide a position-aware intelligent semi-autonomous vehicle (iROV) through to the final option for full autonomy (AUV). Full autonomy was not suitable for operation in the kelp beds as discussed previously, and remains an opportunity for future development.

Low-level

At a low-level, sensor-specific subroutines read the sensor data. The filtered, error-checked, parsed and calibrated data was displayed on a series of easy to read indicators on the operator GUI pictured below in Figure 4.23. This displayed the navigation sensors, for example showing all telemetry, depth, compass, attitude, accelerations and GPS surface position. The GUI also included the machine health sensors, arranged to present a summarised, easy to see at a glance indication of the operating state of the vehicle, rather than confusing the operator with a multitude of data.

Clear, easy to read dials showed normal operating conditions, warning levels and safe operating limits while battery meters showed how much energy was remaining. Various alarms were implemented to alert the user of faults, e.g. leaks, over-temperature situations, etc. A turn count indicator was also implemented to record the number of rotations of the vehicle to prevent the tether becoming unduly twisted and restricting movement.

All mission data, telemetry, sensor readings, video and sonar footage and user commands were synchronised, time-stamped, recorded and archived, either onboard or over the network. This allowed both later inspection and playback as described in section 4.7.6 and kelp bed maps to be compiled from post-processing survey data.

Low-level control allowed a remote operator (either via the wireless or wired link) to control all movements of the vehicle. Individual thruster control was abstracted from the lowest level to a simple holonomic control system of horizontal translation direction (0-360°) and speed (0-100%), (optionally simultaneous) turn rate (100% anticlockwise to 0% through to 100% clockwise) and

vertical movement (100% descend to 0% through to 100% ascend). This interfaced with the holonomic movement control algorithms discussed shortly in section 4.7.4.

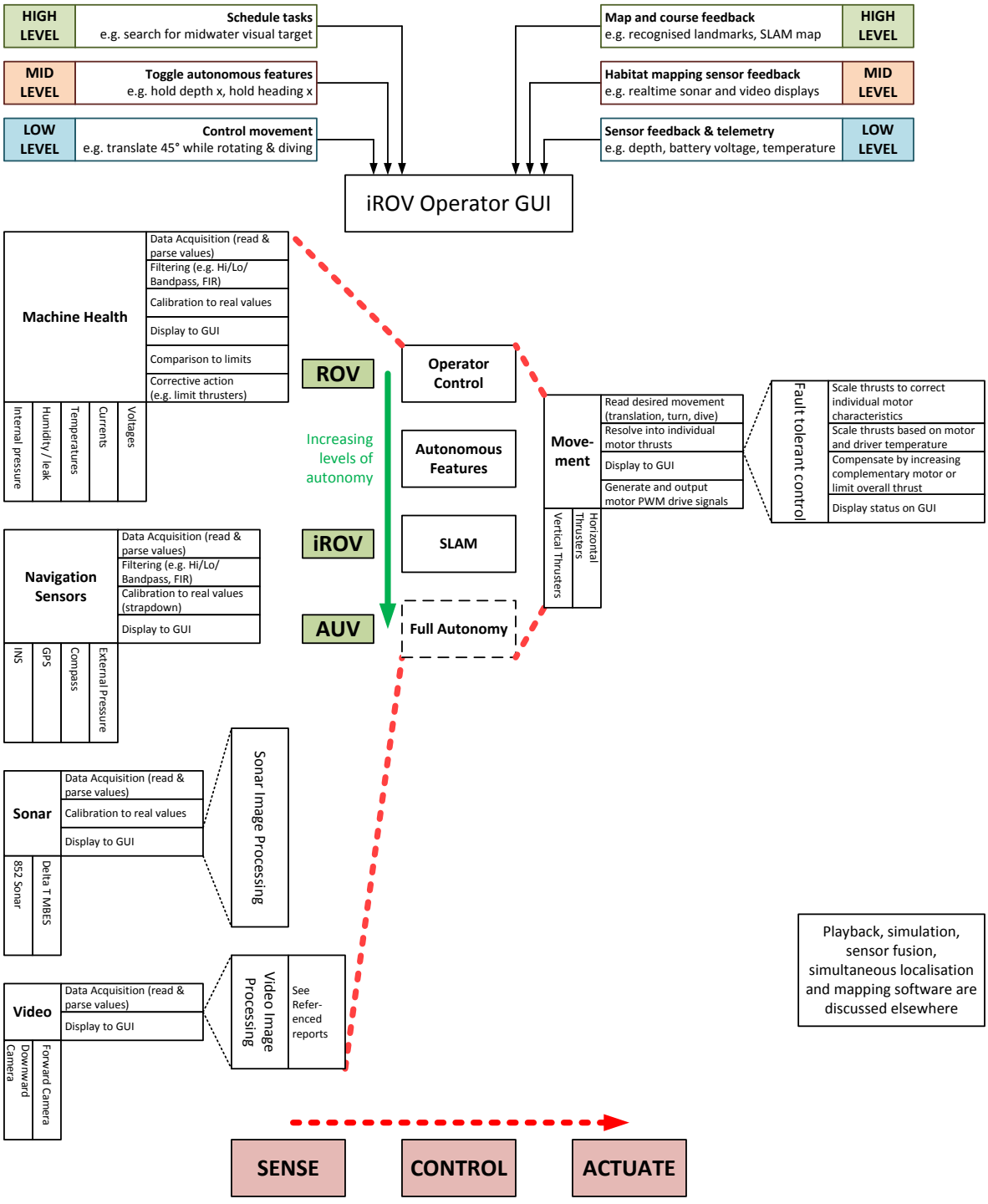

Figure 4.22 - The iROV software architecture for *SeaBiscuit*. All code shown was written in National Instruments LabVIEW, with the video image processing algorithms interacting with C++ subroutines. The code was structured into self-contained projects with a full communication system between projects, allowing code to be flexibly deployed between the different controllers available.

Mid-level

Mid-level sensor feedback included indicators showing the state of enabled autonomous features, for example, the accuracy of holding a depth, or holding a heading. The raw output from the scientific mapping sensors was also displayed; dual camera displays were available, the multibeam display was shown as each image arrived in realtime and the 360° scan from the 852 echosounder was overlaid ping by ping to show the 6-second scan and head angle.

Mid-level control allowed the various autonomous movement features to be toggled and set points controlled to allow the vehicle to hold a course/position despite external influences (water movement, tether drag, etc.). These mid-level autonomous control features included:

- hold a depth while either stationary or moving,
- hold a heading while stationary, diving or manoeuvring (the vehicle always *faces* in the same direction),
- traverse a compass course while rotating (the vehicle always *moves* (*translates*) in the same direction, despite rotating about its axis to orientate the sensors and *face* in different directions).

These mid-level control features were easily sequenced to build up basic missions or transect courses. For example: dive to 10 metres while holding a heading (to avoid the tether tangling), rotate 360° to scan the environment, then translate north west while facing east with a 30° oscillating pan to scan the sensors over a target while transiting a course.

High-level

High-level sensor feedback included processed images, from the sonar and video, with features or landmarks highlighted showing the location of detected objects which were used (either by the autonomous navigation algorithms, or the iROV operator) to aid with reactive navigation. The features included detected landmarks on the video, the seabed detected on the Delta T multibeam sonar, or targets in the midwater on the 852 sonar.

High-level control included scheduling the autonomous movement features (hold a depth, hold a heading, etc.) described above. This also included searching for or tracking objects using the sonars or cameras, or the sophisticated mission planning algorithms described later in section 4.7.3. However, the mission planning algorithms were only implemented for the competition environment for the reasons discussed in the introduction considering the challenges of fully autonomous navigation in kelp beds.

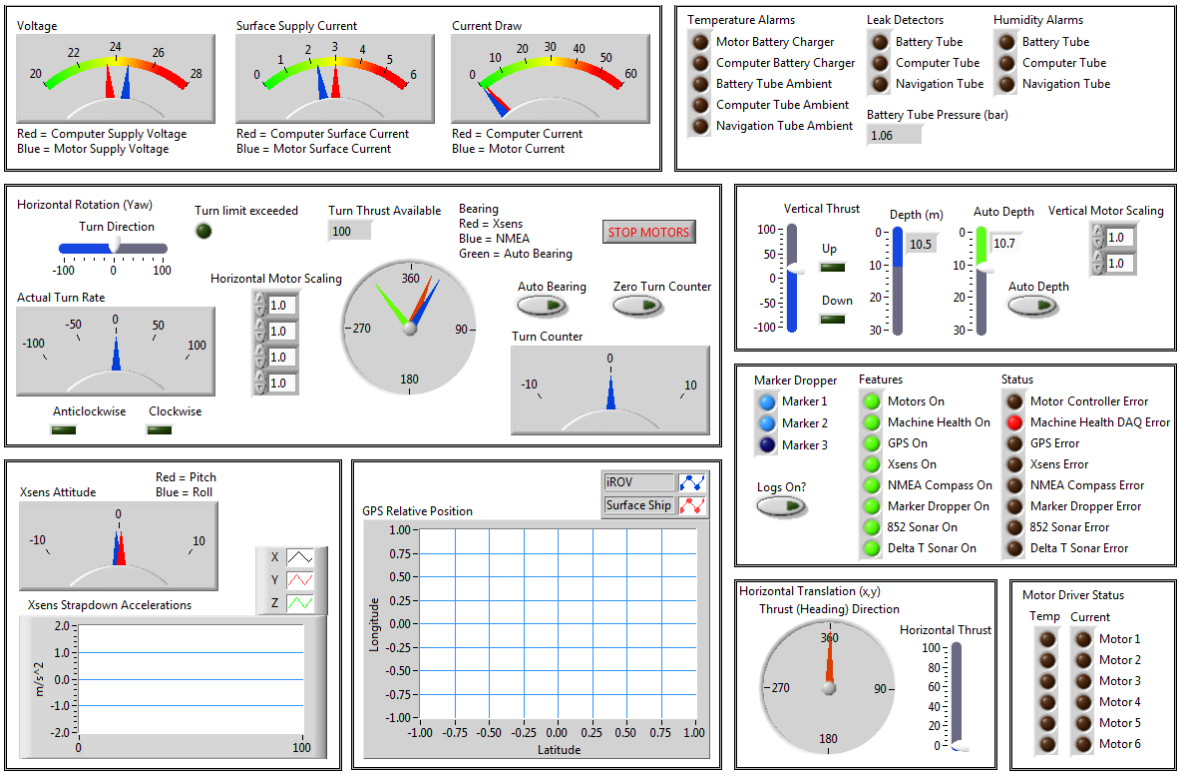

Figure 4.23 - The iROV Remote Operator GUI for *SeaBiscuit*. The video feeds from the two sonars and two cameras were available separately (usually viewed on multiple monitors) streamed over the network and optionally archived.

Through the three levels of control and sensor feedback discussed above, optimal operation of the iROV was achieved. Based on the literature review in Chapter 2 covering the challenges of navigation in kelp beds, this hybridised autonomous control represented the optimal compromise between complete operator control and full independent autonomy.

The final stage in autonomy, to relieve the operator completely, was deemed unsuitable for operation in the kelp beds. It would have required anticipation of all possible situations that the vehicle could encounter, such that the vehicle could autonomously select an action to maximise its chance of success. For reliable operation in the complex and confined kelp bed environment, fully autonomous operation was deemed too unreliable. However, semi-autonomous operation was shown to have great benefits for long and repetitive missions such as searching for a target, traversing survey patterns, mapping areas, and sensor recordings.

The second part of the software architecture diagram shown in Figure 4.22 shows the general framework of sensing, control and actuation. Each block in Figure 4.22 represents a software sub-project of the control architecture dealing with a different category. For each sub-project, the entries beneath the sub-project represent the different categories (e.g. different sensors, or different thrusters) considered, and the entries to the right of the sub-project represent an overview of the operations performed. Thus, for each sub-project the matrix of intersections from the entries at the bottom and the right represent the complexity of the code implemented. It is through the hierarchical program structure, modularity and efficient code-reuse that overall organisational simplicity was preserved.

Considering each block shown:

- The machine health software is discussed in section 4.5
- The navigation sensor software is discussed in section 4.6
- The sonar software is discussed in 4.6.6
- The video software is discussed in section 4.6.7
- The holonomic movement control software is discussed in 4.7.4
- The algorithms for sensor fusion and SLAM are discussed in Chapter 5.

4.7.2 Software stability and performance

Two x86 computers running Microsoft Windows XP and software written in LabVIEW were used for adaptability and flexibility of development and operation. Development was also accelerated by using existing LabVIEW libraries without having to write low-level code from scratch for commonly used operations. Development was simplified through the version control system implemented. Incremental image based software deployment allowed easy recovery to previous versions of both the iROV software and the entire operating system. Each major change was imaged to a separate backup and a version control system was used for minor software updates. This ensured a stable software environment was always available.

4.7.3 Mission planning algorithms

Initial development towards overall autonomous operation at the SAUC-E competitions was mentioned earlier in section 3.4 as part of the confined water trials of *Hawthorne 2.0*. *SeaBiscuit* also successfully competed at SAUC-E 2009 and the results are discussed later in section 6.2. Although autonomous operation at the competition provided a useful set of confined water trials, the task scheduling and autonomous low-level control also proved essential for operation as an

iROV in the eventual nearshore application. Task scheduling in the iROV mode used the same framework as the mission planning for basic autonomous operation at the SAUC-E competition, with software written in LabVIEW for adaptability and flexibility of development. Building on the literature review into mission planning in Chapter 2, the mission planning algorithms for *SeaBiscuit* were implemented in three layers as follows:

- *Strategic level* – provided a mission framework. Tasks were organised in a rational order, allowing for completion in an efficient and effective manner depending on environmental circumstances.
- *Tactical (task) level* – used for completing individual tasks within a mission. This level sequenced a series of operations to complete a given task.
- *Actuation level* – converted tasks from the tactical level into low-level actuation commands.

This tri-layer hierarchical structure afforded robustness in the face of unpredictable conditions and was also reconfigurable, modular and upgradeable for a changing vehicle, changing suite of actuators and peripherals, and for different scenarios.

At the competition, high-level control relied on following a pre-determined mission plan. The current state of the vehicle was compared to the desired state (by fusing the various sensory systems) and the motion required to achieve the desired state was calculated. This recursive process was run continuously until either the desired state was reached, or the system moved onto the next task. This level which provided exploration as well as task selection and scheduling. Although not fully implemented at the SAUC-E competition, this level was replaced by the high-level remote control when operating as an iROV in the nearshore. In the iROV mode, the hierarchical object-orientated modular control system was used to provide hybridised autonomous control while overall supervisory control was maintained by the remote operator. Tasks were scheduled and reconfigured by the operator to build up surveys.

The actuation level determined the thrust vectors required to achieve the desired position change, before finally the low-level control system generated the necessary motor control strings and PWM values. In terms of sensing, the low-level code read and calibrated the sensor data. The mid-level algorithms then converted this sensor data into useful positional information before finally the high-level algorithms performed mapping, localisation and navigation.

Although not fully implemented, some example mission plans to demonstrate the adaptability of the mission planning structure from the SAUC-E competitions are shown in the following figures. Figure 4.24 below shows an example mission plan from SAUC-E 2008 and Figure 4.25 shows the mission plan from SAUC-E 2009. The actuation level is omitted from these diagrams for simplicity. As discussed above, the sub-objectives (the actuation level) were a series of blocks available to the user when defining the mission which reflected the sensing and actuation (including movement) capabilities of the vehicle.

The individual blocks of the flowchart represent sub-VIs (virtual instruments) in the LabVIEW code, which perform different sub-tasks. Each sub-task ran once a series of predefined conditions were met and had a given set of inputs, executed a task and had a set of outputs. This modularity allowed for ease of programming, testing and debugging as well as straightforward task reassignment within the program.

Using the graphical programming language and predefined mission building blocks, building a new mission, or redefining an existing one (on-the-fly) was as simple as drawing a flowchart similar to the one shown in Figure 4.24 into the LabVIEW interface. Predefined mission building blocks represented common sensing, control and actuation tasks and allowed fast definition of a

mission. Blocks ranged in sophistication from 'hold a depth' 'hold a compass heading' to 'move forward at speed *x* for *n* seconds' and 'hold a position' or 'map an area using *x* exploration method'. As more sensory and actuation capabilities are added to the vehicle in future, the palette of mission building blocks can be expanded to exploit these new capabilities. This programming structure also allowed for simulation of the sensing, control and actuation blocks without having to deploy the vehicle.

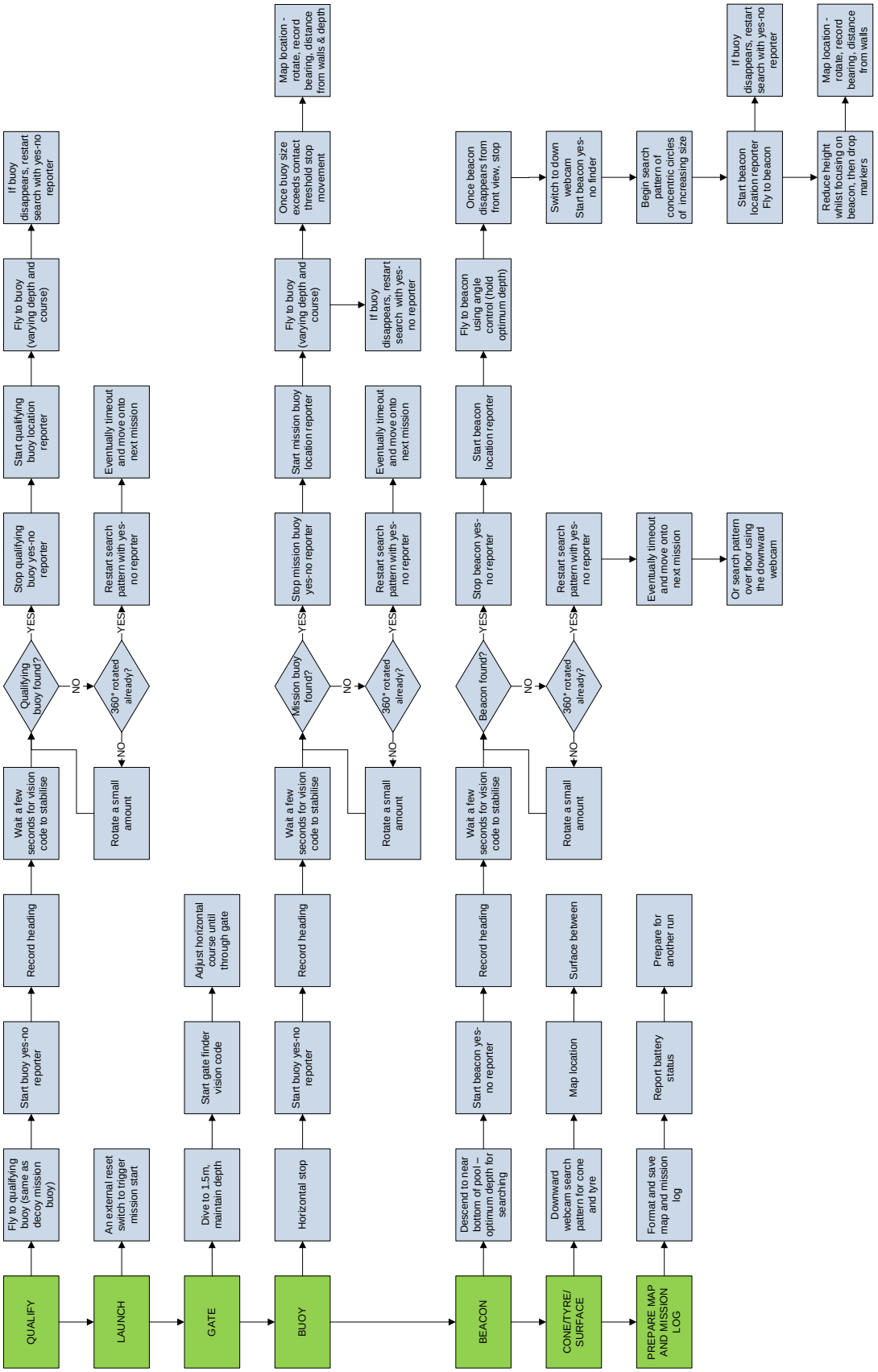

Figure 4.24 - An example mission plan for the 2008 SAUC-E competition which required a number of underwater tasks to be completed. The green boxes show the strategic level and the blue boxes show the tactical layer.

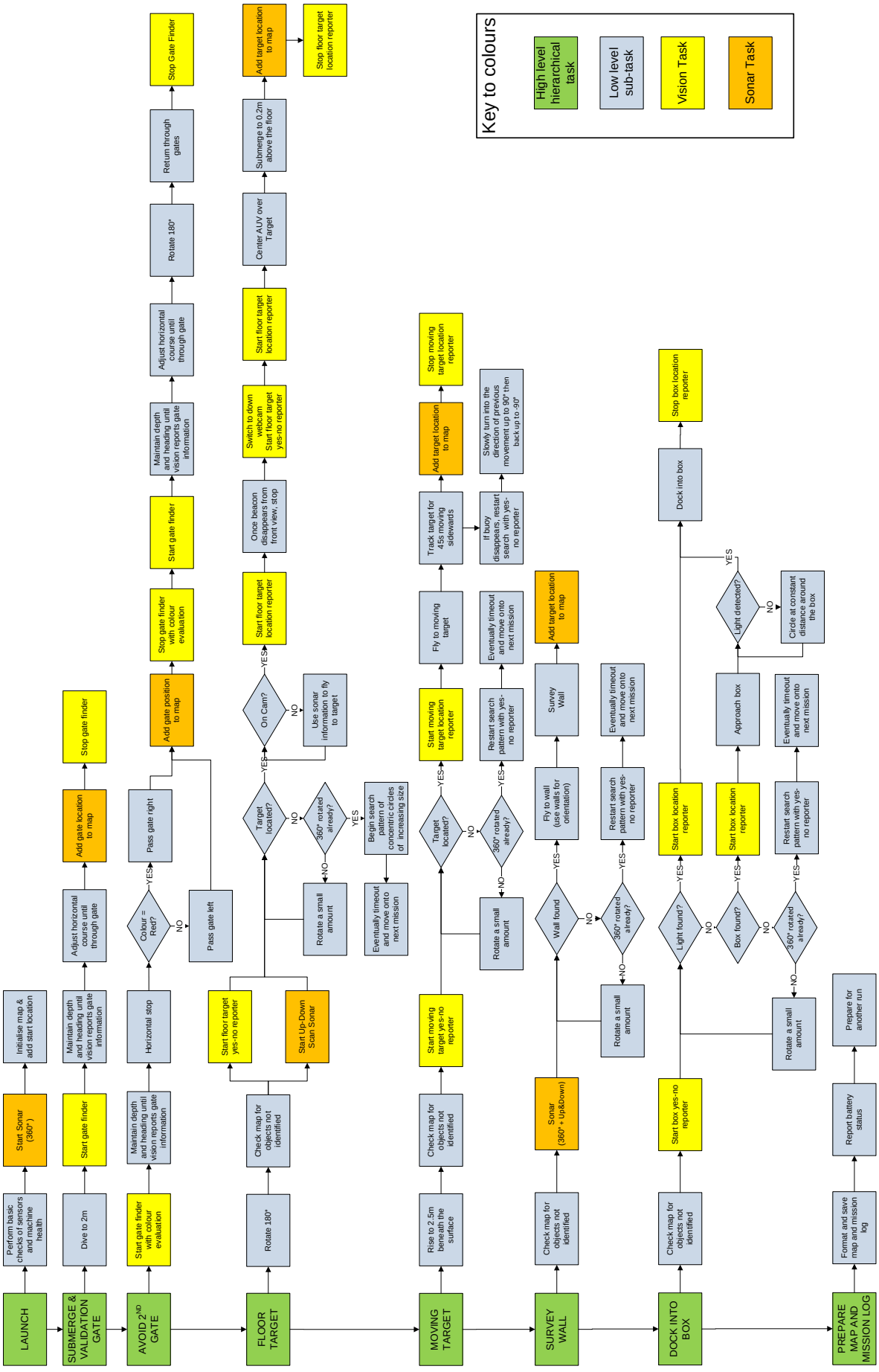

Figure 4.25 - An example mission plan for the 2009 SAUC-E competition which increased the complexity of tasks from previous years to include tracking a moving midwater target and autonomous docking to a box on the seabed.

4.7.4 Holonomic movement control algorithm

Several improvements to the holonomic control algorithm were implemented since the version deployed on *Hawthorne 2.0* and *2.1*. More sophisticated and efficient control was achieved by allowing for the nonlinear relationship between electrical power supplied and motor thrust generated, and for the unequal thrust generated when a motor was used in reverse. The redundancy built into the system was also exploited by the machine health system. Motor thrust scaling allowed an overheating motor or driver to operate at a reduced power until the temperature returned to normal with the other motors providing the supplementary thrust required. Additionally, if a motor or driver failed, the control system could be adapted to exploit the built in redundancy and allow the mission to continue using the remaining functional thrusters. As discussed in section 4.5.1, the wiring was in place but the thruster speed sensors not yet implemented to detect a failed thruster.

The holonomic movement control algorithm directly interacted with the higher-level navigation and control algorithms to provide the required movement despite external (often dynamic) influences such as drag, the effect of the tether and external currents. Horizontal holonomic movement was independent of vertical movement. The control algorithm resolved the desired horizontal translation and the desired horizontal rotation from the world coordinate system into component thrusts in the vehicle coordinate system which were provided by each of the 4 horizontal thrusters. A Proportional Integral Derivative (PID) control system was used to compare the desired heading, bearing and depth with the actual measured values. This allowed for accurate and efficient control with minimal overshoot and fast response.

Different control profiles (PID gain values) were stored for different operating modes. For example, when the tether was detected, the appropriate control profile was used to counteract for the increased drag of the tether, but to provide faster response at the expense of efficiency given that unlimited surface power was available. Higher level control responses to the presence of the tether involved basic items such as maintaining a turn counter to avoid twisting the tether and performing wide sweeping turns to avoid the tether becoming entangled with the vehicle. Control effects included the spring-like nature of the tether, and tail-like effect which served to straighten the vehicle, and pull it backwards and either upwards or downwards at the rear depending on the buoyancy of the tether. In other tasks, a slow response but with little overshoot was more preferable, for example detailed mapping in confined environments. The different control profiles allowed a compromise to be made and adjusted between efficiency, accuracy and speed of response.

4.7.5 Station keeping

The improved holonomic motor control algorithms and navigation accuracy allowed for enhanced station keeping capabilities, allowing the vehicle to hold a position in 3D to a given tolerance despite external forces. These external forces were characterised into two categories.

1. Short term impulses, such as wave movements, swells or sudden forces on the tether
2. Long term drifts such as tides and currents, or a continuous pull from the tether

In each case, there was a trade-off to be made between positional accuracy and energy expended holding the position to a given threshold. Short-term impulses such as wave motion were generally repetitive and comprised swells back and forth (as shown in Figure 3.17 earlier). In this case, it was significantly more energy efficient to correct the *sensor data* rather than try to correct

the *actual movement* of the vehicle. As the movement was repetitive and periodic, overall the average position of the vehicle did not change. Station keeping or course holding was more useful to maintain a position or course despite a long-term drift. The station keeping system was used with great effect to maintain a steady heading, course or position, all to within tolerances determined by the accuracy of the navigation system, despite these long-term drifts.

When the flow rate was too high to hold a position or course, the alternative was a controlled downstream drift. In this case, the support vessel anchored upstream of the survey area, deployed the vehicle and the tether (having strain relief built in) was gradually paid out. As the vehicle moved downstream in the current, its thrusters were used to hold a depth, and to manoeuvre to accurately follow the required transect while tracking its course. At the end of the downstream transect, the vehicle was recovered by the tether. This overcame the limitation of operating in currents greater than the vehicle's propulsive power.

4.7.6 Mission playback and data analysis

During every iROV survey, all navigation data, control data, machine health, telemetry, sonar and video data was recorded and time stamped to allow post processing and review for inspection or analysis of the maps and footage generated. Software was written to index and playback the logged data (sonar, video, navigation sensors) and telemetry in synchronism. For playback, the results were presented in a similar GUI to the mission control interface shown in Figure 4.23 previously, with the addition of an indexed scroll bar to allow missions to be played back at a given speed, stepped through frame by frame, or excerpts to be examined in detail. A version without the GUI also allowed rapid batch processing of results.

Recording the raw footage, as well as processed information, allowed any future development of the analysis and processing software to be applied retrospectively to previous mission data to realise any advances in processing for all previous datasets. The playback software was developed in conjunction with the simulation capabilities discussed in section 5.4 to allow raw data already gathered to be used to aid development of the sensor processing, navigation and exploration algorithms. This permitted algorithm development without necessarily having to deploy the vehicle, of great use given the remote field site.

4.8 Discussion

The benefits of using underwater vehicles for nearshore habitat mapping were established in the literature review presented in Chapter 2. Advantages of coverage and a reduction in labour requirements and cost were discussed over diver surveys [11] and camera drops, and an increased level of survey detail was shown over surface vessel surveys and aerial imaging [13].

From this, the limitations of existing ROVs and AUVs for nearshore operation were explored, trading the risk of autonomous operation with no feedback with the limitations associated with a tethered remote-controlled vehicle [25]. The optimal compromise of a hybrid solution, an intelligent, position-aware ROV (iROV), was proposed to mitigate the limitations from each, and to combine the benefits from both.

The iROV concept combined low-level autonomous control and navigation while maintaining the reliability and data validity from remote operator control and supervision. The security of energy autonomy and the high thrust available from an onboard power supply was combined with the unlimited operating duration in the high currents of the nearshore from a thin, lightweight and

flexible tether providing surface power. With this concept, and building on the background development work into the underwater vehicles *Hawthorne 2.0* and *Hawthorne 2.1*, the iROV *SeaBiscuit* was designed and developed specifically for nearshore habitat mapping.

SeaBiscuit built on the previous strengths and successes of *Hawthorne 2.0* and *2.1* including modular design, holonomic movement and multipurpose flexibility while addressing all of the limitations from these previous generation vehicles. A critical redesign of the mechanical, electrical and software systems specifically to improve operation in the nearshore yielded improved performance, reliability and flexibility over *Hawthorne 2.0* and *2.1*, including:

- **Reliability** – rugged, reliable SEACON wet-mateable connectors, removal of the air pressurisation system, custom made HDPE and aluminium housings, oil-filled thrusters, a re-designed electrical distribution system, extensive machine health and diagnostic sensors, redundant sensing and propulsion and robust, modular communication architectures all extended the reliability of the hybrid iROV concept.
- **Sophistication** – greatly expanded navigation and survey sensor suite (dual sonar & cameras, INS, GPS, pressure), sophisticated navigation algorithms designed for the target nearshore application, modular & upgradeable sensor/accessory suite.
- **Performance** – improved accuracy and efficiency of movement from an upgraded sensor suite (hardware upgrades and improved navigation algorithms), a complementary navigation and holonomic propulsion system to extend the benefits of mapping sensors and to enable reliable nearshore navigation.

Considering the specific objectives identified in section 3.7.1 as opportunities for further development from the test bed vehicles *Hawthorne 2.0* and *2.1*:

1. Improvements to the navigation system were provided by an increased sensor suite (section 4.6), using a variety of absolute and relative sensors together with a sensor fusion algorithm (detailed later in Chapter 5) to combine the navigation data from multiple complementary sensors to improve the overall navigation capabilities of the vehicle.
2. Kelp mapping was provided (and later demonstrated in Chapter 7) by a combination of a forward facing multibeam sonar and a 360° scanning sonar to provide quantitative kelp mapping, using video for realtime target validation.
3. 3D mapping while in transit, independent of station keeping and course holding was enabled by the improvements to the holonomic movement control algorithms (section 4.7.4), the novel sensor arrangement and complementary axisymmetric hull shape and holonomic propulsion system.

SeaBiscuit was built to a total parts budget of approximately £3000, excluding the sonar units. Although this budget included sponsorship of loaned, discounted and evaluation parts, this still represented at least an order of magnitude reduction in cost compared to the commercial offerings described in Chapter 2 with comparable performance [14]. When compared to the objective identified in section 3.3.2.3 of using innovative techniques and sensor fusion to increase the performance of a lower budget vehicle, success can be concluded as the budget was realisable to the target end users, a typical small-scale academic research operation [30, 146].

In many cases, there are significant opportunities for development in the next revision of vehicle. The focus of this research was to develop an iROV prototype to demonstrate the feasibility and benefits of using an iROV for nearshore habitat mapping. As such, generic components such as the thrusters and battery packs were not necessarily optimal, but fit for purpose and designed with a budget constraint. For example, further development to the thrusters to yield a thrust to

electrical power efficiency comparable to similar thrusters of this size [344, 345] will increase the speed of response of the vehicle and permit operation in higher tide speeds. However, the present thrusters were demonstrated as fit for purpose, low-budget and adequate for operation in the kelp beds and station keeping in minimal currents. Techniques were also developed to operate in currents higher than the thrusters can overcome (section 4.7.5). Similarly, higher energy density batteries are available at a significant price increase [333]. However, through the techniques developed using an energy buffer and continual recharge, the relatively small battery capacity has been demonstrated as suitable for the high-power manoeuvring thrust required to operate in the kelp beds, with mission durations of several hours detailed later in Chapter 7.

From the limitations for nearshore habitat mapping identified across the field of existing underwater vehicles, applicability, novelty and benefits have been demonstrated over alternative solutions to nearshore habitat mapping. These are considered across the following key areas of novelty.

4.8.1 iROV hybrid control system

The application and environment determine if control (and energy) autonomy are a benefit or a limitation. The intelligent, position-aware iROV *SeaBiscuit* represented an optimal compromise for the target nearshore environment between remote operator control and full autonomy.

Compared to a basic ROV, which can simply be regarded as a movable sensor platform [25], adding intelligence and position-awareness greatly increased the capability and sophistication of the vehicle, increasing performance and productivity in surveying and mapping underwater environments. Positional awareness allowed survey data to be compiled into useful maps of the environment, both for navigation, scientific comparison and user feedback, rather than simple chronological survey footage [69]. The continual localisation and mapping also allowed realtime feedback to the user of position, exploration and the surrounding environment.

The operator could turn on varying levels of autonomy, for example to hold a position or course despite tether drag and water movement. This allowed a remote operator to focus on the mission and incoming data in realtime, essential to ensuring data validity in the highly dynamic nearshore environments [22]. Whereas a basic ROV is controlled using teleoperation, the iROV concept added sufficient intelligence to allow *teleprogramming* [264], allowing missions to be compiled from a library of elemental manoeuvres and recompiled on the fly in response to changing conditions or scientific data. Further levels of intelligence were transparent to the operator, such as reactive machine health and fault tolerant control, used to increase the reliability and robustness of the vehicle in the hostile nearshore environment.

The additional computational and sensing complexity required to achieve reliable fully autonomous operation in the target nearshore environment would have increased operational unreliability [21], vehicle complexity and most significantly vehicle cost [11]. In high risk areas, or highly dynamic environments, the need for remote operator control and supervision to ensure high quality datasets without redeployments is still (as of 2011) recognised as essential [21]. Based on the justification provided in section 2.3.2.6, a vehicle which was capable of making all of its own decisions unsupervised (exploration, navigation, survey completion and mission planning) for an unknown target application and environment was deemed infeasible for operation in the nearshore environment and not necessarily of benefit.

Instead, the optimal combination of remote supervision and control, yet with varying levels of onboard autonomy, provided a useful scientific and commercial tool for surveying and mapping

the nearshore environment, building on existing hybrid control vehicles [263-265]. As well as reducing vehicle complexity, high-level remote control and supervision ensured data validity, avoiding the need for repeat deployments, as the mission parameters could be adjusted on-the-fly in response to either unexpected or dynamic conditions.

The novel program structure, implemented in LabVIEW, defined missions as flowcharts, with either sequential or conditional transitions between steps intuitively compiled in the 'flowchart' structure of the LabVIEW control system. The inherently modular program structure also allowed data sharing between different program subroutines, and between any number of onboard or surface networked computers. Whereas resource adaptive algorithms are capable of adapting the algorithm (e.g. map resolution) to the computational resources available [150], the novel approach implemented on *SeaBiscuit* through fully networked variables allowed the entire software architecture to be resource adaptive between the onboard (1, 2 or 3 computers) and surface computational power available. For example, if a poor-visibility operating environment favoured sonar operation over video, then the sonar algorithms could be distributed to run on each computer available to maximise the sonar processing frame rate, while continuing to run the lower priority video processing software at a lower frame rate.

The data flow computational model of LabVIEW [346] is inherently parallelisable, for efficient multi-threaded operation when running multiple tasks (e.g. sonar, video, IMU processing), yet also allowing independent (and parallel) deterministic operation when reliable control or data acquisition is required [347]. Through inherent resource management, the architecture developed is scalable, allowing the different computationally intensive (e.g. 1 or 2 cameras, 1 or 2 sonars) to be enabled or disabled with a corresponding increase or decrease in the frame rate of the remaining enabled algorithms, rather than a single sensor causing all other processing to halt. Thus seamless adaptation between the dynamic environmental conditions was ensured and survey speed could be adjusted in realtime by the operator to maintain an acceptable *spatial* survey resolution rather than just a temporal resolution.

4.8.2 iROV hybrid energy system

For the target application in the nearshore environment, energy autonomy with no tether would have imposed a restrictive limitation on survey duration and coverage [13]. The currents and turbulent flow of the nearshore would rapidly exhaust the finite onboard energy supply of batteries of an untethered vehicle. Traditional AUVs are limited to moderate or low current environments and are unable to hold a position or transit an accurate course in the currents typical of kelp beds [13]. For nearshore habitat mapping, the iROV was required to operate in high current tidal conditions, requiring a high degree of manoeuvrability to navigate in and around the kelp beds and to position the sensors in a confined environment surrounded by kelp.

Long mission durations and station-keeping in currents dictated surface power supplied by a tether. However the manoeuvrability required to operate within and map the kelp beds dictated high power thrusters, and thus would have required a thick diameter tether to provide these bursts of high power from the surface. A thick diameter tether would itself have further reduced the manoeuvrability of the vehicle.

Existing hybrid vehicles often offer distinct AUV/ROV modes [266] operating with or without a tether, or provide a lightweight data only tether [251, 252, 267-269]. However, the novel solution implemented on *SeaBiscuit* used a hybrid power supply combining an onboard battery buffer with a continual recharge via a thin lightweight tether. The onboard energy buffer provided the bursts

of power required for manoeuvring, together with the security and data reliability of an onboard power supply in case the tether was damaged or cut. Additionally, the tether afforded security, reducing the risk of data loss when operating in the difficult and challenging shallow water and high current conditions, also allowing recovery of the vehicle by retracting the tether, or by a diver following and disconnecting the tether should the vehicle become entangled.

The thin, lightweight tether allowed an unlimited mission duration and station-keeping in the flows of the nearshore without compromising manoeuvrability. The problems often caused by a trailing tether were also mitigated by the holonomic manoeuvrability of the vehicle, allowing a carefully controlled and recorded path to be navigated to reduce the risk of tangling. Tether drag was reduced by the nature of the thin tether, mitigated by the unlimited energy supply and the control effects overcome by an exact corrective force applied by the holonomic propulsion system. The tether limit on operating range from the surface vessel was not an issue for the small-scale high-detail kelp bed scans. The surface vessel could also be repositioned in the immediate vicinity to extend the survey range without having to recover and redeploy the vehicle.

4.8.3 Complementary holonomic propulsion and navigation system

In the case of surveying and mapping complex nearshore habitats, a high degree of manoeuvrability is required. There is less of a requirement for long distance propulsive efficiency due to the presence of the trickle charging tether discussed previously. Manoeuvrability was realised in *SeaBiscuit* with thrust controlled in 4 degrees of freedom (DoF) and holonomic movement in the horizontal plane, coupled with a complementary 6 DoF navigation system and an accurate and robust control system.

This manoeuvrability had benefits throughout operation, allowing confined spaces and complex 3D environments to be entered and mapped in close proximity increasing survey detail and resolution over surface vessel surveys [10, 247], while maintaining reliability and safety of operation. Reliability was enabled by the novel control system developed in this research to exploit the manoeuvrability, redundancy and fault tolerance of the vehicle. Finally, through the accurate and precise control resulting from the complementary holonomic propulsion and navigation system, *SeaBiscuit* was capable of station keeping and tracking an accurate course in the unsteady flows, tides and currents often found in the target nearshore environment compared to other vehicles [297, 307].

The unique cylindrical shell complemented holonomic movement with homogeneous horizontal drag properties, allowing independent panning of the directional sensors in-transit and provided vertical stability. The holonomic propulsion system also allowed for the novel combination of 2D sonars in the horizontal and vertical planes to be co-registered to provide the benefits of 3D scanning [129, 130], even while the vehicle was in motion. This technique exploited the vehicle configuration, cylindrical hull and holonomic propulsion system to extract maximum benefit from the finite performance limited budget sensors. Sonar frequency separation was used to minimise interference and sonar ping scheduling techniques were developed to mitigate the effects of any interference [132].

In many cases, the drag of ROVs is simply overcome by increased thrust, and little is done to optimise the hydrodynamics of ROVs for manoeuvrability. Similar axisymmetric vehicles exploit homogeneous horizontal drag characteristics to allow movement in any direction [348], yet exploiting an axisymmetric hull and holonomic propulsion to enable 3D ‘spin mapping’ while in transit is rare, with only one vehicle known, the AUV *DepthX* [288]. The vehicle *DepthX* uses

planar arrays of discrete narrow beam (2°) sonars to provide vertical mapping resolution, registered by a radial spin of the vehicle. Although the technique used by DepthX is to rotate while descending/ascending in subterranean flooded tunnels and caves, the principle of panning tightly bound (2° beamwidth) sensors while registering the returns in 3D [303] is similar to that used by *SeaBiscuit*.

SeaBiscuit uses a forward facing multibeam sonar to provide a similar narrow beam (3°) vertical swath. However, the sonar arrays fitted to *DepthX* were primarily used for obstacle avoidance [289]. Significant problems from acoustic noise and interference were encountered using these 32* 600KHz and 24* 300kHz pencil beam sonars, as the entire bank had to be fired at once, particularly in shallow water operation [303]. Conversely, the multibeam sonar fitted to *SeaBiscuit* provided a complete vertical swath at the same time, with no interference or crosstalk. Furthermore, the multibeam fitted to *SeaBiscuit* provided a far greater vertical resolution with 1° vertical beam spacing, compared to the 18° beam spacing of the sonars arranged in three perpendicular rings on *DepthX*. A later fitted downward facing multibeam sonar was used for benthic mapping on the revised vehicle *ENDURANCE* and briefly used in a forward facing orientation for mapping glacier and quarry walls [289].

However, the technique implemented on *SeaBiscuit* allows independent panning of the navigation and mapping sensors and a higher resolution [303]. *SeaBiscuit* uses the forward camera and multibeam sonar to aid navigation, but primarily these are used for habitat mapping, panned with the vehicle yet independently of vehicle course. However, the additional degree of freedom provided by the independently actuated 852 scanning sonar is used for both obstacle avoidance as well as habitat mapping with a far greater angular resolution than the periphery pencil beam sonars used on *DepthX* and *ENDURANCE*, and crucially, with an independent controlled heading. This allowed objects to be scanned while being passed, or sonar contact maintained for absolute drift-free navigation despite movement of the vehicle for either navigating a course or panning the multibeam sonar independently for habitat mapping.

Maintaining sonar contact with a landmark for relative sonar-aided navigation raises another significant advantage of *SeaBiscuit* over vehicles of a similar design. Navigation is performed independently of the expensive Doppler Velocity Log (DVL) solutions often used [258] with no reliance on clear visibility for optical station keeping [305] and no need for expensive or often unreliable acoustic baseline navigation in the nearshore kelp beds [71]. On a lower budget than *DepthX*, but still significantly higher than *SeaBiscuit* [28], the axisymmetric AUV *Charybdis* realises underwater navigation using a DVL, pressure and altimeter sensor to aid visual waypoint navigation [348]. However, no acoustic navigation is implemented, and there is no documentation of exploiting the axisymmetric hull shape to pan directional sensors, such as the multibeam sonar used on *SeaBiscuit*.

The flat saucer shape of *Charybdis* is possible due to the more compact components, for example higher energy density LiPo batteries rather than SLA and a significantly smaller navigation and mapping sensor payload [348]. Although the saucer shape incurs a lower hydrodynamic drag for horizontal translation than the cylindrical shell of *SeaBiscuit*, a saucer hull of dimensions to include the electronic systems of *SeaBiscuit* would be impractical for navigation of a compact vehicle in the confined kelp beds.

Similar to the ROV *Latsis* [27] but significantly smaller, less-expensive and more manoeuvrable, the buoyancy of *SeaBiscuit* was reconfigurable, allowing the vehicle to be operated from the surface or submerged. Surface operation was used to extend the survey capabilities of the surface

vessel into inaccessible (e.g. shallow water), or high risk inaccessible areas (e.g. rocks, kelp, under docks), providing downward facing sonar and video surveys from the surface. *SeaBiscuit* could also be towed at slow speeds (<2 knots) in calm waters between surveys sites to avoid the need for recovery and redeployment between nearby sites. In terms of navigation, a GPS position fix could be obtained at the surface with the sonar units submerged to register sonar targets with a geodetic GPS position, before diving and generating a drift free map of targets relative to the original sonar landmark.

A similar comparison with existing vehicles can be made In terms of budget, dimensions and applicability to habitat mapping in the nearshore kelp beds. The significantly larger *DepthX* and *ENDURANCE* vehicles provide additional payload space for more sophisticated navigation sensors (DVL, precision ring laser gyroscope IMU, USBL) and a much (100 times) larger battery bank of 3.8kWh [288] compared to 0.38kWh used on SeaBiscuit. Although well suited to their target environment of still water and deep water operation, the size (2.13m diameter, 1.52m height) of the *DepthX* and *ENDURANCE* vehicles [29, 288] render them highly unsuitable to operation within the cluttered and complex kelp stipes. Additionally, the size and dry mass in air of 1272kg render them physically impossible for deployment from the size of the research vessels designed to operate in the shallow water coastal kelp beds.

Instead, the 0.7m diameter shell (excluding external peripherals) and a dry mass of 65kg in air of *SeaBiscuit* allowed rapid deployment with a small crew from coastal research vessels. More importantly, rapid, safe and straightforward recovery using a single lift line was possible in the case of changing tides and weather conditions. Not only was the total development cost of *SeaBiscuit* several orders of magnitude lower than the $5m of *DepthX* [349], deployment from a smaller surface vessel also reduces ongoing operational costs.

Similar to other low-cost underwater vehicles [30, 146], *SeaBiscuit* uses a combination of a basic IMU and regular GPS updates to bound errors. However, the example referenced here [30, 146] uses vision to aid IMU/GPS navigation, requiring proximity to a sufficiently diverse seabed and adequate visibility. Instead, to allow operation of *SeaBiscuit* in the kelp beds, steps towards sonar-aided navigation to allow reliable and accurate mapping in poor visibility or from the midwater are later demonstrated using the same sonars used for habitat mapping to minimise cost. Sonar-aided navigation in unmodified environments is used elsewhere, yet often utilises a horizontal swath for tracking benthic features [118]. The novel dual-sonar configuration of *SeaBiscuit*, coupled with the holonomic mapping technique designed specifically for operation in the nearshore and kelp bed habitat mapping does not appear to have been documented elsewhere.

As the *DepthX* and *ENDURANCE* vehicles have no need to manoeuvre in flows their cruising speed of 0.2m/s is acceptable. However, this, coupled with their 4 hour mission duration before the batteries require recharging renders these larger vehicles unsuitable for operation within the currents of the kelp beds [303]. The static and relatively uniform flooded cave and under ice environments into which *DepthX* and *ENDURANCE* were deployed facilitate autonomous control and mapping, and energy and control autonomy leave the vehicle free from the restrictions of a tether to conduct surveys of up to 1000m depths in sinkholes [288], and over several thousand metres horizontally under ice [29]. However, the dynamic and complex kelp beds dictated remote control and supervision, together with a remote trickle battery recharge as discussed above.

Mapping kelp beds of *Nereocystis luetkeana* still poses such a challenge from the full height stipes, canopy [14] and challenging conditions such that modified surface vessels are still widely (as of 2012 [10]) used for survey and mapping of this environment [247]. The field trials

documented in Chapter 6 and Chapter 7 provide a demonstration of using the holonomic iROV *SeaBiscuit* as a successful proof of concept to provide reliable and detailed kelp bed mapping with full manoeuvrability from the midwater. Furthermore, steps towards the outstanding (2011) challenge [210] of sonar aided navigation in an unmodified environment are demonstrated in the absence of a DVL, USBL or precision IMU. The challenges associated with system integration of a variety of devices, interfaces and protocols [240] and sonar integration [27] have been overcome through the novel modular LabVIEW control software.

Chapter 5 Development of Underwater Navigation

5.1 Introduction

The challenges of underwater navigation were identified in Chapter 2, many of which are compounded in the nearshore. The background work in Chapter 3 described the development of a test bed vehicle as a point of comparison from single-sensor navigation and to inform development of the iROV *SeaBiscuit* detailed in Chapter 4. This chapter describes the design and implementation of a complementary nearshore navigation system capable of localisation and mapping in the nearshore.

The justification and implementation of probabilistic sensor fusion are detailed, together with probabilistic characterisation of the navigation sensors. Gaussian functions are used to represent the uncertainty associated with measurements from each sensor, allowing a weighted fusion of multiple measurements, rather than simpler techniques such as voting or a single 'best guess'. This probabilistic framework is extended to simultaneous localisation and mapping (SLAM), allowing the vehicle to correspond observations to previously mapped features in order to compile a map and localise itself, with the uncertainty of each piece of information tracked.

Various algorithms for SLAM are considered for suitability to nearshore navigation, including robust methods for establishing landmark correspondences, together with techniques to use nonlinear data. The extended Kalman filter algorithm for probabilistic SLAM is described and a novel implementation programmed in LabVIEW for use on *SeaBiscuit*. The modular software architecture developed allowed alternative algorithms to be trialled. A simulation environment was constructed as a modular wrapper for the navigation software, using simulated noisy sensor measurements, vehicle motion and environmental variation such as water movement. This allowed the navigation algorithms to be thoroughly tested prior to deployment.

5.2 Sensor fusion

The benefits of sensor fusion in response to the challenges of nearshore navigation were established in the literature review in Chapter 2. In particular the opportunity to use sensor fusion to extend the performance of a limited budget of sensors, together with the requirement to combine absolute and relative measurements were identified. Sensor fusion was used on the iROV *SeaBiscuit* to combine estimates from a *variety of sensors*, each with different complementary *characteristics* (e.g. update frequency, noise, accuracy, etc.). In summary:

- Each sensor's estimate was assigned a *reliability*:
    - this determined its *weighting* (influence) on the overall positional estimate when combining conflicting data
- As environmental conditions changed, the weightings were adjusted (manually at present):
    - turbid water (murky so lower weighting of vision)
    - turbulent water (increased sonar noise)
    - magnetic disturbances (reduced magnetometer accuracy)
- The overall **position estimate** was provided with an accuracy or **uncertainty estimate**

Figure 5.1 below shows the fusion of sensors fitted to *SeaBiscuit*, with the information provided by each sensor described previously in section 4.6.

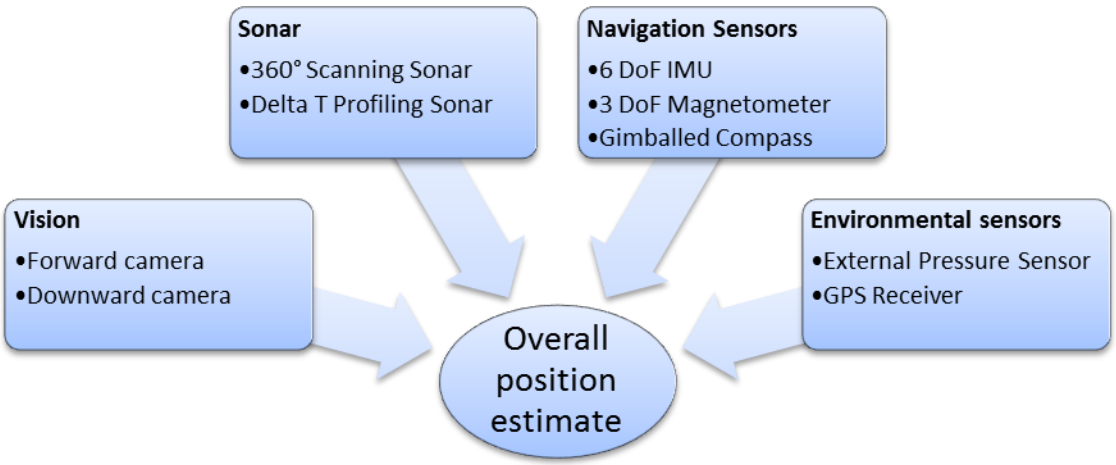

Figure 5.1 - The principle of sensor fusion on the iROV SeaBiscuit.

5.2.1 Justification

Considering the simple example of two sensors measuring the yaw angle of the vehicle, the 2Hz update, mechanically gimballed NMEA compass and the faster yet noisier Xsens IMU (120Hz update, unsynchronised with the 2Hz NMEA compass), then each produced independent observations of the same state, with disparate yet complementary characteristics. Figure 5.2 represents the arrival times of the different measurements.

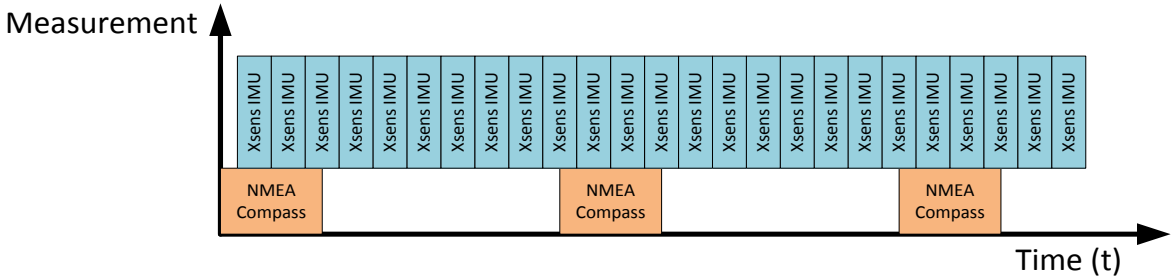

Figure 5.2 - Fusion of the 2Hz NMEA compass the 120Hz Xsens IMU measurements (not to scale).

More frequent estimation of yaw angle was required than the 2Hz update of the NMEA compass, and due to potentially sudden movements of the vehicle, interpolating between observations was not reliable. Instead, the noisier (more uncertain) measurements from the Xsens were used to update the estimate in between NMEA compass updates. Then, each time (every 0.5s) a lower uncertainty NMEA measurement was received, either:

1. the current Xsens estimate was rejected and the NMEA value trusted completely,
2. or, the estimates from each sensor were fused.

The simplistic approach in scenario '1' suggested assuming that the state of the vehicle was the most *recent* measurement, with the NMEA compass measurement taking priority (when available) over the more uncertain Xsens measurement. Scenario '2' which required fusing the data from every measurement from both sensors into an overall estimate had two benefits. No information was 'wasted' or discarded, and if an error, or unnoticed deviation occurred with one sensor, this could be allowed for by comparing and fusing data with the other sensor, rather than just trusting a single measurement or sensor.

Therefore the technique of recursively fusing each measurement (from either sensor) into a maintained state estimate, rather than just accepting a single measurement at each time step, is illustrated in Figure 5.3 below.

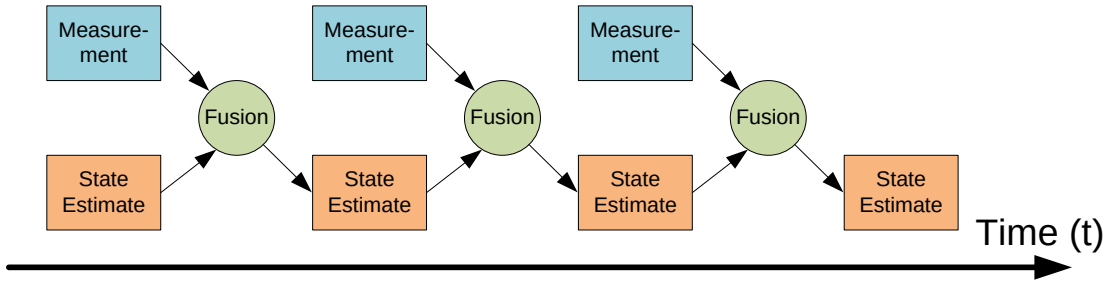

Figure 5.3 - The principle of recursively fusing measurements into the state estimate. An ongoing state estimate was maintained, and each time a new measurement was available, it was fused into the state estimate.

A variety of fusion techniques were identified in the literature review in Chapter 2. Probabilistic methods, including the compact and efficient Extended Kalman Filter (EKF), were proposed to be most applicable for implementation on *SeaBiscuit* for nearshore navigation. The EKF, a parametric filter, represented states, measurements and landmarks as Gaussian (normal) probability density functions which were compactly and efficiently stored with a mean and (co)variance.

5.2.2 Implementation example: fusion of yaw angle (vehicle heading)

Vehicle heading, referred to as the vehicle yaw angle in the World Coordinate System (WCS) is considered here as an example of sensor fusion. The mechanically gimballed NMEA compass and the gyroscopes and magnetometers built into the Xsens Inertial Measurement Unit (IMU) were both capable of measuring yaw angle *directly*.

In addition to these *direct* measurements of yaw angle, *indirect* yaw angle estimates could be made from several of the other sensors. However, these indirect estimates were all reliant on some form of a priori information. For example, given a known map and a uniquely distinctive arrangement of features in the map, subsequent observations of these features could be used to orientate the vehicle using the sonar or vision. Alternatively, assuming stationary landmarks, autocorrelation between sonar scans alone could be used to extract change in yaw angle.

Using the sensor fusion framework, the uncertainty associated with each measurement, landmark, etc. was tracked and data from both direct and indirect sources could be reliably fused. Tracking this uncertainty allowed one sensor to correct another. For example, measurements from the NMEA compass and Xsens IMU were used to estimate the orientation of the vehicle (while tracking the uncertainty of each). Additionally, sonar observations were registered using the orientation estimate. Thus the uncertainty of mapped sonar targets combined the uncertainty from the orientation sensors and the uncertainty associated with the sonar itself. When revisiting and recognising the same location, any observed landmarks which were previously mapped could be used for localisation (with an associated uncertainty) together with the most recent compass and Xsens orientation estimate. Mapped landmarks could also be updated upon reobservation with a lower uncertainty as the position is corrected and confirmed.

This process of constantly using and reusing direct and indirect estimates of state was common to all sensors and the example of fusion of yaw angle is considered here. The first step was determining the magnitude of the uncertainty associated with each measurement for a given set of operating conditions.

5.2.2.1 Yaw sensor characterisation

In order to use the probabilistic framework for sensor fusion and navigation introduced in section 2.3.2.4, the uncertainty associated with each measurement was required. The framework

presented by Thrun et al. [150] stated that 'measurements z_t are usually noisy projections of the state x_t'. Thus, the measurement probability was the probability that the state $X = x$, given that the value of the measurement $Z = z$. Therefore the **measurement probability** $p(z|x)$ for each source of information was required, in this case, each sensor used to measure yaw angle.

The measurement probability was represented with a probability density function (PDF) over the continuous measurement/state space. Although measurements were discrete, limited by the sensor resolution, they were represented by a continuous PDF. The EKF framework required the assumption that the uncertainty associated with measurement data was normally distributed, allowing a Gaussian, or normal PDF to represent the measurement data. Using the canonical parameterisation, this normal PDF was specified by the mean and variance of the normal distribution to provide a concise and efficient representation of the measurement data which accounted for uncertainty.

In order to make these assumptions the following steps were required for each sensor, each change of mounting position, change of sensor setting and each change of operating environment and conditions:

1. Firstly the accuracy of representing the uncertainty associated with the measurement data with a normal distribution was verified analytically by plotting the sensor data for a known position and approximating the data by fitting a normal distribution.
2. The parameters of the normal distribution (mean and variance) were then estimated.

It is important to note the difference between *calibration* and the more detailed *characterisation*.

Calibration refers to the process of relating the sensor output to real-life units (section 4.6.9). For example, the offset between the compass output and the direction the vehicle is facing caused by sensor misalignment in mounting, or the ratio of voltage output and the zero point from the pressure sensor to the vehicle depth. This provided the mean value for the PDF.

Characterisation includes this calibration process (to obtain the mean value for a given state), but also considers the uncertainty (variance) associated with each measurement. The sections below use the example of characterising the NMEA compass and Xsens IMU to allow fusion of the yaw angle of the vehicle. This example describes static characterisation for simplicity in providing a known ground truth measurement for characterisation. This required the assumption that the uncertainty (variance) for each sensor during operating conditions was the same as the uncertainty experienced during static characterisation.

Further developments discussed in Chapter 8 consider improvements to this process, for example automating the characterisation and calibration process to autonomously vary the weighting of each sensor in response to dynamic conditions: e.g. in murky water, vision has a higher uncertainty, when the tether is attached, the control probability is lower, etc.

5.2.2.1.1 NMEA compass characterisation

For the static NMEA compass characterisation, the vehicle was held flat, level and in a known orientation and the output from the NMEA compass was captured over a suitable period. Therefore the state x_t of the robot (the stationary heading of the vehicle) was known and the measurement data z_t was recorded.

Although the accuracy of this calibration process when considering the zero point was not particularly high due to the inevitable error in manually aligning the vehicle, for the purposes of

zeroing the sensor in field conditions it was sufficient. The accuracy of the calibration process only affected the zero-point heading of the map and had no effect on the accuracy of the mapped data as the linearity of the compass was already pre-calibrated to a high accuracy. Additionally, the accuracy of aligning the robot to a known angle had no effect on the accuracy of calibrating the various sensors to each other (co-registration). The same applied to the calibration of the Xsens INS.

Taking the NMEA compass data as an example, several calibration datasets were gathered which recorded the compass data for a known static vehicle position and orientation. Figure 5.4 below shows an example calibration dataset. The vehicle was stationary for a period of approximately 300 seconds with all electrical systems running to simulate electrical and electromagnetic noise during operation.

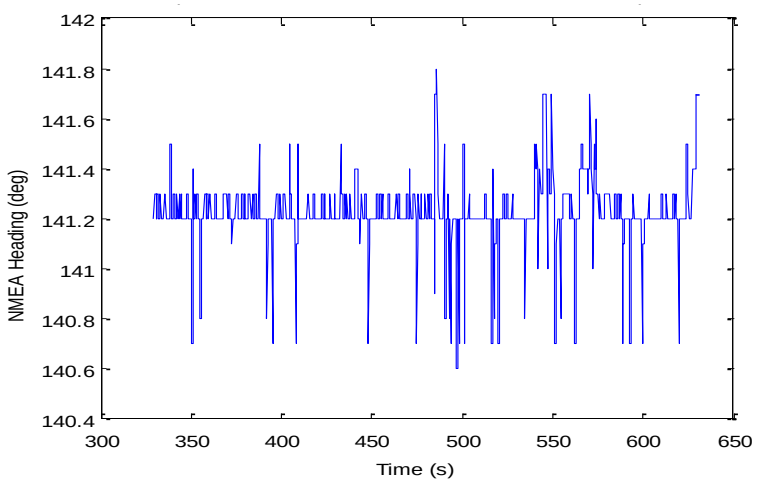

Figure 5.4 - Calibration of the NMEA compass heading. The vehicle was left running in a stationary position on the dock and the (electrical and electromagnetic) noise was recorded.

The calibration dataset shown above in Figure 5.4 is plotted as a histogram in Figure 5.5 below and a Gaussian distribution fitted to it using the MATLAB statistical toolboxes for histogram fitting and normal parameter estimation. The normal distribution shown was parameterised by a mean of 141.2° and a variance of 0.1402.

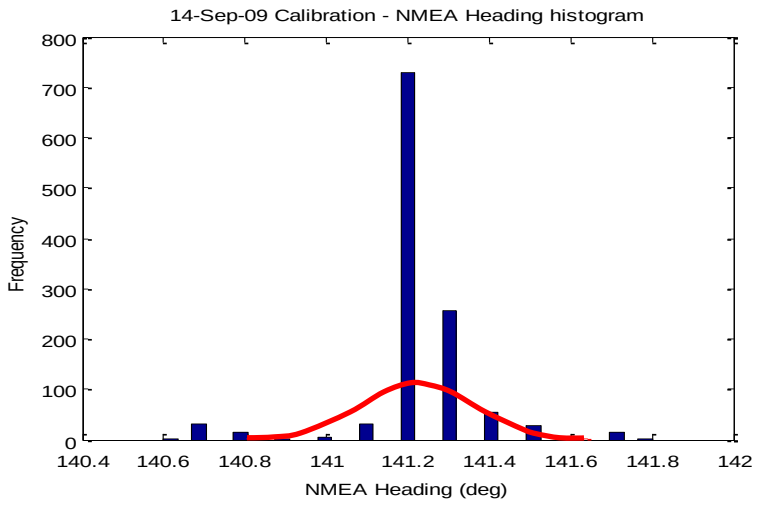

Figure 5.5 - A histogram plot of the NMEA compass calibration dataset shown above in Figure 5.4 with a normal probability density function fitted to the dataset.

The variance was used as a baseline measure of the uncertainty associated with measurements from the NMEA compass in the sensor fusion algorithms as the measurement probability variance. Several factors increased the variance during operation, including operation in close

proximity to ferromagnetic structures and operation of the vehicle's thrusters. However the baseline measure presented above from noise in the sensor was present in all readings. For simplicity at this stage, a static variance for each sensor was assumed, with each sensor characterised under the same conditions. Techniques to detect and correct for dynamic uncertainty are discussed in section 8.3.

5.2.2.1.2 Xsens IMU orientation characterisation

This calibration procedure was repeated for the other navigation sensors and further probabilistic characterisation results are included in Appendix C. To continue the example of fusing yaw angle measurements from the Xsens IMU and NMEA compass, the characterisation of the Xsens orientation measurement is shown below in Figure 5.6. This Xsens orientation measurement was the output of the internally filtered gyroscope and magnetometer readings, as discussed in section 4.6.5.2.

Calibration and characterisation data was acquired for the Xsens IMU simultaneously with the NMEA compass data acquired above to ensure the same conditions throughout, and to calibrate the mounting offset between the two sensors. Although this example only considers the yaw angle measurements from the Xsens IMU, the pitch and roll characterisation values are included for completeness.

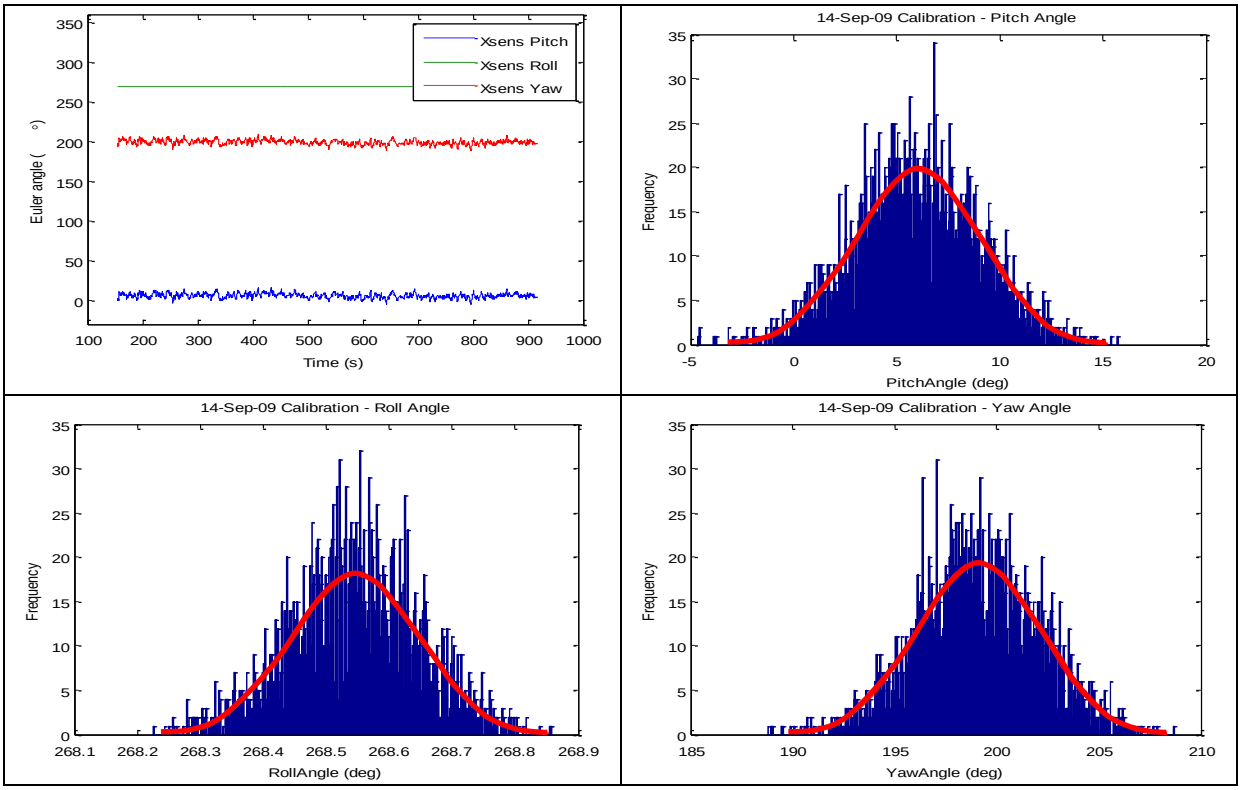

Figure 5.6 - The Xsens orientation characterisation process. The vehicle was held in a stationary position with all electrical systems running to simulate operating conditions and the output from the Xsens inclination estimate was recorded under the same conditions and at the same time as the NMEA compass discussed previously. The top left plot shows the recorded dataset over a period of >700s. The pitch, roll and yaw data are plotted as a histograms. The red trace shows the normal probability density function fitted, the parameters of which are shown inTable 5.1 below.

Table 5.1 - Probabilistic characterisation of the static Xsens and NMEA compass measurements

	Pitch		Roll		Yaw	
	Mean:	**Variance:**	**Mean:**	**Variance:**	**Mean:**	**Variance:**
Xsens IMU:	5.97°	3.0474	268.55°	0.1018	199.09°	2.9779
NMEA Compass:						0.1402

When measuring discontinuous wrapping functions such as orientation, as the orientation reached the range limits e.g. 358°, 359°, 0°, 1°, there was a discontinuity as the function wrapped. The definition of cyclic data (or circular distributions) is that the value (or density) at any point x on the real line is the same as that of $x + k\xi$ where k is any integer and ξ is some real number [350]. This was corrected by the use of 'continuous degrees'. As the orientation increased as the vehicle turned clockwise, e.g. 358°, 359°, etc. and crossed past the zero point, the values continued to be added in the form of 360°, 361°, etc. This allowed the number of rotations to be counted as well – an important point when operating with a tether. The same was true in reverse: for an anticlockwise rotation with the heading decreasing from 2°, 1°, 0°, instead of wrapping, the values continued into negative headings in the form -1°, -2°, etc.

5.2.2.1.3 Characterisation conclusions

The variance (uncertainty) associated with the Xsens IMU orientation measurements was in general higher than that with the NMEA compass, exhibiting greater noise when stationary. However, this did not necessarily mean that the NMEA compass was a 'better' sensor. The NMEA compass exhibited a large degree of mechanical damping which decreased the speed of response but provided a smoothed output. This same effect was demonstrated on the Xsens sensor by applying a moving average filter to the high sample-frequency data. The Xsens had a much faster update (120Hz instead of 2Hz), faster reaction than the mechanically gimballed NMEA compass, could be tilted more than 30° and could measure orientation in 3 DoF (pitch, roll and yaw) rather than just 1 DoF (yaw) as for the NMEA compass. Additionally the Xsens IMU provided robustness to transient magnetic disturbances using the internally filtered combination of magnetometers and gyroscopes to estimate orientation.

Therefore, although the two sensors had disparate characteristics they were an ideal complement to each other through sensor fusion. Gaussians (normal distributions) were also shown to be an adequate approximation of the uncertainty associated with each sensor, allowing representation by a compact computationally-efficient parametric model.

5.2.3 Fusion of Gaussian functions

Techniques for the fusion of normal functions and many of the Gaussian filters based on these principles (e.g. the Kalman filter), required the assumption that the continuous probability distributions were linear not cyclic. If nonlinear wrapped data was used, for example an orientation dataset comprised of alternating values of 359° and 0° would have a high variance as there was a large numerical separation between the values, when in actuality the values were closely spaced by only a degree of orientation. Similarly, if the orientation of the vehicle was represented by a normal distribution with a mean centred on 5°, then there was a relatively high probability that the orientation of the vehicle was 355° (a turn of just 10° anticlockwise). However, when using the standard normal distribution, the probability that the vehicle is at 355° would be appear to be very low (appearing as a turn of 350° clockwise).

The need for circular statistics has long been realised. Techniques such as the *circular normal distribution* described by Gumbel et al. [351] allow the uncertainty associated with directional data in robotics to be represented, and thus the Gaussian filters discussed in previous sections adapted to problems involving directional statistics. A further discussion on directional statistics & cyclic probability distributions is provided in Appendix D.

One technique which is expanded upon later on to allow the non-linear orientation data to be used with a Gaussian filter is to 'linearise' the data before passing it through the filter. For simplicity in the following few sections, the development of the sensor fusion algorithms continues assuming linear data. An evaluation of techniques to perform this linearisation are presented shortly and developed in further detail in section 5.3.6 which considers the extended Kalman filter.

Given Xsens IMU and NMEA compass orientation estimates characterised by Gaussians, each with a respective variance (uncertainty) and complementary characteristics, several techniques exist to intelligently fuse or combine the data from two observations of the same state. For simplicity, the following examples abstract from the specific sensor data provided above and use unit Gaussians to allow the fusion techniques to be easily represented and compared.

The simplest method (introduced previously) accepted the most recent measurement available. When two measurements from different sources arrived at the same time, the measurement with the lower uncertainty was favoured. A development of this based the current estimate on the result of a moving average filter over the previous n measurements, to reduce the effect of spontaneous erroneous results.

The more sophisticated and robust method utilised the probabilistic framework introduced in section 2.3.2.4. Realising that every measurement from every sensor had an associated uncertainty, the amount of uncertainty associated with each measurement determined its influence on the overall position estimate. Representing each measurement as a normal (Gaussian) probability density function (PDF) with a mean μ and variance Σ, two techniques were considered for fusion of the normal distributions:

1. The *addition* of normally distributed PDFs
2. The *multiplication* of normally distributed PDFs

The following two sections consider each of these techniques in summary. The variance is represented by Σ for consistency in the matrix notations developed later rather than the usual σ^2.

5.2.3.1 Addition

Figure 5.7 below shows a generalised continuous example for the *addition* of two normally distributed probability density functions. The red and blue dashed lines represent two sensor measurements characterised by normal PDFs. The red function has a low variance and therefore a high peak, the blue function has a much higher variance and therefore a lower peak and a broader distribution. In this case, the two functions have a coincident mean.

Addition of the two functions yielded the green curve which was normalised to have an integral of 1 (in order to be a valid PDF). However, the result of the addition (the green curve) was no longer a Gaussian. To address this, the black curve was obtained by fitting a Gaussian normal function to the result of the addition using the LabVIEW 'Gaussian Peak Fit Coefficients' subVI, which can be thought of as the Gaussian ***sum*** of the two input normal functions. Two scenarios were considered:

1) The current belief of the state was Sensor 2 (blue-dashed), a relatively uncertain estimate and the measurement (Sensor 1, red-dashed) was obtained which had the same mean as the current estimate but a lower uncertainty. As expected, this corroborating measurement served to

reinforce belief about the current estimate as the mean was the same. The state estimate therefore increased in certainty to the black curve, partway between the two estimates.

2) The opposite scenario was that the current belief was that of Sensor 1 (red-dashed) and a measurement (Sensor 2, blue dashed) was obtained which had the same mean as the current estimate but a larger variance. This would be expected to increase the certainty about the current belief, as re-measuring the same mean was expected to reinforce belief. Instead it weakened belief and the uncertainty increased from the red-dashed function to the broader black function. *This suggested that there was no point in taking the measurement (blue-dashed) as, although it confirmed the current belief (same mean), it weakened the belief distribution.* ***Even though corroborating evidence was received, it lessened belief.***

The justification for this can be seen by examining the curves. By taking the measurement (blue-dashed), the explanation was that although the mean was the same as the current estimate (red-dashed), the measurement could be anywhere within the blue-dashed distribution. The result of adding the functions was therefore correct, but in terms of the robot, there would be no benefit gained in taking the measurement (blue-dashed). The opposite effect was seen when considering combining normal distributions by multiplication in the following section.

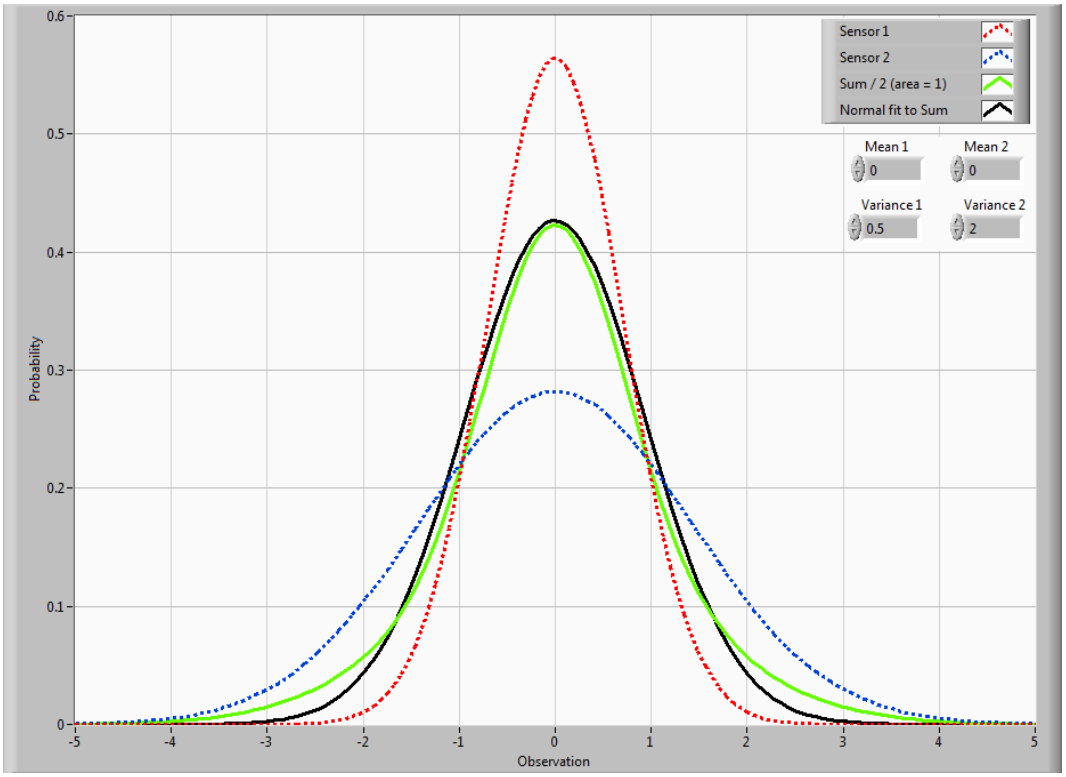

Figure 5.7 - The sum of two normal distributions with a coincident mean.

The case of summing two functions which overlapped but did not have a coincident mean is considered in Figure 5.8 and Figure 5.9 below. Considering Figure 5.8, the current state estimate was centred at '0' (blue-dashed) and had a relatively large uncertainty. If a measurement was taken which suggested that the state was actually centred at '3' (red-dashed), then upon updating the state estimate by summing the two distributions and renormalising, the black curve was obtained. Each new estimate at position '3' pulled the estimate closer and closer to the mean of 3; the higher the certainty of the estimate, the quicker the state estimate converged on '3'.

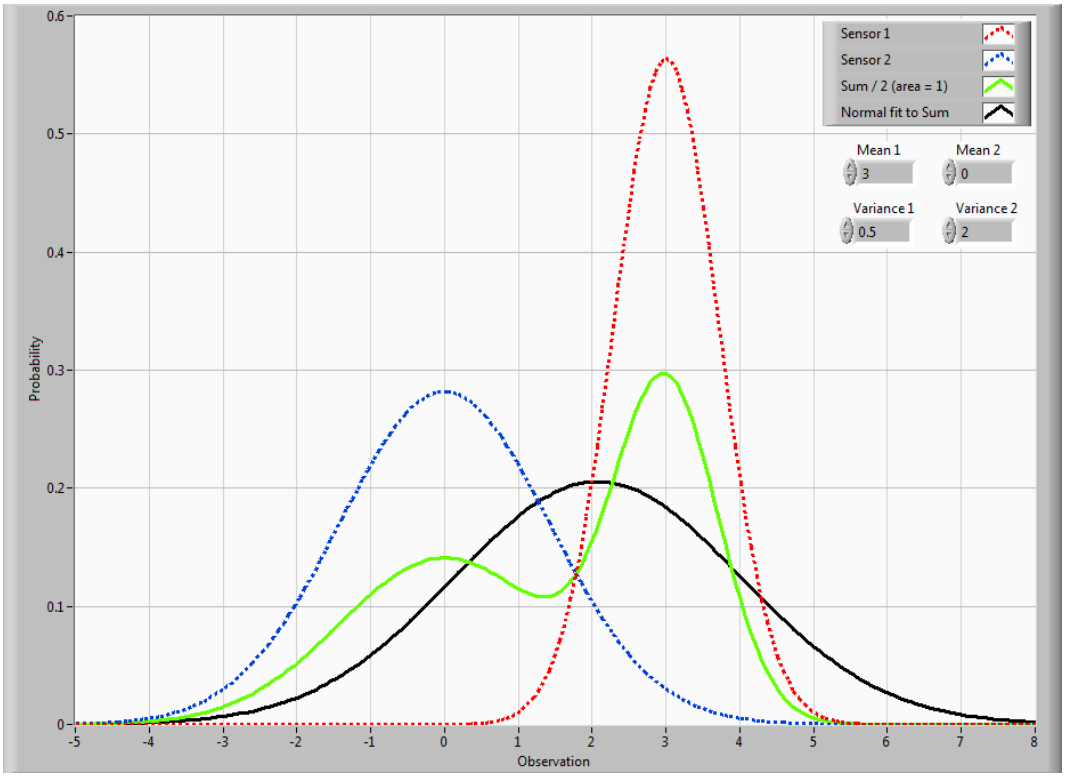

Figure 5.8 - The sum of two normal distributions with an overlapping but non-coincident mean.

Figure 5.9 below shows the same principle, but starting with a relatively certain state estimate (red-dashed) centred at '0' and taking a relatively uncertain (high variance, blue-dashed) measurement at '3'. The effect primarily increased the uncertainty of the state estimate (black-line) but also had the effect of slightly moving the mean of the state estimate towards the new measurement '3'. The speed at which the state estimate converged on '3' depended on the mean and variance of subsequent measurements.

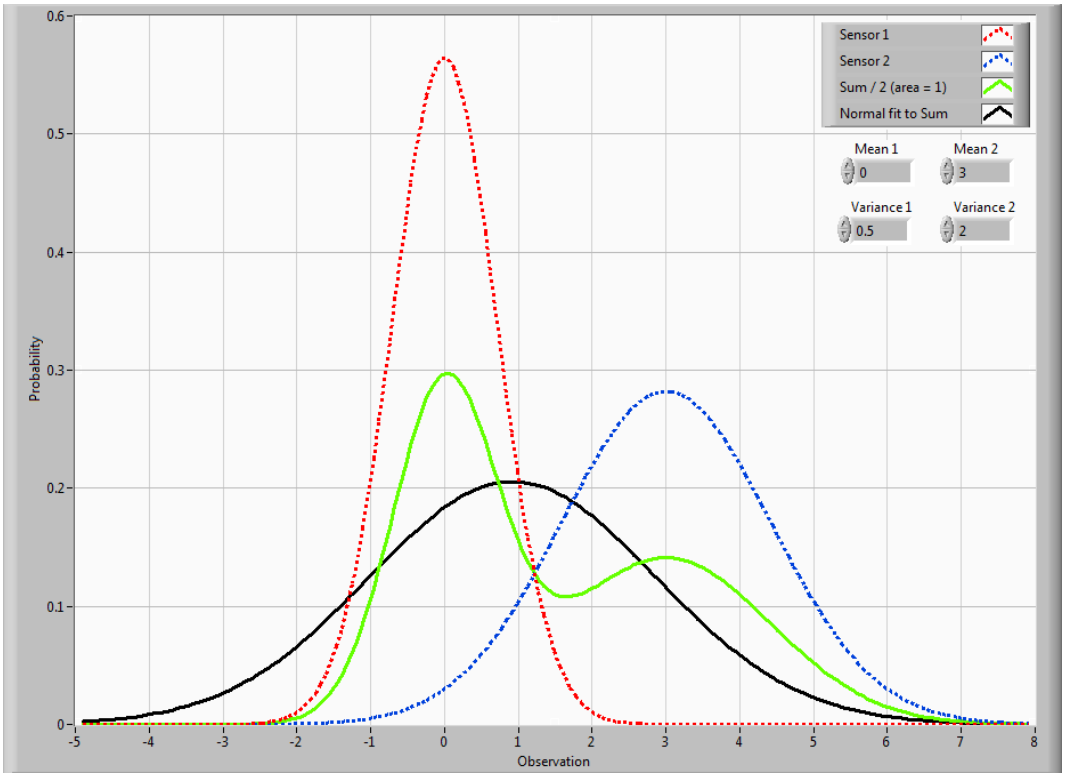

Figure 5.9 - The sum of two normal distributions with an overlapping but non-coincident mean.

5.2.3.2 Multiplication

The same example used for combination of normal functions by addition (Figure 5.7 previously) is repeated below as Figure 5.10 to show the fusion of two normal functions with a coincident mean, one with a small variance, the other with a higher variance, but this time combining the two normal functions through *multiplication*. Considering the same two scenarios from Figure 5.7 when two measurements with coincident means might occur:

1. The current belief of the state was Sensor 2 (blue-dashed), a relatively uncertain estimate and the measurement (Sensor 1, red-dashed) was obtained which had the same mean as the current estimate but a lower uncertainty. The green solid curve shows the result of multiplication of the two measurements to obtain the product. This was normalised to have an integral of one in order to conform to the law of total probabilities and is shown by the black dashed curve. This implied that an uncertain measurement followed by another coincident measurement reinforced belief as the mean was the same. The second measurement therefore increased the certainty of the state estimate to the black curve, more certain than either of the two original estimates. Therefore, both estimates 'improved' knowledge and there was benefit in taking both measurements. (The black dashed curve is coincident with the pink dashed curve, discussed shortly.)
2. The opposite scenario was that the current belief was that of Sensor 1 (red-dashed) and a measurement (Sensor 2, blue dashed) was obtained which had the same mean as the current estimate but a larger variance. Although the second measurement had a high uncertainty, it still suggested that the mean was in the same place and still reinforced the current belief to yield the black-dashed line.

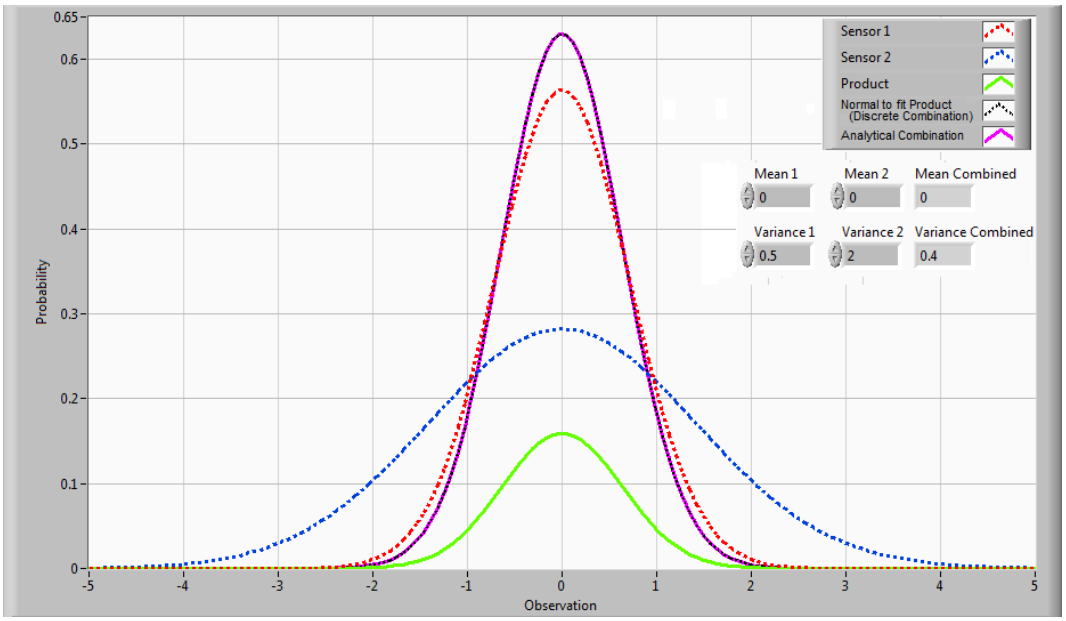

Figure 5.10 - The product of two normal distributions with a coincident mean (red dashed and blue dashed). The green curve represents the numerical product of the two distributions, which was normalised to the black dashed line. This is identical to the pink curve representing the analytical product of the two curves.

The numerical product from element-by-element multiplication of the two distributions in the plot above (the green function) was normalised to obey the rule of total probabilities (the black-dashed function). The shape of the green curve was already a Gaussian, it simply required a scaling factor, the normalisation constant η discussed in more detail in later sections. It was however computationally more efficient to perform the multiplication of normal distributions analytically using the following equation [150]:

$$\left.\begin{array}{l} X_1 \sim N(\mu_1, \Sigma_1) \\ X_2 \sim N(\mu_2, \Sigma_2) \end{array}\right\} \Rightarrow p(X_1) \cdot p(X_2) \sim N\left(\frac{\Sigma_2}{\Sigma_1 + \Sigma_2}\mu_1 + \frac{\Sigma_1}{\Sigma_1 + \Sigma_2}\mu_2, \quad \frac{1}{\Sigma_1^{-1} + \Sigma_2^{-1}}\right)$$

Equation 5.1

This states that if two normally distributed functions are multiplied, the resulting function will be normally distributed and that the parameters of the resulting function can be determined analytically. As can be seen above in Figure 5.10, the pink line (the analytical multiplication) coincides with the black dashed line (the numerical multiplication), showing that the discrete element-by-element technique was correct (provided sufficient samples were taken), yet the analytical solution was much more computationally efficient.

The combination of two normal functions with a different mean using the multiplication function is considered in Figure 5.11 and Figure 5.12 below.

Considering Figure 5.11, the current state estimate was centred at '0' (blue-dashed) and had a relatively large uncertainty. If a measurement which suggested that the state was actually centred at '3' was taken (red-dashed), then upon updating the state estimate by multiplying the two distributions and renormalising, the black curve was obtained. Each new measurement at position '3' pulled the state estimate closer to the mean of 3; the higher the certainty of each new measurement, the quicker the state estimate converged on '3'. Due to the overlap of the normal functions, the certainty of the estimate also increased with each new measurement.

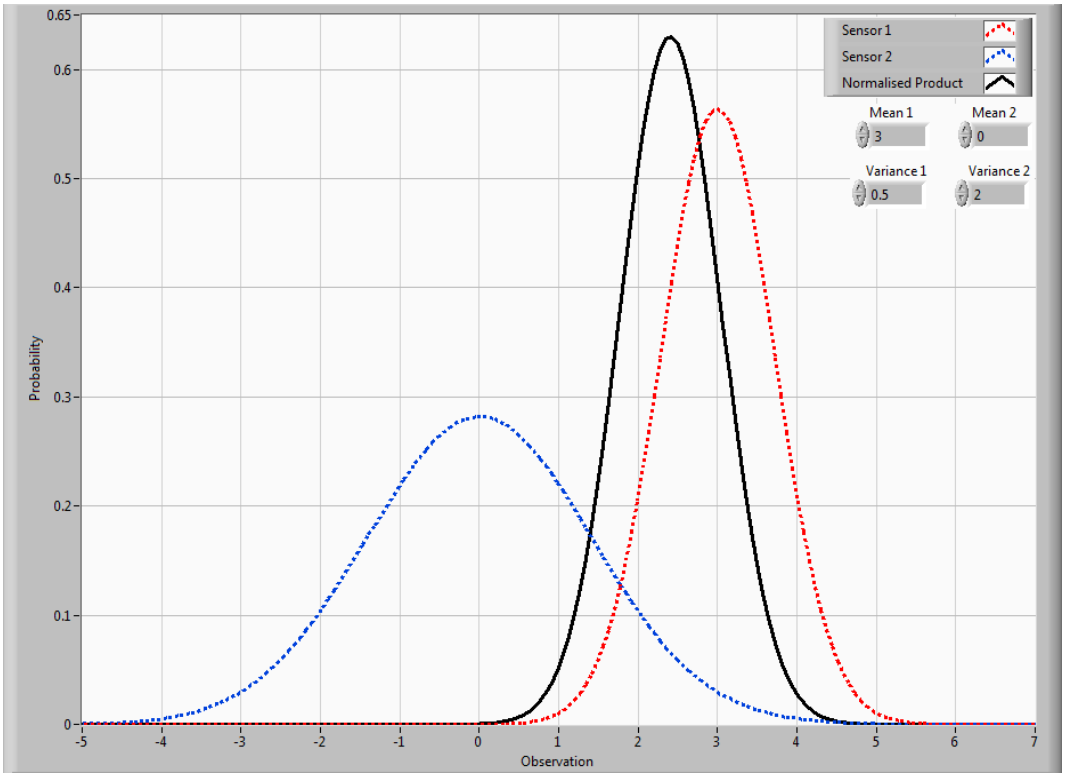

Figure 5.11 - The product of two normal distributions with an overlapping but non-coincident mean.

Similar results can be seen in Figure 5.12 below, this time starting with a relatively certain state estimate (red-dashed) centred at '0' and taking a relatively uncertain (high variance, blue-dashed) measurement at '3'. The new measurement shifted the belief slightly towards the new mean, the amount determined by the variance of the new measurement and, due to the overlap of the normal functions, increased the certainty.

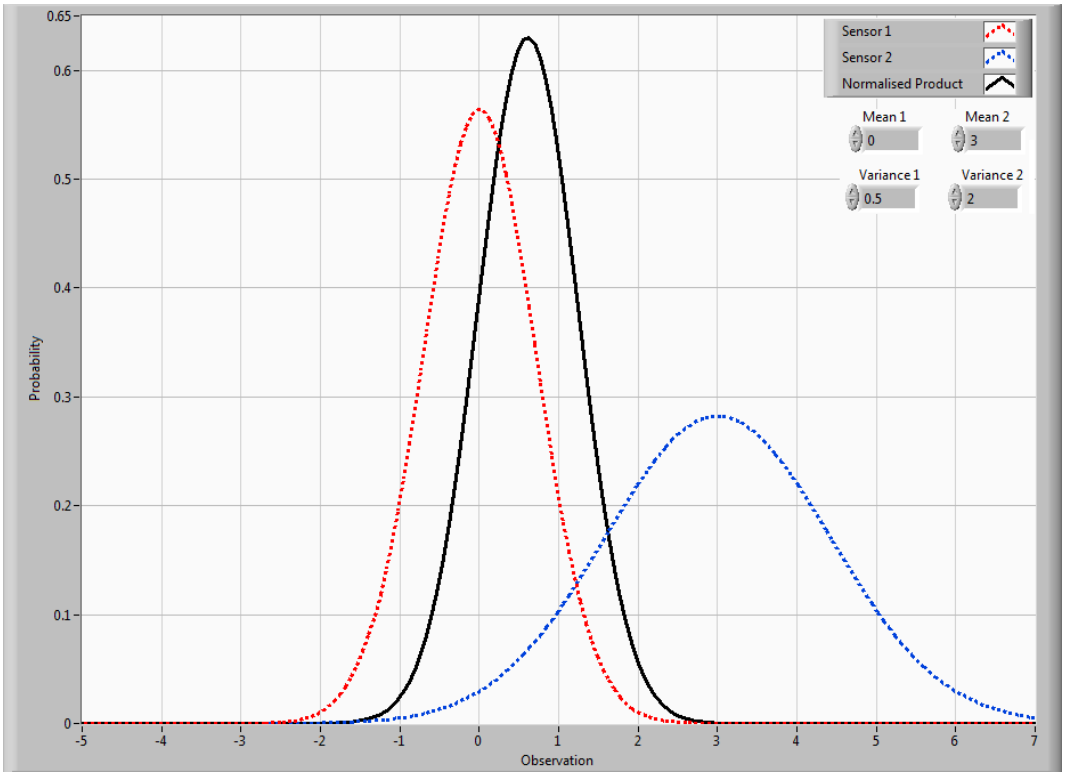

Figure 5.12 - The product of two normal distributions with an overlapping but non-coincident mean.

As the normal function never decays completely to zero over the range $-\infty$ to $+\infty$, any measurement will always overlap to some extent with the existing belief distribution and there will always be some reinforcement of belief. For example, in Figure 5.13 below, two normal functions were combined using the product combination. As expected, the introduction of the blue-dashed function shifted the estimate to the right where the red-dashed estimate was updated as the black solid line. However, the certainty of the black solid line was also increased by the introduction of the blue-dashed function.

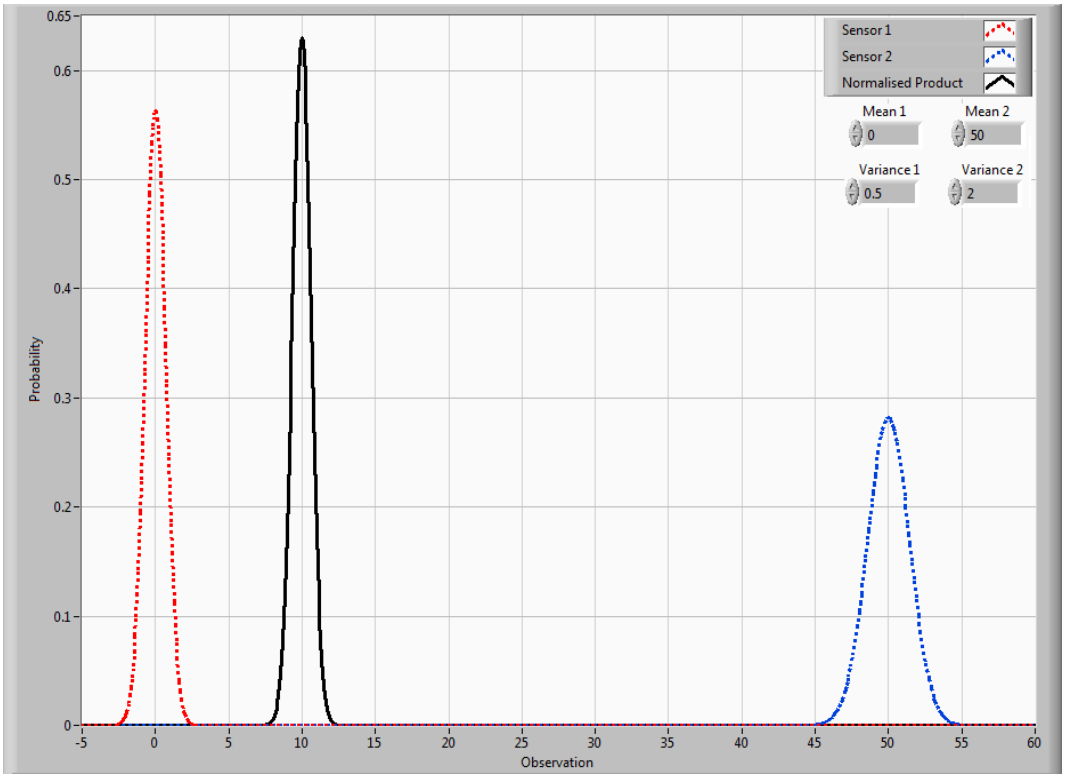

Figure 5.13 - The product of two normal distributions with a non-coincident and widely separated mean.

5.2.3.3 Conclusions

From the examples above, it was concluded that the multiplication of normal distributions was an efficient and valid method for combining the measurements from two sensors, or combining the measurement from a sensor with an existing belief. Using the uncertainty (variance) associated with each sensor reading, or associated with the prior belief, to weight the effect of each input on the combined belief was also demonstrated.

This principle of the weighted combination of normal (Gaussian) functions forms the basis of the Bayesian filtering techniques which are discussed in the following section. The sensor fusion techniques developed above are extended to navigation using Kalman filters to develop the probabilistic representation of uncertainty to localisation and mapping, by including control updates and kinematic models rather than just sensor fusion.

5.3 Theory of Simultaneous Localisation and Mapping (SLAM)

From the techniques for SLAM discussed in the literature review in Chapter 2, the Extended Kalman Filter (EKF) was established as conceptually straightforward and the most applicable to nearshore navigation provided that a series of conditions could be adhered to. The most significant of these was that the state could be accurately represented using Gaussians.

This section begins by establishing the theory required to implement EKF SLAM which is based on the widely accepted theory presented in the recent work by Thrun, Burgard and Fox titled '*Probabilistic Robotics*' [150]. This section then continues by detailing the implementation specific to *SeaBiscuit* with results of field trials presented Chapter 6.

5.3.1 State

State is defined as the collection of all aspects of the robot and its environment that can impact the future [150]. The combined state vector at time t comprises state x_t of the robot at time t and a map m maintained by the robot.

$$x_t = (x\ y\ \theta)^T$$

Where, x, y, and θ are the coordinates and bearing of the robot respectively for localisation in 2 dimensions. This vector, and those used to map landmarks, can be expanded to 3 dimensions as necessary. The map m is comprised of:

$$m = (m_{1,x}\ m_{1,y}\ s_1\ \ m_{2,x}\ m_{2,y}\ s_2\ \ \dots\ \ m_{N,x}\ m_{N,y}\ S_N)^T$$

Where, $m_{i,x}\ m_{i,y}$ are the coordinates of the i-th landmark, for $i = 1, \dots, N$ and s_i is the signature. The signature can be expanded to include any number of defining features of the landmark used to distinguish it from other landmarks. For example, this can be, the colour of the landmark if seen by vision, or the mass and ellipse ratio of an object viewed by sonar, or a unique identifier transmitted by a beacon. The overall combined state vector thus becomes

$$\binom{x_t}{m} = (x\ y\ \theta\ \ m_{1,x}\ m_{1,y}\ s_1\ \ m_{2,x}\ m_{2,y}\ s_2\ \ \cdots\ \ m_{N,x}\ m_{N,y}\ S_N)^T$$

Thrun et al. [150] define a state as being *complete* if it is the best predictor of the future. This entails that knowledge of past states, measurements or controls carry no additional information that would be useful to predict the future more accurately. The concept of state completeness is known as the Markov assumption which states that past and future data are independent if one

knows the current state x_t. This does not require the future to be a *deterministic* function of state – the future may be *stochastic*, but no variables prior to x_t may influence the stochastic evolution of future states, unless this dependence is mediated through the state x_t [150].

The following factors identified by Thrun et al. [150] may have a systematic effect on sensor readings and thus they induce violations of the Markov assumption:

- Unmodelled dynamics in the environment not included in x_t for example moving targets
- Inaccuracies in the probabilistic models
- Approximation errors when using representations of belief functions, e.g. Gaussians

In principle, many of these variables can be included in state representations. It is nearly impossible to specify a *complete state* for any practical robot system. Instead, for practical implementations, often an *incomplete state* is known – a small subset of all state variables [150]. Incomplete state representations are often preferable to more complete ones to reduce computational complexity. In practice, Bayes filters have been found to be surprisingly robust to such violations. As a general rule, the state of x_t should be defined so that the effect of unmodelled state variables has close-to-random effects [150].

5.3.1.1 Environment interaction

There are two fundamental types of interactions between a robot and its environment: *sensor measurements* and *control actions*. The two way interaction is detailed in Figure 5.14 below.

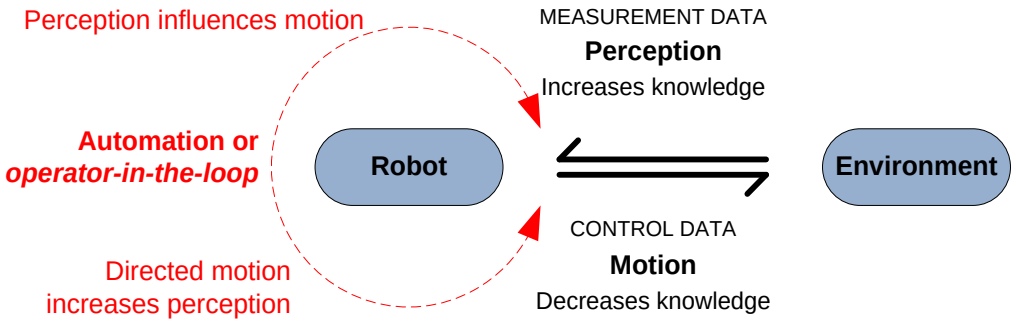

Figure 5.14 - Environment interaction relies on reading sensor measurements (perception), a decision process, which then influences the control action (actuation). In the case of the hybrid iROV, this decision process is a combination of autonomy with the operator-in-the-loop. Figure adapted from [150].

Sensor measurements (*perception*) are the measurements obtained from the sensors about the state of the environment some time ago. Control actions (*actuation*) include robot motion which includes passive or unintended motion such as drift. These two actions co-occur and automation uses sensor measurements to influence control actions. The red dashed automation line which closes the loop between sensor measurements and control actions includes the operator-in-the-loop principle of the iROV.

Two data streams are generated. *Measurement data* provides information about a momentary state of the environment at discrete time t, denoted z_t. This includes camera images, sonar scans, etc. The notation $z_{t_1}{:}z_{t_2}$ denotes the set of measurements acquired from time t_1 to time t_2 as follows:

$$z_{t_1}{:}z_{t_2} = z_{t_1}, z_{t_{1+1}}, z_{t_{1+2}}, \dots, z_{t_2}$$

Control data includes the movement of the vehicle, measured either as the commands sent to the motors, odometry or accelerometer data. While odometers and accelerometers are sensors, the data is treated as control data as its main information conveys an action which caused a change of state. Control data is treated as continuous data represented at discrete time intervals. The variable u_t corresponds to the change of state in the time interval $(t-1):t$. As before, the notation $u_{t_1}:u_{t_2}$ denotes the set of controls from time t_1 to time t_2 as follows:

$$u_{t_1}:u_{t_2} = u_{t_1}, u_{t_{1+1}}, u_{t_{1+2}}, \ldots, u_{t_2}$$

Primarily, measurement increases knowledge by gathering data about the environment whereas motion decreases knowledge due to the uncertainty of robot movement and the change of position to a new location. However, if intelligent control is used to allow perception to influence motion, then directed motion (exploration) can be used to increase perception.

5.3.1.2 Probabilistic generative laws

If it is assumed that the state x_t is conditioned on all past states (x), measurements (z) and controls (u), then the following probability distribution characterises the evolution of state:

$$p(x_t|x_{0:t-1}, z_{1:t-1}, u_{1:t})$$

Equation 5.2

Where: $x_{0:t-1}$ defines all past states prior to the state in question x_t from when the robot started its operation at $t = 0$

$z_{1:t-1}$ defines all measurements taken from $t = 1$, the first measurement up until the most recent measurement before time t

$u_{1:t}$ defines all control actions from the first control action at time $t = 1$ up until the current control action

It is assumed that the robot executes a control action u_1 first, then takes a measurement z_1

If the state x is *complete* then x_{t-1} is a sufficient summary of all that has happened in previous time steps $x_{0:t-1}$ (the Markov assumption discussed in section 5.3.1.) and it is a sufficient representation of all previous controls and measurements up to this point, i.e. the state x_{t-1} represents the datasets $u_{1:t-1}$ and $z_{1:t-1}$. Therefore Equation 5.2 can be simplified; if the state x_{t-1} is known, then only the control u_t matters, and the equation is simplified as follows:

$$p(x_t|x_{0:t-1}, z_{1:t-1}, u_{1:t}) = p(x_t|x_{t-1}, u_t)$$

Equation 5.3

The probability $p(x_t|x_{t-1}, u_t)$y expressed in Equation 5.3 is the *state transition probability*. **It specifies how environmental state x_t evolves over time as a function of robot controls u_t.** Robot environments are stochastic, which is reflected by the fact that $p(x_t|x_{t-1}, u_t)$ is a probability distribution, not a deterministic function.

The property expressed by this simplification in Equation 5.3 is an example of *conditional independence*. It states that certain variables are independent of others if the values of a third group of variables are known, the conditioning variables.

Conditional independence can be used again to model the process by which measurements are being generated. If x_t is complete, the knowledge of the state x_t is sufficient to predict the (potentially noisy) measurement z_t without the need for knowledge of any other variable, such as past measurements, control or even past states.

$$p(z_t|x_{0:t}, z_{1:t-1}, u_{1:t}) = p(z_t|x_t)$$

Equation 5.4

This probability $p(z_t|x_t)$ is called the *measurement probability*. It may not depend on the time index t in which case it is further simplified to $p(z|x)$. The measurement probability specifies the probabilistic law according to which measurements z are generated from the environment state x. **Measurements z_t are usually noisy projections of the state x_t.**

The *state transition probability* and the *measurement probability* defined above together describe the dynamic stochastic system of the robot and its environment. Figure 5.15 illustrates the evolution of states and measurements, defined through these probabilities.

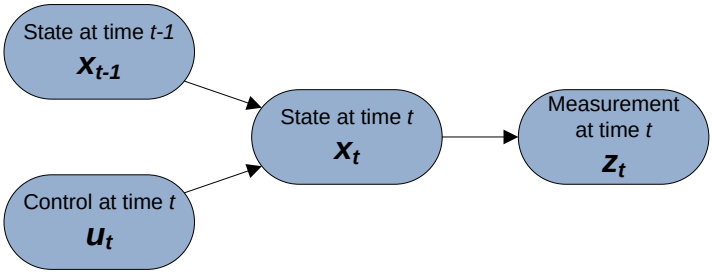

Figure 5.15 - The evolution of states and measurements. In principle, the current state (xt) can be predicted based on the previous state (x_t-1) and the control applied (u_t). This predicted current state can be confirmed / corrected by a measurement (z_t).

Two important relationships from Figure 5.15 are identified:

1. The state at time t is stochastically dependent on the state at time $t-1$ and the control u_t.
2. The measurement z_t depends stochastically on the state at time t.

To specify the model fully, an initial state distribution $p(x_0)$ is also required.

5.3.1.3 Belief distributions

A *belief* represents the robot's internal knowledge about the state of the environment. As state cannot be measured directly, it must be inferred from the data available. Thrun et al. [150] therefore distinguish the true state from the robot's internal *belief*, or its *state of knowledge*.

Probabilistic robotics represents beliefs through conditional probability distributions. A belief distribution assigns a probability (or density value) to each possible hypothesis with regards to the true state. Belief distributions are posterior probabilities over state variables conditioned on the available data. If 'belief of a state variable x_t' is denoted by $bel(x_t)$, then:

Belief: $$bel(x_t) = p(x_t|z_{1:t}, u_{1:t})$$

Equation 5.5

This posterior is the probability distribution over the state x_t at time t, conditioned on all past measurements $z_{1:t}$ and all past controls $u_{1:t}$. This assumes that the belief is generated *after* incorporating the measurement z_t.

To calculate the posterior *before* incorporating the measurement z_t but instead straight after executing the control u_t then the posterior is defined by $\overline{bel}(x_t)$ as follows:

$$\textit{Prediction}: \qquad \overline{bel}(x_t) = p(x_t|z_{1:t-1}, u_{1:t})$$

Equation 5.6

This probability distribution is referred to as the *prediction*, as $\overline{bel}(x_t)$ predicts the state at time t based on the previous state posterior, before incorporating the measurement at time t. Calculating $bel(x_t)$ from $\overline{bel}(x_t)$ is called *correction* or the *measurement update*.

5.3.2 Localisation

From the definitions provided by Levitt and Lawton [201] and Balakrishnan [202], *localisation* is the process of estimating a robot's position in an external reference frame from sensory data when the robot is placed at an unknown location and has to localise itself from scratch **using a map of the environment**. Therefore, localisation in its isolated form assumes that a complete map of the environment is available and the aim is an estimation of the pose of the robot $x_t = (x\ y\ z\ \theta_p\ \theta_r\ \theta_y)$ relative to the map given the robot's perceptions of the environment and its movements.

The difficulty of localisation is that pose can often not be sensed directly. Instead, the robot often has noisy, imperfect and often incomplete sensor measurements of its surroundings and its approximate position. To localise itself, the robot needs to associate these observations with the appropriate part of its map.

Given a map of real-life complexity, a single sensor measurement is often insufficient to determine pose on its own. Instead, the robot often has to use the combination of several sensor measurements and integrate data over time until it has enough information to be able to uniquely identify a single position on the map which corresponds to its current location.

5.3.2.1 Scope

Thrun et al. [150] provide a series of definitions which allow the scope of the localisation problem to be classified across three areas which are applicable to this research.

Local versus global localisation

Global localisation implies the robot begins its mission with no a priori information of its location on the map (there is an equal probability that the robot could be in any location). With each subsequent observation, the global localisation algorithm seeks to reduce the number of possible hypotheses of the robot's pose.

Local localisation is a simpler problem and assumes some a priori knowledge of the robot's position with a given uncertainty. The robot seeks to maintain an accurate estimate of its pose given the errors introduced from subsequent movement and sensing, otherwise known as position tracking. Unimodal distributions are appropriate as long as the uncertainty associated with the robot's pose remains local and confined to the region surrounding the robot. If the uncertainty grows too large, or the pose is lost then the problem becomes global localisation.

To be able to recover from a localisation failure is referred to as the 'kidnapped robot problem' [150], where the robot goes from local localisation to beginning global localisation again. The

difficulty is often detecting the localisation failure. The robot may continue to believe that it knows its position and not realise that it has suffered a localisation failure (being 'kidnapped' and transported to an unknown position without its knowledge). The ability of the localisation algorithm to recognise and recover from failure is essential to robust autonomous operation.

Static versus dynamic environments

When operating in closed tanks it is often possible to make the assumption of a static environment which makes localisation significantly easier. In this case, it can be assumed that the only part of the state which varies is the robot pose and that the position and characteristics of all landmarks remain constant.

However, it is unlikely that a static environment can be assumed in the nearshore environment with the position, configuration and relative position changing of moving boats, debris, wildlife and tethered objects moving in the tides and currents. The tide *height* also has a large effect on tethered and flexible objects such as kelp stipes. At high water, the kelp stipes appear vertical and at rising and falling tides they appear at an angle depending on tide height and flow. At slack water, and exaggerated at low slack water, the stipes 'flop' over on the water surface in a disorganised arrangement.

The localisation algorithm therefore needs to be robust when presented with a dynamic environment and capable of detecting which objects are static and suitable as navigation landmarks and when an object becomes dynamic. Several techniques exist for dealing with dynamic environments which either rely on including dynamic entities in the state at the expense of additional computational and modelling complexity, or filtering out dynamic entities from the sensor data [150]. However, for simplicity in developing the navigation system for the target application, at present, environments will be assumed to be either static over the short scan duration of a typical mission or that any dynamic conditions are momentary and do not persist for more than a few observations and therefore can be accommodated as noise. Long term slow disturbances such as tides are accommodated at a later stage (7.3.4.1).

Passive versus active approaches to localisation

The distinction between passive and active approaches to localisation depends on whether or not the localisation algorithm controls the motion of the vehicle. Passive localisation algorithms observe the environment and the motion of the vehicle without interacting. As the robot is either controlled by an operator, or by the mission planning algorithm, the localisation algorithm seeks to localise the vehicle as well as it can with whatever information is available to it.

The opposite is active localisation, where the localisation algorithm controls the movement of the robot to minimise the localisation error and/or the costs arising from moving a poorly localised robot into a hazardous location [150]. Active localisation can provide a lower localisation uncertainty, for example by avoiding long traverses across sparse landscapes and staying close to distinguishable landmarks (coastal navigation) or, when a high localisation uncertainty develops, seeking a nearby distinctive landmark to resolve any ambiguity. However, active localisation adds complexity to the overall control of the vehicle, requiring a trade-off in time and energy to be made between actively localising the vehicle to an acceptable uncertainty level and carrying out the original mission.

A combination can be used of passive localisation until the uncertainty grows unacceptably large, and then active localisation until the ambiguity regarding the pose of the vehicle is resolved. In

the context of *SeaBiscuit*, a simple example of this occurs when navigating by INS and sonar landmarks when available using passive localisation during a mission. When the error grows too large from a lack of sonar landmarks, active localisation is used and the vehicle surfaces to update a GPS position, thus re-bounding the localisation error.

5.3.3 **Mapping**

The principle of pure mapping is the opposite to that of pure localisation, hence the complementary nature of simultaneous localisation and mapping. Mapping assumes that the position of the robot is known and allows observed objects to be recorded on a map. Critical considerations include: only mapping landmarks or other points of interest rather than spurious observations and sensor noise; mapping objects with a sufficiently high accuracy and with sufficient data for later re-identification; navigation and localisation from the stored map; and finally, data association and correspondences (avoiding mapping the same object on the map several times).

Mapping using multiple sensors is particularly useful when different sensors are sensitive to different features. Multiple maps can be maintained and combined when navigating by techniques such as a logic AND operation for sensors of the same modality or more conservatively, if the sensors are sensitive to different obstacles, by a logic OR operation.

5.3.3.1 Map representation

As introduced earlier, there are several options for representing the map of the environment. These can be loosely grouped into *metric* and *topological* frameworks.

The *metric* mapping framework is how humans generally consider their surroundings – either a 2 or 3 dimensional space is populated with objects and landmarks. Each map feature is placed with precise coordinates. From an accurate map, the distances between objects can be accurately measured and the optimal route between objects calculated, all dependent on the accuracy with which the map was generated.

The *topological* framework considers objects and the relations between them. In a similar manner to a wiring diagram, every object is identified with the connections from one object to another. The map is stored as a graph in which the nodes correspond to locations and the arcs correspond to paths between these locations. In this manner, the length of each arc can be used to record the distance between objects.

When considering the map representation and which landmarks to include on the map, there is often a distinction between the maps which the underwater vehicle can use for autonomous localisation and navigation, and maps for user feedback of survey data. These two maps do not necessarily have to be distinct if the survey points of interest are also used for navigation. However, it does have an effect on the map representation and map maintenance.

Whereas landmarks are often only stored with a position and various descriptors, it is possible to recreate a full 3D representation of the environment following a mission to allow user feedback and inspection. For example, in the dock survey and mapping application discussed in section 6.3, the robot is able to navigate from the fixed dock pilings and thus stores the position and configuration of each landmark (dock piling). However, for user feedback of the survey results, a 3D reconstruction may be more useful.

As Thrun et al. [150] highlight, the *relative* positions of landmarks can be determined with asymptotic certainty, as each re-observation serves to reduce the uncertainty. However, the map is created *relative to the coordinate system defined by the initial robot pose*. A GPS fix from the surface at the start and end of every mission was used to geodetically register underwater maps in the world coordinate system of latitude and longitude.

5.3.4 Simultaneous Localisation and Mapping

In pure localisation (5.3.2) it is assumed that the map is complete and in pure mapping (5.3.3) it is assumed that the position is always known. However, for mobile robots operating in real-world environments, these assumptions can rarely be made. Instead, the robot is usually faced with the problem of concurrently estimating its position and mapping its surroundings, often with no initial a priori knowledge, hence the problem of *simultaneous localisation and mapping* (SLAM) [171].

5.3.4.1 Mathematical definition

The SLAM problem can be defined as:

$$p(x_t, m | z_{1:t}, u_{1:t})$$

Equation 5.7

Which states that the most recent pose of the robot x_t at time t and the map m is estimated given all measurements $z_{1:t}$ and control actions $u_{1:t}$, where $1{:}\,t$ denotes from the start of operation until the current time t. This is referred to as the online SLAM problem as it only involves estimation of variables which persist at time t [150]. Past measurements and controls are discarded once they have been processed (otherwise known as a filter).

The alternative is referred to as the full SLAM problem and seeks instead to expand the pose estimation x_t to include a posterior probability[10] of the entire path taken by the robot since the start of operation. Thus, for the full SLAM problem, x_t becomes $x_{1:t}$ as follows:

$$p(x_{1:t}, m | z_{1:t}, u_{1:t})$$

Equation 5.8

Estimating the full posterior probability provides the maximum possible information and captures all there is to be known about the map and the pose of the robot over all time. However, in practice, the full posterior is rarely calculated due to the large computational complexity which grows rapidly with map complexity in real-world environments.

Thus, online SLAM is performed for navigation of the iROV *SeaBiscuit*. The course of the vehicle can still be recorded by incrementally amending a track – online SLAM simply means that previous positions are not amended after being recorded. In a similar manner to the Markov Assumption (5.3.1), it is assumed that past and future data are independent if the current state x_t is known.

5.3.4.2 Data association

Data association is defined as the process of identifying correspondences between landmarks observed by the sensors and landmarks recorded on the map. Robustness needs to be achieved

[10] To infer the probability of event x prior to incorporating data y is the prior probability $p(x)$. The posterior probability after incorporating the data y is therefore $p(x|y)$ or 'the probability of event x given data y'.

despite imperfect sensing and imperfect representations by approximation to avoid mapping the same landmark twice as two distinct objects, or from confusing two similar landmarks and introducing a localisation error. As Thrun et al. [150] state, the key to successful localisation lies in successful data association.

Correspondences are usually established by a combination of the position of the landmark, its configuration with respect to nearby landmarks and any defining characteristics of the landmark. The formal definition of the SLAM problem introduced earlier as Equation 5.7 is redefined to include correspondences as follows:

$$p(x_t, m, c_t | z_{1:t}, u_{1:t}, m_{t-1})$$

The SLAM problem now seeks to estimate the pose of the robot x_t at time t, the map m and the correspondence c_t of all observed landmarks to those recorded on the map, given all measurements $z_{1:t}$ and controls $u_{1:t}$ since the start of operation until time t, using the previous map m_{t-1} to establish correspondences to previously mapped features.

In some cases, the correspondences are known; this means that every landmark observed is uniquely identifiable and therefore its correspondence with the correct mapped landmark is known. This can often be achieved by artificially placing uniquely identifiable landmarks or locating beacons in the environment. However, in unmodified environments, correspondences are often not uniquely identifiable and in this case the correspondence variable must be estimated.

Two of the most commonly used methods to estimate landmark correspondences are the nearest neighbour (NN) [150] and the joint-compatibility branch and bound (JCCB) [352] algorithms. Each method aims to establish the most-likely correspondence between observation and landmark by minimising the Mahalanobis distance between the observation and the predicted observation based on the mapped landmark being considered. Whereas the Euclidean distance defines the metric distance between two points, the Mahalanobis distance takes into account the correlations and covariance between variables and is scale-invariant [173]. For uncorrelated variables with unit variance, the Mahalanobis distance simplifies to the Euclidean distance.

Using the NN method for estimating correspondences, for each new observation at each time step, a new landmark hypothesis is added to the map using the current estimate of vehicle position, and the range and bearing to the new observation. The correspondence between the new landmark hypothesis and all existing landmarks on the map is calculated using the Mahalanobis distance. The maximum likelihood (ML) estimator then selects the correspondence vector which maximises the likelihood of the measurement. The most common implementation of a ML estimator simplifies maximum likelihood to select the correspondence with the lowest Mahalanobis distance [353]. A new landmark is created if the Mahalanobis distance from the new landmark hypothesis to all existing landmarks in the map exceeds a threshold value α. Implementing the full ML estimator incurs a small computational overhead as it includes calculating the Mahalanobis distance.

Various techniques to select the optimal value of the threshold α, or gating function, exist. The value typically used in the literature is the chi-squared inverse cumulative distribution function $\chi^2_{d,c}$ for a desired confidence level (c), for example c=95%, where d represents the dimensionality of the observation vector [353]. More simply, if false positives are to be avoided, the value of α must be set higher than the smallest expected distance between landmarks plus the vehicle and sensor uncertainty, for a given confidence level.

The ML estimator is prone to errors if there are several similarly-likely hypotheses for the correspondence variable, as it simply uses the most-likely value [150]. Techniques to perform tracking of multiple hypotheses significantly increase complexity, as it is necessary to maintain one map per hypothesis until less-likely hypotheses can be pruned [354]. If the sensor noise plus the vehicle uncertainty is always below the typical distance between a pair of landmarks then the risk of establishing false correspondences is reduced [353]. Thus, errors using the ML-NN estimator from multiple similarly-likely hypotheses can be avoided, to some extent, by maintaining the vehicle localisation error to a minimum and selecting landmarks which are either sufficiently unique and/or far enough apart from each other to avoid confusion. If the environment is to be unmodified, then detecting sufficiently unique landmarks dictates the sensing requirements. Additionally, sufficiently accurate localisation and landmark measurement sensors are required to allow a low threshold value α to be used reliably.

The joint-compatibility branch and bound (JCCB) algorithm accounts for correlation between measurement prediction errors and provides a more robust solution in complex, cluttered environments. When using the NN algorithm, spurious correspondences are easily formed, due to the sensitivity of the NN algorithm to vehicle and sensor errors, and are never reconsidered. The JCCB algorithm allows the validity of correspondences to be reconsidered, providing a more robust rejection of spurious matchings [352]. However, the computational complexity of implementing the JCCB algorithm over the NN algorithm is significantly higher. Implementation for realtime operation is still feasible, provided the algorithm is implemented correctly, which includes processing a limited number of observations using the JCCB algorithm, before associating the remaining observations using the NN algorithm [352].

More recent alternatives have proposed techniques such as the negative logarithm of the matching likelihood (NLML) algorithm. These claim statistically better matching of correspondences with a reduction of false-positive correspondences over using the Mahalanobis distance when operating with higher levels of sensor noise [353]. A small computational overhead is incurred with the higher conceptual complexity of the NLML algorithm.

As an initial implementation of data association for SLAM in this research, the nearest neighbour algorithm [150] was used to estimate landmark correspondences. Although not necessarily optimal [353], the NN algorithm was selected for its conceptual and computational simplicity and ease of implementation [352]. Later sections on implementation (6.3.3.2) demonstrate the suitability of the NN algorithm for the applications of underwater navigation considered in this research. By the nature of the modular algorithms developed, alternative methods for estimating correspondences can be simply ‘slotted-in’ to the simulation and navigation programs in future, and optimisation of the data association algorithm is considered as further research (6.3.5.4).

5.3.4.3 Dimensionality

The initial implementation of the EKF SLAM algorithm with unknown correspondences operated in 2D. All sensor data was still recorded and registered in 3D. However, navigational landmarks were mapped with an x and y coordinate and the position of the robot was tracked using SLAM in 2D as x-position, y-position and yaw angle. Depth was accurately available using the pressure sensor and continually recorded, and pitch and roll were accurately measured by the gyroscopes and magnetometers. Thus sensor data was recorded in 3D for later inspection, but the EKF SLAM provided 2D localisation and mapping of navigational landmarks.

This meant all landmarks observed had to either be assumed constant over the entire z direction (depth) for example, dock pilings and upright kelp stipes, or that the vehicle maintained a constant depth during a survey. In effect, a combination of the two were used. The wide, flat cylindrical shape of the iROV shell afforded high vertical stability for maintaining a constant depth. Furthermore, high vertical thrust with accurate sensing, a fast response and tuned control loops provided good vertical station keeping.

A constant survey depth was not restrictive of scientific results, given that the sonars and cameras were still recording data in 3D. For example the forward-facing Delta T profiling sonar was still recording data over the entire vertical water column for later 3D reconstruction; it was simply that the navigation algorithms for underwater positional estimation (SLAM) were only using 2D planar data to register the x and y position of the vehicle when registering successive sonar scans.

5.3.5 The Kalman filter

The Kalman filter uses multivariate (multi-dimensional) normal distributions to represent beliefs using the moments representation of Gaussian distributions. At time t, the belief is represented by the mean (first moment) μ_t and the covariance (second moment) Σ_t of a Gaussian. The Kalman filter alternates a *prediction step* (or control update step), which modifies the belief in accordance to an action, with a *measurement update step*, in which sensor data is integrated into the present belief.

The **control update (*prediction*)** estimates the belief of state $\overline{bel}(x_t)$ based on the control measurements u_t and the previous belief of the state x_{t-1}, prior to the sensor measurement.

$$\overline{bel}(x_t) = \int p(x_t|u_t, x_{t-1}) bel(x_{t-1}) dx$$

Equation 5.9

The belief $\overline{bel}(x_t)$ which the algorithm assigns to state x_t is obtained by the integral (sum) of the product of two distributions:

- the prior belief of the state denoted by $bel(x_{t-1})$
- and the probability that the control u_t induces a transition from x_{t-1} to x_t

The **measurement update (*correction*)** updates the belief of state $bel(x_t)$ as sensor measurement data z_t becomes available (see Equation 5.6).

$$bel(x_t) = \eta\, p(z_t|x_t)\overline{bel}(x_t)$$

Equation 5.10

The algorithm multiplies the belief $\overline{bel}(x_t)$ by the probability that the measurement may have been observed. It does this for each hypothetical posterior state x_t. The result is normalised by the normalisation constant η to integrate to 1.

The algorithm is recursive in that, the belief $bel(x_t)$ at time t is calculated from the belief $bel(x_{t-1})$ at time $t-1$. To calculate the posterior belief recursively the algorithm requires an initial belief $bel(x_0)$ and time $t = 0$ as a boundary condition. Figure 5.16 shows the principle of combining prediction (control) information with updates (sensor measurements).

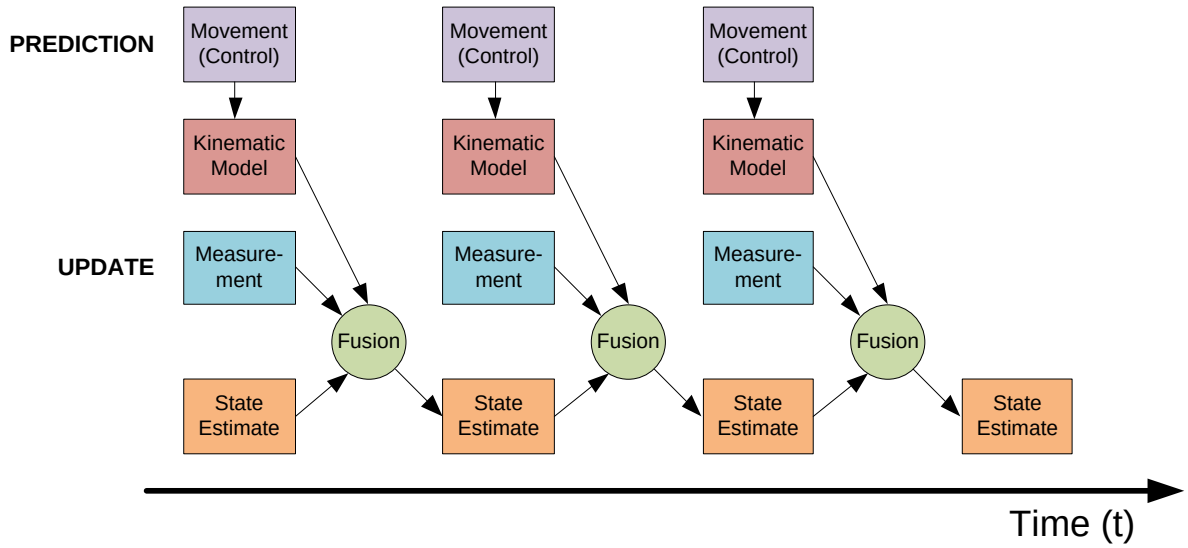

Figure 5.16 - Recursively fusing measurements and control commands into the state estimate. A control command is combined with the kinematic model to predict the effect it will have on the vehicle's state. A measurement can be taken to confirm or correct (update) this predicted change of state and the fusion algorithm combines a weighted combination of this prediction and update with the previous state estimate to recursively calculate the new state. The weightings used for the combination are determined by the uncertainty associated with movement and measurement respectively.

5.3.5.1 Kalman filter assumptions

In addition to the Markov assumption (section 5.3.1 – the complete state assumption: past and future states are independent if one knows the current state), the following three assumptions must be adhered to if the Kalman filter is to be used:

5.3.5.1.1 Assumption 1 – linear dynamics

The next state probability $p(x_t|u_t, x_{t-1})$ must be a *linear* function in its arguments with added Gaussian noise. This is expressed by the following *linear Gaussian* equation:

$$x_t = A_t x_{t-1} + B_t u_t + \varepsilon_t$$

Equation 5.11

Here x_t and x_{t-1} are state vectors and u_t is the control vector at time t. A_t and B_t are both matrices, where:

A_t is a square matrix of size $n \times n$, where n is the dimension of the state vector x_t

B_t is of size $n \times m$ with m being the dimension of the control vector u_t

By multiplying the state and control vector by the matrices A_t and B_t respectively, the state transition function becomes linear in its arguments. Thus, Kalman filters assume linear system dynamics. The random variable ε_t in Equation 5.11 is a Gaussian random vector that models the randomness in the state transition. It has the same dimensions as the state vector $(n \times 1)$, its mean is zero and its covariance is denoted R_t.

A multivariate normal distribution is defined as:

$$p(x) = \det(2\pi\Sigma)^{-\frac{1}{2}} \exp\left\{-\frac{1}{2}(x-\mu)^T \Sigma^{-1}(\mathrm{x}-\mu)\right\}$$

Equation 5.12

And Equation 5.11 defined the state transition probability: $p(x_t|u_t, x_{t-1})$.

Values from Equation 5.11 can be substituted into Equation 5.12 as follows, allowing Equation 5.12 to be rewritten as the linear state transition probability:

$\mu = A_t x_{t-1} + B_t u_t$ The mean of the posterior state

$\Sigma = R_t$ The covariance of the additive Gaussian noise

Performing this substitution

$$p(x_t|u_t, x_{t-1}) = \det(2\pi R_t)^{-\frac{1}{2}} \exp\left\{-\frac{1}{2}(x_t - A_t x_{t-1} - B_t u_t)^T {R_t}^{-1}(x_t - A_t x_{t-1} - B_t u_t)\right\}$$

Equation 5.13

5.3.5.1.2 Assumption 2 – linear measurement functions

The measurement probability $p(z_t|x_t)$ must also be *linear* in its arguments with added Gaussian noise:

$$z_t = C_t x_t + \delta_t$$

Equation 5.14

Where:

C_t is a matrix of size $k \times n$ where k is the dimension of the measurement vector z_t.

δ_t is a multivariate Gaussian used to describe the measurement noise. δ_t has zero mean and its covariance is denoted Q_t.

The measurement probability is thus given by the following multivariate normal distribution (constructed in the same manner as Equation 5.13):

$$p(z_t|x_t) = \det(2\pi Q_t)^{-\frac{1}{2}} \exp\left\{-\frac{1}{2}(z_t - C_t x_t)^T {Q_t}^{-1}(z_t - C_t x_t)\right\}$$

Equation 5.15

5.3.5.1.3 Assumption 3 – normally distributed initial belief

The final assumption to be made if the Kalman filter is to be used is that the initial belief $bel(x_0)$ must be normally distributed. This can be expressed in the following equation, where the mean of this initial belief is μ_0 and the covariance is Σ_0:

$$bel(x_0) = \det(2\pi\Sigma_0)^{-\frac{1}{2}} \exp\left\{-\frac{1}{2}(x_0 - \mu_0)^T {\Sigma_0}^{-1}(x_0 - \mu_0)\right\}$$

Equation 5.16

By making these three assumptions, it is ensured that the posterior belief $bel(x_t)$ is always a Gaussian for any point in time t. The proof of this, and the mathematical derivation of the Kalman filter is commonly available, for example in section 3.2.4 of the work by Thrun et al. [150].

5.3.5.2 Kalman filter algorithm

Figure 5.17 shows the recursive algorithm for Kalman filtering.

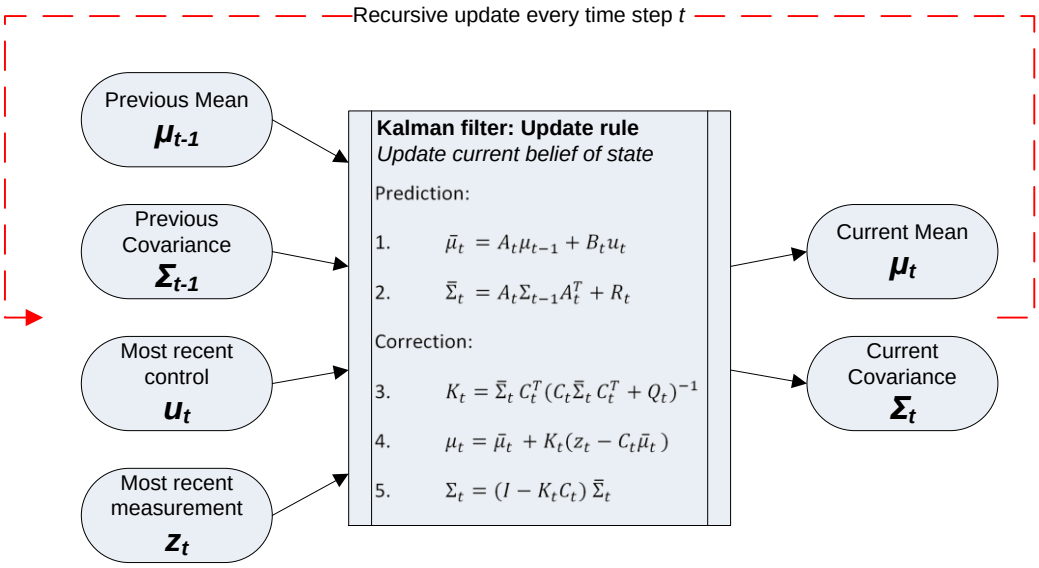

Figure 5.17 - The recursive algorithm for Kalman filtering for linear Gaussian state transitions and measurements.

Lines 1 and 2 of the algorithm predict the mean $\bar{\mu}_t$ and covariance $\bar{\Sigma}_t$ to represent the belief $\overline{bel}(x_t)$ using the control u_t but before incorporating the measurement z_t. The mean is updated using the deterministic version of the state transition function (Equation 5.11) with the mean μ_{t-1} substituted for the state x_{t-1}. The update of the covariance $\bar{\Sigma}_t$ considers the fact that states depend on previous states through the linear matrix A_t. This matrix is multiplied twice into the covariance, since the covariance is a quadratic matrix.

Lines 3, 4 and 5 transform the belief $\overline{bel}(x_t)$ into the output for that iteration $bel(x_t)$ by incorporating the measurement z_t.

The variable K_t defined in line 3 is called the Kalman gain. It specifies the degree to which the measurement is incorporated into the new state estimate.

Line 4 manipulates the mean, by adjusting it in proportion to the Kalman gain K_t and the deviation of the actual measurement, z_t from the measurement predicted according to the measurement probability defined in Equation 5.14.

The difference between the actual measurement z_t and the expected measurement $C_t\bar{\mu}_t$ is defined as the *innovation*.

Finally the covariance of the posterior belief Σ_t is calculated in line 5 adjusting for the information gain resulting from the measurement.

To summarise:

A_t	Matrix $(n \times n)$ that describes how the state evolves from t to $t-1$ without controls or noise.
B_t	Matrix $(n \times l)$ that describes how the control u_t changes the state from t to $t-1$.
C_t	Matrix $(k \times n)$ that describes how to map the state x_t to an observation z_t.
ϵ_t	Random variables representing the process and measurement noise that are assumed to be independent and normally distributed with covariance R_t and Q_t respectively.
δ_t	

5.3.6 The extended Kalman filter

The assumptions imposed by the Kalman filter, chiefly linear state transitions and linear measurements with added Gaussian noise, are rarely fulfilled in practice. Observations are rarely linear functions of the state and the next state is rarely a linear function of the previous state. This, as Thrun et al. state [150], renders plain Kalman filters inapplicable to all but the most trivial robotics problems.

However, it is preferable to keep the computational efficiency of the Kalman filter, which arises from performing state estimation using Gaussians: as any *linear* transformation of a Gaussian random variable results in another Gaussian random variable, the Kalman filter is able to compute the parameters of the resulting Gaussian in closed form. Therefore a way to linearise the transformation is required so that the computationally efficient Kalman filter can continue to be used. It is this linearisation process which allows non-linear data to be used with the techniques of the Kalman filter. This is achieved by the *Extended Kalman Filter*, albeit by only calculating an approximation of the true belief rather than the exact belief as with the Kalman filter.

In the EKF, the assumption is that the next state probability x_t and the measurement probability z_t are governed by nonlinear functions g and h, respectively:

$$x_t = g(u_t, x_{t-1}) + \varepsilon_t$$

Equation 5.17

$$z_t = h(x_t) + \delta_t$$

Equation 5.18

This model generalises the linear Gaussian model underlying Kalman filters introduced in Equation 5.11 defining x_t and Equation 5.14 defining z_t. The function g replaces the matrices A_t and B_t in Equation 5.11 and the function h replaces the matrix C_t. However, by using these arbitrary functions g and h, the belief is no longer a Gaussian.

Taking Equation 5.17 which defines the next state based on a nonlinear function g applied to the control variable u_t and the previous state, then a Gaussian projected through this function is typically non-Gaussian. This is because the nonlinearities in g alter the belief such that the Gaussian shape is distorted.

Figure 5.18 (adapted from Figure 3.3a in [150]) shows the linear transformation of a Gaussian random variable. The original Gaussian random variable (red) shown in the lower right graph is 'updated' using the linear function (blue) shown in the top right graph to give the resulting density function (green) shown in the top left graph. As the update function is linear, the resulting density function is still of Gaussian form, displaying an example of a Kalman filter update.

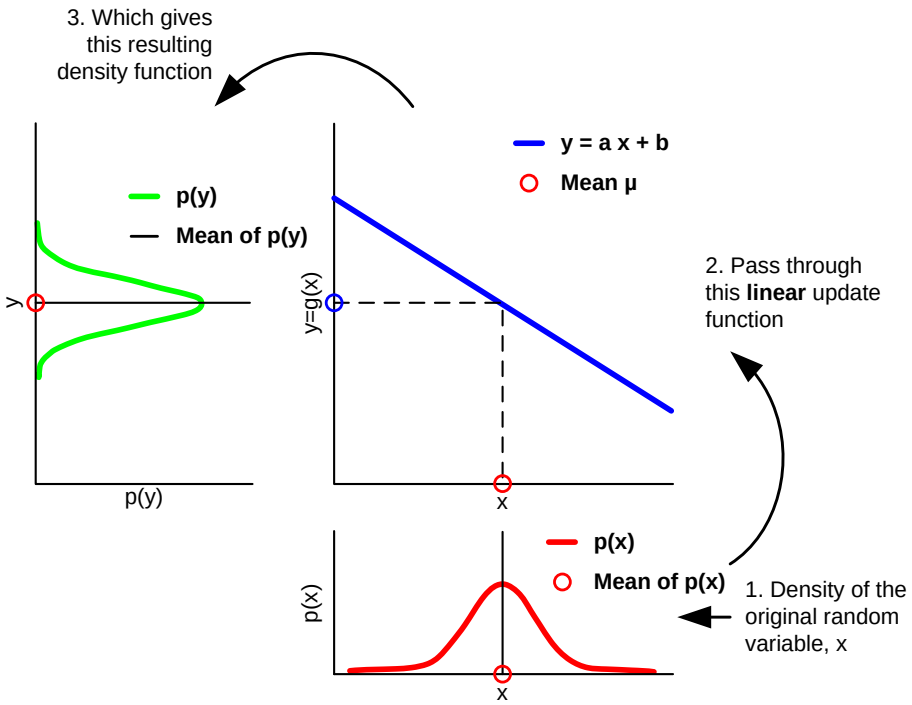

Figure 5.18 - Linear transformation of a Gaussian random variable (figure adapted from [150]). The Gaussian distribution in the lower right (red) is updated by the linear update function (blue) to give the (still Gaussian) density function (green) shown to the top left.

However, if the update function is non-linear, then the resulting random variable is no longer of a Gaussian nature, and a Gaussian is a poor representation of the resulting function as shown in Figure 5.19 (adapted from Figure 3.3b in [150]).

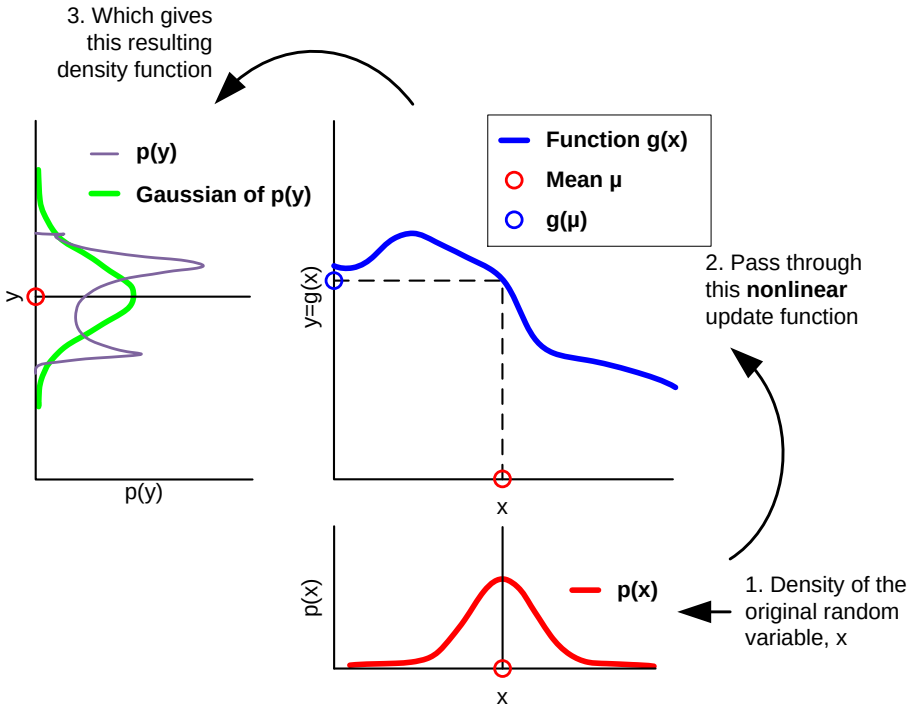

Figure 5.19 - Nonlinear transformation of a Gaussian random variable (figure adapted from [150]). As before, the Gaussian in the lower right (red) is updated by the function shown in the centre (blue), in this case a nonlinear update function. This gives the resulting non-Gaussian density function (green) shown in the top left.

In order to apply the Kalman filter, the update function g is approximated by a linear function. By projecting the Gaussian through this linear approximation, the posterior is Gaussian and the belief propagation is equivalent to the Kalman filter. The same technique is applied to the measurement function h (Equation 5.17 and Equation 5.18). Again the EKF approximates h by a linear function tangent to h, thereby retaining the Gaussian nature of the posterior belief.

5.3.6.1 Linearisation techniques

EKFs linearise nonlinear functions using a method called (first order) *Taylor expansion* which constructs a linear approximation to a function g from the value and slope of g. The slope is given by the partial derivative:

$$g'(u_t, x_{t-1}) \coloneqq \frac{\delta g(u_t, x_{t-1})}{\delta x_{t-1}}$$

Equation 5.19

Figure 5.20 below, adapted from [150], shows an example of linearisation by Taylor expansion of a Gaussian and demonstrates the approximation error resulting from this linearisation against a highly accurate Monte Carlo estimation.

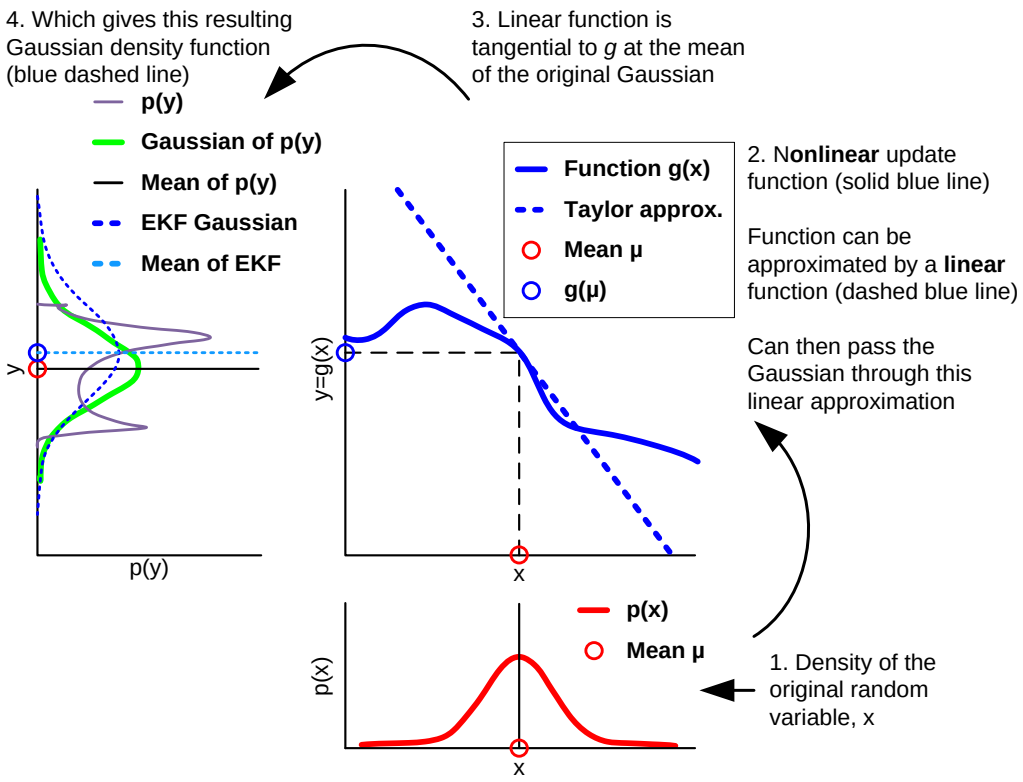

Figure 5.20 - Linearisation applied by the EKF of a nonlinear function g (adapted from [150]). Rather than passing the Gaussian shown in the bottom right (red) through the nonlinear function g (blue solid), it is passed through a linear approximation of g (blue dashed), as calculated by first order Taylor expansion to yield the tangent to g at the mean of the original Gaussian. The resulting linearisation is shown in the upper left plot as the blue dashed Gaussian. This linearisation incurs an approximation error indicated by the mismatch between the blue dashed line and the solid green Gaussian computed by the highly accurate Monte-Carlo estimation.

It can be seen that the actual value of g and its slope (the tangential line, given by Equation 5.19 above) depend on the argument of g (the functions contained within the parentheses). The value of the argument is selected to be the state deemed most likely at the time of linearisation. For Gaussians, the most likely state is the mean of the posterior μ_{t-1} as shown by Figure 5.20.

In other words g, is approximated by its value at μ_{t-1} (and at u_t), and the linear extrapolation is achieved by a term proportional to the gradient of g at μ_{t-1} and u_t:

$$g(u_t, x_{t-1}) \approx \underbrace{g(\quad_t, \mu_{t-1})}_{=\text{the value of } g} + \underbrace{g'(u_t, \mu_{t-1})}_{=:G_t} (x_{t-1} - \mu_{t-1})$$

$$= g(u_t, \mu_{t-1}) + G_t(x_{t-1} - \mu_{t-1})$$

Written as a Gaussian, the **next state probability** is approximated as follows:

$$p(x_t|u_t, x_{t-1}) \approx \det(2\pi R_t)^{-\frac{1}{2}} \exp\left\{-\frac{1}{2}[x_t - g(u_t, \mu_{t-1}) - G_t(x_{t-1} - \mu_{t-1})]^T {R_t}^{-1}[x_t - g(u_t, \mu_{t-1}) - G_t(x_{t-1} - \mu_{t-1})]\right\}$$

Equation 5.20

G_t is called the *Jacobian* matrix and is of size $n \times n$, where n denotes the dimension of the state. The value of the Jacobian depends on u_t and μ_{t-1} hence it differs for different points in time.

EKFs implement the same linearisation for the measurement function h. Here the Taylor expansion is developed around $\bar{\mu}_t$, the state deemed most likely by the robot at the time it linearises h:

$$h(x_t) \approx \underbrace{h(\bar{\mu}_t)}_{=\text{the value of } h} + \underbrace{h'(\bar{\mu}_t)}_{=:H_t}(x_t - \bar{\mu}_t)$$

$$= h(\bar{\mu}_t) + H_t(x_t - \bar{\mu}_t)$$

Where $h'(x_t) = \frac{\delta h(x_t)}{\delta x_t}$

Written as a Gaussian, the **measurement probability** is approximated as follows:

$$p(z_t|x_t) \approx \det(2\pi Q_t)^{-\frac{1}{2}} \exp\left\{-\frac{1}{2}[z_t - h(\bar{\mu}_t) - H_t(x_t - \bar{\mu}_t)]^T {Q_t}^{-1}[z_t - h(\bar{\mu}_t) - H_t(x_t - \bar{\mu}_t)]\right\}$$

Equation 5.21

The 'approximately equal to' symbol remains in both the next step probability (Equation 5.20) and the measurement probability (Equation 5.21) as a reminder that the linearisation process is an approximation.

5.3.6.2 Extended Kalman filter algorithm

The mathematical derivation of the EKF is available in section 3.3.4 of the work by Thrun et al. [150] and an overview of the algorithm is shown below in Figure 5.21.

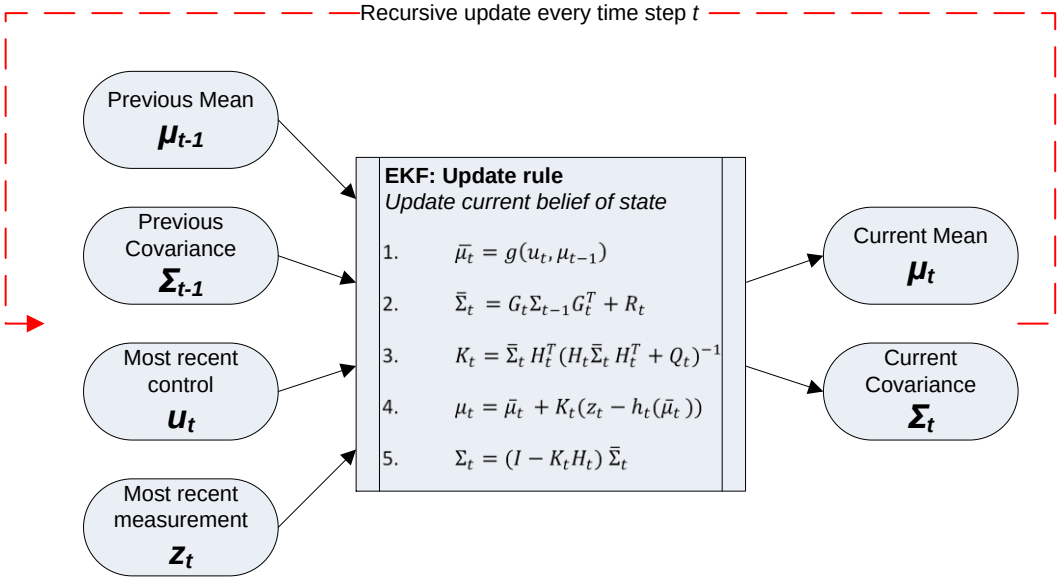

Figure 5.21 - The Extended Kalman Filter algorithm.

The algorithm for implementing the EKF is similar to that for the Kalman filter presented in section 5.3.5.2 except for the following differences:

Table 5.2 - Differences in implementation between the Kalman filter and EKF. Table adapted from [150].

	Kalman Filter (Figure 5.17)	**EKF (Figure 5.21)**
State Prediction Line 1	$A_t\mu_{t-1} + B_t u_t$	$g(u_t, \mu_{t-1})$
Measurement Prediction Line 4	$C_t\bar{\mu}_t$	$h_t(\bar{\mu}_t)$

To summarise, the linear predictions in the Kalman filter are replaced by their nonlinear generalisations in the EKF. Additionally, EKFs use Jacobians G_t and H_t instead of the corresponding linear system matrices A_t, B_t and C_t in Kalman filters. The Jacobian G_t corresponds to the matrices A_t and B_t and the Jacobian H_t corresponds to C_t.

G_t is defined as:

$$G_t = \frac{\delta g(u_t, \mu_{t-1})}{\delta x_{t-1}}$$

H_t is defined as:

$$H_t = \frac{\delta h(\bar{\mu}_t)}{\delta x_t}$$

The accuracy of the linear approximation depends on two main factors: the degree of uncertainty and the degree of local nonlinearity of the functions being approximated. These are considered in turn in the following two sections.

5.3.6.2.1 Dependency on uncertainty

The two graphs in Figure 5.22 illustrate the dependency of the accuracy of the linear approximation on uncertainty. Here, two Gaussian random variables (red) were passed through the same nonlinear function (blue solid) in the same manner as the previous plots. While both Gaussians have the same mean, the variable shown in Figure 5.22a has a higher uncertainty than the one shown in Figure 5.22b as denoted by the wider Gaussian curve (both Gaussians have the same mean, but the one shown in Figure 5.22a has a larger variance).

However, as the Taylor expansion only depends on the mean, both Gaussians were passed through the same linear approximation (blue dashed). The purple lines in the upper left plots of each of the two figures show the densities of the resulting random variable computed by Monte Carlo (MC) estimation. Therefore the green lines (with the mean shown by the black line) represent the resulting Gaussian if the Gaussian in the lower right plot for each figure were accurately passed through the nonlinear function. The blue dashed graphs in the upper left show the Gaussians estimated by the linearisation.

A comparison to the Gaussians resulting from the Monte Carlo (MC) approximations (green) illustrates the fact that higher uncertainty (left plot) typically results in less accurate estimates of the mean and covariance of the resulting random variable. In detail, if the dashed blue line in the upper left plots is compared with the solid green line, that is the Gaussian computed with the EKF compared to the actual MC Gaussian, then it can be seen in Figure 5.22a (high uncertainty) that the EKF provides a poor estimation of the MC Gaussian. However, in Figure 5.22b where the uncertainty is lower, the EKF provides a much better estimation of the resulting Gaussian.

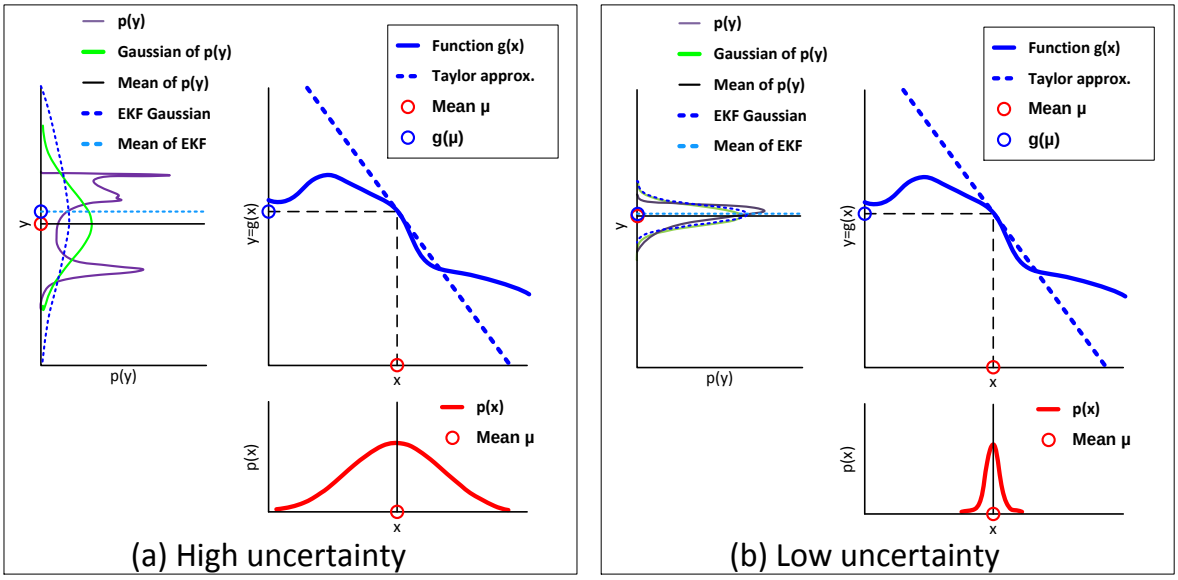

Figure 5.22 - The approximation quality of linearisation by Taylor expansion depends on uncertainty (figure adapted from [150]). In both the left and right plots, the Gaussian in the lower right position (red) is passed through the same linear approximation (blue dashed). The approximation quality can be seen in the upper left plot in each case by any mismatch between the dashed blue line and the solid green line showing the Gaussian of the accurate Monte Carlo estimation. The significantly poorer approximation quality for figure (a) for the high uncertainty case can be seen.

5.3.6.2.2 Dependency on local nonlinearity

The lower plots of Figure 5.23a and Figure 5.23b below show two Gaussians (red) with the same variance but with a slightly different mean. Each Gaussian was passed through the same random variable (blue) shown in the upper right plot (in the same manner as for previous figures). The mean of the first Gaussian (Figure 5.23a) falls in a more nonlinear region of the function *g* than the second Gaussian (Figure 5.23b).

The mismatch between the Gaussian from the accurate Monte Carlo estimation (green) and the Gaussian resulting from the EKF linear approximation (blue dashed) shows that higher local nonlinearities result in larger approximation errors. The EKF Gaussian underestimates the spread of the resulting density.

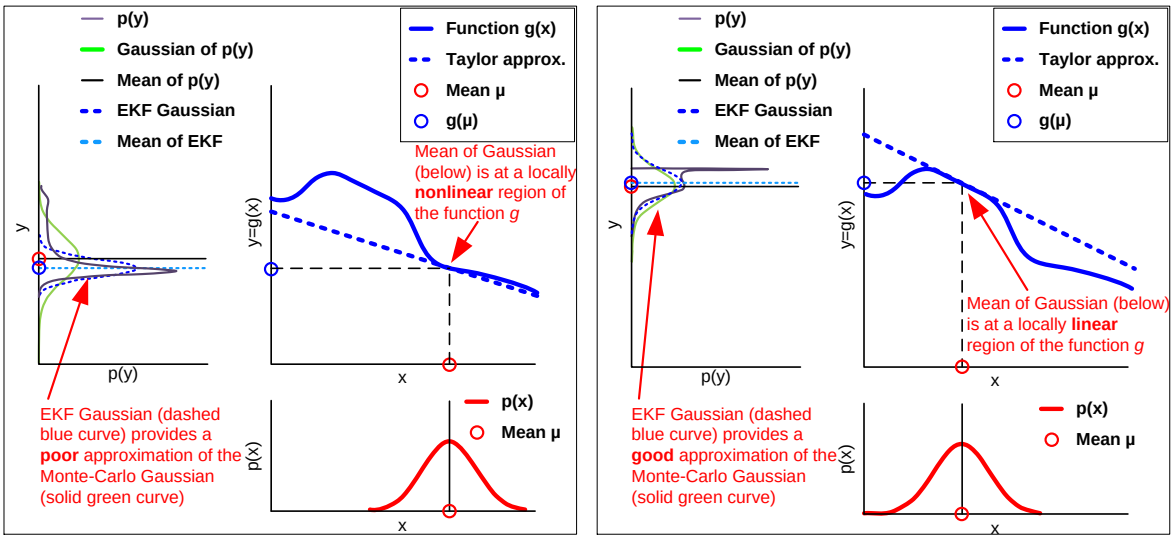

Figure 5.23 - The dependence of EKF approximation quality on local nonlinearity can be seen (figure adapted from [150]). The right plot considers the mean of the Gaussian at a locally linear region of the function g (blue), and correspondingly provides a relatively good approximation, whereas the left plot considers a locally nonlinear region of the function g (blue) with a corresponding poorer approximation quality.

5.4 Implementation

The widely accepted algorithm provided by Thrun et al. [150] for EKF SLAM with unknown correspondences was adapted to the specific application of the underwater navigation of the holonomic iROV *SeaBiscuit*. The algorithm is reproduced below in Table 5.3 and a line-by-line explanation adapted for this application follows in Table 5.4. The full derivation of the EKF SLAM algorithm is commonly available, for example in the work by Thrun et al. [150].

Table 5.3 - The EKF SLAM algorithm with ML correspondences and outlier rejection as presented by Thrun et al. [150]

1	**Algorithm EKF SLAM** $(\mu_{t-1}, \sum_{t-1}, u_t, z_t, N_{t-1})$:
2	$N_t = N_{t-1}$
3	$F_x = \begin{pmatrix} 1 & 0 & 0 & 0 \dots 0 \\ 0 & 1 & 0 & 0 \dots 0 \\ 0 & 0 & 1 & 0 \dots 0 \end{pmatrix}$
4	$\bar{\mu}_t = \mu_{t-1} + F_x^T \begin{pmatrix} -\frac{v_t}{\omega_t}\sin\mu_{t-1,\theta} + \frac{v_t}{\omega_t}\sin(\mu_{t-1,\theta} + \omega_t\Delta t) \\ \frac{v_t}{\omega_t}\cos\mu_{t-1,\theta} - \frac{v_t}{\omega_t}\cos(\mu_{t-1,\theta} + \omega_t\Delta t) \\ \omega_t\Delta t \end{pmatrix}$
5	$G_t = I + F_x^T \begin{pmatrix} 0 & 0 & -\frac{v_t}{\omega_t}\cos\mu_{t-1,\theta} + \frac{v_t}{\omega_t}\cos(\mu_{t-1,\theta} + \omega_t\Delta t) \\ 0 & 0 & -\frac{v_t}{\omega_t}\sin\mu_{t-1,\theta} + \frac{v_t}{\omega_t}\sin(\mu_{t-1,\theta} + \omega_t\Delta t) \\ 0 & 0 & 0 \end{pmatrix} F_x$
6	$\bar{\Sigma}_t = G_t\Sigma_{t-1}G_t^T + F_x^T R_t F_x$
7	$Q_t = \begin{pmatrix} \sigma_r & 0 & 0 \\ 0 & \sigma_\phi & 0 \\ 0 & 0 & \sigma_s \end{pmatrix}$
8	For all observed features $z_t^i = (r_t^i \phi_t^i s_t^i)^T$ do
9	$\begin{pmatrix} \bar{\mu}_{N_t+1,x} \\ \bar{\mu}_{N_t+1,y} \\ \bar{\mu}_{N_t+1,s} \end{pmatrix} = \begin{pmatrix} \bar{\mu}_{t,x} \\ \bar{\mu}_{t,y} \\ s_t^i \end{pmatrix} + r_t^i \begin{pmatrix} \cos(\phi_t^i + \bar{\mu}_{t,\theta}) \\ \sin(\phi_t^i + \bar{\mu}_{t,\theta}) \\ 0 \end{pmatrix}$
10	For $k = 1$ to $N_t + 1$ do
11	$\delta_k = \begin{pmatrix} \delta_{k,x} \\ \delta_{k,y} \end{pmatrix} = \begin{pmatrix} \bar{\mu}_{k,x} - \bar{\mu}_{t,x} \\ \bar{\mu}_{k,y} - \bar{\mu}_{t,y} \end{pmatrix}$
12	$q_k = \delta_k^T \delta_k$
13	$\hat{z}_t^k = \begin{pmatrix} \sqrt{q_k} \\ \text{atan2}(\delta_{k,y}, \delta_{k,x}) - \bar{\mu}_{t,\theta} \\ \bar{\mu}_{k,s} \end{pmatrix}$
14	$F_{x,k} = \begin{pmatrix} 1 & 0 & 0 & 0 \dots 0 & 0 & 0 & 0 & 0 \dots 0 \\ 0 & 1 & 0 & 0 \dots 0 & 0 & 0 & 0 & 0 \dots 0 \\ 0 & 0 & 1 & 0 \dots 0 & 0 & 0 & 0 & 0 \dots 0 \\ 0 & 0 & 0 & 0 \dots 0 & 1 & 0 & 0 & 0 \dots 0 \\ 0 & 0 & 0 & 0 \dots 0 & 0 & 1 & 0 & 0 \dots 0 \\ 0 & 0 & 0 & 0 \dots 0 & 0 & 0 & 1 & 0 \dots 0 \end{pmatrix}$
15	$H_t^k = \frac{1}{q_k} \begin{pmatrix} -\sqrt{q}_k\delta_{k,x} & -\sqrt{q}_k\delta_{k,y} & 0 & \sqrt{q}_k\delta_{k,x} & \sqrt{q}_k\delta_{k,y} & 0 \\ \delta_{k,y} & -\delta_{k,x} & -q_k & -\delta_{k,y} & \delta_{k,x} & 0 \\ 0 & 0 & 0 & 0 & 0 & q_k \end{pmatrix} F_{x,k}$
16	$\Psi_k = H_t^k \bar{\Sigma}_t \left[H_t^k\right]^T + Q_t$
17	$\pi_k = (z_t^i - \hat{z}_t^k)^T \Psi_k^{-1} (z_t^i - \hat{z}_t^k)$
18	End for
19	$\pi_{N_t+1} = \alpha$
20	$j(i) = \underset{k}{argmin}\, \pi_k$
21	$N_t = max\{N_t, j(i)\}$
22	$K_t^i = \bar{\Sigma}_t \left[H_t^{j(i)}\right]^T \Psi_{j(i)}^{-1}$
23	$\bar{\mu}_t = \bar{\mu}_t + K_t^i (z_t^i - \hat{z}_t^{j(i)})$
24	$\bar{\Sigma}_t = (I - K_t^i H_t^{j(i)}) \bar{\Sigma}_t$
25	End for
26	$\mu_t = \bar{\mu}_t$
27	$\Sigma_t = \bar{\Sigma}_t$
28	Return μ_t, Σ_t

Table 5.4 - A description of EKF SLAM with ML correspondences and outlier rejection presented above in Table 5.3

1				
2				
3				Motion Update
4	Manipulate the mean of the belief in accordance with the motion model. This only affects elements of the belief distribution concerned with the robot pose; all mean variables for the map are unchanged.			
5				
6	Manipulate the covariance of the belief in accordance with the motion model. This only affects elements of the belief distribution concerned with the robot pose; all covariance variables for the map are unchanged, as are pose-map covariances.			
7				Measurement Update
8	For each observed feature, a hypothesis is created that the feature is a new landmark with index $N_t + 1$ (an index of one larger than the current number of landmarks tracked in the map).		For all observed features z_t^i	
9	The location and signature of the new landmark is initialized by calculating its expected location given the current estimate of the robot's position and the range and bearing to the landmark.			
10	Then, for all $N_t + 1$ possible landmarks, including the 'new' hypothesised landmark, various update quantities are calculated. For computational efficiency when operating in large environments, this loop can be restricted to landmarks which are close to the robot.	For all landmarks including the new hypothesis		
11				
12				
13	For each measurement, an *expected* measurement is calculated.			
14				
15				
16				
17	The Mahalanobis distance (section 5.3.4.2) between the observed landmark and all mapped landmarks is compiled in an array π indexed by k the loop of all tracked landmarks including the new hypothesis.			
18				
19	If the Mahalanobis distance between the current observed feature to all existing landmarks in the map exceeds the threshold value α then a new landmark is created from the hypothesis of a new landmark.			
20	The ML correspondence between the current observed landmark and all mapped landmarks is selected by selecting the minimum Mahalanobis distance. If a new landmark was created in the previous line then the Mahalanobis distance to this will be 0 and this will be the corresponding landmark.			
21	If the current measurement was associated with a new landmark then the landmark counter N_t is incremented and the various vectors and matrices are enlarged accordingly (not shown).			
22	For each measurement, the Kalman gain is calculated which determines the weighting to assign to the predicted (control) position of mapped the landmark it corresponds to, given the robot's motion and the observed measured position (update) of the landmark. The Kalman gain is a matrix of size 3 by $3N + 3$. The matrix is usually not sparse and information is propagated through the entire state estimate.			
23	The EKF mean is updated by folding the innovation weighted by the Kalman gain back into the belief. (If the map has just been extended then the participating vectors and matrices are extended to suit.)			
24	The EKF covariance is updated by folding the innovation weighted by the Kalman gain back into the covariance. (If the map has just been extended then the participating vectors and matrices are extended to suit.)			
25				
26				
27				
28	The mean μ_t, the covariance Σ_t and the number of landmarks N_t are returned from this time interval.			

Line 22 above, where the Kalman gain is calculated, highlights an important benefit of SLAM using Kalman filters. As Thrun et al. [150] state, the fact that the Kalman gain is fully populated for all state variables, and not just the currently observed landmark and the robot pose, is important. Observing a landmark and reducing uncertainty about the robot's pose does not just reduce uncertainty about the position estimate of this landmark, but also of other landmarks as well. This propagation of information back through the entire state estimate allows maximum use of the information gathered by observing a landmark.

The important benefit in using Kalman filters for SLAM is that, to achieve this reduction in uncertainty for all landmarks by just observing a single landmark, past poses do not have to be modelled explicitly. As Thrun et al. [150] describe, this would involve the full SLAM problem as described in section 5.3.4.1 and make the EKF a non-realtime algorithm. Instead, the dependence (covariance) between the observed landmark and other landmarks is captured in the Gaussian posterior (defined earlier) by the off-diagonal elements of the covariance matrix Σ_t.

The EKF ML SLAM algorithm was implemented in LabVIEW with MathScript nodes used for the matrix manipulation. The modular hierarchical iROV program structure allowed straightforward interfacing to provide the required measurement and control inputs and allowed the output state and map to be plotted in realtime. The modular program nature also allowed development to begin using manually identified correspondences, before development of the maximum likelihood correspondence estimator detailed above.

5.5 Simulation

Throughout development, the algorithms were simulated and tested, where possible with hardware in the loop testing. In previous sections, this focussed on simulation of the sonar and vision image processing algorithms and feature extraction with real-life recorded data used to allow development and tuning. This section details the simulation of the navigation algorithms for SLAM.

The simulation environment generated movement and measurement data with the same uncertainty characteristics as real-life operation. The simulation also allowed real-world data to be played back, to allow tuning, development and an assessment of the performance of the navigation algorithms without having to deploy the vehicle.

The navigation algorithms used on the vehicle were directly interfaced to the simulation environment. The simulation algorithm wrapped around the navigation algorithm, providing simulated inputs, and tracking the vehicle and environment state based on controlled outputs, replacing real world operation in 2 dimensions and 3 DoF as discussed previously.

The actual position of the vehicle and all landmarks were tracked and controlled by the simulation environment exactly, however the exact movements and measurements were corrupted by additive Gaussian noise of the same magnitude and characteristics of the real-world sensor and movement uncertainty. Drift and deviations in the position of the robot from external water movements and uncertain movements of the robot from controlled thrust using additive Gaussian noise were also simulated. Although the kinematics of the vehicle were not included in the simulation, this was tested using hardware in the loop testing.

Landmarks were simulated and observations generated with a range and bearing simulating the output of the sonar units. This range and bearing was generated by the simulation loop based on the measurement the robot would expect to see from its current position and the relative

position of the landmark and combined with additive Gaussian noise to simulate measurement noise (uncertainty). Varying sensor availability, varying landmark observations, dynamic landmarks and unexpected position changes (localisation failures) were also investigated.

In addition to the simulated range and bearing measurement, a signature variable was also simulated with each landmark observation to describe the landmark characteristics. In vision applications, this represented the colour of the object; in sonar applications it comprised the object size and shape.

This signature variable was used, together with the x and y position of the observed landmark, to calculate the maximum likelihood correspondence between an observed landmark and a previously mapped landmark, as described in section 5.3.4.2. The value of α (the threshold for creating a new landmark) was set depending on the expected spacing between landmarks and the sensing error and noise, such that re-observations of the same landmark, but in apparently slightly differing positions, were still corresponded correctly as the same landmark.

5.5.1 Simulation example

Table 5.5 below shows an example of the EKF SLAM algorithm with unknown (ML estimator) correspondences. In this example, operation took place across a Cartesian X-Y plane centred at (0,0). Four landmarks were present at fixed locations (50, 50), (-50, 50), (50, -50) and (-50, -50) respectively. As the robot moved throughout the environment, it could observe any number (or none) of these landmarks. The robot had full x y movement capabilities including yaw angle, although yaw is not shown in the figures below. In addition to continually localising the robot (using the landmarks if present), the SLAM algorithm also mapped and tracked the position of each individually identified landmark continuously.

The colour-coded key to the visualisation is shown in Figure 5.24. The *actual* (static) position of the landmarks is shown by the black dots. In this example, the static landmarks did not vary in position, however the number (if any) of landmarks observed at each time step varied. If a landmark was observed, a simulated measurement was generated. The *actual* position of the robot is tracked by the green trace which was maintained by the simulation algorithm.

The EKF ML SLAM algorithm fused the simulated measurements and the control commands and maintained a position estimate which is displayed by the red trace. The difference in position between the red trace and the green trace is the localisation error.

Together with the position estimate (the red trace) the SLAM algorithm provided an estimate of the uncertainty of the position estimate by plotting an ellipse. The size of the ellipse in the x and y directions is proportional to the covariance of the position estimate in each axis.

In a similar manner, as landmarks were observed and the position of these mapped, landmarks were tracked by a series of coloured ellipses according to the key. Again, the size of the ellipse is proportional to the covariance. The position and covariance of each tracked landmark estimate was maintained, even if it was not observed at that time interval. This allowed the effect of a change in the covariance of the robot's position on the covariance of a landmark to be seen. This effect is discussed below. In the simplified example below, the covariance in the x and y directions is assumed to be equal and so the uncertainty is represented by ellipses with equal proportions, i.e. circles.

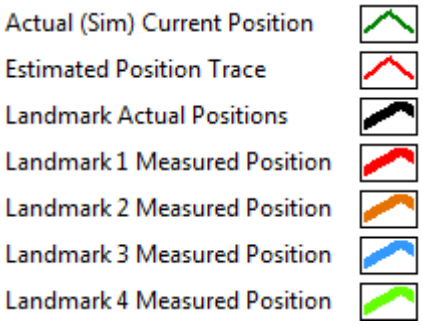

Figure 5.24 - Key to EKF ML SLAM Visualisation.

Table 5.5 - Example simulation implementation of EKF ML SLAM

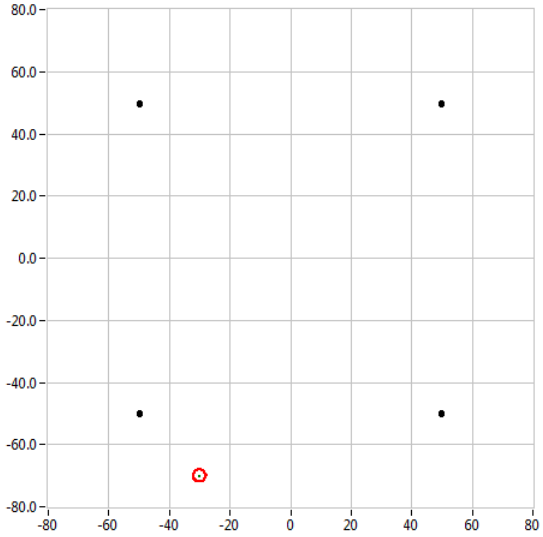	**Frame 1)** The robot began operation at coordinates (-30, -70). The position of the 4 stationary landmarks is shown on the map with black dots at the coordinates (50, 50) … etc. However, the robot had no prior knowledge of its position or the position of these landmarks. The simulation environment was however aware of the robot and landmark positions. The robot's initial estimate of its position serves only to register the map in the WCS, but for this example it was assumed that it started with a GPS position fix on the surface before diving. The uncertainty associated with the initial starting position estimate was relatively low, hence the relatively small red circle (covariance) surrounding the initial position estimate.
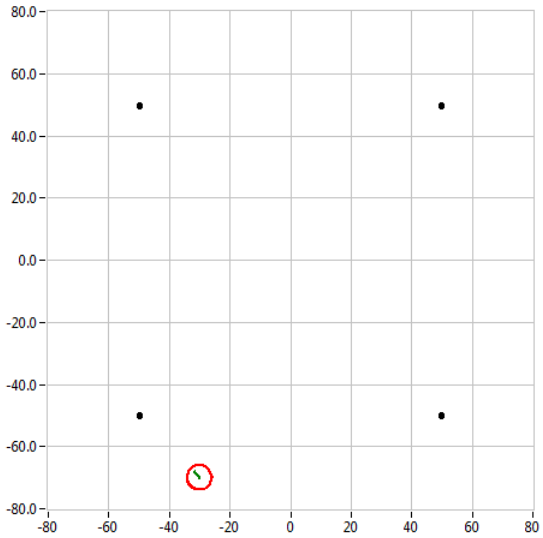	**Frame 2)** The robot has not moved under its own power. It has however been moved by external water movements and is now actually at (-32, -68). This movement is shown by the green simulation line. As the robot could not currently observe any landmarks to localise from and has not commanded this movement it had no knowledge that the movement had occurred. Hence its position estimate remained at (-30, -70). (In real life, the INS would still be providing an estimation of movement.) Due to the increasing uncertainty of this positional estimate over time however, the red circle surrounding its position estimate (covariance) has increased in size.

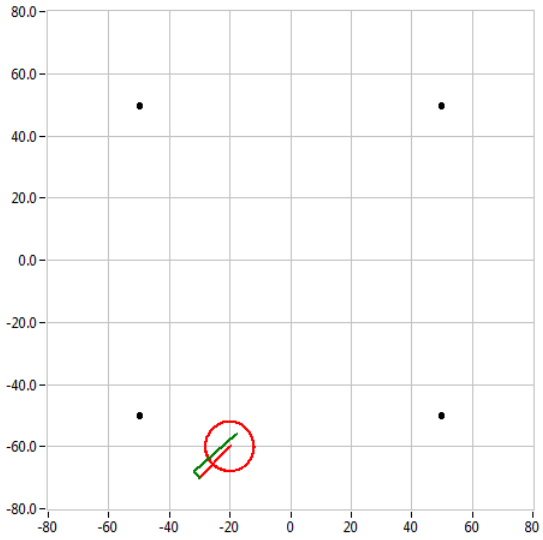

Frame 3) The robot commanded a position change of (+10, +10). As the robot could not currently observe any landmarks, it was only able to predict this position change, hence the red position estimate changed to (-20, -60). Because a change in position introduces a greater uncertainty than just remaining stationary, the red circle (position estimate uncertainty) also increased in size dramatically.

The green trace shows that the commanded change in position was not executed perfectly, and the final actual position was (-18, -56). The red circle of position uncertainty still encompasses the actual position.

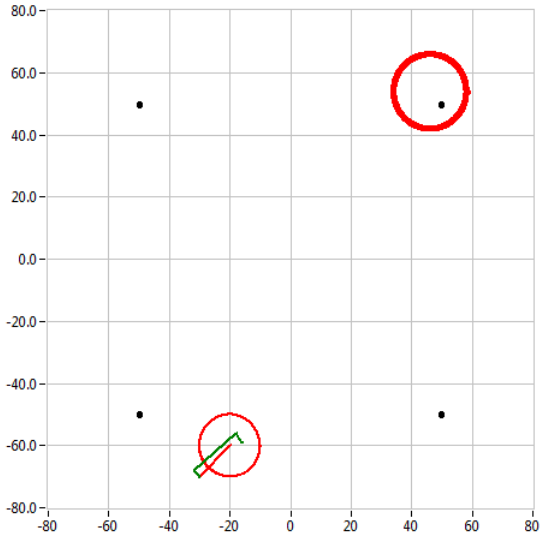

Frame 4) In this frame the robot remained stationary with a corresponding increase in positional uncertainty. A small drift in position occurred which the vehicle was not aware of.

If this operation was to continue in a sparse operating environment with no landmarks to navigate by, the uncertainty associated with the robot position is unbounded and would quickly grow. Although operation could continue, any mapped data would have to be recorded with a very high positional uncertainty.

Landmark 1 (LM1) was observed in this frame. A measurement was simulated by calculating the predicted measurement the robot would see based on its actual simulated (green) position and the relative position of the landmark. This simulated measurement was then corrupted with additive Gaussian noise based on the sensor characteristics (for the sonar, a greater uncertainty at greater range).

The position of LM1 was thus recorded based on the current position estimate of the robot and the simulated measurement. It can be seen that because the position of LM1 could only at this stage be referenced to the current robot position which has a high uncertainty, the uncertainty associated with the position of LM1 was equal to the current robot positional uncertainty combined with the uncertainty associated with the measurement.

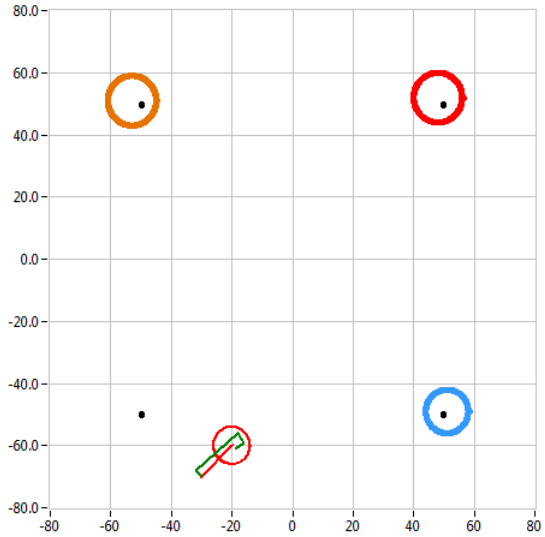

Frame 5) The robot continued to remain stationary and so there was only a small deviation in position from external water movements.

However, the robot re-observed LM1 in approximately the same position (from another simulated measurement from the simulation loop). This allowed it to significantly reduce the uncertainty associated with both its current position estimate and also the uncertainty associated with the mapped position of LM1.

This effect was discussed at the end of section 5.4, but in summary: using Bayesian SLAM, *observing a landmark does not just improve the position estimate of this landmark, but also of other landmarks as well*. This back propagation of information allows maximum exploitation of information gathered by observing a landmark. It not only reduces the uncertainty of other observed landmarks, but also of mapped landmarks which are not observed in this iteration. The benefits occur when a landmark is observed, the robot navigates away from this landmark observing and recording other landmarks, but when the first landmark is *reobserved* the uncertainty associated with the *entire map* and the robot position is greatly reduced.

LM2 and LM3 were also observed at a distance greater than α from existing mapped landmarks so these were recorded as new landmark hypotheses with an uncertainty reflected by the current robot position uncertainty and the respective range of the robot to the landmark.

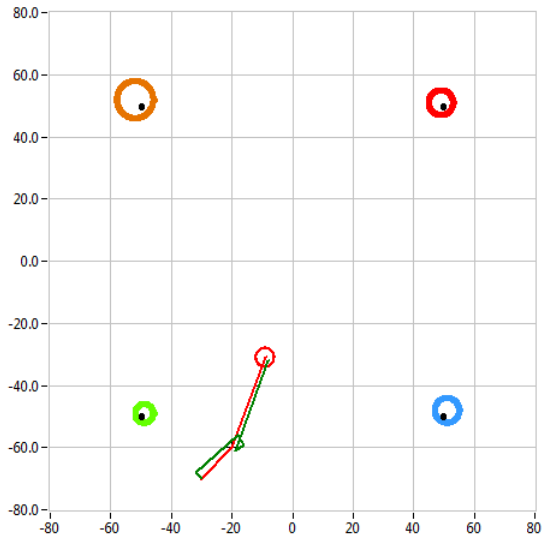

Frame 6) The robot continued its movement while continuing to observe the 3 existing landmarks and observing LM4 for the first time. As the robot approached the landmarks, the error in measurement and the uncertainty associated with the measurements reduced.

Although motion of the robot introduced a larger error in position rather than just remaining stationary, because by this stage, several landmarks were visible and tracked as absolute position references, the localisation error and uncertainty was maintained at a low-level despite continued motion.

The effect of re-observing all landmarks back propagated and reduced the positional uncertainty associated with all tracked landmarks.

5.6 Discussion

The literature review in Chapter 2 developed the justification for sensor fusion to both increase the reliability of navigation in the hostile challenging conditions of the nearshore [15], to provide robust navigation combining idiothetic and allothetic sensors [157] and to maximise the information available from a limited budget of sensors [156]. The benefits of a probabilistic approach to vehicle localisation and mapping, in terms of robustness, applicability to nearshore navigation and computational efficiency were also evaluated [355].

5.6.1 Using sensor fusion to aid navigation in the nearshore

The improvement in navigation made possible by combining the data from multiple complementary navigation sensors over using a single isolated sensor for navigation was discussed in section 2.3.2.4. The underlying principle was that, the more sources of information, the more reliable the overall perception of the environment [15].

The benefits were an increase in reliability (including exploiting sensor redundancy), a reduction in navigation uncertainty (localisation and mapping) and sensor resolution and detail usually only possible from a much higher budget sensors. However, care must be taken to avoid compounding errors, unnecessarily increasing computational complexity [165] and any advantages gained must be weighed against the finite cost, space, weight and power budgets available [200] without compromising the low-cost, highly manoeuvrable vehicle. The sensor fusion implemented on *SeaBiscuit* is considered in the following two sections on high-level and low-level sensor fusion and its benefits.

5.6.1.1 High-level sensor fusion

High-level sensor fusion allows the combination of different sensor modes or different sensor coverage, either to increase sensing capabilities, or to enable reliable sensing in challenging conditions [15].

An example implemented on *SeaBiscuit* was the fusion of video and sonar data. Here the complementary modes and advantages of each sensor [156] were combined to allow for operation in challenging conditions such as dark or turbid water. The sonar units provided long range *detection* and depth perception while the video cameras provided short range *identification* including colour and detailed shape information, whether this was autonomously using the techniques developed for the SAUC-E competition (sections 4.6.6, 4.6.7 and 6.2), or manually for sonar target validation using remote operator control and supervision of the iROV.

The coverage of different sensors was also combined, for example combining the forward facing Delta T *profiling* sonar with the radial 852 *scanning* sonar allowed objects to be registered in both planes, developing a 3D representation of the environment, even while the vehicle was in motion. Techniques to perform this comparison between sonars are demonstrated in the context of the dock mapping as described in section 6.3.4. Using the complementary holonomic navigation and propulsion system, this enabled the benefits of a 3D imaging sonar at a fraction of the price [129, 130].

Combining the coverage of different sensors extended to maximise both submerged and surface sensing. Through the innovative design of *SeaBiscuit,* and the positioning of its angled sonar units and high-profile antennas, the vehicle was able to successfully manoeuvre at the water surface performing detailed sonar scans of the underwater environment while receiving GPS position

updates and communicating via wireless with a remote operator. This bridging of the air-water interface had significant benefits to sensing capabilities, providing drift free absolute GPS registration of sonar targets. The vehicle was capable of observing a sonar landmark underwater from the surface while simultaneously using a GPS position fix to register this object in the world coordinate system. The vehicle could then dive and relate further underwater targets to the originally observed landmark, thus propagating the GPS position fix to all subsequent observed landmarks.

High-level sensor fusion also allowed sensors with complementary characteristics to be combined [157], for example, the positional estimates made by the accelerometers in the INS and estimates made from tracking the successive observation of sonar landmarks. In this case, the accelerometer data was always available, did not require the presence of any external landmarks or features, could be updated as fast as the hardware allowed (120Hz) and was not subject to outside interference such as sonar landmarks moving, or acoustic interference and errors. However, the dead reckoning accelerometer data only estimated position from a previous estimate plus or minus a small measured deviation. While this made it immune to outside interference or errors, it could quickly introduce large cumulative errors, or drift.

In this manner, the sonar unit was complementary; the readings were absolute not relative and thus drift free (the error in each scan was independent and not cumulative with previous measurement errors). However, the sonar required static landmarks to be readily observable and corresponded to subsequent scans, so positional estimates were not always available and are updated much less frequently than the accelerometer data.

Therefore, each of these sensors on their own were not sufficient for robust, reliable underwater navigation. Elsewhere this problem is solved for sparse environments by placing artificial sonar landmarks [17], however the solution implemented on *SeaBiscuit* was required to operate without the additional logistics of environment modification. Instead, the combination of the long term accuracy of the sonar and the short term dynamic response of the INS provided a complementary system.

5.6.1.2 Low-level sensor fusion

Low-level sensor fusion refers to the benefits provided by the probabilistic fusion of different sensor measurements. The precursor to this was to accept that every measurement has an uncertainty associated with it and that any positional estimate, however uncertain, can be useful. Low-level sensor fusion provided a probabilistic framework to combine multiple estimates of the same state from a variety of sensors to reduce the overall uncertainty associated with underwater navigation compared to using the individual sensor measurements in isolation.

Again, the benefit was to make optimal use of all of the information available to the navigation algorithms in the often dynamic conditions of the nearshore environment. Through the algorithms employed, even the location estimate gained from a single sensor observation could be folded back into the algorithm and serve to reduce the uncertainty associated with all mapped features, and hence all future mapped landmarks as well [355].

Alternatives to probabilistic fusion were considered in Chapter 2, including the Dempster Shafer theory [180] and fuzzy set theory [178]. Probabilistic fusion was adopted for its computational simplicity [186] and ease of integration with the algorithms for EKF SLAM.

5.6.2 The design, implementation and simulation of EKF SLAM

Given the suitability of clusters of kelp stipes (and the dock pilings used to test the SLAM algorithms) to a parametric representation and the ability to represent uncertainty, Gaussian filters, in particular the EKF were found to be an efficient and effective solution to nearshore SLAM compared to the higher detail but significantly higher computation complexity of non-parametric filters [139]. The Extended Kalman Filter (EKF) algorithm for SLAM [355] was implemented for the nearshore navigation of *SeaBiscuit*. The benefits of sensor fusion and probabilistic navigation, including an awareness of sensing, movement and environment uncertainty, together with computational efficiency and robustness were all realised. SLAM relative to landmarks with unknown correspondences observed primarily using the two sonars but also using visual landmarks was implemented using the nearest neighbour maximum likelihood estimator [352, 353].

The EKF SLAM algorithm was selected over alternatives such as Graph SLAM [206] for reasons of computational and conceptual simplicity. Although the EKF SLAM algorithm has quadratic complexity with respect to the number of landmarks tracked [208], careful map management and landmark selection, including a correctly set threshold value for associating observed features to tracked landmarks and voting algorithms to avoid mapping spurious noise, were all used to ensure an efficient map, and therefore a map update feasible for computation in realtime.

Although the algorithms for EKF SLAM are long established and widely used for the navigation of mobile robots, the novelty of the modular, flexible implementation in LabVIEW for direct interfacing to the rest of the iROV control system was described in this chapter. In section 2.3.2.5.4 the general consensus was discussed that SLAM for basic structured environments with good sensing is solved as far as basic research is concerned [171], at least at a theoretical and conceptual level [212]. However, SLAM with imperfect sensing in large and/or dynamic environments and without frequent regular landmarks is still a challenge facing mobile robots. In the dynamic nearshore environment with often dynamic sensing and varying sensor availability, and crucially with the constraints of a limited budget and imperfect sensing underwater, SLAM becomes an important and contemporary area of research. It is against this, that novelty in the implementation of EKF SLAM on *SeaBiscuit* is demonstrated in this research. A real world, robust implementation has been developed complementary to the sensing and navigation techniques for the nearshore, with steps towards kelp bed mapping on a limited budget with imperfect sensing demonstrated in the field trials later in Chapter 6 and Chapter 7.

In particular, the ability to not only ignore the effects of dynamic objects but to include them in the model, to monitor and update changes in the environment and to compute semantically meaningful models not just geometric maps of the environment were all identified as opportunities for research [225].

Although significant progress in underwater navigation has been made in recent years, there remain several exciting opportunities for development. Many underwater vehicles do not use sonar/video landmark aided navigation, but instead use DVL or precision INS units [117]. DVL aided sonar navigation has been demonstrated for structured environments [16], or environments modified with sonar markers [211]. Sonar aided SLAM using both multibeam [126] and mechanically panned sonars [125] has also been successfully demonstrated, yet the combined dual-sonar approach implemented on *SeaBiscuit* exploiting holonomicity brings significant benefits, in terms of coverage, robustness, mapping speed and the ability to independently perform 3D habitat mapping while also performing SLAM / obstacle avoidance.

When the environment and application permit, the multi-modal approach of *SeaBiscuit* to register sonar targets with the GPS at the water-air interface, then to navigate from these sonar targets while underwater provides sufficient navigational information at a fraction of the price of comparable DVL and precision INS solutions [63, 77, 82, 83].

It is against this proposition that the research and development into SLAM for nearshore habitat mapping sought to advance the state of the art – to achieve reliable SLAM in the dynamic, unstructured nearshore environment and with the imperfect sensing available in the kelp beds, to achieve robust, reliable results on a low budget through innovative solutions.

It was recognised that there are more efficient and robust algorithms available for SLAM, including those which trade computational efficiency for map detail [206, 355]. Many impose certain assumptions or restrictions on the state, landmarks or operating conditions. This research has investigated the suitability of the EKF ML SLAM for nearshore navigation, demonstrated in the following chapter, and provided both simulation and control software which is modular for the straightforward integration, testing and operation of alternative methods for SLAM. Thus the comparison of alternative algorithms and their potential benefits to nearshore navigation are left as opportunities for further research. In a similar manner, the scalable sensor fusion algorithms allow straightforward integration of either additional sensors or alternative sensors in the future, should the operating environment or budget constraints vary, with a corresponding increase/decrease in performance.

The algorithms were tested in a custom LabVIEW simulation environment which provided a framework where different SLAM algorithms were tested with the benefit that the actual ground truth position of the robot and landmarks were known for comparison to the SLAM algorithm estimates. This allowed the performance, robustness and computational complexity of different algorithms to be tested and accurately compared under different conditions, as algorithms could be ‘slotted in’ to the simulation environment and the vehicle navigation software using a common interface to ensure interoperability. Future development of the simulation environment could include a kinematic model of the vehicle’s movement, together with development of the simulation to operation in full 3D. However, neither of these features were required for the algorithm verification performed in 2D [215] and these remain as opportunities for further work. With the algorithms demonstrated in simulation, the following two chapters describes a staged series of field trials, culminating in the demonstration of SLAM off a piling dock and kelp bed mapping capabilities.

Chapter 6 Field Trials

6.1 Introduction

Following the demonstration in simulation of the navigation algorithms in the previous chapter, the mechanical, electrical and software development from all of the previous chapters were combined for the real-world sea trials of the iROV *SeaBiscuit*. The following two chapters document a real-world successful demonstration of operation in the target nearshore environment.

A staged testing methodology was used, and field trials were conducted over four stages of increasing complexity to ensure reliability throughout.

The first was confined water testing in the SAUC-E competition introduced previously for the vehicle *Hawthorne 2.0* in section 3.4 and now detailed for *SeaBiscuit* in section 6.2. Operation in the closed environment with artificial markers provided a good systems test and allowed the navigation sensors and feature extraction algorithms to be tuned.

Following this, a known but open-water environment was considered. This allowed the performance and navigation (SLAM and sensor fusion) of the vehicle to be assessed under real-world conditions and compared to a ground truth – an absolute position reference and user generated map. For this purpose, the surveying and mapping of a piling dock is documented in section 6.3. The navigation hardware and software developed and simulated over previous chapters was combined with the holonomic motion of the vehicle to provide a capable underwater survey tool. The improvements made from the sensor fusion SLAM algorithms combined with the complementary holonomic navigation and propulsion system were demonstrated. Mapping was achieved using the novel combination of the forward facing multibeam sonar panned by the holonomic propulsion system, and independent control of the 852 scanning sonar, coupled with the LabVIEW implementation of EKF SLAM algorithms.

6.2 Artificial environment: SAUC-E Competition

An exhaustive staged test schedule ensured the iROV *SeaBiscuit* was as ready and reliable as possible for the ocean surveys. The testing started in a laboratory 5m swim flume tank, graduating to a 25m swimming pool, then a 4m deep SCUBA training pool. Finally, as a proof of readiness and as preliminary ocean trials, *SeaBiscuit* entered the annual Student Autonomous Underwater Challenge-Europe (SAUC-E) in 2009.

The SAUC-E competition was sponsored by the Defence Science and Technology Laboratory (DSTL) and the UK Ministry of Defence together with a number of industrial partners [320]. Bath University Racing Submarine Team (BURST) has entered the competition since its inception, competing in 2006, 2007, 2008 and 2009 with increasing degrees of success each year.

The competition involved several AUVs designed by multi-disciplinary student teams from across Europe. Success in the competition was achieved by completing several underwater missions autonomously with speed and accuracy. Marks were also allocated for design and technical merit. The missions included passing through gates, identifying, locating and marking targets and mapping the competition environment [321]. In more recent years, as the field has advanced, so has the standard of the competition and the complexity of the tasks to now involve tracking moving targets, intervention with objects, docking in confined spaces, etc. [356].

Figure 6.1 to Figure 6.3 below show some of the competition targets in a swimming pool clear water test environment while Figure 6.4 shows the typical sonar data available. Competition specific sonar and video image processing and feature extraction algorithms were discussed previously in section 4.6.6 and 4.6.7 respectively, including example footage for each.

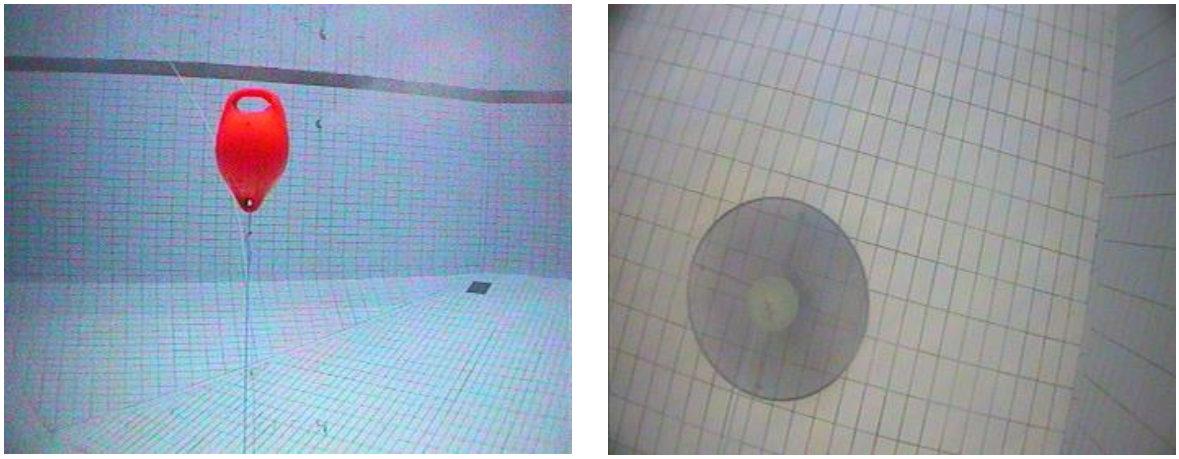

Figure 6.1 - Some of the SAUC-E competition targets. Left: the midwater marker, an air-filled red buoy, Right: the bottom target, both of which had to be detected, identified, mapped and tracked autonomously using video and/or sonar. These images were gathered with a high-resolution camera in the clear waters of a swimming pool test environment. They were intended to illustrate the targets, however the visual quality of operation in the competition environment was significantly lower as seen in previous images. (Image credit [357]).

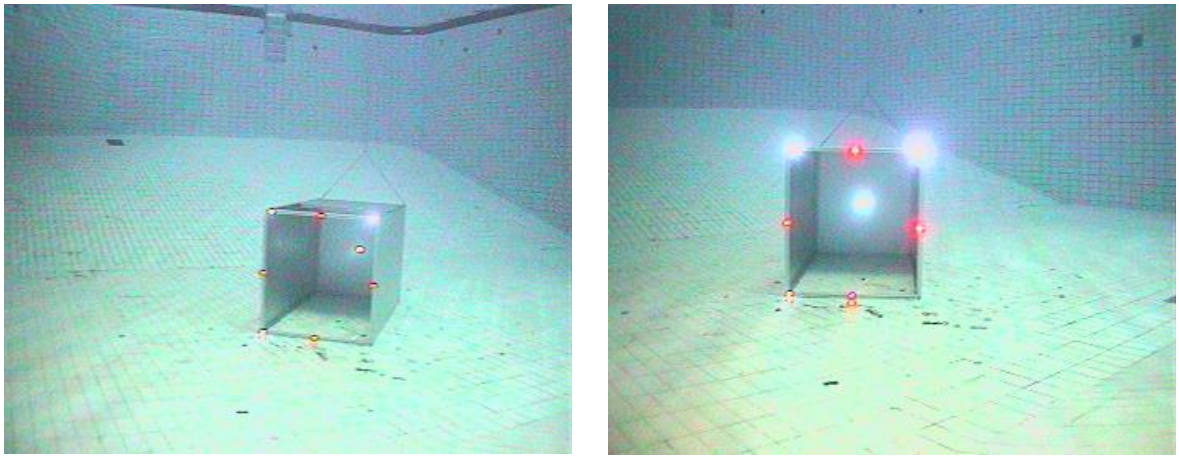

Figure 6.2 - The underwater docking box at the SAUC-E competition. The entrance was marked with red and white LEDs; one of the more challenging tasks was to autonomously dock into this box as a move towards automatic recharging and energy autonomy. As above, these sample images were gathered in clear shallow water and the visual quality of operation in the competition environment was significantly lower. (Image credit [357]).

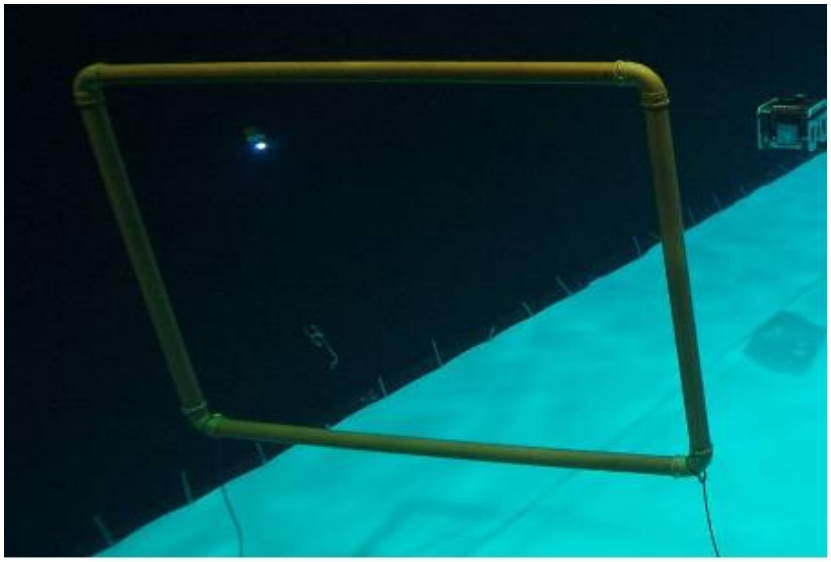

Figure 6.3 - A typical gate at the SAUC-E competition, designed to test navigation and manoeuvrability [358].

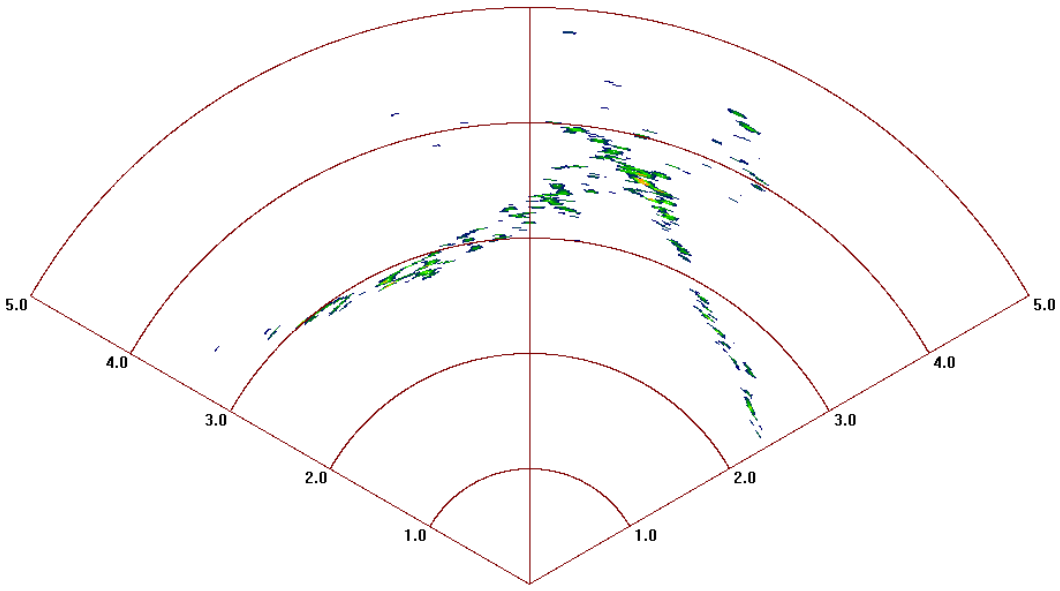

Figure 6.4 - A sample Delta T sonar image of the corner of a test tank in the enclosed SAUC-E competition – range scale is in metres.

The 2009 SAUC-E competition was held at the Ocean Basin Hydrodynamic Test Tank at Qinetiq Haslar, Gosport. This large test tank consisted of relatively clear water, enclosed on all sides and of dimensions 122m long, 61m wide and 5.5m deep [359]. With the addition of some relatively simple mission planning algorithms (section 4.7.3), the competition provided an initial demonstration of autonomy while also demonstrating the field-readiness of the vehicle. Figure 6.5 below shows some images of *SeaBiscuit* at the 2009 competition.

The vehicle demonstrated successful control, manoeuvring, basic sensing capabilities and simple autonomous navigation, including holding and navigating a pre-programmed course in 3D using the navigation sensors.

SeaBiscuit was awarded first place in the second division of vehicles, a successful result and an excellent start to the trials of the vehicle given its rapid development from design to working prototype.

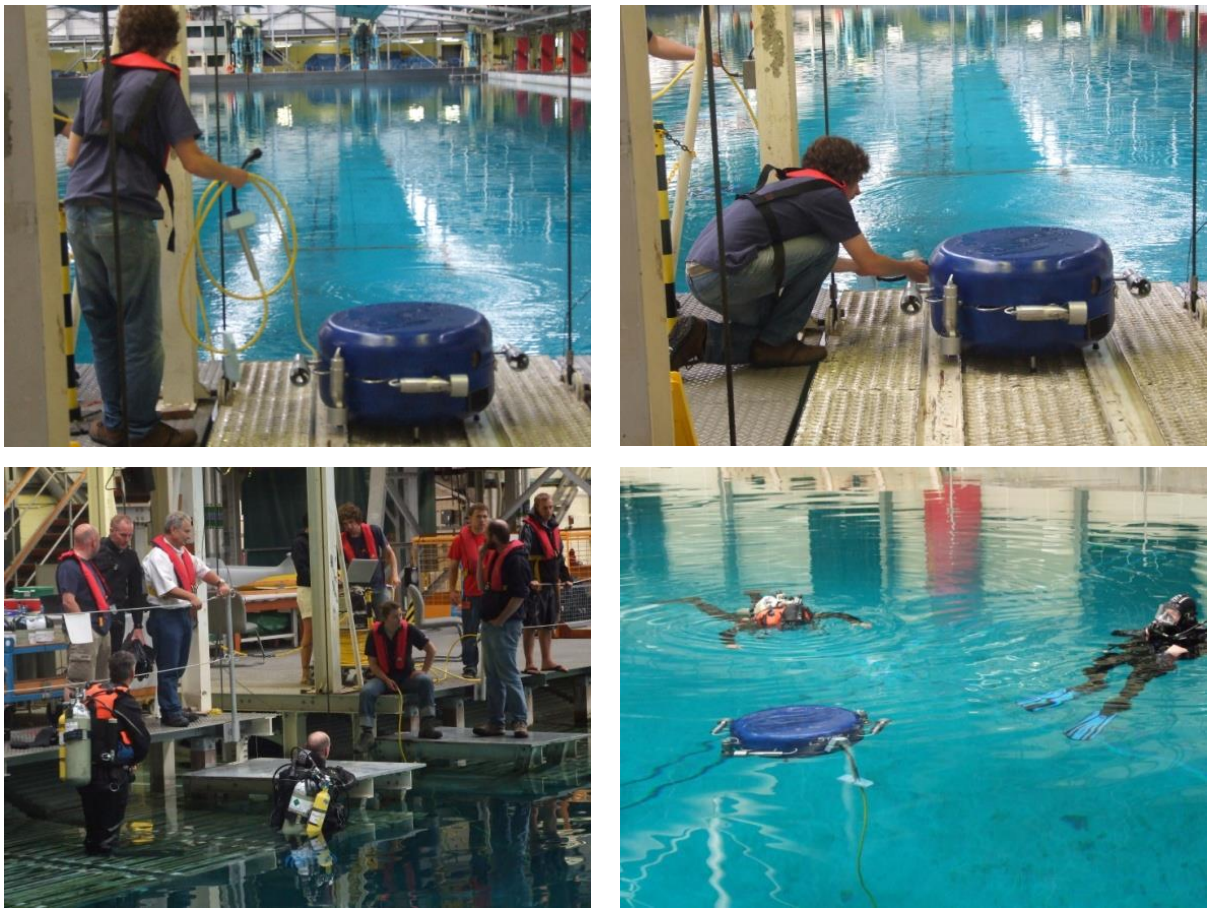

Figure 6.5 - *SeaBiscuit* at the SAUC-E 2009 Competition, Portsmouth, UK. This was a sucessfuly precursor to the 2010 field trials and provided an intial demonstration of autonomy and field-readiness as an iROV. The upper two images show the vehicle being prepared for an untethered launch, with the yellow tether removed in the upper left image and a final check made of the thrusters in the upper right. The vehicle was then lowered into the water using the elevator shown in the bottom left. The lower right figure shows an initial calibration run with the tether attached and support divers on standby.

Following this initial demonstration of basic autonomy and proof of field readiness at the SAUC-E 2009 competition *SeaBiscuit* was flown out to the field site in British Columbia, Canada to begin open ocean trials in the summers of 2009, 2010 and 2011.

6.3 Sheltered environment: Dock survey and mapping

As an initial field trial, the robot was deployed off the dock pictured in Figure 6.6 located close to the field site for the coastal ecosystems research group in Clayoquot Sound, as shown in the map of Flores Island, British Columbia, Canada in Figure 6.7.

Figure 6.6 - The docks at Ahousat, the site for the dock survey and mapping field trial. The left figure shows the sheltered inlet with the docks in the distance. The right figure shows the piling dock from the shore. The dock is aligned north-south with the boom lift crane at the northern most end of the dock facing the open ocean. The walkway leads out from the shore in a north-easterly direction.

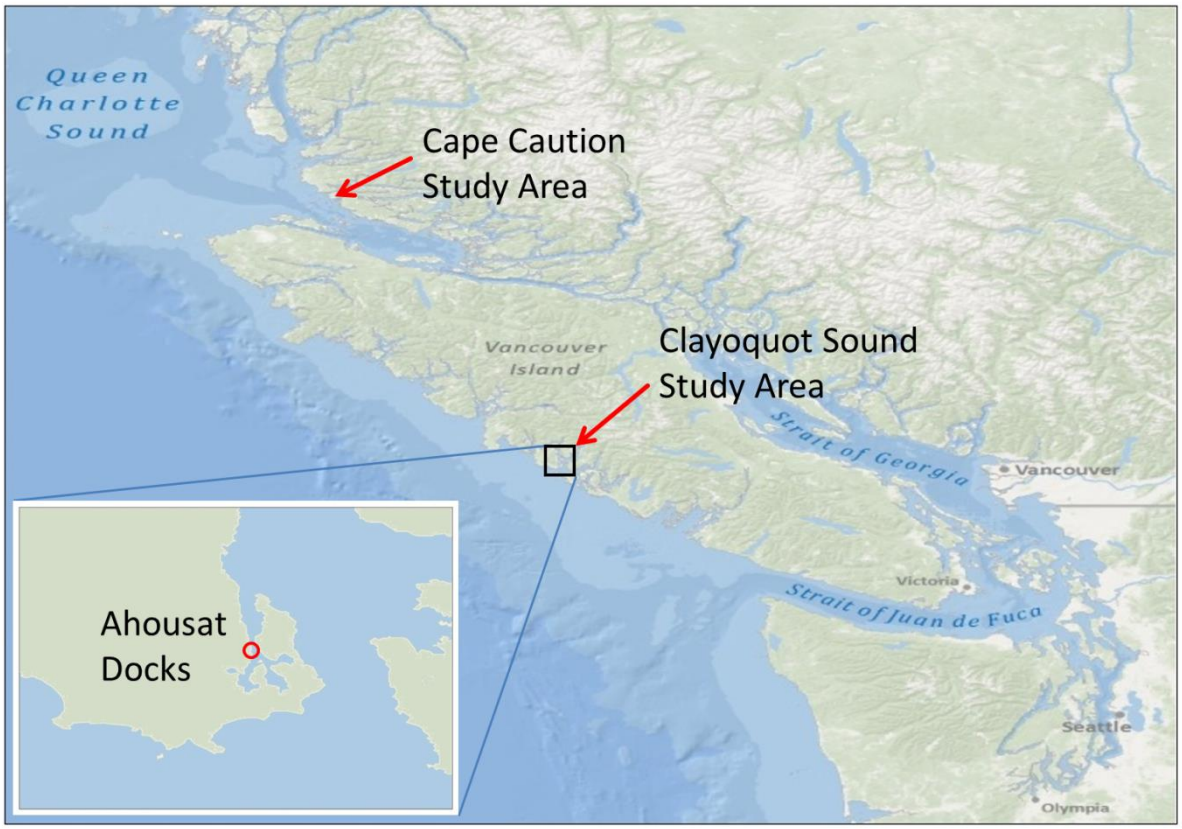

Figure 6.7 - The location of the dock survey and mapping field trials, Ahousat Docks, Flores Island, British Columbia, Canada. The two main grey whale study areas are also shown for reference in the later sections on kelp bed mapping.

This dock provided an ideal operating environment to test the nearshore navigation techniques. A combination of a piling dock in 2-10m of water, a series of floating pontoons anchored by chains, a nearby rocky shoreline with a muddy shallow area, a series of semi-submerged tree trunks and a deep water channel provided a wide variety of targets in close proximity as shown below in Figure 6.8.

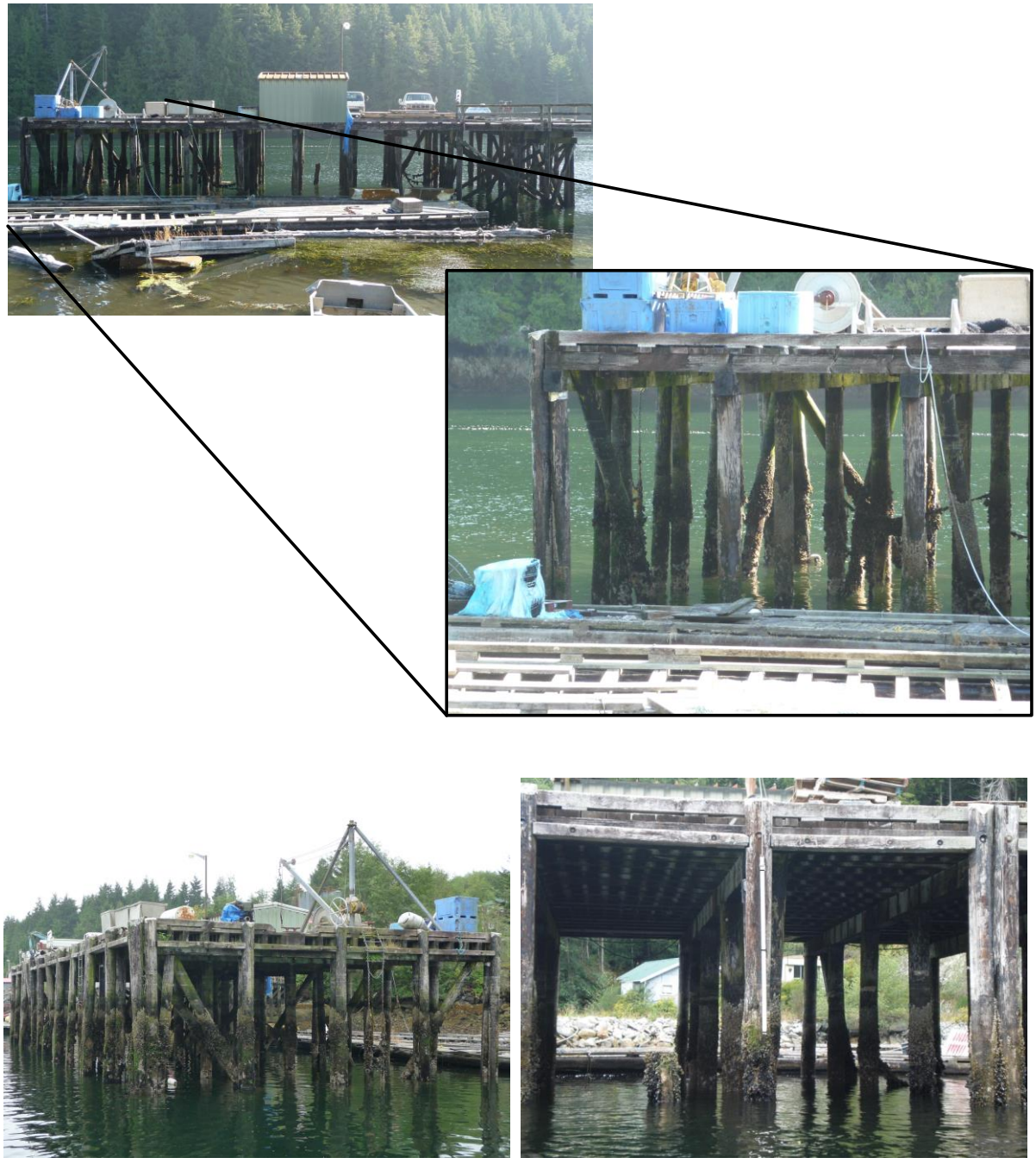

Figure 6.8 - The dock survey test environment. The top image shows the piling dock from the shore, i.e. with the camera facing east. In the foreground the floating dock and shallows approaching the shore can be seen. The zoom of the top figure focuses on the left hand end of the dock, close to the crane used for deployments to show the arrangement of pilings. The lower left figure shows the piling dock from the deep water channel facing into the inlet (south), with the crane end of the dock closest to the camera. Finally, the lower right figure shows a close up facing west, in the middle of the channel looking through the dock towards the shoreline. The floating dock can be seen behind, and further back, the shoreline. Cross pilings and half-height pilings which have broken off can also be seen.

A geometric map of the operating environment was manually surveyed, including the position of all major underwater features, the shoreline and an approximation of the bathymetry. The diagrams in Figure 6.9 below show the configuration of the dock pilings with respect to an approximation of the sloping seafloor. The schematic is geometrically correct except for the approximated seafloor. Double pilings were recorded and a more detailed representation of this diagram shows the cross pilings, and the relative location of the shoreline, the floating docks and other midwater targets. Figure 6.8 above showed underneath the dock at low tide demonstrating the complex configuration of cross pilings and half height vertical pilings.

This manually surveyed geometric map was compared with the datasets gathered by the robot underwater to evaluate the accuracy and performance of the navigation system. The vertical pilings allowed the SLAM and sonar algorithms to be calibrated in real life against a ground truth. The boom lift crane on the end of the dock (shown in Figure 6.10) was also modelled, allowing the robot to be held at known, fixed positions in x, y and z and moved through known arcs of motion. This allowed the comparison of the localisation output to the measured path of the crane, evaluating the SLAM algorithms against a ground truth map and location.

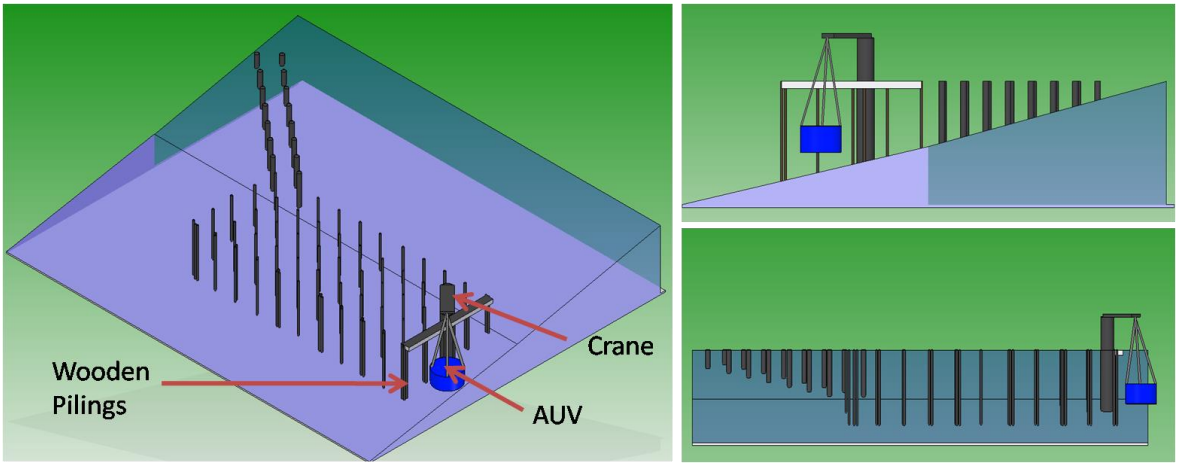

Figure 6.9 - The user generated to-scale map of the docks [340] shown with the sloping seabed from the shore to the deeper water. For scale, the rectangular section of the dock is approximately 31m long by 12m wide. The wooden pilings are approximately 0.3m in diameter and spaced orthogonally at approximately 3m intervals with double pilings along the deep water outside edge and triple pilings on the deep water corners. Cross pilings were present but are not shown in this map for clarity, The dock is aligned north-south with the boom lift crane at the northern most end of the dock facing the open ocean. The walkway leads out from the shore in a north-easterly direction.

Figure 6.10 - Deploying the iROV *SeaBiscuit* from the boom lift crane in British Columbia, Canada.

6.3.1 Generation of ground truth map

The ground truth map, initially in 2D, recorded the centre positions of all of the pilings from the upper level of the dock using measurements made from a square reference frame orientated with the dock and referenced to magnetic north. Figure 6.11 below shows the 2D dock piling map. The position of all features in the water in the vicinity of the dock was included, including the tree stumps, floating docks (including their range of movement on their moorings in the tide), dock ladders descending into the water and the shoreline and shallows.

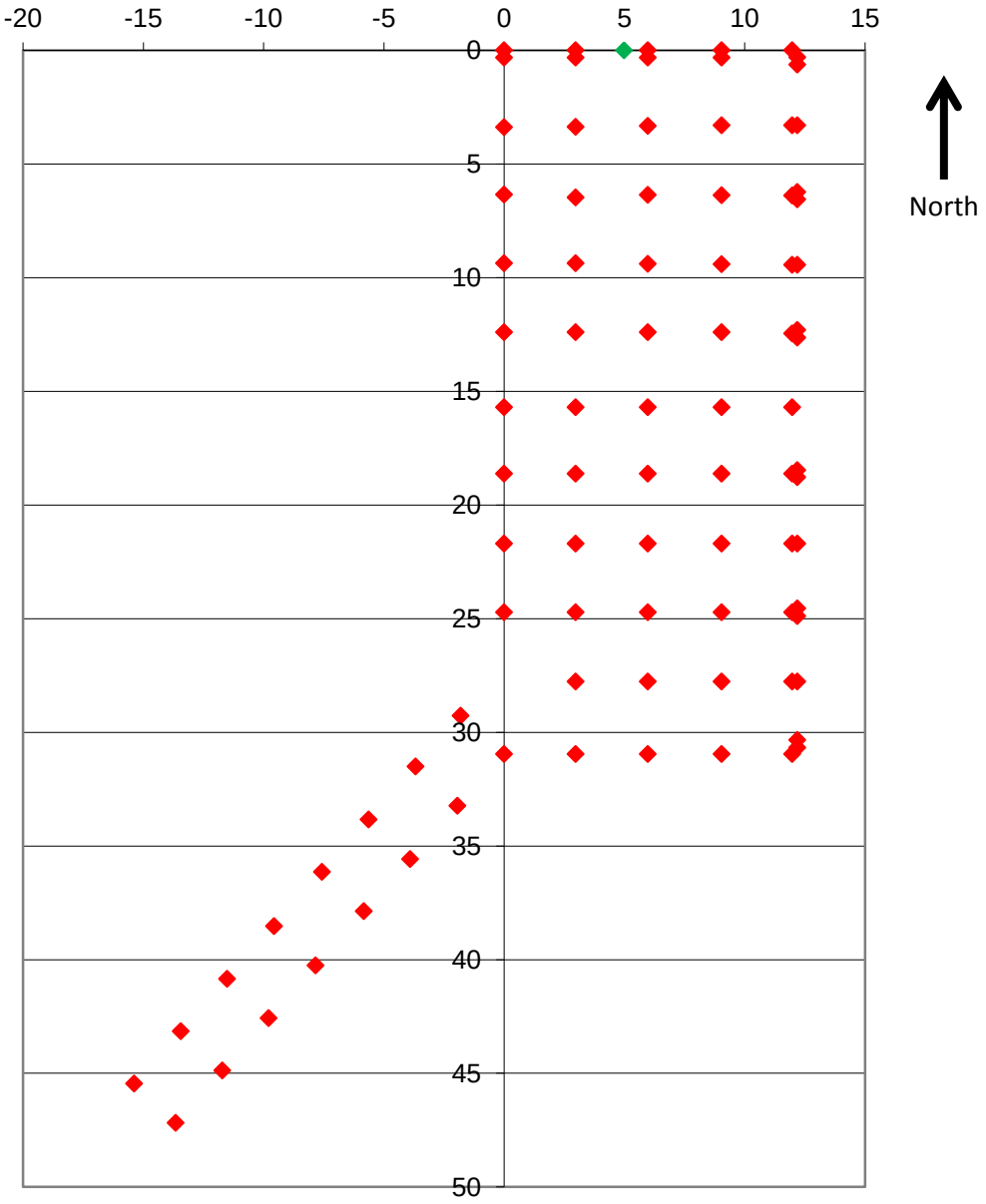

Figure 6.11 - The 2D map of dock piling centres observed at the upper dock level. Alternating double pilings on the outside deep water (right) edge and triple pilings on the deep water corners can be seen. The scale is in metres. The green marker seen at (4.78m, 0m) is the dock ladder.

This map was then extended to 3D by measuring the angle of key pilings to allow for non-vertical leaning pilings. Cross pilings used to brace the vertical pilings together with any half height pilings which had been broken off were also recorded. Measurements from water level using kayaks or a small inflatable boat as well as photographs taken at low tide with a known position reference in the field of view for later analysis and dimensioning were used to validate the map. An example of the structured image used for measurements verification is shown below in Figure 6.12. The effect of perspective was minimised by ensuring perpendicular observations.

Figure 6.12 - An example of the structured image used for verifying dimensions of the dock. A dimensioned marker with metre gradations highlighted in red was held off the dock edge with a series of pictures taken from water level around the dock periphery to ensure a perpendicular image to minimise perspective errors. Dimensions were then approximated in later analysis.

Water depth measurements were also taken at a series of key points around the survey area and the bathymetry interpolated in between. Finally, objects on the seafloor were recorded as far as possible, either by visual surveys using the iROV, or by diver surveys. These objects included discarded equipment and general dock paraphernalia which would either be seen on the sonar surveys and/or which would cause a ferromagnetic disturbance.

6.3.2 **Operation**

This section provides an overview of the operation of the vehicle off the dock demonstrating the performance of the SLAM algorithms. Although the cameras were used in iROV mode for manual corroboration of sonar targets and for user navigation, due to very poor visibility surrounding the dock, autonomous visual recognition of pilings was not feasible. The SLAM algorithms used only the sonar data for this application. Example data from the two sonar units is considered in turn.

6.3.2.1 Example 852 sonar data

Figure 6.13 below shows an example 10m range scan from the 852 sonar. A full 360° scan was performed while suspended on the boom lift crane to maintain a static x & y position together with pitch, roll and yaw angle as close to constant as possible. The raw sonar scan shows a ‘haze’ around the periphery of the scan caused by the diverging conical beam of the sonar interacting with the water surface; the vehicle was relatively close to the surface for this scan, at a depth of approximately 1m.

Several different scan ranges were available with the optimum range selected based on the task, operating conditions, and submerged depth (to reduce reflections from the water surface). The gain was also tuned experimentally based on the range, operating conditions and the expected maximum target strength. The standard method was to maximise the gain to improve detection without saturating the strongest target expected. Values were manually tuned for detecting kelp stipes and dock pilings.

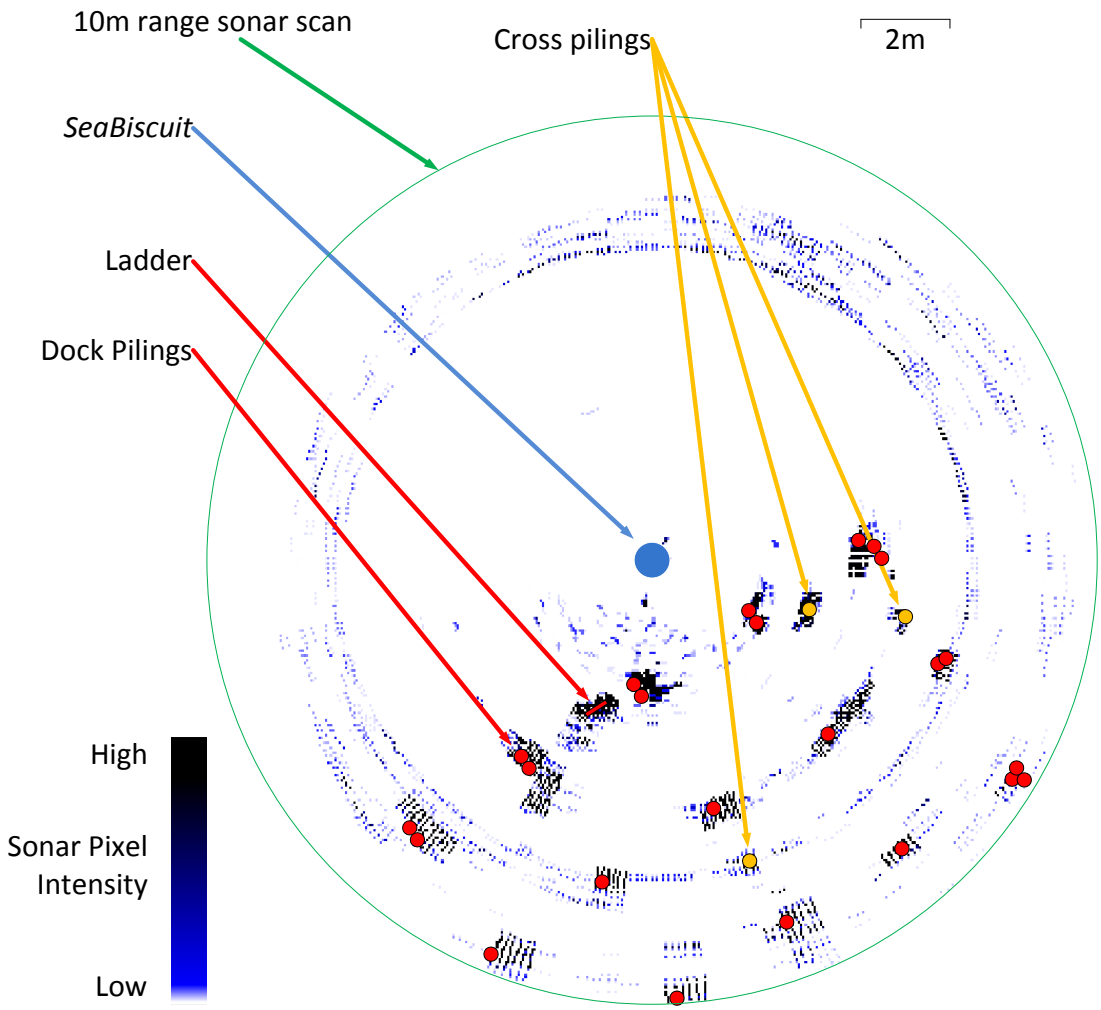

Figure 6.13 - An example 10m range (radius) 852 sonar scan showing a 360° scan around the vehicle. The strong returns with sonar pixel intensity as indicated correspond to dock pilings, spaced approximately 3m apart as shown by the ground truth dock map overlaid onto the sonar scan. Pilings and the dock ladder are shown in red, cross pilings incident on this horizontal plane in orange, and the position of *SeaBiscuit* in blue. Interactions with water surface around the periphery of the scan can also be seen.

The green outline in Figure 6.13 shows the 10m radius sonar scan centred on *SeaBiscuit*. The ground truth dock map was overlaid onto the sonar scan to aid identifying features. The grid of red circles are the dock pilings, correct in scale and position, with the presence of double or triple pilings to strengthen the dock shown, as well as one of the dock ladders.

The yellow circles indicate the typical form of cross pilings which form a diagonal brace between upright vertical pilings. If the cross piling was incident on the current altitude of the vehicle, it appeared as a piling in between the vertical pilings. Were the altitude of the vehicle to change, the apparent x and y position of these diagonal pilings would appear to vary. If SLAM was only being performed in 2D, these would be rejected as dynamic objects. However, when measuring altitude and optionally using the Delta T sonar to image the vertical water column as demonstrated in section 6.3.4, the diagonal nature of these cross pilings becomes apparent. The vehicle was able to utilise non-vertical targets as navigational landmarks rather than having to rely solely on vertical pilings.

Figure 6.14 below shows the same scan registered on the overall dock piling map. The scale is in metres and the ladder (marked as orange) can also be seen just below the x-axis 5m marker in between the regularly spaced pilings. A close correlation between the actual position of the dock

pilings and the sonar scan can be observed. The red overlay omits cross pilings, hence the position of some objects which are seen in between pilings on the sonar scan.

The small differences in position between the ground truth map observed across the sonar scan were caused by uncorrected water movements affecting the vehicle position throughout the 6 seconds required to complete a scan and by any inaccuracies in the ground truth map. These inaccuracies are quantified in section 6.3.5.

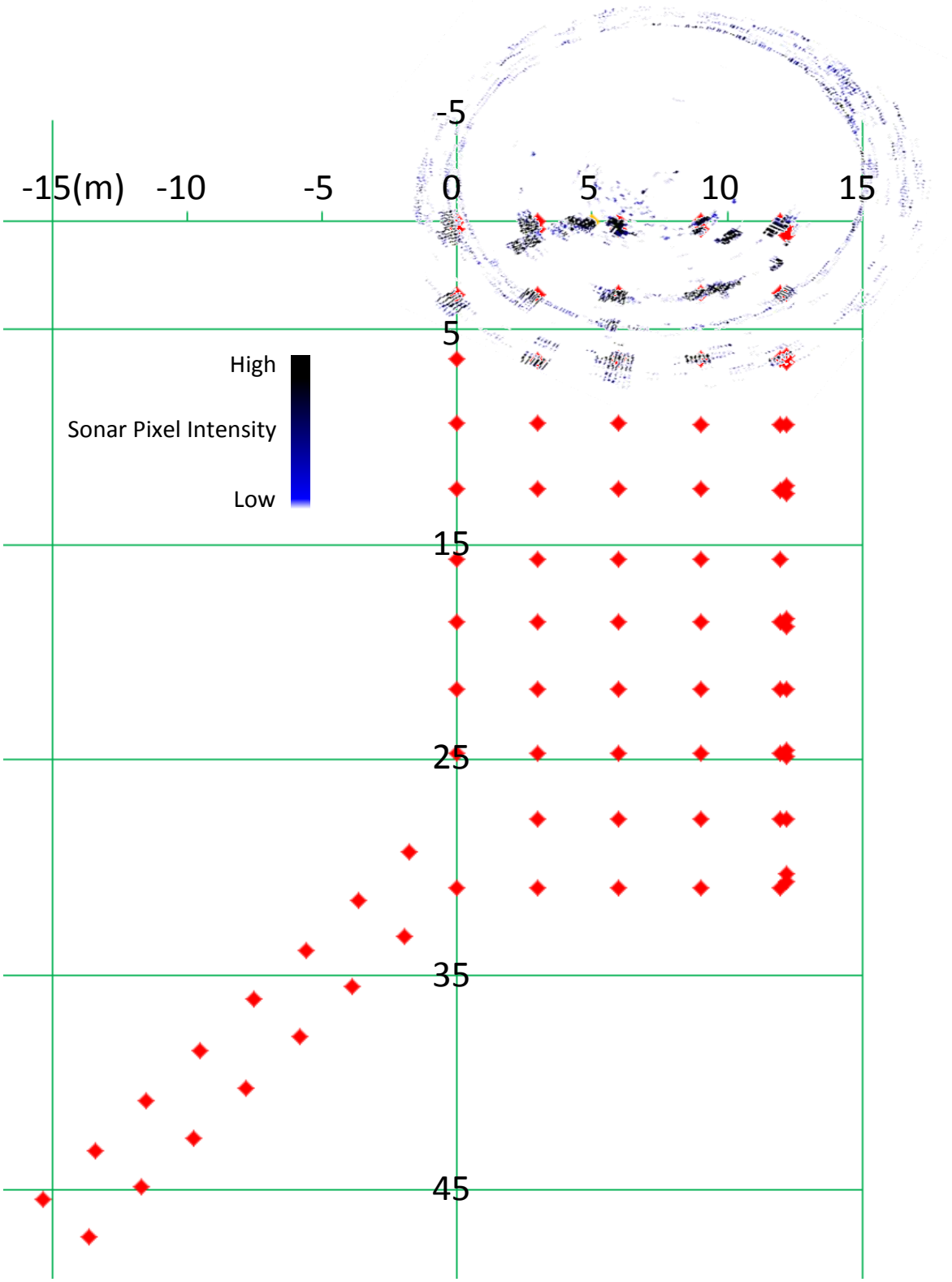

Figure 6.14 - The geometrically correct ground truth dock map was overlaid onto the 10m range (radius) sonar scan from Figure 6.13 showing the presence of multiple clustered pilings. Cross pilings are not indicated. The dock ladder is shown directly underneath the x-axis 5m label in position (4.78m, 0m) as an orange marker.

6.3.2.2 Example long range 852 sonar data

The following two figures show an example scan at a higher range setting of 30m instead of 10m. As before, the vehicle was held in a near-stationary position for the duration of the scan on the boom lift crane. Figure 6.15 shows the raw sonar scan with the approximate perimeter of the dock indicated by the green outline. At close ranges the pilings were clearly visible. As the range increased, occlusion, noise, surface interactions and the poorer spatial resolution caused by diverging beams meant the pilings were less distinct, yet still observable. At this higher 30m range, an area of shoreline and shallows can also be seen in the upper right corner of the scan.

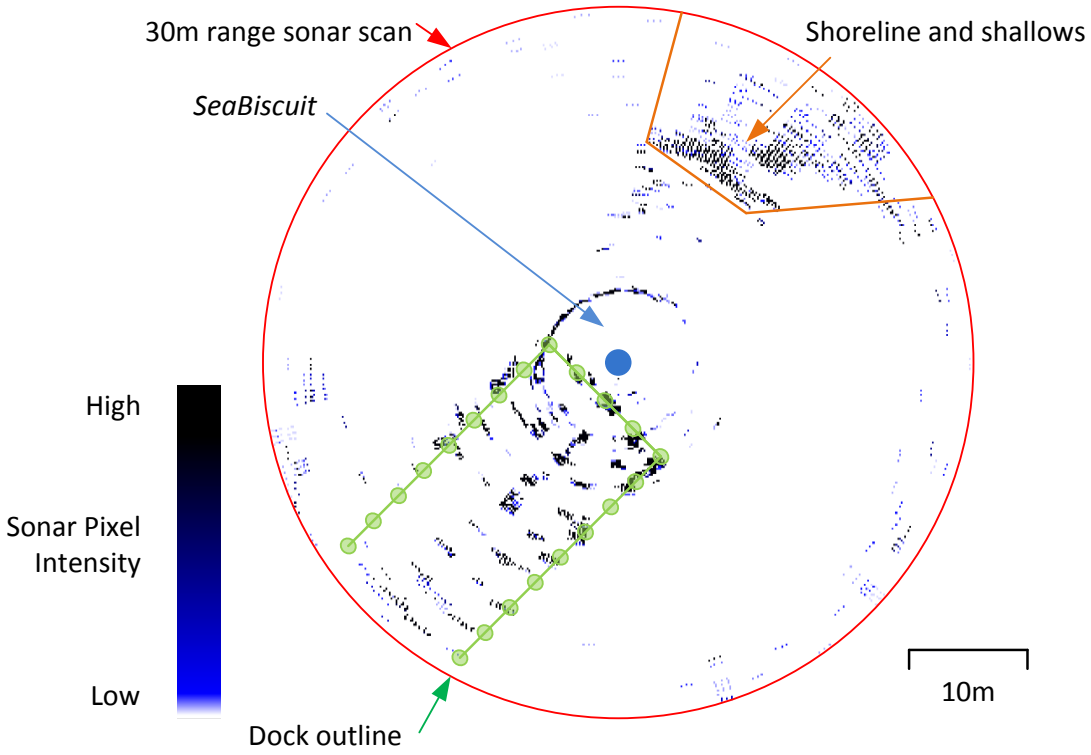

Figure 6.15 - An example 30m range 852 sonar image showing a 360° scan around the vehicle. The strong returns are the dock pilings shown approximately 3m apart, as indicated by the green outline. Double pilings and cross pilings can be seen. The return in the top of the image is an area of shallow water where the seabed was detected.

Figure 6.16 below shows the geometrically accurate map of vertical dock pilings superimposed onto the raw sonar scan. Disparity between the ground truth map and the scan was caused in part by unmapped cross pilings being imaged in between the vertical pilings. This was combined with the occlusion of vertical pilings from this slightly different scan position which caused vertical pilings to not be imaged, but cross pilings to appear as targets in between the mapped position of vertical pilings. The effect of this occlusion and cross pilings was most apparent in the upper pilings of the rightmost column. Techniques to mitigate the effects of occlusion by combining scans from different locations while rejecting cross pilings are covered in the following section on SLAM (6.3.3). Techniques to map cross pilings and other non-vertical targets using the Delta T sonar are then considered in section 6.3.4.

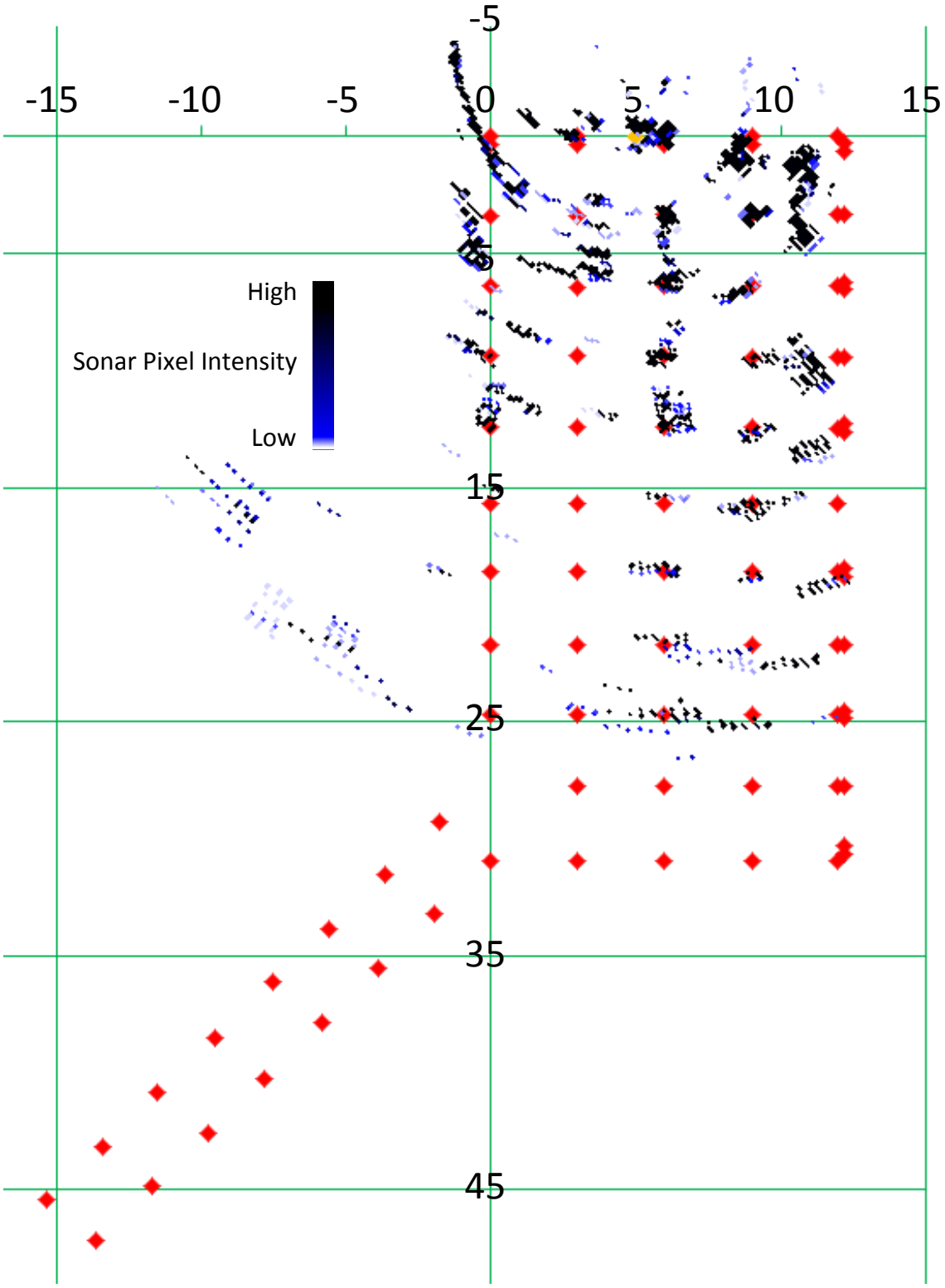

Figure 6.16 - The full geometrically accurate dock map was overlaid onto the 30m range (radius) sonar scan from Figure 6.15 showing the presence of multiple clustered pilings and the geometrically correct spacing of pilings. Cross pilings are not indicated. The dock ladder is shown directly underneath the x-axis 5m label in position (4.78m, 0m) as an orange marker.

Although utilising the higher range setting shown above (and further up to 50m maximum range) reduced the short-range accuracy and resolution, when conditions permitted, long range scans provided much more navigational data in a single scan. This reduced survey effort where conditions allowed, and generated a broad overview map to be later improved with several short range scans of areas of interest while avoiding wasting time generating high-resolution maps of areas with no landmarks.

When considering the 852 sonar scans, often the area of interest (the piling dock) only occupied a small sector of the sonar scan – thus large amounts of the 360° sonar scan and the full 6 second scan period were 'wasted' imaging empty space. This was largely because the scans shown were taken from the periphery of the dock looking inwards. This was improved by taking an initial single long range scan to identify the sector(s) of interest, and then focusing the sonar scan down from the full 360° to a smaller sector which was directed on the area of interest. This reduced the duration of each scan from the full 6 seconds, thus increasing survey speed.

Using the highly manoeuvrable mobile robot rather than a surface vessel allowed further benefits as the vehicle was able to enter the dock structure to scan from within. In this way, the internal structure was scanned at a low range to give a high scan resolution. Objects which might otherwise be occluded or obscured were discovered and scanned. This technique was applicable to both the dock mapping and the kelp mapping discussed later.

6.3.2.3 852 sonar image processing and feature extraction

Image processing algorithms were used to autonomously detect navigational landmarks from both the Delta T and 852 sonar, either in realtime or during post-processing for sonar-aided SLAM. Using the algorithms described in section 4.6.6, the seabed was detected and the water surface calculated from the vehicle attitude and submerged depth. The position and characteristics of useful navigational landmarks were then extracted from the midwater region of interest (ROI). To demonstrate the sonar image processing algorithms, the vehicle was positioned using the crane off the piling dock in three survey positions as shown in Figure 6.17 below.

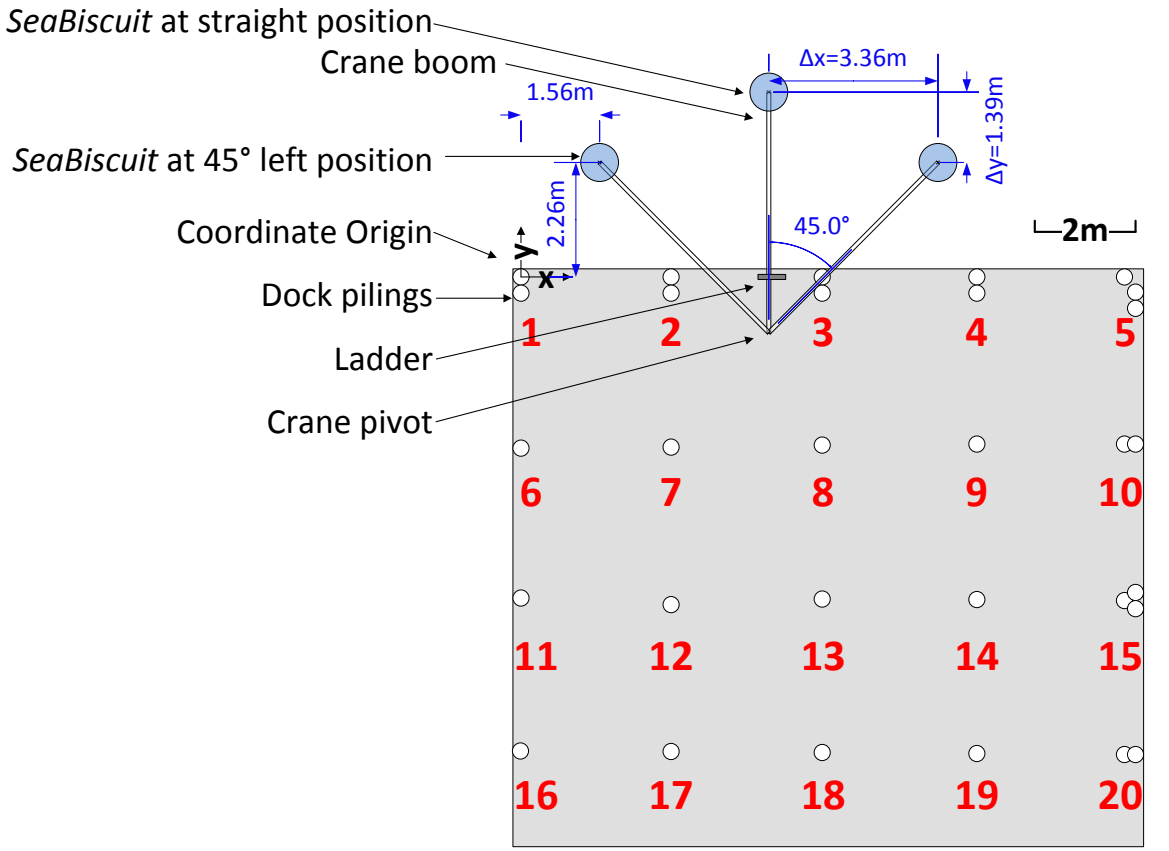

Figure 6.17 - A schematic plan view of the dock pilings (geometrically accurate) with the x and y position of the crane hoist used to hold *SeaBiscuit* at each scan position, 45° apart. The coordinate system origin was defined as the centre of the top left piling as shown. The positive y axis was aligned with magnetic north. Pilings were numbered as shown. When several pilings were clustered in a single position, they were numbered as a single feature.

Figure 6.18 below shows the 852 sonar scans from each survey position. By inspection, several features can be seen in each of the raw scans. The series of images demonstrate the algorithm steps to extract and identify useful features while rejecting the noise present in the image. A range (radius) of 20m and a gain of 15dB were used. The range and gain were tuned in conjunction with the image processing algorithms, operating conditions and expected target strengths. If the gain was set too high, then the scan would be saturated and the intensity of strong returns clipped. Alternatively, if the gain was set too low, then features would be missed. Instead, the aim was to ensure that the strongest expected return used the full intensity scale so that minor details and weak returns would have the best chance of being detected.

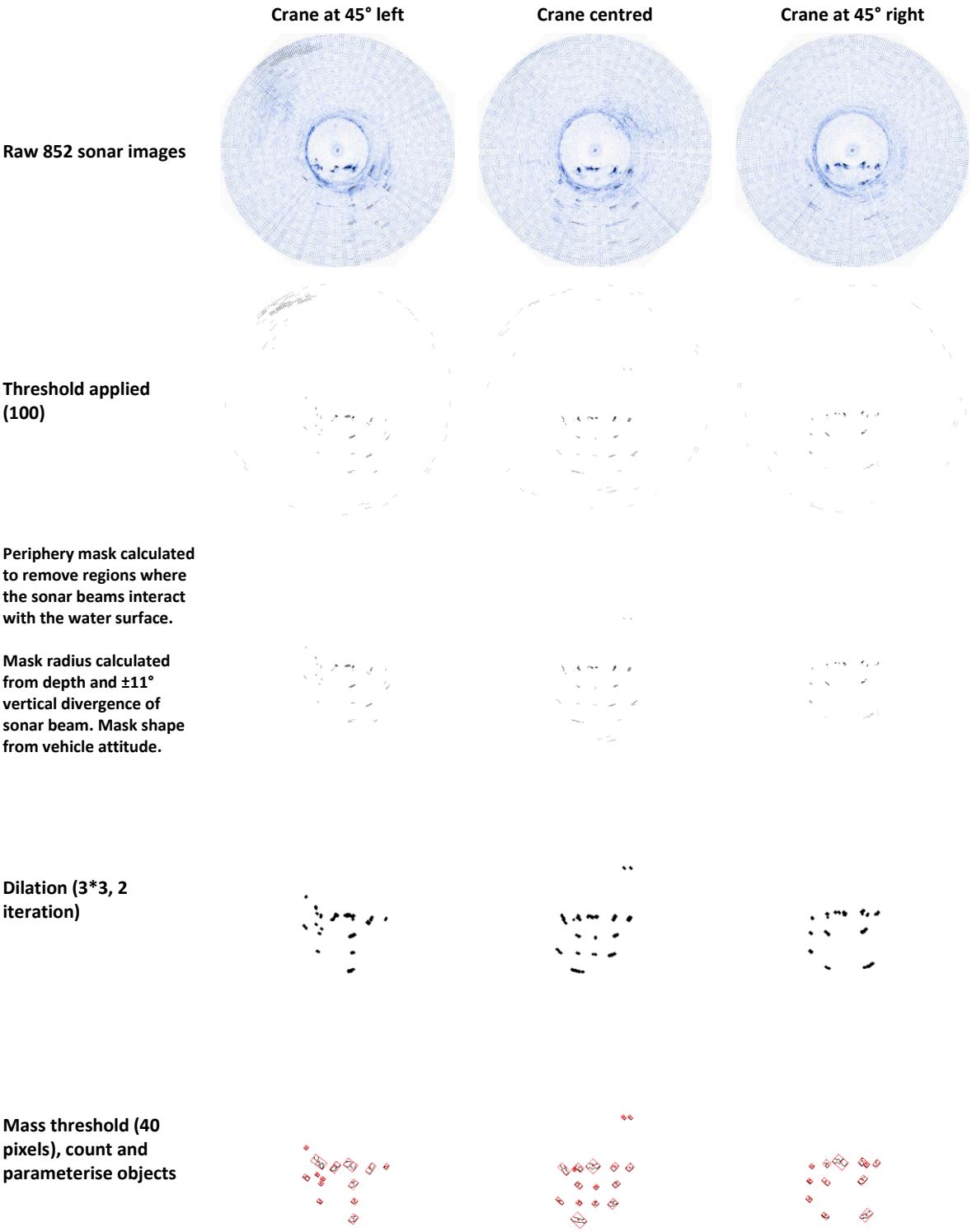

Figure 6.18 - A of three example raw 852 sonar images captured off the end of the piling dock at a range (radius) of 20m and a gain of 15dB to demonstrate the image processing and feature extraction.

The final step in Figure 6.18 above parameterised the scan, labelling each feature, and recording a number of characteristics for each feature (detailed later). Several features which resemble the dock pilings can be seen upon enlarging each of the parameterised scans in turn. Figure 6.19 below shows the parameterised scan from the centre station, registered on the ground truth map of vertical dock pilings using the vehicle navigation sensors. The detected sonar targets are outlined in black and labelled with a red bounding rectangle and a red letter.

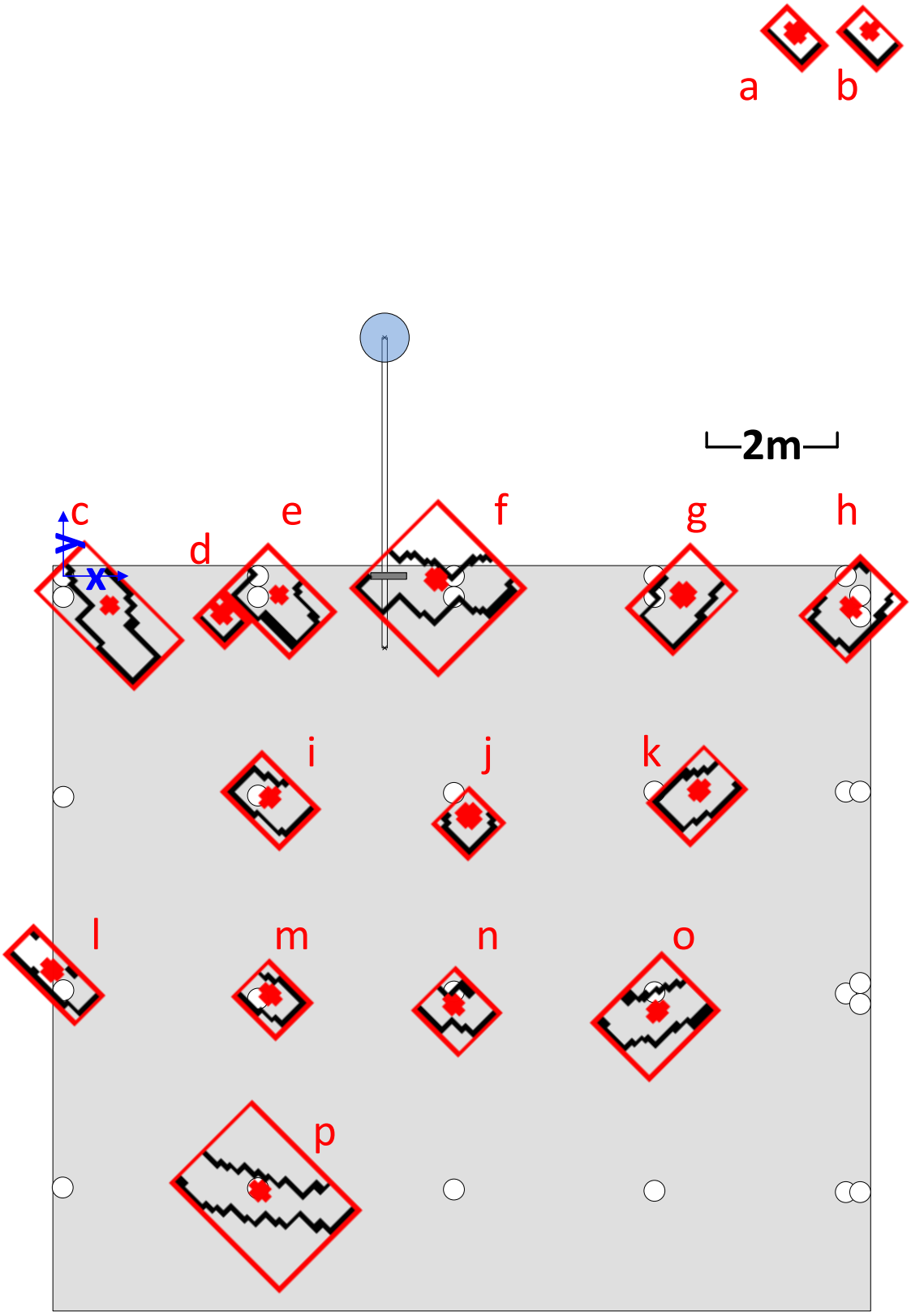

Figure 6.19 - The dock pilings detected from the centre (straight) 20m range sonar scan are shown in black and the geometric dock map is overlaid for comparison. Red bounding rectangles identify each detected sonar target with an identifier and the centre of mass of each target is shown with a red dot. By inspection, there is a good correspondence between the sonar scan and the ground truth map.

By inspection, the agreement between the dock pilings extracted from the sonar scan and the geometric map of the dock was good over approximately 15m of the 20m radius scan. The accuracy is quantified in the following section on SLAM. The dock ladder was also imaged, included in feature ‘f’. The effects of occlusion, causing some pilings to not be imaged, can be seen. The range (radius) was set to 20m and the entire plot area is 500*500 pixels, thus making each metre equal to 12.5 pixels (a resolution of 8cm).

Two targets, labelled ‘a’ and ‘b’, were detected at a range of approximately 8m in the upper right corner of the scan. These targets were transient, and appear only in the scan taken from the straight position, despite the left and right scans imaging the same volume of water. They were assumed to either be objects in the water column, or noise from water surface interactions caused by operating close to the surface combined with either uncorrected vehicle attitude deviations, or wash from a passing boat. Although the SLAM algorithms demonstrated in the following section removed transient features using voting techniques, these spurious features were left in the scan here to demonstrate the characteristics of noise features, both in the raw data, and when spurious features propagate through to the extracted features.

Although the dock map continues much further south beyond the feature identified as ‘p’, these pilings were not detected in this scan. This was partly due to occlusion and the long range which caused weaker returns, but more so, the close proximity of the sonar to the water surface. At this long range, a large amount of the beamwidth was interacting with the water surface and weaker returns were obscured by surface noise.

The elliptical shape of several of the targets was partly caused by clusters of dock pilings in close proximity. Half-height broken pilings which do not extend above the waterline were not included in the ground truth map. Additionally non-vertical pilings, such as cross-pilings appeared as ellipses in the sonar scan. The shape of pilings can also be distorted by uncorrected vehicle yaw deviations from one ping to the next. For example, if the vehicle rotated in the *opposite* direction to the sonar scan and this was not detected, targets would be overestimated, such as target ‘p’ above. An undetected turn in the *same* direction as the sonar scan would cause targets to be underestimated.

A positional error was also unavoidable between the true centre of a piling and the measured centre of the detected sonar target. For any object of non-negligible thickness, the sonar could not measure the true depth of the object and the centre of the recorded feature appeared closer to the sonar that its true position. In effect, the closest edge of the target was being imaged, thus the error was greater for clusters of pilings or larger targets, for example target ‘c’ above. As seen in the maps compiled from several scans in the following section, this was corrected by scanning targets from several different positions to estimate the true target centre.

The parameterised results of the scan in Figure 6.19 are shown in Table 6.1 below:

Table 6.1 - Output characteristics of sonar features from the centre scan location. Explanatory notes follow.

Identifier:	Correspondence (LM #):	Range (m):	Bearing (°):	Actual (ground truth) measurement:		Position Error:		Area (pixels):	Orientation (°):	Aspect Ratio:	Comment:
				Range (m):	Bear-ing (°):	(m):	(%):				
a	None	7.86	53.1					70	135	0.7	Spurious anomaly
b	None	8.79	57.5					70	135	0.7	Spurious anomaly
c	1	5.87	226.0	6.22	232.2	0.74	12.6	222	153	0.5	
d	2	4.56	206.7	4.28	207.0	0.28	6.2	49	151	1	Targets combined (mean) to piling #2
e								165	151	0.706	
f	3	3.76	167.9	3.95	164.5	0.30	7.9	279	86	1	Large error, includes ladder
g	4	6.01	130.6	5.62	133.7	0.50	8.3	174	28	1.417	
h	5	8.22	120.0	8.22	118.8	0.17	2.1	171	38	1.333	
i	7	7.22	194.1	7.27	195.5	0.18	2.5	117	117	0.714	
j	8	7.41	170.0	7.05	171.4	0.40	5.4	75	180	1	
k	9	8.41	145.2	8.10	149.3	0.67	7.9	141	64	1.364	
l	11	10.92	207.9	11.14	206.2	0.39	3.6	146	133	0.421	
m	12	10.19	190.0	10.30	190.9	0.19	1.9	87	111	0.818	
n	13	10.22	174.1	10.07	174.0	0.15	1.5	101	96	0.917	
o	14	11.10	158.0	10.84	157.6	0.27	2.4	187	72	1.357	
p	17	13.18	188.4	13.16	188.5	0.03	0.2	275	102	0.75	
					Average:	0.33	4.8				

In Table 6.1, the **identifier** corresponds to the red labelling of detected targets in Figure 6.19. The sonar scan was registered in the world coordinate system at the x and y coordinates determined by the position of the crane hoist at the centre position. Each ping of the 852 scan was registered in yaw angle using the vehicle navigation sensors. The **correspondence** describes which vertical piling the sonar target matches, according to the numbering scheme in Figure 6.17 previously. There was little ambiguity in the manually established correspondences due to the good matching between sonar scan and ground truth map.

The **range** and **bearing** column of Table 6.1 provide the range and bearing to the centre of mass of each feature detected, indicated by the red spot at the centre of each target. The range was measured relative to the vehicle position. The bearing was registered in the global coordinate system, with every ping corrected for vehicle yaw angle (and attitude) when the scan was taken. The bearing was calculated w.r.t. magnetic north, where clockwise angles increase from 0° (north) along the positive y-axis, as indicated on the figure.

The **actual range** and **actual bearing** column indicate the distance to the matching piling on the ground truth map, again with range relative to the assumed vehicle position on the crane, and bearing w.r.t. magnetic north. The mean (centre) position of multiple clustered pilings was used. Hence, the **position error** lists the difference in metres, and as a percentage of the true range, between the observed position on the sonar and the true position of the target on the ground truth map, both relative to the assumed vehicle position on the crane hoist.

The **area**, **orientation** and **ellipse ratio** were also recorded for each sonar target detected. The **area** was measured in pixels, used for relative comparisons at the same range and gain configuration. Each feature was approximated by an ellipse during parameterisation. The **ellipse ratio** defined the ratio of the long axis of the ellipse to the short axis, so a circle was defined as 1 and a long thin ellipse with a ratio that was noticeably higher or lower than 1. The **orientation** defined the orientation of the long axis of the ellipse over the range 0-180° in the world coordinate system w.r.t. magnetic north.

In summary, the accurate registration of the sonar scan with the ground truth map seen in Figure 6.19 was confirmed, with correspondences established for all sonar targets except features ‘a’ and ‘b’ and an average position error of 0.33m, or 4.8%. Features ‘d’ and ‘e’ were manually corresponded to piling #2 due to their close proximity.

The wide shape of feature ‘f’ was caused by the dock ladder being included in this target, as shown in Figure 6.19. The position errors of >0.5m seen for features ‘c’, ‘g’, and ‘k’ were most likely caused by cross pilings and/or the non-vertical angle of the main pilings. The larger area of feature ‘p’ was caused in part by the spreading of the sonar beam in both the vertical and horizontal direction with range, causing a larger volume of water to be insonified, and hence a larger proportion of the piling and surrounding cross pilings to be detected. In general, pilings off the central axis of the dock (the central column) were imaged over a greater area caused by the angle of the cross pilings relative to the sonar scan.

The scans presented here were taken in calm water with the x, y and z position constrained by the crane, and corrected for vehicle attitude. However, a small uncorrected movement was inevitable and is quantified later in section 6.3.5.2.1, together with an estimation of the uncertainty associated with the method and ground truth map.

The same techniques were applied to the scans taken with the crane at 45° left, as shown below in Figure 6.20 and Table 6.2, and at 45° right, as shown in Figure 6.21 and Table 6.3.

From the left station, as shown in Figure 6.20, fewer landmarks were detected (10 total) with a 50% higher positional error than the straight position. This was partly caused by less of the sonar scan area overlapping the dock, and by the greater effects of occlusion at this closer position. Imaging targets ‘c’, ‘e’ and ‘d’ (which included the dock ladder), all at an oblique angle caused large regions of the cross pilings to be detected. These elliptical returns shown below occluded the majority of the west side of the dock, as seen in the figure by ray tracing the sonar beams. Targets ‘a’, ‘g’ and perhaps part of ‘b’ and ‘h’ were all in the shallow region of water to the east. A floating dock anchored there, together with large areas which dried out at low tide caused these additional targets, as evident in the original raw sonar scan at the left position in Figure 6.15. Target ‘i’ by inspection appeared to be a cross piling, distinct from target ‘j’ over LM6. However, due to its close proximity to target ‘j’ (0.97m separation) the two targets were grouped and an average position recorded, hence the very high (0.97m or 18.8%) positional error to the ground truth map. If the targets were not grouped, and ‘i’ was discounted as a cross piling, then the positional error of ‘j’ on its own became 0.63m or 11.3%, with a corresponding slight reduction in the average positional error for the right hand scan, from 0.43m to 0.39m.

In the right hand scan shown in Figure 6.21, as with the left hand scan, fewer targets (11 total) were detected with a similar 50% higher positional error than the centre position. For the same reasons as the left hand scan, this was most likely due to the oblique angle, occlusion and less of the sonar scan overlapping the dock. Again, the ladder was imaged, and the effect of beam spreading causing apparently larger targets at high ranges can be seen. Target ‘e’ by inspection appears to be a cross piling as it was distinct from target ‘d’ over LM4. However, due to its close proximity to target ‘e’ (0.97m separation) the two targets were grouped and an average position recorded, hence the very high (0.8m or 28.1%) positional error to the ground truth map. If the targets were not grouped, and ‘e’ was discounted as a cross piling, then the positional error of ‘d’ on its own became 0.51m or 21.4%, with a corresponding slight reduction in the average positional errors for the right hand scan from 0.47m to 0.44m.

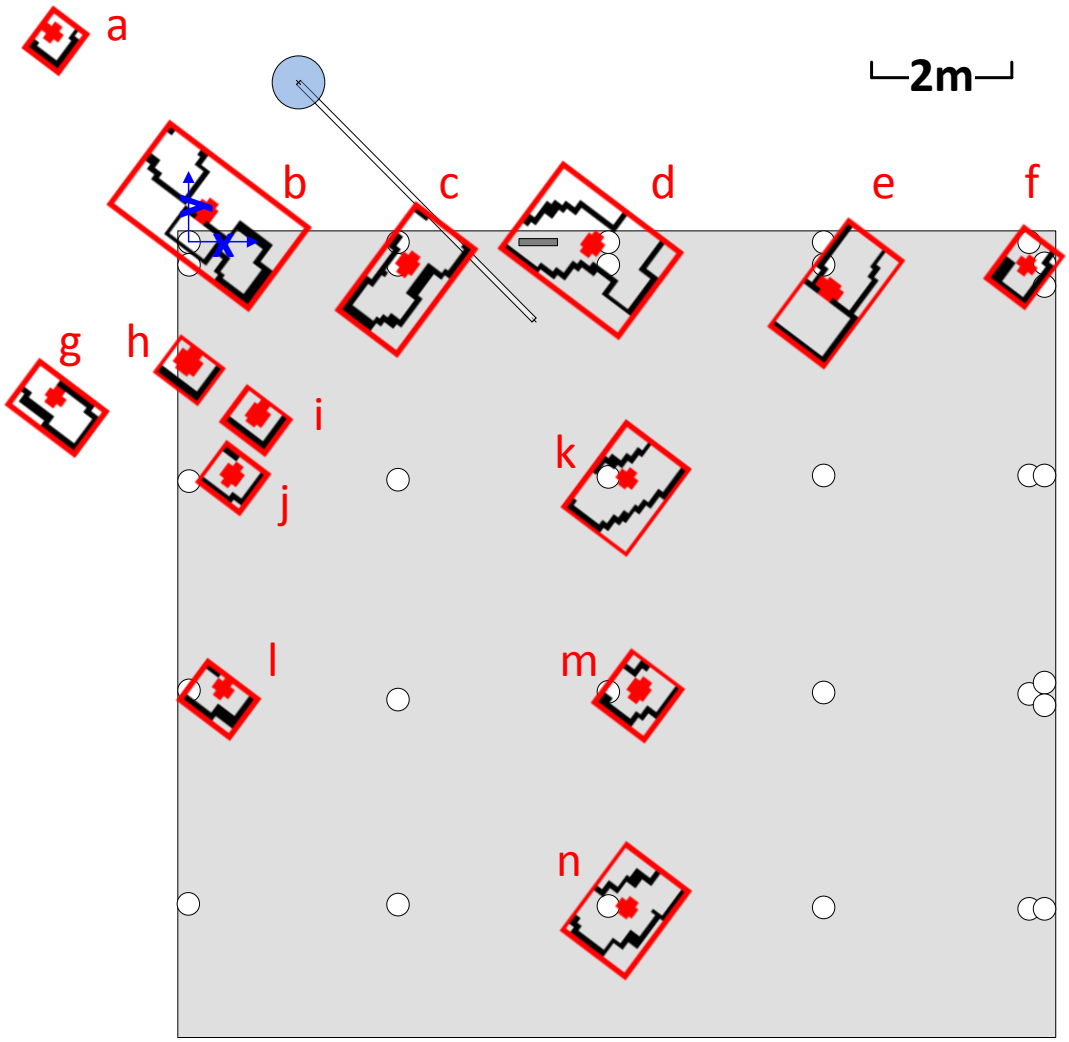

Figure 6.20 - The detected features from the 20m range dock scan with the vehicle aligned at 45° left on the crane are shown in black and the geometric dock map is overlaid for comparison. Red bounding rectangles identify each detected sonar target with an identifier and the centre of mass of each target is shown with a red dot.

Table 6.2 - Output characteristics of objects detected in the scan from the vehicle aligned at 45° left on the crane.

Identifier:	Correspondence (LM #):	Range (m):	Bearing (°):	Actual (ground truth) measurement:		Position Error:		Area (pixels):	Orientation (°):	Aspect Ratio:	Comment:
				Range (m):	Bear-ing (°):	(m):	(%):				
a	None	3.59	281.7					69	34.2	1.125	Shallows & floating dock
b	1	2.25	216.3	2.88	212.8	0.65	28.8	254	165.2	0.6	Large error, includes floating dock
c	2	2.98	148.7	2.80	149.6	0.19	6.2	235	57.2	1.769	
d	3	4.78	118.5	5.04	118.7	0.26	5.5	318	121.2	0.731	Large error, includes ladder
e	4	8.12	111.1	7.87	107.9	0.51	6.3	237	50.2	1.917	
f	5	10.71	104.0	10.87	103.7	0.17	1.6	82	42.2	1.375	
g	None	5.62	218.1					115	154.2	0.6	Shallows & floating dock
h	None	4.22	201.7					63	141.2	0.778	Cross piling
i	6	5.16	188.4	5.85	195.5	0.97	18.8	63	141.2	0.778	Targets combined to include cross piling ‘i’
j								75	128.2	0.8	
k	8	7.30	140.0	7.12	141.6	0.27	3.7	189	80.2	1.286	
l	11	8.61	187.1	8.74	190.3	0.50	5.8	82	132.2	0.727	
m	13	9.87	150.4	9.69	152.9	0.46	4.7	237	50.2	1.917	
n	18	12.57	158.0	12.46	159.2	0.28	2.3	182	82.2	1.286	
					Average:	0.43	8.4				

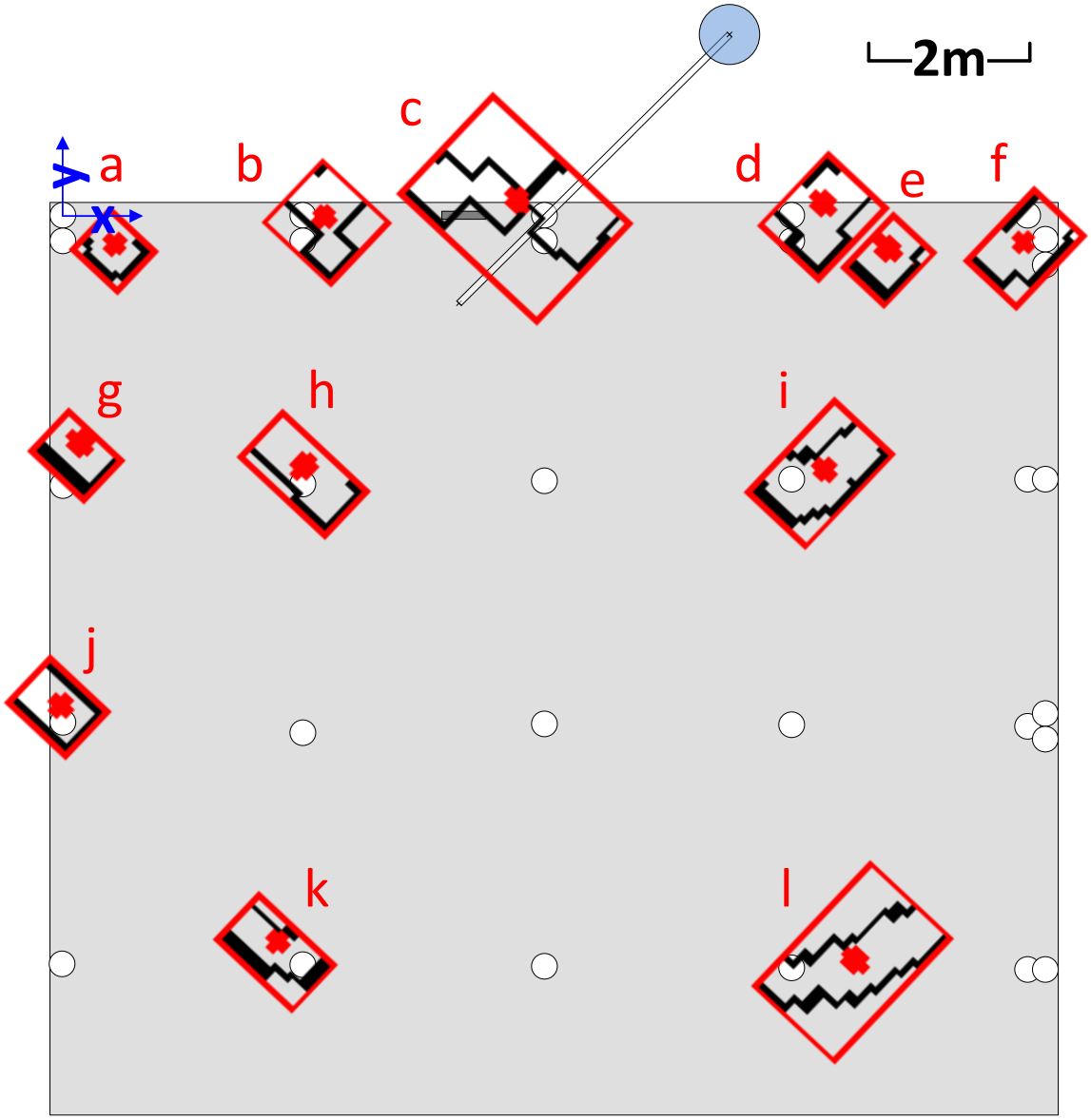

Figure 6.21 - The detected features from the 20m range dock scan with the vehicle aligned at 45° right on the crane are shown in black and the geometric dock map is overlaid for comparison. Red bounding rectangles identify each detected sonar target with an identifier and the centre of mass of each target is shown with a red dot.

Table 6.3 - Output characteristics of features detected in the scan from the vehicle aligned at 45° right.

Identifier:	Correspondence (LM #):	Range (m):	Bearing (°):	Actual (ground truth) measurement:		Position Error:		Area (pixels):	Orientation (°):	Aspect Ratio:	Comment:
				Range (m):	Bearing (°):	(m):	(%):				
a	1	8.07	251.2	8.62	253.7	0.66	8.2	84	158.7	0.9	
b	2	5.52	245.8	5.82	245.5	0.30	5.5	128	176.7	0.929	
c	3	3.33	231.8	3.34	223.5	0.48	14.5	290	107.7	0.714	Large error, includes ladder
d	4	2.85	146.5	2.54	162.3	0.80	28.1	146	31.7	1.25	Targets combined to include cross piling 'e'
e								85	40.7	1.375	
f	5	4.47	125.2	4.63	123.7	0.20	4.5	132	57.7	1.5	
g	6	9.54	237.7	10.02	235.7	0.59	6.2	88	136.7	0.727	
h	7	7.54	224.5	7.72	223.3	0.24	3.2	142	140.7	0.529	
i	9	5.56	167.7	5.61	172.1	0.43	7.8	185	61.7	1.583	
j	11	11.79	224.8	11.94	223.9	0.24	2.0	108	136.7	0.75	
k	17	12.62	206.4	12.78	204.5	0.45	3.6	114	123.7	0.6	
l	19	11.66	172.4	11.70	176.2	0.78	6.7	246	71.7	1.529	
					Average:	0.47	8.2				

Finally to conclude the example 852 sonar image processing example, Figure 6.22 below shows all three scans registered on the same plot as different colours, as a comparison between the information gathered in the parameterised scan from each of the three locations. The targets in a direct line of sight and close to the vehicle were reliably detected from all three positions. However, the effects of occlusion and observing the non-vertical cross pilings from different angles can be seen. The following section uses SLAM techniques to integrate the information gains from several scans to compile a more reliable and more complete map, while simultaneously allowing vehicle localisation.

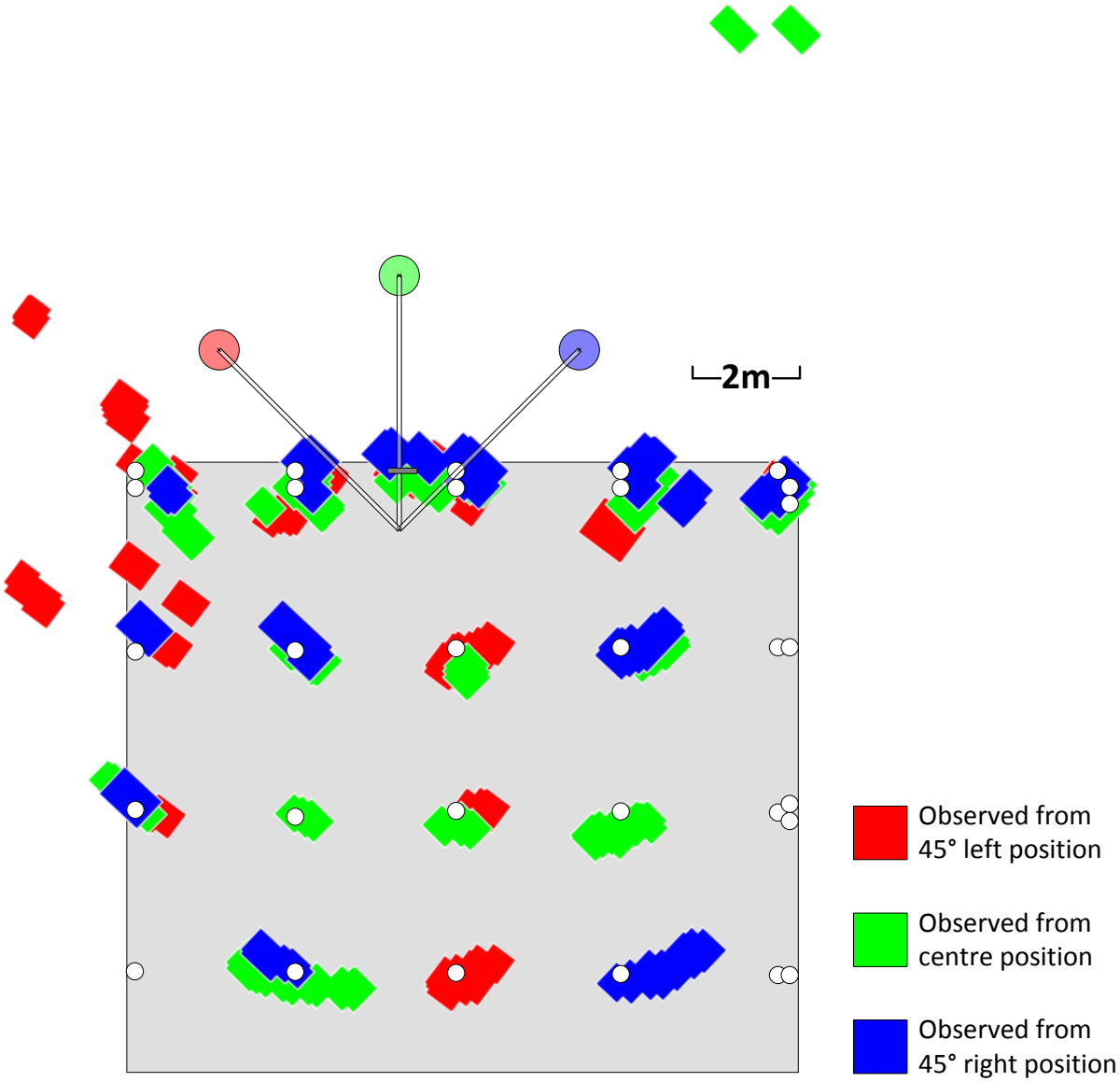

Figure 6.22 - The scans from all three stations are registered on the same plot. Targets observed from the 45° left position are shown in red, from the centre position in green, and finally from the 45° right position in blue, demonstrating the information gains and mitigation of occlusion from combining several scans from different positions.

6.3.3 SLAM operation and results

The piling dock, with its regular and repeated semi-uniform targets, provided an ideal development environment to test the SLAM algorithms in open water conditions. The ground truth dock map allowed a quantified evaluation of the mapping accuracy, while the geometric model of the crane allowed the position of the vehicle to be continually monitored simultaneously. With the above demonstration of sonar image processing and feature extraction

algorithms, the following sections utilise this information to perform sonar-aided localisation and mapping in 2D.

The measurements obtained from each of the three scans in the previous section were used to run the SLAM algorithm step-by-step in an offline mode. The vehicle began at 45° left, then moved to the centre position, before finally to 45° right to demonstrate localisation against the ground truth of crane position and mapping against the user generated dock map (without cross pilings). The results were then compared back to the geometric dock map and the known change in position to evaluate the performance of the algorithms.

6.3.3.1 Landmarks observed

Table 6.4 below shows the observed features at each of the scan positions, according to the numbering of dock pilings shown previously in Figure 6.17.

Table 6.4 - The observed features at each of the three scan positions, using the piling numbers in Figure 6.17. The observed range and bearing in the world coordinate system is shown (0 degrees is along the positive y-axis, that is north). Grey entries were not observed, white landmarks observed from one position only, and orange rows highlight landmarks observed from more than one location.

LM List:	45° Left:		Straight:		45° Right:	
	Range (m):	Bearing (°):	Range (m):	Bearing (°):	Range (m):	Bearing (°):
1	2.25	216.3	5.87	226.0	8.07	251.2
2	2.98	148.7	4.56	206.7	5.52	245.8
3	4.78	118.5	3.76	167.9	3.33	231.8
4	8.12	111.1	6.01	130.6	2.85	146.5
5	10.71	104.0	8.22	120.0	4.47	125.2
6	5.16	188.4			9.54	237.7
7			7.22	194.1	7.54	224.5
8	7.30	140.0	7.41	170.0		
9			8.41	145.2	5.56	167.7
10						
11	8.61	187.1	10.92	207.9	11.79	224.8
12			10.19	190.0		
13	9.87	150.4	10.22	174.1		
14			11.10	158.0		
15						
16						
17			13.18	188.4	12.62	206.4
18	12.57	158.0				
19					11.66	172.4
20						

In Table 6.4 above, for each scan position, a different set of landmarks were observed. The landmarks closer to the vehicle (lower LM numbers) were reliably observed from all stations, with fewer detections at higher ranges. Of importance are the rows highlighted in orange, where a landmark was observed from multiple positions. These multiple observations of the same landmark from different locations were the most useful to localisation; if the SLAM algorithm could establish that the landmark observed in the current scan corresponded to one which had been previously observed, then the robot could use this to estimate a change in position.

6.3.3.2 Establishing landmark correspondences

In section 5.3.4.2, the maximum likelihood (ML) estimation method of establishing landmark correspondences was introduced. Using this method, the position of a newly observed landmark was converted into the world coordinate system and associated to the closest previously-mapped landmark, within a threshold distance (α). This threshold distance provided robustness to realworld sensing inaccuracies. If no previously mapped landmark was detected within the threshold α, then a new landmark hypothesis was created and the new landmark was added to the map. In section 5.5, the ML estimation technique was extended to include landmark signatures and demonstrated in simulation.

However, in section 6.3.2.3, the signature variables extracted for the dock pilings (sonar target characteristics, e.g. area, orientation, ellipse ratio) were deemed too variable with the angle at which the target was imaged. Additionally, the pilings were too similar for the signature variable to be used to establish landmark correspondences. Instead, as Figure 6.22 previously shows, establishing landmark correspondences using relative position alone provided little ambiguity for navigation around the dock.

Taking the three scans presented in Table 6.4 as an example, the vehicle began with no landmarks recorded on its map. The landmarks from scan 1 (the left scan) were initially recorded relative to the vehicle's best estimate of its position at that time. In the open ocean, this could be a surface GPS fix before diving, or if the vehicle was already submerged, the map could be registered in a local coordinate system until surfacing. While in the local coordinate system, full mapping and navigation is still possible, the map is just not registered in a realworld latitude and longitude. In the case of the example above, the initial position estimate was based on the crane position at the left station, thus the relative positions of the landmarks observed from the left scan were recorded on the map.

When integrating the landmarks observed from scan 2, again the relative range and bearing to each landmark was converted to the world coordinate system using the predicted new position of the vehicle. In the open ocean, a combination of the onboard INS, dead-reckoning and GPS updates can be used for the predicted position. For the example here, the predicted new position was the modelled crane centre position. The second stage of the EKF SLAM algorithm later *updated* the map and position with the updated position estimate using the mapped measurements, after data association.

With the second set of landmarks registered using the estimated current vehicle position, the distance from each newly observed landmark to all existing mapped landmarks was considered in turn. If less than the threshold distance (α), the landmark was associated to its nearest neighbour, if greater than α, then a new landmark was added to the map.

The value of α was tuned experimentally for the typical landmark spacing, landmark detection and localisation and mapping uncertainty for operating around the dock. The typical sonar measurement error included the vehicle position estimate uncertainty, as a position estimate is required to register relative range and bearing sonar measurements to the world coordinate system. A value of α=1m was found to provide robustness to sensing uncertainty, while providing reliable mapping results given the typical piling spacing of 3m, excluding cross pilings. Recalling Table 6.1, Table 6.2 and Table 6.3 previously, the position error (the difference between the measured and mapped position of landmarks) was always less than 0.97m with an average of 0.39m, reinforcing the suitability of a value of α=1m. The minimum position difference between landmarks correctly rejected from correspondence to mapped targets (including spurious targets,

cross-pilings, etc.) was 1.22m (feature 'e' on the right hand scan), therefore demonstrating that no-false correspondences were created using a value of α=1m for the example scans above.

When evaluating sonar targets obtained in a single scan, before attempting correspondence to previously mapped targets, the value of α=1m was used to group nearest neighbour targets with a separation of <1m into a combined target. In the example scans above, targets 'd' and 'e' were combined in the centre scan in Table 6.1 and also in the right hand scan in Table 6.3 and targets 'i' and 'j' were combined in the left hand scan in Table 6.2. In each case, targets with a small separation distance (0.92, 0.97 and 0.94m respectively, all <α) were observed.

To the user, by inspection these were most likely either cross pilings, or pilings from the same cluster with either a slight separation, or disjointed in the sonar scan and could easily be removed from the correspondence with a resulting increase in both map and later localisation accuracy. However, to the correspondence algorithm with a separation distance of <α, these were corresponded to their nearest neighbour, rather than recording a new feature representing the cross pilings on the map. Combining features in the raw scan with a separation of <α before establishing correspondences both reduced computational complexity and avoided maintaining a map of several features representing the same landmark.

Figure 6.23 below shows an example for associating landmark 8 between two scans. In the figure, a landmark observed was registered into the map coordinate system using the new predicted vehicle position. The distance to all nearest neighbours of existing mapped landmarks was evaluated. If the newly observed landmark was closer to a previously mapped landmark based on the current predicted vehicle position than the threshold α, then it was associated to its nearest neighbour. The later *update* step of the EKF SLAM algorithm then combined the previous and new position estimates of LM8 and updated the map accordingly. The figure caption provides a full explanation.

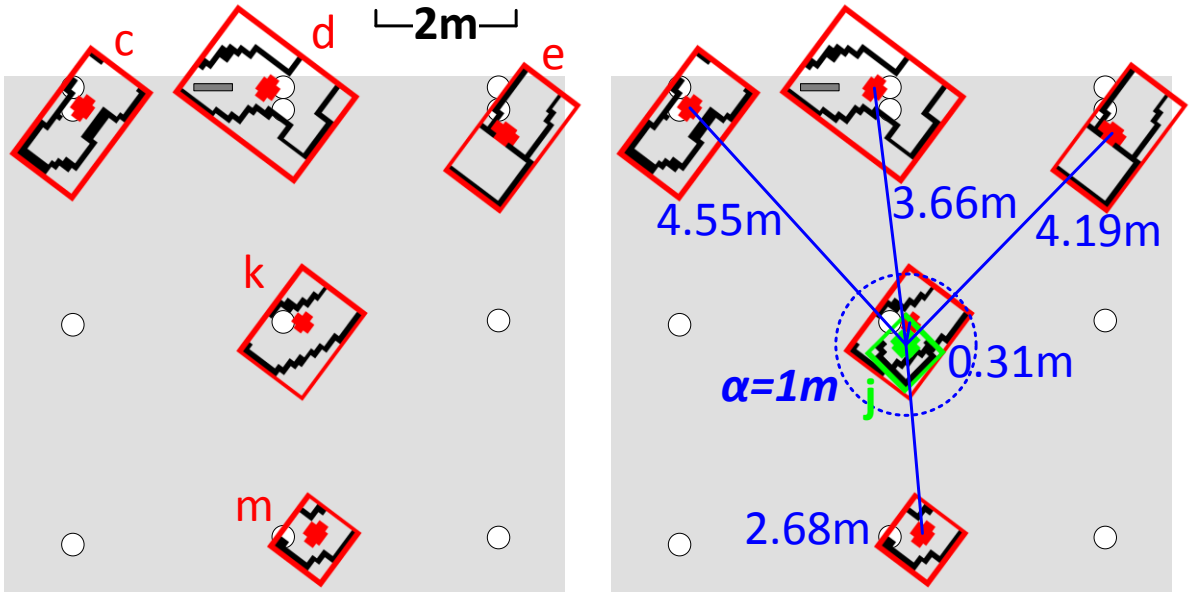

Figure 6.23 - Using the maximum likelihood estimator to establish correspondence to a mapped landmark. The left figure shows a zoomed section of the map centred on LM8 after the scan from the left position. The targets detected from the left scan are labelled in red and registered onto the ground truth map for reference. The right hand figure adds one of the features observed on the subsequent scan from the centre position, feature 'j' shown in green. The distance from feature 'j' to all previously mapped landmarks was evaluated (distances shown in blue) and the closest landmark selected (0.31m). Provided the distance to the closest previously mapped landmark was less than the threshold for creating a new landmark hypothesis (α=1m, shown by the blue dashed circle) then correspondence was assumed to the reobserved landmark.

A second example in Figure 6.24 below shows the case for adding a new landmark to the map. Feature 'i' observed on the scan at the centre position was compared to all existing landmarks recorded on the map from the initial scan from the left hand position. As the threshold α was exceeded, feature 'i' was added to the map as a new landmark hypothesis.

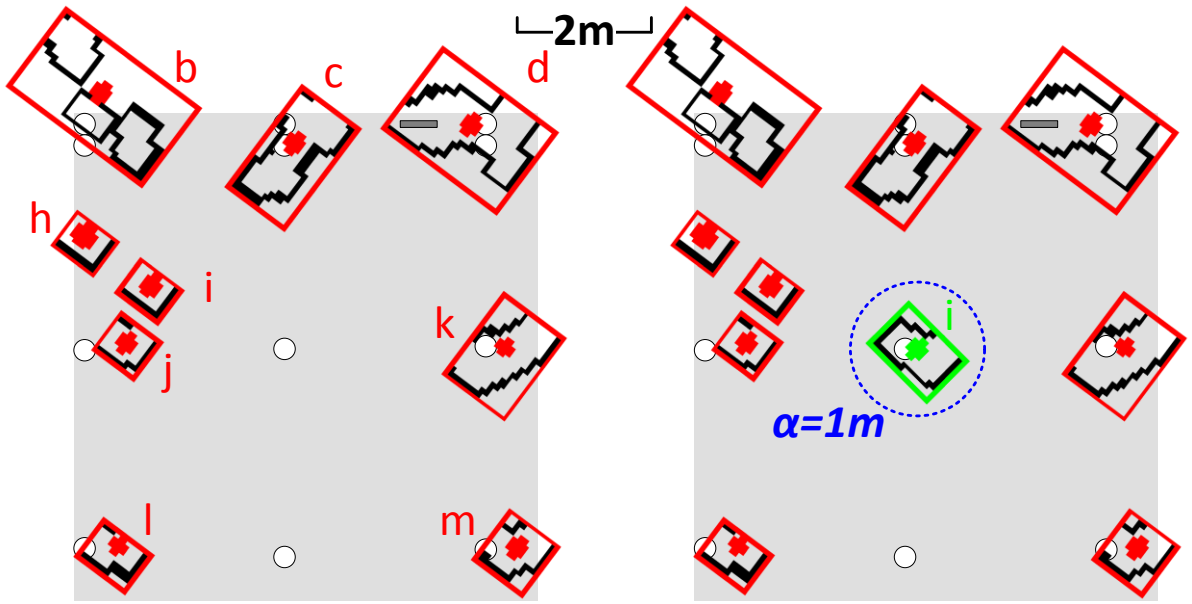

Figure 6.24 - Using the ML estimator to determine the observation of a previously unmapped landmark. The left figure shows a zoomed section of the map centred on LM7 after the scan from the left position. The targets detected from the left scan are labelled in red and registered onto the ground truth map for reference. The right hand figure adds one of the features observed on the subsequent scan from the centre position, feature 'i' shown in green. The distance from feature 'i' to all previously mapped landmarks was evaluated. As no landmarks fell within the blue dashed circle (the threshold α=1m for establishing a landmark correspondence), the feature 'i' was assumed to be previously unmapped and was added to the map as a new landmark hypothesis.

The plot in Figure 6.25 below verifies the selection of α=1m by tracking the change in observed landmark position throughout the three scans, and with reference to the ground truth map position. Each observed landmark is plotted using a different marker, and the apparent mapped positional change between observations of the same landmark is shown. The maximum positional change between observations of the same landmark was verified to be always <1m and with an average of <0.4m.

Of the five sonar targets detected which did not correspond to dock pilings (either anomalies or parts of the floating dock), these all had a positional difference of significantly greater than 1m compared to their nearest neighbour, either previous observations or the ground truth map (2.6, 3.7, 4.5, 8.7, 8.8m) and no false correspondences were established using a threshold of α=1m. Of the four landmarks which were observed only once (the white entries in Table 6.4), these too were consistently observed at >1m from their previously mapped nearest neighbours, validating the selection of α=1m to ensure robust correspondence estimation.

The left hand series of points in Figure 6.25 below shows the position difference between the observations from the left scan position and the ground truth map, with an average of 0.43m. The centre series of points then shows the position difference between landmarks observed in the centre and left hand position with an average change in mapped positions of 0.38m. Finally, the right hand series of points shows the change in mapped position between landmarks observed in the centre and right scans, with an average change in mapped position of 0.37m. Therefore, landmarks were mapped in slightly different positions from each station, of a comparable magnitude difference between stations and compared to the ground truth map.

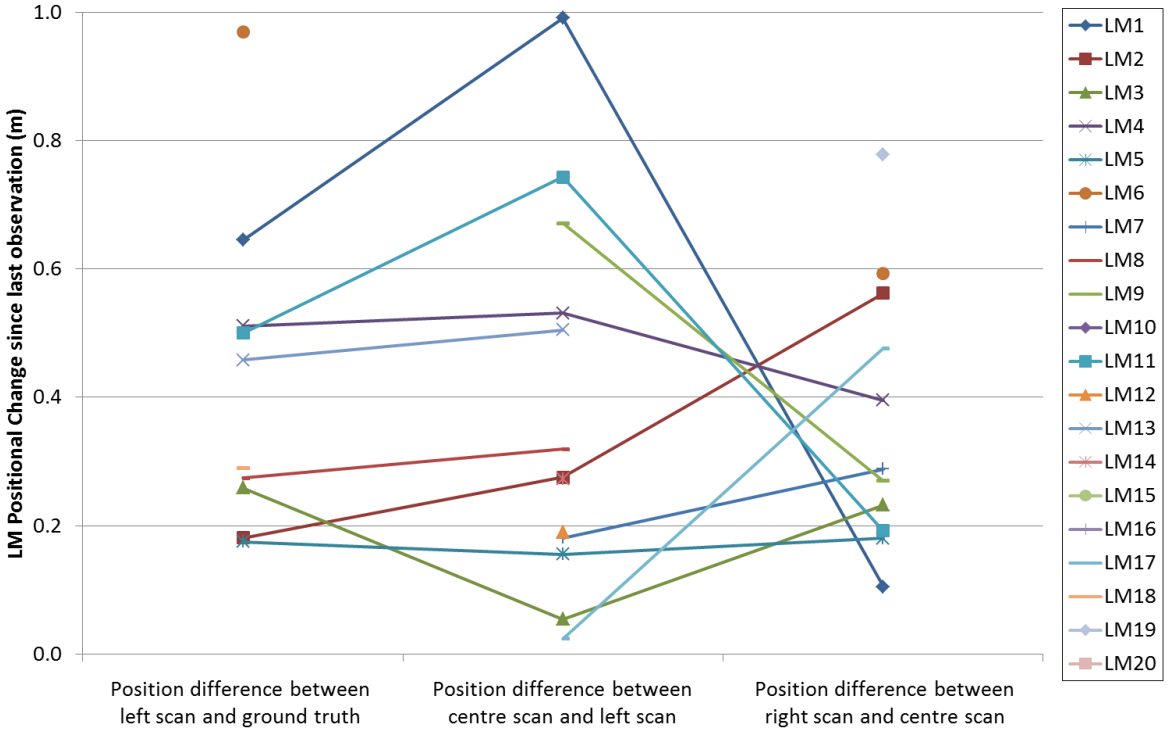

Figure 6.25 - Tracking LM position variation between scans confirmed the selection of α=1m, as the apparent variation in position of correctly corresponded landmarks was consistently <1m. Each coloured marker represents an observed dock piling as indicated in the key, as per the numbering in Figure 6.17. Markers not present correspond to dock pilings not observed. The lines show sequentially observed landmarks. The vertical axis is positional change in the observed position of a landmark between observations, and the horizontal axis shows the evolution of scans.

6.3.3.3 Tracking landmarks to estimate localisation

If a landmark was only observed from a single position then it was mapped for navigational purposes including collision avoidance. In addition, if the landmark was reobserved upon the robot returning to the *same* position, then it was a useful confirmation of the robot returning to the same location and was used to correct any errors accumulated in moving away and returning. Furthermore, if the robot maintained a position, then this singularly observed landmark could be used to aid or confirm station keeping, while other features were being mapped or evaluated to see if *they* were stationary (i.e. static objects suitable for use as landmarks).

Given the correct correspondence, any landmark seen in more than one position (highlighted in orange in Table 6.4 previously) was used to estimate a change in position of the vehicle, or localisation estimate. At least one landmark needed to be tracked between each scan position in order to localise by sonar alone. The more reobservations available, the more robust the localisation and thus, through back propagation in the EKF SLAM algorithm, the more reliable the map of other objects. The more times a landmark was observed, the more useful it was to the mapping algorithm, thus landmarks seen in all three positions were most useful.

The *predicted* movement of the vehicle from the left crane position ($\bar{L}$) to the centre position ($\bar{C}$) can be expressed in vector form as $\bar{C} - \bar{L}$, or as Cartesian coordinates as $(\bar{C}_x - \bar{L}_x, \bar{C}_y - \bar{L}_y)$.

Each of the n landmarks corresponded between the crane position $\bar{L}$ and $\bar{C}$ were used to *update* the predicted movement. For a landmark n observed in the vehicle coordinate system from the left position at (L_{n_x}, L_{n_y}) and the centre position (C_{n_x}, C_{n_y}), the change in vehicle position indicated by corresponding these landmarks was:

$$\text{LM Indicated Change} = (C_{n_x} - L_{n_x}, C_{n_y} - L_{n_y})$$

For each of the landmarks observed from more than one position, the effect of each reobserved landmark on the localisation process in estimating the change in vehicle position is shown in blue in Table 6.6. The actual movement of the vehicle, using the modelled crane positions, was used to ground truth the localisation estimates indicated by tracking landmarks between scan locations. The difference between the change indicated by reobserving the same landmark (the LM indicated change) and the change predicted by the actual movement of the crane shown in Table 6.5 is presented as the position error in Table 6.6.

$$\text{Position Error} = \text{Indicated Change} - \text{Predicted Change from crane movement}$$
$$= (C_{n_x} - L_{n_x}, C_{n_y} - L_{n_y}) - (\bar{C}_x - \bar{L}_x, \bar{C}_y - \bar{L}_y)$$

Table 6.5 - The actual position change between scan positions according to the movement of the crane.

	45° Left:	Straight:	45° Right:
Actual position change (m):	(Δx = 3.36, Δy = 1.39)		(Δx = 3.36, Δy = -1.39)

Table 6.6 - The relative movement of each tracked landmark between scan positions and the position error compared to the actual crane movement.

	45° Left:		Straight:		45° Right:	
LM List:	**Range (m):**	**Bearing (°):**	**Range (m):**	**Bearing (°):**	**Range (m):**	**Bearing (°):**
1	2.25	216.3	5.87	226.0	8.07	251.2
LM Indicated (m):	(Δx = 3.83, Δy = 0.52)				(Δx = 3.30, Δy = -1.30)	
Position Error (m):	(0.47, -0.87) = 0.99				(-0.06, 0.09) = 0.11	
2	2.98	148.7	4.56	206.7	5.52	245.8
LM Indicated (m):	(Δx = 3.12, Δy = 1.25)				(Δx = 3.73, Δy = -0.97)	
Position Error (m):	(-0.24, -0.14) = 0.28				(0.37, 0.42) = 0.56	
3	4.78	118.5	3.76	167.9	3.33	231.8
LM Indicated (m):	(Δx = 3.31, Δy = 1.38)				(Δx = 3.31, Δy = -1.16)	
Position Error (m):	(-0.05, -0.01) = 0.05				(-0.05, 0.23) = 0.24	
4	8.12	111.1	6.01	130.6	2.85	146.5
LM Indicated (m):	(Δx = 3.71, Δy = 1.79)				(Δx = 3.73, Δy = -1.25)	
Position Error (m):	(0.35, 0.40) = 0.53				(0.37, 0.14) = 0.40	
5	10.71	104.0	8.22	120.0	4.47	125.2
LM Indicated (m):	(Δx = 3.44, Δy = 1.26)				(Δx = 3.25, Δy = -1.25)	
Position Error (m):	(0.09, -0.13) = 0.16				(-0.11, 0.14) = 0.18	
6	5.16	188.4			9.54	237.7
LM Indicated (m):	(Δx = 6.12, Δy = 0.01)					
Position Error (m):	(-0.59, 0.01) = 0.59					
7			7.22	194.1	7.54	224.5
LM Indicated (m):					(Δx = 3.19, Δy = -1.16)	
Position Error (m):					(-0.17, 0.23) = 0.29	
8	7.30	140.0	7.41	170.0		
LM Indicated (m):	(Δx = 3.31, Δy = 1.07)					
Position Error (m):	(-0.05, -0.32) = 0.32					
9			8.41	145.2	5.56	167.7
LM Indicated (m):					(Δx = 3.10, Δy = -1.31)	
Position Error (m):					(-0.26, 0.08) = 0.19	
11	8.61	187.1	10.92	207.9	11.79	224.8
LM Indicated (m):	(Δx = 2.67, Δy = 1.67)				(Δx = 3.52, Δy = -1.50)	
Position Error (m):	(-0.69, 0.28) = 0.74				(0.16, -0.11) = 0.47	
13	9.87	150.4	10.22	174.1		
LM Indicated (m):	(Δx = 2.89, Δy = 1.20)					
Position Error (m):	(-0.47, -0.19) = 0.51					
17			13.18	188.4	12.62	206.4
LM Indicated (m):					(Δx = 3.03, Δy = -1.05)	
Position Error (m):					(-0.33, 0.34) = 0.30	

The average localisation estimate between scan locations is presented in Table 6.7 below and compared to the actual change in vehicle position from the movement of the crane.

Table 6.7 - Comparing the average estimated position change with the ground truth actual movement of the vehicle.

	From 45° Left to Straight:	From Straight to 45° Right:
Actual position change (m):	(Δx = 3.36, Δy = 1.39)	(Δx = 3.36m, Δy = -1.39m)
Position change indicated by sonar (m):	(Δx = 3.29, Δy = 1.27) (8 LM used for estimate)	(Δx = 3.35, Δy = -1.22) (9 LM used for estimate)
	From 45° Left directly to 45° Right:	
Actual position change (m):	(Δx = 6.72, Δy = 0)	
Position change indicated by sonar (m):	(Δx = 6.12, Δy = 0.01) (1 LM used for estimate)	

With consideration of the number of landmarks used for the position change estimates above, Table 6.8 below lists the average position error in the localisation estimate using the crane modelled positions as a ground truth.

Table 6.8 - Comparing the average position error for movement between each scan position.

	45° Left:	Straight:	45° Right:
Average Position Error (m):	From 45° Left to Straight: 0.45m		From Straight to 45° Right: 0.30m
	From 45° Left to 45° Right: 0.59m (using single landmark (#6) not observed from centre) From 45° Left to 45° Right: 0.09m (using the cumulative localisation estimate)		

The position *estimates* were compared to the *actual* position of each scan location in Table 6.9:

Table 6.9 - A comparison of the actual vehicle position on the crane with the localisation estimates. The SLAM algorithm assumed an initial location of the left position with prior knowledge (e.g. surface GPS) to zero the map in the Dock Coordinate System. The straight scan position estimate was calculated using the change in position estimate from left to centre (Table 6.7) and the right position estimate was calculated using the cumulative change in position to the straight station *and* the subsequent estimated change in position to the 45° right position.

	Actual crane position:	Position estimate using the sonar scans of landmarks and localisation:
45° Left:	(1.56, 2.26)	(1.56, 2.26) – a priori knowledge of the initial state was assumed (for example a surface GPS fix used to register the map in the world coordinate system)
Straight:	(4.92, 3.65)	(4.85, 3.53) – this was the original position + the estimated change in position using the localisation algorithms
45° Right:	(8.28, 2.26)	(8.20, 2.31) – the original position + the estimated change in position to the straight position + the estimated change in position to the 45° right position = the *cumulative* localisation position. (7.68, 2.27) – this was the position estimate using just the single LM observed from 45° left and 45° right but not observed in the straight position

6.3.3.4 Mapping features

The EKF SLAM algorithm allowed tracked landmarks to be used for localisation while simultaneously mapping landmarks. At each station, the map of tracked landmarks was updated and new landmarks were recorded with an uncertainty estimate as discussed previously. In the example discussed here, the covariance in the x and y directions was assumed to be equal and so the uncertainty was represented by ellipses with equal proportions – circles. During operation, the uncertainty associated with each mapped landmark was proportional to the number of times it was reobserved in the 'same' position, and the uncertainty associated with the location

estimate of the robot each time the landmark was observed (the position of a landmark can only be mapped as accurately as the current robot location is known). Figure 6.26 below integrates the localisation process shown previously with the SLAM algorithm and overlays the results onto the ground truth dock map.

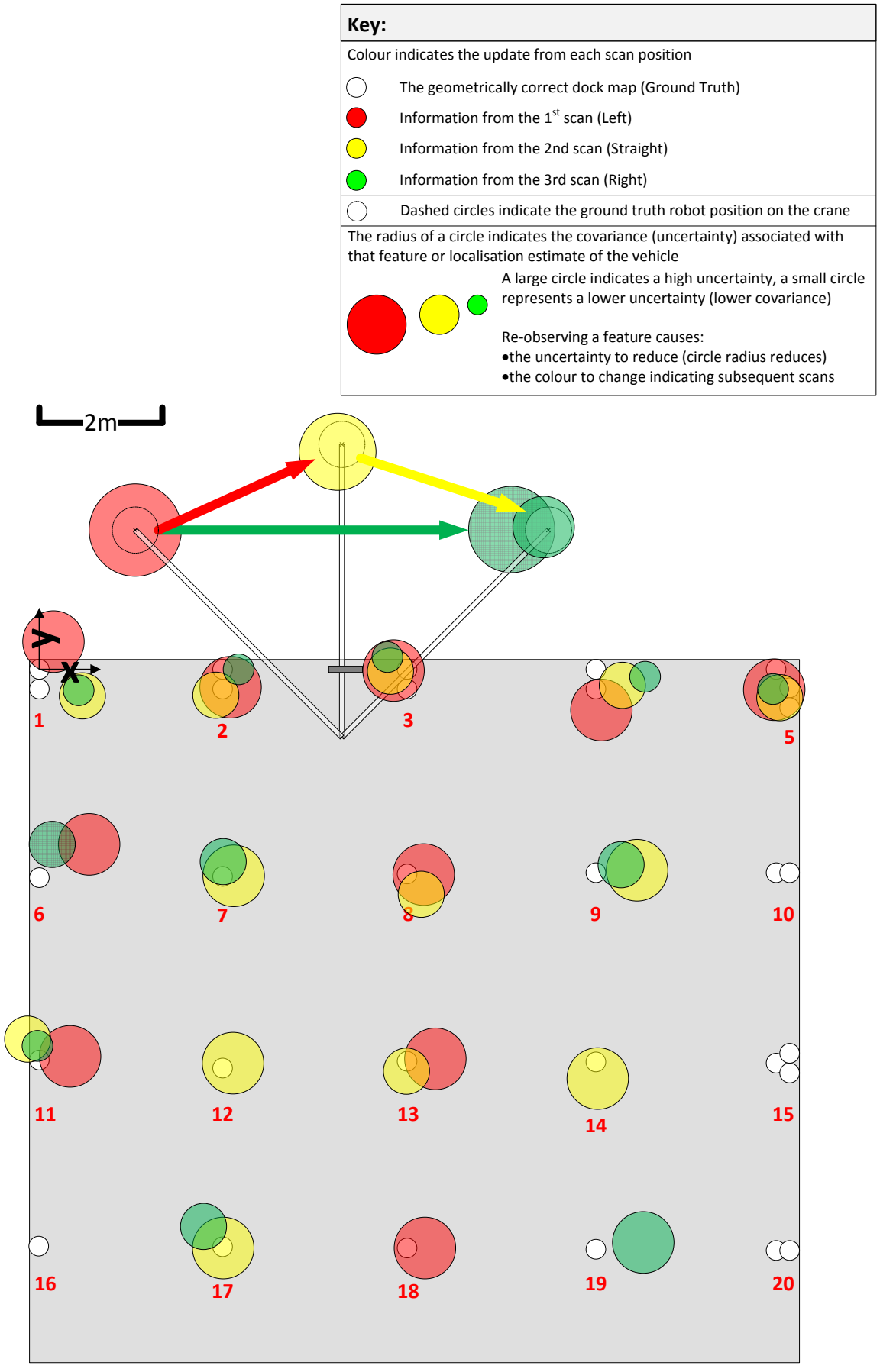

Figure 6.26 - The sequential compilation of a dock map and localisation estimate using SLAM. For a full description, see the text below.

Figure 6.26 above shows the evolution of the localisation estimate and dock map between the three stations using the SLAM algorithm. The cumulative SLAM process is shown using sonar tracked landmarks corrected by the vehicle navigation sensors. The localisation estimate of the vehicle using observed landmarks between scans is shown at the top of the plot by the shaded vehicle positions. As before, the hashed green vehicle position was estimated using only the hashed green landmark (LM6) which was only observed in the 45° left and the 45° right position, i.e. localisation without any landmarks observed in the straight position. As only a single landmark suggested the green hashed vehicle position, this had little effect on the final localisation estimate (1 landmark weighted against 10 landmarks which suggested the green non-hashed estimate).

The localisation error at each station is the difference in the coloured position of *SeaBiscuit* from each of the crane positions (dashed circles). The reduction in localisation uncertainty at each station as more landmarks were reobserved is represented by the reducing radius of the localisation estimates. This reduction in localisation uncertainty had a corresponding effect on the mapping uncertainty of observed landmarks.

The coloured landmarks correspond to the station from which they were observed. Red landmarks were observed at 45° left, yellow landmarks from the straight position and green landmarks from 45° right. The manually mapped positions of the dock pilings from the ground truth map are shown in white. A reduction in the radius of shaded landmarks represents a reduction in mapping uncertainty, caused by reobservations of a successfully corresponded landmark from different stations. Each reobservation reduced the mapping uncertainty.

From the left station (red), the vehicle recorded all observed landmarks with a high uncertainty corresponding to the high uncertainty of its location estimate and the fact that all LM had only been seen once (high uncertainty = large covariance circles).

At the centre station (yellow), newly observed landmarks were added to the map with a high uncertainty. Several landmarks which corresponded to LM observed in previous scans were reobserved. The position of these was corrected based on the reobservation and the mapped uncertainty reduced from reobservation with a lower localisation uncertainty. Concurrently, the position of the vehicle was estimated by tracking these reobserved landmarks and the uncertainty associated with the localisation estimate was reduced accordingly. Whereas movement of the vehicle increased localisation uncertainty, the large number of landmarks tracked throughout this movement reduced the localisation uncertainty.

At the right station (green), the position of landmarks which were reobserved was adjusted and the uncertainty reduced. New landmarks were recorded and LM which had been previously observed but not seen on this scan remained at the same position with the same uncertainty. The position and uncertainty of the vehicle was also updated based on the tracked landmarks.

Figure 6.26 above showed the observations taken at each of the three stations by *overlaying* the different scans. The SLAM algorithm *combined* the information at each time step with the previous knowledge of the map and vehicle location to produce an overall updated state estimate. This is referred to as online SLAM (5.3.4.1). The combination process avoided the need to store all previous states of the vehicle and map, which would use large amounts of memory. Figure 6.27 below shows the result of the combination process, previously demonstrated in simulation in section 5.4. Successive observations of landmarks were corresponded to previously observed features and their mapped position and uncertainty updated, while simultaneously using these landmarks to localise the vehicle and to track the localisation uncertainty.

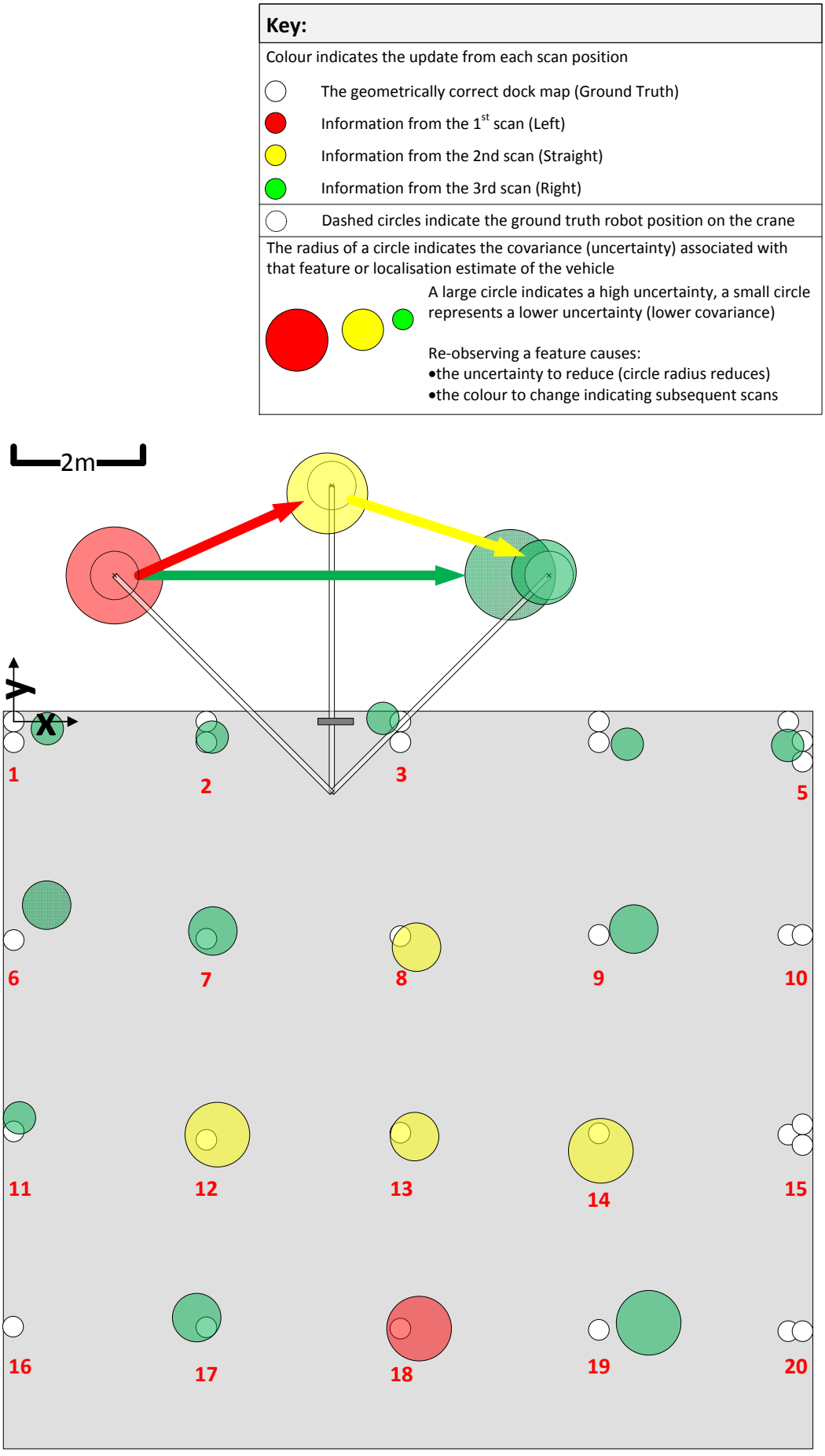

Figure 6.27 - The combined SLAM dock map and localisation estimate upon reaching the final station. At each station, the new information was integrated and a single updated state estimate was maintained (online SLAM). Reducing circle radii (of mapped landmarks and the vehicle) shows the reduction in mapping and localisation uncertainty. The red-yellow-green colour transition represents the different stations for vehicle localisation shown at the top, and from where the most recent landmark observation occurred for landmarks.

6.3.4 Integrating Delta T sonar data

Data from the forward facing multibeam Delta T sonar was complementary to the 852 sonar data in many respects. The update rate was much faster (up to 20 scans per second), the range was higher (up to 100m) and the sonar imaged the entire vertical water column, rather than just the ±11° vertical beam opening of the 852 sonar. Figure 6.28 below provides an example 20m range raw image from the forward facing Delta T sonar with a user generated overlay. Different ranges were selected depending on the application and conditions.

In Figure 6.28 below, the horizontal line of intermittent returns at the bottom of the image is the seabed and the vertical returns extending up from this are the dock pilings spaced approximately 3 metres apart in a uniform pattern. The reflections of objects and the seabed above the waterline are also identified. Although this overlay was user generated, it was the task of the Delta T sonar image processing algorithms to extract the same features for survey, localisation and mapping purposes – these algorithms are discussed in the following section.

At higher ranges, the dock pilings provided a weaker return and were harder to detect. However, the spacing shown correctly matches the ground truth map of the pilings observed. This scan was taken with the vehicle very close to the surface of the water. The faint horizontal line at the centre of the scan is the water surface. This was barely visible and only for the first few metres of range. The much stronger horizontal line at the top of the image is a reflection of the seabed.

Figure 6.28 is the raw data capture and is shown before any image processing or filtering operations have been performed. Additionally, the image has not been corrected for the pitch and roll of the vehicle; the image shows the vehicle pitched up by 7° so the water surface and the seabed extend away from the vehicle in a slight upward inclination. Correction of vehicle inclination is applied before the image processing algorithms to aid in detection of the water surface. All returns above the water surface, the reflection of the seabed, and all noise below the seabed (secondary echoes) were removed by the sonar image processing software to leave the water column region of interest.

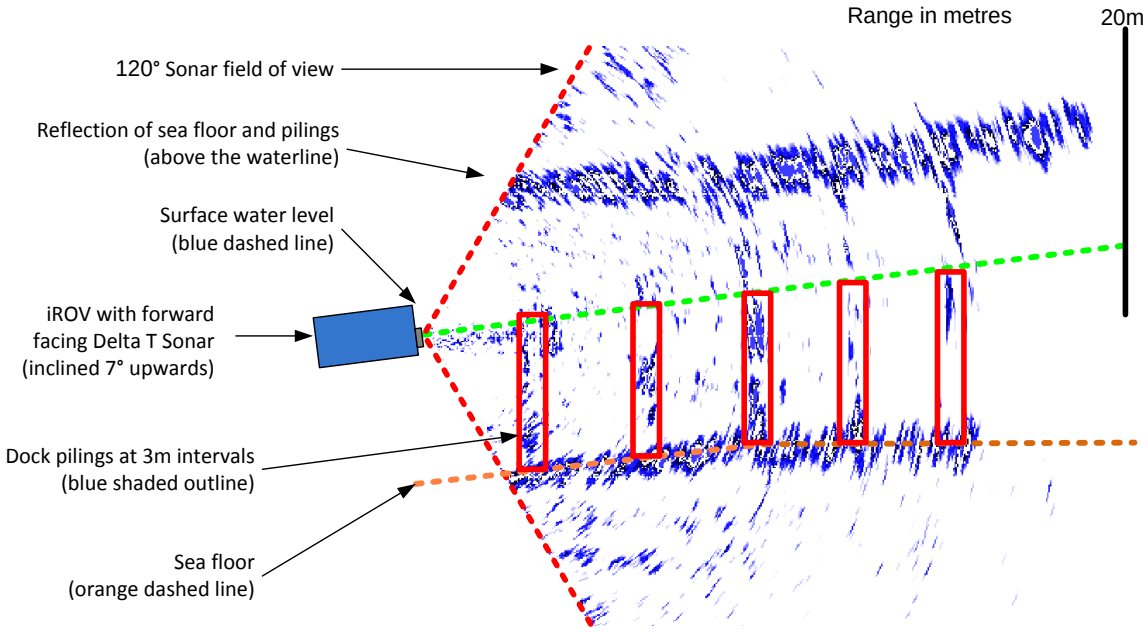

Figure 6.28 - An example annotated 20m range Delta T image of the dock pilings. The seabed, water surface and dock pilings are highlighted with the user generated overlay, together with the reflections shown above the waterline. The iROV is not shown to scale.

6.3.4.1 Delta T sonar image processing

Depending on the range setting of the Delta T sonar, the vehicle depth and altitude, it was expected to see the seabed and/or the water surface. In Figure 6.29 below the Delta T was orientated so that 60° of the beamwidth went upwards and 60° downwards. This was optimal when the vehicle was operating at depth. However when operating close to the surface, the sonar was usually orientated at 40° downwards. This allowed the vehicle to image more of the seabed and objects directly beneath it, and reduced the amount of 'wasted' beams exiting the water surface. 40° was selected rather than 60° so that there were still some upward facing beams to allow for semi-submerged operation, while still imaging directly below the vehicle.

Various image processing and feature extraction algorithms were applied to the raw sonar data from the Delta T, as described in section 4.6.6. The principle was to calculate the position and angle of the water surface, given the attitude and depth of the vehicle (from other sensors), and remove any regions above this. The seabed was then detected if in range, and any secondary echoes below this removed. Finally, any features (objects, landmarks) were extracted for navigational purposes.

These features were split into objects either connected to the seafloor, such as the dock pilings dimensioned below in Figure 6.29, or objects which were distinct from the seafloor, such as midwater targets, cross (diagonal) dock pilings and floating objects. Cross pilings appeared as 'floating' objects which appeared to change in depth as the vehicle panned the sonar across the diagonal target. Targets which were connected to the seafloor were detected by segmenting the continuous return into separate features comprising a separate floor and object. Sufficiently prominent bathymetric features, such as rocks, were also segmented into distinct landmarks.

Figure 6.29 below shows the example scan used previously and adds dimensions extracted from the sonar scan. Table 6.10 below compares the dimensions extracted from the sonar scan with the ground truth values from the manually dimensioned dock map.

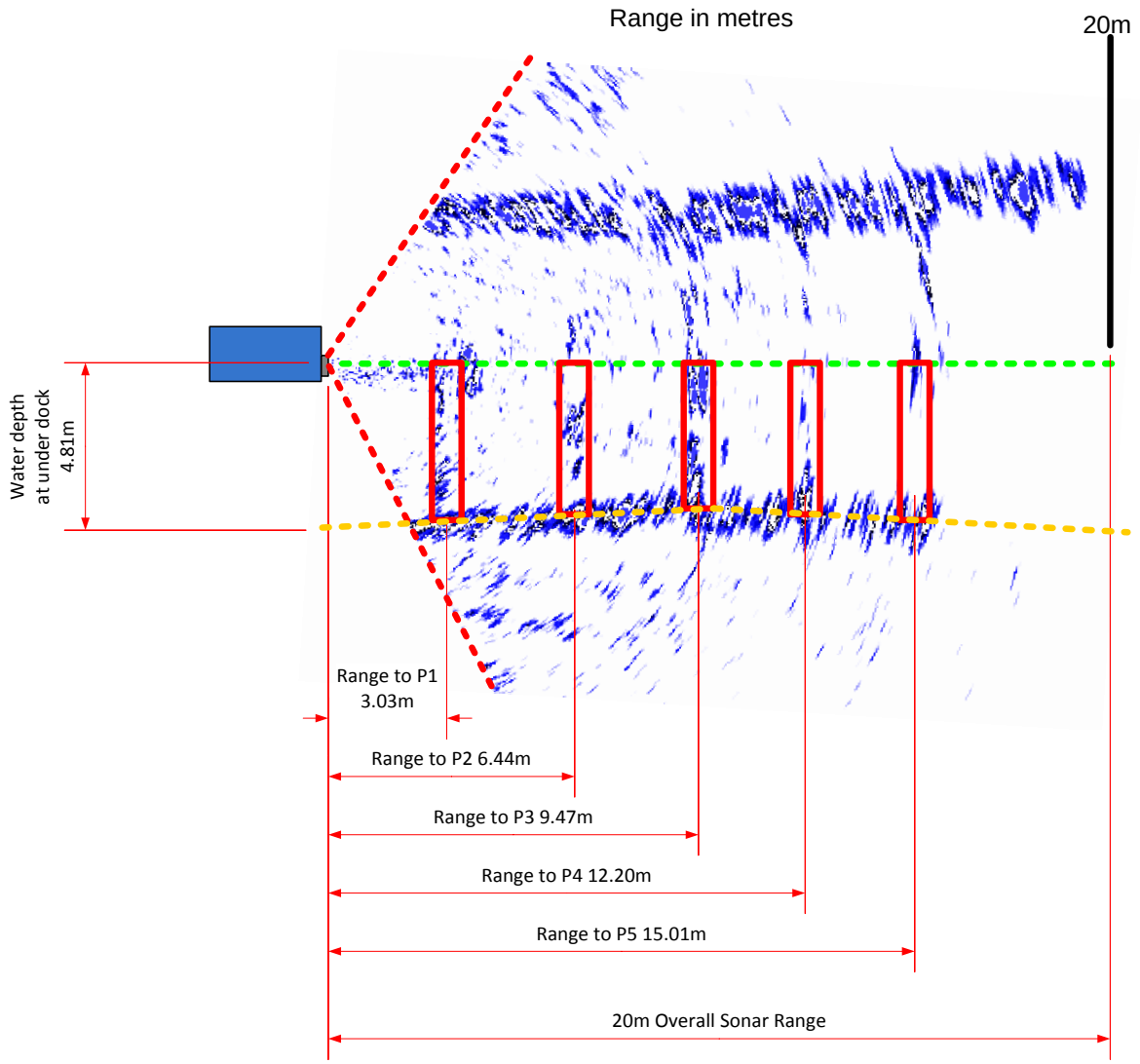

Figure 6.29 - An example dimensioned Delta T image taken with the dock pilings (P1, P2, …) in view. The seabed, water surface and dock pilings are highlighted with the user generated overlay, together with the reflections shown above the waterline. The Delta T sonar image processing algorithms were used to extract this information for survey, localisation and mapping purposes. The iROV is not shown to scale.

Table 6.10 - Example output data (summarised) from the Delta T scan shown in Figure 6.29. The range to the seafloor was combined with the mounting position of the sonar and the depth estimated using the external pressure sensor, and used to estimate water depth at the current position.

Object:	Range from sonar image processing algorithm (m):	Range from ground truth (m):	Position error to ground truth (m):
Range to seafloor (converted to water depth at current state of tide)	Combined to give water depth of 4.81		
Piling 1 (defined as zero point)	0.00	0.00	
Piling 2	3.41	3.32	+0.09
Piling 3	6.44	6.36	+0.08
Piling 4	9.17	9.39	-0.22
Piling 5	Object not detected	12.40	N/A

Column 3 of Table 6.10 contains data from the manually generated geometric dock map as described in section 6.3.1. This was used as a ground truth estimate for the sonar data (column 2). The increasing error with range can be seen, as it was harder for the algorithm to detect the pilings given the irregular shape and lower intensity return on the weaker (higher range) sonar returns. In the scan shown above, particularly due to coincident pilings occluding others, piling 5

was almost completely indistinguishable. Whilst the user is able to 'fill in the gaps' in the sonar image, the algorithm was operating without any a priori knowledge of the pattern and shape of the dock. It was impossible for the current algorithm to detect this piling without detecting many other false positives. However, the general accuracy was good with an average error of 0.13m which was within the map ground truth uncertainty discussed later in section 6.3.5.1.

The first step in integrating the Delta T multibeam compressed the 3D data from the vertical water column to 2D which allowed co-registration and correlation with the 852 sonar scans. The examples below used the dock pilings but the technique was later successfully applied to kelp mapping. Taking the example Delta T scan shown previously in Figure 6.28 and Figure 6.29, the compression to 2D algorithm first corrected the scan for pitch angle. This was important, otherwise a vertical piling would appear as a large weak return when compressed to 2D if it was at an angle, potentially causing it to be overlooked if it blurred into the background noise.

The second step removed the reflections caused by the beams interacting with the water surface and removed the scan region above the surface (above the green dashed line in Figure 6.29). The surface was approximated as a flat line, with an adjustable threshold used to remove the effects of rough surface conditions. The surface intersection was calculated using the vehicle inclination from the attitude sensor and depth from the pressure sensor.

The third step removed the seabed using automated image processing algorithms as discussed in section 4.6.6.6. The result at this intermediate stage is shown below in Figure 6.30 using data from the example image above in Figure 6.28.

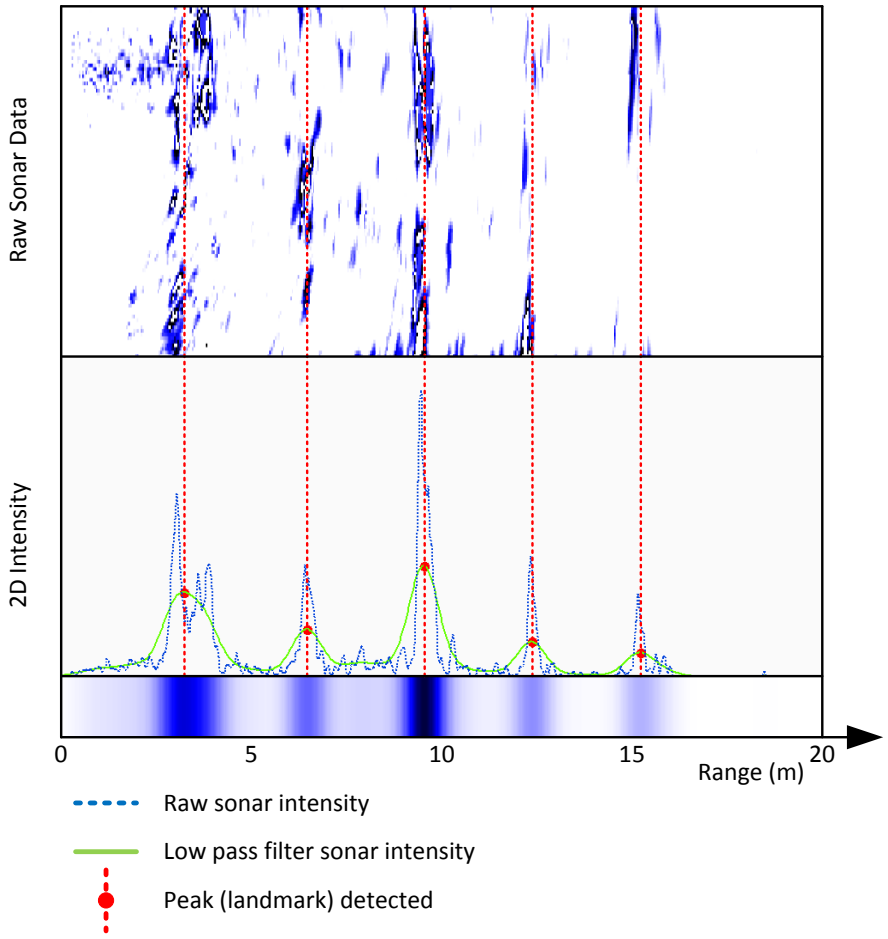

Figure 6.30 - The stages in compressing the 3D Delta T scans to a 2D representation. The upper figure shows the example Delta T scan from Figure 6.28 with the region of interest (ROI) between the water surface and the seabed extracted and corrected for vehicle pitch. The image was then compressed to 2D and the intensity varying with range is shown below. Landmarks were detected using a peak detection algorithm from the low pass filtered intensity data. The colour bar at the bottom represents the sonar intensity compressed to 2D over range using an intensity plot.

Figure 6.30 above shows three plots. The upper plot shows the example Delta T sonar scan from Figure 6.28 with the region of interest (ROI) between the water surface and the seabed extracted, other regions removed and the image corrected for the pitch of the vehicle to extract the rectangular ROI shown above. The horizontal scale shows the range in metres. This ROI was compressed into 2D, where the sonar scan shown in the upper part of the image was converted to an array, and each column represented the mean of all entries in that column.

The middle figure then shows a plot of these mean values using the same horizontal range scale and a vertical scale of the 2D sonar intensity. The blue dashed line in this middle plot shows the raw sonar intensity varying with range and the green line shows the result of a 50-tap FIR low pass filter corrected for phase. The red dots highlight the result of a peak detection algorithm, which searched the green filtered data for peaks exceeding a threshold minimum width and height. These threshold values were application-specific to the background noise present on the sonar and the typical characteristics of landmarks present. The red dots highlight the 5 peaks detected, and the red dashed lines correspond correctly to the 5 dock pilings which can be recognised in the top sonar scan by inspection.

The extraction of the ROI, including tuning the parameters of the seabed and surface removal routines, as well as tuning the low pass filter parameters were important as these steps increased the signal to noise ratio (SNR) of the feature detection algorithms. If there was a large level of background noise in the intensity plots shown in the lower parts of Figure 6.30, then this could obscure faint features, or cause false detection of objects.

If the scan was parameterised at this stage, the output from the peak detection algorithm was a list of the landmarks detected, their range and intensity. These values were registered in the world space and either passed to the SLAM algorithm for navigation, or used to generate the map for user inspection. However, more reliable landmark detection and identification of correspondences was possible if several Delta T scans of the water column compressed to 2D were combined and registered into a radial plot before parameterisation.

6.3.4.2 Combining several 2D scans

The colour bar at the bottom of Figure 6.30 above shows the sonar intensity compressed to 2D and varying with range as an intensity plot, using the same colour scale as the top plot of Figure 6.30. Figure 6.31 below registers several-hundred of these Delta T scans compressed to 2D in the world coordinate system to build up a radial 2D scan as shown. The vehicle was suspended using the dock crane at a stationary x y position and a constant depth. This allowed the 852 sonar to pan over the dock from a known stationary position, but also allowed the vehicle to rotate about its axis using its thrusters to pan the Delta T sonar over the dock at approximately 1°/second. With a repetition rate of 13 Hz, this equated to an angular resolution of 0.08°, or one Delta T scan at every 0.08° of pan.

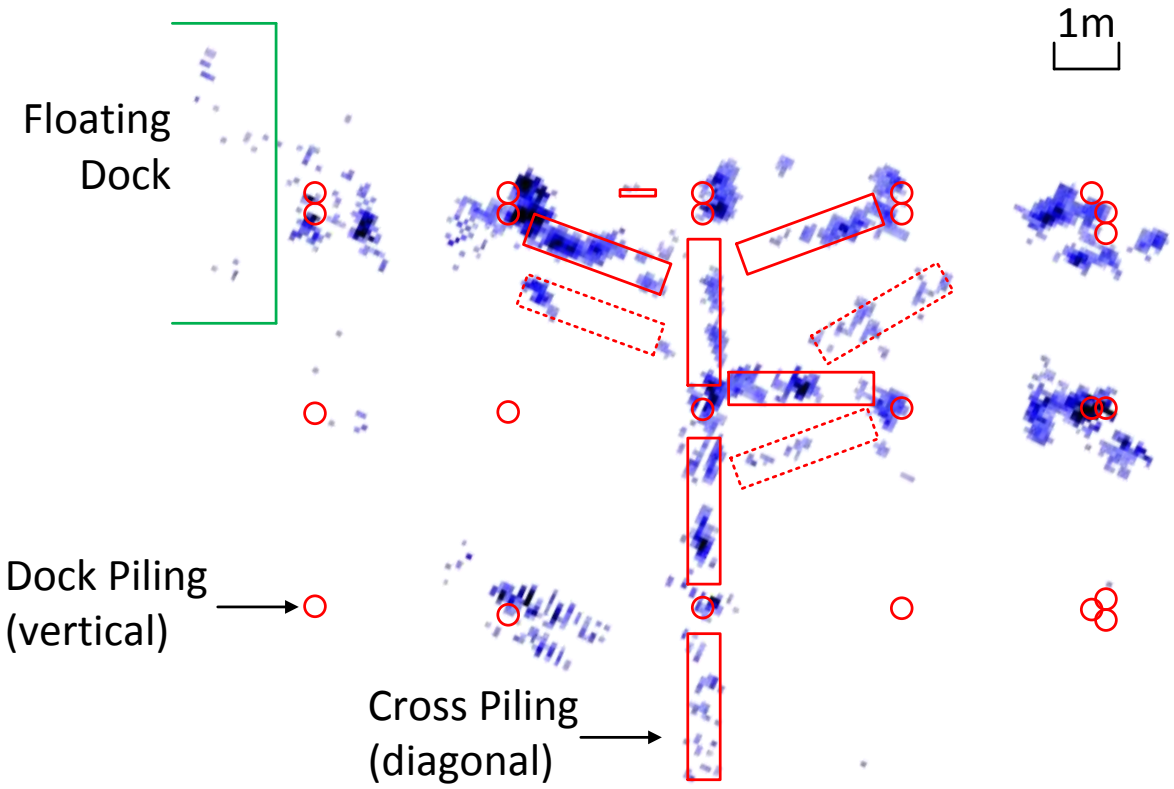

Figure 6.31 - Several hundred Delta T pings were compressed to 2D and registered into a 2D radial scan of the dock pilings. The red circles indicate the geometrically accurate position of the near-vertical dock pilings from the ground truth map. The red rectangles indicate cross pilings which diagonally brace between the vertical pilings, often spanning three pilings. Dashed red rectangles show fainter cross pilings, either at higher ranges or partially occluded.

The 20m range compiled scan in Figure 6.31 was overlaid onto the ground truth dock map which included the position of the vertical dock pilings surveyed at the dock walkway level. Considering the not exactly-vertical angle of these pilings, and that the Delta T sonar was scanning the midwater ROI as indicated in Figure 6.28 earlier, the agreement between the ground truth map and the Delta T scan is generally very good, with the typical position error between the observed and ground truth piling centre <1m.

Cross pilings were also apparent on the scan and are highlighted by red rectangles. These cross pilings generally spanned three vertical pilings at a diagonal angle close to 45°. The cross pilings on the Delta T map above are more apparent than the 852 sonar scans previously shown, again due to the greater vertical ROI surveyed by the Delta T. The 852 sonar scanned a sector ±11° vertically, centred on the horizontal plane only imaging cross pilings almost directly incident on the same horizontal plane as the vehicle. However, the Delta T sonar imaged the entire water column, and diagonal cross pilings were imaged over their entire height.

Some occlusion can be seen when pilings are occluded behind larger, closer range targets. However, techniques to reduce the effects of occlusion by integrating several scans from different locations using SLAM have been demonstrated in the previous section. The same techniques used for the 852 sonar in the previous section for landmark detection, parameterisation and identification were applied to the Delta T radial scans to provide an additional source of information, as shown in Figure 6.32 below. The figure uses similar image processing algorithms to parameterise targets above a certain pixel mass threshold within the closest 10m range of the vehicle. The threshold and range mask were adjustable depending on operating conditions,

however for the dock scan shown below, the variability of target position was minimised within this 10m range due to reduced beam spreading and therefore greater spatial resolution.

The use of cross pilings for navigation with the 852 sonar is limited as the position of non-vertical landmarks will appear to change when imaged from different heights and will be discounted as dynamic landmarks in the SLAM algorithm. However, cross pilings and other non-vertical targets can be used as a navigational landmarks when imaged with the Delta T sonar as the entire water column is imaged.

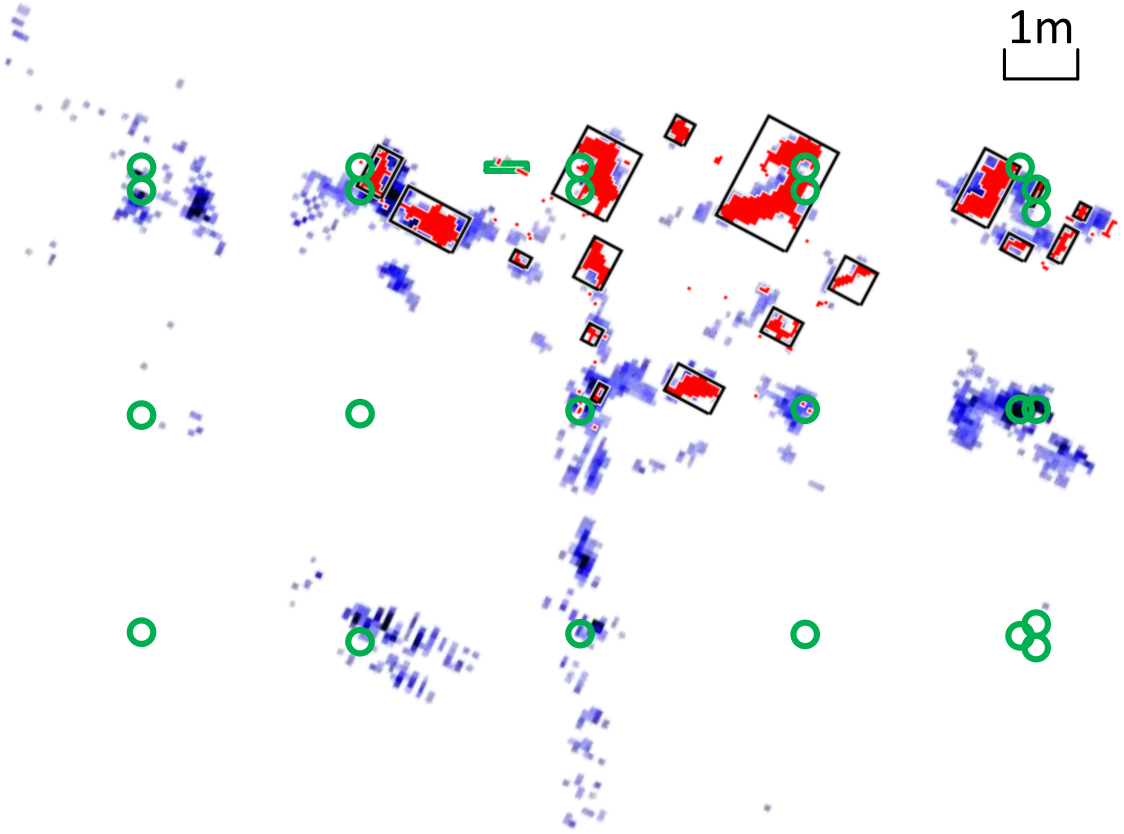

Figure 6.32 - Image processing and feature extraction algorithms were used to extract navigational landmarks from the compiled Delta T scans, similar to those used for the 852 sonar. The blue pixels show the compiled 20m range Delta T scan, overlaid onto the green map of dock pilings (without cross pilings shown). The red targets show features above a certain mass threshold detected as navigational landmarks within a 10m radius of the vehicle, where there was higher reliability of detecting landmarks.

The information gains by integrating data from the Delta T sonar scans in addition to the 852 sonar scans can be seen by comparison to Figure 6.33 below. In this plot, a 20m 852 scan taken from approximately the same position as the Delta T scan above was registered onto the same ground truth map of the dock pilings, demonstrating relatively good (<1m average) correspondence between the mapped piling position and the sonar scan.

Together with a controllable scan direction independent of vehicle heading, the other information gains from the 852 sonar arose from imaging a different ROI of the water column. Given the ±11° ROI imaged by the 852 sonar about the horizontal plane compared to the adjustable vertical ROI of the Delta T sonar, several objects were present in the 852 scan shown in Figure 6.33 below, which were not present in the Delta T scan in Figure 6.32 above. The area of strong returns to the left, delineated by a green line in Figure 6.33 below, is the shallow water and shoreline, where a floating dock was anchored. These were not surface interactions or noise at higher ranges as they were not present on the right hand side in deeper water.

The region of shallow water and the seabed was excluded from the Delta T scan by tuning the vertical ROI extracted. The semi-circular ring in the centre of the scan was caused from water surface interactions from a slight attitude deviation of the vehicle. Again, this was excluded from the Delta T scan by selecting the ROI to exclude the water surface. However, for the 852 sonar, the vertical ROI could not be adjusted. Instead, an annulus mask was calculated based on vehicle depth and 852 sonar range, and excluded in the image processing algorithms. It was left in the raw scan in Figure 6.33 below to show the differences between the two sonar returns including (albeit removable) noise.

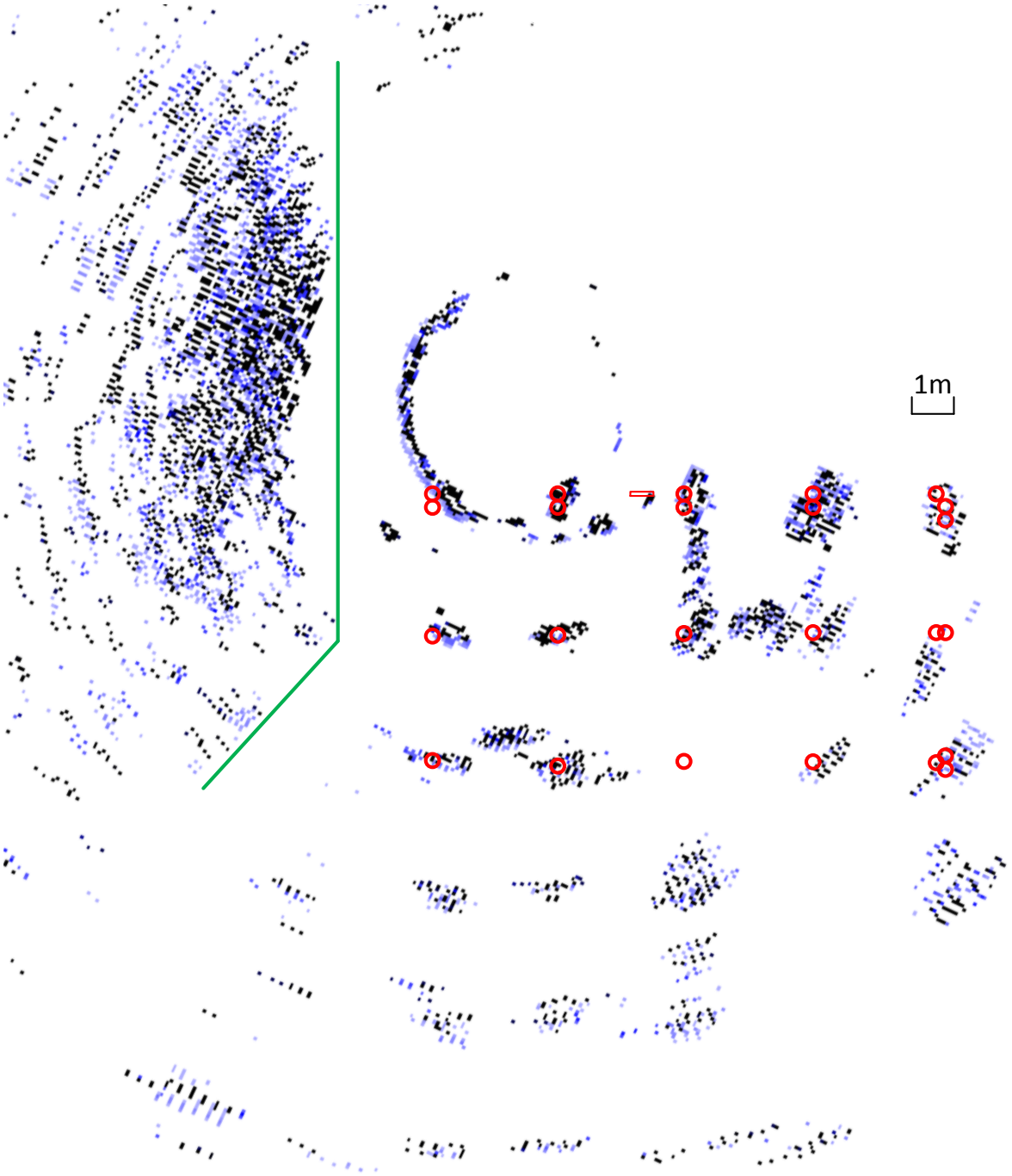

Figure 6.33 - An example 20m range 852 scan taken from approximately the same position off the dock. Relatively good (<1m) correspondence between observed pilings and the ground truth piling centres shown by red circles can be seen, as can the presence of several cross pilings between the vertical dock pilings. The area bounded by the green line to the left is the shallow shoaling seabed and shoreline, with a floating dock anchored in shallow water.

The differences between the Delta T sonar scans and the 852 scans were partly due to the different frequencies of the sonars, 260 and 675/850 kHz respectively, causing a different return strength from different targets. However, the most significant difference resulted from the sonars imaging different regions of the water column. Figure 6.34 below shows a view from the side of the vehicle representing the ±11° vertical beam opening of the 852 sonar and the 120° vertical swath of the Delta T sonar. The beamwidth over increasing range is shown represented at the depth and altitude which the above scans were taken.

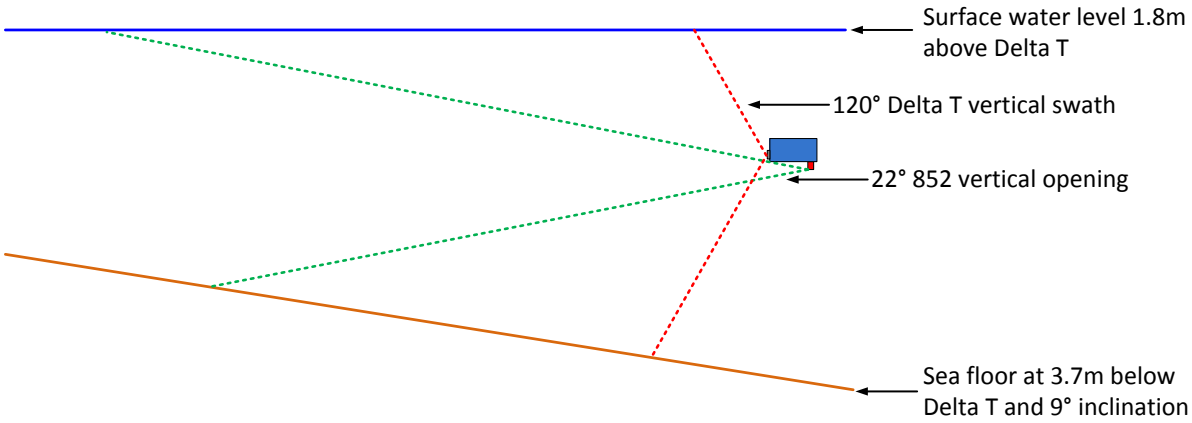

Figure 6.34 - The 852 and Delta T sonars image an overlapping volume of the water column. Of the 120° vertical swath of the Delta T, a region of interest is calculated between the surface and seabed using vehicle altitude, depth and attitude, with threshold values set to exclude seabed and surface noise.

Although, as Figure 6.34 shows, the two sonars overlapped, they were imaging different aspects of the same spatial area and thus providing different yet complementary information. Rather than just using the 2D 852 data, the Delta T profiling sonar, even in this compressed 2D mode, added useful additional information. At the very least, the Delta T sonar provided corroborating information of the same space imaged by the 852 sonar, provided a higher sampling rate, a different frequency for reliable detection, and imaged a far greater vertical swath, which was particularly useful when operating in deeper water than the 5-6m shown above.

Figure 6.35 below provides a comparison of the 2 sonar scans, by displaying the presence of thresholded returns on the 852 sonar in blue, thresholded returns on the Delta T sonar in red and thresholded returns on both sonars (i.e. targets observed in exactly the same location on both sonars) in green. The information gains from using each sonar to image different ROI of the water column can be seen as distinct areas of red and blue, while corroboration between the sonars is possible using areas of green shading. In particular, the Delta T sonar was able to accurately map non-vertical targets and to discriminate between the seabed and water column in areas of shallow water by varying the vertical ROI. Conversely, the large regions of blue shading to the left of Figure 6.35 below indicate that the 852 sonar was unable to discriminate between the seabed due to the fixed vertical beam opening, but had a better performance of imaging dock pilings at higher ranges, with pilings imaged over the entire 20m range setting.

	Difference from ground truth (m)	
Piling number:	**Delta T:**	**852:**
1	Not detected	Not detected
2	0.23	0.02
3	0.25	0.23
4	0.44	0.28
5	0.32	0.40
6	Not detected	0.41
7	Not detected	0.08
8	0.26	0.09
9	Not detected	0.33
10	Not detected	0.77
Mean position difference:	**0.30**	**0.29**

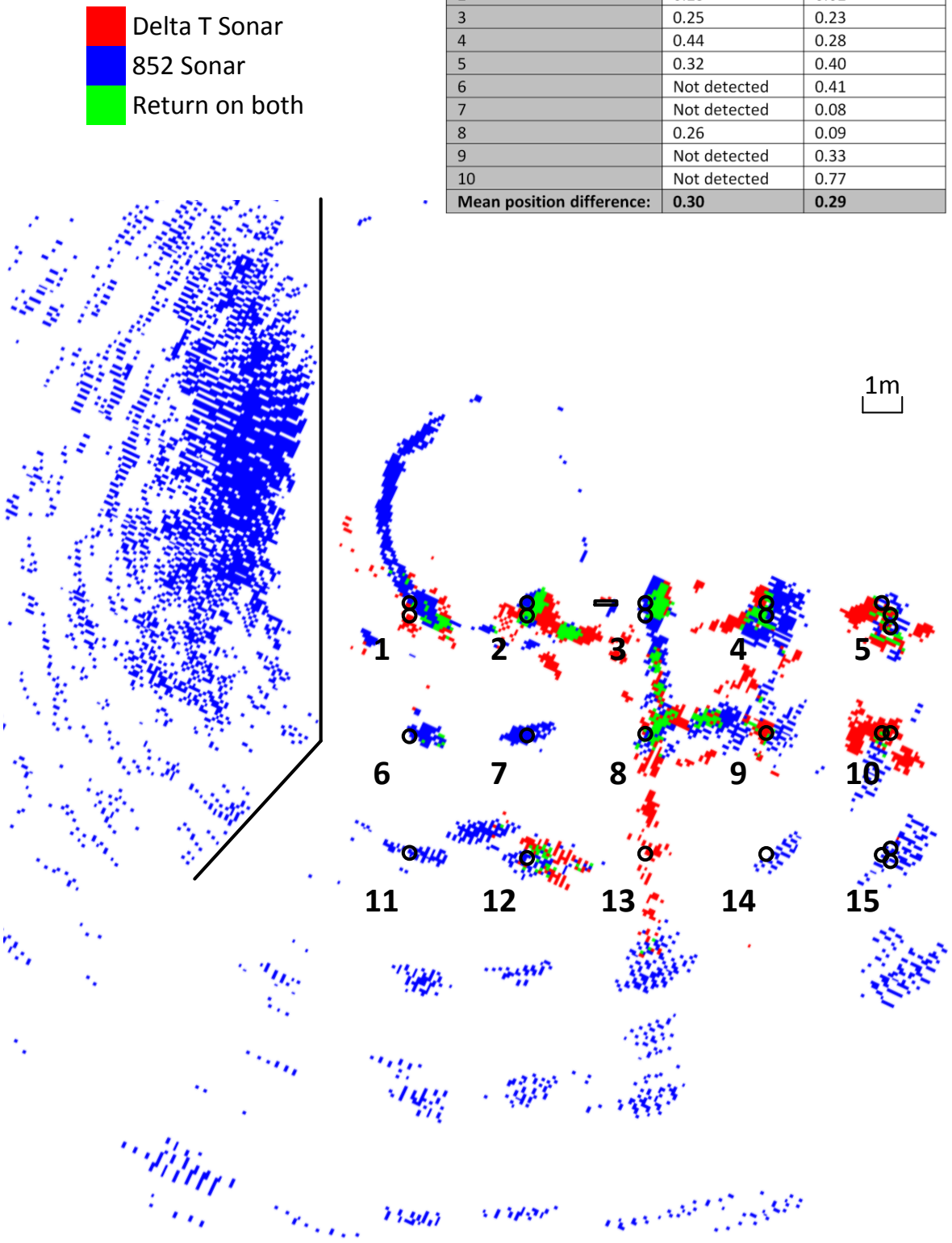

Figure 6.35 - The combined dock scans from the 852 and Delta T sonar registered on the same map. Thresholded returns from the 852 sonar are shown in blue, from the Delta T sonar in red and thresholded returns from both sonars shown in green. The information gains from each sonar can be seen as distinct areas of red and blue, while corroboration between the sonars was possible using areas of green shading. The difference between the ground truth piling positions and the positions detected using the 852 and Delta T sonar is shown in the inset table.

The combined 2D scan was parameterised and landmarks detected using both the Delta T and 852 sonar scans, using the techniques described previously. The position error between the pilings detected using each sonar and the ground truth mapped position of each piling is shown in the inset table.

Several conclusions can be drawn from Figure 6.35. The 852 sonar provided more reliable detection of dock pilings, in particular at higher ranges for this water depth, with a comparable position accuracy to the Delta T sonar. The reduced detection on the Delta T sonar was in part due to occlusion, but also due to a narrow water column ROI. If the ROI was set to a wider vertical region of the water column, sensitivity was increased at high ranges, but errors and noise from the water surface and seabed easily caused false detection of pilings.

However, the lack of vertical resolution on the 852 sonar caused errors when imaging non-vertical targets from different altitudes (the scans above were taken at a constant altitude). For the scans taken above, cross pilings could be excluded from the detection algorithms using an ellipse ratio threshold, but are left in the scan shown in Figure 6.35.

Additionally, 852 sonar scans taken in shallow water were masked by the seabed, as shown to the left part of the scan, which required the region to be excluded. Using the Delta T sonar allowed the water column to be reliably extracted, even in shallow water, and allowed non-vertical targets to be accurately imaged.

Given the comparable mean position difference for both sonars, it was proposed that the errors present in the ground truth map were comparable to the errors in the sonar position estimation of piling centres. These errors in the ground truth map are discussed further in section 6.3.5.1.3. In brief, they comprised errors from unmodelled underwater half-height or broken pilings, unmodelled cross pilings and biological growth on pilings (verified by video and diver inspection). Additionally, the ground truth map was measured from the piling centre at the dock walkway level and pilings assumed to be vertical. A small off-vertical angle of a piling of just a few degrees caused a large positional error at depth, several metres below. Finally, visual inspection using the iROV of the seabed surrounding the dock discovered large amounts of unmapped debris, including submerged engine blocks and sections of iron railway tracks.

6.3.5 **Discussion**

The previous section has detailed the field trials of the iROV *SeaBiscuit* in the sheltered waters of a piling dock. The shallow water conditions were similar to nearshore kelp beds, yet the vertical dock pilings presented a series of clearly detectable near-vertical sonar targets as analogues to the kelp stipes, in a regular pattern. The mapping results were compared to a known ground truth map of the piling positions. Modelling of the crane was used to constrain the vehicle position during the survey, allowing ground truthing of the vehicle localisation estimate.

6.3.5.1 Mapping performance and accuracy

A map of the dock was surveyed using the 852 sonar from three different positions from the midwater. A total of 16 out of a possible 20 vertical pilings within range were successfully mapped (Table 6.4), with the remaining 4 pilings occluded at high ranges by closer pilings (Figure 6.27). Correspondences were correctly identified for all pilings observed from more than one position, using the nearest neighbour maximum likelihood method for establishing landmark correspondences. The pilings were mapped with an average position error from the ground truth map of 0.40m or, expressing the positional error as a percentage of target range, 7%.

When interpreting the mapping error seen in Figure 6.27 previously, two observations were made. The first was that the landmark mapped error correlated very poorly ($R^2 = 0.02$) with the number of times the landmark was observed, as shown below in Figure 6.36. However, it was

expected that the more times a landmark was reobserved, the more accurate the mapped position would be, as errors were averaged out with each observation. The poor correlation suggests that another source of errors outweighed the mapping uncertainty. Outliers with particularly high position errors in Figure 6.36 below were caused by adjacent cross pilings being included in the piling position.

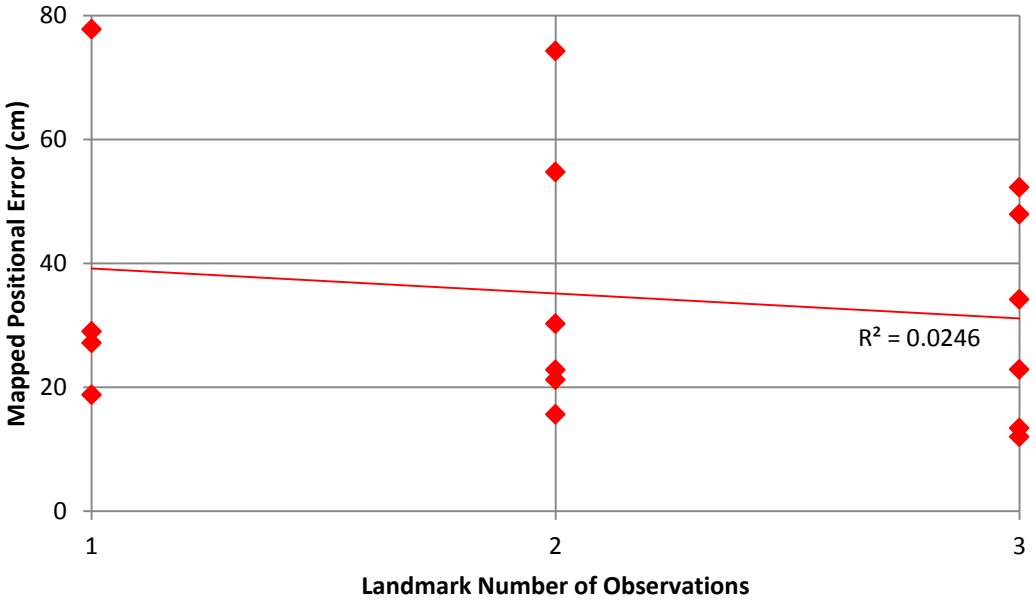

Figure 6.36 - Plotting the mapped position error of landmarks against the number of times a landmark was observed for the map shown in Figure 6.27 shows a very poor correlation. It would be expected that the more times a landmark was observed, the more accurate the mapped position would be, averaging both spurious errors and mis-measurements of the centre of non-negligible diameter sonar targets.

The second observation was that the mapped position error was not correlated with target range, as shown in Figure 6.37 below. This is the opposite of what was expected, as the diverging sonar beams at greater ranges imaged a greater height of non-vertical targets and a greater volume of adjacent cross pilings, coupled with unremovable beam interactions with the surface. As with Figure 6.36 above, this suggested that another source of error was outweighing the typical sonar measurement uncertainty.

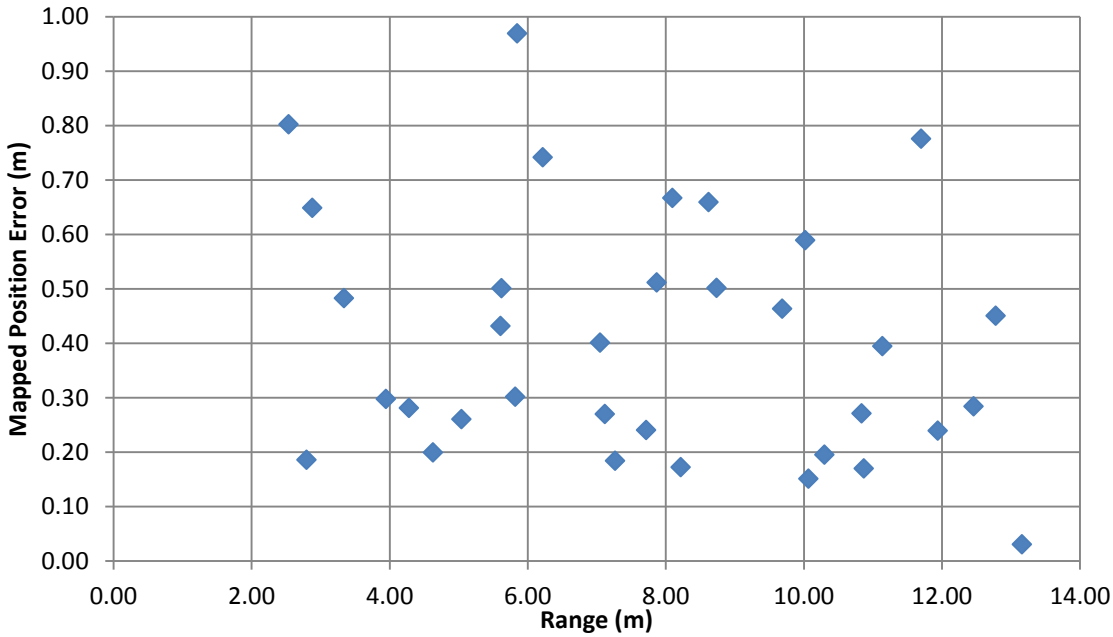

Figure 6.37 - Plotting mapped position error against target range shows no correlation. This is the opposite to what was expected, given the diverging sonar beams at greater ranges imaging a greater water volume with a poorer spatial resolution, coupled with increased noise, weaker returns and beam interactions with the water surface.

Although the accuracy of mapped landmarks compared to the ground truth map was relatively poor (0.4m averaged for all LM and all stations), the mapped *repeatability* between scans, or the accuracy with which a landmark was remapped in the *same* location was slightly better (0.38m), as shown in Figure 6.25 previously. However, generally landmarks were mapped in slightly different position from each station, of a comparable magnitude difference between stations and compared to the ground truth map.

The following three subsections propose three sources of these errors in addition to the typical sonar measurement uncertainty model, and attempt to quantify the effect of each error source.

6.3.5.1.1 Errors from uncorrected vehicle position deviations

Wherever possible, the effect on the sensor measurements of deviations in vehicle position and attitude was corrected. This included, for example, registering every Delta T and 852 sonar ping for yaw angle, correcting Delta T pings for vehicle attitude and examining 852 pings against a pitch and roll threshold. Attempts were also made to correct for external water movements varying the x, y and z position of the vehicle. This is the principle of the SLAM algorithms discussed previously which were able to estimate the vehicle position change as well map the landmark position.

The relatively still water and use of the crane hoist ensured that dynamic transient pitch and roll deviations were minimised during the surveys. However, uncorrected pitch and roll deviations from 0° will cause position errors between landmarks observed on the same scan. For example, if on the same scan, some landmarks appear too close and some too far from the vehicle, but for a subsequent scan this pattern changes, then this suggests an uncorrected vehicle attitude angle *as the LM positions relative to each other vary within a scan*.

Even if the deviation in attitude remains constant between scans, because the dock pilings change in yaw angle with respect to the vehicle between scans as the vehicle is moved on the crane, image distortion will occur. An example static distortion caused by an uncorrected pitch would cause objects in front of and behind the vehicle to appear further away whereas objects on either side of the vehicle would appear at the correct distance, thus severely distorting the image. However, as the vehicle moves on the crane and the relative position of the dock pilings change with respect to the yaw angle of the vehicle, different pilings will be in front of the vehicle in the new scan position and so the distortion will be applied to a different set of pilings. For example, an uncorrected variation of ±5° in pitch would cause *vertical* targets directly in front of and behind the vehicle at a range of 20m to appear with a position error of +8cm, but if the 852 sonar was panning rather than the vehicle, this error would not appear on targets imaged to the side of the vehicle.

A combination of pitch and roll, either varying in between scans, or even worse, varying during a scan can introduce serious errors. An uncorrected attitude deviation can cause as many errors as an uncorrected change in position, and the distortion method is more complex.

6.3.5.1.2 Measuring the centre of non-negligible thickness sonar targets

Sonar is incapable of measuring the true depth of objects incident with a beam, and instead detects the abrupt change in density from the surrounding water column [11]. Therefore, the true centre of an object of non-negligible thickness will not be correctly measured, as instead, the return will be centred on the closest boundary of the density change. This causes objects of a non-negligible density (for example the 0.32m diameter dock pilings) to be mapped closer to the sonar

than the true centre. This can be corrected by scanning from angles around the periphery of the landmark and averaging the detected position to the true centre. However, the scans taken off the dock were only taken from a 90° arc around the landmarks as shown in Figure 6.38 below, with several landmarks occluded from one or more positions.

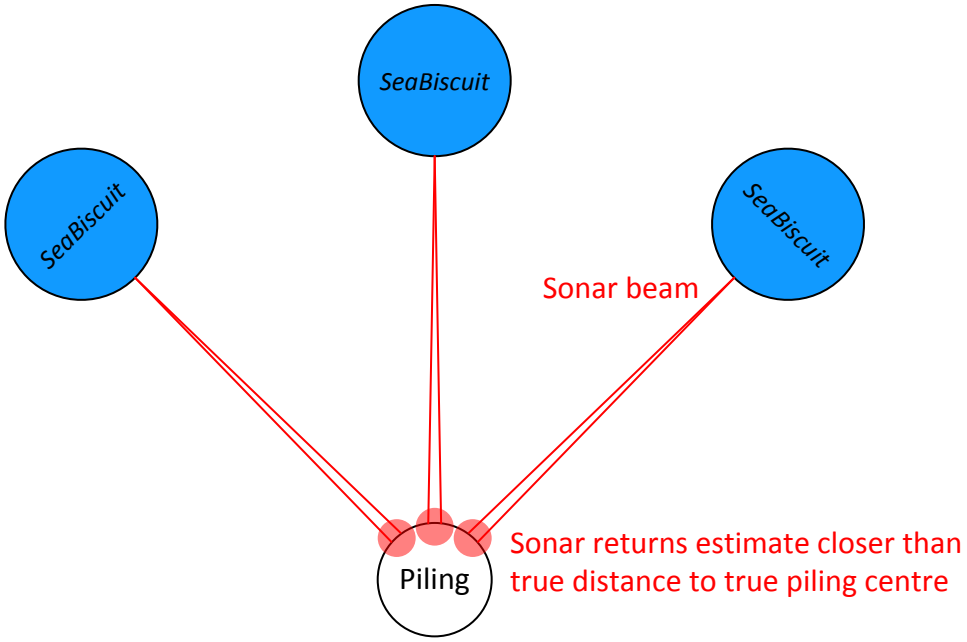

Figure 6.38 - Imaging a target of non-negligible thickness from a variety of angles will result in differing (all incorrect) estimates of the target centre position as it is the density change from the water to the target which is being detected. If the target is imaged from all sides, the average position will converge on the true centre for a symmetrical target.

This explains in part, the trend for objects to be detected at ranges closer to their true range, as shown in Table 6.11 below. Apart from outliers caused by cross pilings seen in the final map in Figure 6.27, the average positional error seen in Figure 6.36 is close to the radius of the pilings (>0.32m). The negative number for the centre scan in Table 6.11 (targets imaged at higher ranges on average than their mapped position) could be attributed to either a mispositioning of the vehicle on the crane (discussed below) or one of the other error sources discussed in this section.

Table 6.11 - Comparing the average error between mapped and measured range across all three stations. A positive number means landmarks were, on average, measured at a closer proximity than the ground truth map suggested.

Survey station:	Average LM map range – LM measured range (metres):
Left	0.10
Centre	-0.07
Right	0.16

6.3.5.1.3 Errors in the ground truth map, including unmapped features

The accuracy of the manually generated ground truth map itself is also considered. The map used for 2D SLAM ground truthing has the known limitation of not modelling cross pilings or old pilings which have broken off beneath the waterline. This includes those which have since been replaced with adjacent clustered pilings but the original half height piling remains.

These unmapped pilings can appear as anomalies in a scan. More importantly, if they appear in close proximity to a piling which is modelled, they cannot be distinguished by the sonar and so will cause the modelled piling to appear as one large feature, encompassing the un-modelled piling. This is acceptable until the large feature is approximated by a centre of mass. The effect of the additional pilings will distort the centre of mass from the centre of the modelled piling and thus introduce a systematic error in the x-y position of that piling.

Further errors can be introduced from observing the same feature from different angles using the sonar. The far side of the object, including unmapped cross pilings or half height pilings can be occluded from some angles, or the overall size obscured, both causing apparent errors when compared to the ground truth map. The SLAM map was updated as the same landmark was reobserved from different angles and the position incrementally corrected to the true object centre. Should cross pilings only be present on one side of a vertical piling, then imaging the target from different sides will not necessarily cause the mapped position to converge on the true vertical piling centre. Instead the mapped position will converge on the centre of mass of the cross piling and vertical piling combined, causing an error when the map is compared to the ground truth map which includes only vertical pilings. This effect occurs in both the 852 and Delta T scans, but is particularly noticeable on the Delta T scans, for example Figure 6.32 previously.

Additionally, as shown in particular by the Delta T plots (6.3.4 earlier in this section), there are a large number of underwater targets which are not included in the manually gathered ground truth map. As the ground truth map only includes full-height vertical pilings, these 'unmapped' targets appear on the scans yet are not corresponded to pilings on the ground truth map. However, these are mapped in a repeatable and reliably constant position, (as shown by Figure 6.35 earlier) and so will not introduce errors in the iROV maintained SLAM map.

The case of pilings not being exactly vertical is also important to consider, either from inaccurate installation or from damage by boats, tides and subsidence over time. Over the entire 8-10 metre height of a piling, a vertical misalignment of even a few degrees will cause the position of the top of the piling (where the ground truth map was measured) to the middle of the piling (where the sonar map was surveyed) to differ by several centimetres. For example, the row of pilings on the edge of the dock underneath the crane (and therefore the closest targets to the vehicle) were surveyed to have alignment errors in various directions of up to 3°. This caused a ≈21cm error in various directions in the ground truth position of the corresponding piling at the survey height, an important source of error to consider when evaluating the SLAM positional errors in Table 6.8.

The results of the SLAM proof of concept can be interpreted with an awareness of these sources of error, and any estimates of the vehicle mapping accuracy need to consider the accuracy of the ground truth map it is being evaluated against. Measurement of the ground truth map from the midwater would be required to increase the accuracy of the ground truth map, with a corresponding *potential* increase in the *apparent* accuracy of mapping performed by the vehicle for the reasons discussed above. Incorporation of the non-vertical nature of pilings, half-height broken pilings and cross pilings into the ground truth map will provide a more complete measure of the ground truth. At present, the vehicle mapping is proposed to have better small scale accuracy than the ground truth map, however, the ground truth map does show pilings which were occluded and therefore not mapped by the vehicle.

6.3.5.2 Localisation performance and accuracy

Simultaneous localisation was also performed, using landmarks associated between more than one scan to estimate the movement of the vehicle. An overall localisation error of 0.09m was calculated with respect to the modelled ground truth position of the crane used to constrain the movement of the vehicle through an arc of motion between three stations spaced at 3.62m apart (Table 6.8). This overall localisation error of 0.09m expressed as a percentage of the total vehicle displacement through the arc of 6.72m is 1.3%. This error is attributed to the differing apparent position of non-negligible thickness sonar targets observed from different angles and the effect of adjacent cross pilings observed and occluded from different angles, both of which are discussed

above. In the same manner as errors in the manually surveyed map used for ground truthing the mapping process were analysed above, errors in the ground truth location are analysed here as inaccuracies and errors in positioning of the vehicle on the crane.

The significantly lower localisation error than the mapping error is primarily attributed to the fact that errors in the ground truth mapped position of pilings (which dominate the mapping error above) have no effect on the localisation error as only the *relative* observed piling positions were used for the localisation estimate. Crucially, compared to localisation performed by inertial navigation alone, this localisation error is independent of drift, provided that sonar targets can be reliably observed. GPS updates from the surface were used to register the map in the world coordinate system, with an accuracy associated with the GPS position fix, typically of the order of a few metres. Thus the average map accuracy of 0.4m above was an average local map accuracy of the relative positions of landmarks, and the map was globally registered with an accuracy of a few metres.

6.3.5.2.1 Errors in the positioning of the vehicle on the crane

By the nature of aligning the crane to the 3 scan positions, there was an inevitable source of position error in the ground truth position measurement which introduced apparent errors in the results from the SLAM algorithm.

The boom lift crane had three controlled degrees of freedom comprising the pivot angle of the base, the lift angle of the boom and the height of the crane hook (connected to the vehicle). The pivot angle of the base determined the x and y position of the vehicle, tracing an arc through the water.

The boom lift angle also determined the x and y position of the vehicle as the radius of the arc varied in x and y. The boom lift angle also varied the height of the vehicle (z position), although the vehicle height was controlled and corrected independently by the hoist. The boom lift angle was controlled by a cable, thus the position was measured and controlled by the amount of cable released from the winch.

Although the crane hook was on a pivot, and the vehicle was suspended on a rope such that it could rotate independently of the crane boom tracing a radial arc, the pivot did not rotate freely and the radial arc of the crane affected the vehicle yaw angle to some extent.

The position of the three controlled aspects of the crane (yaw angle, boom lift angle and hoist height) were measured and controlled. However, the accuracy at which they could be positioned was relatively poor and no instrumentation was present on the crane. An approximation of uncertainty of these three controls is provided in the table below:

Table 6.12 - A measure of crane positional errors and their effect on the positional accuracy of the vehicle.

Controlled crane degree of freedom	Local positional accuracy	Effect on vehicle position	Transferred effect on vehicle position accuracy
Boom pivot angle	±3°	X & Y position in a radial arc around crane centre	±24.9cm in X & Y position in a radial arc around crane centre
Boom lift angle	±1°	X & Y position in a radius extending out from the crane centre Z position	±0.7cm in X & Y position in a radius extending out from the crane centre ±8.3cm in Z position
Hoist height	±1cm	Z position	±1cm in Z position

From Table 6.12 it can be seen that the uncertainty in boom pivot angle had a large effect (±24.9cm) on the vehicle X and Y position and that the cumulative total of these positional errors was comparable to the SLAM positional error of 0.09-0.45m in (x,y) position observed in Table 6.8 at the end of the SLAM results (section 6.3.3.3) earlier.

Although the errors introduced in z position shown in Table 6.12 are smaller in magnitude, and did not directly affect the (x,y) *position*, they could still have a significant effect on the (x,y) position estimate. In particular, the vertical error is significant when considering non-vertical targets, including cross pilings. When viewed from a different height, these diagonal targets appear to have a different (x,y) position in the 2D plane, thus introducing an error to the (x,y) position estimate of the vehicle and targets.

This error is compounded by any off-horizontal mounting angle of the base of the crane as it will introduce the same effect: a change in (x,y) position will introduce a change in z position as the boom rotates. The angle of the crane mount could not be accurately measured in the field using the tools available; it was assumed to be close to level, yet should still be considered.

There are also errors caused by unconstrained degrees of freedom. These included external water movement, turbulence and drag from the tether pulling the vehicle to be not directly underneath the hook, a sustained flow of tide causing the same effect, and a non-level attitude when suspended on the harness underneath the hook.

While every effort was taken to minimise these during the ground truth process, such as operating under constant minimal tide and weather conditions, in calm water and suspending the scan during boat wakes, inevitably some errors were still introduced. Table 6.13 presents estimates of the magnitude of some of these errors.

Table 6.13 - Positional errors and their effect on the uncertainty of the positional estimate of the vehicle.

Positional error	Effect on vehicle position estimate	Transferred effect to vehicle position estimate uncertainty
Boat wakes, waves and turbulence	Scan suspended if ≥±0.25m in (x,y,z) vehicle position or ≥±15° of vehicle pitch, roll & yaw angle. Errors highly transient and dependent on instantaneous scan conditions. High-speed movement can be missed by sensors. Also causes significant movement (apparent as positional errors) in observed non-fixed targets, either free-floating or anchored.	<±0.25m in (x,y,z) position or <±15° of pitch, roll & yaw angle
Tidal flow	A sustained drag with the vehicle moving as a pendulum on the crane hoist. Scan suspended if ≥±0.25m in (x,y,z) vehicle position or ≥±15° of vehicle pitch, roll & yaw angle. Errors are sustained and predictable to some extent. Also causes significant movement (apparent as positional errors) in observed non-fixed targets, either free-floating or anchored.	<±0.25m in (x,y,z) position or <±15° of pitch, roll & yaw angle
Cable drag	Errors are sustained with periods of high-dynamics (as coiled cable 'snaps' around) and depend on vehicle movement. High-speed movement can be missed by sensors.	<0.05m in (x,y,z) position or <±15° of pitch, roll & yaw angle
Harness attitude deviations	Caused by mounting error on the 4-point harness used to hoist the robot. Errors are sustained and dependent on vehicle movement.	<0.05m in (x,y,z) position or <±5° of pitch, roll angle

Although attitude errors will not directly cause a position error, in the same manner as errors in z position can introduce an error in the (x,y) position estimate as previously discussed, uncorrected vehicle attitude deviations can have a similar effect.

It can be seen that the combined effect of the errors in Table 6.13 above, even more so when combined with those in Table 6.12, can approach the positional error measurement of the SLAM ground truth. Thus the apparent errors when comparing the results to the ground truth map and location estimate can be explained by a number of factors, both inherent in the vehicle and its operation but also to the method of ground truthing the navigation system.

Alternative methods of ground truthing vehicle position are possible, including laser tracking of a surface marker [30], USBL and DVL solutions. However, the crane provided a rapid and zero-expenditure method to quickly verify the principle of sonar-aided SLAM of the iROV *SeaBiscuit*. Although the accuracy was relatively low, the uncertainty with each degree of freedom was quantified, allowing the results to be interpreted accordingly.

6.3.5.3 Sonar fusion

Data from the Delta T multibeam sonar was used to provide vertical discrimination of the seabed, non-vertical targets and the water surface, as well as imaging a far greater volume of the water column (Figure 6.34). Techniques to correct and extract the water column and compress the Delta T data to 2D for registration with the 852 sonar map were demonstrated, together with algorithms to extract navigational landmarks from the scan (Figure 6.32). Fusion of the data from the two sonars provided a more complete map of the piling dock (Figure 6.35). The information gains from using each sonar were seen, including the higher range and scan angle independent of vehicle heading of the 852 sonar, together with the vertical discrimination, higher resolution and faster mapping speed of the Delta T sonar.

As shown in Figure 6.35, this sonar fusion, exploiting the holonomic axisymmetric mapping technique, not only provided information gains, but also allowed corroboration and correction of targets co-registered on both sonars. The difference between the ground truth mapped position of landmarks and that observed with the Delta T sonar (0.30m) and the 852 sonar (0.29m) was comparable. This suggested that the actual mapping accuracy was very good, of the order of the difference between these two values, but that other errors were causing these large deviations.

These errors included the average piling diameter of 0.32m causing an inaccurate measure of the true centre position, the effect of non-vertical pilings causing errors in the ground truth map surveyed from the dock walkway and the effect of cross pilings and broken-off half-height pilings adjacent to the vertical pilings. Each of these error sources affected both sonars in a similar manner, and it was estimated that the errors associated with the ground truth map were larger than any true mapping errors.

6.3.5.4 Development of landmark association

As well as considering positional accuracy, it was also important to consider landmark correspondence accuracy. Techniques to autonomously establish the correspondence of observed landmarks to previously observed mapped features were implemented using the maximum likelihood nearest neighbour estimation technique, described in section 5.3, demonstrated in simulation in section 5.5 and demonstrated off the piling dock here. Using the threshold value of $\alpha = 1$, correct correspondences were established with zero false positives / negatives. The value of α was chosen to be higher than the smallest expected distance between landmarks plus the sensor and vehicle uncertainty [353].

A common limitation of the ML estimator occurs if there are several similarly-likely hypotheses [150]. However, for the sea trials of navigation off the piling dock, the dual sonar system provided reliable detection of distinct, stationary landmarks, allowing the ML estimator to be used without the need to track multiple correspondence hypotheses [354]. Should future deployments require navigation in more complex, cluttered environments, alternative techniques such as the joint-compatibility branch and bound (JCCB) algorithm and the negative logarithm of the matching likelihood (NLML) algorithm are able to provide more robust estimation of landmark correspondences [352, 353], at the expense of increased computational complexity. The modular navigation algorithms provide a common interface for alternative correspondence estimators to be 'slotted in' in future operation.

The implementation of EKF ML SLAM included the option of recording each landmark with a signature variable (section 5.5) to describe additional features of the landmark to aid with feature correspondence beyond simply relying on observed position. The characteristics commonly extracted to define sonar features vary with the sonar configuration and typical landmark form [360]. However, these commonly comprise: perimeter, area, area-to-perimeter ratio and radial signature (the distance from the feature's centroid to its boundary as a function of angle, a more detailed measure of shape than the ellipse ratio described previously) [361].

The sonar measurement of area, orientation and ellipse ratio was comparable between scans for the same object, under the same conditions, at the same range and imaged from the same angle. However, too many factors affected the sonar return to reliably use these characteristics to identify landmark correspondences *alone*, particularly with an unknown catalogue of similar targets (dock pilings or kelp stipes). Landmark descriptors are less reliable when the landmarks have similar characteristics; the example of pier legs is given [362] similar to the dock pilings presented here. Instead, an opportunity for future work uses these characteristics in conjunction with the feature position to *aid* estimating landmark correspondences.

6.3.5.5 Development of landmark weighting

The effect of each individual estimate on the overall localisation estimate from tracking each landmark would usually be determined by the weighting assigned to each estimate, according to the EKF framework introduced in 5.3.6. This weighting is calculated by the uncertainty associated with the measurement. Therefore, landmarks where the measurement is uncertain (for example due to high range) or where the correspondence is uncertain (for example due to few unique features) would have a low weighting. That way, their uncertain estimate of the change in position would have a lesser effect than landmarks which were deemed to be more reliable indicators. However, in this example, as the uncertainty of measurements taken by the sonar was not weighted according to range, each position estimate had an equal weighting.

As the uncertainty of all measurements was assumed to be equal, the uncertainty of the position estimate was inversely proportional to the number of tracked features (the more features tracked between positions, the less uncertain the position estimate was). When presenting the estimated position change in Table 6.7, the number of LM used by the SLAM algorithms to calculate the localisation estimate was also presented. This value determined the uncertainty associated with the localisation estimate, for example a single LM was tracked from left to right but which was not observed in the intermediate straight position. Although only a single LM was tracked and there is only a relatively uncertain localisation estimate from this single observation, it still reinforced the estimate from the other landmarks tracked between consecutive stations.

Further characterisation and ground truthing of the uncertainty associated with each sonar measurement has the potential to increase navigation robustness, by allowing landmark (and localisation) uncertainty to be correctly weighted.

6.3.5.6 Development to 3D mapping

For nearshore navigation, 2D SLAM was justified to be adequate in section 5.3.4.3. The 2D SLAM implementation tracked position in x, y and vehicle yaw angle. However, the vehicle still had a highly accurate and reliable estimation of depth (pressure sensor) and altitude (Delta T sonar). 3D orientation was also measured (Xsens INS & magnetometers) and stability in pitch and roll ensured through the high metacentric height and cylindrical hull design.

All survey and map data was still gathered in 3D (for example the 3D Delta T sonar scans), it was just the SLAM navigation system which navigated and localised *from landmarks in 2D*. Simplification of *SLAM* to 2D without simplifying *operation* to 2D afforded a significant reduction in computational complexity using a pair of assumptions to avoid perceptual aliasing [74]:

a) the vehicle operates at a constant height, referenced to the seabed if there are significant variations in tide height or referenced to the surface if the bathymetry is very uneven,
b) or, that all landmarks are uniform over the entire vertical height.

For the dock survey and mapping, both of these assumptions were valid, with the exception of cross (diagonal bracing) pilings. For the kelp bed application, landmarks were not necessarily vertically uniform, requiring more accurate depth holding during a survey.

Referring back to the original requirement which prompted the development of sonar-aided SLAM, the need for a combination of absolute and relative sensors for each degree of freedom was established in Chapter 2. The navigation sensor suite on its own can provide accurate and absolute (drift free) measurements of z position and pitch, roll and yaw angle. However, sonar aided SLAM was required to provide absolute position data in x and y. The 2D sonar-aided SLAM implementation fulfilled this requirement precisely. *Sonar-aided SLAM for nearshore environments provided the solution to drift free navigation in x and y thus completing the navigation system without the need for 3D SLAM.*

Further benefits are also available as the algorithm development advances to realise sensor fusion of the full Delta T 3D vertical swath data. The limitation with compression to 2D is that only vertical features can be reliably identified. A diagonal feature which is parallel to the sonar swath, i.e. a piling aligned with the vehicle and leaning either directly towards the vehicle or away from it, will appear as a ‘smeared’ feature on the intensity plot, a large object of a lower intensity, when in fact this is a distinctive landmark when viewed in 3D. Although this limitation is mitigated by overlaying several scans from various directions taken from various locations, it would be avoided altogether by techniques for full 3D object detection and registration in 3D space using the vehicle’s navigation sensors. 3D object detection is considered as future development.

6.3.5.7 Comparison with existing nearshore survey and mapping

The dock surveying and mapping application discussed here provided an excellent test of the hardware and software systems and demonstrated many successes, including providing an evaluation of the performance of the navigation system against a ground truth. When compared to the results available from dead reckoning INS navigation between GPS fixes alone (including the results discussed in Chapter 3), sonar-aided SLAM provided a significant improvement. From

the individual position changes and the associated errors shown in Table 6.6 and from the summaries shown in Table 6.7 and Table 6.8, it can be seen that the average localisation error was 0.45m at the intermediate station and 0.09m overall (1.3% of the total arc of displacement). When compared to the equivalent positional estimates which could be gained from dead reckoning INS sensors alone, this is very good, and more importantly, this is independent of drift over time and does not require high-rate detectable movements. Typical high budget INS systems exhibit a drift of approximately 1100 metres / hour CEP [79] and the low budget Xsens IMU used on *SeaBiscuit* is several orders of magnitude worse.

SLAM using a scanning sonar in structured shallow water environments has been demonstrated elsewhere. However, this often uses a DVL to aid navigation [16] in the absence of clearly defined landmarks such as the dock pilings. In this case [16], a 50 minute duration, 600m transect was performed in a marina, with the vehicle always operating with at least one marina wall in range of the scanning sonar. Drift-free localisation over the 50 minute survey was maintained with an x, y error of <±5m evaluated against a GPS ground truth, and SLAM was used to register maps of the marina walls. Although the accuracy and scanning sonar technique of *SeaBiscuit* is comparable, the frequent sonar landmarks present on the dock survey allowed accurate drift-free operation without an expensive DVL, which has the potential for unreliability in the kelp beds discussed in section 2.3. When sufficient sonar landmarks are available, DVL free navigation using artificially deployed sonar landmarks has also been demonstrated elsewhere with an accuracy of approximately 5m [211].

A comparable accuracy is possible using DVL-aided *visual* seafloor tracking to provide time-independent (drift-free) error characteristics [147], or in the absence of a DVL [30]. Similar to the sonar-aided SLAM requirement for sonar landmarks, visual seafloor tracking requires operation in proximity to a sufficiently diverse seafloor, coupled with good visibility, both of which render visual seafloor tracking unsuitable to operation in kelp beds. Similarly, bathymetric-aided SLAM is feasible to provide a drift-free source of information to augment navigation [126], yet requires an unobstructed sonar view of a sufficiently bathymetrically diverse seabed. Although this may be possible in the kelp beds, it cannot be solely relied upon due to the risk of the vegetation obscuring the seabed.

The axisymmetric hull and holonomic motion of *SeaBiscuit* allowed the integration of vertical multibeam sonar data, to both expand the sonar coverage and angular resolution and to provide vertical resolution. On a budget several orders of magnitude greater than *SeaBiscuit*, with dimensions and weight infeasible for deployment and operation in the kelp beds, the AUV *DepthX* provided a demonstration of axisymmetric holonomic spin mapping [288]. *DepthX* uses a navigation sensor suite comprising an INS, DVL, a 56-beam radial sonar array and USBL as described previously. Accuracy measures are not well documented from the significantly more sophisticated (and higher budget) sensing suite, in particular due to the lack of ground truth available during the field trials of *DepthX*. The accuracy is however sufficient to create high detail maps of vertical flooded cave environments, operating to depths of several hundred metres [288].

The later revision of *DepthX* to *ENDURANCE* quotes a nominal navigation accuracy of 0.04% of the distance travelled [29], but again there is little further documentation of operational navigation accuracy. Whilst the quoted figure is significantly better than that of *SeaBiscuit*, the budget and sensor suite dimensions are also significantly higher. In the case of *DepthX* and *ENDURANCE*, drift-free navigation is realised from the USBL update relative to a surface transmitter, deemed infeasible for operation in the kelp beds, as discussed in section 2.3.

6.3.6 **Conclusions**

These field trials have demonstrated SLAM with previously acquired survey footage. Through the common standard of log files and time stamping, survey footage can be gathered from any location, and reprocessed at a later date as more advanced algorithms are developed. In this way, any development to the SLAM and habitat mapping algorithms can be applied retrospectively to all previously gathered datasets with the corresponding benefits, without the need for a costly and time consuming redeployment. Although only a single proof of concept is presented here, datasets were gathered for a variety of conditions, depths and positions around the dock, including a variety of movements, including pans at stationary positions, oscillating and continuous pans while translating around the dock. Processing of these datasets is left as future work, coupled with the further development of the SLAM algorithms. The SLAM and image processing algorithms are feasible for realtime operation given the onboard computing power and a map of this complexity, allowing the opportunity for online realtime SLAM around the piling dock in future deployments.

Overall, the piling dock field trial provided a successful proof of concept of the benefits of the holonomic iROV mapping technique for a structured environment. The information gains from using sensor fusion, and a mapping accuracy comparable to the individual sensor resolution and accuracy were demonstrated. Thus accurate mapping was achieved on a budget, with the accuracy of results proposed to be scalable with an increased sensing budget, with straightforward integration of alternative sensors facilitated by the modular hardware and software structure. The near-vertical pilings provided a useful proof of concept of nearshore navigation and mapping prior to the first kelp bed deployments of the iROV *SeaBiscuit* in an unstructured open ocean nearshore environment.

Chapter 7 Kelp Mapping

7.1 Introduction

Following the demonstration using the iROV to survey a dock in the previous chapter, the focus moved to kelp bed mapping to support a coastal ecosystems research group. As part of the staged field trials, *SeaBiscuit* was initially calibrated and tested on an 'artificial' kelp bed of kelp stipes transplanted to a sheltered but open-water real-world environment, described in section 7.2.

Calibration and verification of detection using a known dimensioned arrangement of kelp stipes reduced uncertainty and increased accuracy when compared to methods which do not compare detection against an exact sonar target, such as diver surveys and camera drops in the general area surveyed, or manually surveying areas which dry out at low tide [20]. The only reference in the literature to using a known arrangement of kelp stipes as verification refers to a different species (giant kelp) and was only used to verify manual detection using a single beam echosounder log from a ship based survey [8]. The process described later in this chapter was extended to bull kelp, to multibeam sonar surveys from the midwater, used not only to verify detection but also to tune *autonomous* detection and parameterisation algorithms, and to relate a sonar measurement to an absolute measure of kelp biomass and biovolume.

In the summer of 2011, the first successful open ocean kelp bed maps were gathered. It was possible to identify clusters of stipes, to convert this into a useful measure of biomass and to generate a density surface across the kelp bed as discussed in section 7.3. Autonomous kelp detection algorithms were used to detect and parameterise kelp stipes mapped using both sonars, and manual registration was used to mosaic scans from surveys taken on different days of the same kelp beds. Areas of rock and raised bathymetry were delineated by target mass, and realtime verification of kelp stipe targets was provided by co-registered dual video feeds.

Referring back to the original research aim in section 1.1, to develop a tool capable of detailed mapping of kelp beds from the midwater with a resolution of individual stipes, the iROV *SeaBiscuit* was a successful proof of concept. Comparing the iROV solution to alternative techniques discussed in the literature review in Chapter 2, detail and resolution benefits were demonstrated over ship based [7, 8] and aerial surveys [4, 5], and cost, coverage and positioning benefits were demonstrated over divers [1, 11] and camera drops / tows [3], providing quantitative mapping of kelp stipes from the midwater.

Compared to existing ROVs and AUVs which often specifically avoid operating under canopy forming kelp [14], the hybrid iROV technique developed ensured reliable and robust kelp mapping. A hybrid control architecture, combining onboard position-awareness and low-level autonomy, allowed survey data to be registered with a position reference and relieved the operator of station-keeping and course-holding. Data validity in dynamic conditions was ensured by remote supervision and realtime data verification. Robust, reliable high-level control was provided by maintaining the operator-in-the-loop. A hybrid power-supply also provided the unlimited mission duration and security of a tethered vehicle, with the high-powered manoeuvring thrust required to navigate reliably in and around the full height kelp stipes.

Mapping in transit, independent of course was enabled by sonar fusion, exploiting the holonomic movement capabilities of the vehicle, and realtime validation of the exact sonar targets reduced ambiguity when mapping kelp stipes and allowed reliable autonomous detection.

7.2 Calibration and test: Artificial kelp bed

Following the successful proof of underwater navigation and mapping in sheltered waters with clearly defined semi-structured targets (dock pilings), the staged sea trials continued with mapping an artificial kelp bed, still in sheltered waters. This allowed calibration of the habitat mapping sensors in constant ground truth conditions to relate sonar scans to an absolute kelp biomass and biovolume estimate, rather than just measurements of relative density.

The sonar image processing algorithms could also be tuned in constant ground truth conditions to enable optimal and reliable detection of the kelp stipes for autonomous mapping. Manual visual validation was also employed, both for the artificial kelp bed and for open ocean scans, as an aid to tuning the image processing and feature extraction algorithms to reliably extract kelp stipes, and to ground truth the density estimates. Video footage was reviewed, either in realtime or during later analysis to confirm that (visibility and target range permitting) the targets observed on the sonar (kelp stipes, fish, jellyfish, mysids, seabed) were correctly identified.

7.2.1 Calibration kelp bed setup

A known quantity and known arrangement of intact kelp stipes were anchored in a known position in sheltered waters off the calibration piling dock discussed in the previous section. The five kelp stipes used were transplanted to a comparable water depth and care was taken to ensure that the stipe and pneumatocyst structure remained intact.

Figure 7.1 below shows the arrangement of the kelp stipes relative to the calibration piling dock. The position was measured from the surface relative to the dock pilings, and verified by divers underwater. The figure is to scale and geometrically accurate. The five individual stipes are numbered in this diagram and dimensioned in the following section.

The stipes were anchored to a circular frame, 1.08m in diameter and at known positions around the frame circumference. A 10mm diameter nylon rope holding a marker buoy at the water surface was anchored to the centre of the frame.

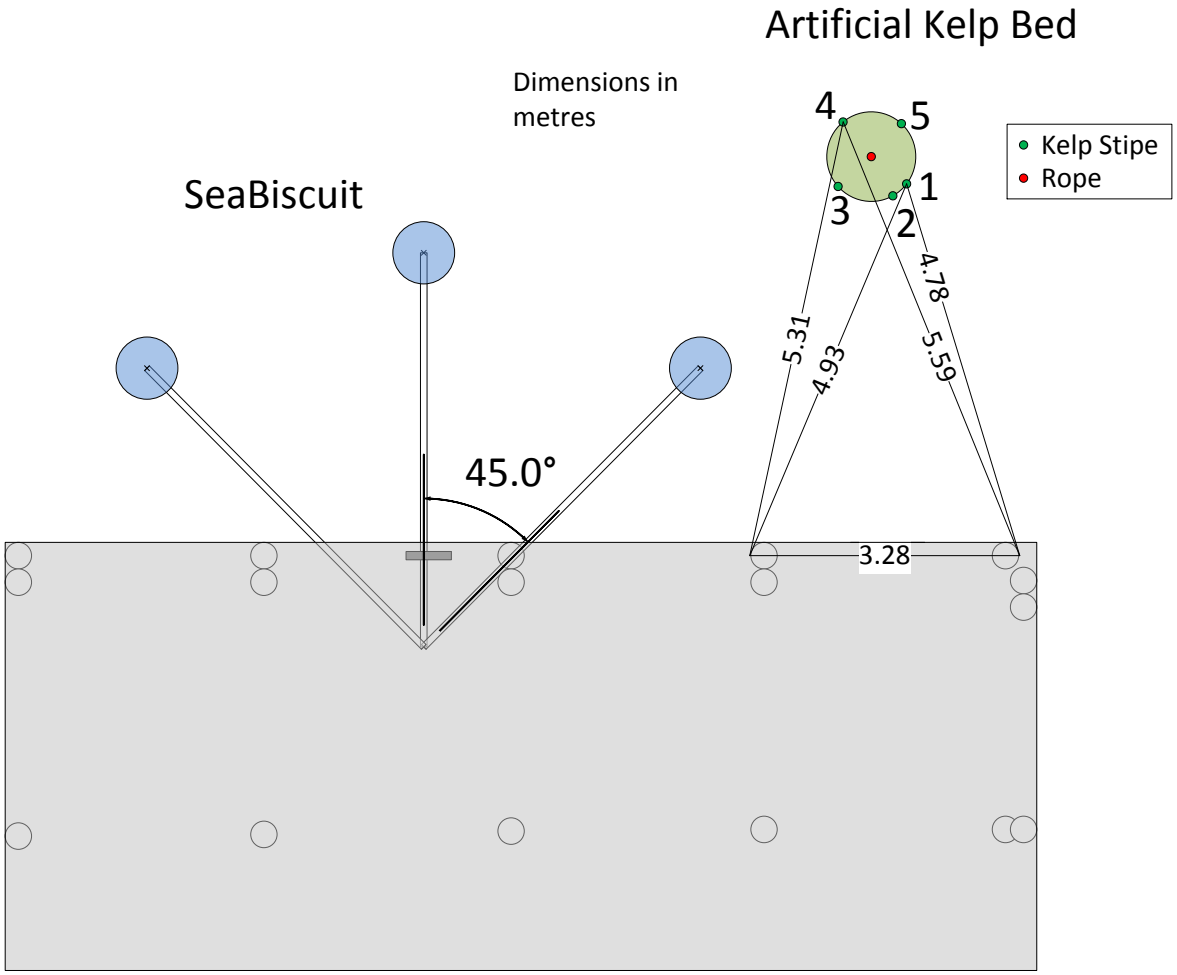

Figure 7.1 - The location of the artificial kelp bed at a known position and known orientation/arrangement off the calibration piling dock. The figure is to scale and geometrically accurate from diver surveys and surface measurements. Dimensions are shown in metres.

7.2.1.1 Kelp measurement

The 5 stipes forming the artificial kelp bed were fully dimensioned, both upon installation, and after a period of 4 days to ensure that no degradation had occurred. No measurable change in dimensions was observed between measurements taken when the kelp was first transplanted to when it was removed for dissection. The gas volumes were also intact. Therefore, it was assumed that no significant change in biovolume or gas volume occurred during the 4 days in which calibration scans took place [363].

The overall height, diameter across this height at 30 cm intervals, wall thickness, longitudinal cavity volume, pneumatocyst volume, tissue density, biomass and biovolume were all measured. The internal measurements required dissection of the kelp and were performed only once during recovery of the artificial kelp bed. Figure 7.2 below shows the internal and external diameter of the 5 stipes, measured at 30cm intervals from the seabed up to and including the pneumatocyst.

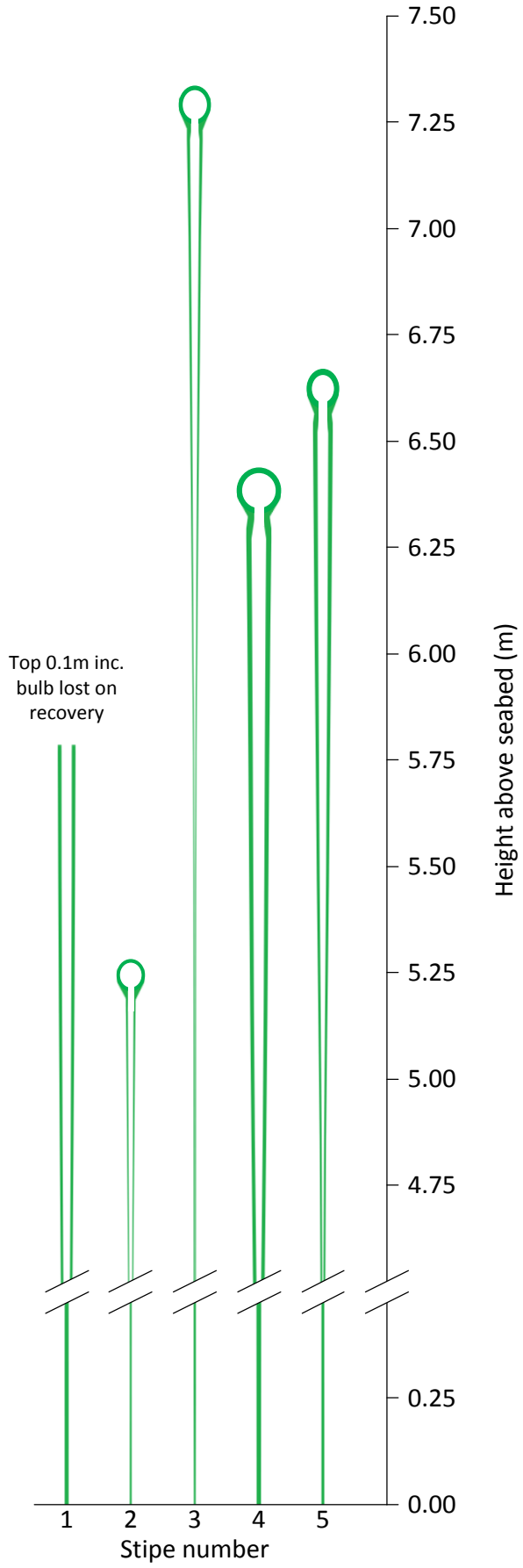

Figure 7.2 - The artificial kelp bed was made up of 5 stipes, shown here drawn to scale. The lower section (0.25-4.75m) of the kelp stipes (the majority of which was not gas-filled and followed the same trend as above) is omitted from the diagram in order to preserve image scale and clarity. Although internal and external diameter, pneumatocyst internal and external dimensions, overall height and gas volume are all drawn to scale, the minimum line thickness has been increased for clarity in print, hence the very thin walls and very thin diameter stipes appear slightly thicker in this diagram.

Figure 7.3 below shows a zoomed in detail of the pneumatocyst of stipe 5 showing the measurements taken. The varying wall thickness including at the widest and narrowest point (the neck) of the stipe were dimensioned, as were the pneumatocyst inside and outside horizontal and vertical diameters.

The kelp fronds are not shown, nor were these dimensioned – the fronds had a much weaker acoustic target strength compared to the gas-filled stipe and pneumatocyst, and were not considered at this stage of the model.

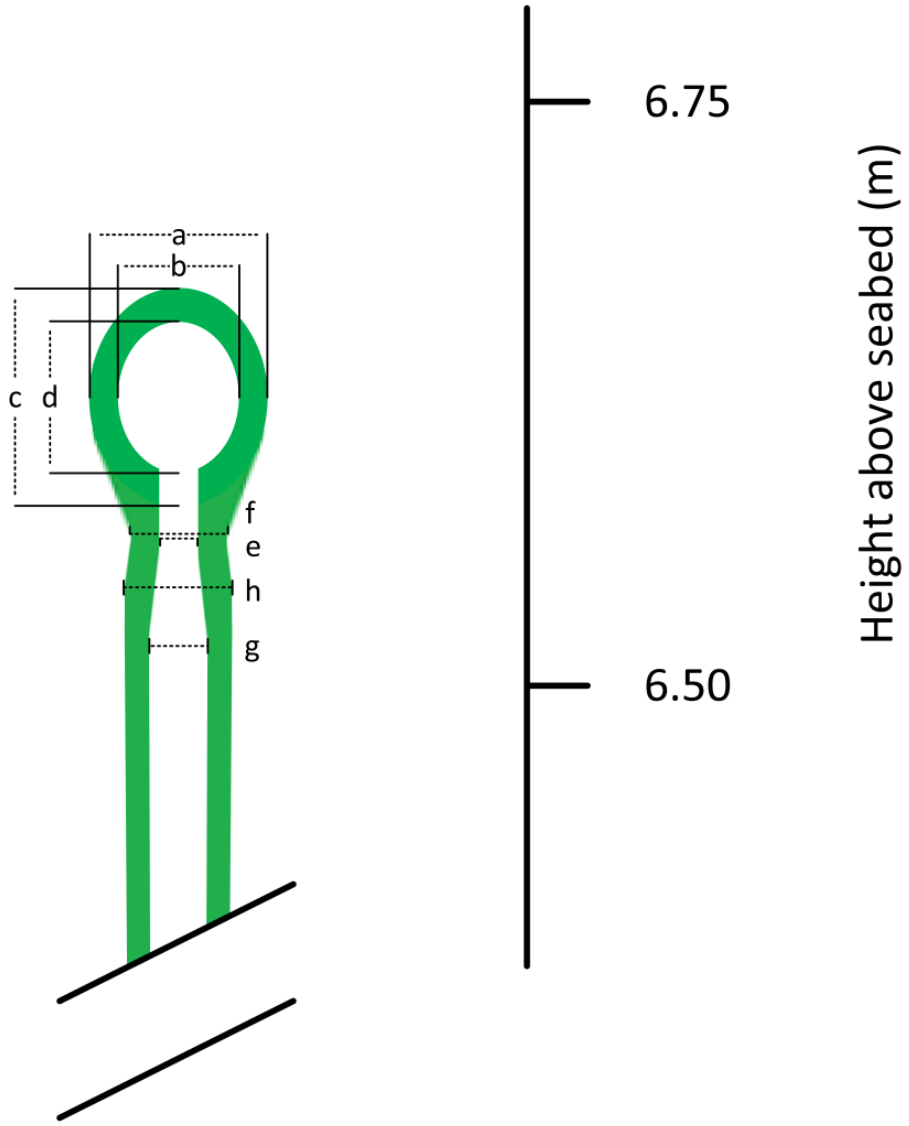

Figure 7.3 - A zoomed in dimensioned diagram showing the pneumatocyst of stipe 5. The labelled dimensions are below in Table 7.1.

Table 7.1 - Pneumatocyst detailed dimensions for stipe 5.

a	Pneumatocyst	External width	73.8 mm
b		Internal width	54.4 mm
c		External height	91.0 mm
d		Internal height	71.7 mm
e	Neck (narrowest point internally)	Internal diameter	16.2 mm
f	Neck (narrowest point externally)	External diameter	35.8 mm
g	Widest point internally	Internal diameter	25.5 mm
h	Widest point externally	External diameter	46.0 mm

7.2.2 **Sonar calibration**

The dimensioned artificial kelp bed allowed the sonar units to be calibrated, allowing the open ocean kelp bed scans to be related to actual estimates of biomass and biovolume.

Figure 7.4 below shows an example 10m range sonar scan of the artificial kelp bed using the 852 sonar. The raw scan is shown on the left, an overlay identifying the targets in the middle and a zoomed detail of the artificial kelp bed on the right. The 5 stipes with numeric identifiers arranged radially around the central rope marker can be seen. These numbers match the stipe numbers in Figure 7.2. This scan was taken at an approximate height of 4.5m above bottom of the kelps stipes shown in Figure 7.2, the lowest point where all 5 stipes had a measurable gas pocket.

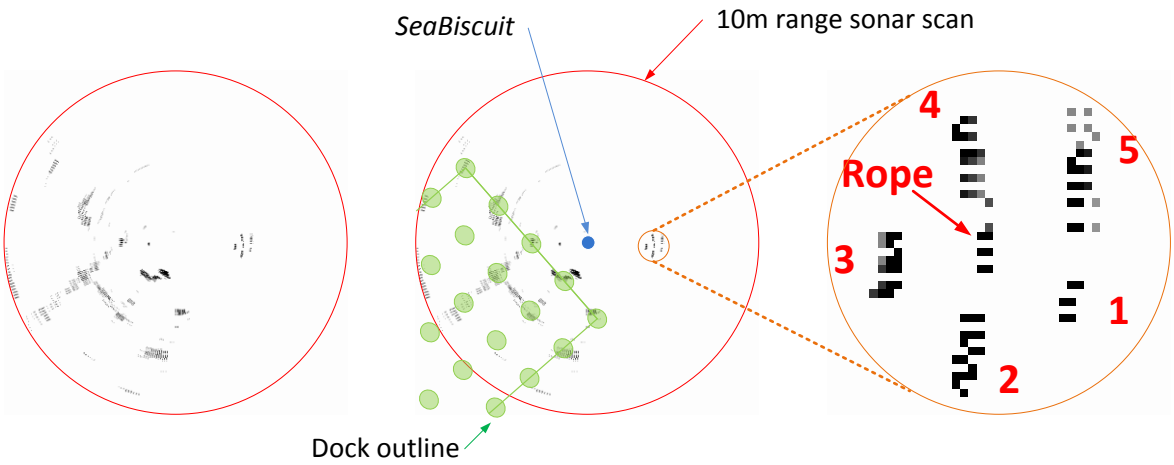

Figure 7.4 - Example 852 10m range sonar scan showing the 5 stipes of the artificial kelp bed arranged radially around a central rope marker adjacent to the piling dock. The raw scan is shown on the left, an overlay identifying the targets is shown in the middle and the right hand scan shows a zoomed detail of the artificial kelp bed. Each stipe is identified as per the numbering system developed in Figure 7.2 and continued into Table 7.2 below.

The stipe and gas pocket cross sectional area (CSA) for each stipe at this height are shown in Table 7.2 below, as is the 'pixel mass' of the kelp stipes as detected by the sonar scan. The 'pixel mass' in this case was defined as the sum of the intensities of the pixels making up that feature.

Table 7.2 - Kelp stipe data at 4.5m above the base of the stipes, from the 852 sonar scan shown in Figure 7.4.

Feature:	Tissue CSA (mm^2):	Gas pocket CSA (mm^2):	Sonar Pixel Mass:	Sonar Pixel Mass / Gas Pocket CSA:	Sonar Pixel Mass / Tissue CSA:	Sonar Pixel Mass / Overall (Gas + Tissue) CSA:
Stipe 1	345.63	174.60	350	2.00	1.01	0.67
Stipe 2	61.97	37.90	819	21.61	13.22	8.20
Stipe 3	18.00	1.24	745	600.34	41.38	38.71
Stipe 4	417.60	86.32	819	9.49	1.96	1.63
Stipe 5	85.96	7.69	849	110.34	9.88	9.07
Rope	10mmØ 78.54mm^2 CSA		397			5.05

As seen from the zoomed detail in Figure 7.4 and the data in Table 7.2, the resolution of the 852 sonar was sufficient to distinguish individual stipes, yet too poor to accurately quantitatively represent the individual stipes. This was compounded at greater ranges as the radial beams diverged reducing spatial resolution, and compounded further at higher *range settings* as the same number of range bins were used to represent greater spatial areas. While the scans above show a 10m range, the majority of scans taken at sea used a 20m range to increase coverage rate.

However, although the resolution limited individual stipe measurement, in practical open-ocean settings, this was not a problem. Due to the turbulent nature of the kelp beds, stipes were often twisted and intertwined, presenting a cluster of stipes, indistinguishable by sonar. Instead the

broader density and distribution of kelp stipes was more important for the ecological surveys of the kelp beds. This density and distribution data was represented as a surface, an average of each cluster of kelp stipes, to give the overall density and distribution picture, accounting for the clusters of intertwined kelp stipes as well as individual stipes.

For the example calibration kelp bed shown above, the stipes were combined into a cluster of 5 stipes and the rope was subtracted to provide a calibration value to relate kelp tissue CSA and kelp gas pocket CSA in the plane with pixel mass.

The acoustic characteristics of the kelp at the scanning frequency, (675kHz and 850kHz in this case), the output power and gain of the sonar and the image processing algorithms all affected the sonar return. The calibration process was repeated for a series of ranges, range settings and gain values to generate several calibration datasets which were then applied to scans taken in the open ocean. For the examples presented above taken under the conditions detailed, the following calibration values were obtained.

Table 7.3 - Summary of 852 sonar kelp stipe calibration values.

Sonar Parameters:	Σ Sonar Pixel Mass (w/o rope):	Σ Tissue CSA (mm^2):	Σ Gas pocket CSA (mm^2):	Sonar Pixel Mass / Tissue CSA:	Sonar Pixel Mass / Gas Pocket CSA:	Sonar Pixel Mass / Overall (Gas + Tissue) CSA:
R10 G10 F675	3582	929.2	307.8	3.85	11.64	2.90
R20 G10 F675	2390	929.2	307.8	2.57	7.76	1.93

In Table 7.3 above, the sonar parameters in column 1 are designated as follows: R = range in m, G = gain in dB, and F = frequency in kHz. The sonar pixel mass refers to the sum of the intensities of all pixels which made up the 5 stipes of the artificial kelp bed from the scan taken at this specific height with the pixels which made up the marker rope removed by inspection. Σ Tissue CSA refers to the sum of the cross sectional area (CSA) of the tissue of all 5 stipes at this height, Σ Gas pocket CSA to the gas pocket cross sectional area. From these figures, the calibration values relating pixel mass to tissue CSA and gas pocket CSA were calculated.

Although the calibration model was made up of a low number of samples, the process demonstrated using the 852 scanning sonar for kelp detection and identification, as well as relating the strength of the return to kelp biomass / biovolume. Expansion of the table shown above and a more detailed calibration model are discussed as future work in section 8.2.

An accurate measure of the entire biomass / biovolume of the kelp stipe depended on the 3D full shape of the kelp stipe (i.e. its thickness over the entire vertical height). However, planar scans still provided a useful comparative estimate. For preliminary results, the 2D planar data gathered at a constant and repeatable depth under constant repeatable conditions was used for direct comparison of density and distribution between kelp beds. The constant survey height was chosen to be representative and to provide good scan results.

In the same manner as for the dock survey and mapping application, the Delta T sonar allowed 2D planar maps of the kelp distribution to be registered in 3D and expanded to include the full vertical characteristics of the kelp bed. Initially the same technique compressing the Delta T data to 2D using the algorithms discussed in section 6.3.4 was used to incorporate the additional information provided by the Delta T profiling sonar. These information gains, realised through sensor fusion, included imaging of the entire water depth, an alternative frequency to the 852 sonar and a much faster sampling rate. Additional calibration datasets were gathered using the Delta T sonar and for correlation with the scans obtained with the 852 sonar.

7.3 Open ocean: Kelp bed mapping

The initial field trials off the dock demonstrated the mapping accuracy, reliability and benefits of the intelligent, position-aware iROV. They allowed the performance of the vehicle to be assessed under real-world conditions and compared to a ground truth, an absolute position reference and the user generated geometric dock map.

Following the successful results described above, the focus shifted to the surveying and mapping of kelp beds. The aim was to use the iROV to provide a useful underwater survey and mapping tool while also developing and evaluating the mapping and navigation algorithms for operation in the target nearshore ocean environment. The kelp beds, vast underwater forests of seaweed, extending from the seabed up to the surface in shallow waters (<30m) support populations of mysids, one of the food sources of grey whales.

7.3.1 Grey whale research in Canada

The pacific population of grey whales (*Eschrichtius robustus*) are migratory animals, which travel north from their breeding grounds in Mexico to the coast of British Columbia, Canada and beyond into Alaska to feed over the summer months [364]. Relatively little is still known about the feeding habits, food sources, activity budgets and behaviour of these great mammals. More importantly in recent years, their interaction with the increasing volume of whale-watching tourism boats has become a further topic for study, with some concerns that these whale-watching boats may be affecting the behaviour of the grey whales [365].

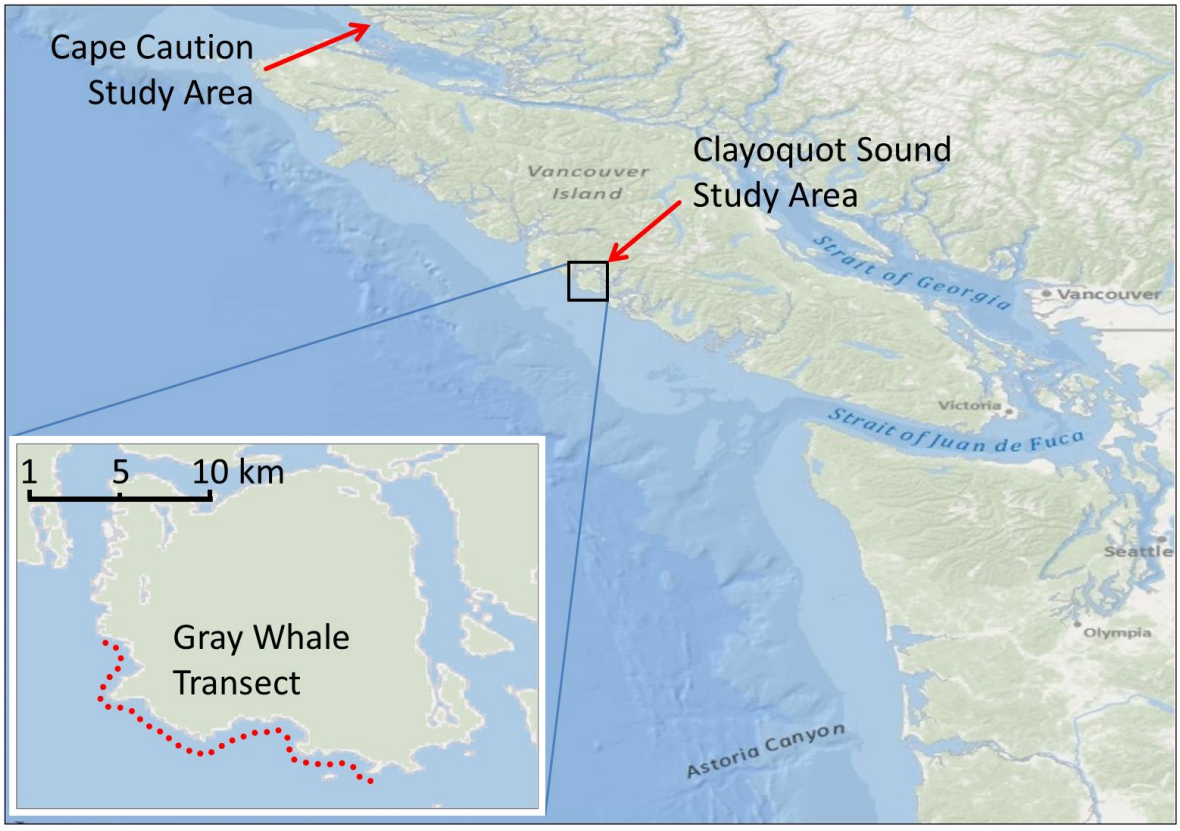

Figure 7.5 - Map of Vancouver Island, Canada showing the Cape Caution and Clayoquot Sound study areas. The zoomed section shows Flores Island, the location of the dock survey application discussed in the previous section. The dotted line shows the grey whale transect, a route surveyed bi-weekly during the grey whale feeding season to evaluate the abundance, distribution and behaviour of any grey whales present [2]. This transect route passes several large kelp beds.

For nearly 20 years, the *Coastal Ecosystems Research Foundation* (CERF) has combined grey whale research with a successful eco-tourism venture focusing on the Cape Caution area of British Columbia, Canada [366]. In recent years, CERF joined with a group from the Department of Geography at the University of Victoria [367] and moved its operations to Clayoquot Sound off the coast of Tofino, Vancouver Island, British Columbia, Canada. Figure 7.5 above shows the location of the two study areas in relation to Vancouver Island, Canada.

The research operation consisted of a small group of researchers and crew (typically 5-10) and various small boats. The fleet comprised *Stardust*, a 37ft research vessel, *Drifter*, a 22ft aluminium speedboat, a fleet of four kayaks and a small dinghy, *Silvia*. This was representative of the typical intended users of the underwater vehicle developed – a relatively small-scale research group working on a limited budget.

Much of the existing underwater surveying and mapping conducted by the group was performed by either SCUBA divers or by instruments lowered from the boats. The use of an underwater vehicle had the potential to both improve the data quality and to increase the survey coverage. Using the iROV *SeaBiscuit* as a position-aware steerable instrument platform, under remote control from the surface provided realtime video and sonar feedback of the underwater environment, allowing the survey to be directed in realtime. Using sonar fusion, both the area and the density of the kelp beds was measured. Concurrent video was also used for an insight into the contents of the kelp beds, for example species distribution. Further work to extend the sonar mapping to estimate the volume and density of mysid swarms is discussed in section 8.6.2.

7.3.2 Study site overview

The open ocean kelp bed sea trials were intended to provide a useful scientific dataset, while also evaluating the performance of the vehicle in the target nearshore environment. Three of the kelp beds surveyed in the Clayoquot Sound study area are shown below in Figure 7.6. The dataset was extended to approximately ten further kelp beds in 2011.

These kelp beds were selected with the research scientists to be kelp beds where grey whales had been seen feeding, and were therefore of interest in terms of the kelp and mysid abundance and distribution. These kelp beds were also selected for the initial trials due to their relatively small and manageable size, both for this mapping application, but also for several of the related acoustic experiments investigating ambient noise. These acoustic experiments (discussed in section 8.6.1) also required a map of the distribution of kelp stipes.

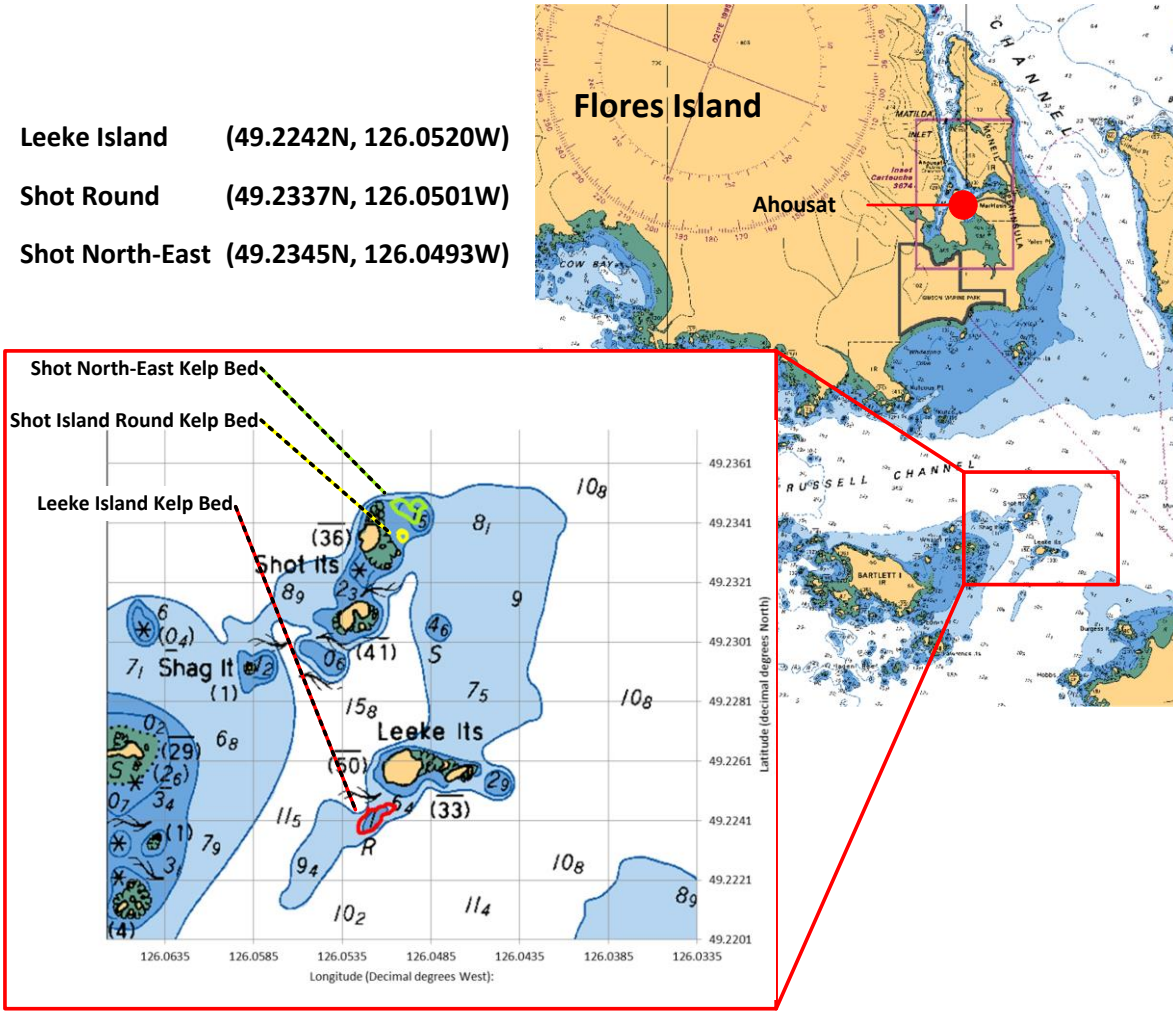

Figure 7.6 - The location of three of the kelp beds surveyed in Clayoquot Sound. The GPS marked kelp bed perimeters are shown on the inset in red, yellow and green tracks.

7.3.3 Objective and context

Kelp beds range in size from a few tens of square metres up to square kilometres. Their occurrence is widely dispersed along the coast where conditions permit (water depth, tide and current speed, benthic composition, etc.) and the location of most of the major kelp beds in the study area was known. However, relatively little was known beyond this, and it was this extended information and understanding which could be used to support the other coastal ecosystems research. Specific to the tasks performed by the underwater vehicle, the objectives were to:

1. Generate a map of the kelp bed perimeter (delineate).
2. Add the topography of the seafloor (bathymetry).
3. Populate the map with an estimate of the density and distribution of kelp.

The outcome of the research was thus a populated kelp bed map which could be used for inspection, calculating spatial and temporal trends and populated with further data. For example, whale feeding and behaviour observations, other marine life, change in mysid/kelp density and makeup over time (e.g. with whale feeding and over winter), diver collected samples, water chemistry (conductivity, temperature, fluorometry) could all be added and co-registered on the kelp bed map. Many of these additional modes of data could be gathered by the underwater vehicle simultaneously to compiling the kelp map through the modular expansion of the sensing system of the *SeaBiscuit*. For example, sensors to measure conductivity, temperature, fluorometry as well as high-resolution cameras can all be easily interfaced.

7.3.4 **Methods**

As an example and proof of concept of the benefits of using the iROV *SeaBiscuit* for kelp bed mapping, the method and example results are presented below for the Leeke Island kelp bed. Taking each of the objectives listed above, an overview is provided of the data gathered, the data processing and analysis techniques, and examples of the integration of the data from different sensors to construct the overall populated map. Figure 7.7 documents deploying the iROV *SeaBiscuit* into the kelp beds from the research vessel *Stardust* during the 2010 field season.

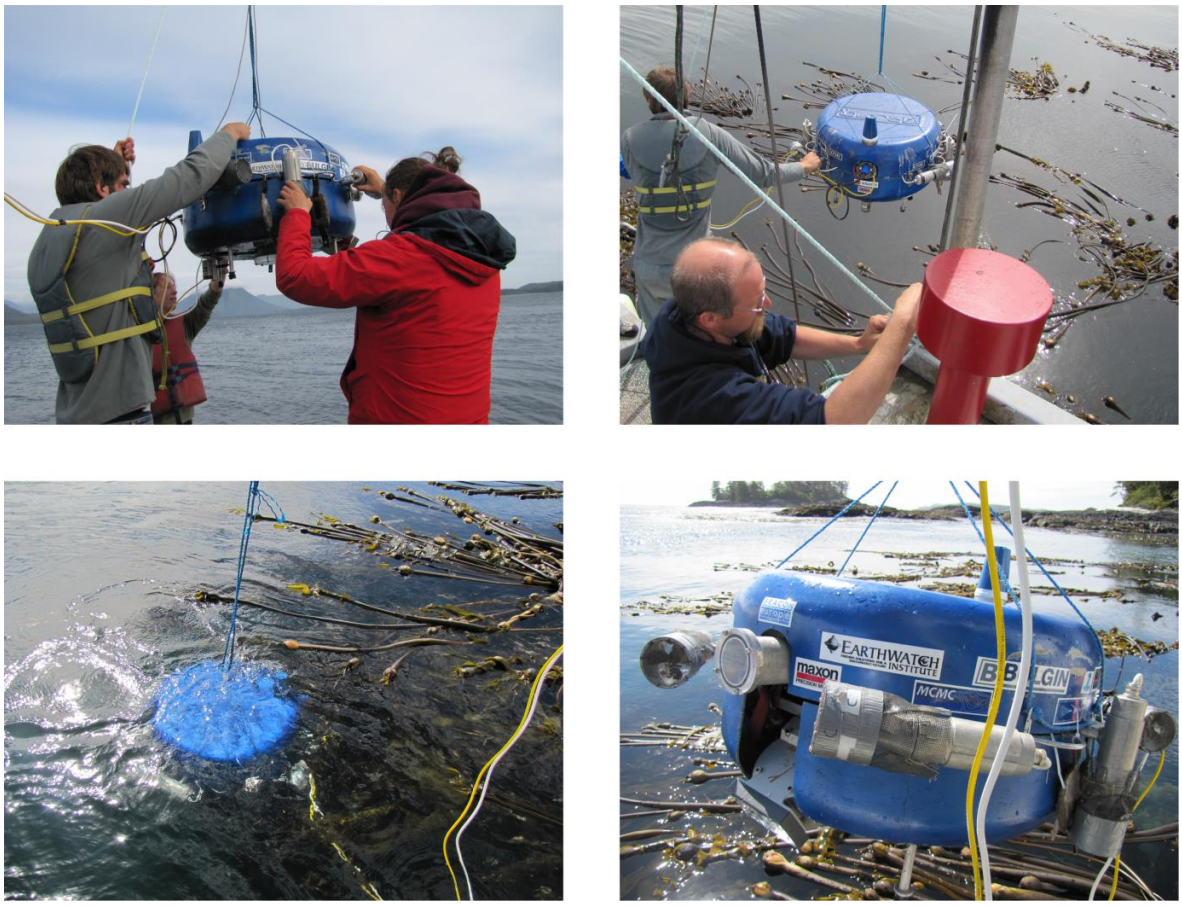

Figure 7.7 - Deploying the iROV *SeaBiscuit* into the Leeke Island kelp bed, British Columbia, Canada (2010).

7.3.4.1 Mapping the kelp bed perimeter

The first stage of mapping the kelp bed was to establish the perimeter, or delineate the boundary. As seen in Figure 7.6 earlier, although some kelp beds are indicated on marine charts, there is no information covering their expanse or perimeter. Delineating large kelp beds using the underwater vehicle was time consuming. It was usually more efficient to map an approximate perimeter at the surface by manoeuvring the surface vessel around the perimeter of the kelp bed while recording position using GPS. For complex perimeters, or in shallow water, the small inflatable boat and kayaks were used to establish the perimeter using a handheld GPS receiver. Given the approximate perimeter created by the surface vessel, the scan areas of interest were then established and accurately mapped from the midwater using the underwater vehicle.

The effect of external water movement and tides on the flexible kelp stipes was considered on two different scales. The effect of water movement on individual kelp stipes, including techniques to correct for deviations during a survey are discussed in later sections. However, on a larger scale, tidal flows also had a significant effect on the kelp bed perimeter, as shown in Figure 7.8 below.

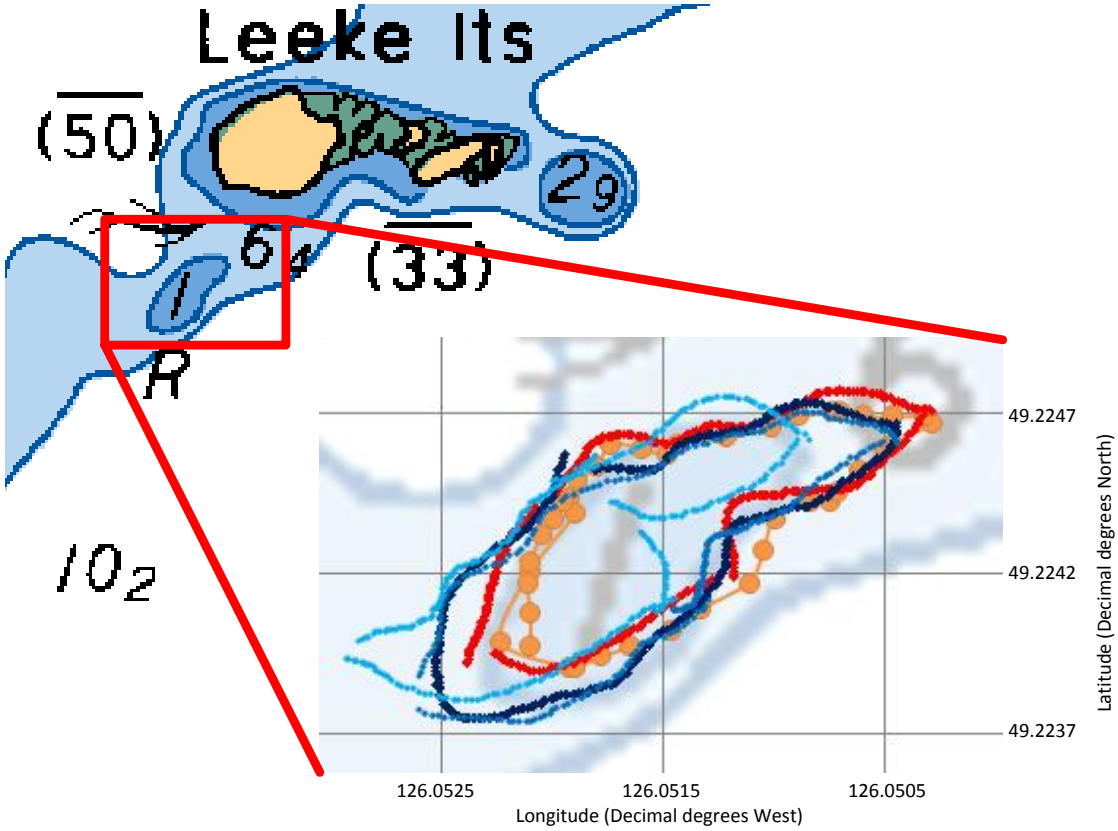

		Tide State:	Survey Time & Date:	Time to High Slack Water (HSW)	Tide Height:
Rising Tide	-3:30	Fast Rising Tide	13Sep10 12:04-12:14	3h42-3h32 before HSW	2.15 – 2.25m
	-2:00	Rising Tide	24Aug10 10:38-10:52	2h02-1h50 before HSW (Kayaked perimeter)	2.4 – 2.5m
High Slack Water	0:00	High Slack Water	8Sep10 12:33-12:40	13-20 minutes after HSW	3.6m
	+1:00	Falling Tide	13Sep10 16:48-16:54	62-68 minutes after HSW	3.25 - 3.2m
Falling Tide	+3:30	Fast Falling Tide	13Sep10 19:16-19:24	Falling Tide 3h30-3h38 after HSW	2.05 – 1.95m

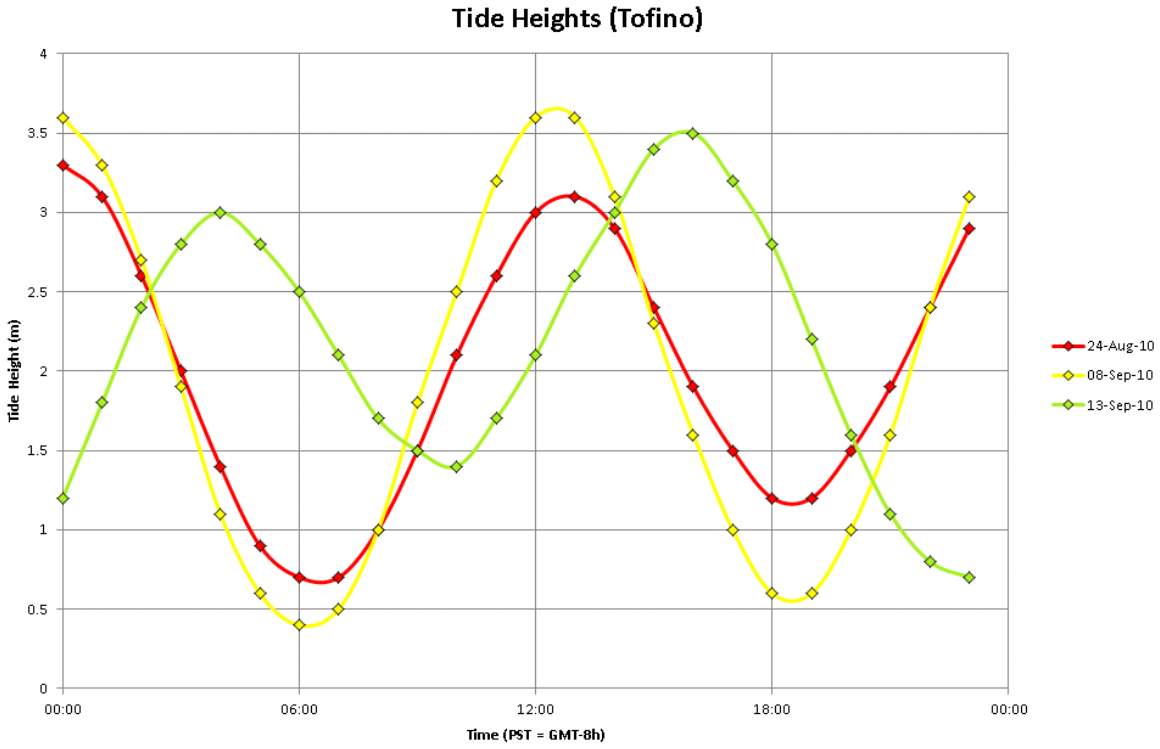

Figure 7.8 - Surveying the perimeter of the Leeke Island kelp bed at different tide heights and directions. Surveys were taken using a surface vessel or a kayak [1] as indicated in the key. The tide heights for the perimeter survey are shown in the lower plot [368]. The time and duration of the perimeter scan was compared against this and used to estimate the height and the flow speed/direction of the tide.

The effect of the tide height and flow speed/direction can be seen in Figure 7.8 above. The different colour plots indicate the kelp bed perimeter observed at different tide heights and directions according to the key shown. The red then orange plots show a rising tide until a minimum deviation was reached at the dark blue plot a few minutes after high slack water. The pale blue plot shows the reverse sway of the kelp bed approximately 1 hour after high-slack water and the turquoise plot 3h30 after high slack water. The perimeter measured by Wladichuk using a kayak and a handheld GPS receiver is shown in orange [1].

The plot in the lower part of Figure 7.8 shows the tide heights for the local port, Tofino, approximately 10 nautical miles away for the days on which the scans were conducted.

The large deviation in perimeter with tide height and flow can be seen. Tidal flow caused the flexible kelp stipes to drift over a large radius, all in the same direction. When viewed underwater, the vertical kelp stipes appeared at an angle, the obliqueness of the angle dependent on the height of the tide and the strength of the current. When viewed from above, for example when taking aerial or surface photographs to ground truth the sonar and maps, the strength of the flow, and particularly low tide heights caused the canopy of stipes and fronds to 'flop over' at the surface, thus reducing the accuracy of aerial photography mapping techniques.

Several techniques were used to ensure data quality and validity in tidal areas. The first was to ensure that all surveys were taken at the same conditions, the same tide height and the same flow. This was either at slack water (when the tide direction was changing and thus there was no flow), or at the same strength of flow and tide height. This required careful synchronisation of the tides with wind to ensure repeatable conditions.

When operating in approximately the same conditions proved too restrictive, the alternative was to model the effects of tides on the kelp stipes. The tide height and flow was predictable at every site, either interpolated from tide tables of surrounding areas or measurable on site. The trends in movement seen on Figure 7.8 were compared with the tide curves to generate an approximate model to correct scans taken at different times on subsequent days. However, a full tidal model of the kelp stipes is complex, requiring inputs of tide height, direction and flow speed to determine both the drift causing movement of the kelp stipes, but also the water height available to support the buoyant stipes. The effects of wind speed and sea state would also need to be considered. Research into modelling kelp stipes to determine wave and current interactions was reviewed in Chapter 2, yet a full tidal model of the kelp was considered infeasible at this stage, given the potential inaccuracies of using an overly simplistic approximation. Steps towards modelling the kelp stipes are discussed as future work in section 8.2.

Instead, for the surveys presented here, scans were taken at a repeatable tide state. High slack water was often used as this also provided the highest water level to ensure that the stipes were as vertical as possible. Using the tide plots shown above in Figure 7.8, a comparable tide height and flow could be found between different days. Subsequent plots detailing the map of the Leeke Island kelp bed as an example use the dark blue perimeter from the above map in Figure 7.8 (the perimeter at high slack water). To mitigate the effect of wind, scans were taken under repeatable (usually negligible) wind conditions.

7.3.4.2 Seafloor topography (bathymetry)

Given the delineated kelp bed perimeter in the x and y axes, the next step was to map the seafloor topography (bathymetry) in the z-axis over the kelp bed. During normal survey operation, many of these tasks were performed concurrently to improve efficiency and are only discussed separately here for clarity.

The bathymetry not only defined the operating region in the z-axis when surveying the kelp bed, but also provided useful scientific data. Benthic composition was estimated by video. Several techniques were used to provide bathymetric data, either corrected for, or at constant tides. Although *SeaBiscuit* could estimate water depth while underwater by adding the submerged depth (pressure sensor) to the distance to the seafloor (altitude) estimated using the Delta T sonar to get total water depth, it was as straightforward to perform this operation from the surface, which allowed the map to be registered using GPS.

The bathymetry was also surveyed from a kayak or a small RIB, using a handheld depth sounder, or by the surface support vessel *Stardust* using its echosounder. Each technique provided an increase in map coverage and survey speed over the underwater vehicle bathymetric survey, but with a corresponding decrease in map resolution. As the data output was of a common form (water depth measured at a series of points), different techniques were used depending on how varied the bathymetry was, the kelp density, and the map resolution required. The depth measurements taken by the surface vessels were also used for ground truthing and verification of the measurements made by *SeaBiscuit*.

The techniques to extract the seafloor and to estimate altitude from the Delta T sonar data were the same as those used for the dock survey and mapping application as shown in Figure 6.29 in the previous chapter. Figure 7.9 below shows an example bathymetric map presented as a 2D surface in MATLAB for the Leeke Island kelp bed. The 2D plot can also be viewed in 3D showing the peaks and troughs of the seabed by panning and rotating the camera. The markers shown on the plot represent manual depth measurements made throughout the kelp bed from a surface kayak survey in conjunction with the acoustic studies performed by Wladichuk [1] on the same kelp bed. Depth measurements were made over three days and were corrected for tide height. The colour bar describes the bathymetry, where redder colours indicate shallow water at rocky peaks within the kelp bed and bluer colours indicate deeper water towards the periphery of the kelp bed. From diver inspection, the interpolation between this resolution of sampling was deemed to be a valid representation.

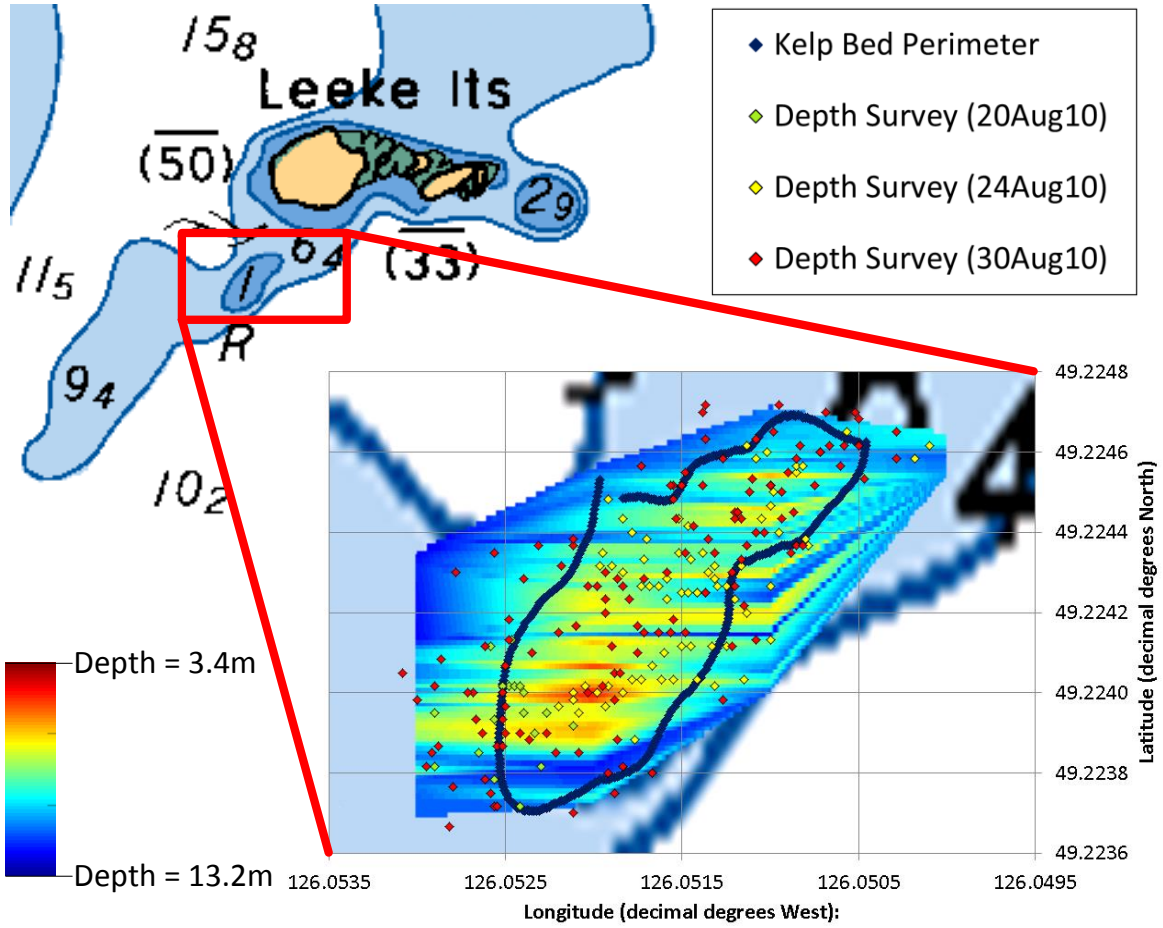

Figure 7.9 - The combined 223 point bathymetric survey of the Leeke Island kelp bed corrected for tide height. The kelp bed perimeter is shown in blue and the red, green and yellow markers represent depth measurements gathered over three days corrected for tide height. The colour bar describes the 2D surface plot of bathymetry. This bathymetric data was gathered in conjunction with Wladichuk [1].

7.3.4.3 Density and distribution of kelp

Given the bathymetric map of the kelp bed, with the perimeter delineated, the map was then populated with an estimate of the density and distribution of kelp. *SeaBiscuit* used the 852 sonar to detect objects in the horizontal plane while correcting observations for vehicle attitude and storing them with the vehicle position. The Delta T sonar was used, as before, to co-register objects from the 2D horizontal scan in the vertical plane, providing a faster update rate and allowing different regions of the vertical water column to be extracted for mapping. Finally, the cameras were used for realtime target identification and confirmation to verify close range sonar targets, when visibility permitted.

7.3.4.3.1 Acoustic mapping of kelp stipes

Figure 7.10 below shows an example 20 metre range (radius) 852 sonar scan in the centre of the Leeke Island kelp bed. This example scan was performed with *SeaBiscuit* suspended from the boom of the surface vessel (shown in orange) to allow a stationary known GPS reference position to be held during testing. The typical appearance of kelp stipes is highlighted by the green circles distributed throughout the left half of the scan. The blue shaded sector is the region of the kelp bed which was partially occluded by the surface vessel hull. The kelp stipes provided an acoustic return distinct from any background noise, facilitating reliable detection, either by manual inspection or by autonomous image processing.

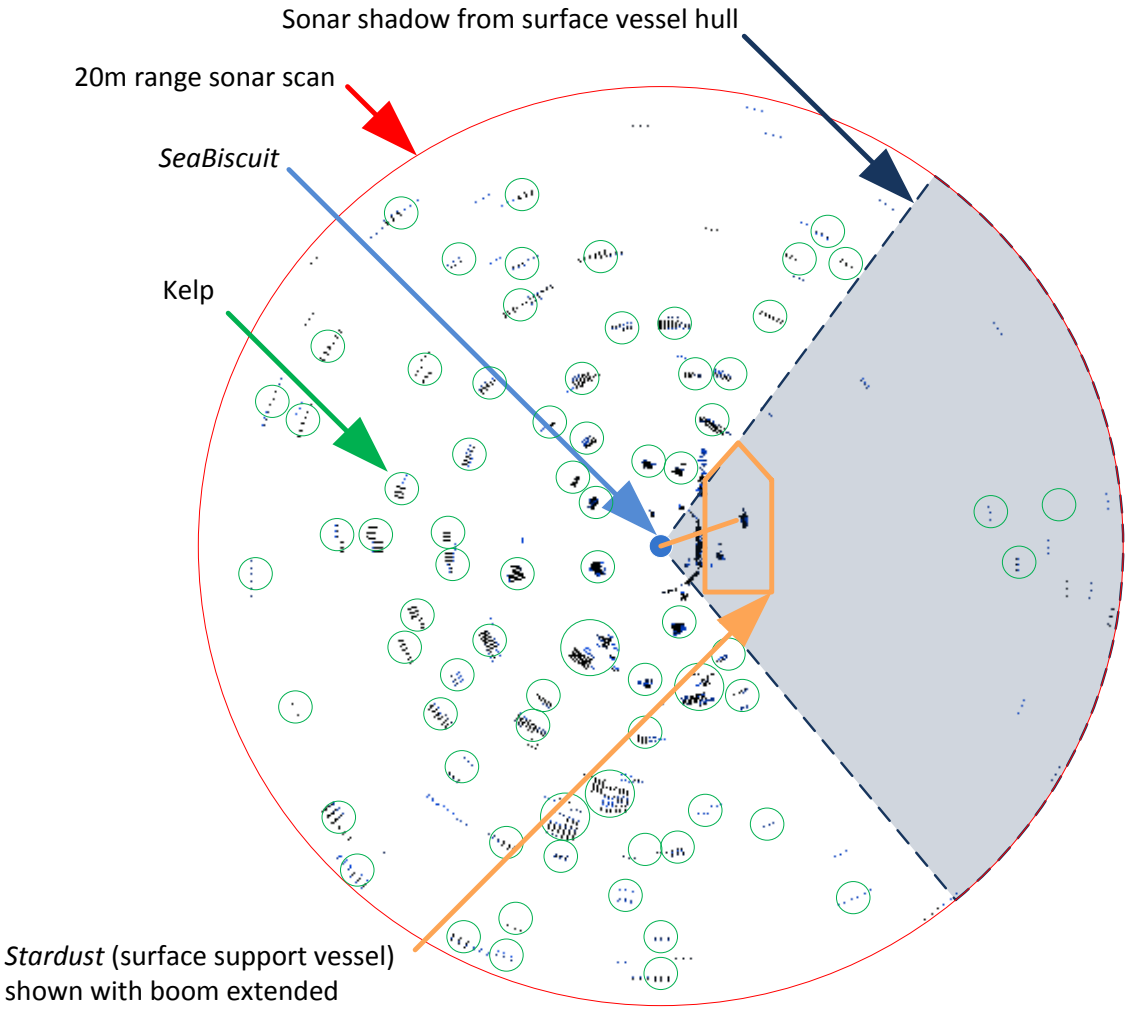

Figure 7.10 - An example 20m range 852 sonar scan of the Leeke Island kelp bed. The overlay highlights areas of kelp stipes with green circles and shows the launch configuration of the underwater vehicle. The blue shaded sector is the region of the kelp bed which was partially occluded by the surface vessel hull.

7.3.4.3.1.1 Manual extraction of kelp stipes

The development of techniques for manual extraction of kelp stipes enabled robust development of later autonomous feature extraction routines, allowing comparison of the autonomous estimates with a ground truth estimate of the same scan area. In challenging conditions, the data was still processed manually to ensure reliable operation or for validation of the autonomous algorithms. To enable efficient manual extraction of kelp stipes from a large number of sonar scans in post-processing, a graphical user interface (GUI) was written in LabVIEW. The GUI, as shown below in Figure 7.11, presented the user with a series of sonar scans while displaying the sensor data for that time (depth, attitude, position).

A number of steps were prompted. Firstly, the user defined a circular mask to represent the radius of useful scan information (for example, when operating close to the surface or with large scan ranges, the periphery of the scan can become corrupted with noise). Regions outside the mask were discarded. Secondly, an optional sector mask (or multiple sectors) was applied to exclude regions of the scan, for example the area of the kelp bed in the acoustic shadow of the surface vessel as shown in Figure 7.10 previously.

The remaining unmasked area was the area scanned for kelp stipes, and the region marked as ‘surveyed’ on the overall kelp bed map. The important distinction was made between areas surveyed to have no kelp stipes present, and areas which had no stipes recorded on the map as

they had yet to be surveyed. The next step of the GUI prompted the user to identify the position and size of kelp stipes by defining a series of circles of varying radii similar to those shown in Figure 7.11. The parameterised results were recorded, either for further analysis or to compile the overall map.

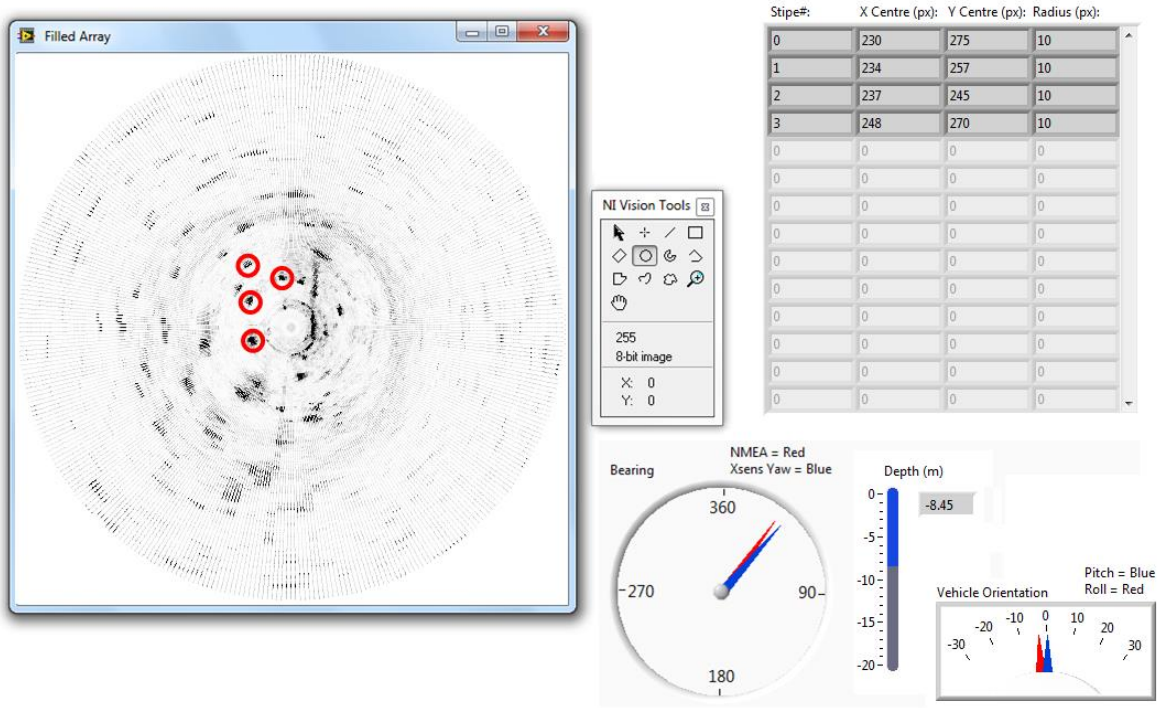

Figure 7.11 - The GUI for manual kelp stipe extraction is shown for the Leeke Island kelp bed scan used previously. A sonar scan and the corresponding vehicle sensor data is displayed, and the user is prompted to identify the radius and position of any kelp stipes present, together with the useful range of the sonar scan.

7.3.4.3.1.2 Autonomous extraction of kelp stipes

Given the large areas of kelp bed to cover, autonomous image processing and feature extraction algorithms provided great benefits in reducing the labour requirements for post-processing scans.

Many of the techniques and algorithms used for extracting the density and distribution of kelp were similar to those used for the dock piling survey application. The parameters and specific details were tuned to reflect the change in conditions, target strength, acoustic characteristics and the non-uniformity of the kelp stipes. The image processing algorithms were required to estimate the position and 'mass' (area & density) of the kelp stipes and the navigation sensors and algorithms were used to register the individual sonar scans to create the overall map. It was assumed that any object present in the midwater above a given intensity threshold was kelp (seen either on the Delta T sonar or the 852 sonar). Filtering was used to eliminate the majority of noise, and it was unlikely that spurious features (e.g. fish) were present on successive scans.

The steps detailed above in the manual image processing were replicated in the autonomous feature extraction algorithms. A brief overview using the same example scan from the Leeke Island kelp bed is presented below in Table 7.4.

The manually processed scans were used to tune and verify the development of the autonomous kelp stipe detection algorithms. To ensure robust, reliable and accurate estimates of the kelp density and distribution, the sonar image processing and feature extraction algorithms were also verified against video footage gathered concurrently by the iROV (some example images were shown in Figure 4.16).

Table 7.4 - An example of autonomous image processing and feature extraction to estimate kelp density and distribution from the Leeke Island kelp bed sonar scan.

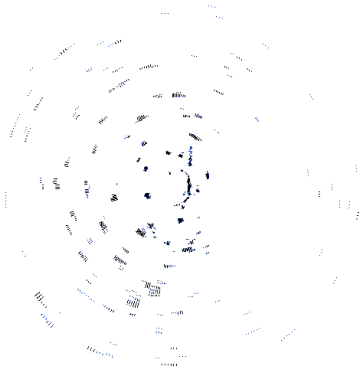	Raw sonar scan.
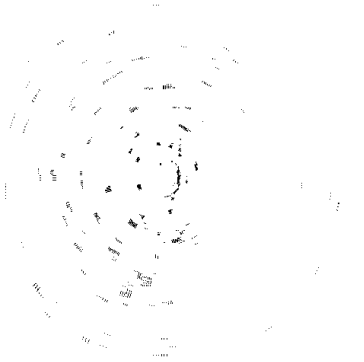	Threshold (100) to remove noise.
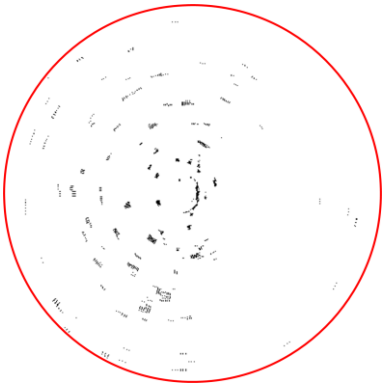	Circular mask to remove noise at the periphery of the scan, for example water surface interactions for scans at a shallow depth and regions where beams have exited the water surface. The mask radius was calculated from the submerged depth and the 22° vertical divergence of the sonar beam. The shape of the mask (circular or elliptical) was calculated from the attitude of the vehicle as each ping was acquired. Automatic inspection routines were used to detect noise in the immediate periphery of the vehicle and to apply an annulus mask to remove this.
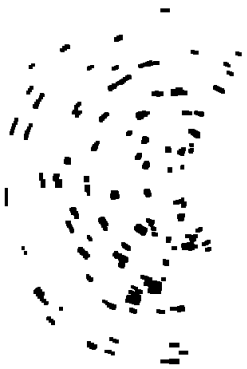	Dilation (3*3, 2 iteration) The features in the dilated image are then labelled with a unique identifier as shown below in Figure 7.12.

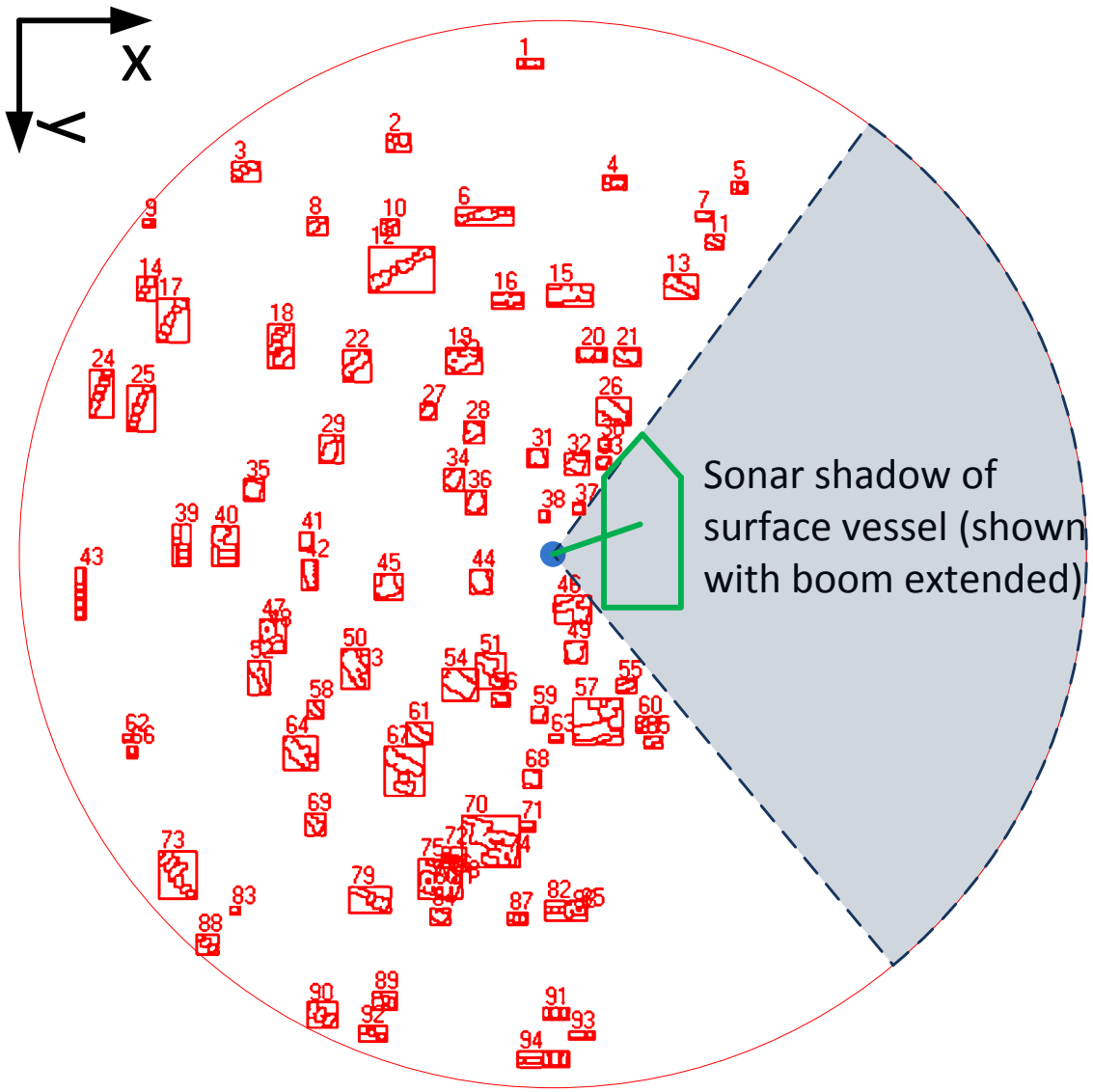

Figure 7.12 - An example output of the autonomous kelp stipe detection algorithm. Each stipe was recorded with a numeric identifier, together with its range, bearing, pixel mass, bounding ellipse ratio, orientation, etc. No mass threshold was applied as specific known objects (such as pilings) were not being searched for; provided the noise was reliably removed, any return, however small, was a valid midwater target.

The parameterised results of the autonomous kelp detection algorithm were stored in an array, with each stipe or cluster of stipes labelled with a unique identifier. The first 10 objects detected are listed below in Table 7.5 out of a total of 94 for the scan shown in Figure 7.12. This data was saved, together with the scan location and time, to be able to recreate an overall map of the density and distribution of kelp throughout the kelp bed. Efficient mapping and storage was achieved by processing the data and recording features with appropriate descriptors to enable a full reconstruction without having to store the memory-intensive raw sonar scans.

Table 7.5 - A summary of the feature data from the Leeke Island kelp bed scan shown above in Figure 7.12.

Object Identifier	X Centre (m):	Y Centre (m):	Pixel Mass:	Orientation (°):	Aspect Ratio:
1	9.53	0.84	0.061	0	2.40
2	7.08	2.32	0.067	27	1.22
3	4.25	2.84	0.070	26	1.44
4	11.12	3.06	0.053	169	1.83
5	13.41	3.14	0.042	162	1.33
6	8.68	3.67	0.126	9	3.00
7	12.77	3.69	0.035	173	1.60
8	5.58	3.86	0.051	33	1.25
9	2.44	3.82	0.022	0	1.25
10	6.92	3.88	0.048	27	1.29
…continues to object 94					

In Table 7.5 above, detailing the information associated with each kelp stipe, the x and y positions are listed in the coordinate system shown in the sonar scan above in Figure 7.12, with the origin in the top left corner as shown. These local sonar coordinate system locations were then combined with the current estimate of the robot position and orientation to record the position of objects in the global coordinate system. The 4th column of Table 7.5 lists the pixel mass of the observed feature, or the number of pixels comprising the feature (as the image is binary).

The aspect ratio was the ratio of the long side to the short side of the ellipse used to represent each cluster of kelp stipes. The orientation of this bounding ellipse is listed in column 5 and is the orientation of the long axis of this bounding ellipse relative to the local coordinate system axis. For the purposes of labelling features in Figure 7.12, a bounding rectangle was used together with the numeric object identifier.

Figure 7.13 below compares the results of the autonomous image processing algorithms to detect the kelp stipes with the manually generated overlay for the same scan. By inspection, the algorithms were seen to be a reliable and accurate autonomous measure of the kelp present in the image.

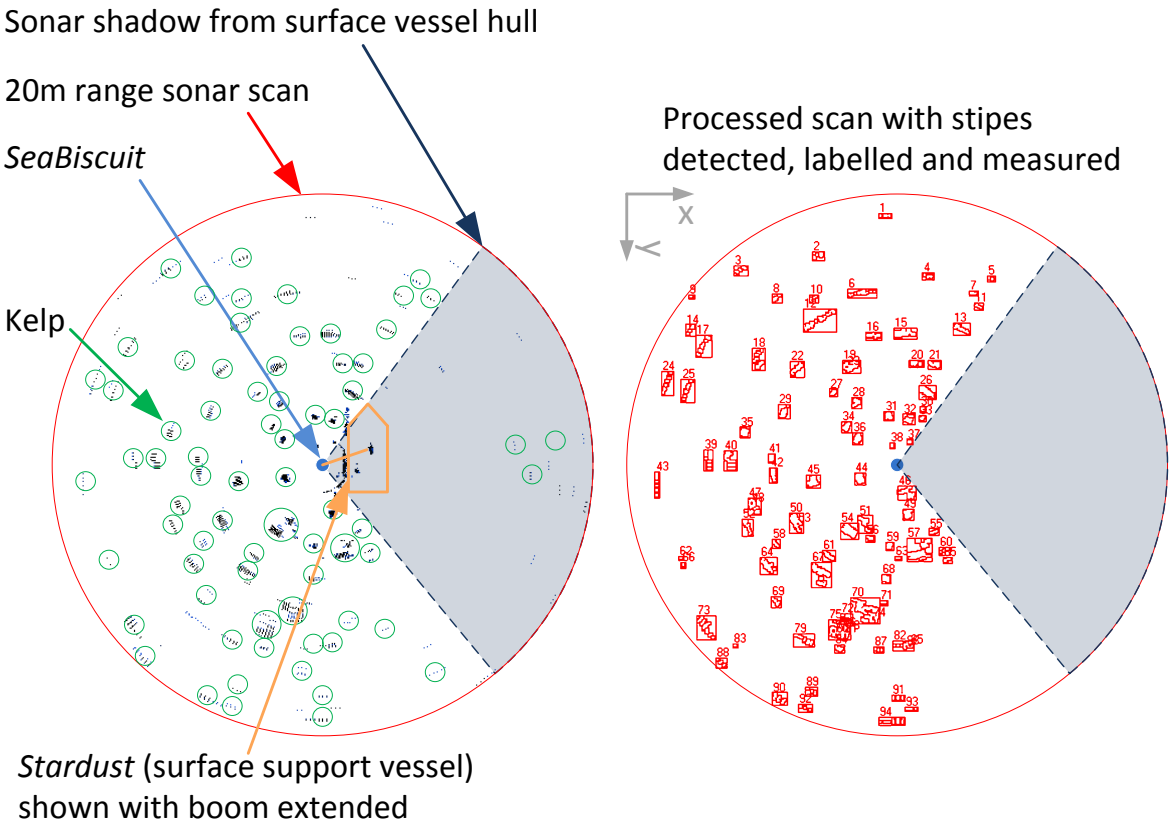

Figure 7.13 - Comparing the autonomous kelp detection algorithms with the result of the manually processed scan. By inspection, the autonomous estimate (shown on the right) was a reliable and accurate measure of the kelp distribution and density.

7.3.4.3.2 Integrating Delta T multibeam data

As demonstrated in the dock mapping application, data from the forward facing multibeam sonar was used to map the entire vertical water column of the kelp bed, and to confirm and corroborate the mapping using the 852 sonar. Using the techniques discussed in section 6.3.4, the Delta T data was initially compressed to 2D to provide an additional source of mapping information, imaging a greater volume of the water column as shown in Figure 6.34, and providing a faster update rate of up to 20Hz. Once compressed to 2D, the data was directly integrated with the 852 sonar scans.

Figure 7.14 below shows an example 20m range Delta T scan taken from the midwater from within a kelp bed. The water surface is indicated by the blue line, calculated by the pressure sensor and vehicle attitude. The bathymetry was approximated by the orange line, and detected by the algorithms discussed previously in the dock mapping section to be 1.1m below the vehicle at an angle of 12.6°.

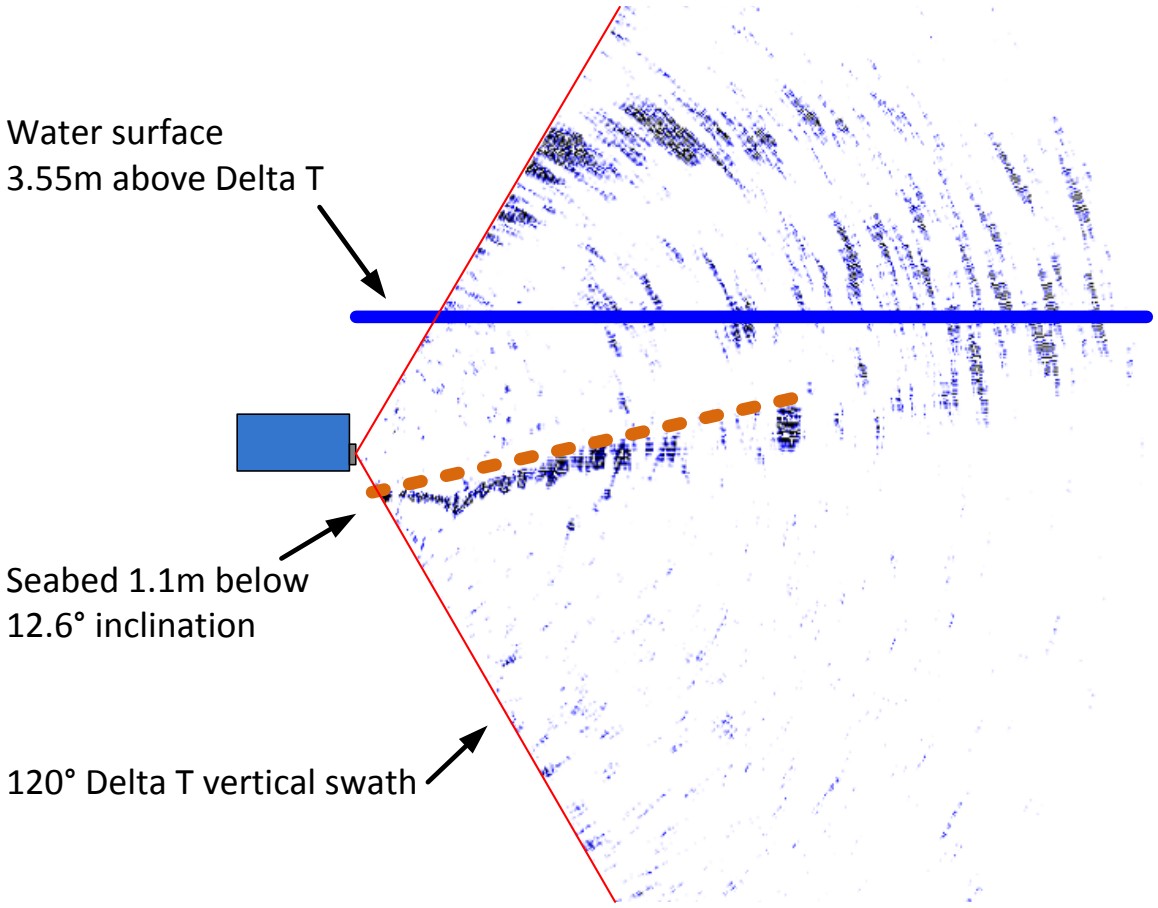

Figure 7.14 - An example 20m range Delta T kelp bed scan in shallow water (approximately 4.6m water depth). The water surface is indicated by the blue line and the bathymetry approximated by the dashed orange line.

As with the dock survey, the water column was bounded vertically by the calculated surface and the detected seabed as the region of interest for mapping. This region of interest was compressed to 2D using the same techniques discussed earlier in section 6.3.4. Figure 7.15 below shows the compression to 2D process for the example scan shown above in Figure 7.14. The water column was extracted as the region of interest between the seabed and water surface, before being compressed to 2D. The middle graph plots pixel intensity (the sum of pixel intensity at that range bin) against range. Point features seen in the raw sonar plot can be matched to peaks in the graph, which is also displayed as a colour bar at the bottom of the figure.

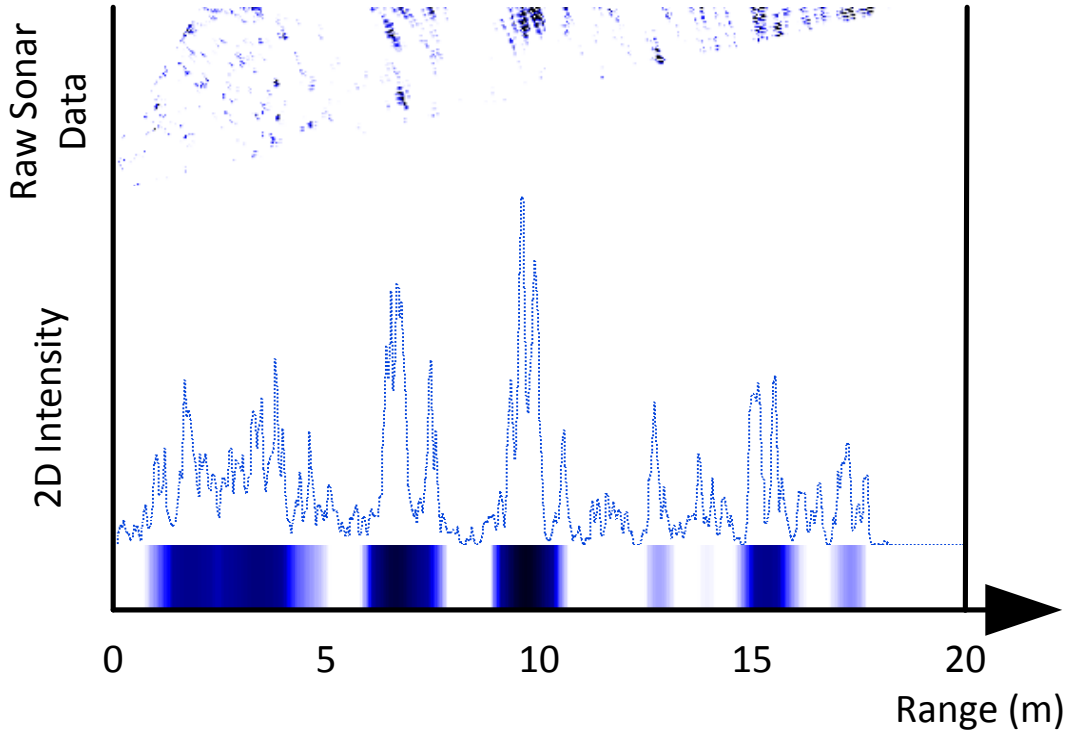

Figure 7.15 - Compression of forward facing Delta T multibeam kelp scans to 2D. The upper plot shows the region of interest (ROI) between the seabed and water surface extracted from the example scan shown above in Figure 7.14. The middle plot shows the ROI compressed to 2D and plots pixel intensity against range. The colour bar at the bottom of the plot represents increasing intensity with darker colours.

Although the compression to 2D process was similar to the dock survey application, the filtering and image processing performed after compression was different when mapping kelp stipes. The dock pilings provided a large, fixed and high intensity return which could be detected by peak detection algorithms, given a threshold amplitude and peak width. However, in the kelp mapping application, all midwater targets were mapped. Parameterisation and detection of the kelp stipes was not performed until successive Delta T compressed 2D scans were registered using the vehicle position and attitude into a 2D radial scan.

Figure 7.16 below shows an example 20m radial Delta T scan which was compiled of 307 individual Delta T scans over a sector of 309°. For each scan, the water column region of interest (ROI) was extracted as shown in Figure 7.14 and the ROI compressed to 2D as shown in Figure 7.15 before being registered in yaw angle on the radial scan shown in Figure 7.16 below. The red sector indicated in Figure 7.16 below was the individual ping used in the examples above demonstrating the ROI extraction and compression to 2D. The intensity characteristics varying with range can be verified between the plots.

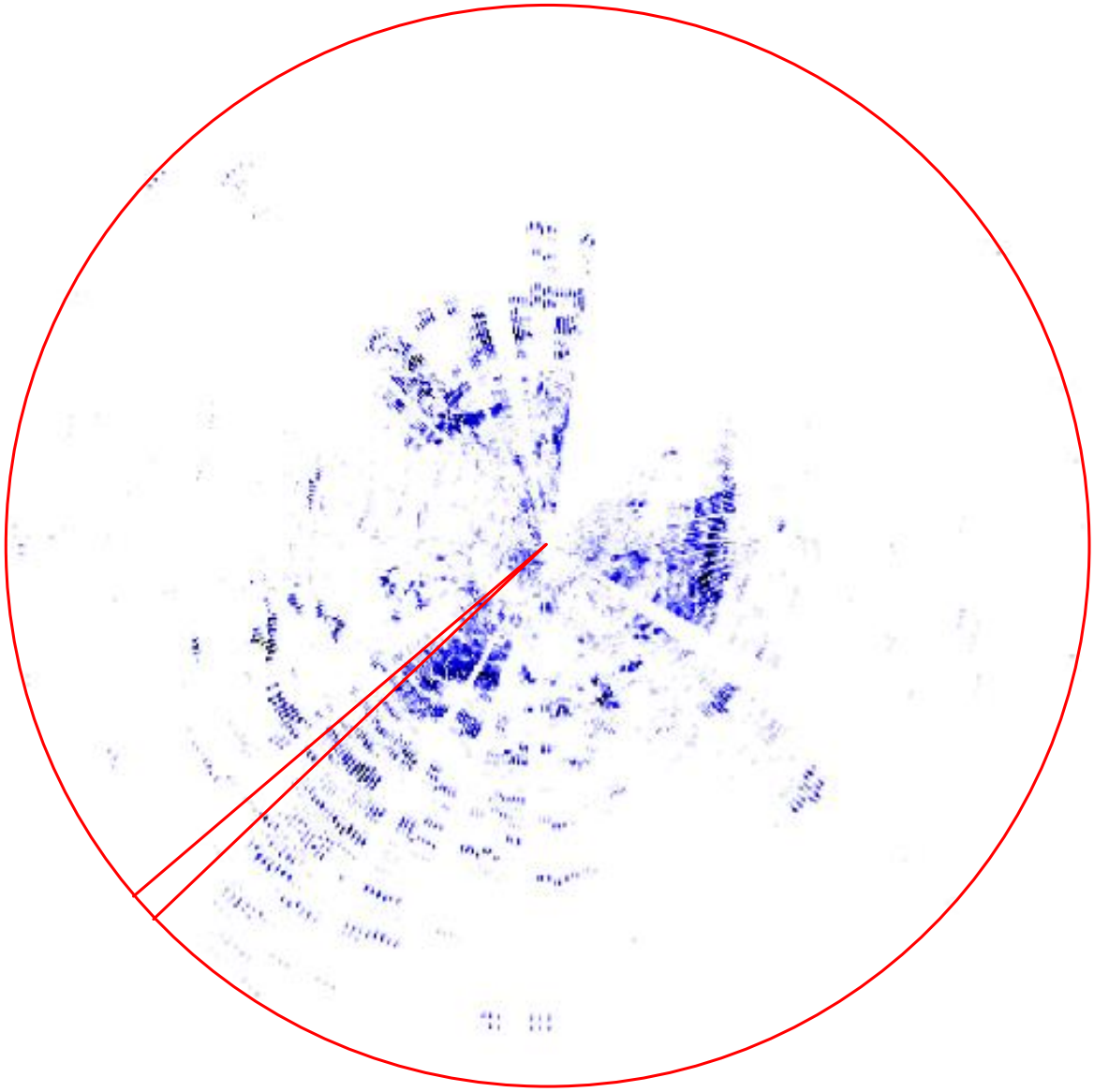

Figure 7.16 - An example 20m radial scan compiled from successive Delta T scans compressed to 2D and registered with vehicle attitude. The highlighted sector shows the single ping used in the previous example and shown in Figure 7.14 and Figure 7.15.

The compiled Delta T radial scan was either recorded on the map in its raw form, or parameterised using similar autonomous kelp detection algorithms as used for the 852 sonar image processing. Figure 7.17 below shows the result of parameterising the example Delta T radial scan shown above in Figure 7.16. The sonar scan is shown in the background and the overlay shows the result of the kelp stipe detection algorithm. As for the 852 sonar scans previously, each feature was labelled with a unique identifier and the output was an array of all relevant characteristics.

As before, the benefits of parameterisation were computational and memory efficiency, provided that the object detection was reliable and sufficient data was preserved to enable a full reconstruction of the kelp bed from the parameterised data output.

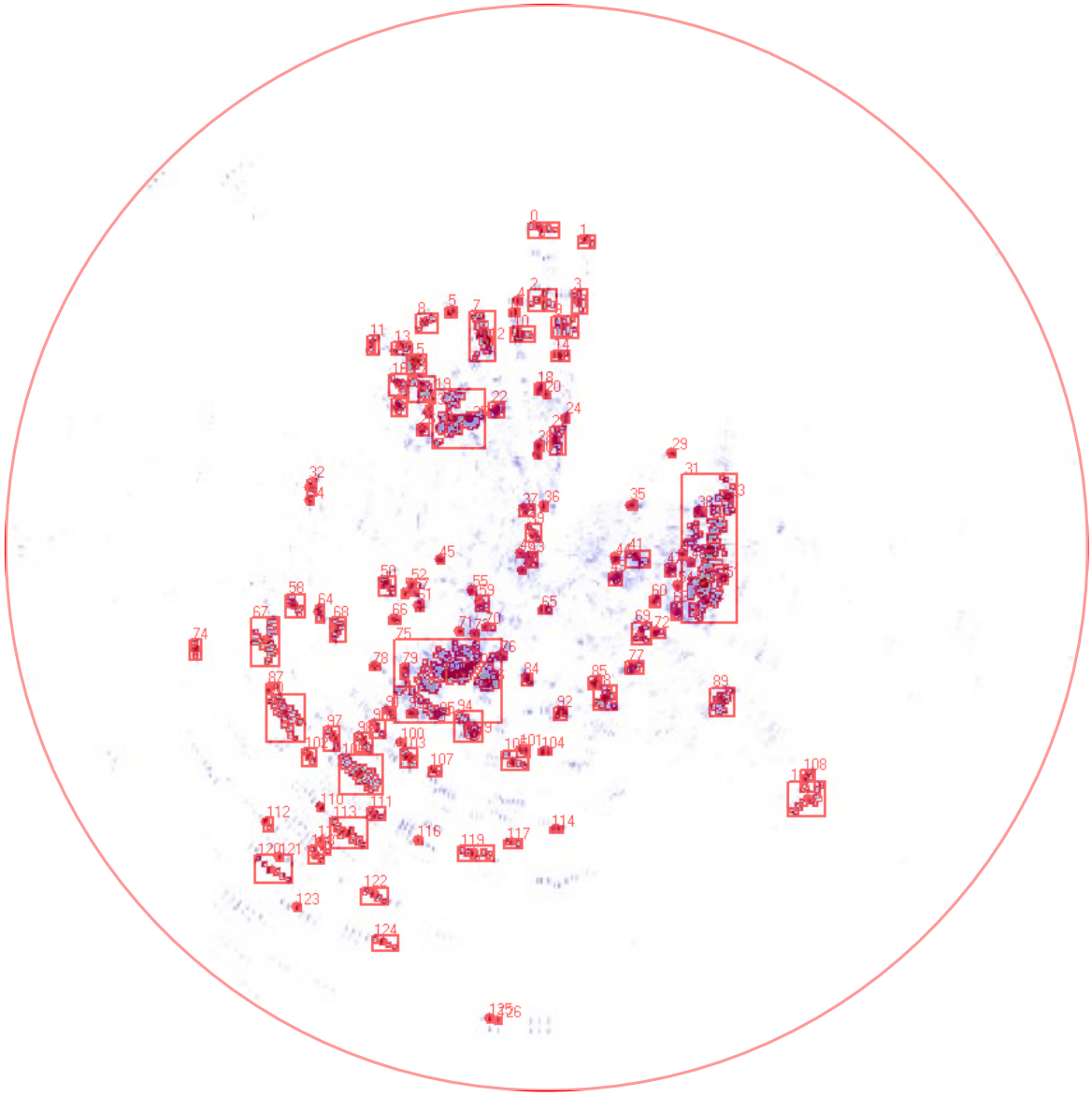

Figure 7.17 - Autonomous kelp stipe detection from a radial Delta T scan. The background shows the scan from the previous example in Figure 7.16. The red overlay shows the result of the autonomous kelp detection algorithm set with a relatively high pixel mass threshold for clarity. All objects (kelp stipes) detected in the scan were parameterised and recorded with their characteristics.

7.3.4.3.3 Combining several 2D scans

As the majority of kelp beds were larger than a single scan radius, registration of several overlapping scans allowed an overall map of the kelp bed to be compiled.

Whether 852 radial scans, Delta T radial scans or Delta T vertical scans were used, the correct registration of successive scans was important to avoid over-estimating kelp density. Figure 7.18 below shows this effect. If the apparent kelp density increased with the number of scans performed then the scan registration was likely to be incorrect. The exception to this was the occlusion of stipes which may become observable as the vehicle and targets move between successive scans. Figure 7.18 demonstrates one method to avoid recurring targets in successive scans being interpreted as an overly high density estimate. Provided correspondence can be achieved between successive observations of the same target in slightly different positions, the recurring targets were mapped only once at a mean observed position.

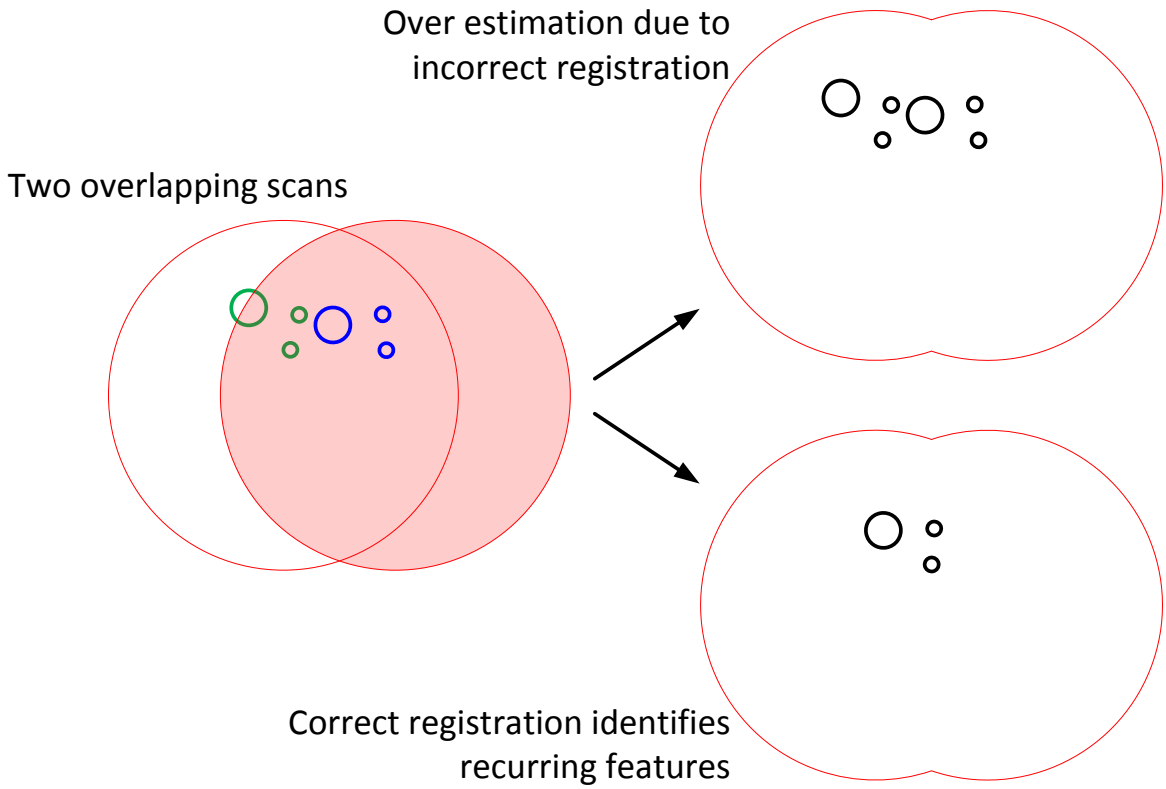

Figure 7.18 - Correct registration of successive scans was important to avoid over-estimating kelp density. The left figure shows two successive scans which overlapped with the same arrangement of 3 targets observed in green in the first scan and blue in the second scan in a slightly different position. If the scans were simply overlaid, with vehicle movements not corrected, then the top right figure shows the over-estimation of kelp density resulting from incorrect registration. The lower right figure shows one solution: provided correspondence between scans could be achieved, the mean observed position of the targets was used.

A combination of accurate measurement of vehicle position, an understanding of the periodic wave movement of the kelp stipes, and registration of uniquely identifiable patterns within the scan were used to register maps of several successive scans. For the kelp bed scans, initially this registration was performed manually using a GUI written specifically for this task, part of which is shown below in Figure 7.19. The software processes 852 and Delta T pings into radial 2D plots, each corrected for vehicle attitude and orientation while displaying the vehicle depth over time. The scans were initially registered using the estimated vehicle position recorded during the survey. The user then toggled the scans over time, while adjusting the threshold and fine control of the scan x and y position and yaw angle correction to verify the alignment.

Correct registration of mosaicking was ensured by monitoring a series of plots of the compiled map. In environments when a high accuracy was possible, the logic AND of all scans displayed pixels which were above a preset thresholded level in either all scans, or more than one scan. For lower accuracy scans (e.g. more water movement, more flexible targets, higher sonar ranges), the thresholded pixel frequency (as shown in the top left plot in Figure 7.19) displayed the sum of pixels above a threshold level from all scans. Whereas the AND plot was maximised from mosaicking, the thresholded pixel frequency was maximised with high intensity point targets rather than low intensity coverage, thus showing targets which were present in the same position on multiple scans.

The upper right plot of Figure 7.19 shows the mean pixel value for all enabled scans and the larger lower plot shows the colour coded occurrence of pixels above a thresholded level in different scans.

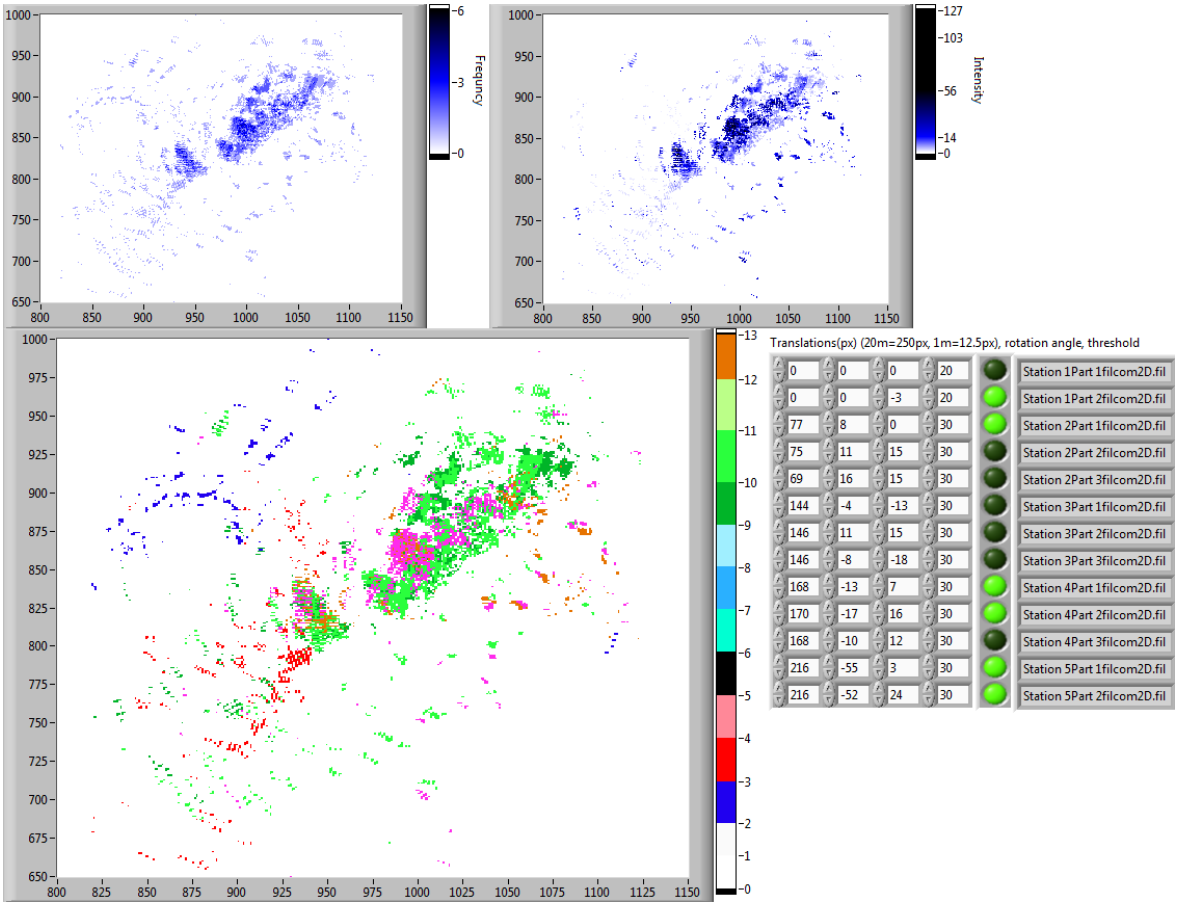

Figure 7.19 - Scan mosaicking was performed manually using the GUI shown. The vehicle position estimate was used as a starting point, with confirmation in post-processing (right hand data array and toggle switches) using a combination of the thresholded pixel frequency (top left), the mean pixel intensity (top right) and the thresholded presence of returns (lower left). This example shows four 20m range 852 sonar scans over partially overlapping sectors, taken from three stations approximately 5 metres apart. The majority of returns present were verified by diver inspection to be kelp stipes.

Techniques to perform this registration and mosaicking autonomously, are discussed in future work section 8.1. As an initial proof of concept of kelp bed mapping, the process continued using the vehicle position estimate, together with manual scan mosaicking and correction when required. Given the compiled map, registered from several mosaicked scans, the final step was calibration of the relative pixel intensities to an actual estimate of kelp biomass and biovolume using the calibration processes discussed in section 6.3.5.

7.3.4.3.4 Survey methods

A variety of survey methods were employed as the incremental development and field trials advanced. Initial scans were performed in calm waters by suspending the vehicle from the research vessel boom. These scans were either performed at the surface utilising the adjustable declination angle of the Delta T, or from the midwater. The surface vessel boom provided a known x, y position, tracked using the surface vessel GPS, with the surface vessel either in transit or at anchor. A swivel harness and the holonomic propulsion capabilities allowed the vehicle to rotate about its axis to pan the sensors across the kelp beds and generate a series of radial pans. The vehicle could also move in the proximity of the boom hoist to mitigate occlusion of kelp stipes by scanning from a slightly different x, y position.

Operation then moved to free transects through and around the kelp beds, with survey methods dependent on the current and conditions. When operating at slack tide or in regions of low current, the vehicle was launched and transited a course around the periphery of the kelp bed

facing in. Facing a constant position in the centre of the kelp bed provided a complete map or an oscillating pan of the directional sensors across the kelp bed while in transit increased coverage and reduced occlusion. Straight transects around the perimeter of the kelp bed to form a bounding polygon were also performed, using the vehicle's holonomic capabilities to maintain the directional sensors facing a constant heading (or an oscillating pan back and forth) facing the kelp bed, while transiting a course around the kelp bed. Alternatively, the vehicle entered the kelp bed orientating the directional sensors outwards to increase survey detail.

In regions of low current, the holonomic propulsion system was used to make course corrections to mitigate external water movements. However, in higher currents (limited by the available vehicle thrust), the surface vessel anchored upstream of the kelp bed and allowed the iROV to drift, either past or through the kelp bed, using its onboard thrusters for course corrections. The speed of the iROV was controlled by gradually paying out the strain-relieved tether from the surface vessel and the thrusters used to effect minor movements and course corrections, rather than attempting to move directly against the overall current. When large distances had to be covered, it was normally more time efficient to manoeuvre the surface vessel to the approximate position, anchor and drift to a stable anchorage before launching the underwater vehicle.

As discussed throughout Chapter 4 and Chapter 5, the iROV navigation system is in development. Realtime navigation using the kelp stipes as landmarks remains an opportunity for further work (section 8.1). Instead, a variety of techniques were used to supplement and corroborate the navigation of the vehicle while developing the iROV concept and habitat mapping techniques in the absence of a DVL or USBL navigation system. Frequent GPS updates from the surface, as well as registering sonar targets from the surface using GPS before diving and navigating relative to these GPS referenced targets were both discussed earlier. These were used to bound the drift from navigation using dead-reckoning alone, and to bound the search area when manually or autonomously mosaicking the sonar scans.

During development, external position observations synchronised with the onboard vehicle clock were also frequently used to supplement the onboard vehicle navigation to aid post-processing when compiling the map. In the same manner as above, these observations were used to bound cumulative errors and the search area for sonar mosaicking and allowed confirmation of the vehicle navigation estimates. Relative vehicle position estimates were made from the stern of the research vessel at approximately 15-30 seconds intervals. These relative estimates, e.g. (x=-5m, y=10m), were combined with the surface vessel GPS and compass in post-processing to convert to absolute vehicle position. Tracking of the vehicle while underwater using a surface vessel such as a kayak or small RIB to allow movement over the kelp stipes also allowed the vehicle position to be tracked using a synchronised GPS log.

7.3.5 **Results**

Figure 7.20 below shows an example kelp bed map taken by *SeaBiscuit* from the midwater, at an altitude of approximately 1m, in a water depth of 5m. A series of nine scans taken by the 852 scanning sonar were compiled from single pings into radial scans, each made up of over 120 radial pings corrected for vehicle attitude. These scans were taken at five stations spaced approximately 5m apart and were manually mosaicked using the GUI shown earlier to maximise regions of local pixel intensity which represented kelp stipes.

The plot in Figure 7.20 shows the mean pixel intensity when all 9 scans are combined, using the pixel intensity scale shown, where darker colours indicate a stronger acoustic return. The 20m radius of each individual scan is shown by the colour key on the right. The zoomed section shows a region of distinct kelp stipes, apparent in the same location on several successive scans. 1 pixel in all of the 20m range 852 sonar scans presented here is equal to 8cm.

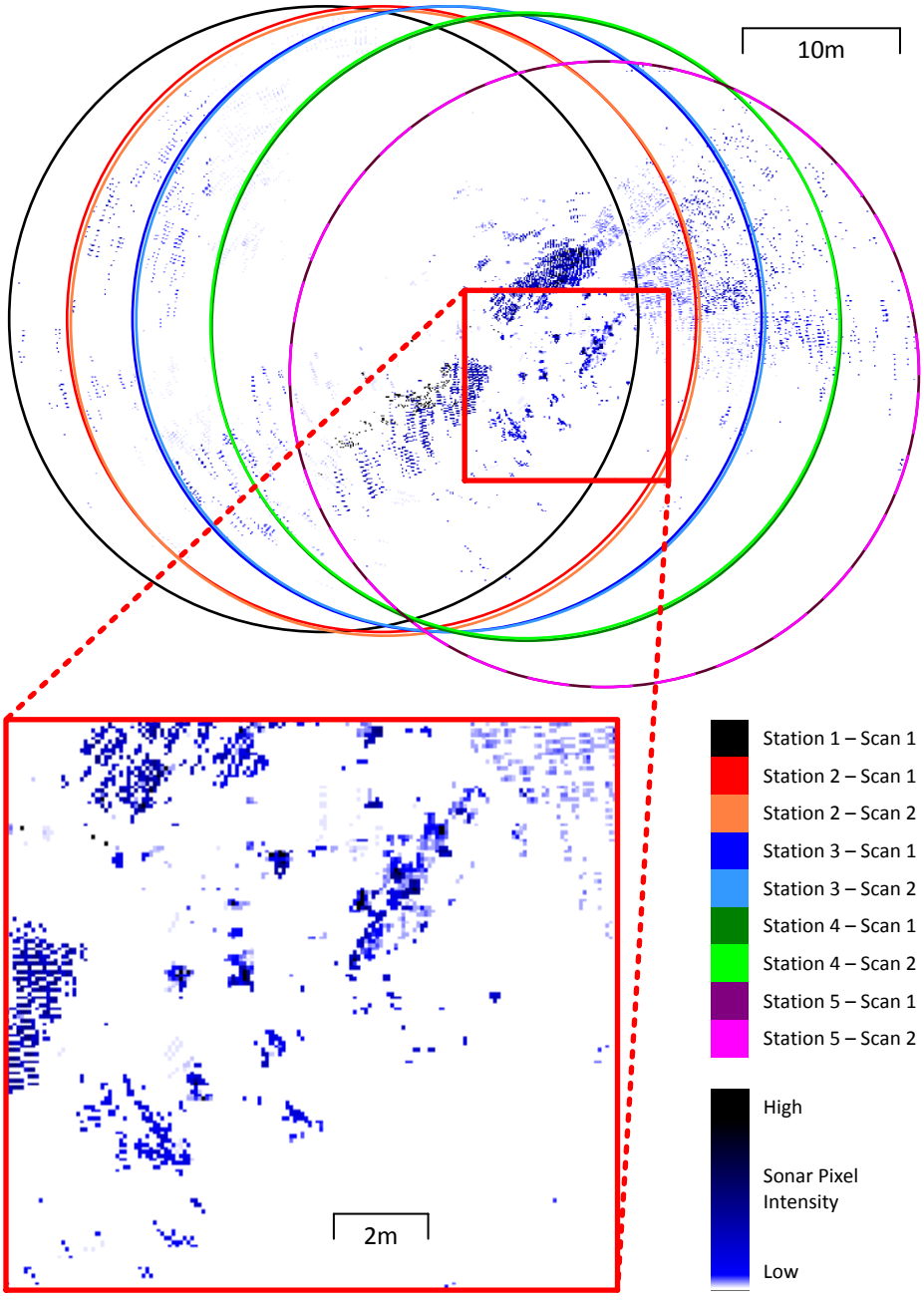

Figure 7.20 - A kelp bed scan compiled from 9 overlapping mosaicked 852 sonar scans taken at 5 stations, spaced approximately 5 metres apart. The plot shows the mean pixel intensity from all 9 registered scans, as per the key on the right. The zoomed inset shows a region of distinct kelp stipes.

Figure 7.21 below shows the same kelp bed map, but compiled using the maximum pixel intensity rather than the mean pixel intensity between scans. Comparison between Figure 7.20 and Figure 7.21 shows the effect of spurious or dynamic targets causing an overestimation of the kelp density if the maximum pixel intensity was used. The same intensity scale was used in both plots, yet in the maximum pixel intensity plot shown in Figure 7.21 below, a spurious target appearing in a single scan has a large effect on the overall compiled map and, if undetected, could also lead to incorrect mosaicking.

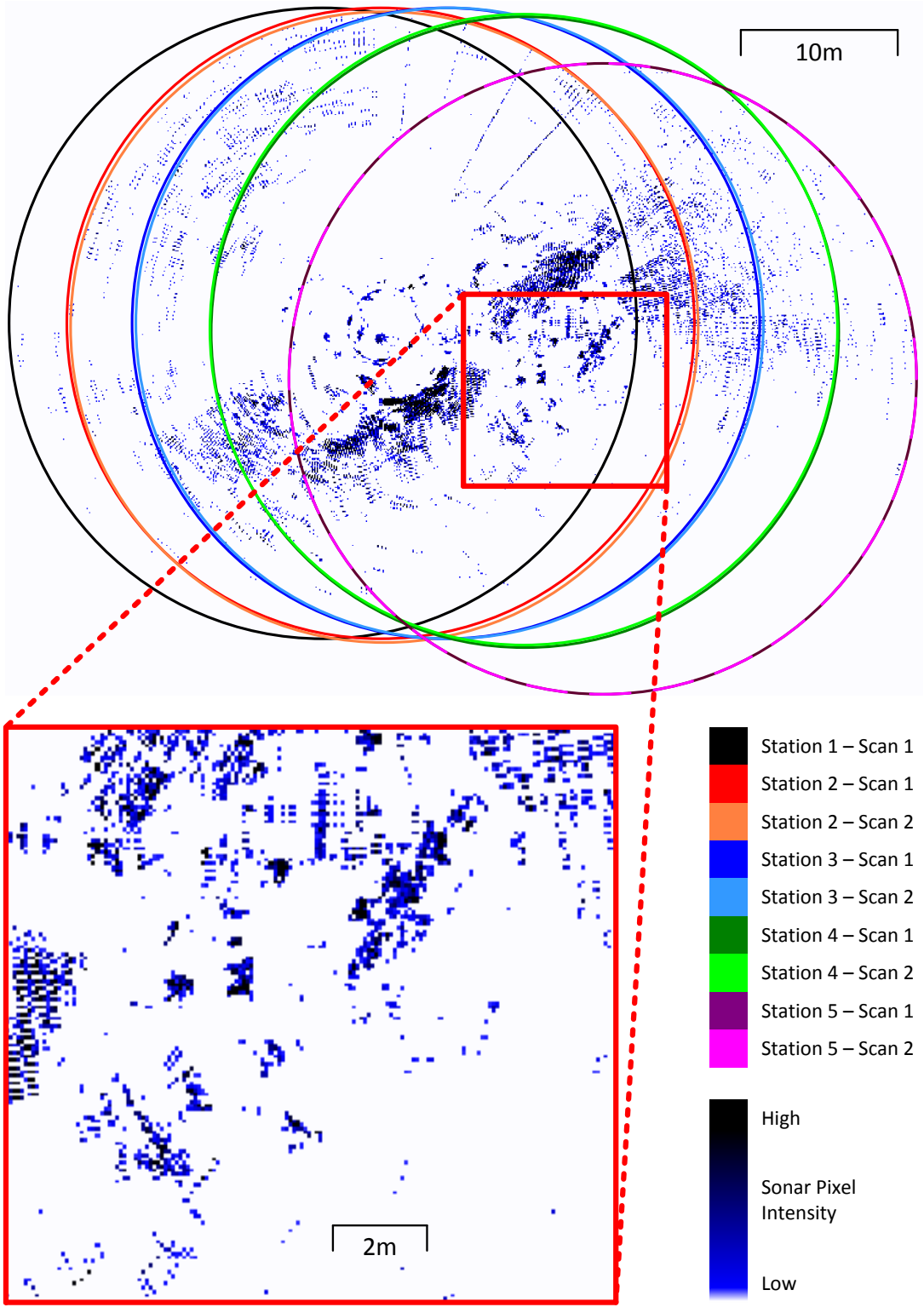

Figure 7.21 - The 9 scan kelp bed map shown earlier is presented as maximum pixel intensity. Comparison with the mean pixel intensity shown in Figure 7.20 above shows the effect of spurious or dynamic targets causing an overestimation of the kelp density if the maximum pixel intensity was used. The intensity scale used here was the same as in Figure 7.20 above.

Figure 7.22 below shows the thresholded pixel count between the 9 overlapping scans of the kelp bed map shown earlier. The green and red pixels, in particular in the zoomed section, show the occurrence of targets present in exactly the same location in at least one successive scan.

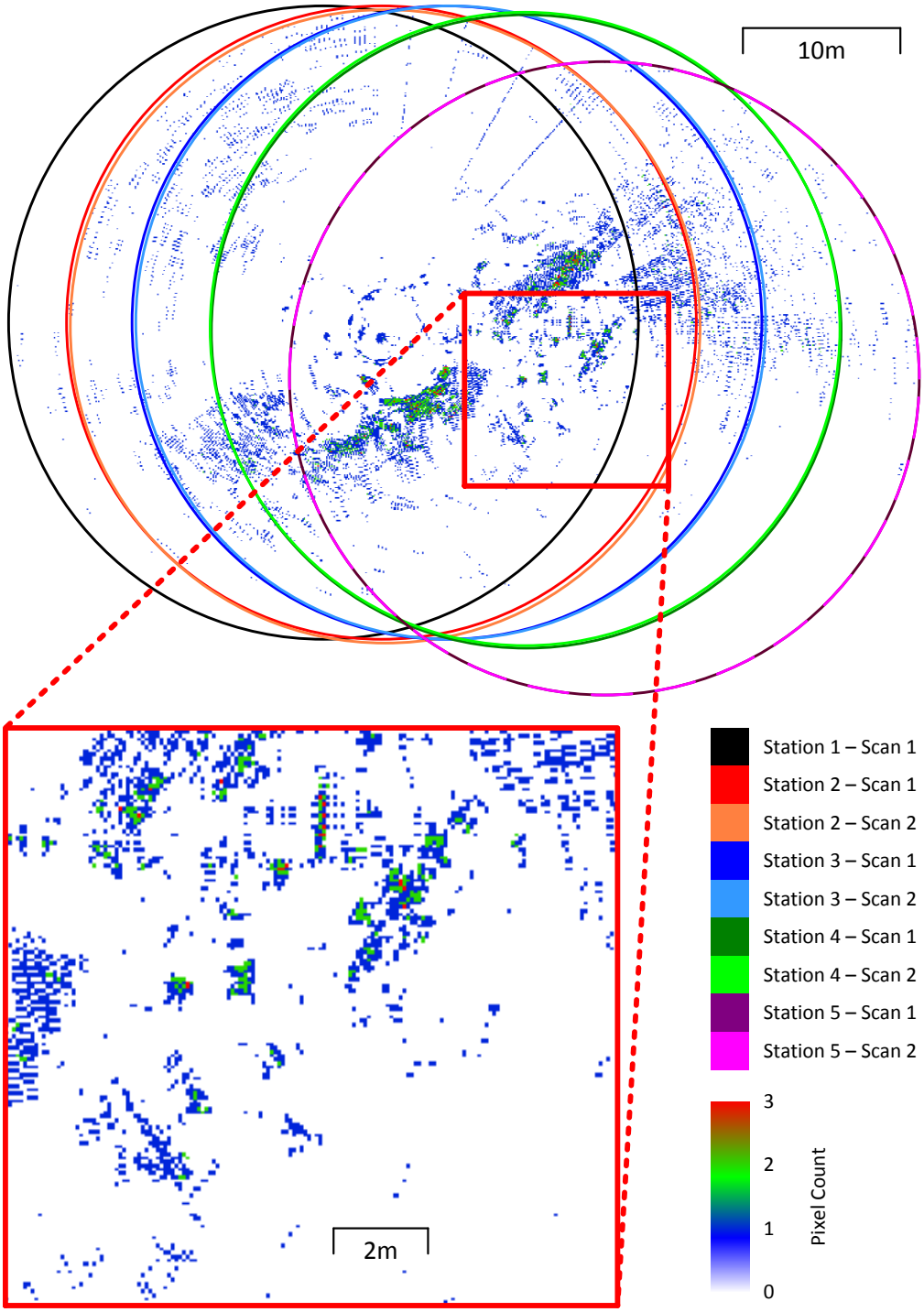

Figure 7.22 - The pixel colour shows the thresholded pixel count from the 9 overlapping scans of the kelp bed map shown earlier. The green and red pixels, in particular in the zoomed section, show the occurrence of targets present in exactly the same location in at least one successive scan. 1 pixel is equal to 8cm.

The large amount of blue pixels in Figure 7.22 above shows thresholded pixels present in only one scan. However, the grouping of these into coherent targets between scans, often with some overlap, even if not exactly overlapping, shows the small scale movement of the vehicle and kelp stipes during operation. Although Figure 7.22 shows a relatively small number of thresholded pixels present in *exactly* the same location in successive scans, coherent targets were formed from stipes appearing in *approximately* the same location in several scans. This was verified by the high intensity targets in the mean plot shown earlier in Figure 7.20 and in Figure 7.23 below.

Figure 7.23 below shows the occurrence in each scan of pixels above a thresholded level as per the key on the right. Stipes made up of several colours represent recurring targets observed in the same place, as seen in Figure 7.22 above showing the thresholded pixel count. These recurring distinct targets, for example in the zoomed inset, were used to guide the registration and mosaicking of the successive scans. Targets made up of fewer colours were either dynamic targets only present on some scans, or targets only visible from some positions due to occlusion. A combination of successive overlapping scans, together with the thresholded pixel count shown above were used to aid this distinction. The principle is similar to the voting techniques introduced earlier in map management.

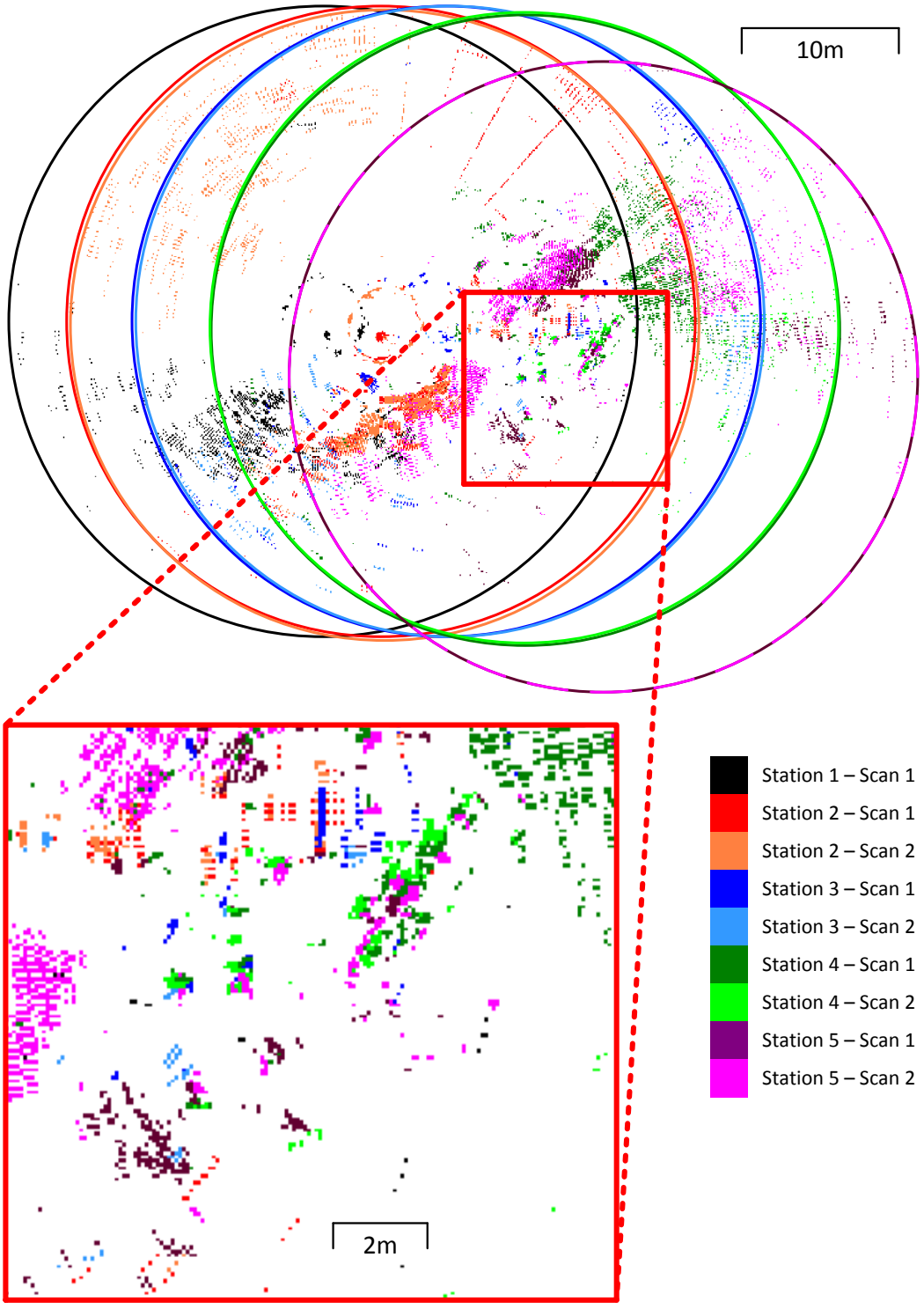

Figure 7.23 - The occurrence of pixels above a thresholded level on each scan as per the key on the right. The zoomed inset shows a region of distinct kelp stipes demonstrating the mosaicking and registration between different scans.

The Delta T was used to aid distinction in the 852 scans between spurious, dynamic and occluded targets. Figure 7.24 below shows the mean pixel intensity from thirteen Delta T 20m range scans acquired concurrently with the previous 852 sonar data. The vehicle held an approximately stationary position for the radial 852 sonar pan, before rotating about its axis to pan the Delta T sonar over the kelp bed at each station, before a further 852 sonar scan, and then moving to the next station approximately 5m away. All Delta T pings were registered and corrected for vehicle attitude, compressed to 2D and used to reconstruct a radial Delta T scan. The zoomed section shows the same region as above in the 852 sonar scans where distinct kelp stipes can be seen.

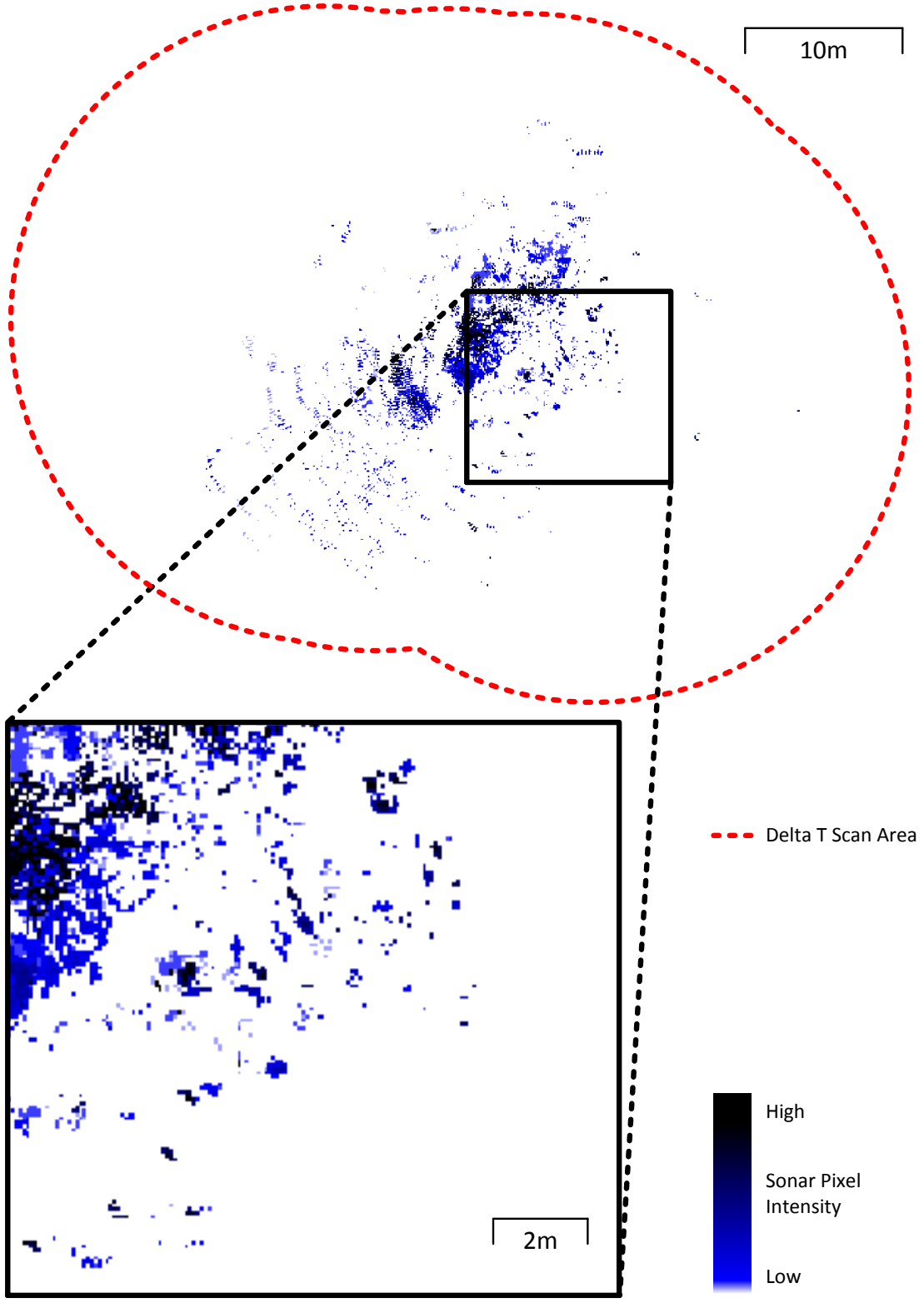

Figure 7.24 - The mean pixel intensity from 13 Delta T 20m range scans taken at stations overlapping with the 852 kelp bed map. Darker colours correspond to higher sonar pixel intensities. The zoomed section shows a region of distinct kelp stipes.

The occurrence of each target on the 852 and Delta T sonar scans can be seen below in Figure 7.25. The thresholded returns from the Delta T sonar scans in red have been overlaid onto the blue 852 sonar scans and the region mapped for each sonar is shown. Thresholded returns present on both sonars are shown in green.

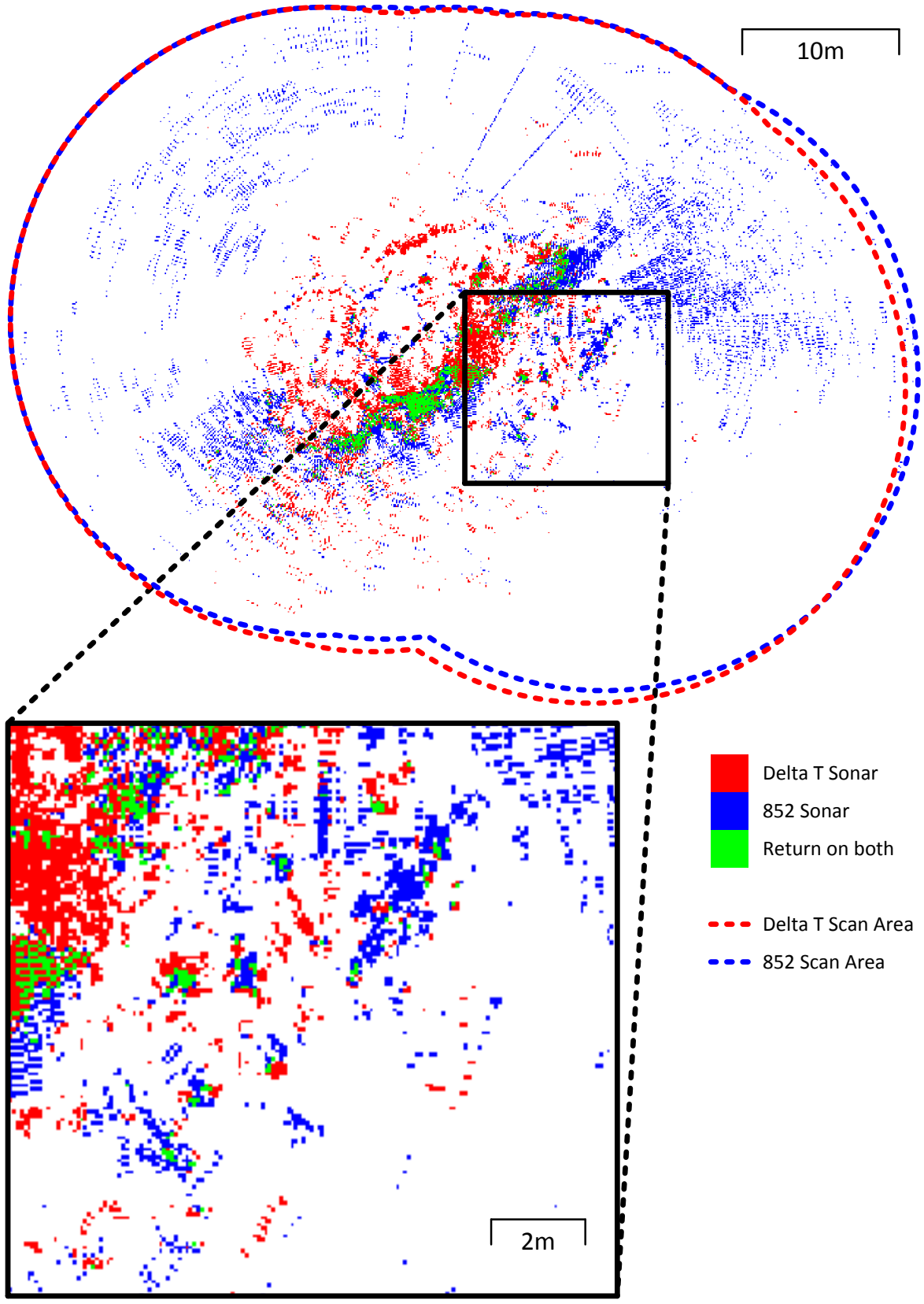

Figure 7.25 - The combined scans from the 852 and Delta T sonar registered on the same map. Thresholded returns from the 852 sonar are shown in blue, from the Delta T sonar in red and thresholded returns from both sonars shown in green. The zoomed section shows several of the kelp stipes have been imaged by both sonars at the same location.

The zoomed section in Figure 7.25 above shows several of the kelp stipes have been imaged by both sonars at the same location (green pixels). This was used to aid map registration and mosaicking, as well as distinguishing between spurious targets by using a combination of the mean, thresholded pixel count, maximum and thresholded colour coded scans for each sonar individually, and for the combined results.

Differences between the thresholded returns from each sonar and between stations were attributed to a number of factors. Although the scans spatially overlapped they were conducted at different times. The total survey lasted 20 minutes, including periods in between when these scans were taken, with slow movement between stations while scanning. As the Delta T scans were taken during a vehicle pan, but the 852 scans taken before and after the vehicle pan, differences between the targets observed in each were partly due to movement of the stipes back and forth in the water, together with any uncorrected vehicle movements.

As Figure 6.34 on page 247 illustrated, the 852 and Delta T sonars imaged different but overlapping regions of the water column. Thus the red and blue returns shown in Figure 7.25 above, in particular at higher ranges, were imaging different regions of the water column, and so an overlap (green pixels) was not necessarily expected. Instead, the complementary information from each sonar was integrated into the map, and targets at a closer range where the two sonars do overlap were used to aid registration between scans from the two sonars.

In particular, at higher ranges, the 852 beams interact with the seabed as seen by faint blue shading at high ranges. For the example scans shown here, at an altitude of 1m above an assumed flat seabed, the outer 852 vertical beams interacted with the seabed after 11m. The Delta T multibeam sonar provided vertical resolution and the seabed was excluded by restricting the vertical region of interest, resulting in much less seabed interaction seen on the red Delta T return.

Figure 7.26 below shows the final kelp bed map compiled from the registered set of 852 and Delta T sonar scans presented as mean pixel intensity. Noise at long ranges and spurious targets were minimised using the mean pixel intensity and the combined dual-sonar scan provided clear, distinct mapping of kelp stipes, as seen in the zoomed inset.

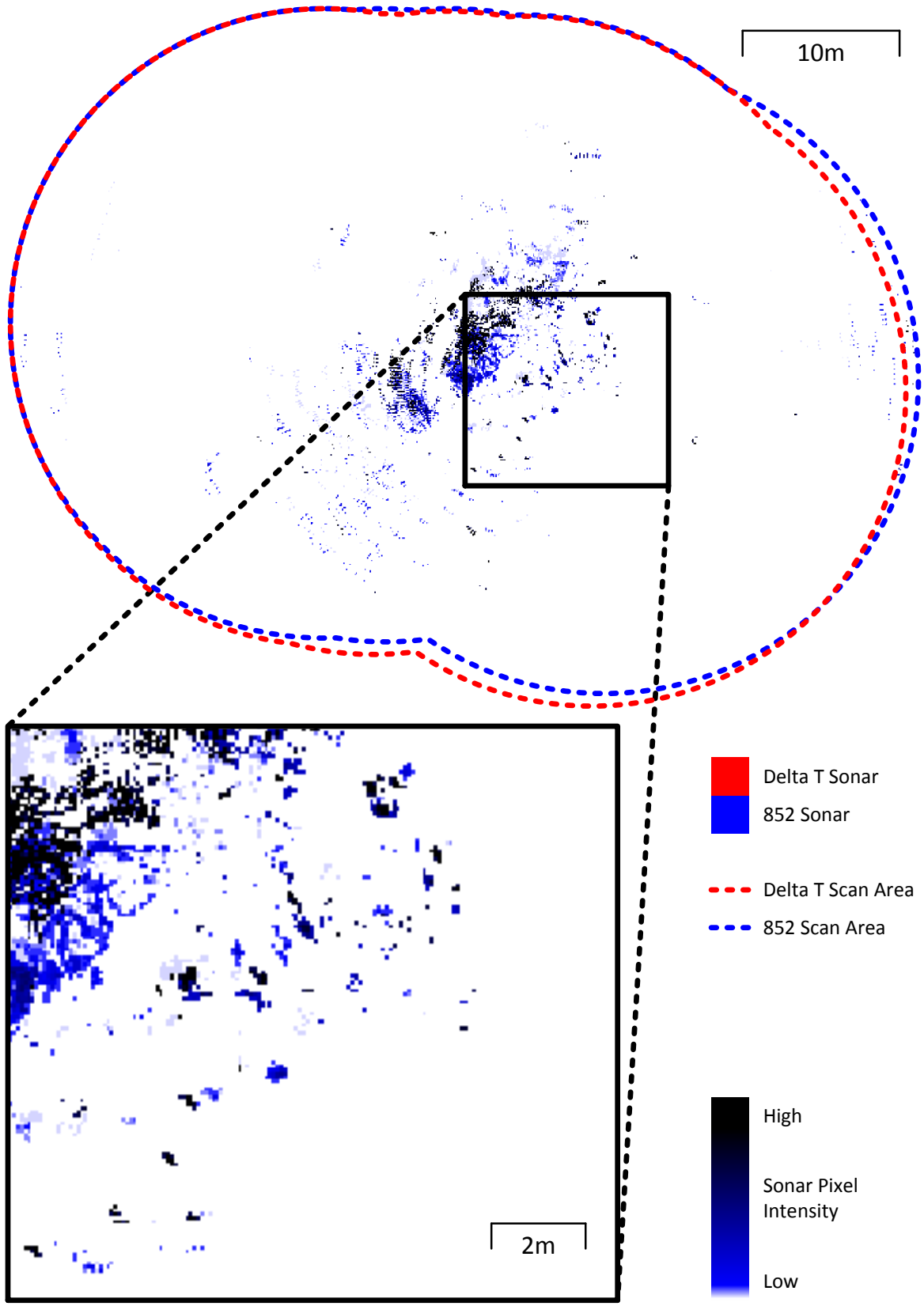

Figure 7.26 - The final kelp bed map, compiled from the registered set of 852 and Delta T sonar scans presented as mean pixel intensity using the scale shown. Noise at long ranges and spurious targets were minimised using the mean pixel intensity. The zoomed inset shows a region of distinct kelp stipes.

For comparison, Figure 7.27 below shows a map of a different region of the same kelp bed surveyed on a different day, presented as mean sonar pixel intensity. The map below was compiled from nine 852 20m range sonar scans and twelve Delta T 20m range scans, again all corrected for vehicle attitude, compiled into 2D radial scans and registered into the map shown. The scans were taken at 4 stations, approximately 5m apart with the overlapping regions used for registration. Although there was a greater water movement on this day, the zoomed inset still shows a region of distinct kelp stipes observed between both sonars, on all scans.

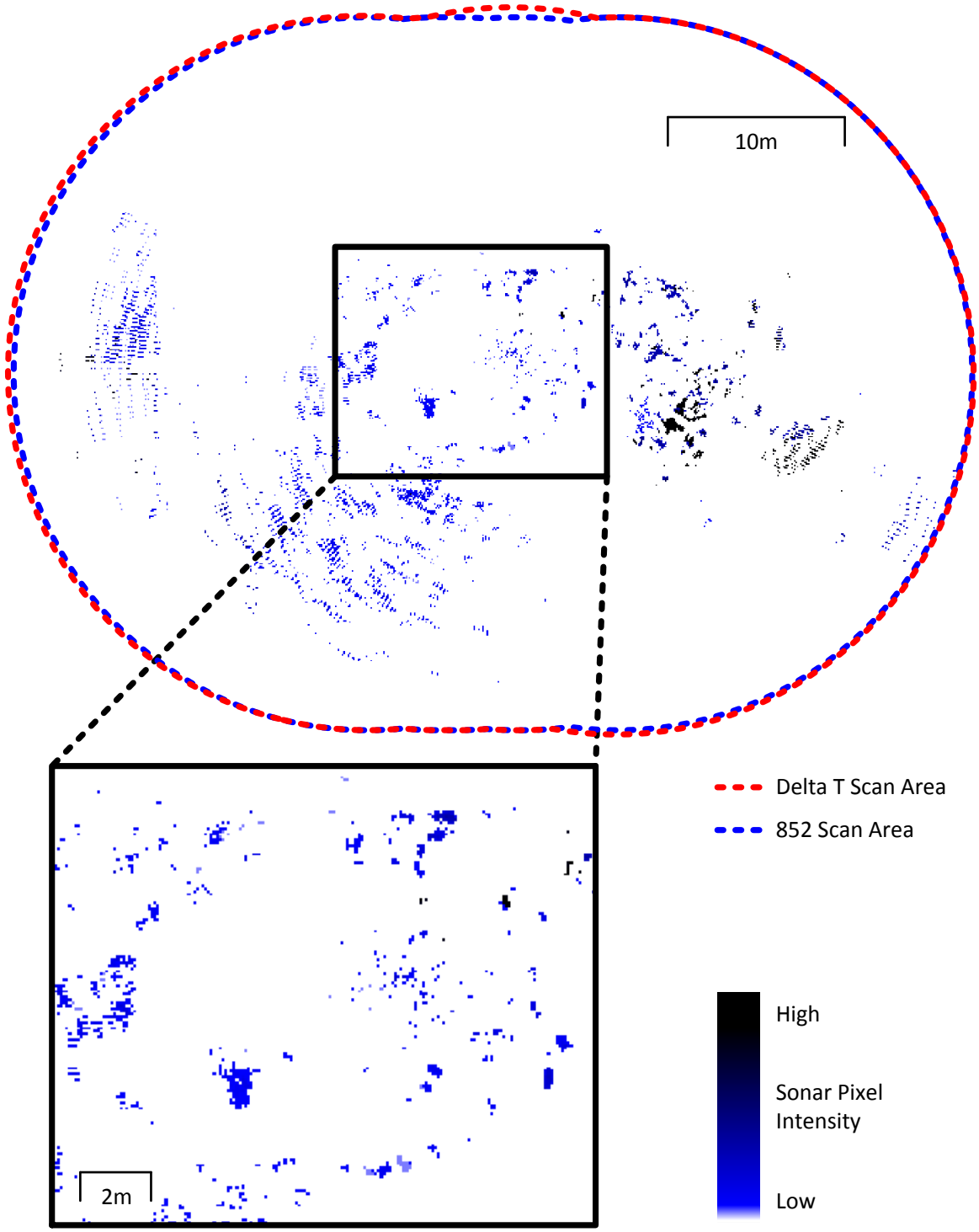

Figure 7.27 - The combined map of a different region of the kelp bed mapped previously but surveyed on a different day is presented as mean pixel intensity from nine 20m range 852 sonar scans and twelve 20m range Delta T sonar scans, taken from 4 stations, each spaced approximately 5m apart.

The scans from each sonar, including the overlapping region used for scan registration is shown below in Figure 7.28.

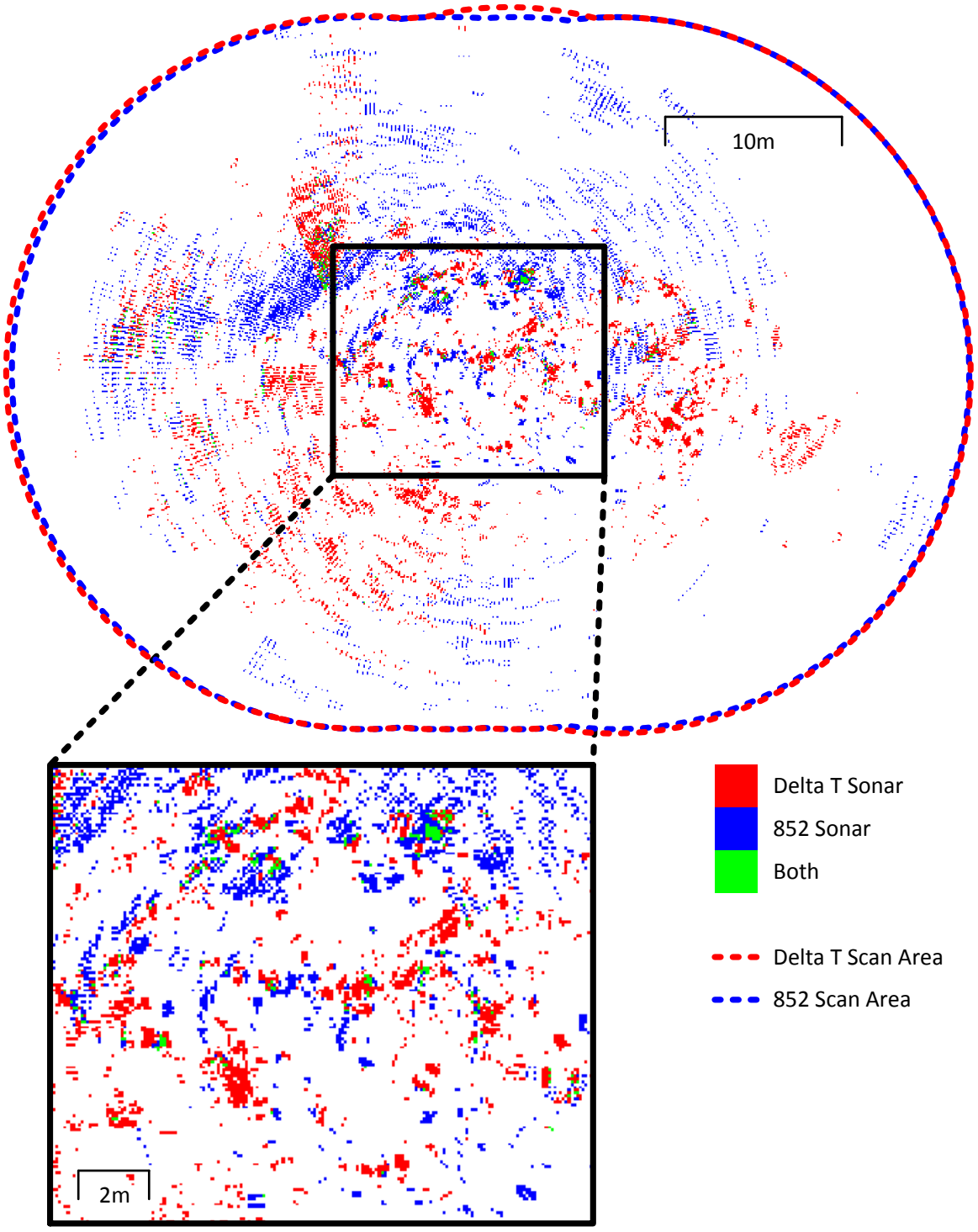

Figure 7.28 - The scan data from each sonar across all scans is identified by colour, with pixel returns present on both sonars shown in green. Although the conditions were not as calm as for the previous survey, sufficient regions of distinct kelp stipes are still present for manual mosaicking of the sonar scans.

The two scans shown previously were taken on different days but of the same kelp bed. On the second day, the surface support vessel anchored 16.25m away from the anchorage on the first day and *SeaBiscuit* was deployed in approximately the same region of the kelp bed. The figures below demonstrate registration between the kelp bed scans from the two different days using manual sonar mosaicking, given sufficient overlap. The offset in registration between the plots was calculated to be 19.78m which was plausible given, the tether length and surface support vessel anchored positions. The registration between sonar plots on different days was performed using the mean pixel intensity from all 852 and Delta T scans combined on each day.

This provided the most reliable map of stipes, with spurious and dynamic targets minimised. The registration can be seen in Figure 7.29 below in particular in the zoomed inset, using a colour code for thresholded pixel intensity from each day. The green pixels represent targets observed in the same location between the two days once each day was registered. Although not all of the targets were observed in exactly the same location, many further targets were observed in sufficiently close proximity between days to be used for manual registration. These can be seen as coherent distinct clusters of red and blue pixels, in particular in the zoomed inset.

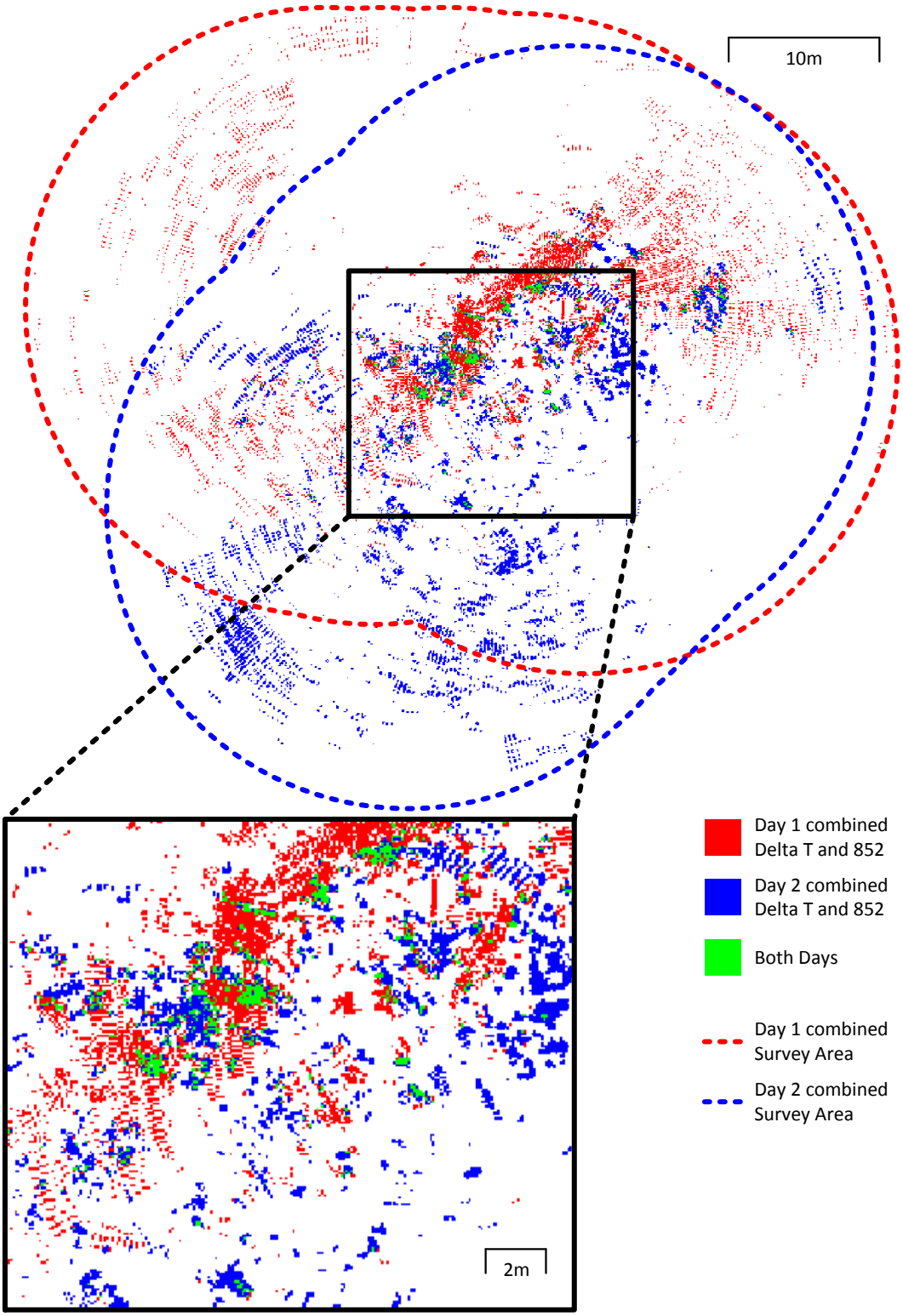

Figure 7.29 - The scans of the same kelp bed from two separate days are registered on the same map. The zoomed section shows the region primarily used for manual sonar mosaicking of the two scans, where several coherent targets were observed in a similar location between days. The upper left region of the zoomed section shows the same seabed feature, but imaged from a different (45°) angle and different position. The lower right region of the zoomed section shows a region of kelp stipes imaged over the two days.

The final combined kelp bed map plotted using mean pixel intensity from both days can be seen in Figure 7.30 below. The zoomed inset shows the same region as above, where the lower right region of the inset shows the kelp stipes.

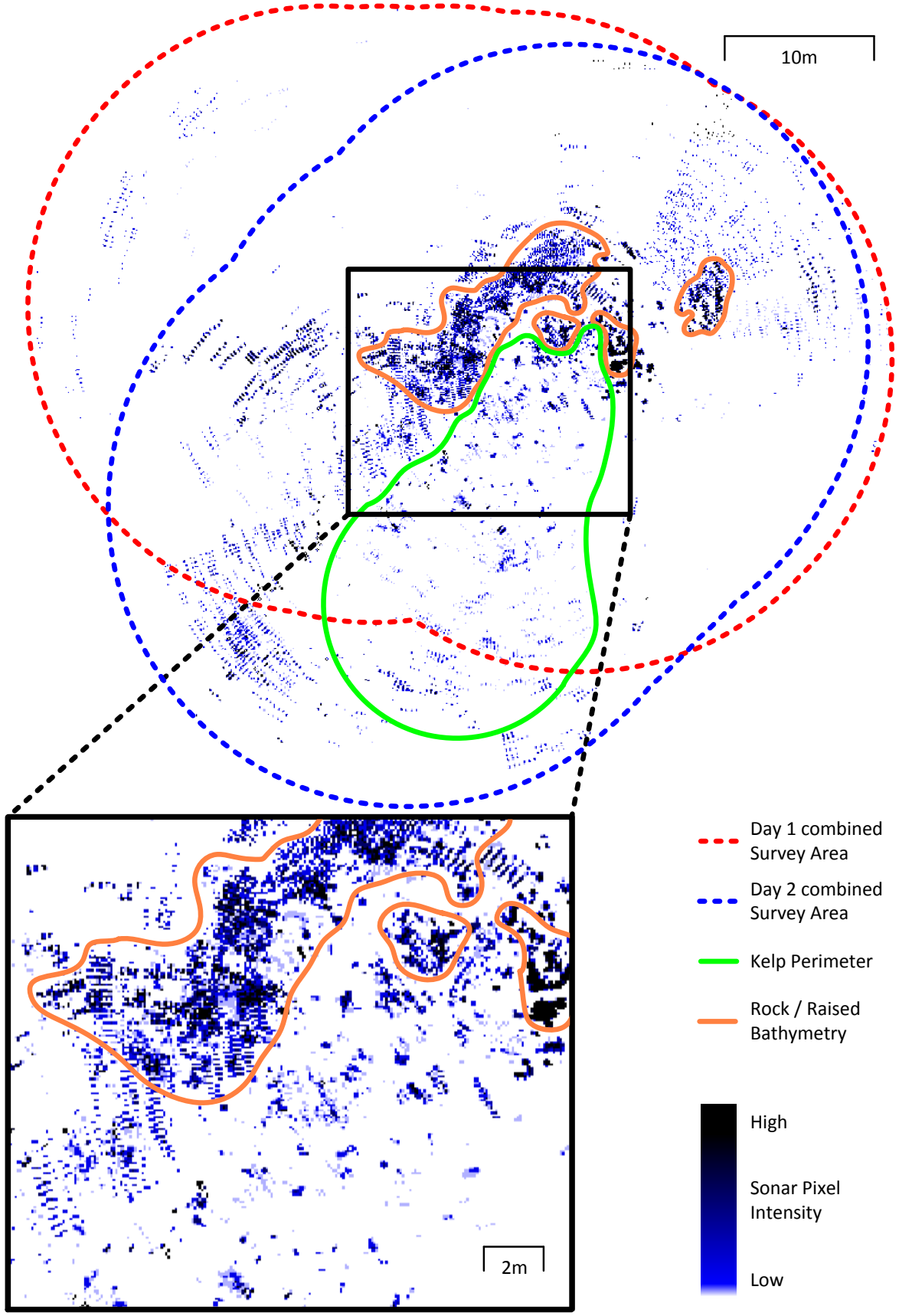

Figure 7.30 - The final combined kelp bed map from 2 days, 2 sonars and several mosaicked scans is plotted using mean pixel intensity. The zoomed inset shows the same region as above, where the lower right region of the inset shows the kelp stipes imaged between days. This manually interpreted map delineates regions of kelp with a green line and rocks / raised areas of bathymetry with orange lines. Noise at high sonar ranges is indistinguishable, and other unidentified targets require confirmation (either by video or further inspection) to reliably identify kelp stipes.

Figure 7.30 above shows the region of kelp stipes manually delineated by a green perimeter, and significant rocks and regions of raised bathymetry delineated with an orange line.

The Delta T vertical region of interest was selected to exclude the average seabed height. However, significant outcroppings and areas of raised bathymetry were still detected where they entered the midwater, coincident with the same depth as kelp stipes elsewhere. The large oblong rock in the centre of the scan was observed on the scans on both days.

These rocks and outcroppings were not removed from the final scan, both forming important habitat information, as well as being useful static navigational landmarks. The regions of kelp and rocky outcroppings in Figure 7.30 above were identified manually, using information gathered by diver surveys in the same area and video footage gathered concurrently by the iROV during the survey as ground truthing tools. However, the distinction was not absolute –noise at high sonar ranges is indistinguishable, and other unidentified targets on the scan require confirmation, either by video or further inspection, to reliably identify kelp stipes.

When operating at this altitude (1m in a total water depth of 6m), the kelp stipes appear as distinct targets, as seen in Figure 7.30 above. These were notably distinct from rocks and seabed outcroppings which appear as much larger mass targets. This distinction was used to aid autonomous distinction of kelp stipes.

Figure 7.31 below shows the result of a basic operation to detect large mass objects. Sonar targets larger than a typical kelp stipe were assumed to be rocks, or seabed features. The image shown above in Figure 7.30 was thresholded and objects above a specified pixel mass (in this case 250 pixels) were identified by a brown bounding rectangle. These rocks (as with kelp stipes) were represented as ellipses, with an associated x and y coordinate, pixel mass, ellipse ratio and orientation – the bounding rectangle was simply used below for labelling. Features labelled ‘0’ through to ‘8’ match up correctly with seabed features confirmed as rocks by ground truthing.

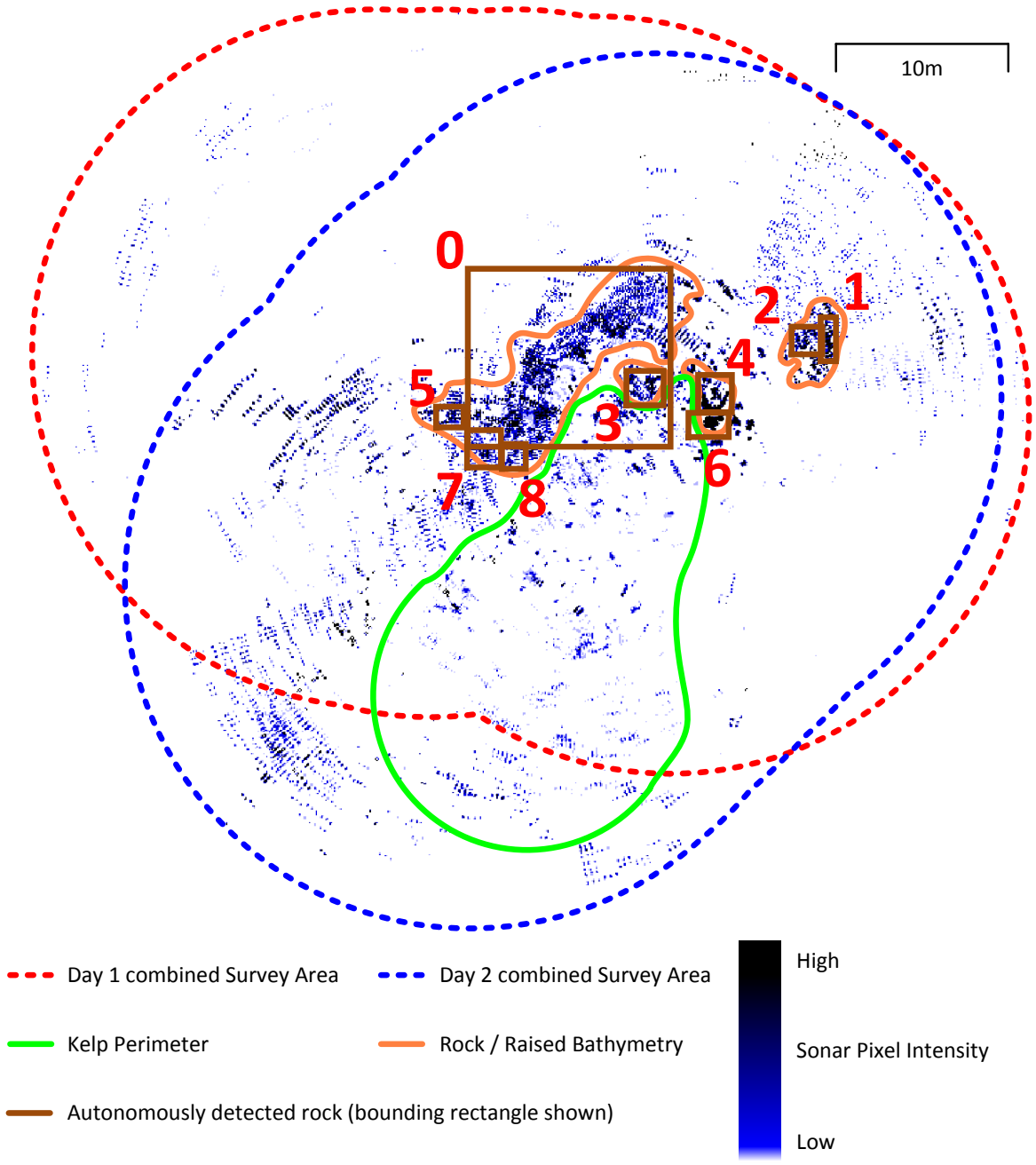

Figure 7.31 - Rocks and seabed features were detected autonomously based on a thresholded pixel mass. The brown bounding rectangles added to the kelp bed map delineate rocks detected by the algorithm using a pixel mass threshold of >250 pixels. The rocks were labelled with red numeric identifiers.

The resulting map thus comprised three areas, delineated either manually or using the steps towards autonomous detection discussed above. These three regions were seabed features, kelp, and areas which required further investigation to confirm the contents. In particular, regions at the periphery of the overall map, which were only scanned a few times, often required further scans to reliably distinguish clusters of kelp stipes from seabed features.

The regions identified as kelp above were quantified and parameterised using the techniques demonstrated in section 7.3.4.3.1.2, and the results are shown below in Figure 7.32. The algorithm detected 576 kelp stipes, or clusters of kelp stipes, within the manually delineated region of kelp shown by the green perimeter. Each stipe is highlighted in red, and bounded by a black rectangle for labelling purposes. The stipes were represented as ellipses, and recorded with a numeric identifier, x and y coordinates, pixel mass and ellipse ratio for each stipe allowing efficient storage. The steps towards a calibration model established in section 6.3.5 were used to relate the detected stipes to a real life estimate of kelp biomass and biovolume.

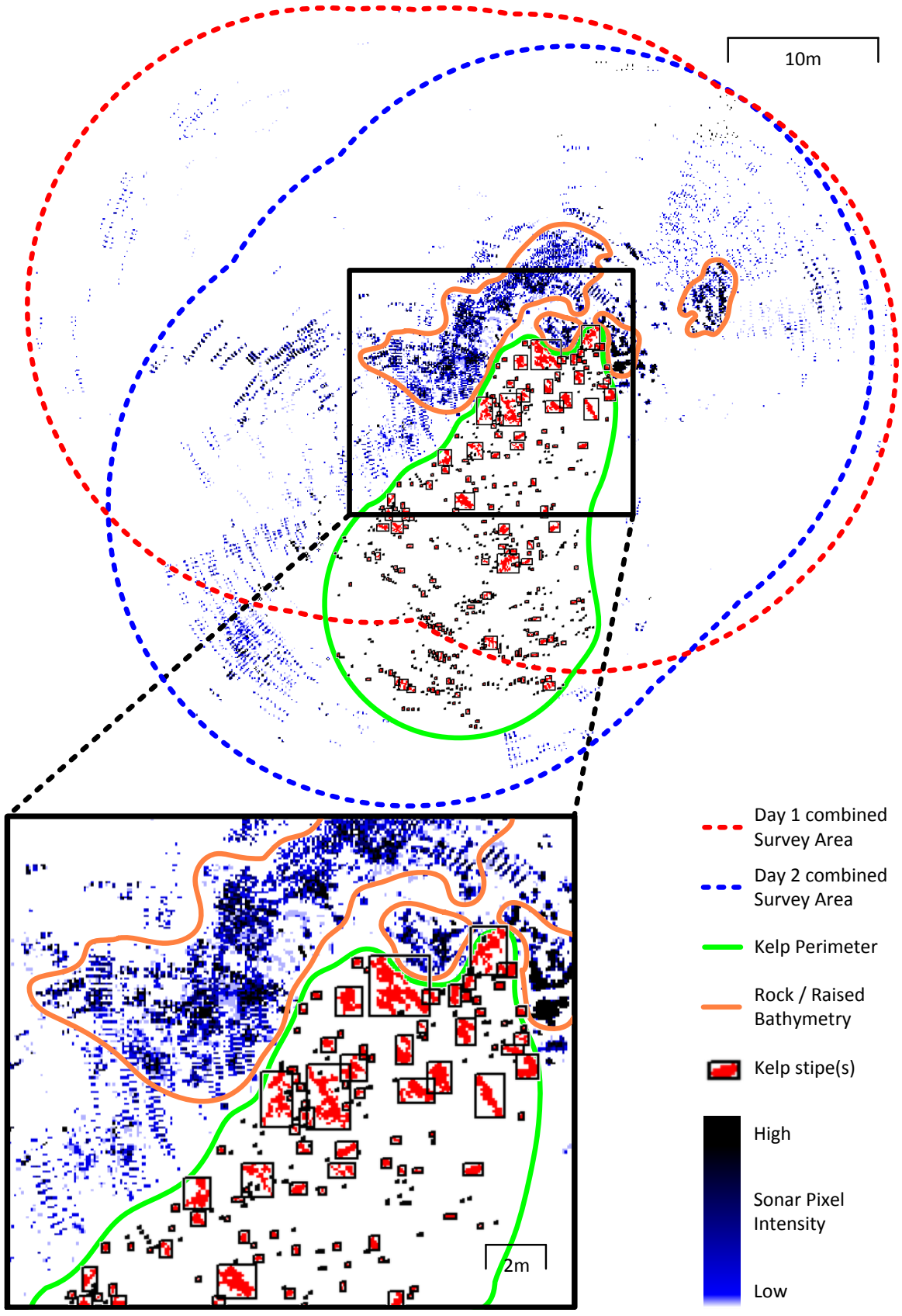

Figure 7.32 - Kelp stipes were detected and parameterised autonomously using the algorithms developed earlier. The green line delineates the manually identified kelp perimeter, and the red targets bounded in black bounding rectangles are autonomously detected kelp stipes.

7.3.6 **Discussion**

The summer of 2010 saw the first open ocean field trials of the iROV *SeaBiscuit*, deployed to map the density and distribution of kelp beds in the nearshore.

7.3.6.1 Survey methods

A variety of survey methods was used to provide the full spectrum of coverage versus detail. At the upper end of the spectrum, high coverage was achieved by instrumenting the surface vessel *Stardust* with the same habitat mapping multibeam and navigation sensors as used on *SeaBiscuit* to provide high-coverage surface transects around the kelp beds. The autonomous sonar processing algorithms for kelp detection and quantification developed for *SeaBiscuit* were applied to the sonar data gathered by *Stardust* and full motion correction from the *SeaBiscuit* navigation sensor suite was used to provide small scale correction of the GPS track. Individual clusters of stipes were mapped, and a measure of kelp density and distribution was possible with higher detail than other ship based kelp bed mapping [8], made possible using the Delta T multibeam sonar. However, as with other ship based habitat mapping, the lack of small scale manoeuvrability, restrictions imposed by the canopy forming kelp and need to conduct surveys from the surface looking downwards rather than from the midwater all reduced detail [48].

Using reconfigurable buoyancy to provide flotation, surface scans using the iROV were also performed, providing the holonomic manoeuvrability of the iROV and freedom to operate around the kelp canopy and in shallow water, while providing surface GPS updates. Other significantly larger and higher-budget ROVs are able to perform this surface mapping, bridging the air-water (or GPS-sonar) boundary [27], yet none are able to offer the holonomic axisymmetric spin mapping technique of *SeaBiscuit*.

Midwater scans provided a significantly increased level of detail, allowing quantification of kelp stipes, rather than occlusion from the canopy. Similar vehicles of this size are typically limited to operation in currents of 1 knot or less [13], and the relatively high lateral translation drag of *SeaBiscuit* coupled with sub-optimal thrusters [344, 345] imposed a similar limit on the currents which could be overcome by the onboard thrusters. Through the hybrid power supply, combining an unlimited operating duration with a thin, flexible tether and the onboard energy buffer for high powered manoeuvring thrust, missions of unlimited duration were possible in current speeds up to this limit.

Midwater operation in currents beyond this would normally exclude the use of underwater vehicles of this size and manoeuvrability [13] and towfish are often used to provide high-coverage midwater habitat mapping [9]. However, given the full height stipes and canopy, coupled with the requirement for small-scale high-detail maps, towfish were unsuitable due to the lack of small scale manoeuvrability and the high risk of tangling. Instead, the surface vessel anchored upstream of the kelp bed and allowed the iROV to drift, either past or through the kelp bed, using its onboard thrusters for course corrections and controlling the downstream speed of the iROV using the strain-relieved tether.

Finally, free-swimming midwater mapping with concurrent video feedback to the remote operator was demonstrated using vertical station keeping and course holding to navigate through kelp beds. When larger coverage was required, the surface support vessel either followed or towed the underwater vehicle at slow speeds between transect sites [14].

7.3.6.2 Evaluation

The habitat mapping was split into three objectives: delineation, bathymetry estimation and populating the map with stipe density.

Surface vessel transects were often used to delineate the perimeter of the kelp beds, registering the boundary using GPS and allowing regions of interest to be defined for high-detail midwater mapping using the iROV. The significant effect of tides on the kelp stipes, both on the kelp bed perimeter and the angle of the kelp stipes was investigated with initial steps towards modelling the effect of tides (Figure 7.8). Techniques for bathymetric mapping of the kelp beds were also demonstrated (Figure 7.9), again using either the surface vessel or the iROV depending on the area to be covered.

Finally, reliable and quantitative acoustic kelp detection was demonstrated using sonar fusion of the 852 and Delta T sonar units. Techniques for manual extraction of the kelp stipes were developed (Figure 7.11) which also allowed verification of later autonomous detection algorithms. While manual processing of sonar footage to extract the density of other kelp species is common [8, 19], the advantages of autonomous image processing providing a reduction of labour requirements and potential increase in accuracy were clear given the large areas to be covered. The 852 (Figure 7.13) and Delta T (Figure 7.17) image processing algorithms were adapted from those developed earlier for landmark sonar-aided SLAM to isolate and extract kelp stipes for mapping and parameterisation. As with landmark SLAM, the benefits of parameterisation are computational and memory efficiency, allowing a full reconstruction of the kelp bed map without having to store the memory intensive raw sonar scans.

Techniques for registration of more than one overlapping scan, from both the 852 and Delta T sonar were developed (Figure 7.19), including metrics for evaluating the quality of registration (mean pixel intensity, maximum pixel intensity, thresholded pixel count). Using a common scan format, coupled with scale and attitude correction, registration of several scans from different positions, different sonars and even different days were all demonstrated (Figure 7.29).

Exploiting the information gains from each sonar, including the different region of water imaged and the vertical discrimination of the Delta T, regions of kelp and seabed features were identified and delineated both manually (Figure 7.30) and basic autonomous techniques were also demonstrated (Figure 7.31). From this, the delineated regions of kelp were parameterised and the algorithm results evaluated against the raw sonar scans (Figure 7.32).

The parameterised maps allow the calibration methods developed in section 7.2 to be applied to the open ocean kelp bed surveys to provide a quantitative estimate of kelp density. Additionally, the parameterised kelp maps enable the future work proposed towards using the kelp stipes themselves as navigational landmarks (section 8.1).

This section has used two examples from the datasets gathered to demonstrate successful open ocean nearshore kelp mapping, compiling a map from two surveys conducted on different days. The holonomic axisymmetric survey technique was exploited and sonar fusion, together with techniques for autonomous map interpretation and kelp detection, served as a proof of concept of the benefits of using the iROV *SeaBiscuit* for nearshore habitat mapping.

7.3.6.3 Validation

Ground truthing was performed across two stages, calibration and validation [20].

Calibration against a known ground truth was used to confirm sonar target identification and to provide a quantitative estimate of kelp biomass / biovolume. The transplanted artificial kelp bed provided a known quantity and arrangement of fully dimensioned kelp stipes to validate detection, similar to the work performed by Zabloudil et al. for an alternative species (*Macrocystis pyrifera*) [8]. This allowed the manual detection criteria of kelp stipes to be verified and the sonar settings tuned with a known target presence [8]. However, the artificial kelp bed in this research also allowed development and verification of the autonomous kelp detection algorithms, used for later autonomous kelp bed surveys, and calibration of the sonar returns to a known biovolume and biomass of kelp at that height. With further calibration datasets to expand the model, this novel technique has the potential to apply real life kelp biovolume estimates to all previously gathered sonar kelp bed maps.

Validation was performed during each survey, to verify the quality of data and interpretations and to resolve ambiguous target classification. Data quality verification included both identifying the number and position of stipes correctly, together with verification of localisation estimates used to register the sonar scans into an overall map. A combination of diver verification, concurrent video verification and camera drops / tows were used to verify habitat classification and to verify sonar target identification, in particular in areas of ambiguous targets or challenging conditions.

The staged development in the confined environment, through to navigation off the piling dock and calibration of the sonars to the artificial kelp bed allowed comparison to a known ground truth at each stage of development. For the open ocean field trials, several validation techniques were employed to verify correct operation.

Realtime video verification of sonar targets was possible for both the 852 and Delta T sonar when visibility and range permitted using the realtime feedback of video footage from the forward and downward facing cameras, as seen earlier in section 4.6.7.

Diver kelp bed surveys, coupled with camera drops of the kelp beds were also used to provide verification. Ground truth positioning for calibration and verification of the scans was also performed using diver support as pictured in Figure 7.33 below.

Figure 7.33 - Diver positioning of the vehicle at a series of known pre-measured positions at a known distance and orientation from the kelp bed was used to ground truth the kelp bed surveys and navigation.

The vehicle was held at a series of pre-measured positions, referenced to the surface via marker buoys and thus to GPS, and a series of controlled known movements performed for comparison to the results obtained. These included holding stationary positions over a grid of known positions measured and marked on the seafloor in a known kelp bed arrangement, or performing a series of constrained scans, for example a 360° scan, or an oscillating pan, either stationary or any

combination of these while moving at a known speed between stations. Visual communication between the divers to the surface operator and the logged data for later reference of the operations performed was provided by the onboard cameras, which also allowed verification of the movements and sonar targets observed. It is this diver ground truthing which forms the basis towards sonar-aided SLAM from kelp discussed in section 8.1.

7.3.6.4 State of the art

The suitability of using a holonomic highly-manoeuvrable underwater vehicle for operating in the difficult and complex, often enclosed, hostile nearshore environment of kelp beds has been demonstrated. The manoeuvrability provided allowed detailed sonar and video scans to be taken at-depth and from within the kelp bed, thus increasing the coverage and detail when compared to surface vessel scans [8, 48]. It also allowed an accurate course to be transited despite external water movement. Holonomic movement and the axisymmetric shell allowed the directional sensors to be exploited and was used to extend the coverage of the limited-budget sensor suite to gather results typical of a much higher budget sensor. This included extending the 2D multibeam footage to register full 3D maps of the environment *while the vehicle was independently in-transit* [129, 130].

Through the results achieved from the field trials, an improvement in the coverage, quality and detail of the kelp bed maps gathered using the iROV has been demonstrated over SCUBA diver transects or kayak surveys [1]. iROV surveys provide time and labour savings when compared to other methods and fulfil the niche in between the level of detail provided by a manual diver survey and the speed of a surface vessel sonar survey [11]. Sonar mapping provided increased coverage over diver surveys [11], particularly in low visibility. This is of particular importance in the high biological intensity, therefore high turbidity kelp beds [49, 50]. Furthermore, sonar scans performed by an underwater vehicle rather than a surface vessel increase manoeuvrability and provide independence from surface conditions. It also allows horizontal scans to be taken through the kelp bed, station keeping, operation in shallow water and controlled movements with a lower risk of damage or tangling [13].

The compromise between the security and control of a tether with remote high-level operator control, realtime feedback & supervision and on-the-fly reaction to changing conditions provided a reliable nearshore survey method when evaluated against AUV/ROV techniques for nearshore habitat mapping in Chapter 2 [251, 252, 267-269]. Operational reliability was ensured in the dynamic conditions of the nearshore, and crucially data validity could be verified during acquisition. This avoided only discovering errors or reduced quality during post-processing, both costly in time and budget if a redeployment was required [11]. Coupled with the buffered high-power holonomic thruster system, the benefits of an intelligent, position-aware iROV have been demonstrated for operation in the hostile nearshore environment.

Long established [369] methods for estimating canopy forming kelp distribution still rely on surface vessel sonar surveys [8] using manual processing of results to estimate kelp density and distribution. Due to the survey method, which requires either the surface vessel to pass over the canopy forming kelp, or to image stipes from an oblique angle using side-looking sonar, clutter and occlusion cause inaccuracy in the kelp estimate in areas of high plant density, quoted as >20 stipes / 100m² [8]. This is chiefly caused by the beam spreading of the surface mounted echosounders requiring a clear beam in between positive kelp returns to distinguish one stipe from another.

Instead, the iROV survey method, using a combination of scanning and multibeam sonar footage gathered from the midwater, was capable of distinguishing greater stipe densities using the adjustable range of each sonar, and vertical and horizontal discrimination. Small scale manoeuvrability was also used to mitigate the effects of occlusion. Surface sonar techniques also risk underestimating density for juvenile or small stipes [8], yet it is proposed that mapping from the midwater, with video verification provides a more reliable method to ensure all stipes are detected.

Whereas other underwater vehicles utilise video for nearshore habitat mapping and classification [12], the combined dual-sonar and dual-video approach used on *SeaBiscuit* allows robust operation in a greater variety of environments, including turbid water, under the kelp canopy and with greater penetration of the kelp beds from the periphery, both increasing coverage and reducing the risk of tangling. More traditional AUV torpedo hull configurations for operation in the nearshore have a known susceptibility to significant pitch and roll due to wave action with a corresponding reduction in survey data quality [12]. However the high metacentric height [297] of *SeaBiscuit* coupled with the holonomic propulsion system and cylindrical hull minimised the effect of wave action, allowing station keeping and course holding in flows with the onboard inertial sensors used to correct for wave action. Habitat mapping was performed in the absence of acoustic navigation transponders and without environmental modification often used in the nearshore [11].

Surface canopy area is used to describe the distribution of kelp, on a scale typical of an entire kelp bed or series of kelp beds [369]. On a smaller scale, at higher detail, the distribution of kelp is presented as an averaged density surface, with the resolution varying with the application, typically as stipes per 100m² [8]. On a smaller scale again, the results of diver surveys and manual video processing are typically processed at 10 second intervals along an assumed constant diver transect speed between two surface markers, with the stipes visible in each video frame counted assumed to be a 4m² area using a SCUBA diver for scale [1]. However, the assumed swim speed and course, lack of a position reference, visibility dependent observability, grouping of several clustered stipes into a single target and lack of stipe size measurement all present opportunities for accuracy improvements using the iROV, coupled with the benefits of coverage, detail and labour reduction from autonomous processing.

Using the iROV method, kelp bed area and stipe density as an averaged surface are both possible, yet with a proposed higher detail from midwater scans. Furthermore, at the very high-detail level to augment the diver video surveys discussed above [1], the iROV allows surveys of this detail, with stipes registered with a positional accuracy of <1m, yet with a coverage of >20m per scan, a continual position estimate and realtime video footage for verification using the method discussed above [1].

A relative measure of stipe diameter is also provided using the iROV method, allowing clustered stipes to also be quantified. The calibration techniques discussed in section 7.2 provide a method to convert this relative measure to a real life estimate of kelp biomass / biovolume as the calibration dataset is extended.

Although the capital cost of an underwater vehicle is high, through the exploitation of sensors for both habitat mapping and navigation and the hybrid iROV techniques, the cost of *SeaBiscuit* has been minimised, and is significantly less than vehicles of a comparable specification and functionality [14]. When compared to the commercial costs of diver surveys, quoted at up to $10k per day [11], the financial benefits of the iROV for habitat mapping can also be seen.

Chapter 8 Conclusions and Future Work

Practical evaluation of existing techniques for nearshore habitat mapping throughout four field seasons has provided a demonstration of the limitations of existing solutions as well as an insight into the dynamic conditions and challenging environment of kelp beds. The extensive literature review in Chapter 2 into existing methods and applicable techniques from similar fields, coupled with the field trials of *Hawthorne 2.1* described in Chapter 3, informed the development of a solution to this challenging problem.

The iROV *SeaBiscuit*, described in Chapter 4, exploited hybrid techniques from the fields of AUVs and ROVs to provide a robust solution for mapping the challenging kelp bed environment. A hybrid control architecture, combining onboard position-awareness and low-level autonomy, allowed survey data to be registered with a position reference and relieved the operator of station-keeping and course-holding. Data validity in dynamic conditions of tide, waves, visibility and kelp density was ensured by remote supervision and realtime data feedback. Robust, reliable high-level control was provided by maintaining the operator-in-the-loop. A hybrid power-supply also provided the unlimited mission duration and security of a tethered vehicle, with the high-powered manoeuvring thrust required to navigate reliably in and around the full height kelp stipes despite currents.

Designed on a budget feasible for small-scale research teams, and utilised for three field seasons by the Coastal Ecosystems Research Foundation in Canada, *SeaBiscuit* was designed to exploit the maximum benefit from a limited budget. The complementary axisymmetric hull, holonomic propulsion system and sonar-fusion allowed 3D mapping while in transit, with station-keeping and course-holding provided independently of panning the directional sensors over the kelp stipes. Utilisation of the same sensors for navigation as well as mapping was developed in Chapter 5 and later demonstrated off a piling dock.

Sensor fusion provided benefits over using a single sensor, or using sensors in isolation. These benefits included combining drift-free navigation with the robustness and availability of idiothetic information, the combination of detail and coverage by fusing sonar for detection and video for identification, the extended coverage and resolution in 3D realised by sonar fusion and bridging the air-water boundary to register sonar targets with an absolute GPS position.

A staged series of field trials of increasing complexity guided the development of the iROV *SeaBiscuit* while ensuring reliable progress as described in Chapter 6 and Chapter 7. These began as confined water trials with the addition of basic mission planning algorithms demonstrating a move towards autonomy at the SAUC-E competition. Following confined water trials, the benefits of sensor fusion and SLAM were shown in the sheltered waters of the dock survey and mapping application, allowing the sonar feature extraction algorithms to be tuned to autonomously detect and map underwater vertical targets. Successful simultaneous localisation and mapping off the dock demonstrated the capabilities of nearshore navigation using a combination of sensors to provide drift free reliable underwater navigation.

The move towards kelp bed mapping started with calibration and verification of a known arrangement of kelp stipes to ground truth the sensors and mapping algorithms, detailed in Chapter 7. Following this, several successful field trials deploying the vehicle in a variety of conditions demonstrated the capability and benefits of kelp bed mapping using an iROV. Techniques were developed and demonstrated to delineate the kelp bed perimeter, to map the bathymetry while correcting for tide height and to map the density and distribution of kelp stipes

using co-registered data from the Delta T multibeam and 852 scanning sonars. Methods were proposed to calibrate the acoustic data to an estimate of kelp biomass and biovolume using the artificial kelp bed. Validation and verification of the results were also explored, using realtime video validation of sonar target classification and ground truthing using diver surveys and camera drops / tows.

Compared to the existing field of nearshore habitat mapping, the iROV *SeaBiscuit* provided a compromise between detail and coverage which was ideally suited to navigation in the kelp beds of *Nereocystis luetkeana*. A significant increase in coverage was demonstrated over diver surveys, with financial savings and an unlimited survey duration. Data gathered using video was of a comparable detail to that gathered by the divers, yet a continuous position estimate was provided. However, sonar fusion provided high coverage rates of data co-registered with video, with a quantitative estimate of the position and size of each stipe or cluster of stipes.

Although acoustic mapping from surface vessels provided high-coverage surveys complementary to the iROV surveys, the level of detail available from midwater mapping using the iROV was much greater. Data was acquired free from the occlusion and restrictions of imaging through the kelp canopy, and without the movement and shallow water restrictions of a surface vessel transecting through the kelp bed. Furthermore, small-scale manoeuvrability provided data with a greater spatial resolution and reduced the effects of occlusion, decoupling the survey data from surface conditions.

Several general opportunities for further development were identified earlier. These included improvements to the known limitation of the existing thrusters to yield more efficient operation and a higher thrust to allow surveys and station-keeping in higher currents. Improvements to the ruggedness of the prototype vehicle to allow reliable deployment, operation and recovery in the open ocean conditions are also required. In future, as either the mapping requirement dictates or budget permits, the addition and integration of either further or alternative sensors is also straightforward due to the inherently scalable algorithms and software. Through the matrix orientated SLAM and sensor fusion algorithms, provided any additional sensor is properly characterised, integration can be as simple as another element in the matrix or recursively fusing an additional sensor measurement to incorporate the benefits.

However, as a proof of concept of the benefits of iROVs for nearshore habitat mapping, the current iROV prototype *SeaBiscuit* has been proven successful through a staged series of field trials. Several opportunities for further research are identified below towards full-scale open ocean kelp bed mapping, together with several further applications of the iROV.

8.1 Autonomous kelp scan registration

In section 7.3.4.3.3, the technique for registering (mosaicking) several overlapping sonar scans of the kelp bed to form a larger overall map comprised of several scans was described. During the initial kelp bed deployments, this registration was performed manually during post-processing, using the GUI shown in Figure 7.19. This GUI presented the operator incrementally with a series of sonar scans, allowing different scans to be toggled and registered onto the overall compiled map. The x and y position of scans could be adjusted and the yaw angle corrected to optimise registration. The estimated vehicle position for the time when the scan was taken was used to bound the search space for registration and a variety of metrics were used to evaluate the quality of fit and to confirm the optimum estimate of registration. Registration was compounded by errors from either dynamic targets, movement of the flexible stipes either between scans and/or

during a scan and uncorrected vehicle movement during a scan. Manual registration was demonstrated for several kelp bed scans in section 7.3.5 as an initial solution to compiling kelp bed maps.

However, the opportunity for autonomous kelp scan registration has the potential to reduce error, reduce labour requirements by eliminating manual processing and to allow the realtime compilation of a kelp bed map during a survey. Bounding the search area from a global search with an initial 'best guess' of the registration using the estimated vehicle position, to a far computationally simpler local search, is equally applicable to autonomous registration. The extra step required is the algorithm to autonomously evaluate the different possibilities of registration and use the 'quality of fit' metrics to select the optimum registration.

Techniques to estimate the relative vehicle movement from successive sonar scans are already well established, including probabilistic techniques specifically optimised for mechanically scanning sonars [124, 125]. An opportunity for future work is to develop these algorithms for the dual sonar geometry of *SeaBiscuit* using the combination of the 852 scanning and Delta T multibeam sonar, specifically for operation in the kelp beds. Autonomous registration of successive sonar scans enables the exciting opportunity of 'SLAM from kelp' or using the kelp stipes themselves to aid navigation.

Using the probabilistic framework for SLAM and sensor fusion developed in Chapter 5, it was proposed that any piece of navigational information could be used to further knowledge, if it was correctly characterised. Dynamically estimating the uncertainty of position estimation from the kelp stipes during operation is required, in order to correctly weight any localisation information inferred from the kelp stipes.

The targets are non-uniform, of varying size and far from being in a regular ordered pattern. Not only do the kelp stipes tangle and clump together, but unlike a dock piling, the kelp stipes sway back and forth in waves, currents and tides. This effect can cause the kelp stipes to appear as dynamic objects. The exceptions to this are in calm water, when the kelp stipes remain still enough for the duration of a survey that they can be used for navigation, or when the current is strong enough, and steady enough in direction and magnitude that the stipes are pulled in a single, repeatable and constant direction.

In these cases, the kelp stipes may be static enough to navigate from. A sonar scan at the surface can relate a known arrangement of stipes to the world coordinate system using GPS and then the vehicle can dive and the underwater scan can begin. A sustained current providing repeatable navigation from kelp stipes can be verified by surfacing regularly to compare the positional estimate with a GPS update and by monitoring the *relative* position of stipes with respect to each other to detect random, turbulent or periodic flow.

An apparent shift in position of all of the kelp stipes can be compared to short duration accelerometer readings to decide if it is a shift in the position of the vehicle, an external water movement shifting the kelp bed, or a combination of the two. An apparent positional change of a single area of kelp stipes can be interpreted as external water movement, these targets can then be regarded as dynamic and not used for navigation. In this way, even in high currents, provided that the currents are sustained and relatively constant, the kelp stipes themselves can be used for brief navigation and localisation, to correct for drifting INS data in between GPS updates.

Initial work towards investigating the feasibility of SLAM from kelp was performed during the 2011 field season which included generating a ground truth dataset of a kelp bed using diver held

positions. The next stage considers the processing of this ground truth data to investigate the feasibility of recognising patterns of kelp stipes as navigational landmarks. As with the dock survey and mapping, sonar-aided SLAM has the potential to provide drift free position information to reduce positional uncertainty when surveying and mapping the kelp beds.

8.2 Kelp modelling

In section 6.3.5, the dimensioning and arrangement of a series of five kelp stipes was described to provide an 'artificial' kelp bed of known characteristics to calibrate the sonars. Within the main document, the target strength (recorded as intensity on the sonar bitmap) at different ranges, gains, depths and angles was used to generate a calibration dataset. This lookup table related a given sonar intensity under the specified conditions to a corresponding amount of kelp (gas pocket cross sectional area, biomass and biovolume) *in the current horizontal plane* imaged by the swath. Provided the same horizontal height was maintained throughout a survey, this allowed relative comparisons to be made.

An opportunity for further work seeks to create a generalised model for kelp stipes, to allow interpolation within the calibration lookup table already created. If a sufficiently reliable and accurate model is possible, this could also allow an observed biovolume / biomass at the current depth, coupled with vehicle altitude and water depth to be extrapolated to estimate the overall kelp stipe biovolume / biomass which would relax the requirement of operating at a constant vertical height. This generalised model could then be applied to all *Nereocystis luetkeana* kelp in open ocean scans to augment and correct measurements from the Delta T sonar over the entire vertical height of the kelp stipes.

8.3 Dynamic evaluation of sensor noise and uncertainty

The nearshore environment is highly dynamic and environmental conditions can change quickly with little warning. The aim of future work is to develop a dynamic model of sensor uncertainty, which can adapt on-the-fly while a mission is in progress to autonomously adjust the uncertainty characteristics in response to changing environmental conditions.

This allows the navigation algorithm to respond to changes in environmental conditions and reactively shift the weighting of the sensor fusion algorithms to ensure the most reliable and robust navigation at all times, despite dynamic environmental conditions. Robustness and reliability is gained over assuming that a single static model of sensor uncertainty is valid for all conditions; an improvement in navigation accuracy will result from the optimal weighting of each sensor by the sensor fusion algorithms. Additionally, the navigation and mapping algorithms will be aware of the variation in overall localisation uncertainty caused by the variation in environmental conditions and can act accordingly.

For each sensor, techniques need to be developed to autonomously estimate the sensor noise and uncertainty. For some sensors, for example the compass, this is relatively straightforward and a low-level evaluation of sensor noise can be applied – the compass output can be monitored for a known yaw angle measured by another mode of sensing, for example the INS or 852 sonar. However, for more sophisticated sensors, such as the cameras and sonar units, more complex high-level autonomous evaluation of noise and uncertainty are required. As environmental conditions change, the weightings are adjusted, for example:

- turbid water (murky so lower weighting of vision)
- turbulent water (increased sonar noise)

- magnetic disturbances (reduced magnetometer accuracy)

For the cameras, a reduction in light level and an increase in water turbidity can be detected which will both serve to increase visual uncertainty. For the sonar units, increasing sea-state, operation close to the water surface and long range landmarks will all increase uncertainty. Finally, for the accelerometers, long, gentle slow movements will all increase uncertainty through undetected drift. The equivalent high-level evaluation of noise and uncertainty for the earlier compass example is to detect operation in rough seas using the INS which will affect the gimballed compass. Additionally, sonar scans and deviations in orientation between the gyroscopes and compass can be used to detect when the vehicle is in close proximity to large ferromagnetic objects, for example the surface support vessel or underwater structures.

If a sensor is deemed either to have failed or to be temporarily unusable due to a change in conditions, then the bias can be adjusted to zero so as to ignore that sensor. The failure of a sensor which is still generating measurements but which are incorrect (the opposite to fail-silent behaviour) can be detected through the co-registration of common states between sensors. If sensing redundancy exists, the mission can continue despite failures.

8.4 SLAM controlled sensor focussing

The benefits of extending the coverage of directional sensors using the complementary navigation and holonomic propulsion capabilities were explored earlier in this document. These included the ability to extend the coverage of the 2D forward facing Delta T multibeam sonar towards the results available from a 3D imaging sonar, as well as the ability to independently orientate and pan the directional sensors independently of the vehicle's course or transect.

At present, high-level control of the sensor orientation, scan mode and vehicle movement is performed manually with low-level autonomy. This means the operator selects the vehicle course (the translation direction) and the vehicle heading (the angle the vehicle will face while transiting this course, or the movement while transiting, e.g. an oscillating pan or slow rotation) and the vehicle carries out these movements using feedback from the navigation sensors (INS, compass, depth, etc.) to close the feedback loop.

In developing the autonomy of the vehicle for operation in the nearshore while maintaining the security of remote high-level control and supervision, one exciting area of research is SLAM controlled sensor focusing. This allows the autonomous navigation algorithms to influence the direction of the sensors to autonomously seek to reduce ambiguity about the information gathered or the map created.

To consider an example: if the vehicle is transiting through open water seeking to map its surroundings with no a priori information, then typically the Delta T will be facing forward to provide information on the bathymetry and for collision avoidance, and the 852 sonar will be continually scanning around the vehicle every 6 seconds.

If an object is detected on the 852 sonar, the sector of interest of the 852 sonar can be immediately reduced to focus on this object, reducing from the full 360° to for example ±45° about the object with a corresponding increase in update rate to 1.5 s. This increase in update rate provides faster feedback, and reduces mapping uncertainty. An occasional full 360° scan can still be performed intermittently to ensure no other objects are missed. A second stage can then be to pan the vehicle and the forward facing Delta T sonar (including the forward facing camera if in range) over the object of interest while still transiting the original course.

In principle the sensors, holonomic movement capability and software frameworks are in place to achieve this SLAM controlled sensor focusing and it is already performed manually to some extent by the remote operator. The additional autonomy required to enable this is an exciting opportunity for development of the control architecture.

8.5 Active buoyancy control

Efficiency benefits can be realised by coupling the vertical thrust system with an active buoyancy control system. A buoyancy control system will eliminate the difficulties of trimming the buoyancy and vehicle attitude each time a peripheral is changed (such as a new sensor or actuator), or the vehicle moves from saltwater to freshwater operation, and will also yield efficiency gains. The existing fixed buoyancy provides a small positive buoyancy for reliability, which is continually countered with a small amount of downward thrust. However, if reliability can be achieved otherwise, then a buoyancy control system can provide vertical station holding and depth control using changes in buoyancy rather than thrust. This will yield significant energy savings, particularly for vertical station keeping when the energy expenditure to hold a position is zero.

The optimal solution to provide long-term efficient vertical station keeping while maintaining the instantaneous high-thrust required for manoeuvring in the nearshore environment is a hybrid system coupling the benefits of both a buoyancy control system with a vertical thruster system. In this way, manoeuvring and reaction to sudden water movements can be provided by the thrusters while the buoyancy control system provides long-duration station keeping.

8.6 Further applications

Given the delineated kelp bed, the underlying bathymetric data and the density and distribution of kelp stipes, the further development of the map depends on the application. This can include further sonar and visual surveys, the addition of species identification by diver surveys and towed nets, or benthic composition from ponar grabs. Two studies being supported are an investigation of the underwater acoustics of kelp beds and the corresponding navigation of grey whales by ambient noise, and a study of the density and distribution of mysid shrimp in the kelp beds, the food source of the grey whales as introduced in Chapter 2.

8.6.1 Kelp bed acoustics

Grey whales are known not to use active echo-location like other marine mammals and are thought to navigate using ambient noise [1, 41]. Research is underway into the underwater soundscape in proximity to and within kelp beds, including acoustic transmission and attenuation through the kelp beds [1]. In each case, the density and distribution of the surrounding kelp bed is required to be able to correlate any acoustic measurements made. Both the overall general map of the kelp bed is important, but also high-resolution transects in specific regions.

Figure 8.1 shows a typical experimental setup for acoustic transmission experiments through the kelp bed. In these experiments, a known acoustic signal was broadcast from a known point and the received signal was recorded for analysis at a series of known distances away. The attenuation of different frequencies can be compared to the density and distribution of kelp along the transmission path. For this experiment, the blue circles show the centres of 4 scan locations where high-resolution 2D maps, of the form shown in Figure 7.17 earlier, were generated of the distribution of the kelp stipes to provide an indication of the transmission pathway. All points were GPS referenced and were recorded at equivalent tides to ensure repeatability.

From the kelp bed maps created to support the acoustic research, significant benefits from the iROV survey method were seen. Compared to surface observations using kayaks and handheld GPS units [1], the actual midwater stipe position was measured using the iROV rather than surface canopy position. Compared to surface vessel sonar scans, the iROV provided a more directed, controllable sensor platform which could be positioned accurately and manoeuvred within the kelp bed easily. As with other applications, when compared to diver transects, significant time and labour savings from using the iROV were seen, allowing for a greater coverage with the same resources [1, 11]. Through the optimal compromise of a tethered, yet intelligent iROV, the underwater vehicle was capable of surveying and mapping continuously without interruption for extended periods of time and manoeuvring to a new site without requiring recovery and redeployment.

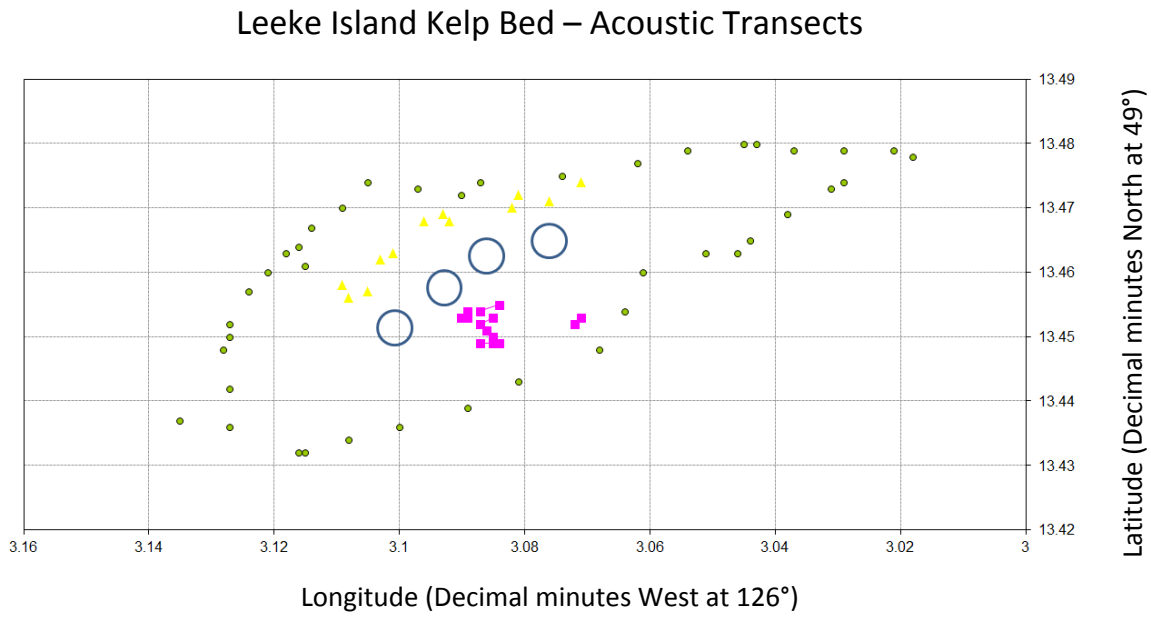

Figure 8.1 - An experimental setup for acoustic transmission experiments in the Leeke Island kelp bed. Green dots mark an approximate perimeter of the Leeke Island kelp bed, pink markers show the source of several transmissions and the yellow markers show corresponding receiver stations [1]. For this experiment, the 4 blue circles show the centres of 4 scan locations where high-resolution 3D maps were generated of the distribution of the kelp stipes to provide an indication of the transmission pathway.

8.6.2 Density and distribution of mysids

Grey whale feeding ecology studies [3, 40] are investigating the temporal and spatial relationship between the distribution of grey whales, the distribution of kelp and the distribution of mysid shrimp, the food source of the grey whales. The kelp bed maps are a useful tool for supporting research into the population distribution of mysid shrimp which occupy the kelp beds. Other studies have demonstrated detecting swarms of mysids with a 110kHz and 220kHz single beam echosounder using surface vessel surveys [2]. Post-processing software was developed in conjunction with Feyrer [2] to extract the mysid density and to co-register it with the surface vessel track information to convert the density estimate to a mapped distribution of mysids. Future work could include overlaying the mapped distribution of mysids onto the kelp bed map for analysis of the density and distribution of the grey whale food source on a temporal and spatial scale.

As the mysid swarms are often found close to the seabed, in 10+ metres of water with poor visibility, visual validation that the target being insonified is actually a mysid swarm is not possible

from the surface vessel surveys. Instead validation presently relies on net drops and diver surveys in the coarsely approximate area.

The modular hardware and software design of *SeaBiscuit* allows straightforward integration of other instruments such as these 110/220kHz echosounders. Surveys can then be performed from the midwater, with a corresponding increase in detail and manoeuvrability within the complex kelp bed environment, independent of any constraints of the surface vessel. The attitude and position of the vehicle is continually recorded allowing the mysid data to be registered on a 3D world coordinate system map with the kelp bed map. On-the-fly target validation of mysid swarms using realtime video feedback is also possible.

Promising initial results using the 260kHz Delta T multibeam sonar currently fitted to *SeaBiscuit* for mysid detection have been demonstrated in the 2012 field trials. Using the same multibeam sonar simultaneously for kelp mapping, mysid mapping and to aid navigation minimises the overall cost, but also automatically co-registers all maps.

Figure 8.2 below shows an example sonar scan using the Delta T multibeam sonar mounted on a keel pod on the surface support vessel as an initial demonstration of mysid detection at 260kHz. Although full 3D water column data was gathered, for simplicity here the results are presented as an echosounder plot using the central beams. Water depth is on the vertical axis, time is on the horizontal axis and the backscatter intensity is represented using the pixel intensity as shown. The surface vessel was instrumented using the navigation sensors and algorithms from *SeaBiscuit* for positioning in 3D. The visual display of backscatter intensity is shown with a mysid swarm highlighted above the seabed. The strong continuous red line of high intensity is the seabed, the largely white area above is the midwater. The position of the surface vessel was recorded with a synchronised timestamp to allow the swarm density to be mapped, and estimates of the biomass / biovolume to be generated.

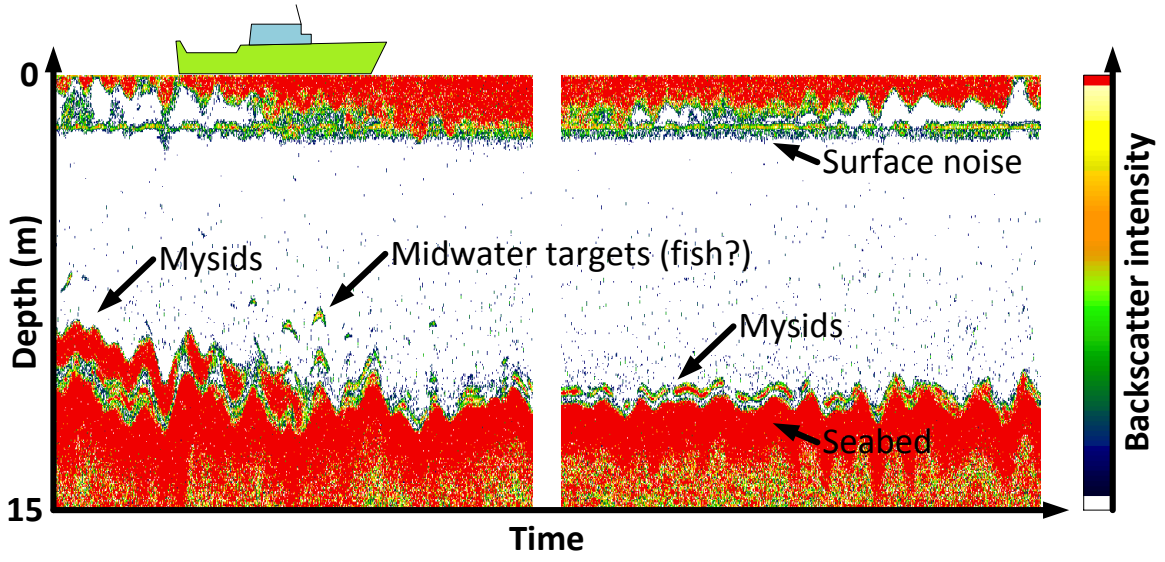

Figure 8.2 - Mysid swarms, detected with the Delta T sonar in an area free from kelp, are highlighted on the two scans adjacent to the seabed. These were gathered with the Delta T sonar keel-mounted on the surface vessel facing downwards, with attitude and position registered using the navigation sensors from *SeaBiscuit*. The central beams of the multibeam return were used to form the echosounder plot as shown. The backscatter intensity scale is shown, with the display gain increased for printing.

Similar results are proposed with *SeaBiscuit* and mysid specific survey data has been gathered in several of the kelp beds surveyed in 2012. Using the iROV trades reduced survey coverage for a greatly increased small scale manoeuvrability and also allowed target corroboration using video. Using the onboard cameras fitted to *SeaBiscuit*, any potential echosounder return could be quickly verified by the operator visually to ensure the correct target classification. Realtime autonomous extraction of mysid density from video footage is still in development. Figure 8.3 shows a set of example images during a mysid sampling dive, and Figure 8.4 shows a series of images detailing the mysid swarms.

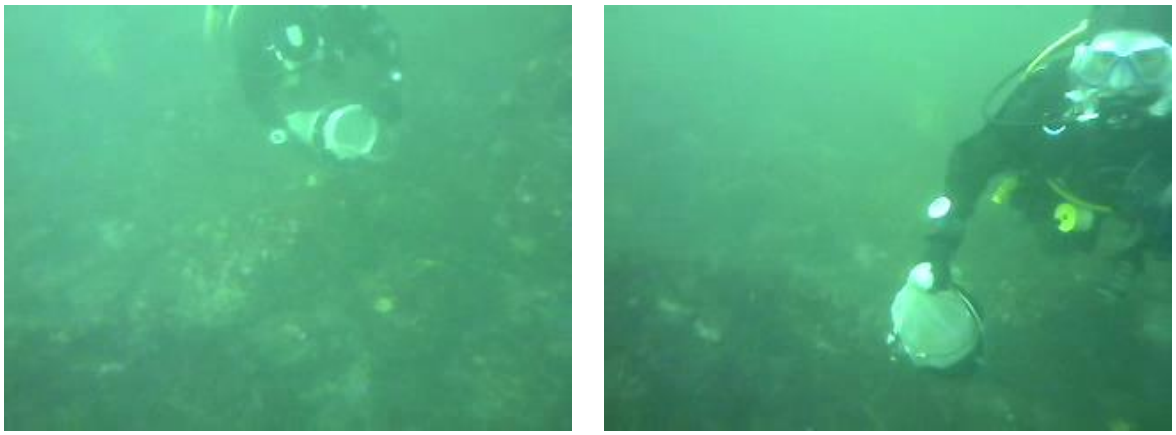

Figure 8.3 - Two sample images captured using *SeaBiscuit* showing the mysid sampling process using a net. By co-registering video and sonar data in both time and space, with a continual log of position as the mysid sampling is carried out, the density and distribution of mysids from the sample area can be mapped.

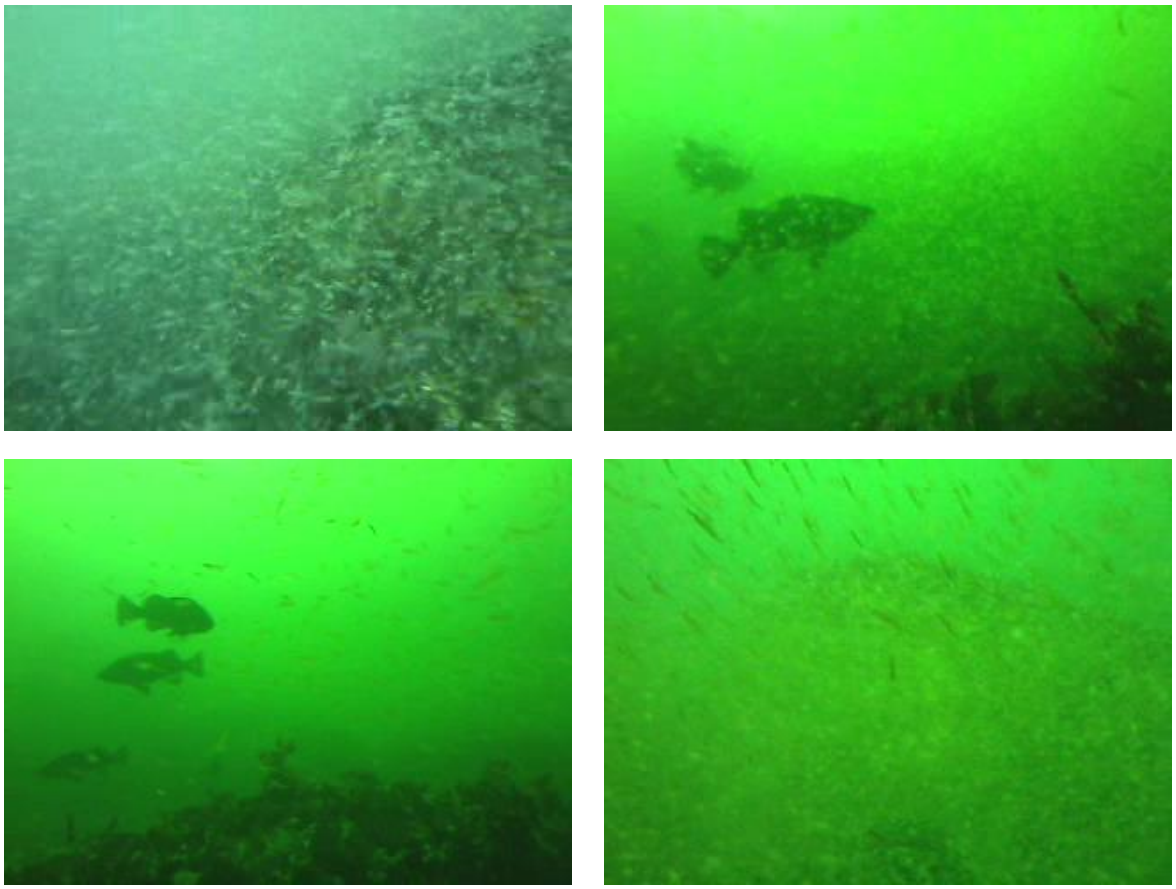

Figure 8.4 - Four sample images captured using *SeaBiscuit* showing the density and distribution of mysids extending a few metres above the seafloor in regions of kelp and rocky pinnacles. The swarm boundary can be delineated by video and the pressure sensor, and the extent mapped in a similar manner to kelp stipes using visual and acoustic techniques.

Dissemination

SAUC-E Journal Papers:

B. Sykes, D.I. Hall, K.M. Collins, B.J. Williamson, G. Brindlinger, K. Hogg, P.R. Riggs, W.M. Megill. (2007) *Hawthorne – The Second BURST AUV.* DSTL Student Autonomous Underwater Challenge – Europe 2007 Journal Paper.

K.M. Collins, H.J. Brassington, M.T. Ferris, P. Glockner, J. Middleton, B.J. Williamson, J. Yao, S.C. Dolan, W.M. Megill. (2008) *Hawthorne 2.0.* DSTL Student Autonomous Underwater Challenge – Europe 2008 Journal Paper & Associated Presentation.

B.J. Williamson, S.J. Bailey, K. Collins, R. Ladd, T. Ruckser, A. Webster, S.C. Dolan, W.M. Megill. (2009) *SeaBiscuit – The 2009 University of Bath AUV.* DSTL Student Autonomous Underwater Challenge – Europe 2009 Journal Paper & Associated Presentation.

Publications:

B.J. Williamson, W.M. Megill, M.J. Balchin. (2012) *Towards mapping Nereocystis luetkeana kelp beds: using the holonomic iROV SeaBiscuit and sonar fusion.* A conference presentation and full technical proceedings paper for the July 2012 Institute of Acoustics European Conference on Underwater Acoustics, Edinburgh, UK.

B.J. Williamson, W.M. Megill, M.J. Balchin. (2013) *From a Racehorse to a Ploughshare: Adapting the University of Bath AUV for Field Research.* Draft paper currently being prepared for submission to the Journal of Field Robotics, Wiley Blackwell, presenting the development of the iROV *SeaBiscuit*, its complementary sensor suite and holonomic propulsion scan technique and successful sea trials for nearshore habitat mapping.

Field Season Reports:

W.M. Megill (2008) *Whales of British Columbia - 2008 field report.* Prepared for Earthwatch Institute, Maynard, MA.

W.M. Megill, R.E. Burnham, L.L. Stelle, D.A. Duffus (2009) *Whales of British Columbia - 2009 field report.* Prepared for Earthwatch Institute, Maynard, MA.

W.M. Megill, R.E. Burnham, J.L. Wladichuk, B.J. Williamson, L.L. Stelle, D.A. Duffus (2010) *Whales of British Columbia - 2010 field report.* Prepared for Earthwatch Institute, Maynard, MA.

W.M. Megill WM, K.D. Bachen, R.E. Burnham, T.G. Lawson, J.L. Wladichuk, B.J. Williamson (2010) *Surveys for grey whales, Eschrichtius robustus, near Cape Caution, BC, Summer 2010.* Report prepared for National Marine Fisheries Service, Seattle, WA.

Selected Presentations:

W.M. Megill, K.M. Collins, P. Glockner, S. Graf, J.L. Maud, B.J. Williamson, J.L. Wladichuk (2008) *Mapping the nearshore, underwater environment.* A poster presentation at the Sensors and Sensing Poster Exhibition organised by the EPSRC 'Bridging the Gaps' Initiative, University of Bath, UK.

B.J. Williamson (2009) *A holonomic propulsion and guidance system for a miniature Autonomous Underwater Vehicle.* A presentation to the Department of Electronic and Electrical Engineering, University of Bath, UK.

B.J. Williamson, S.J. Bailey, T. Ruckser, A. Webster, W.M. Megill, M.J. Balchin, S.C. Dolan (2009) *SeaBiscuit – The 2009 University of Bath Autonomous Underwater Vehicle.* A presentation to the Bath Artificial Intelligence group, Department of Computer Science, University of Bath, UK.

Related Publications:

B.J. Williamson, M.A. Redfern, R.K. Aggarwal, J. Allinson, C. Harris, R. Hotchkiss (2011) *Project Edison: SmartDC.* A conference presentation and full technical proceedings paper presented at the December 2011 IEEE PES Innovative Smart Grid Technologies Europe 2011 Conference, Manchester, UK.

> This paper developed many of the techniques for efficient computing, DC power management, instrumentation and distribution to a much larger scale to consider local DC Networks.

B.J. Williamson, P.S. Blondel (2012) *Multibeam imaging of the environment around marine renewable energy devices.* A conference presentation and full technical proceedings paper for the July 2012 Institute of Acoustics European Conference on Underwater Acoustics, Edinburgh, UK.

> This paper developed the multibeam imaging, instrumentation and long-duration high-efficiency remote sensing techniques for a moored installation, together with techniques for ping synchronisation of the Delta T multibeam sonar with other acoustic devices.

References

1. Wladichuk, J.L., *Investigation of ambient noise in the underwater coastal environment and its potential for use as a navigational aid by grey whales, Eschrichtius robustus, foraging in British Columbia, Canada*, in *Department of Mechanical Engineering*. 2010, University of Bath: Bath.
2. Feyrer, L.J., *The foraging ecology of gray whales in Clayoquot Sound: interactions between predator and prey across a continuum of scales*, in *Department of Geography*. 2010, University of Victoria: Victoria.
3. Maud, J., *The distribution and abundance of mysid shrimp as the primary prey of the grey whale (Eschrichtius robustus) at Cape Caution, British Columbia*, in *School of Ocean Sciences*. 2008, University of Bangor: Bangor.
4. Deysher, L.E., *Evaluation of remote sensing techniques for monitoring giant kelp populations.* Hydrobiologia, 1993. **260-261**(1): p. 307-312.
5. Stekoll, M.S., L.E. Deysher, and M. Hess, *A remote sensing approach to estimating harvestable kelp biomass*, in *Eighteenth International Seaweed Symposium*, R. Anderson, et al., Editors. 2007, Springer Netherlands. p. 97-108.
6. Fyfe, J.E. and S.A. Israel. *A window on an underwater habitat: quantifying differences in giant kelp beds using colour aerial photographs and image processing software*. 1996.
7. Kruss, A., P. Blondel, and J. Tegowski, *Mapping macrophytes and habitats: single-beam and multibeam imaging in the Arctic*, in *Underwater Acoustic Measurements: Technologies and Results* 2011: Kos, Greece.
8. Zabloudil, K., J. Reitzel, S. Schroeter, J. Dixon, T. Dean, and T. Norall. *Sonar mapping of giant kelp density and distribution*. 1991: ASCE.
9. Nelson, T.A., S.N. Gillanders, J. Harper, and M. Morris, *Nearshore Aquatic Habitat Monitoring: A Seabed Imaging and Mapping Approach.* Journal of Coastal Research, 2011: p. 348-355.
10. Kvitek, R.G. and J. Weiner. *Research vessel works in uncharted waters*. 2012 [cited 2012 28/01/2012]; The use of a surface vessel with air-propeller propulsion to map kelp beds.]. Available from: http://news.csumb.edu/news/2011/sep/23/research-vessel-works-uncharted-waters.
11. Jones, M.E., L. Miller, D.L. Woodruff, and D.W. Ewert. *Mapping of Submerged Aquatic Vegetation Using Autonomous Underwater Vehicles in Nearshore Regions*. in *OCEANS 2007*. 2007.
12. Denuelle, A. and M. Dunbabin. *Kelp Detection in Highly Dynamic Environments Using Texture Recognition*. in *Australasian Conference on Robotics and Automation*. 2010. Brisbane, Australia.
13. Barrett, N., J. Seiler, T. Anderson, S. Williams, S. Nichol, and S.N. Hill. *Autonomous Underwater Vehicle (AUV) for mapping marine biodiversity in coastal and shelf waters: Implications for marine management*. in *OCEANS 2010 IEEE - Sydney*. 2010.
14. Pacunski, R.E., W.A. Palsson, H.G. Greene, and D. Gunderson, *Conducting visual surveys with a small ROV in shallow water.* Marine habitat mapping technology for Alaska. Alaska Sea Grant College Program, University of Alaska Fairbanks, 2008.
15. Loebis, D., R. Sutton, and J. Chudley, *Review of multisensor data fusion techniques and their application to autonomous underwater vehicle navigation.* Proceedings of IMarEST - Part A - Journal of Marine Engineering and Technology, 2002. **2002**(1): p. 3-14.
16. Ribas, D., P. Ridao, J.D. Tardos, and J. Neira, *Underwater SLAM in man-made structured environments.* Journal of Field Robotics, 2008. **25**(11-12): p. 898-921.
17. Williams, S.B., P. Newman, J. Rosenblatt, G. Dissanayake, and H. Durrant-Whyte, *Autonomous underwater navigation and control.* Robotica, 2001. **19**(5): p. 481-496.
18. Thurman, E., J. Riordan, and D. Toal, *Multi-Sonar Integration and the Advent of Senor Intelligence*. 2009, I-Tech Education and Publishing, Vienna, Austria. p. 151-164.
19. Elwany, M.H.S., W.C. O'Reilly, R.T. Guza, and R.E. Flick, *Effects of Southern California kelp beds on waves.* Journal of waterway, port, coastal and ocean engineering, 1995. **121**(2): p. 143-150.
20. Saade, E.J. *Seafloor Habitat Mapping Nearshore San Diego County*. in *California and the World Ocean '02: Revisiting and Revising California's Ocean Agenda*. 2002. Santa Barbara, California, USA: American Society of Civil Engineers.
21. Meinecke, G., V. Ratmeyer, and J. Renken. *HYBRID-ROV - Development of a new underwater vehicle for high-risk areas*. in *OCEANS 2011*. 2011.
22. Bowen, A., M. Jakuba, D. Yoerger, C. German, J.C. Kinsey, L.L. Whitcomb, and L. Mayer. *Lightly tethered unmanned underwater vehicle for under-ice exploration*. in *Aerospace Conference, 2012 IEEE*. 2012.
23. Zanoli, S.M. and G. Conte, *Remotely operated vehicle depth control.* Control Engineering Practice, 2003. **11**(4): p. 453-459.
24. Toal, D., E. Omerdic, and G. Dooly. *Precision navigation sensors facilitate full auto pilot control of Smart ROV for ocean energy applications*. in *Sensors, 2011 IEEE*. 2011.
25. Christ, R.D. and R.L. Wernli, *The ROV manual: a user guide to observation-class remotely operated vehicles*. 2007: Elsevier.
26. Fletcher, B., C. Young, J. Buescher, L.L. Whitcomb, A. Bowen, R. McCabe, and D.R. Yoerger. *Proof of concept demonstration of the Hybrid Remotely Operated Vehicle (HROV) light fiber tether system*. in *OCEANS 2008*. 2008.
27. Toal, D., J. Riordan, E. Thurman, and H. Ahmad, *Novel Multi-Sonar Controller and Other Advanced Features Developed and Tested on Latis, a Smart, Remotely Operated Vehicle.* Proceedings of the Institution of Mechanical Engineers, Part M: Journal of Engineering for the Maritime Environment, 2010. **224**(4): p. 309-325.

28. Johnston, J. *The AUV Charybdis*. 2005 [cited 2012 09/10/2012]; Available from: http://www.duke.edu/web/robotics/html/auv.htm.
29. Stone, W., B. Hogan, C. Flesher, S. Gulati, K. Richmond, A. Murarka, G. Kuhlman, M. Sridharan, V. Siegel, R.M. Price, P.T. Doran, and J. Priscu, *Design and Deployment of a Four-Degrees-of-Freedom Hovering Autonomous Underwater Vehicle for sub-Ice Exploration and Mapping.* Proceedings of the Institution of Mechanical Engineers, Part M: Journal of Engineering for the Maritime Environment, 2010. **224**(4): p. 341-361.
30. Dunbabin, M., J. Roerts, K. Usher, G. Winstanley, P. Corke, and Ieee, *A hybrid AUV design for shallow water reef navigation*, in *2005 IEEE International Conference on Robotics and Automation*. 2005, Ieee: New York. p. 2105-2110.
31. Schwing, F., M. O'Farrell, J. Steger, and K. Baltz, *Coastal upwelling indices, west coast of North America 1946–1995.* NOAA Technical Memorandum NMFS-SWFSC, 1996. **231**: p. 207.
32. Varela, M., M.T. Álvarez-Ossorio, A. Bode, R. Prego, P. Bernárdez, and C. Garcia-Soto, *The effects of a winter upwelling on biogeochemical and planktonic components in an area close to the Galician Upwelling Core: The Sound of Corcubión (NW Spain).* Journal of Sea Research, 2010. **64**(3): p. 260-272.
33. Steneck, R.S., M.H. Graham, B.J. Bourque, D. Corbett, J.M. Erlandson, J.A. Estes, and M.J. Tegner, *Kelp forest ecosystems: biodiversity, stability, resilience and future.* Environmental Conservation, 2002. **29**(4): p. 436-459.
34. Mann, K.H., *Seaweeds: their productivity and strategy for growth.* Science, 1973. **182**: p. 975-981.
35. Gunderson, D.R., A.M. Parma, R. Hilborn, J.M. Cope, D.L. Fluharty, M.L. Miller, R.D. Vetter, S.S. Heppell, and H.G. Greene, *The Challenge of Managing Nearshore Rocky Reef Resources.* Fisheries, 2008. **33**(4): p. 172-179.
36. Raffaelli, D.G. and S.J. Hawkins, *Intertidal ecology*. 1999: Kluwer Academic Pub.
37. Schoch, G.C., *The Spatial Distribution of Bull Kelp (Nereocystis leutkeana) in the Kachemak Bay Research Reserve.* Kachemak Bay Research Reserve, Alaska Department of Fish and Game, Homer, AK, 2001.
38. Rigg, G.B. and L.A. Swain, *Pressure-Composition Relationships of the Gas in the Marine Brown Alga, Nereocystis luetkeana.* Plant Physiology, 1941. **16**(2): p. 361.
39. Langdon, S.C., *Carbon Monoxide, Occurrence Free In Kelp (Nereocystis luetkeana).* Journal of the American Chemical Society, 1917. **39**(1): p. 149-156.
40. Stelle, L.L., *Behavioral ecology of summer resident gray whales (Eschrichtius robustus) feeding on mysids in British Columbia, Canada*. 2001, University of California, Los Angeles
41. Wladichuk, J.L., W.M. Megill, and P. Blondel, *Passive acoustic localization techniques of Eastern Pacific grey whales.* Journal of the Acoustical Society of America, 2008. **123**(5): p. 3207.
42. Dayton, P.K., *Ecology of Kelp Communities.* Annual Review of Ecology and Systematics, 1985. **16**: p. 215-245.
43. Lorentsen, S.-H., K. Sjøtun, and D. Grémillet, *Multi-trophic consequences of kelp harvest.* Biological Conservation, 2010. **143**(9): p. 2054-2062.
44. Jensen, J., J. Estes, and L. Tinney, *Remote sensing techniques for kelp surveys.* Photogrammetric Engineering and Remote Sensing, 1980. **46**(6): p. 743-755.
45. Seymour, R., M. Tegner, P. Dayton, and P. Parnell, *Storm wave induced mortality of giant kelp, Macrocystis pyrifera, in southern California.* Estuarine, Coastal and Shelf Science, 1989. **28**(3): p. 277-292.
46. Lurton, X., *An introduction to underwater acoustics: principles and applications*. 2002: Springer-Praxis.
47. Noel, C., C. Viala, M. Coquet, B. Zerr, and T. Perrot, *Acoustic data fusion devoted to underwater vegetation mapping.* Journal of the Acoustical Society of America, 2008. **123**(5): p. 3951.
48. Hass, H. and I. Bartsch, *Acoustic kelp bed mapping in shallow rocky coasts - case study Helgoland.* Observing the Coastal Sea - an Atlas of Advanced Monitoring Techniques. LOICS Reports & Studies, 2008. **33**: p. 50-53.
49. Platt, T., C. Fuentes-Yaco, and K.T. Frank, *Marine ecology: Spring algal bloom and larval fish survival.* Nature, 2003. **423**(6938): p. 398-399.
50. Smayda, T.J., *Ecological features of harmful algal blooms in coastal upwelling ecosystems.* South African Journal of Marine Science, 2000. **22**(1): p. 219-253.
51. Rebikoff, D. and F. Lauderdale. *30 Years of ROV Development*. in *ROV'83: remotely operated vehicles:" A technology whose time has come"*. 1983.
52. Metzler Sr, A. and G. Shaefer, *XN-3-- the U. S. Navy's first ROV.* INTERVENTION/ROV'92: A Decade Of Achievement, 1992, 1992: p. 93-101.
53. McFarlane, J.R. *ROVs and AUVs: tools for exploring, exploiting and defending the ocean frontier*. in *Underwater Technology, 2000. UT 00. Proceedings of the 2000 International Symposium on*. 2000.
54. McFarlane, J.R. *Tethered and untethered vehicles: The future is in the past*. in *OCEANS 2008*. 2008.
55. Roberts, G.N. and R. Sutton, *Advances in unmanned marine vehicles*. IEE Control Engineering Series. Vol. 69. 2006: IET.
56. Wernli, R.L. *AUV commercialization-who's leading the pack?* in *OCEANS 2000 MTS/IEEE Conference and Exhibition*. 2000.
57. Wernli, R.L. *AUVs-a technology whose time has come*. in *Underwater Technology, 2002. Proceedings of the 2002 International Symposium on*. 2002.
58. Blidberg, R., *The Development of Autonomous Underwater Vehicles (AUVs); A Brief Summary*. 2001, Autonomous Undersea Systems Institute. p. 12.
59. Brooks, R., *A robust layered control system for a mobile robot.* Robotics and Automation, IEEE Journal of, 1986. **2**(1): p. 14-23.
60. International Organization for Standardization (ISO), *International vocabulary of basic and general terms in metrology (VIM)*. 2004.
61. Karleskint, G., R. Turner, and J. Small, *Introduction to marine biology*. 2009: Brooks/Cole Pub Co.
62. Sabol, B.M., R.E. Melton, Jr., R. Chamberlain, P. Doering, and K. Haunert, *Evaluation of a Digital Echo Sounder System for Detection of Submersed Aquatic Vegetation.* Estuaries, 2002. **25**(1): p. 133-141.

63. Lykens, T., T. Sisk, and C. Tomichek. *Acoustic Doppler Current Profiler Technology*. 2005 [cited 2012 22/01/2012]; Available from: www.saludahydrorelicense.com/documents/ADCP_presentation.ppt.
64. Utter, B. and M. Denny, *Wave-induced forces on the giant kelp Macrocystis pyrifera (Agardh): field test of a computational model.* Journal of Experimental Biology, 1996. **199**(12): p. 2645-54.
65. Erdey-Heydorn, M.D., *An ArcGIS Seabed Characterization Toolbox Developed for Investigating Benthic Habitats.* Marine Geodesy, 2008. **31**(4): p. 318-358.
66. Bickers, A.N., *Cost effective marine habitat mapping from small vessels using GIS, sidescan sonar and video.* Coastal GIS, 2003.
67. Tan, H.-P., R. Diamant, W.K.G. Seah, and M. Waldmeyer, *A survey of techniques and challenges in underwater localization.* Ocean Engineering, 2011. **38**(14–15): p. 1663-1676.
68. Pan-Mook, L., J. Bong-Huan, K. Kihun, L. Jihong, T. Aoki, and T. Hyakudome, *Simulation of an Inertial Acoustic Navigation System With Range Aiding for an Autonomous Underwater Vehicle.* Oceanic Engineering, IEEE Journal of, 2007. **32**(2): p. 327-345.
69. McLeod, D. and J. Jacobson. *Autonomous UUV inspection - Revolutionizing undersea inspection*. in *OCEANS 2011*. 2011.
70. Newman, P. and H. Durrant-Whyte. *Using sonar in terrain-aided underwater navigation*. 2002: IEEE.
71. Leonard, J., A. Bennett, C. Smith, and H. Feder. *Autonomous underwater vehicle navigation*. 1998: Citeseer.
72. Filliat, D. and J.-A. Meyer, *Map-based navigation in mobile robots: I. A review of localization strategies.* Cognitive Systems Research, 2003. **4**(4): p. 243-282.
73. Meyer, J.-A. and D. Filliat, *Map-based navigation in mobile robots: II. A review of map-learning and path-planning strategies.* Cognitive Systems Research, 2003. **4**(4): p. 283-317.
74. Crook, P. and G. Hayes, *Learning in a state of confusion: Perceptual aliasing in grid world navigation.* Towards Intelligent Mobile Robots, 2003. **4**.
75. Kuipers, B. and P. Beeson. *Bootstrap learning for place recognition*. 2002: Menlo Park, CA; Cambridge, MA; London; AAAI Press; MIT Press; 1999.
76. Titterton, D. and J. Weston, *Strapdown inertial navigation technology*. 2004: Peter Peregrinus Ltd.
77. Gebre-Egziabher, D., R.C. Hayward, and J.D. Powell. *A low-cost GPS/inertial attitude heading reference system (AHRS) for general aviation applications*. in *Position Location and Navigation Symposium, IEEE 1998*. 1998.
78. Panish, R. and M. Taylor. *Achieving high navigation accuracy using inertial navigation systems in autonomous underwater vehicles*. in *OCEANS, 2011 IEEE - Spain*. 2011.
79. IXSEA, *PHINS Inertial Navigation System Datasheet*. 2011.
80. Kearfott, *T-24 Inertial Navigation System Datasheet*. 2011.
81. Brokloff, N.A. *Matrix algorithm for Doppler sonar navigation*. in *OCEANS '94. 'Oceans Engineering for Today's Technology and Tomorrow's Preservation.' Proceedings*. 1994.
82. Teledyne RS Instruments, *Phased Array Explorer Doppler Velocity Log Datasheet*. 2010.
83. Snyder, J. *Doppler Velocity Log (DVL) navigation for observation-class ROVs*. in *OCEANS 2010*. 2010: IEEE.
84. Abbott, E. and D. Powell, *Land-vehicle navigation using GPS.* Proceedings of the IEEE, 1999. **87**(1): p. 145-162.
85. Shallberg, K. and S. Fang. *WAAS measurement processing; current design and potential improvements*. in *Position, Location and Navigation Symposium, 2008 IEEE/ION*. 2008.
86. Enge, P., T. Walter, S. Pullen, K. Changdon, C. Yi-Chung, and T. Yeou-Jyh, *Wide area augmentation of the Global Positioning System.* Proceedings of the IEEE, 1996. **84**(8): p. 1063-1088.
87. Lehtinen, M., A. Happonen, and J. Ikonen. *Accuracy and time to first fix using consumer-grade GPS receivers*. in *Software, Telecommunications and Computer Networks, 2008. SoftCOM 2008. 16th International Conference on*. 2008.
88. Bennamoun, M., B. Boashash, F. Faruqi, and M. Dunbar. *The development of an integrated GPS/INS/sonar navigation system for autonomous underwater vehicle navigation*. in *Autonomous Underwater Vehicle Technology, 1996. AUV '96., Proceedings of the 1996 Symposium on*. 1996.
89. Honghui, Q. and J.B. Moore, *Direct Kalman filtering approach for GPS/INS integration.* Aerospace and Electronic Systems, IEEE Transactions on, 2002. **38**(2): p. 687-693.
90. Yun, X., E.R. Bachmann, R.B. McGhee, R.H. Whalen, R.L. Roberts, R.G. Knapp, A.J. Healey, and M.J. Zyda, *Testing and evaluation of an integrated GPS/INS system for small AUV navigation.* Oceanic Engineering, IEEE Journal of, 1999. **24**(3): p. 396-404.
91. Kwak, S.H., J.B. McKeon, J.R. Clynch, and R.B. McGhee. *Incorporation of global positioning system into autonomous underwater vehicle navigation*. in *Autonomous Underwater Vehicle Technology, 1992. AUV '92., Proceedings of the 1992 Symposium on*. 1992.
92. Crowell, J. *Small AUV for Hydrographic Applications*. in *OCEANS 2006*. 2006.
93. Norton, N.A., *Evaluation of Hardware and Software for a Small Autonomous Underwater Vehicle Navigation System (SANS)*. 1994, Naval Postgraduate School, Monterey, California: Monterey, California.
94. Frank, J.E., R. Geiger, D.R. Kraige, and A. Murali, *Smart Tether System For Underwater Navigation And Cable Shape Measurement*. 2008, US Patent App. 20,080/300,821.
95. *Smart Tether Navigation and Positioning Systems for ROVs and Divers*. 2011 [cited 2011 30/05/2011]; Available from: http://www.smarttether.com/.
96. White, C., D. Hiranandani, C.S. Olstad, K. Buhagiar, T. Gambin, and C.M. Clark, *The Malta cistern mapping project: Underwater robot mapping and localization within ancient tunnel systems.* Journal of Field Robotics, 2010. **27**(4): p. 399.
97. *Smart Tether - Frequently Asked Questions*. 2011 [cited 2011 30/05/2011]; Available from: http://www.kcftech.com/products/tether-positioning-system-faq.shtml.

98. Hagen, O.K., K.B. Anonsen, and M. Mandt. *The HUGIN real-time terrain navigation system*. in *OCEANS 2010*. 2010.
99. Li, Y., P. Chen, and Z. Dong, *Sensor Simulation of Underwater Terrain Matching Based on Sea Chart. Advances in Computer Science, Environment, Ecoinformatics, and Education*, S. Lin and X. Huang, Editors. 2011, Springer Berlin Heidelberg. p. 89-94.
100. Zhang, T. and J.-x. Gao. *Multi-sensor data fusion approach for terrain match navigation of autonomous underwater vehicles*. in *Industrial Mechatronics and Automation (ICIMA), 2010 2nd International Conference on*. 2010.
101. Fong, D.A. and N.L. Jones, *Evaluation of AUV-based ADCP measurements.* Limnology and Oceanography: Methods, 2006. **4**: p. 58-67.
102. Kukulya, A., A. Plueddemann, T. Austin, R. Stokey, M. Purcell, B. Allen, R. Littlefield, L. Freitag, P. Koski, and E. Gallimore, *Under-ice Operations with a REMUS-100 AUV in the Arctic.*
103. Purcell, M., C. von Alt, B. Allen, T. Austin, N. Forrester, R. Goldsborough, and R. Stokey. *New capabilities of the REMUS autonomous underwater vehicle*. in *OCEANS 2000 MTS/IEEE Conference and Exhibition*. 2000.
104. Whitcomb, L., D. Yoerger, H. Singh, and D. Mindell. *Towards precision robotic maneuvering, survey, and manipulation in unstructured undersea environments*. 1998: Citeseer.
105. Youngberg, J.W., *Method for extending GPS to underwater applications*. 1992.
106. Hubert, T., *Method and device for the monitoring and remote control of unmanned, mobile underwater vehicles*. 1996.
107. Thomas, H.G. *GIB buoys: an interface between space and depths of the oceans*. in *Autonomous Underwater Vehicles, 1998. AUV'98. Proceedings Of The 1998 Workshop on*. 1998.
108. Heckman, D. and R. Abbott. *An acoustic navigation technique*. in *Engineering in the Ocean Environment, Ocean 73 - IEEE International Conference on*. 1973.
109. Hunt, M.M., W.M. Marquet, D.A. Moller, K.R. Peal, W.K. Smith, and R.C. Spindel, *An acoustic navigation system*. 1974, Woods Hole Oceanographic Institution.
110. Vickery, K. *Acoustic positioning systems. A practical overview of current systems*. in *Autonomous Underwater Vehicles, 1998. AUV'98. Proceedings Of The 1998 Workshop on*. 1998.
111. Vickery, K. *Acoustic positioning systems. New concepts-the future*. in *Autonomous Underwater Vehicles, 1998. AUV'98. Proceedings Of The 1998 Workshop on*. 1998.
112. Bellingham, J.G., T.R. Consi, U. Tedrow, and D. Di Massa. *Hyperbolic acoustic navigation for underwater vehicles: implementation and demonstration*. 1992.
113. Gagan, *Submarine Image*. 2009.
114. Geyer, E., P. Creamer, J. D'Appolito, and R. Rains. *Characteristics and capabilities of navigation systems for unmanned untethered submersibles*. in *Unmanned Untethered Submersible Technology, Proceedings of the 1987 5th International Symposium on*. 1987.
115. Balloch, R., *Baseline*, Sonardyne, Editor. 2007, Sonardyne.
116. *UM-8025-02 System Manual for Fusion USBL Navigation System*. 2005, Sonardyne.
117. Willemenot, E., P.Y. Morvan, H. Pelletier, and A. Hoof. *Subsea positioning by merging inertial and acoustic technologies*. in *OCEANS 2009 - EUROPE*. 2009.
118. Johannsson, H., M. Kaess, B. Englot, F. Hover, and J. Leonard. *Imaging sonar-aided navigation for autonomous underwater harbor surveillance*. 2010: IEEE.
119. Maurelli, F., Y. Petillot, A. Mallios, P. Ridao, and S. Krupinski. *Sonar-based AUV localization using an improved particle filter approach*. in *OCEANS 2009 - EUROPE*. 2009.
120. Aulinas, J., X. Llado, J. Salvi, and Y.R. Petillot. *Feature based slam using side-scan salient objects*. in *OCEANS 2010*. 2010.
121. Mahon, I. and S. Williams. *SLAM using natural features in an underwater environment*. 2004. Kunming, China: Institute of Electrical and Electronics Engineers Inc.
122. Woock, P. and C. Frey. *Deep-sea AUV navigation using side-scan sonar images and SLAM*. in *OCEANS 2010 IEEE - Sydney*. 2010.
123. Smith, C.M., *Integrating mapping and navigation*. 1998, Massachusetts Institute of Technology.
124. Hernandez, E., P. Ridao, D. Ribas, and A. Mallios. *Probabilistic sonar scan matching for an AUV*. in *Intelligent Robots and Systems, 2009. IROS 2009. IEEE/RSJ International Conference on*. 2009.
125. Mallios, A., P. Ridao, D. Ribas, F. Maurelli, and Y. Petillot. *EKF-SLAM for AUV navigation under probabilistic sonar scan-matching*. in *Intelligent Robots and Systems (IROS), 2010 IEEE/RSJ International Conference on*. 2010.
126. Barkby, S., S. Williams, O. Pizarro, and M. Jakuba. *An efficient approach to bathymetric SLAM*. in *Intelligent Robots and Systems, 2009. IROS 2009. IEEE/RSJ International Conference on*. 2009.
127. Petillot, Y., I. Ruiz, and D. Lane, *Underwater vehicle obstacle avoidance and path planning using a multi-beam forward looking sonar.* IEEE Journal of Oceanic Engineering, 2001. **26**(2): p. 240-251.
128. Quidu, I., L. Jaulin, A. Bertholom, and Y. Dupas, *Robust Multitarget Tracking in Forward-Looking Sonar Image Sequences Using Navigational Data.* Oceanic Engineering, IEEE Journal of, 2012. **37**(3): p. 417-430.
129. *EchoScope Real-time 3D Sonar*. 2011 [cited 2011 18/01/2011]; Available from: http://www.codaoctopus.com/3d_ac_im/index.asp.
130. *First Four Echoscope 3D Real-Time Underwater Imaging Sonars are Delivered*. 2005 October 25, 2005 [cited 2011 18/01/2011]; Available from: http://www.rovworld.com/article703.html.
131. Lurton, X. and J.C. Le Gac, *The CALIMERO project: scientific objectives and first at-sea results.* Proc. SeaTechWeek, Brest, 2004.

132. Williamson, B.J. and P. Blondel. *Multibeam imaging of the environment around marine renewable energy devices*. in *11th European Conference on Underwater Acoustics*. 2012. Edinburgh, UK: Institute of Acoustics.
133. Horgan, J., F. Flannery, and D. Toal. *Towards real time vision based UUV navigation using GPU technology*. in *OCEANS 2009 - EUROPE*. 2009.
134. Dalgleish, F., S. Tetlow, and R. Allwood. *Vision-based navigation of unmanned underwater vehicles: a survey. Part I: Vision Based Cable-, Pipeline-and Fish Tracking*. 2004: Institute of Marine Engineering, Science and Technology.
135. Negre, A., C. Pradalier, and M. Dunbabin, *Robust vision-based underwater homing using self-similar landmarks.* Journal of Field Robotics, 2008. **25**(6-7): p. 360-377.
136. Perrier, M., *The visual servoing system "CYCLOPE" designed for dynamic stabilisation of AUV and ROV.* Oceans 2005 - Europe, Vols 1 and 2, 2005: p. 334-338.
137. Negahdaripour, S., X. Xu, and L. Jin, *Direct estimation of motion from sea floor images for automatic station-keeping of submersible platforms.* IEEE Journal of Oceanic Engineering, 1999. **24**(3): p. 370-382.
138. Xu, X. and S. Negahdaripour, *Automatic optical station keeping and navigation of an ROV; sea trial experiments.* Oceans Conference Record (IEEE), 1999. **1**: p. 71-76.
139. Wirth, S., A. Ortiz, D. Paulus, and G. Oliver. *Using particle filters for autonomous underwater cable tracking*. in *2nd IFAC Workshop Navigation, Guidance and Control of Underwater Vehicles*. 2008. Ireland: The International Federation of Automatic Control.
140. Negahdaripour, S., X. Xu, A. Khamene, and Z. Awan. *3-D motion and depth estimation from sea-floor images for mosaic-based station-keeping and navigation of ROVs/AUVs and high-resolution sea-floor mapping*. 1998. Piscataway, NJ, USA: IEEE.
141. Marks, R.L., S.M. Rock, and M.J. Lee. *Real-time video mosaicking of the ocean floor*. in *Autonomous Underwater Vehicle Technology, 1994. AUV '94., Proceedings of the 1994 Symposium on*. 1994.
142. Wallis, C.L., *An Investigation into Computer Vision Techniques for Underwater Object Recognition*, in *Department of Mechanical Engineering*. 2006, University of Bath: Bath.
143. Yao, J., *Investigation into underwater object recognition and tracking for the SAUC-E competition*, in *Department of Computer Science*. 2008, University of Bath: Bath.
144. Ruckser, T., *Vision System for Student Autonomous Underwater Mini-Submarine*, in *Department of Electronic and Electrical Engineering*. 2009, University of Bath: Bath.
145. Baruwa, L., *Advanced Computer Vision System for Autonomous Underwater Vehicle*, in *Department of Electronic and Electrical Engineering*. 2010, University of Bath: Bath.
146. Dunbabin, M., P. Corke, and G. Buskey. *Low-cost vision-based AUV guidance system for reef navigation*. in *Robotics and Automation, 2004. Proceedings. ICRA '04. 2004 IEEE International Conference on*. 2004.
147. Eustice, R.M., O. Pizarro, and H. Singh, *Visually augmented navigation for autonomous underwater vehicles.* IEEE Journal of Oceanic Engineering, 2008. **33**(2): p. 103-122.
148. Huster, A., S.D. Fleischer, and S.M. Rock. *Demonstration of a vision-based dead-reckoning system for navigation of an underwater vehicle*. 1998. Piscataway, NJ, USA: IEEE.
149. Shkurti, F., I. Rekleitis, and G. Dudek. *Feature Tracking Evaluation for Pose Estimation in Underwater Environments*. in *Computer and Robot Vision (CRV), 2011 Canadian Conference on*. 2011.
150. Thrun, S., W. Burgard, and D. Fox, *Probabilistic Robotics*. 2005, Cambridge, Mass.: MIT.
151. Caccia, M., *Low-cost high-precision motion control for ROVs*, in *Advances in unmanned marine vehicles*, G.N. Roberts and R. Sutton, Editors. 2006, IET.
152. Caccia, M., *Handling uncertainty in underwater robotics: the example of ROV bottom following*, in *Mobile Robots: New Research*, J.X. Liu, Editor. 2005, Nova Publishers. p. 143-175.
153. Luo, R.C. and M.G. Kay. *A tutorial on multisensor integration and fusion*. in *Industrial Electronics Society, 1990. IECON '90., 16th Annual Conference of IEEE*. 1990.
154. Luo, R.C., Y. Chih-Chen, and S. Kuo Lan, *Multisensor fusion and integration: approaches, applications, and future research directions.* Sensors Journal, IEEE, 2002. **2**(2): p. 107-119.
155. McKee, G.T., *What can be fused?* NATO ASI Series F Computer and Systems Sciences, 1993. **99**: p. 71-71.
156. Majumder, S., S. Scheding, and H.F. Durrant-Whyte, *Multisensor data fusion for underwater navigation.* Robotics and Autonomous Systems, 2001. **35**(2): p. 97-108.
157. Cox, I.J., *Blanche-an experiment in guidance and navigation of an autonomous robot vehicle.* Robotics and Automation, IEEE Transactions on, 1991. **7**(2): p. 193-204.
158. Bachmann, E.R., R.B. McGhee, R.H. Whalen, R. Steven, R.G. Walker, J.R. Clynch, A.J. Healey, and X.P. Yun. *Evaluation of an integrated GPS/INS system for shallow-water AUV navigation (SANS)*. in *Autonomous Underwater Vehicle Technology, 1996. AUV '96., Proceedings of the 1996 Symposium on*. 1996.
159. Olfati-Saber, R. and J.S. Shamma. *Consensus Filters for Sensor Networks and Distributed Sensor Fusion*. in *Decision and Control, 2005 and 2005 European Control Conference. CDC-ECC '05. 44th IEEE Conference on*. 2005.
160. Hackett, J.K. and M. Shah. *Multi-sensor fusion: a perspective*. in *Robotics and Automation, 1990. Proceedings., 1990 IEEE International Conference on*. 1990.
161. Von Neumann, J., *Probabilistic logics and the synthesis of reliable organisms from unreliable components.* Automata studies, 1956. **34**: p. 43-98.
162. Kopetz, H., H. Kantz, G. Grunsteidl, P. Puschner, and J. Reisinger. *Tolerating transient faults in MARS*. in *Fault-Tolerant Computing, 1990. FTCS-20. Digest of Papers., 20th International Symposium*. 1990.
163. Bosse, E., J. Roy, and D. Grenier. *Data fusion concepts applied to a suite of dissimilar sensors*. in *Electrical and Computer Engineering, 1996. Canadian Conference on*. 1996.

164. Magee, M.J., B.A. Boyter, C.-H. Chien, and J.K. Aggarwal, *Experiments in Intensity Guided Range Sensing Recognition of Three-Dimensional Objects.* Pattern Analysis and Machine Intelligence, IEEE Transactions on, 1985. **PAMI-7**(6): p. 629-637.
165. Rao, N.S.V. *A fusion method that performs better than best sensor*. in *Conference on Multisource-Multisensor Data Fusion*. 1998.
166. Rao, N.S.V., *On fusers that perform better than best sensor.* Pattern Analysis and Machine Intelligence, IEEE Transactions on, 2001. **23**(8): p. 904-909.
167. Elmenreich, W., *Sensor fusion in time-triggered systems*. 2002, Technische Universität Wien.
168. Elfes, A., *Using occupancy grids for mobile robot perception and navigation.* Computer, 1989. **22**(6): p. 46-57.
169. Smith, R.C. and P. Cheeseman, *On the Representation and Estimation of Spatial Uncertainty.* The International Journal of Robotics Research, 1986. **5**(4): p. 56-68.
170. Kalman, R.E., *A new approach to linear filtering and prediction problems.* Transactions of the ASME--Journal of Basic Engineering, 1960. **82**(Series D): p. 35-45.
171. Durrant-Whyte, H. and T. Bailey, *Simultaneous localization and mapping: Part I.* IEEE Robotics and Automation Magazine, 2006. **13**(2): p. 99-108.
172. Durrant-Whyte, H. *Consistent integration and propagation of disparate sensor observations*. in *Robotics and Automation. Proceedings. 1986 IEEE International Conference on*. 1986.
173. Mahalanobis, P.C. *On the generalized distance in statistics*. in *Proceedings of the National Institute of Sciences of India*. 1936: New Delhi.
174. Crowley, J.L. and Y. Demazeau, *Principles and techniques for sensor data fusion.* Signal Processing, 1993. **32**(1–2): p. 5-27.
175. Rendas, M.J. and I.M.G. Lourtie. *Hybrid navigation system for long range operation*. in *Autonomous Underwater Vehicle Technology, 1994. AUV '94., Proceedings of the 1994 Symposium on*. 1994.
176. Balasuriya, A. and T. Ura. *Multi-sensor fusion for autonomous underwater cable tracking*. in *OCEANS '99 MTS/IEEE. Riding the Crest into the 21st Century*. 1999.
177. Durrant-Whyte, H., *Multi sensor data fusion*. Springer Handbook of Robotics. 2008. 585-610.
178. Lu, Z.Y., Z.C. Hu, and K. Uchimura, *SLAM Estimation in Dynamic Outdoor Environments: A Review.* Intelligent Robotics and Applications, Proceedings, 2009. **5928**: p. 255-267.
179. Duda, R.O., P.E. Hart, and N.J. Nilsson, *Subjective Bayesian methods for rule-based inference systems*, in *Proceedings of the June 7-10, 1976, national computer conference and exposition*. 1976, ACM: New York, New York. p. 1075-1082.
180. Shafer, G., *A mathematical theory of evidence*. Vol. 1. 1976: Princeton University Press, Princeton.
181. Zou, Y., K. Ho Yeong, S. Chua Chin, and W. Zhou Xiao. *Multi-ultrasonic sensor fusion for mobile robots*. in *Intelligent Vehicles Symposium, 2000. IV 2000. Proceedings of the IEEE*. 2000.
182. Challa, S. and D. Koks, *Bayesian and Dempster-Shafer fusion.* Sadhana, 2004. **29**(2): p. 145-174.
183. Cremer, F., E. Den Breejen, and K. Schutte. *Sensor data fusion for anti-personnel land-mine detection*. 1998: Citeseer.
184. Braun, J.J. *Dempster-Shafer theory and Bayesian reasoning in multisensor data fusion*. 2000.
185. Duckett, T. and A. Saffiotti. *Building globally consistent gridmaps from topologies*. 2000.
186. Koks, D. and S. Challa, *An introduction to Bayesian and Dempster-Shafer data fusion.* 2003.
187. Zadeh, L.A., *A Theory of Approximate Reasoning (AR)*. 1977: Electronics Research Laboratory, College of Engineering, University of California.
188. Ribo, M. and A. Pinz, *A comparison of three uncertainty calculi for building sonar-based occupancy grids.* Robotics and Autonomous Systems, 2001. **35**(3–4): p. 201-209.
189. Oriolo, G., G. Ulivi, and M. Vendittelli, *Real-time map building and navigation for autonomous robots in unknown environments.* Systems, Man, and Cybernetics, Part B: Cybernetics, IEEE Transactions on, 1998. **28**(3): p. 316-333.
190. Kobayashi, K., K.C. Cheok, K. Watanabe, and F. Munekata, *Accurate differential global positioning system via fuzzy logic Kalman filter sensor fusion technique.* Industrial Electronics, IEEE Transactions on, 1998. **45**(3): p. 510-518.
191. Pham, D. and D. Karaboga, *Optimum design of fuzzy logic controllers using genetic algorithms.* Journal of Systems Engineering, 1991. **1**(2): p. 114-118.
192. Sutton, R. and G.D. Marsden, *A Fuzzy Autopilot Optimized Using a Genetic Algorithm.* The Journal of Navigation, 1997. **50**(01): p. 120-131.
193. Sutton, R., S.D.H. Taylor, and G.N. Roberts, *Neuro-Fuzzy Techniques Applied to a Ship Autopilot Design.* The Journal of Navigation, 1996. **49**(03): p. 410-430.
194. Sutton, R., G.N. Roberts, and S.D.H. Taylor, *Tuning fuzzy ship autopilots using artificial neural networks.* Transactions of the Institute of Measurement and Control, 1997. **19**(2): p. 94-106.
195. Sistiaga, M., J. Opderbecke, M. Aldon, and V. Rigaud. *Map based underwater navigation using a multibeam echosounder*. 2002: IEEE.
196. Karlsson, R. and F. Gustafsson, *Bayesian surface and underwater navigation.* Signal Processing, IEEE Transactions on, 2006. **54**(11): p. 4204-4213.
197. Di Massa, D.E., *Terrain-relative navigation for autonomous underwater vehicles*. 1997.
198. Fowler, C.A., *Comments on the Cost and Performance of Military Systems.* Aerospace and Electronic Systems, IEEE Transactions on, 1979. **AES-15**(1): p. 2-10.
199. Theil, A., L.J.H.M. Kester, and E. Bosse. *On measures of performance to assess sensor fusion effectiveness*. in *Information Fusion, 2000. FUSION 2000. Proceedings of the Third International Conference on*. 2000.

200. Dasarathy, B.V. *More the merrier...or is it? Sensor suite augmentation benefits assessment*. in *Information Fusion, 2000. FUSION 2000. Proceedings of the Third International Conference on*. 2000.
201. Levitt, T.S. and D.T. Lawton, *Qualitative navigation for mobile robots.* Artificial intelligence, 1990. **44**(3): p. 305-360.
202. Balakrishnan, K., O. Bousquet, and V. Honavar, *Spatial Learning and Localization in Rodents: A Computational Model of the Hippocampus and its Implications for Mobile Robots.* Adaptive Behavior, 1999. **7**(2): p. 173-216.
203. Choset, H.M., K.M. Lynch, S. Hutchinson, G. Kantor, W. Burgard, L.E. Kavraki, and S. Thrun, *Principles of robot motion: theory, algorithms, and implementation*. 2005: The MIT Press.
204. Leonard, J.J. and H.F. Durrant-Whyte. *Simultaneous map building and localization for an autonomous mobile robot*. in *Intelligent Robots and Systems '91. 'Intelligence for Mechanical Systems, Proceedings IROS '91. IEEE/RSJ International Workshop on*. 1991.
205. Bailey, T. and H. Durrant-Whyte, *Simultaneous localization and mapping (SLAM): Part II.* IEEE Robotics and Automation Magazine, 2006. **13**(3): p. 108-117.
206. Thrun, S., *Simultaneous localization and mapping.* Robotics and Cognitive Approaches to Spatial Mapping, 2008. **38**: p. 13-41.
207. Yi, C. and B.-U. Choi, *Detection and Recovery for Kidnapped-Robot Problem Using Measurement Entropy*, in *Grid and Distributed Computing*, T.-h. Kim, et al., Editors. 2011, Springer Berlin Heidelberg. p. 293-299.
208. Shuai, G., M. Shugen, L. Bin, S. Rongchuan, and W. Yuechao. *VorSLAM: A new solution to simultaneous localization and mapping*. in *Information and Automation (ICIA), 2010 IEEE International Conference on*. 2010.
209. Cheeseman, R.S.M.S.P., R. Smith, and M. Self. *A stochastic map for uncertain spatial relationships*. 1987.
210. Folkesson, J. and J. Leonard, *Autonomy through SLAM for an Underwater Robot - Robotics Research*, C. Pradalier, R. Siegwart, and G. Hirzinger, Editors. 2011, Springer Berlin / Heidelberg. p. 55-70.
211. Folkesson, J., J. Leonard, J. Leederkerken, and R. Williams. *Feature tracking for underwater navigation using sonar*. in *Intelligent Robots and Systems, 2007. IROS 2007. IEEE/RSJ International Conference on*. 2007.
212. Matsebe, O., S. Holtzhausen, C. Kumile, and N. Tlale. *Modeling the kinematics of an autonomous underwater vehicle for range-bearing Simultaneous Localization and Mapping*. 2009: IEEE.
213. Sipser, M., *Introduction to the Theory of Computation*. 2006: Thomson Course Technology Boston, MA.
214. Guivant, J.E. and E.M. Nebot, *Optimization of the simultaneous localization and map-building algorithm for real-time implementation.* Robotics and Automation, IEEE Transactions on, 2001. **17**(3): p. 242-257.
215. Thrun, S., Y. Liu, D. Koller, A.Y. Ng, Z. Ghahramani, and H. Durrant-Whyte, *Simultaneous Localization and Mapping with Sparse Extended Information Filters.* The International Journal of Robotics Research, 2004. **23**(7-8): p. 693-716.
216. Shoudong, H., W. Zhan, and G. Dissanayake, *Sparse Local Submap Joining Filter for Building Large-Scale Maps.* Robotics, IEEE Transactions on, 2008. **24**(5): p. 1121-1130.
217. Nieto, J., T. Bailey, and E. Nebot, *Recursive scan-matching SLAM.* Robotics and Autonomous Systems, 2007. **55**(1): p. 39-49.
218. Aurenhammer, F., *Voronoi diagrams—a survey of a fundamental geometric data structure.* ACM Computing Surveys (CSUR), 1991. **23**(3): p. 345-405.
219. Reid, D., *An algorithm for tracking multiple targets.* Automatic Control, IEEE Transactions on, 1979. **24**(6): p. 843-854.
220. Leonard, J.J., B.A. Moran, I.J. Cox, and M.L. Miller. *Underwater sonar data fusion using an efficient multiple hypothesis algorithm*. in *Robotics and Automation, 1995. Proceedings., 1995 IEEE International Conference on*. 1995.
221. Pace, D.W., M. Mallick, and W. Eldredge. *Spectral feature-aided multi-target multi-sensor passive sonar tracking*. in *OCEANS 2003. Proceedings*. 2003.
222. Blanco, J.L., J.A. Fernandez-Madrigal, and J. Gonzalez, *Toward a Unified Bayesian Approach to Hybrid Metric--Topological SLAM.* Robotics, IEEE Transactions on, 2008. **24**(2): p. 259-270.
223. Tully, S., G. Kantor, and H. Choset, *A unified Bayesian framework for global localization and SLAM in hybrid metric/topological maps.* The International Journal of Robotics Research, 2012.
224. Chen, L. and H. Hu, *Towards Localization and Mapping of Autonomous Underwater Vehicles: A Survey*. 2011, University of Essex.
225. Frese, U., *Interview: Is SLAM Solved?* KI - Künstliche Intelligenz, 2010. **24**(3): p. 255-257.
226. Dissanayake, M.W.M.G., P. Newman, S. Clark, H.F. Durrant-Whyte, and M. Csorba, *A solution to the simultaneous localization and map building (SLAM) problem.* Robotics and Automation, IEEE Transactions on, 2001. **17**(3): p. 229-241.
227. Dissanayake, M., P. Newman, H. Durrant-Whyte, S. Clark, and M. Csorba, *An experimental and theoretical investigation into simultaneous localisation and map building*, in *Experimental Robotics VI*. 2000, Springer Berlin / Heidelberg. p. 265-274.
228. Dissanayake, G., H. Durrant-Whyte, and T. Bailey. *A computationally efficient solution to the simultaneous localisation and map building (SLAM) problem*. in *Robotics and Automation, 2000. Proceedings. ICRA '00. IEEE International Conference on*. 2000.
229. Dissanayake, G., S.B. Williams, H. Durrant-Whyte, and T. Bailey, *Map Management for Efficient Simultaneous Localization and Mapping (SLAM).* Autonomous Robots, 2002. **12**(3): p. 267-286.
230. Thrun, S., *Robotic mapping: A survey.* Exploring artificial intelligence in the new millennium, 2002: p. 1–35.
231. Jiang, Y., G.R. Liu, S.H. Luo, and L. Zhou, *A Review on Localization and Mapping Algorithm Based on Extended Kalman Filtering.* 2009 International Forum on Information Technology and Applications, Vol 2, Proceedings, 2009: p. 435-440.

232. Bonin-Font, F., A. Ortiz, and G. Oliver, *Visual Navigation for Mobile Robots: A Survey.* Journal of Intelligent & Robotic Systems, 2008. **53**(3): p. 263-296.
233. Tolman, E.C., *Cognitive maps in rats and men.* Psychological review, 1948. **55**(4): p. 189-208.
234. Endo, Y. and R.C. Arkin. *Anticipatory robot navigation by simultaneously localizing and building a cognitive map*. in *Intelligent Robots and Systems, 2003. (IROS 2003). Proceedings. 2003 IEEE/RSJ International Conference on*. 2003.
235. Trullier, O., S.I. Wiener, A. Berthoz, and J.-A. Meyer, *Biologically Based Artificial Navigation Systems: Review and Prospects.* Progress in Neurobiology, 1997. **51**(5): p. 483-544.
236. Chitre, M., S. Shahabudeen, L. Freitag, and M. Stojanovic. *Recent advances in underwater acoustic communications networking*. in *OCEANS 2008*. 2008.
237. Jun, L., T. Yardibi, S. Xiang, H. Hao, and L. Jian. *Enhanced Channel Estimation and Symbol Detection for High Speed MIMO Underwater Acoustic Communications*. in *Digital Signal Processing Workshop and 5th IEEE Signal Processing Education Workshop, 2009. DSP/SPE 2009. IEEE 13th*. 2009.
238. McDowell, P., J. Chen, and B. Bourgeois. *UUV teams, control from a biological perspective*. in *OCEANS '02 MTS/IEEE*. 2002.
239. Wilson, M., *Deep sea habitat mapping using a remotely operated vehicle: Mapping and modeling seabed terrain and benthic habitat at multiple scales in the Porcupine Seabight, SW Ireland*. 2006, PhD Thesis, National University of Ireland, Galway.
240. Toal, D. *Challenges of ROV System Integration for Deep Water Habitat Mapping: Mapping cold water corals at 800 - 1,200 m on the margins of the continental shelf off west coast Ireland*. [cited 2012 26/01/2012]; Available from: http://www.searchmesh.net/pdf/SWToal.pdf.
241. Parry, D.M., M.A. Kendall, D.A. Pilgrim, and M.B. Jones, *Identification of patch structure within marine benthic landscapes using a remotely operated vehicle.* Journal of experimental marine biology and ecology, 2003. **285–286**: p. 497-511.
242. Smith, S.E. and D.H. Shull, *Survey of Whatcom County, Washington Nearshore Rockfish by Remotely Operated Vehicle and Implications for Marine Protected Areas.* Report prepared by Huxley College of the Environment, Western Washington University, Bellingham, Washington, 2009.
243. Harrold, C., K. Light, and S. Lisin, *Organic Enrichment of Submarine-Canyon and Continental-Shelf Benthic Communities by Macroalgal Drift Imported from Nearshore Kelp Forests.* Limnology and Oceanography, 1998. **43**(4): p. 669-678.
244. Reynolds, J.R., R.C. Highsmith, B. Konar, C.G. Wheat, and D. Doudna. *Fisheries and fisheries habitat investigations using undersea technology*. in *OCEANS, 2001. MTS/IEEE Conference and Exhibition*. 2001.
245. Blidberg, D., S. Mupparapu, S. Chappell, R. Komerska, J.C. Jalbert, and R. Nitzelm. *The SAUV II (solar powered AUV) test results 2004*. in *Oceans 2005 - Europe*. 2005.
246. Crimmins, D.M., C.T. Patty, M.A. Beliard, J. Baker, J.C. Jalbert, R.J. Komerska, S.G. Chappell, and D.R. Blidberg. *Long-Endurance Test Results of the Solar-Powered AUV System*. in *OCEANS 2006*. 2006.
247. Kvitek, R.G., P.J. Iampietro, E. Sandoval, C.K. Bretz, A. Derose, and D. Ventresca, *Transducers, cables and kelp: acoustic mapping of shallow water rockfish habitat in California kelp forests.* Environmental Geosciences, 1999. **6**(3): p. 147-147.
248. Johansson, B., Siesjo, x, J., and M. Furuholmen. *Seaeye Sabertooth A Hybrid AUV/ROV offshore system*. in *OCEANS 2010*. 2010.
249. Reed, S., J. Wood, and C. Haworth. *The detection and disposal of IED devices within harbor regions using AUVs, smart ROVs and data processing/fusion technology*. in *Waterside Security Conference (WSS), 2010 International*. 2010.
250. Young, C., B. Fletcher, J. Buescher, L.L. Whitcomb, D. Yoerger, A. Bowen, R. McCabe, M. Heintz, R. Fuhrmann, C. Taylor, and R. Elder. *Field Tests of the Hybrid Remotely Operated Vehicle (HROV) Light Fiber Optic Tether*. in *OCEANS 2006*. 2006.
251. Murashima, T., T. Aoki, S. Tsukioka, T. Hyakudome, H. Yoshida, H. Nakajoh, S. Ishibashi, and R. Sasamoto. *Thin cable system for ROV and AUV in JAMSTEC*. in *OCEANS 2003. Proceedings*. 2003.
252. Murashima, T., H. Nakajoh, H. Yoshida, J.N. Yamauchi, and H. Sezoko. *7000 m class ROV KAIKO7000*. in *OCEANS '04. MTTS/IEEE TECHNO-OCEAN '04*. 2004.
253. Bowen, A.D., D.R. Yoerger, C. Taylor, R. McCabe, J. Howland, D. Gomez-Ibanez, J.C. Kinsey, M. Heintz, G. McDonald, D.B. Peters, J. Bailey, E. Bors, T. Shank, L.L. Whitcomb, S.C. Martin, S.E. Webster, M.V. Jakuba, B. Fletcher, C. Young, J. Buescher, P. Fryer, and S. Hulme. *Field trials of the Nereus hybrid underwater robotic vehicle in the challenger deep of the Mariana Trench*. in *OCEANS 2009, MTS/IEEE Biloxi - Marine Technology for Our Future: Global and Local Challenges*. 2009.
254. Whitcomb, L.L., M.V. Jakuba, J.C. Kinsey, S.C. Martin, S.E. Webster, J.C. Howland, C.L. Taylor, D. Gomez-Ibanez, and D.R. Yoerger. *Navigation and control of the Nereus hybrid underwater vehicle for global ocean science to 10,903 m depth: Preliminary results*. in *Robotics and Automation (ICRA), 2010 IEEE International Conference on*. 2010.
255. Conte, G. and G. Orlando. *A variable structure control of a remotely operated vehicle*. in *OCEANS '94. 'Oceans Engineering for Today's Technology and Tomorrow's Preservation.' Proceedings*. 1994.
256. Bong-Hwan, J., L. Pan-Mook, L. Ji-Hong, H. Seok-Won, K. Yeon-Gyu, and L. Jihong. *Multivariable optimal control of an autonomous underwater vehicle for steering and diving control in variable speed*. in *OCEANS 2003. Proceedings*. 2003.
257. Yuh, J., *Learning control for underwater robotic vehicles.* Control Systems Magazine, IEEE, 1994. **14**(2): p. 39-46.

258. Riedel, J.S. and A.J. Healey. *Shallow water station keeping of AUVs using multi-sensor fusion for wave disturbance prediction and compensation*. 1998. Piscataway, NJ, USA: IEEE.
259. Yoerger, D. and J. Slotine, *Robust trajectory control of underwater vehicles.* Oceanic Engineering, IEEE Journal of, 1985. **10**(4): p. 462-470.
260. Harsamizadeh Tehrani, N., M. Heidari, Y. Zakeri, and J. Ghaisari. *Development, depth control and stability analysis of an underwater Remotely Operated Vehicle (ROV)*. in *Control and Automation (ICCA), 2010 8th IEEE International Conference on*. 2010.
261. Heping, L., G. Zhenbang, and L. Min. *The Anti-wave control of small open-frame underwater robot*. in *Intelligent System and Knowledge Engineering, 2008. ISKE 2008. 3rd International Conference on*. 2008.
262. Silvestre, C., A. Pascoal, and A. Healey. *AUV control under wave disturbances*. in *10th International Symposium on Unmanned Untethered Submersible Technology*. 1997: University of New Hampshire - Marine Systems.
263. De Souza, E.C. and N. Maruyama, *Intelligent UUVs: Some issues on ROV dynamic positioning.* Aerospace and Electronic Systems, IEEE Transactions on, 2007. **43**(1): p. 214-226.
264. Fraga, S.L., J.B. Sousa, A. Girard, and A. Martins. *An automated maneuver control framework for a remotely operated vehicle*. in *OCEANS, 2001. MTS/IEEE Conference and Exhibition*. 2001.
265. Martin, S.C., L.L. Whitcomb, D. Yoerger, and H. Singh. *A Mission Controller for High Level Control of Autonomous and Semi-Autonomous Underwater Vehicles*. in *OCEANS 2006*. 2006.
266. Veruggio, G. and F. Grassia. *ROMEO: a versatile unmanned underwater vehicle for marine research*. in *OCEANS '95. MTS/IEEE. Challenges of Our Changing Global Environment. Conference Proceedings.* 1995.
267. Tsukioka, S., T. Aoki, Y. Kasutani, K. Ryouke, and T. Nakae. *The navigation system for an expendable fiber cable ROV "UROV"*. in *OCEANS '95. MTS/IEEE. Challenges of Our Changing Global Environment. Conference Proceedings.* 1995.
268. Webster, S.E. and A.D. Bowen. *Feasibility analysis of an 11,000 m vehicle with a fiber optic microcable link to the surface*. in *OCEANS 2003. Proceedings*. 2003.
269. Toumelin, N. and J. Lemaire. *New capabilities of the REDERMOR unmanned underwater vehicle*. in *OCEANS, 2001. MTS/IEEE Conference and Exhibition*. 2001.
270. Forrester, N.C. *Power Transformer Design For Tethered Underwater Vehicles*. in *OCEANS '92. 'Mastering the Oceans Through Technology'. Proceedings.* 1992.
271. Silva, J., A. Martins, and F. Pereira. *A reconfigurable mission control system for underwater vehicles*. 2002: IEEE.
272. El Jalaoui, A., D. Andreu, and B. Jouvencel. *A control architecture for contextual tasks management: application to the AUV Taipan*. 2005: IEEE.
273. Palomeras, N., M. Carreras, P. Ridao, and E. Hernandez. *Mission control system for dam inspection with an AUV*. 2007: IEEE.
274. Patron, P., E. Miguelanez, Y.R. Petillot, D.M. Lane, and J. Salvi. *Adaptive mission plan diagnosis and repair for fault recovery in autonomous underwater vehicles*. in *OCEANS 2008*. 2008.
275. Hagen, P. *AUV/UUV mission planning and real time control with the HUGIN operator system*. 2002: IEEE.
276. Pang, S., J. Farrell, R. Arrieta, and W. Li. *AUV reactive planning: deepest point*. 2004: IEEE.
277. Arkin, R.C., *Behavior-based robotics*. 1998: MIT press.
278. Evans, J., P. Patrón, B. Smith, and D. Lane, *Design and evaluation of a reactive and deliberative collision avoidance and escape architecture for autonomous robots.* Autonomous Robots, 2008. **24**(3): p. 247-266.
279. Collins, K., *Autosub under Greenland Ice*, Autosub1_lg.jpg, Editor. 2005, National Oceanography Centre, Southampton.
280. Lea, R.K., R. Allen, and S.L. Merry, *Comparative study of control techniques for an underwater flight vehicle.* International Journal of Systems Science, 1999. **30**(9): p. 947-964.
281. Refsnes, J.E. and A.J. Sorensen. *Design of control system of torpedo shaped ROV with experimental results*. in *OCEANS '04. MTTS/IEEE TECHNO-OCEAN '04*. 2004.
282. Cazenave, F., R. Zook, D. Carroll, M. Flagg, and S. Kim, *The skinny on SCINI: Development of the ROV SCINI and deployment in McMurdo Sound, Antartica.* Journal of Ocean Technology, 2011. **6**(3): p. 39-58.
283. Sanderson, A.C. and R. Blidberg, *Solar-powered Autonomous Underwater Vehicle*, sauv_h.tif, Editor. 2004, National Science Foundation.
284. Webb, D.C., P.J. Simonetti, and C.P. Jones, *SLOCUM: an underwater glider propelled by environmental energy.* Oceanic Engineering, IEEE Journal of, 2001. **26**(4): p. 447-452.
285. Schilling Robotics, *Schilling Robotics UltraHeavy-Duty (UHD) Work-Class ROV System Datasheet*. 2011.
286. Toal, D., E. Omerdic, J. Riordan, and S. Nolan, *Multi-Mode Operations Marine Robotic Vehicle - A Mechatronics Case Study*, in *Mechatronics in Action: Case Studies in Mechatronics - Applications and Education*, D. Bradley and D.W. Russell, Editors. 2010, Springer.
287. HydroVision & Herriot Watt University Ocean Systems Laboratory. *The Offshore Hyball ROV*. 2012 [cited 2012 30/01/2012]; Available from: http://osl.eps.hw.ac.uk/images/uploads/wrex3.jpg.
288. Stone, W. *Design and deployment of a 3D autonomous subterranean submarine exploration vehicle*. in *15th International Symposium on Unmanned Untethered Submersible Technology 2007 (UUST '07)*. 2007. Durham, New Hampshire, USA: Autonomous Undersea Systems Institute (AUSI).
289. Richmond, K., S. Gulati, C. Flesher, B.P. Hogan, and W.C. Stone. *Navigation, control, and recovery of the ENDURANCE under-ice hovering AUV*. in *16th International Symposium on Unmanned Untethered Submersible Technology 2009 (UUST '09)*. 2009. Durham, New Hampshire, USA: Autonomous Undersea Systems Institute (AUSI).

290. Licht, S.C. *Biomimetic Robots for Environmental Monitoring in the Surf Zone and in Very Shallow Water*. in *2010 IEEE/RSJ International Conference on Intelligent Robots and Systems (IROS), Workshop on Robotics for Environmental Monitoring, IROS 2010*. 2010.
291. Vainio, M., P. Appelqvist, and A. Halme, *Mobile robot society for distributed operations in closed aquatic environment.* Robotica, 2000. **18**(3): p. 235-250.
292. Wang, S., J. Ai, W. Dai, and Y. Li, *Robust Model for the Design of Controller in Saucer UAV.* Journal of Software, 2010. **5**(7): p. 753-760.
293. Kumar, R.P., S.S. Babu, Y. Srilekha, C.S. Kumar, A. Sen, and A. Dasgupta, *Test-bed for navigation and control of a thruster based AUV.* Oceans 2006 - Asia Pacific, Vols 1 and 2, 2006: p. 908-911.
294. Palmer, A., G.E. Hearn, and P. Stevenson, *Modelling tunnel thrusters for autonomous underwater vehicles.* 2008.
295. Alvarez, A., A. Caffaz, A. Caiti, G. Casalino, L. Gualdesi, A. Turetta, and R. Viviani, *Fòlaga: A low-cost autonomous underwater vehicle combining glider and AUV capabilities.* Ocean Engineering, 2009. **36**(1): p. 24-38.
296. Damus, R., S. Desset, J. Morash, V. Polidoro, F. Hover, C. Chryssostomidis, J. Vaganay, and S. Willcox, *A new paradigm for ship hull inspection using a holonomic hover-capable AUV.* Informatics in Control, Automation and Robotics I, 2006: p. 195-200.
297. Aguiar, A.P. and A.M. Pascoal. *Dynamic positioning and way-point tracking of underactuated AUVs in the presence of ocean currents*. in *Decision and Control, 2002, Proceedings of the 41st IEEE Conference on*. 2002.
298. Fossen, T.I. and T.A. Johansen. *A Survey of Control Allocation Methods for Ships and Underwater Vehicles*. in *Control and Automation, 2006. MED '06. 14th Mediterranean Conference on*. 2006.
299. Simon, D., V. Rigaud, A. Santos, B. Espiau, and P. Rives, *Sensor-Based Control of Holonomic Autonomous Underwater Vehicles.* 1995.
300. Schill, F.S., *Distributed communication in swarms of autonomous underwater vehicles*. 2007, The Australian National University.
301. Fossen, T.I., *Marine Control Systems: Guidance.* Navigation and Control of Ships, Rigs and Underwater Vehicles, Marine Cybernetics AS, 2002.
302. The ABB Group, *Product Introduction to Compact Azipod*. 2008: Helsinki.
303. Fairfield, N., G. Kantor, D. Jonak, and D. Wettergreen, *DEPTHX autonomy software: design and field results.* Robotics Institute, Carnegie Mellon University, Pittsburgh, PA, Tech. Rep. CMU-RI-TR-08-09, 2008.
304. Conte, G., A.M. Perdon, and S. Zanoli. *A navigation and inspection systems for ROVs*. in *OCEANS '95. MTS/IEEE. Challenges of Our Changing Global Environment. Conference Proceedings.* 1995.
305. Leabourne, K.N., S.M. Rock, S.D. Fleischer, and R. Burton, *Station keeping of an ROV using vision technology.* Oceans '97 Mts/Ieee Conference Proceedings, Vols 1 and 2, 1997: p. 634-640.
306. Kruger, D., R. Stolkin, A. Blum, and J. Briganti. *Optimal AUV path planning for extended missions in complex, fast-flowing estuarine environments*. 2007.
307. Witt, J. and M. Dunbabin. *Go with the flow: Optimal AUV path planning in coastal environments*. 2008.
308. Benjamin, M., J. Curcio, and P. Newman. *Navigation of unmanned marine vehicles in accordance with the rules of the road*. 2006: IEEE.
309. Petres, C., Y. Pailhas, P. Patron, Y. Petillot, J. Evans, and D. Lane, *Path planning for autonomous underwater vehicles.* Robotics, IEEE Transactions on, 2007. **23**(2): p. 331-341.
310. Hamilton, K., D.M. Lane, K.E. Brown, J. Evans, and N.K. Taylor, *An integrated diagnostic architecture for autonomous underwater vehicles.* Journal of Field Robotics, 2007. **24**(6): p. 497-526.
311. Healey, A. *Towards an automatic health monitor for autonomous underwater vehicles using parameter identification*. 2009: IEEE.
312. Changting, S., Z. Rubo, and Y. Ge. *Fault Diagnosis of AUV Based on Bayesian Networks*. in *Computer and Computational Sciences, 2006. IMSCCS '06. First International Multi-Symposiums on*. 2006.
313. Xu, H., Y. Zhang, and X. Feng. *Research on the decentralized supervisory control of autonomous underwater vehicle*. 2004: IEEE.
314. Nana, L., L. Marcé, J. Opderbecke, M. Pettier, and V. Rigaud. *Investigation of safety mechanisms for oceanographic AUV missions programming*. 2005: IEEE.
315. Kanti Podder, T. and N. Sarkar. *Fault tolerant decomposition of thruster forces of an autonomous underwater vehicle*. in *Robotics and Automation, 1999. Proceedings. 1999 IEEE International Conference on*. 1999.
316. Li-ping, Y., Z. Ming-jun, W. Yu-jia, and W. Juan. *Study on simultaneous Fault Tolerant Control of AUV thrusters*. in *Automation and Logistics, 2008. ICAL 2008. IEEE International Conference on*. 2008.
317. Rae, G.J.S. and S.E. Dunn. *On-line damage detection for autonomous underwater vehicles*. in *Autonomous Underwater Vehicle Technology, 1994. AUV '94., Proceedings of the 1994 Symposium on*. 1994.
318. Sykes, B., D.I. Hall, K.M. Collins, B.J. Williamson, G. Brindlinger, K. Hogg, P.R. Riggs, and W.M. Megill, *Hawthorne - The second BURST AUV*. 2007, University of Bath.
319. British Standards, *BS EN 60529:1992 Specification for degrees of protection provided by enclosures (IP code)*. 1992, British Standards Online.
320. *Student Autonomous Underwater Challenge - Europe (SAUC-E)*. 2008 [cited 2010 29/10/2010]; Available from: http://www.dstl.gov.uk/news_events/competitions/sauce/index.php.
321. *SAUC-E 2008 Mission and Rules*. 2008 [cited 2008 28/01/2008]; Available from: http://www.dstl.gov.uk/news_events/competitions/sauce/mission-and-rules.doc.
322. Collins, K.M., H.J. Brassington, M.T. Ferris, P. Glockner, J. Middleton, B.J. Williamson, J. Yao, S.C. Dolan, and W.M. Megill, *Hawthorne 2.0 - Same Boat, New Guts*. 2008, University of Bath.

323. *IFREMER Deep Wave Basin*. 2008 16/01/2008 [cited 2010 06/11/2010]; Available from: http://www.ifremer.fr/metri/pages_metri/infrastructure/brest_basin.htm.
324. Webster, A., *Competition Submersible: AUV Sonar*, in *Department of Mechanical Engineering*. 2009, University of Bath: Bath.
325. *MMA7260Q Datasheet*. 2005, Freescale Semiconductor.
326. *ADXRS300 Datasheet*. 2004, Analog Devices.
327. SparkFun Electronics, *SparkFun Electronics IMU 6 Degrees of Freedom v2 Data Sheet*. 2008.
328. Yeh, K.C. and K.C. Kwan, *A comparison of numerical integrating algorithms by trapezoidal, Lagrange, and spline approximation.* Journal of Pharmacokinetics and Pharmacodynamics, 1978. **6**(1): p. 79-98.
329. Majumder, S., S. Scheding, and H. Durrant-Whyte. *Sensor fusion and map building for underwater navigation*. in *Proc. Australian Conf. on Robotics and Automation*. 2000.
330. Pattinson, C.P., *High Efficiency Propulsion for Autonomous Underwater Vehicles*, in *Department of Mechanical Engineering*. 2006, University of Bath: Bath.
331. IEEE, *IEEE 802.3: ETHERNET*, in *802.3ab 1000BASE-T Gbit/s Ethernet over twisted pair at 1 Gbit/s*. 2008.
332. Bradley, A.M., M.D. Feezor, H. Singh, and F. Yates Sorrell, *Power systems for autonomous underwater vehicles.* Oceanic Engineering, IEEE Journal of, 2001. **26**(4): p. 526-538.
333. Hasvold, Ø., N.J. Størkersen, S. Forseth, and T. Lian, *Power sources for autonomous underwater vehicles.* Journal of Power Sources, 2006. **162**(2): p. 935-942.
334. *NASA NMEA Clipper Marine Compass*. 2011 [cited 2011 12/01/2011]; Available from: http://www.mesltd.co.uk/nasa-clipper-compass-system-p-687.html.
335. *Keller Series 21 R Pressure Sensor Datasheet*. 2011, Keller Druck.
336. Xsens, *MTi and MTx User Manual and Technical Documentation*. 2009.
337. Podder, T.K. and N. Sarkar, *Fault-tolerant control of an autonomous underwater vehicle under thruster redundancy.* Robotics and Autonomous Systems, 2001. **34**(1): p. 39-52.
338. Gebre-Egziabher, D., R.C. Hayward, and J.D. Powell, *Design of multi-sensor attitude determination systems.* Aerospace and Electronic Systems, IEEE Transactions on, 2004. **40**(2): p. 627-649.
339. Thong, Y.K., M.S. Woolfson, J.A. Crowe, B.R. Hayes-Gill, and D.A. Jones, *Numerical double integration of acceleration measurements in noise.* Measurement, 2004. **36**(1): p. 73-92.
340. Birtles, P., *Sonar Mapping*, in *Department of Mechanical Engineering*. 2010, University of Bath: Bath.
341. *2010 SAUC-E Competition Sample Images*. 2010 [cited 2011 23/05/2011]; Available from: http://www.nurc.nato.int/events/sauce10/download.htm.
342. Williamson, B.J., S.J. Bailey, K. Collins, R. Ladd, T. Ruckser, A. Webster, S.C. Dolan, and W.M. Megill, *SeaBiscuit - The 2009 University of Bath AUV. A report to the fourth annual SAUC-E competition hosted by DSTL and the MoD.* 2009, University of Bath: Bath.
343. Hough, P.V.C., *Method and means for recognizing complex patterns*, U.S.P. Office, Editor. 1962: USA.
344. SeaBotix Inc., *SeaBotix BTD150 Thruster Specification*. 2012.
345. Brand, B., K. Brower, J. Langevin, and J. Le, *Autonomous Robotic Submarine*. 2012, Washington State University.
346. Hils, D.D., *Visual languages and computing survey: Data flow visual programming languages*. Journal of Visual Languages & Computing, 1992. **3**(1): p. 69-101.
347. Muecke, K. and B. Powell. *Feasibility of LabVIEW as a scalable robot programming language*. in *Resilient Control Systems (ISRCS), 2011 4th International Symposium on*. 2011.
348. Duke Robotics, *Charybdis AUV Poster*. 2004, Duke University.
349. Stone Aerospace. *Robo-explorer goes deep*. 2010 [cited 2012 27/11/2012]; DepthX Press Kit]. Available from: http://www.stoneaerospace.com/news-/news-press-kit.php.
350. Shatkay, H. and L. Kaelbling. *Heading in the right direction*. 1998: Citeseer.
351. Gumbel, E., J. Greenwood, and D. Durand, *The circular normal distribution: Theory and tables.* Journal of the American Statistical Association, 1953. **48**(261): p. 131-152.
352. Neira, J. and J.D. Tardos, *Data association in stochastic mapping using the joint compatibility test.* Robotics and Automation, IEEE Transactions on, 2001. **17**(6): p. 890-897.
353. Blanco, J.L., J.A. Gonzalez-Jimenez, and J.A. Fernandez-Madrigal, *An Alternative to the Mahalanobis Distance for Determining Optimal Correspondences in Data Association.* Robotics, IEEE Transactions on, 2012. **28**(4): p. 980-986.
354. Cox, I.J. and J.J. Leonard, *Modeling a dynamic environment using a Bayesian multiple hypothesis approach.* Artificial intelligence, 1994. **66**(2): p. 311-344.
355. Thrun, S., *Probabilistic robotics.* Communications of the ACM, 2002. **45**(3): p. 52-57.
356. *SAUC-E 2010 Mission and Rules*. 2010 [cited 2010 29/10/2010]; Available from: http://www.nurc.nato.int/events/sauce10/Mission_Rules_2010_v3.pdf.
357. Heriot-Watt University Ocean Systems Laboratory. *SAUC-E Support Pages - Sample Target Images*. 2009 [cited 2009 01/05/2009]; Available from: http://osl.eps.hw.ac.uk/SAUC-E.php.
358. *SAUC-E 2007 Competition Images*. 2007 [cited 2008 28/01/2008]; Available from: http://www.dstl.gov.uk.
359. *Ocean Basin & Rotating Arm Datasheet*. 2012 05/05/2012]; Qinetiq Haslar, Gosport Ocean Basin Specifications]. Available from: http://www.qinetiq.com/what/capabilities/maritime/Documents/Ocean-Basin-and-Rotating-Arm.pdf.
360. Ribas, D., P. Ridao, and J. Neira, *Underwater SLAM for structured environments using an imaging sonar*. Vol. 65. 2010: Springer Verlag.
361. Carpenter, R.N. *Concurrent mapping and localization with FLS*. in *Autonomous Underwater Vehicles, 1998. AUV'98. Proceedings of the 1998 Workshop on*. 1998.

362. Tena Ruiz, I., Y. Petillot, D.M. Lane, and C. Salson. *Feature extraction and data association for AUV concurrent mapping and localisation*. 2001: IEEE.
363. Fallis, A.L., *Growth of the fronds of Nereocystis luetkeana*. 1915, University of Washington.
364. Stelle, L., W. Megill, and M. Kinzel, *Activity budget and diving behavior of gray whales (Eschrichtius robustus) in feeding grounds off coastal British Columbia.* Marine Mammal Science, 2008. **24**(3): p. 462-478.
365. Malcom, C.D., *The current state and future prospects of whale-watching management, with special emphasis on whale-watching in British Columbia.*, in *Department of Geography*. 2004, University of Victoria.
366. Megill, W.M. *Coastal Ecosystems Research Foundation*. 2008 [cited 2008 05/10/2008]; Available from: http://www.cerf.bc.ca.
367. Duffus, D. *The University of Victoria Whale Research Laboratory*. 2010 [cited 2010 29/10/2010]; Available from: http://www.geog.uvic.ca/whalelab/.
368. Canadian Hydrographic Service, *Tofino Tidal Prediction*. 2010, Fisheries and Oceans Canada.
369. Grove, R.S., K. Zabloudil, T. Norall, and L. Deysher, *Effects of El Niño events on natural kelp beds and artificial reefs in southern California.* ICES Journal of Marine Science: Journal du Conseil, 2002. **59**(suppl): p. S330-S337.
370. SubConn Inc., *SubConn Series of Underwater Connectors*. 2012.
371. Mini-Box.com. *picoUPS-120-ATV Manual*. 2012 [cited 2012 28/08/2012]; Available from: http://resources.mini-box.com/online/PWR-PicoUPS-120-ATV/PWR-PicoUPS-120-ATV-manual.pdf.
372. Batschelet, E., *Circular statistics in biology*. 1981: Academic Press, 111 Fifth Ave., New York, NY 10003.
373. Batschelet, E., *Statistical methods for the analysis of problems in animal orientation and certain biological rhythms*. 1965: American Institute of Biological Sciences.
374. Berens, P., *CircStat: A MATLAB Toolbox for Circular Statistics.* Journal of Statistical Software, 2009. **31**(10): p. 1-21.
375. Von Mises, R., *Über die "Ganzzahligkeit" der Atomgewichte und verwandte Fragen.* Physikal. Z., 1918. **19**: p. 490-500.
376. Fisher, N., *Statistical analysis of circular data*. 1996: Cambridge Univ Press.

Appendix A Standards

One of the design concepts of *SeaBiscuit* was flexibility to adapt between operating modes, environments, applications and to support additional peripherals and sensors. To enable this flexibility, as well as allowing the power, navigation, control and propulsion suite of *SeaBiscuit* to be applied to other vehicles, a series of standards were developed over the course of this research. These standards defined electrical, mechanical, and software protocols and interfaces, adapting recognised best practice to the underwater environment allowing components to be easily interchanged in the field, or redeployed in other applications. For example, the navigation suite of *SeaBiscuit* was regularly used to augment the navigation suite of the research vessel *Stardust*, and there are plans to deploy it to other underwater vehicles developed in the Ocean Technologies Laboratory at the University of Bath.

The three most applicable standards for reuse throughout the vehicle, and beyond to other underwater vehicles and instrumentation are the standards developed for underwater peripheral interfaces, inter-device communications and the tether. These three are detailed in the following sections.

A.1 Peripheral interface

A 4 pin waterproof connector was used as a general peripheral interface providing power to the USB bus and peripherals at 5V DC at up to 6A per root host connector (on the main computer tube). The USB bus allowed devices to be multiplexed using USB hubs, and non-USB peripherals (RS232 and RS485) were easily converted to USB using commercial off the shelf converters. The USB bus provided sufficient bandwidth (480Mb/s) for multiple video streams. The typical power limitation of USB (0.5A) was overcome by replacing the USB controller supplied current with a high-current (6A) 5V line. Peripherals included machine health USB DAQ boards, cameras and RS232 and RS485 sensors & motor controllers via converters. 4 pin waterproof bulkhead connectors used male pins, peripheral cables used sockets as shown in Figure A1 below. Blanking plugs are available for each.

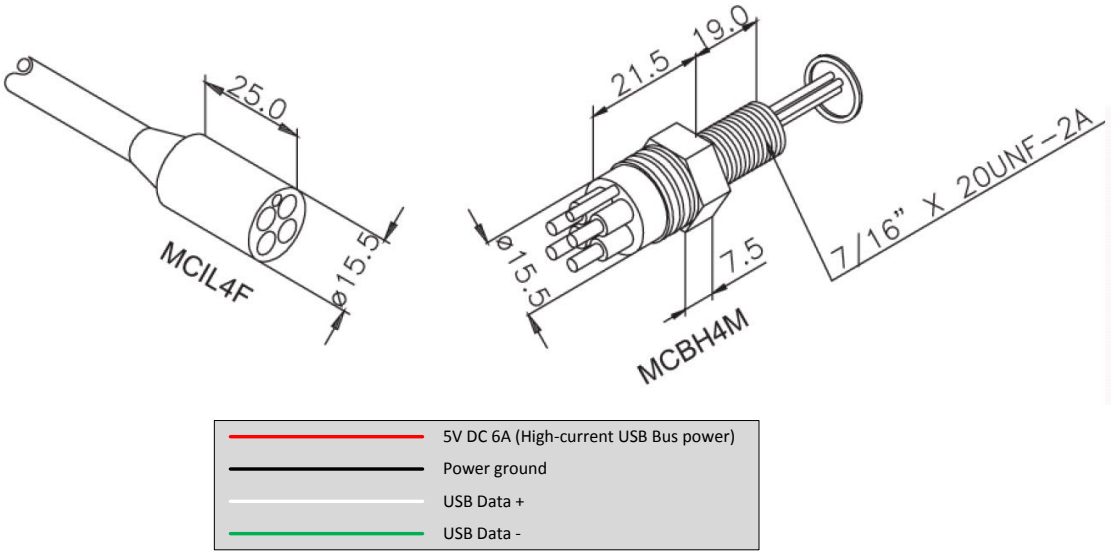

Figure A1 - 4 pin USB peripheral interface (connector images adapted from [370]). Dimensions shown are in mm except the imperial thread.

A 6 pin revision to include 12V at 6A was developed for devices which required higher power than the 5V 6A from the 4 pin standard defined above. This was used for the 12V NMEA peripherals (e.g. compass). The pinout is shown below in Figure A2.

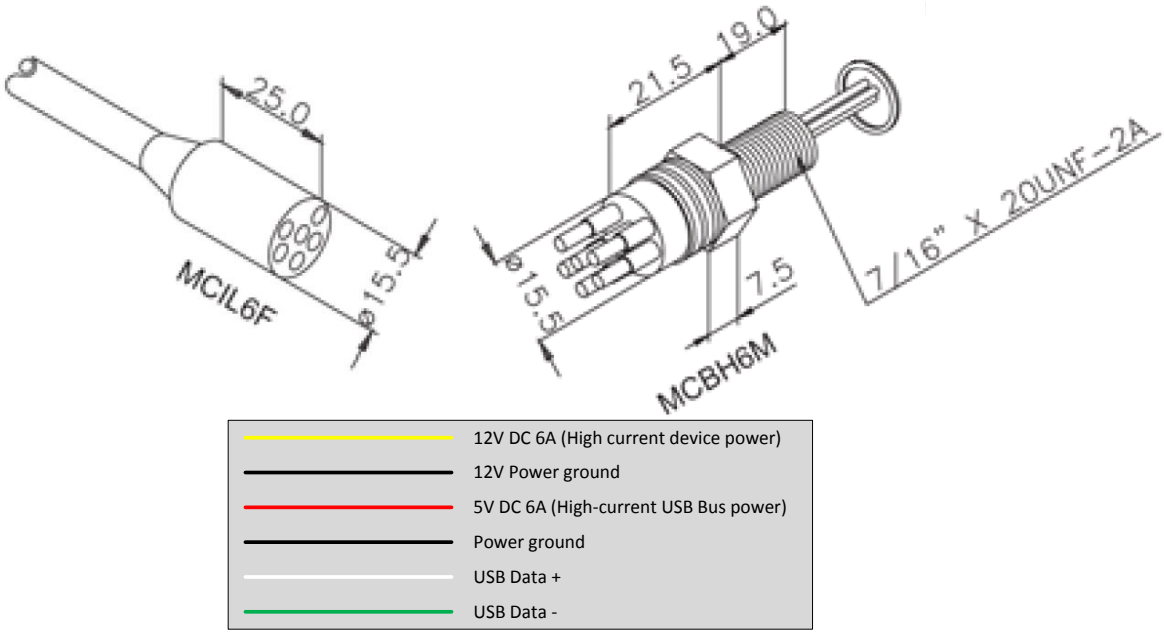

Figure A2 - 6 pin USB peripheral interface with 12V power line (connector images adapted from [370]). Dimensions shown are in mm except the imperial thread.

A.2 Communications interface

For higher bandwidth peripherals, an Ethernet interface was used for the multibeam sonar, inter-computer communication and developed later to the surface tether. Auto-configuring MDI/MDIX (straight through Ethernet or cross-over wired cables) switches were used. Ethernet used 4 connectors and the remaining 4 were used to transmit 24V and 12V power for Ethernet peripherals (e.g. the 24V multibeam Delta T sonar). This was limited to 6A by the waterproof connectors and where standard Category 5/6 cabling was used, limited to 0.5A per cable. The pinout is shown in Figure A3 below.

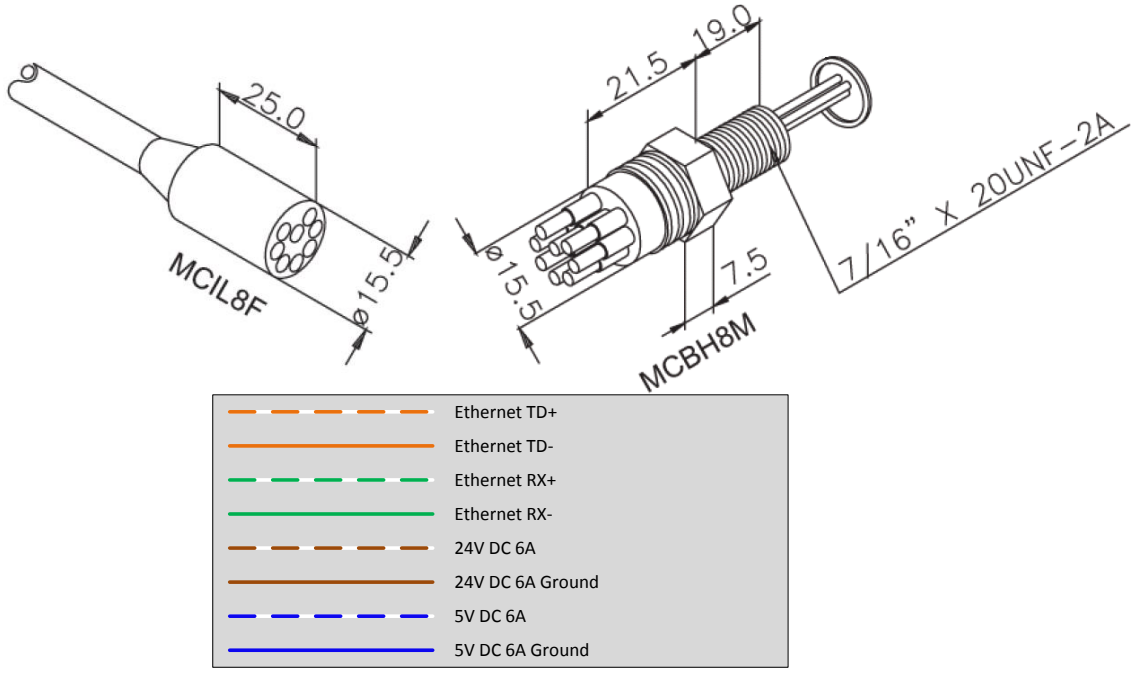

Figure A3 - 8 pin Ethernet communications interface with 24V and 5V power lines (connector images adapted from [370]). Dimensions shown are in mm except the imperial thread.

A.3 Tether

The 8 pin Ethernet standard developed above was extended to provide the communications link for the tether. The power and communications tether was split into distinct cables to reduce interference, and to allow operation with just power, just communications or the full combined tether. This also allowed inexpensive cable to be used for the tether (6A 4-core mains flex and standard Category 5/6 Ethernet cable, often bound together to form a single tether with strain relief and flotation). This inexpensive cable was used in lengths of up to 100m (determined by the Ethernet specification for communications, and by voltage drop for power). Tether lengths over 100m are possible using Ethernet repeaters, fibre optic transceivers and DC-DC converters but are not currently implemented.

There was no need to separately stream video over expensive and fragile coaxial cable, as multiple video streams could be encoded, streamed and archived over Ethernet for lossless transmission to multiple clients.

The pinout for the communications cable is shown below in Figure A4. Standard Ethernet signals were transmitted over 4 of the cores, and the remaining 4 cores were used to provide low-level (computer independent) communication of a remote reset of the computers, remote toggling of the power to the vehicle and a remote power good indicator for diagnostics.

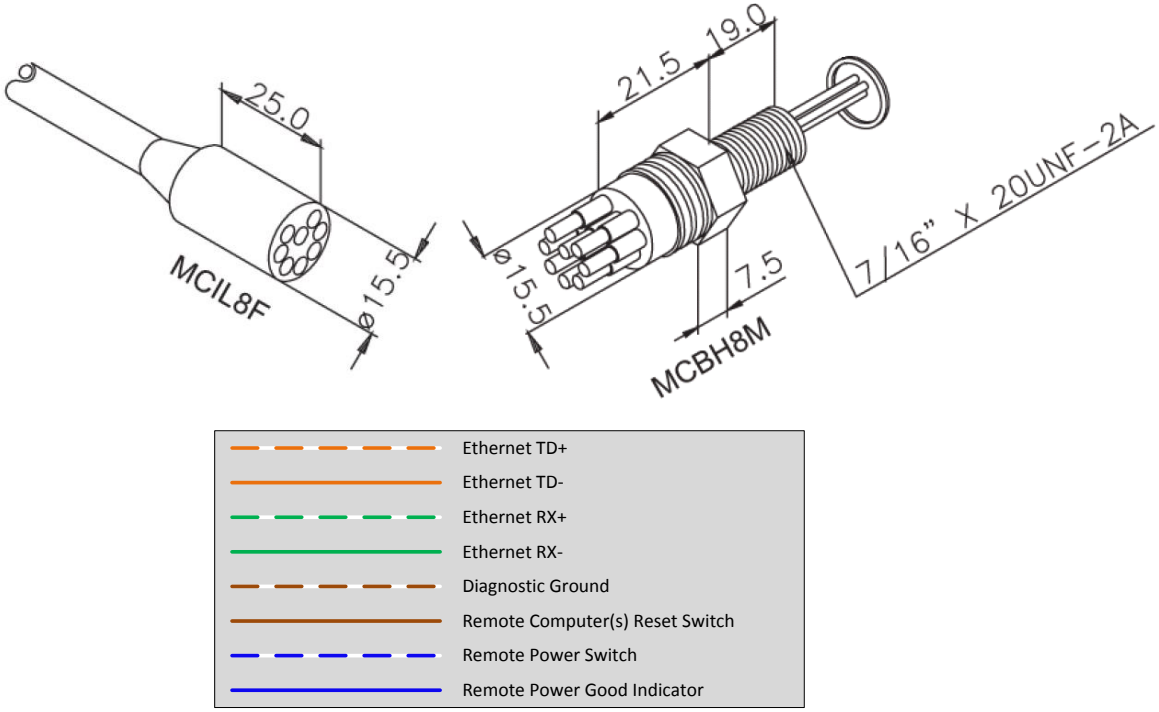

Figure A4 - 8 pin Ethernet tether interface with low-level power, diagnostic and reset lines (connector images adapted from [370]). Dimensions shown are in mm except the imperial thread.

As mentioned above, power was transmitted using a separate optional cable with a distinct connector, as shown in Figure A5 below. In some circumstances, for example for short mission durations when high tether flexibility was required, the power tether could be removed, using just the lightweight highly flexible communications tether. However, in the nearshore environment, this was rare.

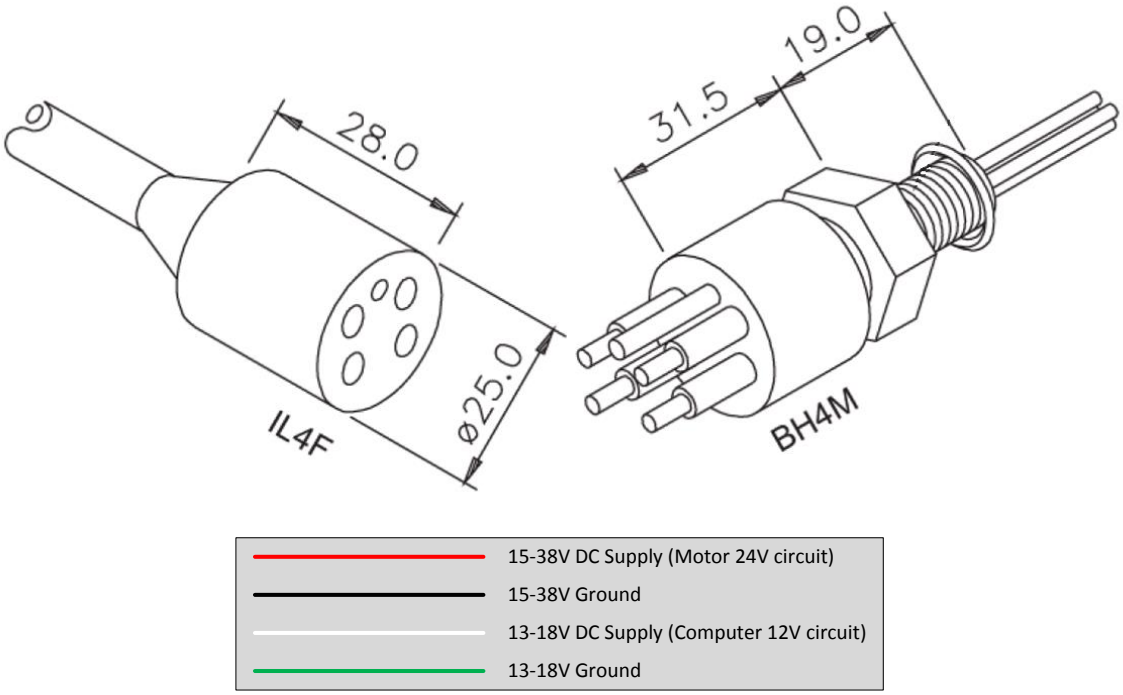

Figure A5 - 4 pin power tether interface with combined charge and supply lines for the 15-38V (27.6V nominal) motor circuit and 13-18V (13.8V nominal) computer circuit (connector images adapted from [370]). Dimensions are in mm.

The 4-core 6A cable provided two power circuits. This separate power supply system isolated the sensitive computers, sensors and signal processing from any noise introduced on the motor circuit, and ensured data and mission integrity if the motor batteries were inadvertently exhausted faster than they could be recharged.

DC-DC converters onboard the vehicle allowed a flexible supply voltage to be used, allowing the system to be charged from an alternator output or battery bank and mitigating any effects of voltage drop in the tether.

A series of relay isolators disconnected the pins on the rear of the vehicle when the tether was unplugged preventing electric shocks and avoiding electrolysis of the pins. This allowed the tether to be removed or refitted underwater. Blanking plugs were available.

Appendix B Power distribution system

Figure B1 on the following page details the circuit diagram for the motor power distribution system (PDS). Working from the left hand side (the tether) to the right (the vehicle), the systems are detailed as follows:

The surface tether supplies DC power over the range of 15-38V at a 6A maximum determined by the tether cable and connectors, fused on the surface. The input passes through a high efficiency (90%) DC-DC converter which provides a stable 13.8V output.

The surface isolator relays disconnect the entire downstream (vehicle side) of the circuit from the exposed tether connector on the rear of the vehicle until the tether power source is connected avoiding electrolysis of the pins on the rear of the vehicle.

The dual battery system has an 80A fuse to protect the high current output and lower current fuses to protect the lower current circuitry (represented by the thinner wires in Figure B1). The batteries are charged separately as 12V units for safety and to maximise the life of the batteries. Charging is controlled using a PICO UPS 120 battery charger [371] configured for a 1.2A constant current, constant voltage charge which bulk charges the batteries quickly, then maintains them on a float charge.

The relay labelled centre breaker in Figure B1 separates the batteries for charging at 12V when the surface power is applied, and reconnects them in series to provide 24V to the motors when the surface power is disconnected.

When the surface power is connected, as well as powering the battery chargers, the batteries are disconnected from the load to avoid them being discharged during charging. The small remainder of the 6A supply current not being used for charging the batteries is available for manoeuvring the vehicle in a specific low power mode where motor thrust commands are limited. Should full manoeuvring thrust be required, the surface charge is quickly toggled by a single switch on the surface station.

Finally, the output, either from the surface power supply or the batteries is controlled by a double pole relay isolator to disconnect the supply to the vehicle. These relays are toggled by a reed switch operated by magnets from the outside of the vehicle. This can be operated by a diver for safety, and the motors can be isolated for servicing without interrupting the supply to the computers.

The output of the isolators is distributed to the motor drivers via a fused distribution block. Individual fuses prevent a fault with one thruster from affecting the redundancy of the vehicle propulsion.

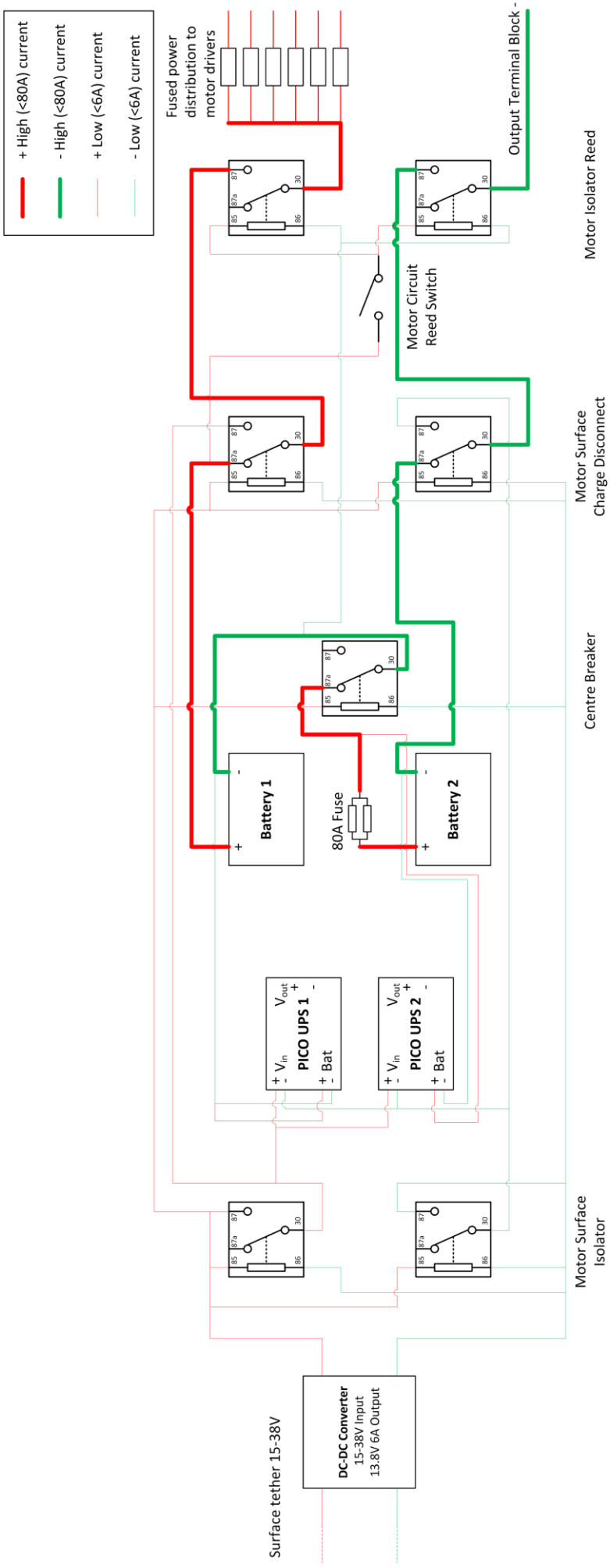

Figure B1 - The power distribution system for the motor circuit.

The computer power distribution (PDS) is a simplified version of the motor PDS. As the peak current is much lower, all circuits are rated at 6A with lower rated relays, cabling and fuses. The structure of the circuit is the same, but as the computers are configured to run off a 12V bus, a single battery, single battery charger and single low-voltage disconnect are used, removing the need for the relay labelled centre breaker in Figure B1.

The low voltage disconnect for the motor batteries was implemented through the machine health system, warning the user when the motor battery voltage reaches a low-level at risk of damaging the batteries.

As the current draw of the computers is lower than that of the motors (<6A) the Vout terminal of the PICO UPS battery charger board [371] was used to supply the computers, providing a continuous power supply to the computers when the surface tether was connected and disconnected. Any interruption would cause the computers to reset and so a smooth supply was essential. Through the MOSFET design of the PICO UPS units, there is no interruption to the power (switching time 100ns [371]).

The higher current motor circuit tolerates a momentary break in power to avoid the need to potentially sustain a 24V 80A load. This would otherwise either require large and expensive power electronics, or a large and therefore bulky smoothing capacitor to sustain power during the relay changeover.

The computer PDS uses the same arrangement as the motor PDS of surface isolator relays, a charger disconnect and overall isolators controlled by the reed switches on the rear of the vehicle. For safety, the remote low-level power switch can only be toggled using the diagnostic lines on the tether when the magnets controlling the reed switches are inserted. The output still goes to a fused distribution block, however rather than high current motor drivers, the outputs are the computers, networking and signal processing equipment, with DC-DC converters stepping from 12V down to 5V and up to 24V for the various buses required.

Appendix C Navigation sensor probabilistic characterisation

Probabilistic characterisation of the pressure sensor and Xsens accelerometers are presented below as further examples to those in the main document.

C.1 Pressure sensor calibration & characterisation

Calibration of the pressure sensor was performed for the mounting position on the vehicle, and to relate the output voltage to submerged depth (incorporating pressure, salinity, temperature). Constant values of an average salinity of 3% and an average temperature of 11°C were assumed and verified regularly. As with other sensors, different operating conditions required recalibration.

The pressure sensor was characterised by taking a static evaluation of the noise measured by the sensor in a tank of still water with all other electrical systems running. Calibration was performed by lowering the vehicle to depths measured by an external reference (tape measure) while recording the voltage change. The measurement probability was thus determined for the state being a certain depth, given the voltage observed from the sensor.

Noise and therefore uncertainty was present from a number of sources including, nonlinearities inherent in the sensor, electrical noise, water height fluctuations caused by waves and movement of the vehicle (although this was mitigated as far as possible by shrouding the sensor inside the fibreglass hull).

Figure C1 below shows the raw pressure measurement over a 15 minute duration, which is plotted as a histogram on the right. Gaussian noise was verified and the data approximated by the normal distribution function shown in red.

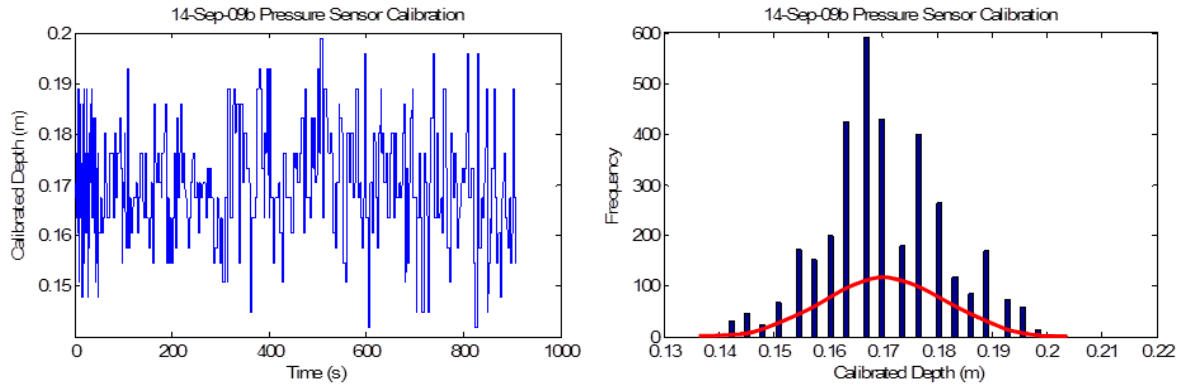

Figure C1 - Pressure sensor characterisation. The left plot shows the raw data recorded in still water over 15 minutes. This data was plotted as a histogram and approximated by a normal distribution as shown in the right plot.

The characterisation was repeated several times to ensure valid data. The results from three examples are shown in Table C1 below as parameterised normal distributions. The final row uses the data from Figure C1 above.

Table C1 - Probabilistic characterisation of pressure sensor measurement uncertainty.

	Calibrated Depth (m)	
	Mean:	**Variance:**
13-Sep-09 120sec run	0.278m	0.013357
14-Sep-09 300sec run	0.187m	0.012444
14-Sep-09 900sec run	0.170m	0.011139

C.2 Xsens accelerometer characterisation

Static calibration of mounting angle and noise characterisation of the Xsens accelerometers was performed under the same conditions as above. However, the raw output from the Xsens IMU was not the strapdown accelerations (with gravity removed), but the raw measurements which still included the acceleration due to gravity. Therefore the measurement probability for the raw accelerations *and* for the orientation outputs was required to calculate the strapdown accelerations – the mean of each was used and the uncertainty associated with each original measurement propagated through to the strapdown acceleration estimate.

Figure C2 below shows an example characterisation dataset. The top left figure shows the raw data from a >700s recording when the vehicle was static on the dock with all electrical systems running to simulate operating conditions. The acceleration data is plotted as a histogram and the distribution was approximated by a normal distribution function shown by the red curve.

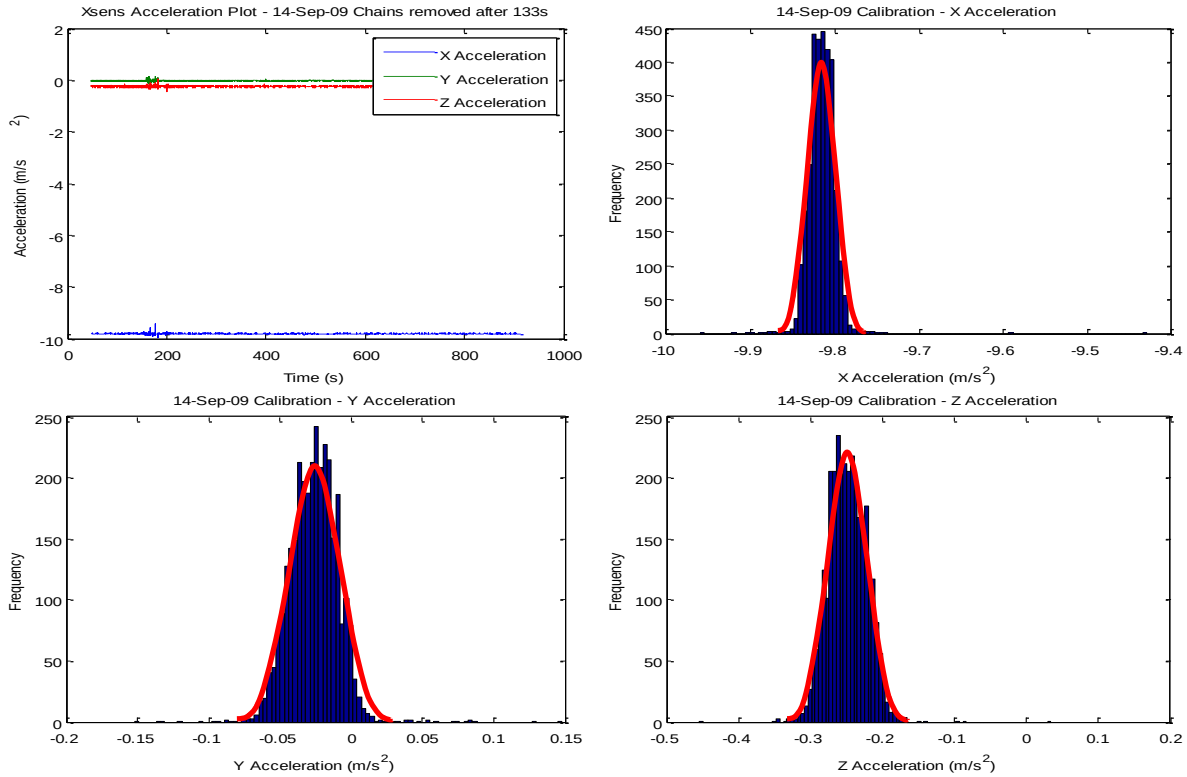

Figure C2 - An example probabilistic characterisation of the Xsens accelerometer measurement uncertainty. The top left figure shows raw data from a static >700s recording. Noise was observed in the X, Y and Z accelerometers. The data was plotted as a histogram in the remaining three plots. Using the methods described earlier in the main body of this document, the distribution was approximated by a normal distribution function shown by the red curve. (The acceleration due to gravity of 9.81m/s² appears in the x-axis due the sensor mounting orientation for this characterisation run. The mounting was later corrected.)

The characterisation was repeated over several datasets to ensure repeatability. Table C2 below summarises the parameters of the normal Gaussian distributions used to represent the measurement probabilities. A high degree of repeatability was seen, and as with the other sensors, the variances shown below were used as the measurement uncertainty when weighting the effect each sensor had on the overall position estimate.

Table C2 - Xsens accelerometer characterisation summary.

	X Acceleration		Y Acceleration		Z Acceleration	
	Mean:	**Variance:**	**Mean:**	**Variance:**	**Mean:**	**Variance:**
13-Sep-09	-9.8118m/s²	0.009957	-0.0447m/s²	0.014798	-0.2662m/s²	0.027645
14-Sep-09	-9.8153m/s²	0.016393	-0.0257m/s²	0.017726	-0.2484m/s²	0.027180

Appendix D Directional statistics & cyclic probability distributions

The definition of cyclic data (or circular distributions) is that the value (or density) at any point x is the same as that of $x + k\xi$ where k is any integer and ξ is some real number [350].

Circular statistical techniques, such as the circular normal distribution described by Gumbel et al. [351], allow the uncertainty associated with directional data to be represented.

D.1 Circular mean

In many cases the arithmetic mean of angles is an inconsistent representation of the mean (average direction) of the set of angles. With reference to Batschelet section 1.3 [372], a method for calculating the circular mean using vectors can be derived.

If a sample of 3 angles is considered, ($\theta_1 = 0^\circ, \theta_2 = 90^\circ, \theta_3 = 315^\circ$) as shown in Figure D1 then the arithmetic mean is 135°.

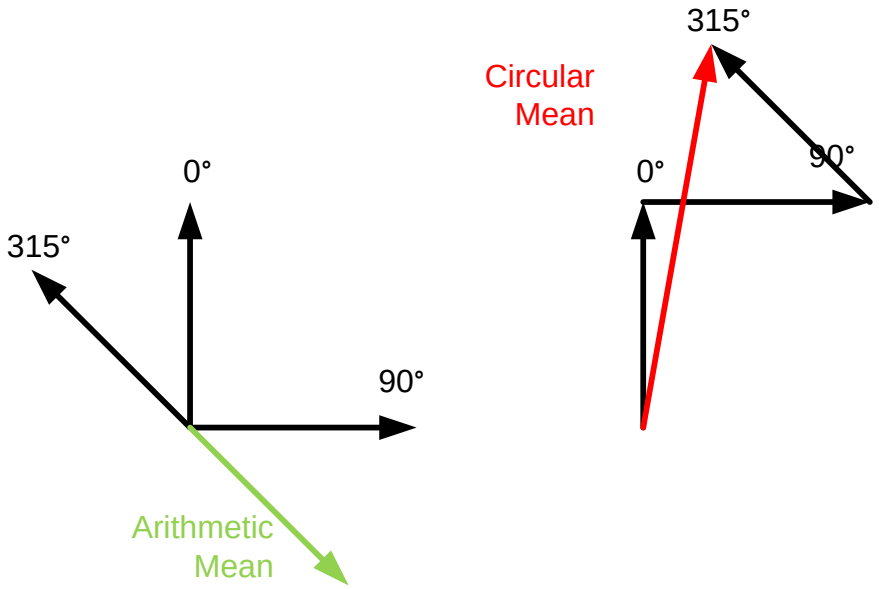

Figure D1 - Calculating the arithmetic and circular mean of 3 angles.

If each angle in the sample is plotted as a vector of unit length and of angle specified by the angle of the sample (as shown in Figure D1) then it can be seen by inspection that the arithmetic mean (plotted in green) is an incorrect measure of the 'average direction'. However, if the vectors are drawn one after another, then the overall resultant vector can be calculated. The angle of this resultant vector (plotted in red in Figure D1) is the *circular mean*.

As Batschelet describes [372], if a rectangular coordinate system is considered with X and Y axes and origin O. Additionally, ϕ_i is one of the n angles in the sample, and e_i is therefore the vector of unit length which corresponds to the sample ϕ_i. Therefore the corresponding x and y components of the vector in question can be calculated using the following equations:

$$x_i = \cos\phi_i$$

$$y_i = \sin\phi_i$$

If all of the vectors are summed (as in the right hand side of Figure D1) but additionally divided by the number of samples (n) then the rectangular coordinates of the centre of mass of all of the vectors ($\bar{x}$ and $\bar{y}$) is obtained, as follows:

$$\bar{x} = \frac{1}{n}(x_1 + x_2 + \cdots + x_n) = \frac{1}{n}(\cos\phi_1 + \cos\phi_2 + \cdots + \cos\phi_n)$$

$$\bar{y} = \frac{1}{n}(y_1 + y_2 + \cdots + y_n) = \frac{1}{n}(\sin\phi_1 + \sin\phi_2 + \cdots + \sin\phi_n)$$

From these two resultant vectors $\bar{x}$ and $\bar{y}$ the mean angle of the sample denoted by $\bar{\phi}$ can be calculated using the following equations:

$$\bar{\phi} = \begin{cases} \tan^{-1}\left(\bar{y}/\bar{x}\right) if\ \bar{x} > 0 \\ 180° + \tan^{-1}\left(\bar{y}/\bar{x}\right) if\ \bar{x} < 0 \\ 90° if\ \bar{x} = 0\ and\ \bar{y} > 0 \\ 270° if\ \bar{x} = 0\ and\ \bar{y} < 0 \\ undetermined\ if\ \bar{x} = 0\ and\ \bar{y} = 0 \end{cases}$$

D.1.1 Circular variance and circular deviation

If the length of the *resultant vector* which is the sum of all of the individual vectors is defined as R with components $\sum x_i$ and $\sum y_i$ then the length of the *mean vector* is defined as $r = R/n$ with components $\bar{x}$ and $\bar{y}$. Therefore, the length of the mean vector is:

$$r = (\bar{x}^2 + \bar{y}^2)^{\frac{1}{2}}$$

And as $r = R/n$, the length of the resultant overall vector is:

$$R = \left[\left(\sum x_i\right)^2 + \left(\sum x_i\right)^2\right]^{\frac{1}{2}}$$

Which can also be expressed as:

$$r = \frac{1}{n}\left[\left(\sum \cos\phi_i\right)^2 + \left(\sum \cos\phi_i\right)^2\right]^{\frac{1}{2}}$$

A special case occurs when $\bar{x} = 0$ and $\bar{y} = 0$ and thus $r = 0$. In this case the mean vector is equal to the zero vector. However, for all other cases r is defined.

The length of the mean vector r can be used as a measure of concentration and thus, from this, the circular variance introduced.

Considering some examples, if all of the samples lie in the same direction then the length of the mean vector r is equal to 1. If the samples all lie in roughly the same direction, e.g. within an arc of 20°, then the r value is still close to 1. As the concentration reduces and the samples become more disperse, then the r values reduces. When $r = 0$ then there is no concentration of samples around a single direction.

Therefore if r is a measure of concentration, $1 - r$ can be thought of as a measure of dispersion. However, in equations 1.4.5 and 1.4.6 presented in Batschelet [372], it is demonstrated that

$2(1-r)$ is equal to the angular variance (otherwise referred to as the circular variance), defined as:

$$s^2 = 2(1-r)$$

In the same way that the square root of the variance is taken in linear statistics to obtain the standard deviation, the square root of the circular variance is taken in circular statistics to obtain the following measure of dispersion:

$$s = [2(1-r)]^{1/2}$$

Or in degrees:

$$s(degrees) = \frac{180^\circ}{\pi}[2(1-r)]^{1/2}$$

This measure was introduced by Batschelet in 1965 [373] and is now widely used.

The MATLAB Circular Statistics Toolbox 2010b [374] provides program code for calculating the circular mean and variance from a population of samples using MATLAB. In particular 'circ_mean.m' and 'circ_var.m'. These algorithms were translated to LabVIEW code 'Circular Mean and Variance.vi' for integration with the navigation software.

D.2 Circular distributions

In the same manner as samples are represented in linear statistics with a probability density function (PDF) to aid data reduction and efficiency, samples from a circular space can be represented with a circular distribution.

Circular distributions are finite (ranging from 0 to 360° or 0 to 2π) and continuous in that there exists a probability density for every angle ϕ):

$$f(\phi), 0 \leq \phi < 2\pi$$

Additionally, the density is always positive (or zero) and the integral over the whole range equals the total probability 1:

$$\int_0^{2\pi} f(\phi)d\phi = 1$$

In the same manner as for linear statistics, the distribution used to represent the entire population needs to be verified as an appropriate representation. As with all probability density functions, either linear or circular, representing the population by a PDF is an approximation and it needs to be ensured that it is a valid approximation. This can either be verified by inspection or by applying 'goodness of fit' tests.

As much of the uncertainty associated with the sensors, state estimation and map representation is unimodal, symmetric and normally distributed, it makes sense to use a circular version of the normal distribution. The most commonly used circular normal distributions is the von Mises distribution which is discussed in the following section. A discussion of alternative circular unimodal symmetric distributions follows in section D.2.2 and includes the wrapped normal distribution.

D.2.1 The von Mises distribution

The von Mises distribution is a unimodal probability distribution defined over a cyclic space and is discussed in section 15.3 of reference [372]. In the same manner as for linear statistics, the parameters of the von Mises distribution can be estimated and then suitability verified by using statistical tests for goodness-of-fit. Chapter 4 of reference [372] provides an overview of these statistical tests. These tests of goodness-of-fit can also be applied to the application of linear statistics to the other probabilistic representations used in Chapter 5.

The von Mises distribution was introduced in 1918 [375] and is frequently used in the analysis of directional statistics as the closest analogue to the normal distribution. For this reason, the von Mises distribution has also been named the 'circular normal distribution' [351]. However, this should not be confused with a bivariate normal distribution with $\sigma_1 = \sigma_2 = 1$ and correlation coefficient $\rho = 0$. In this case, the contour lines of the probability distribution are circles.

The von Mises distribution is defined over a cyclic space by the distribution:

$$f(\phi) = \frac{1}{2\pi I_0(\kappa)} \exp[\kappa \cos(\phi - \theta_1)]$$

The distribution is characterised by two parameters: the mean angle θ_1 and the parameter of concentration, κ.

The function takes on its maximum value at $\phi = \theta_1$ hence $\theta_1$is the mode, and, as the distribution is symmetric and unimodal about the mode, θ_1 is therefore also the mean angle.

κ is the 'parameter of concentration' and the larger κ is, the more concentrated the distribution is about the mean angle. If $\kappa = 0$, the von Mises distribution becomes a uniform distribution.

$I_0(\kappa)$ is the modified Bessel function of order 0 and is described elsewhere, including section 16.4 of reference [372].

As stated in section D.1.1, the length of the mean vector r of a population defines a parameter of concentration. In terms of the von Mises distribution, a 'mass' of unit size spread over the circumference of a unit circle can be considered (see figure 15.1.2 from reference [372]). The mean vector μ_1 of the von Mises distribution (with angle θ_1) points to the 'centre of mass' of the mass drawn. The length of this mean vector μ_1 is defined by ρ_1 and is a measure of concentration (as with r):

$$|\mu_1| = \rho_1$$

The length of the mean vector ρ_1 can be converted into κ, the von Mises parameter of concentration, by using the function $A(\kappa)$ as follows:

$$|\mu_1| = \rho_1 = A(\kappa)$$

$A(\kappa)$ is discussed as equation 16.4.13 in reference [372] and again involves modified Bessel functions. The equation is reproduced below. Lookup tables are provided in reference [372] or the solution can be computed.

$$A(\kappa) = I_1(x)/I_0(x) \qquad (x \geq 0)$$

D.2.1.1 Generating von Mises distributions

The MATLAB Circular Statistics Toolbox 2010b [374] provides program code 'circ_vmpdf.m' for generating a von Mises distribution from a specified parameter of mean angle θ_1 and the parameter of concentration, κ. These algorithms have been translated into LabVIEW code in 'Create and Analyse von Mises Distribution.vi'.

This LabVIEW program allows a von Mises PDF to be generated and compared to a linear (non-circular, non-wrapped) normal distribution centred on the same mean angle. The total probability (integral) can also be inspected and verified to be equal to 1 for a variety of different parameters of θ_1 and κ.

D.2.1.2 Estimating the parameters of von Mises distributions

The aim of modelling populations with a probability density function is to assume that the sample is an accurate representation of the entire population and to then estimate the parameters of the model, in this case, the von Mises distribution. This data redundancy adds efficiency to the representation but the assumption that the sample accurately represents the population must be valid and the parameters of the model must be accurately estimated.

Given a pre-existing sample of angles (e.g. sensor measurements) the following notation can be used for the hypothetical parent population:

	Statistic (sample)	**Parameter (population)**
Mean vector	m	μ_1
Mean vector length	r	ρ_1
Mean angle	$\bar{\phi}$	θ_1

The subscript '1' is from the theory of trigonometric moments of the distribution discussed in section 16.2 of reference [372] and is included here for consistency only.

The estimates of the parameters of the population are defined by the $\widehat{\ }$ notation, therefore the estimates of μ_1, ρ_1 and θ_1 are defined by $\hat{\mu}_1$, $\hat{\rho}_1$ and $\hat{\theta}_1$ respectively.

Provided that the sample is a sufficient representation of the entire population, it is plausible to base the estimates of the *parameters* on the corresponding *statistics*. Therefore, in accordance with section 3.2 of reference [372], it may be tentatively suggested that:

$$\hat{\mu}_1 = m$$

$$\hat{\rho}_1 = r$$

$$\hat{\theta}_1 = \bar{\phi}$$

These assumptions can be made for a von Mises distribution by finding a *maximum likelihood estimate* of the theoretical population mean vector length ρ_1 and the theoretical population mean angle θ_1. Section 17.2 of Batschelet [372] provides a detailed discussion of the parameters of a von Mises distribution.

The maximum likelihood estimations, r and $\bar{\phi}$ respectively, are therefore accepted as valid estimates. As Batschelet [372] states in section 3.2, maximum likelihood estimates are 'consistent,

efficient and sufficient' for estimating the parameters of a von Mises distribution to represent an existing sample.

However, as Batschelet [372] highlights, biasing of the estimates can occur. The estimate of the theoretical mean angle is unbiased in that it is always valid that the mean angle of the sample is the mean angle of the population, given that the sample is an accurate and representative one.

However, in the same manner as for calculating the variance of a sample in linear statistics, for the estimate of r, the theoretical mean vector length, is heavily biased. On an average of many samples, r is too large. This is especially true for a small sample size.

Batschelet [372] discusses the problem of biasing in detail and reviews a number of possible solutions. However, Fisher [376] provides an alternative approach to parameter estimation for a von Mises distribution which is more recent, and builds upon the previous work. The method is adapted from section 4.5.5 in reference [376] as follows:

Using the same notation as previously in this section, the (maximum likelihood) estimate $\hat{\theta}_1$ of the mean direction of the population θ_1 can be assumed to be the mean direction of the sample $\bar{\phi}$ (the circular mean is calculated of all of the angles in the sample using the method discussed in section D.1).

The maximum likelihood estimate of κ is given by $\hat{\kappa}_{ML}$ as follows:

$$A_1(\hat{\kappa}_{ML}) = r$$

Where r is the mean vector length of the sample and the function A_1 is defined as the ratio of two modified Bessel functions as follows:

$$A_1(x) = I_1(x)/I_0(x)$$

Equation D1

These Bessel functions can be calculated programmatically, or an approximation to the solution is given by Fisher in equation 4.40 in reference [376] as follows:

$$\hat{\kappa}_{ML} = \begin{cases} 2r + r^3 + 5r^5/6 & r < 0.53 \\ -0.4 + 1.39r + 0.43/(1-r) & 0.53 \leq r < 0.85 \\ 1/(r^3 - 4r^2 + 3r) & r \geq 0.85 \end{cases}$$

Equation D2

This method discussed by Fisher is valid, however Fisher notes the same problem with biasing as Batschelet in that $\hat{\kappa}_{ML}$ can be seriously biased when the sample size n and the mean vector length of the sample r are small ($r < 0.7$ and particularly $r < 0.45$), in that it can substantially over-estimate the true value of κ. For $n \leq 15$, the following estimate is preferred:

$$\hat{\kappa} \begin{cases} \max(\hat{\kappa}_{ML} - 2(n\hat{\kappa}_{ML})^{-1}, 0) & \hat{\kappa}_{ML} < 2 \\ (n-1)^3\hat{\kappa}_{ML}/(n^3 + n) & \hat{\kappa}_{ML} \geq 2 \end{cases}$$

Equation D3

In section 4.5.5(i) of reference [376], Fisher discusses two approaches to calculating the confidence interval for the mean direction.

D.2.1.2.1 Parameter estimation in LabVIEW and MATLAB

The file 'circ_vmpar.m' in the MATLAB Circular Statistics Toolbox 2010b [374] provides program code for estimating the parameters of a von Mises distribution for a given sample of data. The output is $\hat{\theta}_1$ (the estimated mean angle of the population) and κ, the concentration parameter. The LabVIEW file 'Von Mises Parameters.vi' implemented the above in LabVIEW.

$\hat{\theta}_1$ is estimated using the method for calculating the circular mean as described in section D.1. κ is calculated using the method specified in Equation D2 and D3 above. Equation D2 estimates the value of κ using an approximation instead of calculating the ratio of the two modified Bessel functions as described by Equation D1. Equation D3 then attempts to remove the effect of biasing on the value of κ when $n \leq 15$.

D.2.2 Alternative symmetric unimodal distributions:

From section 15.4 of reference [372] it can be seen that there are several alternatives to the von Mises distribution for unimodal symmetric probability distributions. These include the wrapped normal distribution, wrapped Cauchy distribution and the cosine distribution (otherwise called the sine-wave or cardioid distribution). In Figure D2, the mean in all four plots is zero, the mean vector is of length 0.4464, and so the four distributions correspond in angular deviation. Specifically to the von Mises distribution, the parameter of concentration discussed earlier $\kappa = 1$. The symmetric pair of dots on each plot are at the points of inflection. Although the shapes of the distributions are similar, the points of inflection are closest in the wrapped Cauchy distribution but separated much further in a cosine distribution.

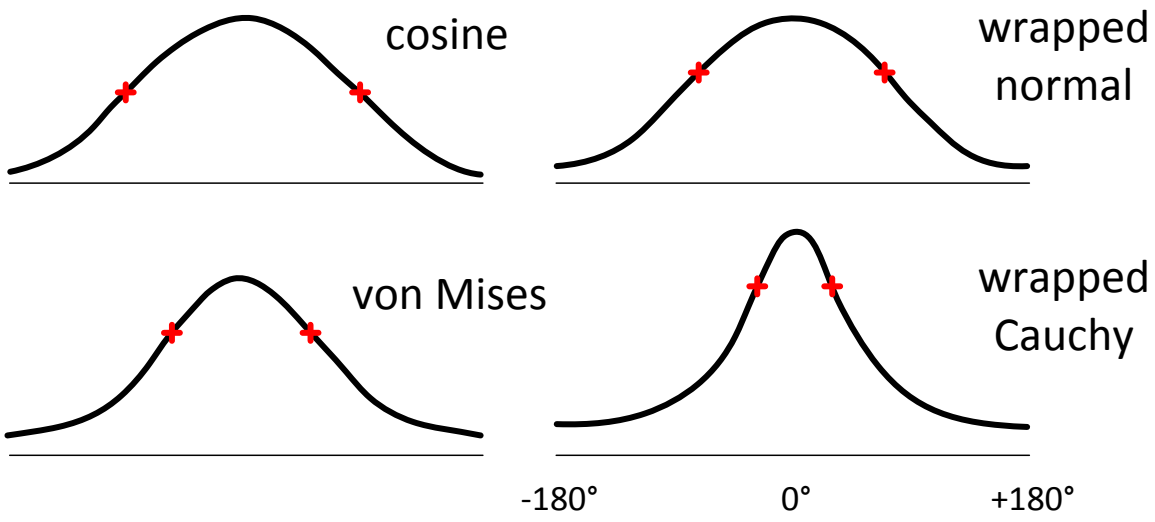

Figure D2 - Four common unimodal symmetric circular distributions, the cosine, wrapped normal, von Mises and the wrapped Cauchy distribution. The mean in all four plots is 0, the mean vector length is 0.4464, and so the four distributions correspond in angular deviation. The von Mises distribution parameter of concentration $\kappa = 1$. The symmetric pair of dots on each plot at the points of inflection. Figure adapted from [372].

Thus these four unimodal symmetric probability distributions, and others, provide alternative distributions to represent uncertainty when using circular distributions within the probabilistic framework discussed in Chapter 5. However, principally for computational simplicity, and as discussed in further detail in Chapter 5, the linearisation step of the Extended Kalman Filter was used to linearise non-linear data to allow the linear Kalman filter to be used. Thus these circular distributions are not considered in further detail at this stage, but provided here for comparison.